Seismological and Engineering Effects of the M 7.0 Samos Island (Aegean Sea) Earthquake

Report Coordinators/Editors

K. Onder Cetin, Middle East Technical University, Turkey

George Mylonakis, University of Bristol, UK

Anastasios Sextos, University of Bristol, UK

Jonathan P. Stewart, University of California, Los Angeles, USA

Hellenic Association of Earthquake Engineering: Report 2020/02

Earthquake Engineering Association of Turkey

Earthquake Foundation of Turkey

Earthquake Engineering Research Institute (USA)

Geotechnical Extreme Events Reconnaissance Association: Report GEER-069

https://doi.10.18118/G6H088

December 31, 2020

Revised June 18, 2021

Table of Contents

Preface

The Samos Island (Aegean Sea) earthquake struck at 13:51/14:51 local time in Greece and Turkey, respectively, on 30 October 2020. It produced wide-ranging effects including tsunami run-up, ground shaking with local zones of high intensity that led to collapse of structures and 118 fatalities in both countries, and various geotechnical effects including liquefaction, rockfalls and landsliding.

The earthquake occurred during the global COVID-19 pandemic, which necessitated a different response than would be typical for an earthquake of this size. With global travel restricted, international agencies did not send reconnaissance teams to the region. However, reconnaissance was performed. In Greece, the Hellenic Association of Earthquake Engineering (HAEE/ETAM) mobilized a 12-member team to Samos Island and neighboring islands in two successive missions. Similarly, the Earthquake Engineering Association of Turkey and the Earthquake Foundation of Turkey (EEAT/EFT) mobilized teams to affected regions of the Aegean coast, with the main focus being the highly impacted city of Izmir.

While these reconnaissance missions were underway, discussions began to take place between HAEE/ETAM and EEAT/EFT, which was facilitated and encouraged by US-based international organizations (Earthquake Engineering Research Institute, EERI, and Geotechnical Extreme Events Reconnaissance Association, GEER). The information exchange was productive, and it became evident that this significant event could only be understood in depth by mobilizing scientists on both sides of the fault, while integrating data and interpreting field evidence collectively. Moreover, over the course of these three-way discussions (Greece-Turkey-USA), a genuine enthusiasm developed to collaborate and produce joint reports for future events that reflects our common purpose of turning disaster into knowledge. This can-do spirit is shared by the large and diverse group of contributors to this report, who view the boundary between the two countries as a “natural laboratory” that overcomes historical tensions in the region and provides unique opportunities for transnational/cross-border research and collaborations.

Initially, EEAT/EFT, HAEE and several university research centers prepared reports summarizing their reconnaissance activities. To facilitate the production of this report, four representatives of the partnering organizations were charged with organizing, facilitating the preparation of, and editing a joint document. This report is the result of that process; it presents in a combined document the principle seismological, engineering, and social impacts of this important event both on the Greek islands and the Aegean part of the Turkish mainland.

On behalf of the sponsoring organizations, the report coordinators would like to express their gratitude to the chapter coordinators, authors, and reviewers that made this collaboration and document possible. Any opinions, findings, and conclusions or recommendations expressed in this report are those of the authors and do not necessarily reflect the views of the sponsoring organizations. Likewise, any use of trade, firm, or product names is for descriptive purposes only and does not imply endorsement by the sponsoring organizations and their governments.

Sponsoring associations:

Earthquake Engineering Association of Turkey
Earthquake Foundation of Turkey
Earthquake Engineering Research Center, Middle Eastern Technical University, Turkey

Hellenic Association of Earthquake Engineering, Greece

Earthquake Engineering Research Institute, USA

Geotechnical Extreme Events Reconnaissance Association, USA

Chapter Coordinators and Contributors

Burak Akbaş, Middle East Technical University, Turkey

Mustafa Akgün, Dokuz Eylül University, Turkey

Sinan Akkar, Boğaziçi University, KOERI, Turkey

Murat Aksel, Alanya Alaaddin Keykubat University, Turkey

Ahmed Al-Suhaily, Middle East Technical University, Turkey

Abdullah Altındal, Middle East Technical University, Turkey

Selim Altun, Ege University, Turkey

Erhan Altunel, Eskişehir Osmangazi University, Turkey

Ayşegül Askan, Middle East Technical University, Turkey

Bekir Özer Ay, Middle East Technical University, Turkey

Seckin Aydin, State Hydraulic Works (DSI), Turkey

Alper Baba, Izmir Institute of Technology, Turkey

Ece Eseller Bayat, Istanbul Technical University, Turkey

Barış Binici, Middle East Technical University, Turkey

Elife Çakır, Middle East Technical University, Turkey

Gizem Can, Middle East Technical University, Turkey

Erdem Canbay, Middle East Technical University, Turkey

Alp Caner, Middle East Technical University, Turkey

Ozan Cem Celik, Middle East Technical University, Turkey

Kemal Önder Çetin, Middle East Technical University, Turkey

Marinos Charalampakis, National Observatory of Athens, Geodynamic Institute, Greece

Faik Cuceoglu, State Hydraulic Works (DSI), The General Directorate, Turkey

Gözde Güney Doğan, Middle East Technical University, Turkey

Cemalettin Donmez, Izmir Institute of Technology, Turkey

Nurhan Ecemis, Izmir Institute of Technology, Turkey

Alaa Elsaid, Middle East Technical University, Turkey

Emre Ercan, Ege University, Turkey

Michalis Foumelis, Aristotle University of Thessaloniki, Greece

Athanasios Ganas, National Observatory of Athens, Geodynamic Institute, Greece

Christos Giarlelis, EQUIDAS Consulting Engineers, Greece

Marilia Gogou, National Kapodistrian University of Athens, Greece

Işıkhan Güler, Dolfen Engineering and Consultancy Ltd., Turkey

Zeynep Gülerce, Middle East Technical University, Turkey

Mustafa Ümit Gümüşay, Alanya Alaaddin Keykubat University, Turkey

Makbule Ilgaç, Middle East Technical University, Turkey

Tahir Serkan Irmak, Kocaeli University, Turkey

Alper İlki, Istanbul Technical University, Turkey

Doğan Kalafat, Boğaziçi University, KOERI, Turkey

Özkan Kale, Ted University, Turkey

Nikos Kalligeris, National Observatory of Athens, Geodynamic Institute, Greece

Ioannis Kalogeras, National Observatory of Athens, Geodynamic Institute, Greece

Utku Kanoğlu, Middle East Technical University, Turkey

Vasilis Kapetanidis, National Kapodistrian University of Athens, Greece

Andreas Karakonstantis, National Kapodistrian University of Athens, Greece

Vasilis Karakostas, Aristotle University of Thessaloniki, Greece

Ilektra Karasante, National Observatory of Athens, Geodynamic Institute, Greece

Shaghayegh Karimzadeh, Middle East Technical University, Turkey

Nikolaos Karveleas, Earthquake Planning and Protection Organization (EPPO), Greece

Ercan Serif Kaya, Alanya Alaaddin Keykubat University, Turkey

Cem Kıncal, Dokuz Eylül University, Turkey

Mustafa Kerem Kockar, Hacettepe University, Turkey

Anastasia Kiratzi, Aristotle University of Thessaloniki, Greece

Charalambos Kkallas, Aristotle University of Thessaloniki, Greece

Maria Kleanthi, Ministry of Infrastructure Transport and Networks, Greece

Nikos Klimis, Democritus University of Thrace (DUTh), Greece

Kiriaki Konstantinidou, Institute of Engineering Seismology and Earthquake Engineering (ITSAK), Greece

Asimina Kourou, Earthquake Planning and Protection Organization (EPPO) , Greece

Vasiliki Koussi, Ministry of Infrastructure Transport and Networks, Greece

Vassilis Lekidis, Institute of Engineering Seismology and Earthquake Engineering (ITSAK), Greece

Efthymios Lekkas, National and Kapodistrian University of Athens (NKUA) / Earthquake Planning and Protection Organization (EPPO), Greece

Maria Manousaki, Earthquake Planning and Protection Organization (EPPO), Greece

Basil Margaris, Institute of Engineering Seismology and Earthquake Engineering (ITSAK), Greece

Spyridon Mavroulis, National Kapodistrian University of Athens, Greece

Nikolaos Melis, National Observatory of Athens, Geodynamic Institute, Greece

George Mylonakis, University of Bristol, United Kingdom / Khalifa University, UAE / University of California, Los Angeles, USA

Engin Nacaroglu, Pamukkale University, Turkey

Öcal Necmioğlu, Boğaziçi University, KOERI, Turkey

Evi Nomikou, National Kapodistrian University of Athens, Greece

Arda Özacar, Middle East Technical University, Turkey

Berguzar Ozbahceci, Izmir Institute of Technology, Turkey

Aristidis Papachristidis, 3DR Engineering Software Ltd., Greece

Eleftheria Papadimitriou, Aristotle University of Thessaloniki, Greece

Achilleas Papadimitriou, National Technical University of Athens, Greece

Panayotis Papadimitriou, National Kapodistrian University of Athens, Greece

Costas Papazachos, Aristotle University of Thessaloniki, Greece

Panagiotis Pelekis, University of Patras, Greece

Ali Pınar, Boğaziçi University, KOERI, Turkey

Orhan Polat, Dokuz Eylül University, Turkey

Prodromos Psarropoulos, National Technical University of Athens, Greece

Seyhun Püskülcü, Earthquake Foundation of Turkey

Constantinos Repapis, University of Western Attica, Greece

Zafeiria Roumelioti, University of Patras, Greece

Emmanouil Rovithis, Institute of Engineering Seismology and Earthquake Engineering (ITSAK), Greece

Cihan Sahin, Yıldız Technical University, Turkey

Anastasios Sextos, University of Bristol, United Kingdom

Alper Sezer, Ege University, Turkey

Vassilios Skanavis, University of Southern California, USA

Egemen Sonmez, Izmir Institute of Technology, Turkey

Eyüp Sopacı, Middle East Technical University, Turkey

Dimitris Sotiriadis, Democritus University of Thrace (DUTh), Greece

Berkan Söylemez, Middle East Technical University, Turkey

Hasan Sözbilir, Dokuz Eylul University, Turkey

Ioannis Spingos, National Kapodistrian University of Athens, Greece

Jonathan P. Stewart, University California, Los Angeles, USA

Halûk Sucuoğlu, Middle East Technical University, Turkey

Costas Synolakis, University of Southern California, USA / Academy of Athens, Greece

Onur Tan, Istanbul University Cerrahpasa, Turkey

Nikolaos Theodulidis, Institute of Engineering Seismology and Earthquake Engineering (ITSAK), Greece

Thekla Thoma, Earthquake Planning and Protection Organization (EPPO), Greece

Reviewers

Atilla Ansal, Özyeğin University, Turkey

Nuray Aydınoğlu, Boğaziçi University, KOERI, Turkey

David M. Boore, US Geological Survey (retired)

George Bouckovalas, National Technical University of Athens, Greece

Murat Altug Erberik, Middle East Technical University, Turkey

Mustafa Erdik, Boğaziçi University, KOERI, Turkey, President of the Earthquake Foundation of Turkey [General Reviewer of the entire report]

Haluk Eyidoğan, Istanbul University, Turkey

Michael Fardis, University of Patras, Greece [General Reviewer of the entire report]

Michalis Fragiadakis, National Technical University of Athens, Greece

Andreas Kappos, Khalifa University, United Arab Emirates, European Association for Earthquake Engineering (EAEE), Greece [General Reviewer of the entire report]

Konstantinos Makropoulos, University of Athens, Greece

Kyriazis Pitilakis, Aristotle University of Thessaloniki (AUTH), European Association for Earthquake Engineering (EAEE), Greece [General Reviewer of the entire report]

Ioannis Psycharis, National Technical University of Athens, Greece

Bilge Siyahi, Gebze Institute of Technology, Turkey, President of Earthquake Engineering Association of Turkey

Kosmas Stylianidis, Aristotle University of Thessaloniki (AUTH), Greece

George Tsiatas, University of Patras, Greece

Panos Tsopelas, National Technical University of Athens, Greece

Dimitrios Vamvatsikos, National Technical University of Athens, Greece

Executive Summary

On 30 October 2020, a moment magnitude 7.0 earthquake occurred on a previously mapped normal fault north of Samos Island (variously referred to as the North Samos Fault or the Kaystrios Fault) in the Aegean Sea. The tectonic setting for this region is trans-tensional where active extension and strike-slip deformations coexist. The event magnitude of 7.0 slightly exceeds the maximum magnitude anticipated for this fault in source models. Historical archives do not indicate an event of this magnitude on this or other local faults in the last 19 centuries (since AD47). We present two similar finite fault models derived from ground motion data and geodetic data, both of which show the rupture as occurring on a fault dipping 40-45^{o} to the north, with an along-strike length of 32-38 km and down-dip width of 15 km. Several primary phenomena (e.g. coastal uplift of approximately 10 cm on west Samos footwall) were observed.

The fault rupture lowered the seafloor, which produced a tsunami that impacted nearby Samos Island as well as a series of Anatolian towns along the Çesme and Seferihisar coast of Kuşadası Bay, with maximum runup and penetration distance of about 3.8 m and 2500 m measured in Akarca and along the Alacati Azmak stream, respectively, resulting in substantial property losses. The tsunami occurred as a sequence of sea level lowering and surge, which is documented in detail from post-event reconnaissance as well as eyewitness reports and videos. Due to relatively short distances between the source and affected cities, wave travel times were relatively short for the affected coastal locations (10-30 min), challenging the ability of tsunami warning systems to alert the public, and contributing to substantial property losses and causing one fatality.

The mainshock was recorded by 11 and 66 stations in Greek and Turkish strong-motion networks, respectively, within 200 km from the fault rupture and by > 200 accelerometers from both national networks (Turkey & Greece) for distances up to 600 km. Two of the Greek instruments were located in the near-fault region, about 10 km from the fault rupture plane, and provided the strongest recordings (PGA of approximately 0.23g, PGV of approximately 22 cm/s). Overall levels of ground shaking, and their variation with distance, are consistent with expectation from global and regional ground motion models, and reinforce previous findings of regional anelastic attenuation effects. The intensity of ground shaking was near design levels in Samos Island, but well below design levels for reference rock conditions in the Anatolian coastal regions due to large source-site distances (30 to 70 km). Where site conditions were favorable (rock or shallow stiff soils), these ground motions did not damage structures. However, pronounced site effects locally amplified ground shaking at site frequencies near 0.7-1.6 Hz throughout the Izmir Bay region for both stiff and soft soil sites. This amplification was particularly pronounced on soft soils in the Bayrakli district, which led to significant structural damage. We also document an apparent localization of site amplification (possibly from surface topography and bedrock morphology) on Samos Island at Ano Valley suggested by damage concentration in low- rise buildings.

The earthquake produced isolated incidents of rockfalls and landslides, mainly in the northern part of Samos Island. We document these ground failures, as well as several “no-ground failure”

case histories in Anatolia, where liquefaction was anticipated given the poor geotechnical conditions and high groundwater levels. Liquefaction was observed in different parts of Samos island. Ports on the north side of Samos Island were damaged by displacements/rotations of quay walls towards the water, pavement cracks and backfill settlements behind the walls, and some signs of ejecta associated with liquefaction. The source of these movements (soil liquefaction, foundation deformations from wall inertial response) remains under investigation. On the Anatolian coast, despite tsunami-induced damage in port facilities, no geotechnical engineering related permanent ground deformations or failures of quay walls were observed.

The earthquake impacted a diverse inventory of structures on Samos Island and the Aegean part of Anatolia. In Samos Island, because of its proximity to the source, the strength of the shaking in the period range of the predominantly masonry structures was near that used in their design. We document damage that occurred to these structures, mainly for residential use, although collapses were rare and the performance was generally good and consistent with expectation for the level of shaking. Earthquake effects in Anatolia were concentrated in Izmir, a city of 4 million with a range of geotechnical conditions. Structures of all types performed well in most of Izmir, with the notable exception of the Bayrakli district, which has soft soil conditions that amplified ground shaking in the 0.6-1.5 s period range. Structures in this same period range (7 to 10 stories) experienced much higher demands than what was typical in Izmir. Even though these demands were below the levels of design spectra in place at the time of structural design, they nonetheless produced a series of collapses and appurtenant loss of life (116 fatalities), suggesting the structural performance is below the level that would be expected, possibly because of design and/or construction process deficiencies. To the extent that future earthquakes will produce strong shaking over a wider frequency range, many more structures will experience large demands. As such, retrofit/replacement campaigns are needed to address this risk.

In contrast to building structures, major lifeline systems in Anatolia, including dams and pipelines do not appear to have been damaged. This is largely expected, because the modest ground shaking levels in the region did not produce ground failures (e.g., from liquefaction), which has been shown to be a principal cause of damage to such systems elsewhere.

The emergency responses in Greece and Turkey provided housing, food, and related assistance to residents displaced from their homes due to actual or perceived structural collapse risk. In both regions, educational efforts with local government officials and residents had been undertaken prior to the event. Future research could investigate the beneficial impacts of these efforts on the responses of organizations and citizens during and immediately following the event, as well as other public policy measures including mandatory earthquake insurance (Turkey), building code enforcement, and retrofit policy.

1.0 Regional Tectonics and Seismic Source

Chapter Coordinators: Anastasia Kiratzi, A. Arda Özacar, Costas Papazachos, Ali Pınar

Authors / Contributors:

Aristotle University of Thessaloniki: Anastasia Kiratzi, Costas Papazachos, Vasilis Karakostas, Eleftheria Papadimitriou, Michalis Foumelis, Charalambos Kkallas

Boğaziçi University, KOERI: Ali Pınar, Doğan Kalafat

Dokuz Eylül University: Hasan Sözbilir, Bora Uzel

Eskişehir Osmangazi University: Erhan Altunel

İstanbul University – Cerrahpaşa : Onur Tan

Kocaeli University: Serkan Irmak

Middle East Technical University: A. Arda Özacar, Eyüp Sopacı, Zeynep Gülerce

National Kapodistrian University of Athens: Panayotis Papadimitriou, Vasilis Kapetanidis, Ioannis Spingos, Andreas Karakonstantis, Nicholas Voulgaris, Efthymios Lekkas, Evi Nomikou, Spyridon Mavroulis, Marilia Gogou

National Observatory of Athens, Geodynamic Institute: Athanasios Ganas, Varvara Tsironi, Ilektra Karasante

Sakarya University: Murat Utkucu

1.1 Introduction

On 30 October 2020 11:51 UTC (13:51 local time) an earthquake of moment magnitude **M**7.0 (GCMT solution) occurred offshore the northern coast of Samos Island, in the Gulf of Ephesus/Kuşadasi. Initial magnitude estimates by various agencies were in the range 6.6 to 7.0. The here relocated epicenter (Origin Time=11:51:25.2; Latitude= 37.8919°; Longitude=26.8066°, hypocentral depth= 8.2 km; Simulated Wood-Anderson magnitude M_L = 6.7) lies 9 km north of the coast of Samos; 14 km SE from the closest coast of Turkey; 34 km south of Seferihisar and 58 to 76 km SW from the metropolitan area of Izmir, that suffered the heaviest damage. The earthquake reportedly caused 2 fatalities and 19 minor injuries at Samos Island, along with several injuries and significant damage to the building stock. In Western Turkey, the effects of the event were detrimental, with 116 fatalities, over 1,030 injuries and structural damage that included at least six collapses, in Izmir, approximately 70 km away from the epicenter. While several strong earthquakes had recently affected both Greece and Turkey along the eastern Aegean (e.g. the 2017 Kos **M**6.6 and Lesvos **M**6.3 mainshock), this was the first **M**7.0 event that had an important impact in both countries since the 1957 April 25 **M**7.2 that affected significantly both Rhodes (Greece) and Fethiye (Turkey) areas (Papazachos and Papazachou, 2003).

1.1.1 *Regional tectonic setting*

The Aegean Sea and Western Anatolia are among the most seismically active areas in Eastern Mediterranean and have been the site of devastating earthquakes in both recent and historical times. The region is affected by; a) the escape of the Anatolia block towards the Aegean (escape-tectonics), b) the rollback of the subducting eastern Mediterranean plate under the Aegean in the south, provoking extension of the Aegean and Western Anatolian crust and, c) by gravitational forces acting in western Anatolia. Recent studies on tomography suggest that slab edge process and related back-arc extension is the dominant driving force for the Western Anatolia and Aegean tectonics (Wortel and Spakman, 2000; van Hinsbergen et al., 2010; Facenna et al., 2006; Biryol et al., 2011; Ganas et al., 2009; Jolivet et al., 2013). In terms of strain, the amount of crustal extension between Samos and Western Anatolia (the broader Izmir area) is 7.4 mm/yr based on GNSS data modeling (Vernant et al., 2014). The extension in the region is mainly compensated by large-scale extensional detachments and high-angle normal faults, while crustal-scale strike-slip faults (such as İzmir-Balıkesir Transfer Zone) accommodate lateral motions (Figure 1.1).

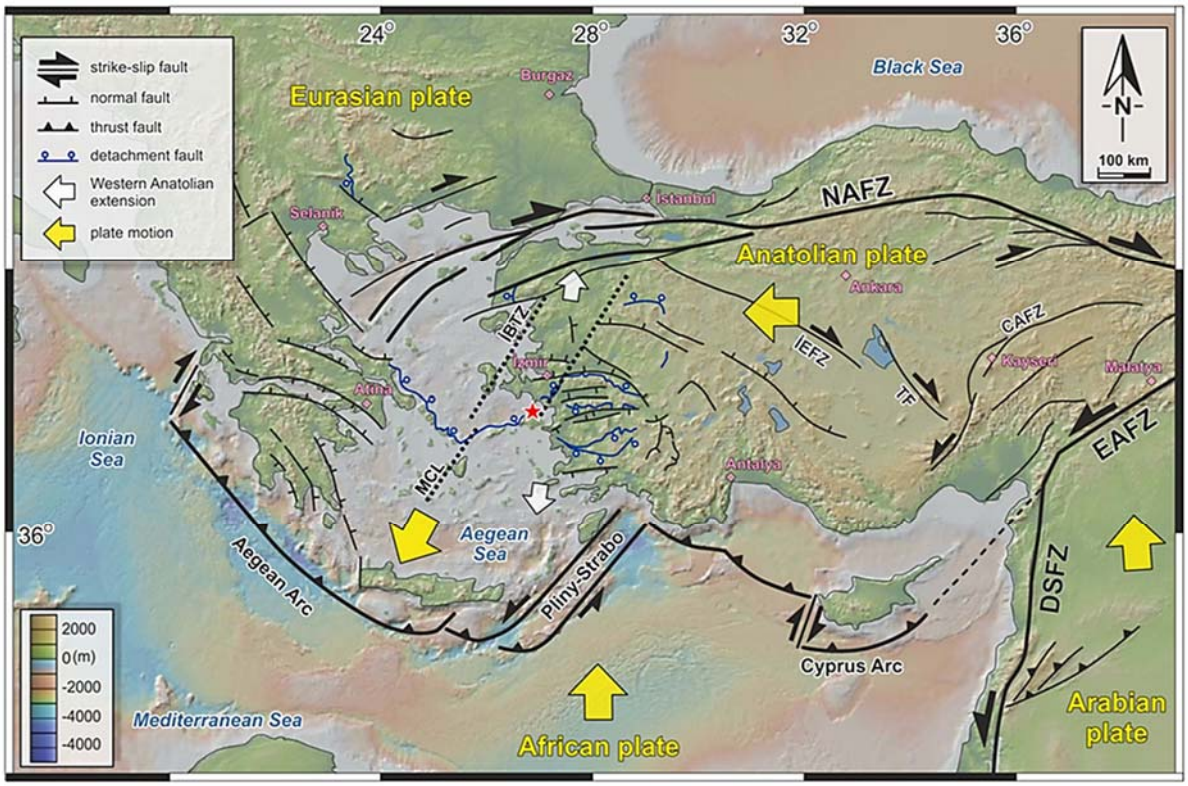

Figure 1.1. Tectonic setting of Eastern Mediterranean (modified from Uzel et al., 2013). NAFZ: North Anatolian Fault Zone, EAFZ: East Anatolian Fault Zone, DSFZ: Dead Sea Fault Zone, CAFZ: Central Anatolian Fault Zone, TF: Tuz Gölü Fault, IEFZ: İnönü Eskişehir Fault Zone, IBTZ: İzmir-Balıkesir Transfer Zone, MCL: Mid-Cycladic Lineament.

Available earthquake focal mechanisms (Figure 1.2 a-c) clearly support the coexistence of active extension and strike-slip deformation along the coastal region of western Anatolia and eastern Aegean Sea. Seismic activity is mainly concentrated on normal faults that are formed due to active N-S extension, while strike-slip faults accommodate shear motions associated to west-southwest motion of Anatolia. Active splays of the North Anatolian Fault act as the source of the strike-slip stress regime in the North Aegean, which extends down to Samos Island. In inland areas, the active tectonic regime is mainly extensional and the region is characterized by several horst graben systems, bounded by normal faults (Figure 1.2c).

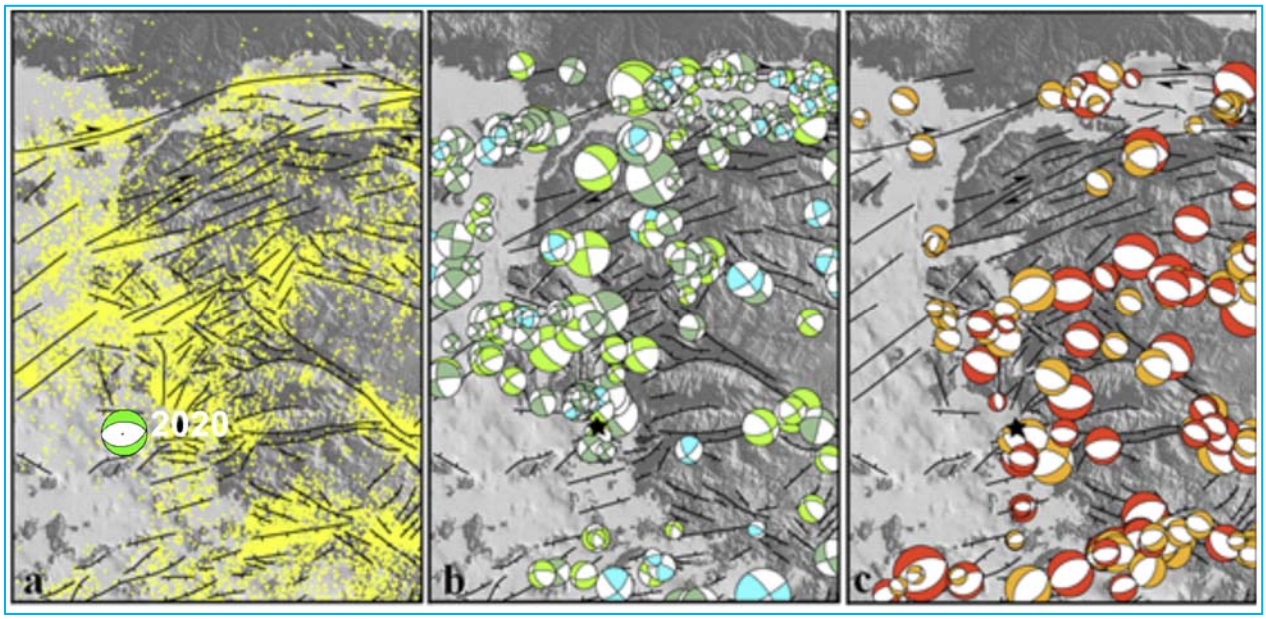

Figure 1.2.a) Seismicity (KOERI catalogue) and fault structure (Ozacar, 2011) in the broader region. The beach ball shows the mechanism and the location of the Samos earthquake. **b)** Earthquake focal mechanisms indicating strike-slip faulting and, **c)** normal faulting. Data from Ozacar (2011) for the period 1909-2010.

To this end, the 30 October 2020 Samos earthquake occurred in the cross-border region between the eastern Aegean Sea islands and Western Turkey, where the active tectonic regime is transtensional, that is to say, it is deforming due to both extensive and transtensive shear (Chatzipetros et al. 2013; Kiratzi, 2002, 2014; Ozacar, 2011, Tur et al., 2015). More specifically, transtensional shear zones are those, which are characterized by the co-existence of different structures, related to both strike-slip shear and extension. End member structures include pure strike-slip faults and purely extensional ("normal") dip-slip faults, as was the case of the Samos earthquake. Moreover, note that this area is a transition zone, regarding the observed crustal thickness. It marks the boundary between the thinned continental crust (~20-25km) of the southern Aegean Sea (e.g. Bohnhoff et al., 2001; Karagianni et al., 2005; Sodoudi et al., 2006), with the thicker crust of western Anatolia (~30km), which has a typical Moho depth of ~28km at the broader Buyuk Menderes Graben region (e.g. Zhu et al., 2006b; Karabulut et al., 2019).

1.1.2 *Off-shore faults in the vicinity of the mainshock - identifying the fault that ruptured*

From the spatial distribution of the aftershock sequence (Figure 1.3), it is evident that the fault that ruptured during the **M**7.0 2020 mainshock is located offshore the northern coast of Samos Island. This fault has been previously identified, mainly based on morphotectonic information. More specifically, in the work of Chatzipetros et al. (2013) a fault to the north of Samos is identified as ***North Samos Fault***, dipping to the north (SA05 in their publication). Moreover, in the GreDaSS database (Caputo et al., 2012; Sboras, 2012) and the GEM-Faults database, a composite fault source (GRCS912) is identified in this area, named ***Kaystrios Fault***, which is a good candidate for the fault that ruptured during the 2020 sequence. The geometric characteristics of Kaystrios Fault are: strike in the range 260° to 290°, dip 45° to 70° and rake in the range -100° to -80°, while the maximum depth of the fault is estimated as 14.5 Km. The estimated slip rate of this fault is 0.10 to 2 mm/y and the estimated max magnitude is **M**6.9.

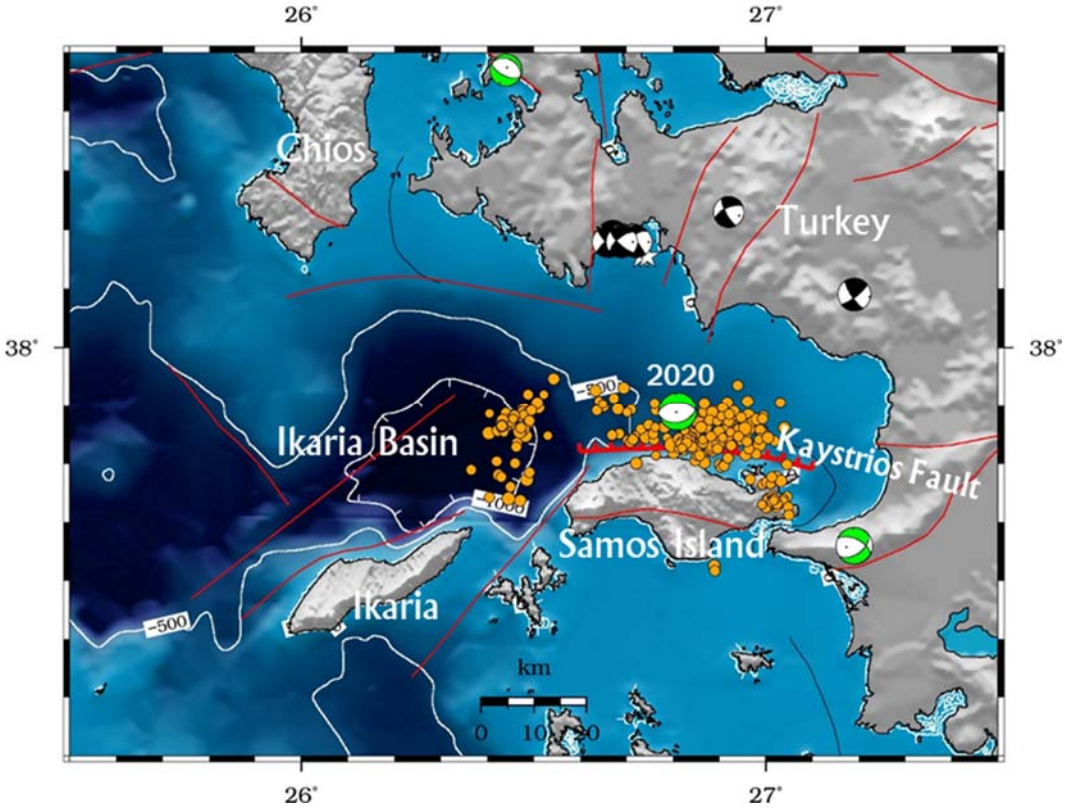

Figure 1.3. Relocated seismicity of M≥3 (AUTh relocation) and mapped-inferred off-shore faults of the region (GreDAsSS, Caputo et al., 2012; Sboras, 2012). Overall, the characteristics of the 2020 sequence are compatible with the geometry of the Kaystrios Fault, which dips to the north and bounds the northern coastline of Samos, showing a compatible geometry with the proposed source and slip models.

A detailed hydrographic survey of the northern coastal margin of Samos Island (Greece) was conducted at the beginning of December 2020 by R/V NAUTILOS of the Greek Hydrographic Services. The main morphological characteristic of the northern margin of Samos Island is a sub-

parallel to the coast-elongated basin, 22 km long, 10 km wide and 690 m deep, as seen in the preliminary, unprocessed swath data of Figure 1.4.

The southern margin of the basin is rather steep, with morphological slopes of more than 10°, following the major E-W normal fault surface running along the coastal zone, with an overall throw of more than 500m. In contrast, the northern margin of the basin shows a gradual slope increase from 1° to 5°.

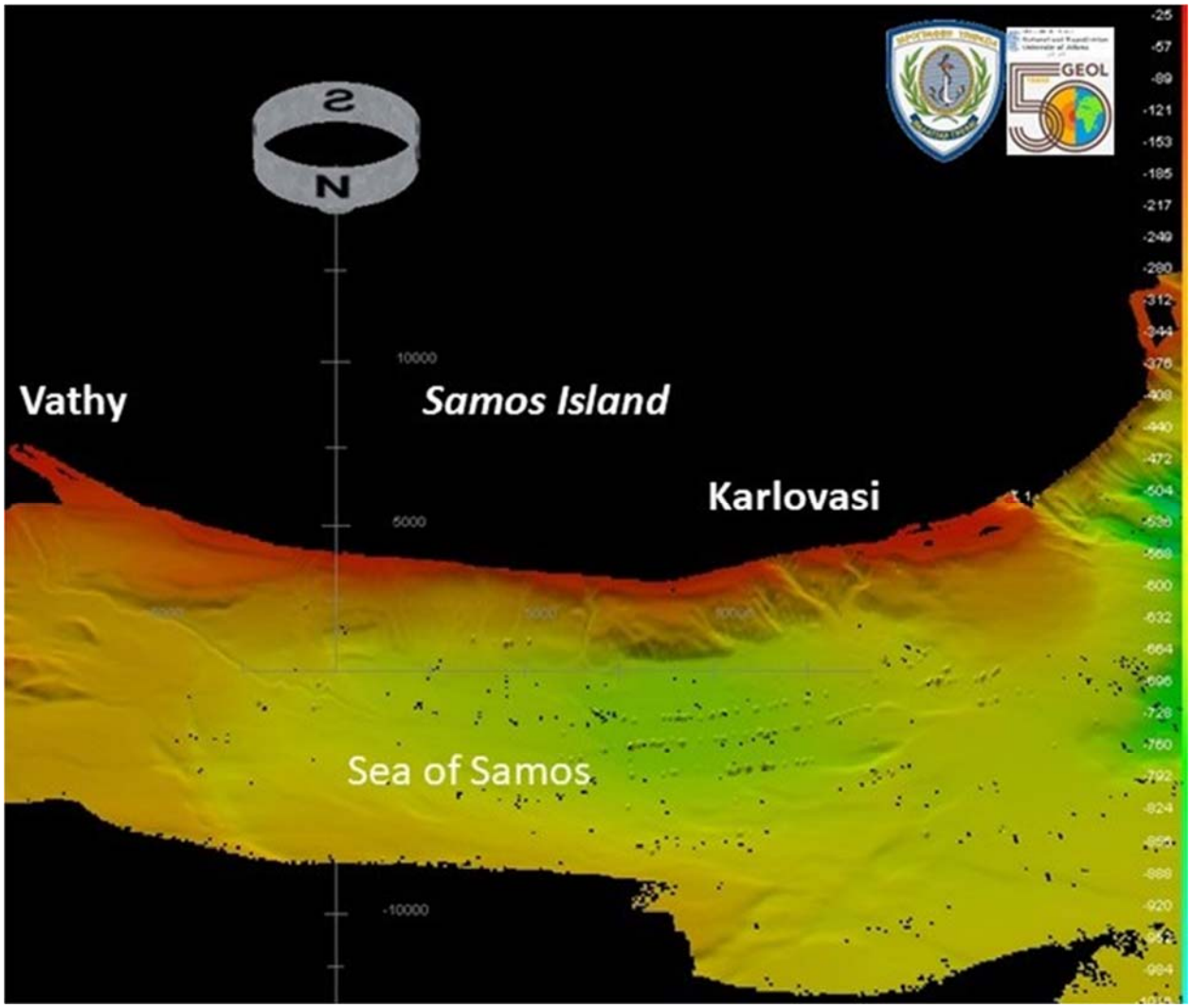

Figure 1.4. Shaded relief swath map at the Sea of Samos, showing the seismic fault zone at the northern part of Samos (unprocessed swath data).

The continental platform is developed mainly in the northern slopes of the Gulf and its depth spans from 80 to 200 m, being the widest at its N and NE sections. However, the continental platform is absent from the abrupt slopes of the coast of northern Samos, from Karlovasi up to Vathy. This absence is presumably justified by the existence of a marginal fault of approximately W-E direction along the northern coast, which creates the abrupt slopes. In contrast, the

northern margin of the basin is very gradual. Numerous small canyons trending N-S transversal to the main direction of the Gulf are observed along the southern margin, between 100 and 500 m water depths. These canyons have a length around 2.7 km and width between 100-300 m. Two large submarine landslides with a width of 1.3 km and 0.8 km, respectively, are located to the north of Karlovasi. The creation of the canyons is probably due to the uplift of Northern Samos Island and their 400 m vertical height difference corresponds to the throw of the Northern Samos Fault, which has controlled the steep margin slopes.

1.1.3 *Geologic and Tectonic Setting of İzmir Bay Area*

In the Turkish side, the main damage was observed in Izmir, and the interpretation of the damage pattern should be mainly sought in the basin and site effects, alongside the characteristics of the structural inventory. The Izmir bay is formed by the junction of the E-W-trending extensional normal faults (Uzel et al., 2013).

Figure 1.5. *Upper***:** satellite view of İzmir Bay with geology (Uzel et al., 2013). *Lower:* a field photo of faults bounding İzmir Bay. KaF: Karşıyaka Fault, IZF: İzmir Fault. Historical seismicity shows that damaging earthquakes occurred near the broader İzmir metropolitan area.

The metropolitan area of İzmir, with a population of 4 million, lies on the inner part of the bay, which is a morphological depression situated on the subsiding hanging wall block bounded by active normal faults from both sides (Figure 1.5). At the base, stratigraphy is characterized by

rocks of the Bornova Flysch Zone, which is made up of a highly sheared, flysch-type matrix with sandstone-mudstone alternations and recrystallized limestone olistholits. The basement rocks of Bornova Flysch Zone and Miocene volcano-sedimentary units are elevated with ~E-W trending normal faults along the northern and southern margins and Quaternary alluvium and fan-delta to shallow marine deposits accumulate within the İzmir Bay depression. The alluvial fans, which are controlled by the Karşıyaka Fault to the north and the İzmir Fault to the south, are characterized by unconsolidated coarse-grained debris flow sediments. The fluvial deposits are coarse- to fine-grained axial river deposits carried by the rivers on the footwall. The lateral fans and the axial river deposits, which are controlled by the present-day drainage system, inter-finger laterally and vertically with fine-grained fan-delta and shallow marine deposits through the bay. In the middle part of the Bornova plain, the basin fill exceeds 300 meters in thickness and computed predominant periods are in excess of 1 sec (Pamuk et al., 2017). Based on the Mid-Holocene marine sediments, the coastline of Bornova plain was passing 1.5 km inland from the present day (Karadaş, 2012 and 2014), which correlates well with the heavily damaged area.

1.2 Seismic History of the Region

1.2.1 *Historical seismicity near Samos Island*

As earlier discussed, the broader Samos island area is situated in a trans-tensional regime, resulting in the presence of a large number of ~E-W trending active normal faults, which locally interact with strike-slip faults, which are mostly dextral, characterized by a dominant NE-SW orientation, varying from almost N-S to ENE-WSW. As a result, the area is seismically active, often with large events, like the **M**7.0 2020 mainshock north of Samos. Based on recent seismicity models for the Aegean (e.g. Vamvakaris et al., 2016), for an area with a radius of 40km around Samos, the average return period for an event with a minimum magnitude of **M**6.0 (typical damaging event in the Aegean) is 25-30yr, increasing to ~80-100yr for a strong **M**6.5 mainshock (which often inflicts heavy damage in the area). This seismic activity has been observed since antiquity, though information for strong events from the main active faults near the island of Samos is mainly available for the last 3 centuries.

The earliest information for earthquakes in Samos dates back to 200BC, where information from inscriptions and historical reports (Bousquet and Pechoux, 1978) suggests the generation of a strong (**M**6.0-6.5) event, with significant impact on the island (macroseismic intensity ~7-8 in the Modified Mercalli scale, denoted as I_{MM} hereinafter). The strongest event in antiquity is the 47AD **M**~7.0 earthquake, which is very similar to the recent 2020 **M**7.0 mainshock: The earthquake caused heavy damage in Samos (I_{MM}~8), but also in Izmir, Ephesus (present-day Selçuk), Miletus, Chios and several Ionian cities of Asia Minor (Papazachos and Papazachou, 2003). The earthquake was very strongly felt ($I_{MM}\geq 4$) in Laodicea and Hierapolis (close to present day Denizli) at a distance of ~200km (Guidoboni et al. 1994), an observation that (together with the extent of heavy damage) is compatible with proposed mainshock magnitude (**M**6.9-7.1). While the

available information for this event is reliable and originates from various sources (Greek and Roman inscriptions, Romans Philostratus and Plinius, Byzantine Malalas and Syncellus), it is difficult to identify the associated active fault that generated this event. The damage pattern suggests that it may have been generated on the 2020 **M**7.0 Samos earthquake fault (Kaystrios fault), but alternative faults on the Turkish coast could be also associated with the observed damage distribution.

Information on historical seismicity for the broader region of Samos Island is mainly available after the mid-18th century. It includes various historians and resources: for example local historian Stamatiadis and the historical local "Samos" newspaper, as well as seismologists who have worked on the compilation of historical seismicity catalogues and macroseismic maps (e.g. Schmidt, 1867; Sieberg, 1932a, b; Karnik, 1971; Shebalin et al., 1974; Ambraseys, 1988; Makropoulos et al., 1989; Guidoboni et al. 1994).

We have used the information for Samos historical and 20th century mainshocks, as summarized by Papazachos and Papazachou (2003), and employed macroseismic information to perform a preliminary re-appraisal of the historical mainshock seismicity of Samos Island. Magnitude estimations were based on the macroseismic intensity-magnitude relations proposed by Papazachos and Papaioannou (1997), while event locations were adjusted using the observed macroseismic information.

A typical example is presented in Figure 1.6a, where the meizoseismal area ($I_{MM}\geq 8$) is presented for the strong 1751/06/18 Samos earthquake. This event is the first mainshock for which detailed information exists since antiquity in the Samos region. Large parts of Chora and Vathy in Samos, as well as Kuşadasi on the Turkish coast collapsed (several churches and mosques), while the heaviest damage was observed in Agacli, where nearly all buildings collapsed. Significant rockfalls occurred in mount Dilek (Mykali) and the presence of surface ground fissures is reported in documents from Agia Zoni monastery in Samos. The dimensions of the $I_{MM}\geq 8$ area and additional data and descriptions suggest that the event is **M**~6.8, stronger than originally proposed by Papazachos and Papazachou (2003) (**M**6.4). The proposed epicenter in Figure 1.6a is likely associated with the Yavansu Fault and its possible continuation towards the Aegean Sea.

Following a similar approach, we present in Figure 1.6b the major historical and 20th century earthquakes in Samos since mid-18th century. Fault Plane Solutions (FPS) for events with **M**>4.5, as well as major active faults from various databases (GreDaSS, Caputo et al.; NOAv3.0, Ganas et al., 2020) and publications (e.g. Mountrakis et al., 2003; Sakellariou and Tsampouraki-Kraounaki, 2019) are also depicted.

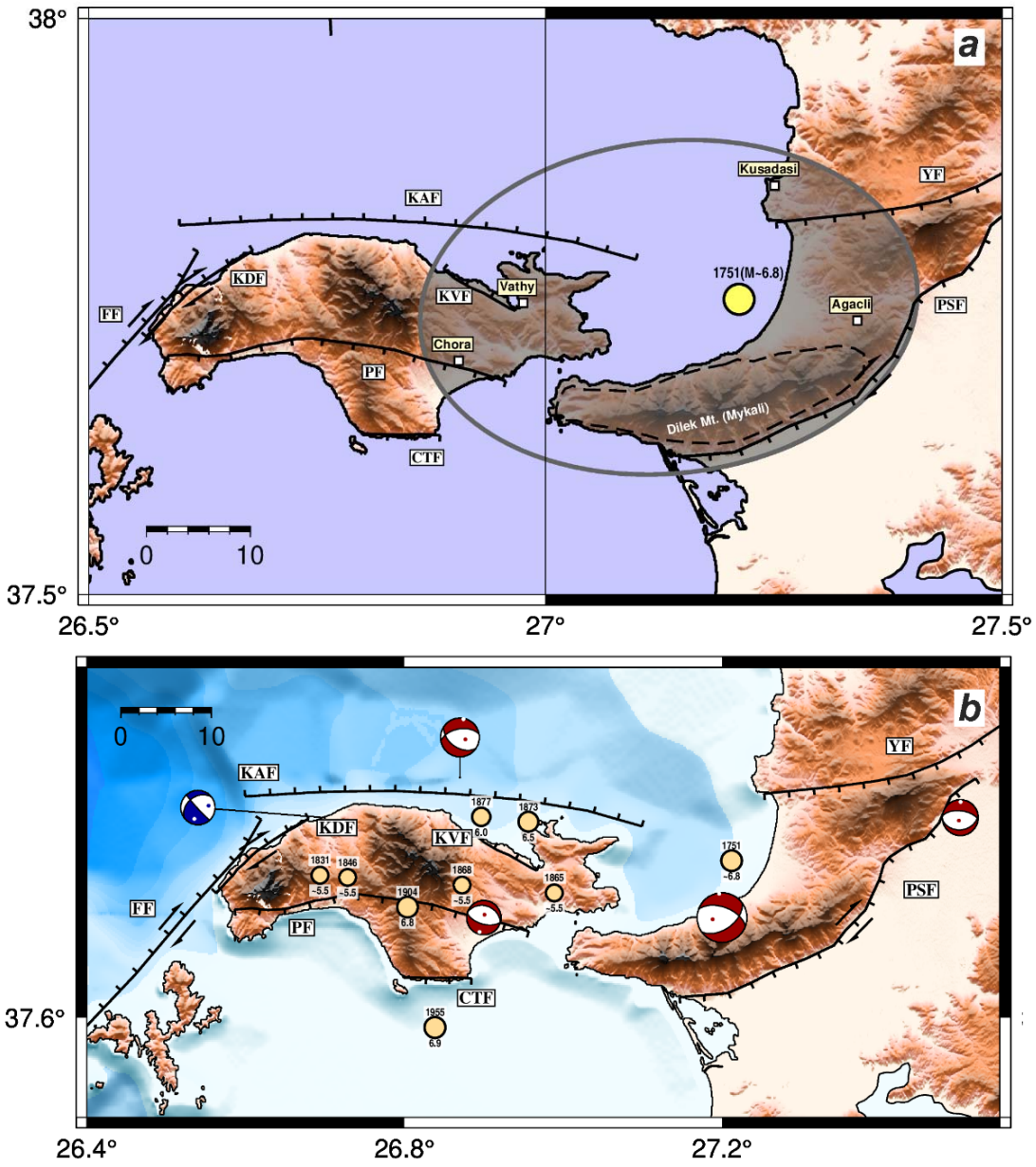

Figure 1.6. a) Meizoseismal area ($I_{MM} \geq 8$) of the 1751/06/18 **M**~6.8 mainshock. The main cities, which suffered heavy damage in Samos and coastal Turkey, as well as the Mt. Dikek (Mykali) area (dashed line) where rockfalls were observed, are also depicted. **b)** Major historical and 20th century earthquakes in Samos since mid-18th century. Fault Plane Solutions (FPS) for events with **M**>4.5, as well as major active faults are also depicted (KAF: Kaystrios fault [which hosted the 2020 sequence], FF: Fourni fault, PF: Pythagorion fault, KDF: Karlovasi-Drakeon Fault, KVF: Kokkari-Vathy Fault, CTF: Cape Tsopelas Fault, YF: Yavansu Fault, PSF: Priene-Sazli Fault).

The information presented in Figure 1.6, depicts a rather complex and interesting evolution of seismic activity in the late 18th, 19th and 20th century for Samos, as well as the lack of known (at

least for this period) significant events for the Kaystrios fault that hosted the 2020 **M**7.0 seismic sequence. Most specifically:

a) Between 1831 and 1868 a significant number of moderate earthquakes (**M**<6.0) occurred in Samos, most of them near the Pythagorion fault. This is clear from: the reported strong rockfall phenomena in mountain Kerketeas of western Samos (1831 and 1846 events); the occurrence of aftershocks that were felt only in the central part of the island (1831 event); the presence of surface fissures in southern Samos (1846 event); the localized damage in villages of southern Samos (1868 event, with heavy damage in the Pagondas village); alongside the limited impact (no damage, only occasional strong shaking) of these shocks along coastal Turkey. Very few of the mainshocks were felt in Izmir. Several of these events are associated with extended (in time) seismic sequences, resembling earthquake swarms, with foreshocks starting up to 9 months before each event and strong aftershocks up to 7 months after the mainshocks.
b) Seismicity migrated to the north, with the occurrence of the strong 1873 earthquake (**M**~6.5), which resulted into heavy damage in the eastern part of the island and was very strongly felt in Izmir. The earthquake was also felt in the Greek mainland, up to Thessaloniki in the north (almost 500km away from the epicenter), while several of its aftershocks were also strongly felt along coastal Turkish cities. While the epicenter of this event is very poorly constrained, it may be associated with the strong (**M**~6.0) event that occurred 4 years later (1877), which has a significant impact in northwestern Samos, with several collapsed buildings in the coastal villages of Avlaki and Kokkari, located to the west of the city of Vathy. Although both these events may have occurred in the eastern part of the Kaystrios fault (KAF in Figure 1.5b), they are most probably associated with other faults in northeastern Samos, like the Kokkari-Vathy normal fault (KVF in Figure 1.5b).
c) The strong 18th century activity seems to culminate with the generation of the 1904 August 11 large (**M**6.8) mainshock. This event is clearly associated with the Pythagorion fault (PF in Figure 1.5b) in central Samos; with peak damage along a line following the fault trace in the settlements of (from west to east) Koumeika, Skoureika, Pirgos and Chora, as well as along its extension towards the east in the area of Ano Bathy and Agia Triada. The earthquakes killed 4 people, injured 7, and had a clear energy propagation towards the south (hanging wall), as it caused also damage in Patmos island, was felt up to the Suez Canal and Red Sea (more than 1000km away), while only being lightly felt in Athens. It should be noted that this pattern (Aegean events been strongly felt in northern Africa) is well known since ancient times and is typically attributed to the propagation of strong Lg waves trapped in the very high-Q/high-velocity eastern Mediterranean crust south of the Hellenic arc. Preliminary modelling (see next event for details) of the available macroseismic information from the database of Papazachos et al. (1997), as well as the lack of any reference for a tsunami, confirm the proposed large earthquake magnitude, as well as its association with the Pythagorion onshore fault.
d) The last significant event in Samos was the large 1955 July 16 **M**6.9 earthquake. This event was considered to have occurred to the south of Samos and close to the delta of the Büyük Menderes River (Turkey) (Papazachos and Papazachou, 2003). The heaviest damage (I_{MM}=8) was observed in the island of Agathonisi, south of Samos, with significant impact

also in southern Samos (I_{MM}=7+ locally also 6+/7). We have employed the macroseismic data collected by the Geodynamic Institute of the National Observatory of Athens, as compiled and reported by Papazachos et al. (1997), in an attempt to verify the proposed fault location. Figure 1.7 presents the simulated (contour map) and observed (colored circles) macroseismic information (I_{MM} values) for this event. For the simulation, we have employed the finite-fault stochastic simulation approach of Motazedian and Atkinson (2005), as adapted by Boore (2009). Source and path parameters were calibrated from previous work based on regional GMPEs (Skarlatoudis et al., 2003). Though not critical for the overall assessment, site effects were approximated using generic transfer functions for Greece from Klimis (1999, 2006). These functions were based on V_{S30} values derived from topographic slope proxies, following Wald and Allen (2007), shown to be appropriate for the area of Greece by Stewart et al. (2014). Finally, we employed typical κ_0 values proposed for A/B, C and D NEHRP soil classes for Greece by several authors (Margaris and Boore, 1998, Margaris and Hatzidimitriou, 2002; Klimis et al., 1999, 2006). The simulation results shown in Figure 1.7, as well as the details of the near-fault reconstructed damage pattern, presented in the top-left inset Figure, show that we can adequately model the damage distribution with the adopted fault geometry, as also verified by the quantitative comparison of observed and simulated macroseismic intensity values in the upper-right inset Figure. This agreement suggests that the causative fault is most probably associated with the Cape Tsopelas Fault (CPF) in southern Samos and the westward edge of the Priene-Sazli Fault (PSF). This activation of an offshore normal fault is further supported by the observation of strong tsunami phenomena reported for south-eastern Samos (Pythagorion and Ireon areas), with a runup of ~2m and inundation distances exceeding 20m (Psilovikos, 1996*, unpubl. report*).

The previous historical information provides some important constraints with respect to the 2020 **M**7.0 Samos sequence:

a) A similar, large earthquake (**M**~7.0) has not occurred along the Kaystrios Fault (KAF) during the last ~270 years. While some strong events (1873, **M**~6.5) may be associated with eastern segment of this fault, it appears that no known large event of similar magnitude can be associated with this fault (during this period), suggesting that the recent 2020 **M**7.0 event occurred on a fault that was rather "mature".
b) The similar (in dimensions), and sub-parallel large Pythagorion fault was activated through a series of moderate events in the mid-late 19th century, culminating in the large 1904 **M**6.8 mainshock, that had a significant impact in the broader Samos area.
c) In 1955, a similar magnitude earthquake also occurred along the southern Samos coast, at a second, sub-parallel, east-west trending offshore normal fault, dipping to the south.
d) In all these three **M**6.8-7.0 events, despite their large magnitude and extended damage throughout the island, the number of casualties on Samos was rather small (4 people in 1904, none for the 1955 event, 2 people for the recent 2020 mainshock). While the 1904 onshore fault event not only had a complex preshock and foreshock seismic activity but also large aftershocks (**M**~5.8-5.9 one week and 2 months after the mainshock), the two

offshore fault events appear to have rather subtle aftershock sequences, with the 1955 event having its largest aftershock (**M**5.1), roughly 1.5 month after its generation. Moreover, both offshore fault events (1955 and 2020) are associated with a similar tsunami phenomena (e.g. runups of ~2m), with a significant but localized impact along the Samos coasts.

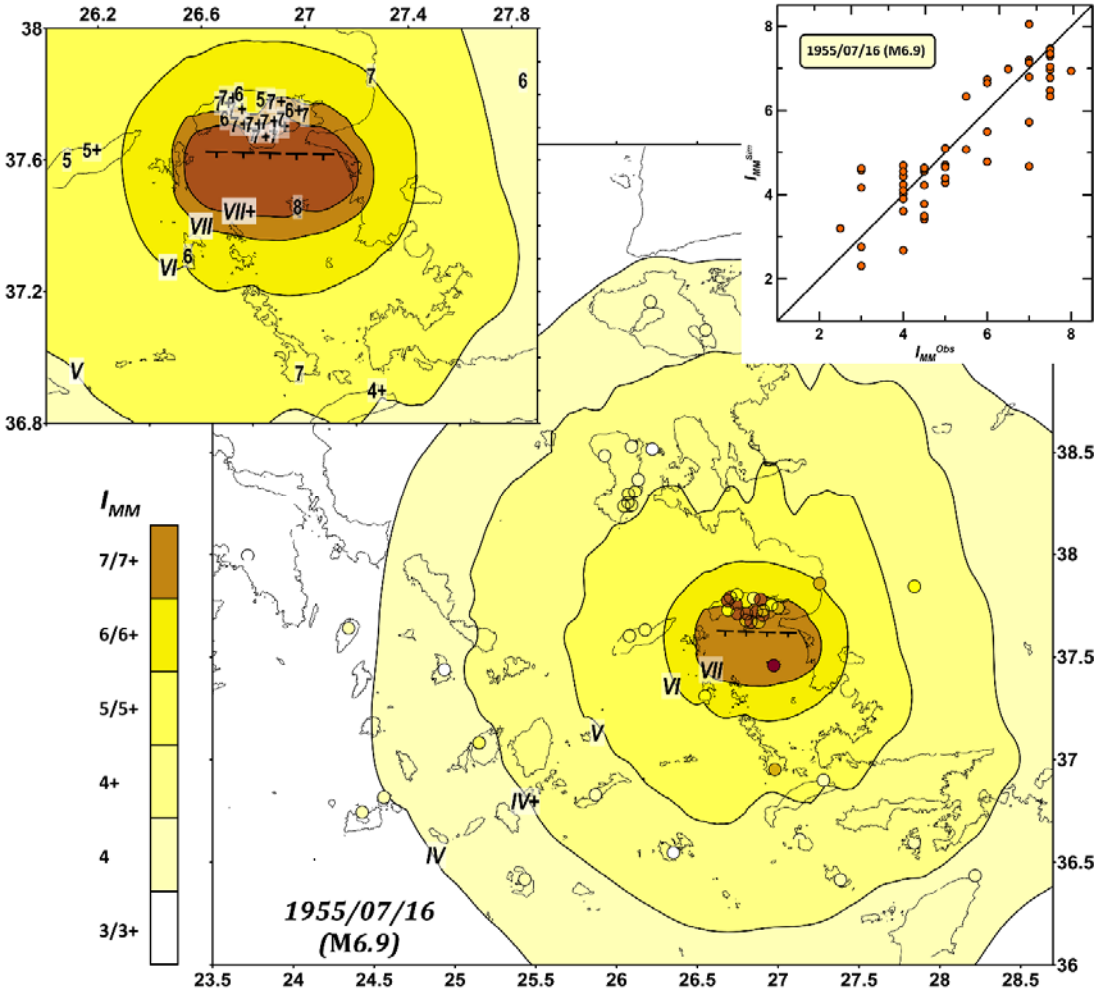

Figure 1.7. Isoseismals (labels in Latin numbers) from the stochastic simulation of the macroseismic information (damage distribution) for the 1955/07/16 **M**~6.9 mainshock (see text for modeling details) and original I_{MM} observations for the same event (colored circles). The top-left inset Figure presents the same comparison for the near-fault area (observed intensities are shown with numbers), while the top-right Figure shows the quantitative comparison of observed (I_{MM}^{Obs}) and simulated (I_{MM}^{Sim}) values (bisector depicted with solid line). The comparison supports the generation of the 1955 event along an offshore normal fault, associated with the faults Cape Tsopelas (CPF) and Priene-Sazli (PSF).

1.2.2 Historical seismicity near the İzmir Bay Area

The İzmir Bay Area has been affected by strong earthquake occurrence in the past, especially during the period 1600-1800 (Figure 1.8). It is worth mentioning nine events which had reported intensities, I_{MM} >8 (Pınar and Lahn, 1952; Soysal et al., 1981; Ambraseys, 2009; Duman et al., 2016 and references therein).

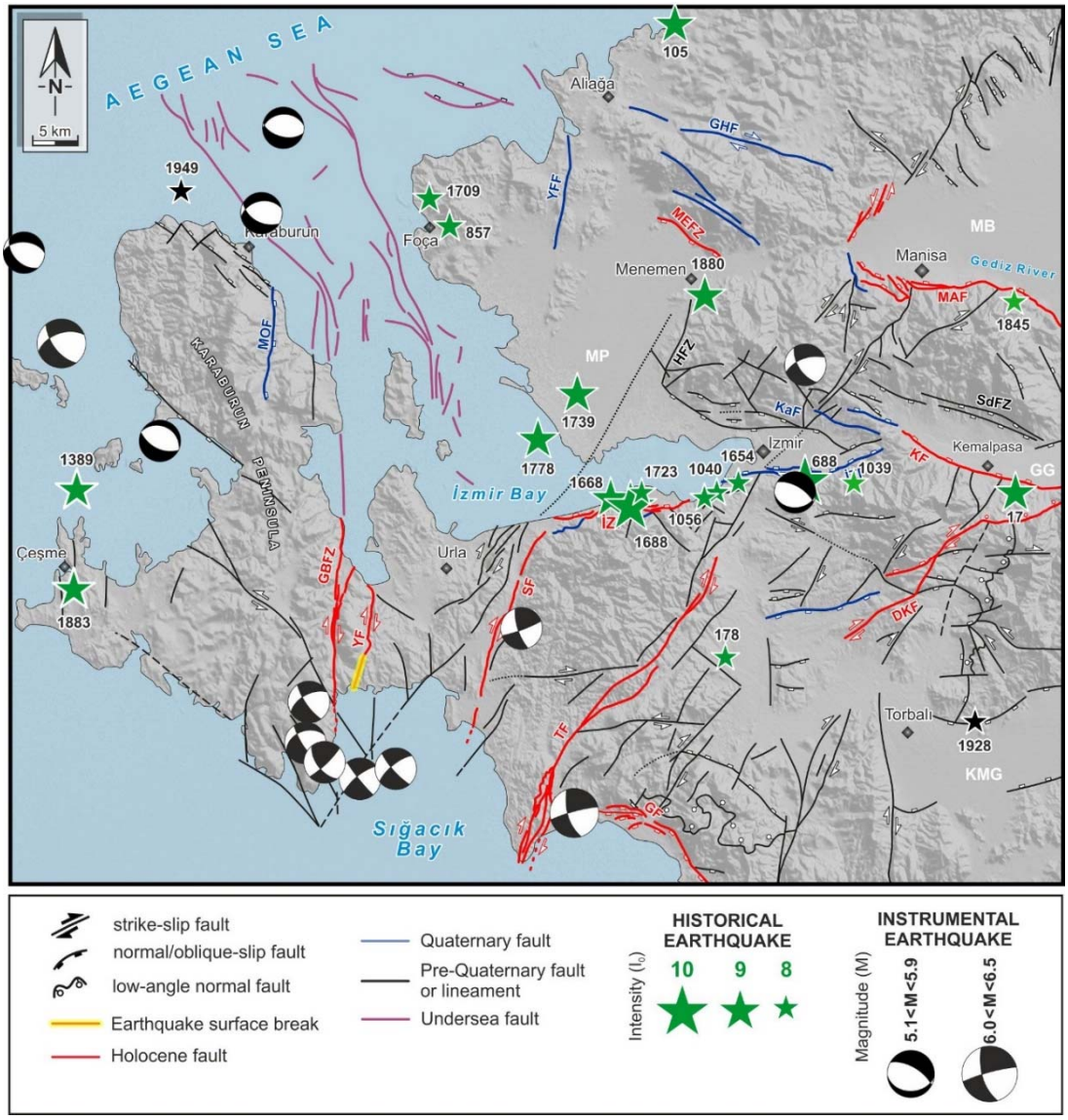

Figure 1.8. Seismotectonic map of İzmir region. Faults are taken from Uzel et al. (2013) and Emre et al. (2018). Damaging historical earthquakes are compiled from Duman et al. (2016). Focal mechanisms of earthquake are taken from Tan et al. (2008).

The strongest event, in terms of intensity, occurred in 1688 near Izmir, most probably along the İzmir Fault. It caused heavy damage to the mosques, churches, and city walls; invoked a major fire in the city and caused over 2000 causalities (Pınar and Lahn, 1952). The major destruction

occurred across Bornova plain (between Narlıdere and Bayraklı) where large ground cracks have been reported. Multiple landslides along the coastal part of the city were triggered. Moreover, tsunami waves have been reported which is consistent with activation of the offshore İzmir fault segment imaged by Coskun et al. (2017) using high-resolution seismic data. The maximum macroseismic intensity of this event was estimated to be 10.

The earthquakes of 17, 688, 1389, 1668, 1739, 1778, 1880, 1883, with I_{MM}~9, have epicenters along the coastal part of the Aegean Sea (Figure 1.8). The 17AD event near Kemalpaşa caused damage in 13 cities including Ephesus (Pınar and Lahn, 1952; Ergin et al., 1967; Ambraseys, 2009). The İzmir Bay area was also damaged heavily during another significant earthquake in 688, which is located on the Bornova plain. This event, caused 20000 fatalities, and could be associated with the eastern segment of İzmir fault that bounds Bornova plain from south (Ergin et al., 1967). Among events (1389, 1883) that occurred near Çeşme, the devastating November 1883 event led to around 1500 fatalities (Soysal et al., 1981; Ambraseys, 2009). İzmir Bay and Menemen Plain were also shaken by the 1668, 1739, 1778, 1880 events that led to destruction in the area (Ergin et al., 1967). According to a note written in Patmos, the 1739 earthquake lasted significantly long causing house collapses in İzmir and Chios Island, and submerging the delta mouth of the Gediz (Agria) River (Papazachos et al., 1997; Eyidoğan et al., 1991).

During the instrumental period (after ca 1926), seismic activity in the Izmir region includes five significant earthquakes (Figure 1.8). These are in chronological order: 1928 (**M**=6.5) Torbalı, 1949 (**M**=6.6) Karaburun, 1992 (**M** 6.0) Doğanbey, 2003 (**M** 5.7) Seferihisar and 2005 (**M** =5.4 – 5.8) Sığacık events. The epicenter of the 1928 Torbalı earthquake located at the westernmost tip of Küçük Menderes Graben likely originated from the activation of the normal fault bounding the graben to the north. According to reports, 2000 houses had been damaged (Pınar and Lahn, 1952). The 1949 Karaburun earthquake occurred in the northernmost part of the Izmir Bay, at the northern offshore of the Karaburun Peninsula. Seven fatalities and severe damage (2200 houses) is reported around Çeşme, Mordoğan, Karaburun and Chios Island (Ergin et al., 1967). The 1992 Doğanbey earthquake occurred along the Tuzla Fault with right lateral strike-slip mechanism (Türkelli et al., 1995). The earthquake damage was rather limited but according to field observations, geothermal fluids and underground waters were affected.

The 2003 Seferihisar earthquake, which caused damage to ~ 100 buildings in the Urla-Seferihisar area, ruptured a conjugate fault between the Seferihisar and Tuzla Faults (Figure 1.8). The aftershock parameters and focal mechanism solution indicated the activation of an ENE–WSW-trending, near-vertical right-lateral strike-slip fault (Zhu et al., 2006a). Two years later, an earthquake sequence, which caused a 5 km-long surface rupture (Duman et al., 2016) happened in the vicinity. The 2005 Sığacık earthquake sequence included three strong events. Initially, **M**=5.4 event occurred on 17 October 2005 at the western coast of Sığacık Bay. It was followed 4 hours later by an **M**=5.8 event, then 3 days later, on 20 October by another **M**=5.9 event (Aktar et al., 2007). Both these later events occurred in the central part of Sığacık Bay, east of the initial shock. Many destructed buildings and earthquake-related soft-sediment deformations have

been reported (Sözbilir et al., 2009). The sequence migrated roughly to the east and aligned roughly in two clouds, in the NNW-SSE and NE-SW directions. Focal mechanism solutions of the event sequence indicated activation of both NE-trending dextral and NNW-trending sinistral strike-slip faults that are subparallel to Gülbahçe and Seferihisar faults (Benetatos et al., 2006; Aktar et al., 2007). It is also important to note that focal mechanism solutions of small earthquakes recorded within the İzmir Bay area are highly variable but mainly in agreement with dominant normal faulting associated to N-S extension (Gok and Polat, 2014).

Compiled long-term seismicity clearly displays the abundance of damaging earthquakes, occurring on both normal and strike-slip faults in the broad İzmir area (Figure 1.8). The abundance of active faults that can generate moderate to large earthquakes, combined with poor site conditions, pose a significant seismic risk for the area. In this respect, site characterization efforts and multidisciplinary active fault studies that will reveal their seismic cycle pattern and present their state of stress are essential to develop a more accurate seismic hazard assessment and guide seismic risk mitigation plans of İzmir and nearby districts.

1.3 Characteristics of the 2020 Seismic Sequence

1.3.1 Relocation of the sequence

Initial sequence relocation: 322 events of the 2020 Samos sequence were detected and manually analyzed (SL-NKUA). The collected travel times were merged with catalogue and arrival-time data collected from other Greek and Turkish institutes (Geodynamics Institute of the National Observatory of Athens, GI-NOA and the Turkish Disaster and Emergency Management Presidency, AFAD). Events were initially located using the HypoInverse-2000 code (Klein, 2002) and a custom velocity model that was constructed for this sequence, determined through the error minimization technique (e.g. Kissling et al., 1994), starting with a 1D model for the region of Karaburun (Erythres), Turkey (Karakonstantis, 2017).

Although the aftershocks were located at the eastern margins of HUSN, the integration of data from stations located at both Greece and Turkey allowed to obtain much better average azimuthal gap of 68°, being narrower than 100° for most events. However, the lack of data from local stations, especially during the first days of the sequence, limited the capability to constrain focal depths and resolve the geometries of the activated structures from the distribution of hypocenters. Furthermore, this caused foci locations to be strongly biased by the selection of the velocity model, which is preliminary. To improve the relative locations of hypocenters, the sequence was relocated using the HypoDD code (Waldhauser, 2001). This algorithm reduces uncertainties caused by discrepancies between the 1D velocity model and the real structure by minimizing the double difference between calculated and observed travel-times for pairs of neighboring events. To this purpose, waveform cross-correlation data were also incorporated from available stations in the region. Figure 1.9 presents the preliminary results for 322 events that were successfully relocated. The epicentral distribution reveals the existence of several

distinct spatial clusters. A dense cluster of aftershocks has occurred east of the mainshock, about 10 km north of Samos Island. This group is associated with the major aftershocks (**M**≥4.5; stars in Figure 1.9), which have been reported for this sequence, including the largest aftershock. An approximately 20-km-long area with very sparse to no aftershock seismicity can be observed to the west of the mainshock. Further west, a significant cluster of events is also observed, while two additional, smaller, isolated clusters were also located, one at the eastern tip of Samos Island and another to the north of Ikaria Island. According to this initial relocation, most seismicity is located between depths of 6 to 14 km, with very few events occurring at smaller or larger depths. Although a planar geometry could not be clearly yet being resolved from the available hypocenters, their distribution in the eastern spatial groups along with the hypocenter of the mainshock was consistent with a north-dipping fault plane, outcropping near the northern coast of Samos Island. The latter result was also consistent with reported preliminary deformation observations, showing subsidence at the northern tip of Samos Island and mainly uplift to its western part (Papadimitriou et al., 2020, *see later discussion*).

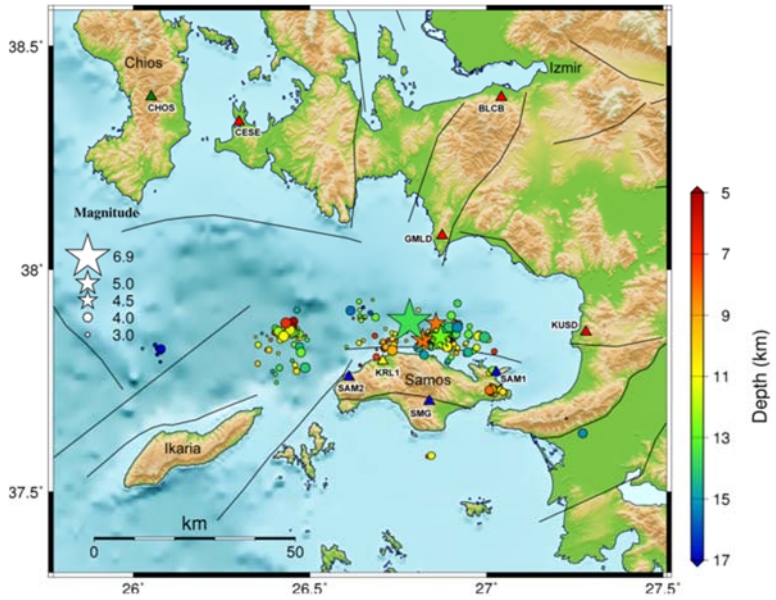

Figure 1.9. Preliminary relocation of 322 events (by SL-NKUA) that occurred during the period between 30 October and 8 November 2020. The seismological stations used for the region are presented by triangles (Network codes: blue=HL, yellow=HI, green=HT, red=KO), while major events of the aftershock sequence (**M**≥4.5) are depicted by stars.

Updated relocation of the M7.0 2020 seismic sequence: To improve previous results, as well as to expand the time interval considered in the analysis, an updated relocation approach was applied for the **M**7.0 2020 Samos sequence by the Geophysical Laboratory of the Aristotle University of Thessaloniki (GL-AUTh). For this reason, the complete travel time dataset from the date of the mainshock, 30 October 2020 until 1 December 2020 was used, as this was initially available in the database of the GL-AUTh, consisting of 997 earthquakes, with ~10500 P and S phases. This dataset was merged with the corresponding catalogue and arrival-time data

collected from the Geodynamics Institute of the National Observatory of Athens (GI-NOA), resulting in an updated catalogue of 1039 events, with a significantly larger P and S phase dataset (~17200 phases). Finally, the dataset was merged with data from: the Turkish Disaster and Emergency Management Presidency (AFAD; the Kandilli Observatory and Earthquake Research Institute, Boğaziçi University (KOERI); the Seismological Laboratory of the National and Kapodistrian University of Athens (SL-NKUA); the University of Patras/Seismological Laboratory (UPSL); and other regional institutes. All data were retrieved from the database of the European Mediterranean Seismological Centre (EMSC-CSEM). This additional information increased the number of events to 1282 for the period 30 Oct to 01 Dec 2020, and the number of phase data to almost 31000 P and S phases, resulting in an average number of 24 P and S phases for each aftershock, with an excellent azimuthal coverage.

This enhanced dataset, created by merging seismological metadata and products (e.g. picked seismic phases, epicenters, etc.) from both Greek and Turkish providers, *strongly suggests that there is a need for an efficient real-time/ near real-time exchange and sharing mechanism, allowing to obtain reliable, critical information about similar near-border seismic sequences*.

Earthquake relocations for aftershock sequences often suffer from poor knowledge of the local velocity structure, especially for the shallow part of the crust. This was an important factor in the case of the Samos sequence, as the permanent network is rather sparse in this area. The traditional approach, i.e. application of linearized inversions using conventional 1D velocity model algorithms (e.g. VELEST) often suffers from the impact of the initial reference models, which has been shown to critically bias the obtained results (e.g. Kissling et al., 1994). To overcome the sensitivity of the linearized inversions on the starting (initial or a priori) velocity model, the typical approach is to use a large family of “realistic” starting models, that sample a significant part of the parametric space (Kissling et al., 1995), and consider the variability of all resulting models. This approach attempts to determine which part of the recovered model is more robust i.e. independent (more or less) of the initial model.

For the Samos 2020 sequence we followed the idea proposed by Jansky et al. (2010) and employed a Monte Carlo parametric search of the velocity model space, realized through an adapted neighborhood algorithm (Wathelet, 2008), together with a conventional location code (Hypoinverse-2000, Klein, 2002). In this approach, the regional velocity model is simultaneously estimated (non-linear optimization) with the relocation of the complete seismic sequence. While Monte Carlo inversions are much more demanding, they also allow obtaining a better control of the model, without worrying for models trapped in local minima of the traveltime misfit function. The 50 best minimum misfit (traveltime RMS) P velocity models (out of a total number of >2500 models) obtained with this approach, as well as their average, is presented in Figure 1.10. The models show a rather small variability in the crust, with velocities increasing from ~2.5km/s at the surface to ~5.8km/s at the depth of 4km, and a smaller increase to ~6.3km/s at lower crustal depths. The Moho depth, not so well constrained, varies between 20 and 30km, with a mean

value around 25km, in good agreement with previous results for the Moho depth in the study area (e.g. Sodoudi et al., 2006) that suggest a crustal thickness of 25-30km.

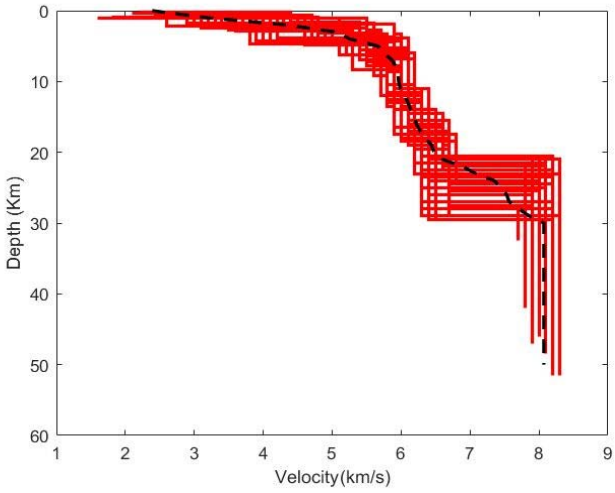

Figure 1.10. Distribution of the 50 best P-wave velocity models obtained from a non-linear Monte-Carlo traveltime inversion of the 2020 **M**7.0 aftershock sequence dataset (1282 events, 30786 P and S phases). The average model is depicted with a dashed line.

The resulting relocated events were also processed with the HypoDD code (Waldhauser, 2001), to improve relative locations of hypocenters and minimize the impact of traveltime data outliers. To reduce the impact of poor traveltime data, this relocation step was limited to events with small initial location errors (RMS<0.8 sec, ERH<5km, ERZ<10km). This led to a subset of 989 events (see Table S1-Appendix), ~80% of the original dataset, mainly the large magnitude events with an adequate number of phases, that were further processed with HYPODD and the model presented in Figure 1.10. The average relative relocation horizontal and depth error is less than 1km. Figure 1.11 depicts the relocated aftershock sequence for the first day, the first week and the first month after the **M**7.0 Oct 30, 2020 mainshock. It also shows the adopted fault geometry for the final finite-fault modeling (dashed line polygon). The distribution, especially for the first week is similar with the one presented in Figure 1.9 (practically the same time span), revealing a rather complex evolution of the aftershock sequence. More specifically, during the first day the western segment of the fault rupture is characterized by the almost complete absence of aftershocks (see blue dashed-line polygon in Figure 1.11a), in very good agreement with results presented later, suggesting that the largest slip occurred in this area. Moreover, no activity is observed on other secondary faults on Samos island during the first 24 hours, except for the westernmost cluster (number 1 in Figure 1.11a), which exhibits a rather clear NE-SW alignment, and is most probably related with the morphotectonic anomaly (canyon, dashed yellow line in Figure 1.11c) observed in the sea-floor bathymetry. During the next weeks, the aftershock sequence expanded spatially, with clear triggering of other active faults of the area (clusters 2, 3 and 4 in Figure 1.11), or distributed seismicity in neighboring regions (cluster 5). While these

aftershocks are relatively small in magnitude, they clearly demonstrate the presence of stress triggering from the mainshock.

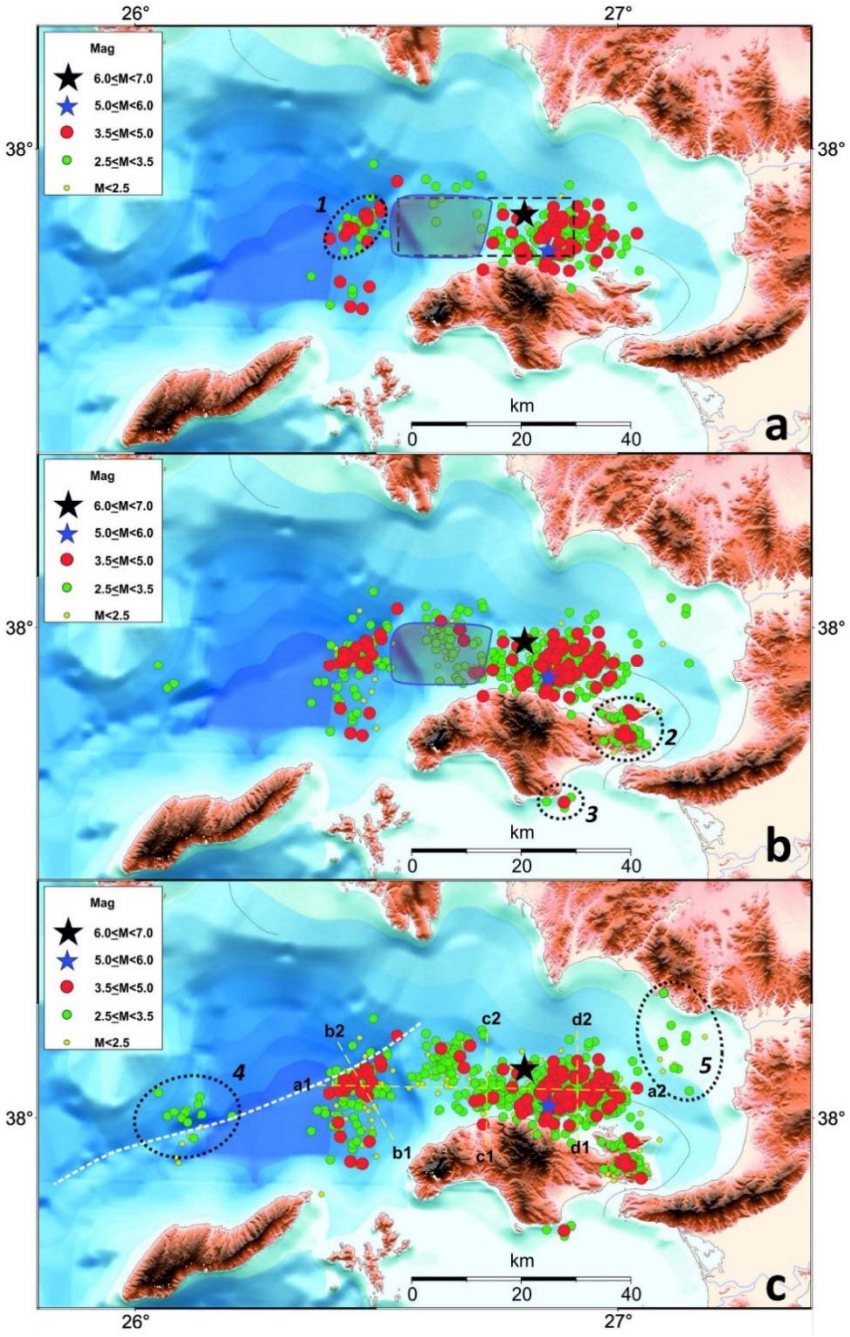

Figure 1.11. Spatial distribution of the relocated **M**7.0 2020 aftershock sequence, including 989 events with best locations: a) 1st day, b) 1st week, c) 1st month. The gap in the aftershock sequence during the first 24h and the adopted fault geometry for the final finite-fault modeling are depicted with blue solid-line (in *a* and *b*) and black dashed-line polygons (*a*), respectively. Several off-fault secondary seismicity clusters are depicted with numbered dotted-line ellipses (*see text for details*). The morphotectonic feature (canyon) associated with clusters 1 and 4 is also depicted with a yellow dashed line in c.

Figure 1.12 presents the depth distribution of the relocated aftershock sequence along the selected cross-sections shown in Figure 1.11c.

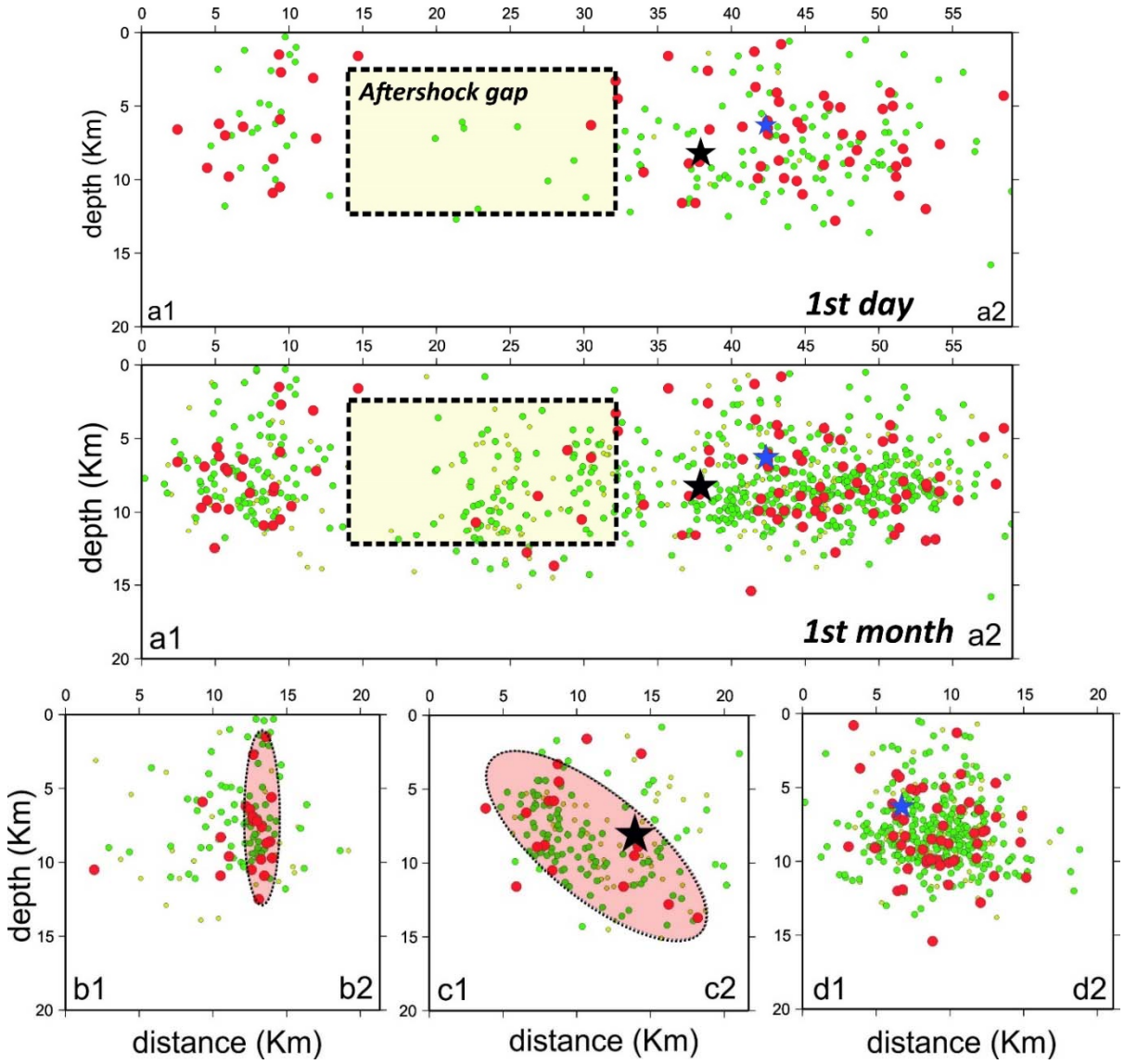

Figure 1.12. Depth plots of the aftershock sequence along the selected cross-sections shown in Figure 1.11c for the first month of the aftershock sequence. The along fault cross-section (a1-a2) is also presented for the first day (top plot) of the sequence. In both plots along fault plots (a1-a2) the area of low-aftershock seismic activity is depicted by a dashed polygon. We can also identify the off-fault activity of cluster 1, which occurred along a nearly vertical strike-slip fault (see section b1-b2). While the overall fault dip to the north is recognized for the western part of the fault (section c1-c2), the aftershock seismicity in its eastern segment is more diffuse, suggesting the secondary triggering of several small-scale structures (section d1-d2).

Aftershocks extend from ~1km up to the depth of 11-12km, slightly shallower that the initial locations of Figure 1.9, in better agreement with the finite-fault modes later presented. In the

along fault cross-section (a1-a2) for the first day after the mainshock, we can identify the area of low aftershock seismic activity (dashed-line polygon). When the same cross-section is considered for the first month of the seismic sequence, this "gap" area is partially filled with aftershocks. In the same along-fault depth cross-section, we can identify the off-fault activity of cluster 1 (see Figure 1.11a), which occurred along a nearly vertical fault (see section b1-b2) that was also activated during the first day. This cluster is most probably a trans-tensional feature, with significant dextral strike-slip motion, as indicated by the fault-plane solution information (e.g. Figure 1.14), as well as the fault geometry, which is very similar with the trans-tensional dextral Fourni Fault (FF) and the similar Karlovasi-Drakeon Faults (KDF) to the south.

Regarding the fault geometry, while a clear dipping of the seismic activity at an angle of ~45^{o} is recognized for the western part of the fault (cross-section c1-c2), the aftershock seismicity along its eastern segment is much more diffuse (section d1-d2), even during the initial phase of the sequence. This rather "fuzzy" pattern indicates the possible secondary triggering and activation of several small-scale fault structures at the eastern edge of the fault. This is supported by the gradual change from the more normal fault plane solutions (FPS) that characterize the central fault segment, to the more strike-slip dominant FPS seen along its eastern edge, as is depicted in Figure 1.14.

1.3.2 Focal mechanisms

Mainshock. The published focal mechanisms for the mainshock, from a number of agencies (Table 1.1), converge on the activation of a normal fault that strikes mainly E-W and is connected with pure dip slip (the strike-slip component was in most cases very weak). The strike angle of the fault plane that dips to the north varies from 260° to as much as 294°. The dip angle of this north dipping fault plane varies from 29° to 55°. The mean mechanism is s/d/r = 274°/43°/-88°.

Table 1.1 Published moment tensor solutions for the mainshock (ordered in ascending dip angle).

Origin Time	Lat°N	Lon°E	H (km)	Mo (Nm)	**M**	strike	dip	rake	strike	dip	rake	Agency
11:51:44	37.80	26.70	12f	4.09e+19	7.0	275	29	-87	93	60	-91	USGS
11:51:26	37.90	26.80	14	3.76e+19	7.0	260	36	-116	111	58	-72	IPGP
11:51:34	37.80	26.70	12f	4.01e+19	7.0	270	37	-95	96	53	-86	GCMT
11:51:26	37.80	26.80	11	3.90e+19	7.0	289	40	-69	82	53	-107	INGV
11:51:26	37.90	26.80	10	--	7.2	275	45	-96	103	45	-85	OCA
11:51:24	37.90	26.80	11	3.26e+19	6.9	270	46	-91	95	43	-87	AFAD
11:51:27	37.90	26.80	15	3.50e+19	7.0	272	48	-93	97	41	-85	GFZ
11:51:26	37.90	26.80	13	2.81e+19	6.9	270	50	-81	76	41	-101	UOA
11:51:24	37.90	26.81	6	2.65e+19	6.9	294	54	-65	76	43	-120	NOA
11:51:27	37.90	26.80	10	3.00e+19	6.9	272	55	-93	97	34	-85	KOERI

Aftershocks. Focal mechanisms of 28 major aftershocks (**M**≥3.7) were determined (Table S2 - Appendix and Figure 1.13) from routine analysis (SL-NKUA), using data only from Greek networks. The fault plane solution of the largest aftershock (**M**5.0) that occurred a few hours after the main event (30 October 2020 15:14:57 UTC), is similar with the mainshock, (264°/37°/-126°), with a centroid depth of 15 km. The average source parameters for the aftershocks, as determined from the distribution of strike, dip and rake angles, seem to agree with the modeling results for the mainshock, indicating E-W to WNW-ESE, almost pure dip-slip normal faulting. It should be noted that the herein presented results for the focal mechanisms are still preliminary and subject to revision, where possible, with additional data from stations mainly located at Turkey to reduce contingent effects of the current azimuthal bias.

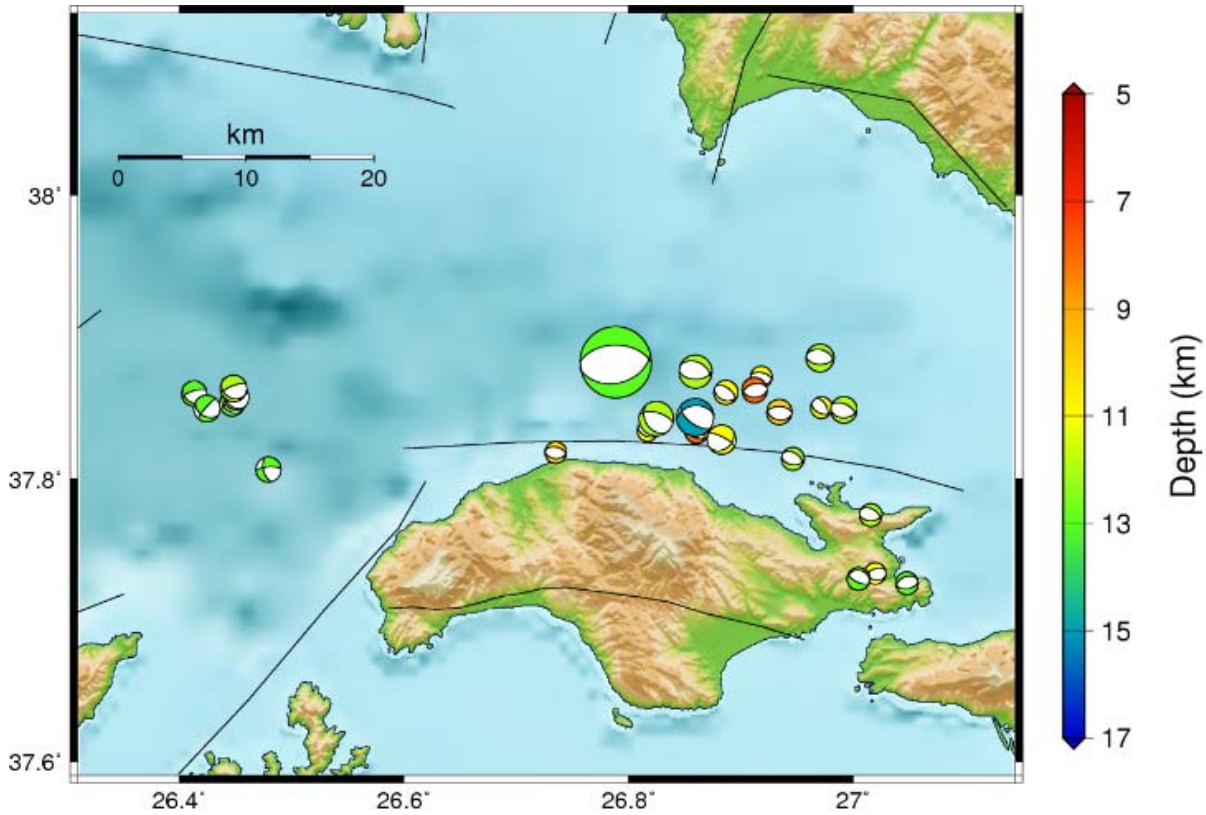

Figure 1.13. Focal mechanism solutions of the 2020 Samos mainshock and 28 major aftershocks (**M**≥3.7). Beach-ball locations are from the preliminary epicentral locations of routine analysis at SL-NKUA.

Another set of moment tensor solutions for major aftershocks, obtained using regional data from stations on Turkey, was determined by Altunel and Pınar (2020), listed in Table S3-Appendix and shown in Figure 1.14. The aftershocks investigated in these analyses are largely the same as those evaluated using the Greek data.

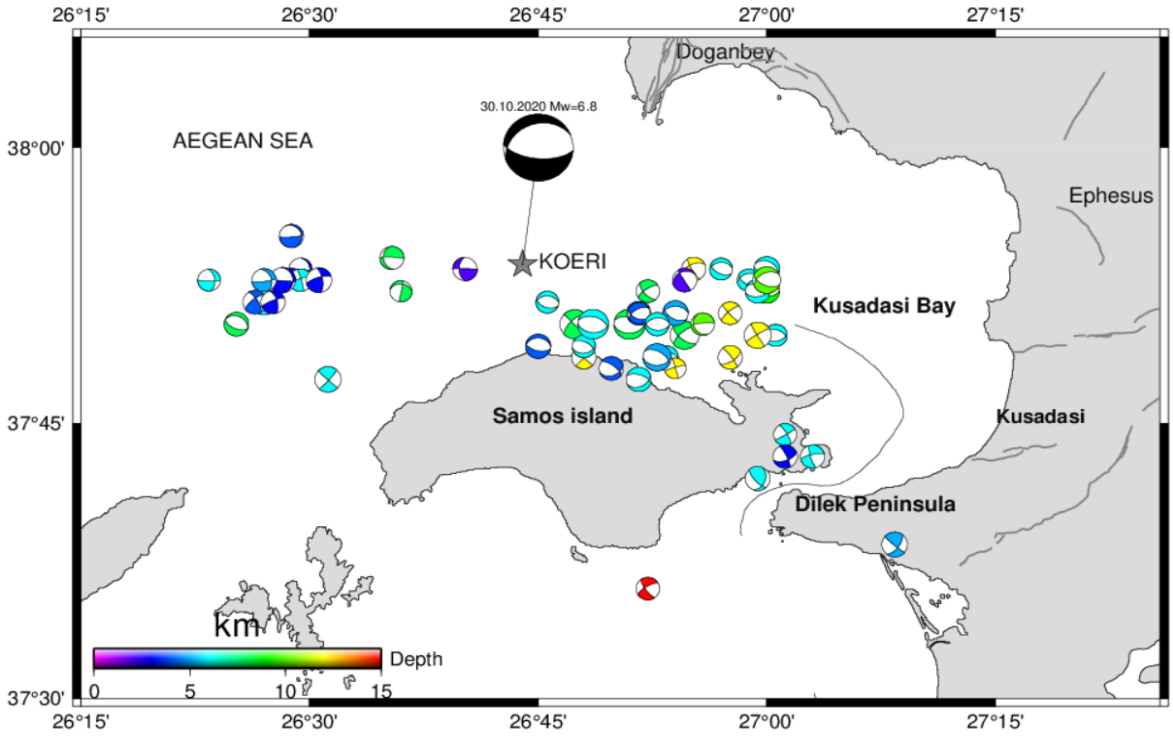

Figure 1.14. Focal mechanism solutions of aftershocks around Samos Island until November 11, 2020 by Altunel and Pınar (2020) (mainshock epicenter and aftershock locations are also from the KOERI database).

Comparison of Figures 1.13 and 1.14 shows several similar features, but also some differences. More specifically, all events show an N-S extension, with the majority of events being normal with more or less E-W striking fault planes. However, a large number of strike-slip events exist in Figure 1.14, mainly on the mainshock rupture edges, in agreement with regional tectonics, as well as the relocated seismicity distribution. This observation suggests that *it is necessary to perform similar computations using waveform data from both Greek and Turkish networks, in order to obtain more robust and reliable Fault Plane Solution (FPS) information for similar, along-border seismic sequences.*

1.4 Finite Fault Models: Seismic Results

An earthquake invokes slip over a fault area rather than at a point. The amplitude of the slip and the dimensions of the area that slipped, scale with the magnitude of the event – in fact, seismic moment is the product of slip, fault area, and shear modulus, a variable related to the geophysical properties of rock in the earthquake source region. The slip magnitude and extent of the area are usually modeled through a "finite fault inversion", which uses digital waveforms to reconstruct the slip history onto the fault plane. The resulting "finite fault models" can be static (if using non-continuous geodetic data, like InSAR, campaign or low sample rate GPS data) or kinematic (using seismic, high-rate GPS or tsunami data). The shaking caused by an earthquake is related to the

spatial extent of slip on the fault. This and the next section examine finite fault models for the Samos mainshock.

1.4.1 Teleseismic modeling

The inversion scheme employed for finite-fault models is described by Yoshida et al. (1996), Yagi and Kikuchi (2000) and Yagi et al. (2003). The data are digital recordings of teleseismic P- body waveforms, which are clearly visible at 41 seismic stations (Figure 1.15), retrieved from the Global Seismic Network (GSN). The data were band-passed between 0.01 and 0.5 Hz using a zero phase-shift Butterworth band-pass filter to remove long-period drift and high frequency noise, and subsequently converted to ground displacement. Data and synthetics (Green's functions) were sampled at dt= 0.2 s.

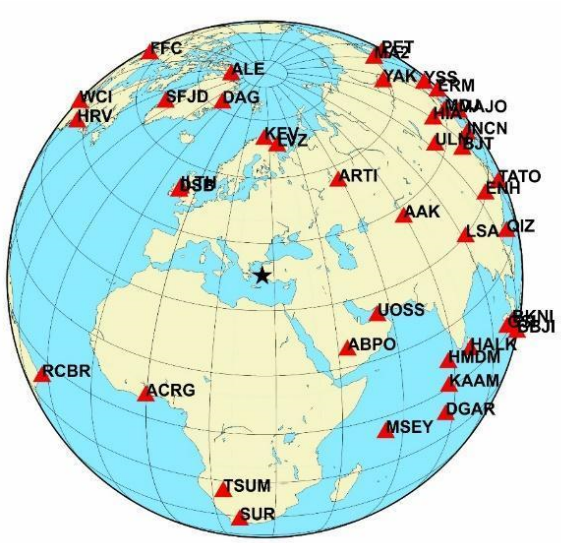

Figure 1.15. Teleseismic stations that were used in waveform inversion. Black star indicates the epicenter of the 30 October 2020 **M**7.0 earthquake.

The basic modeling assumptions include rupture propagation along a single fault, while the adopted fault parameters are from the GCMT solution and the hypocenter parameters from KOERI. For the discretization of the region to be modelled, an optimal fault dimension with a total number of 60 sub-faults were selected, with grid sizes of 5 km x 5 km, consisting of 12 sub-faults in the strike direction and 5 sub-faults in the dip direction. It was assumed that the rupture started at the hypocenter. The Green's functions were calculated as in Kikuchi and Kanamori (1991) and the Jeffrey's-Bullen model, with an additional water layer of 0.5 km. The slip rate function of each sub-fault is expanded into a series of 12 triangle functions, with a rise time of 1.0 s. A rupture velocity of 3.2 km/s was also selected by trial and error in order to determine the initiation time of the basis function at each sub-fault.

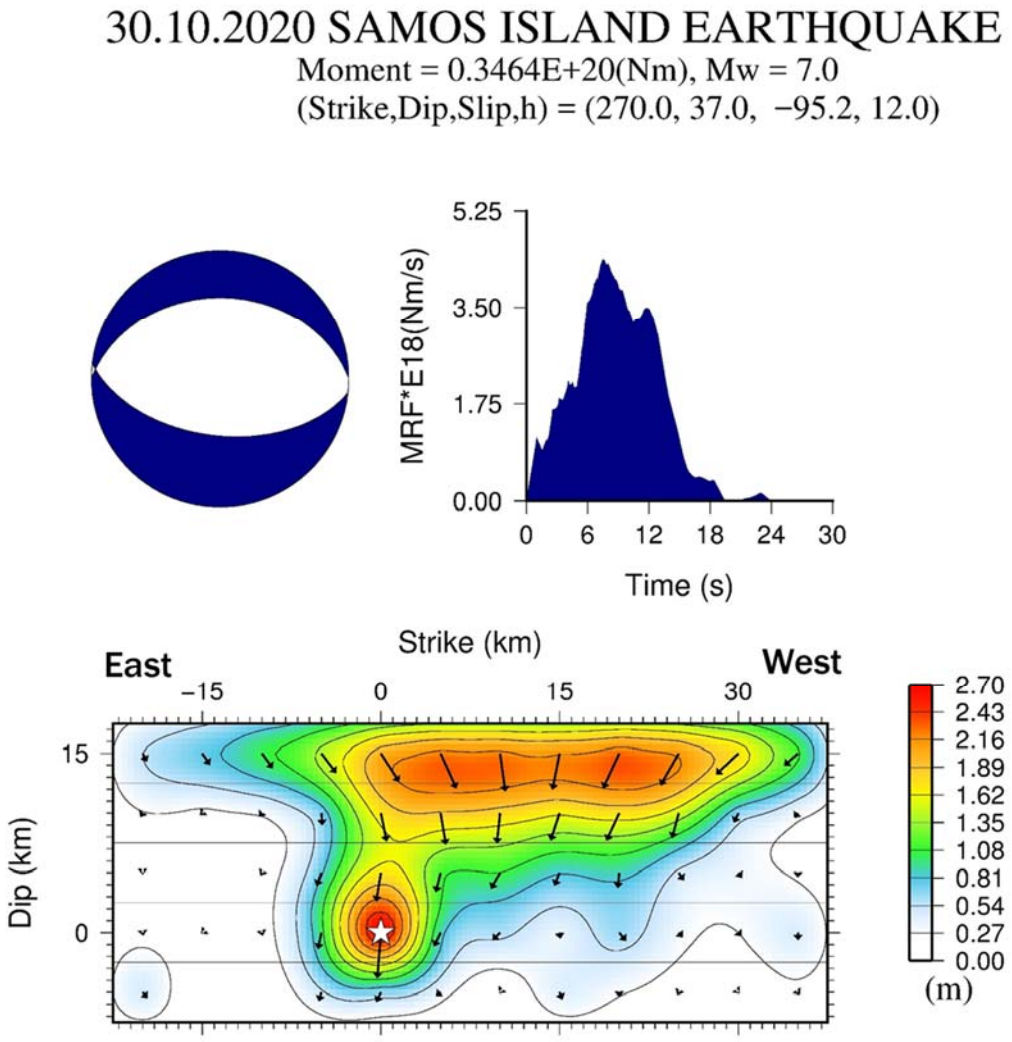

Figure 1.16. Focal mechanism, moment-rate function, and co-seismic slip distribution of the 30 October 2020 **M**7.0 Samos Island earthquake for north dipping nodal plane, adopting the GCMT solution. The white star indicates the hypocenter at 12 km depth. The vertical scale near the slip model shows the displacement values in meters. Note that the major slip is located updip from the hypocenter and in the western part of the fault plane.

The slip model for the north-dipping plane is summarized in Figure 1.16. The moment release and slip distribution indicate that the rupture initiated around the hypocenter and continued bilaterally on the east-west direction but also asymmetrically, mainly towards the west. The obtained seismic moment is 3.464 x 10^{19} Nm, comparable with the seismic moment proposed by different agencies. While the largest displacement, which is around 2.7 m if the shear modulus is assumed to be 30 GPa, occurs close to the hypocenter, it is seen that the slip with large amplitudes occurs at shallow depths and towards the west. The model source duration is 19 s.

The finite fault model published by USGS for the north N276°E dipping plane (Figure 1.17), also shows a two-lobe pattern of the Moment Rate Function and the presence of double slip patches.

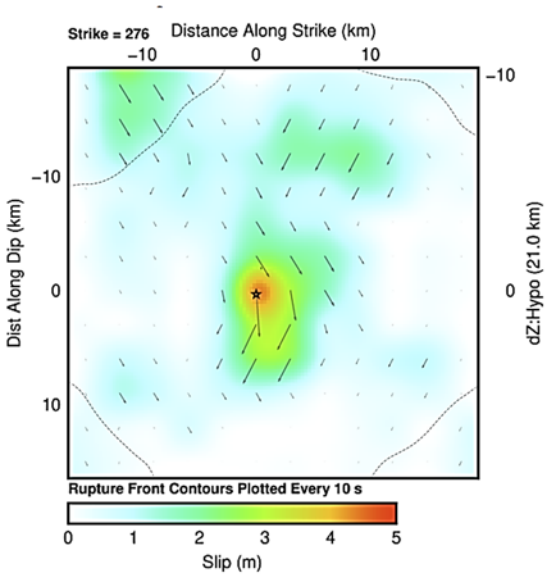

(a)

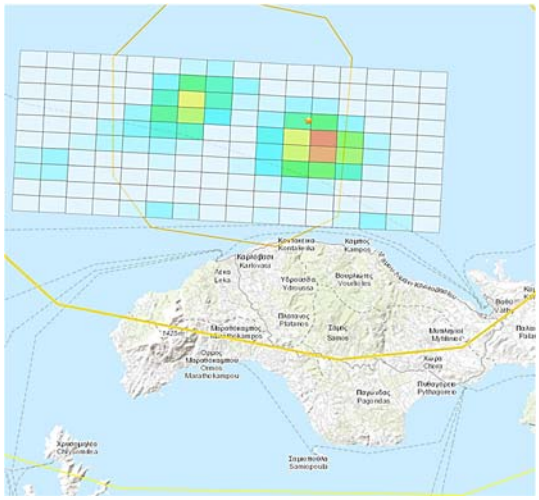

(b)

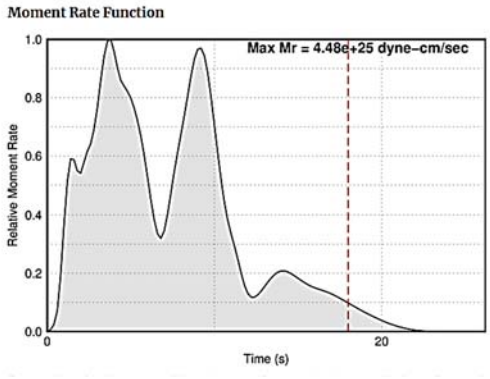

(c)

Modelling parameters:
12×12 subfaults along strike and dip, of 3 km length each.
Earthquake at cell [6,7].
Lon: 26.7953° Lat: 37.8973°
Fault coordinates:

Lon.	Lat.	Depth
26.95760	37.73800	10.93150
26.56060	37.77100	10.93150
26.59600	38.03660	29.47870
26.99290	38.00370	29.47870

(d)

Figure 1.17 Finite- fault modeling for the mainshock, as published by USGS. (a) Cross section of slip distribution. Slip amplitude is shown in color and the motion direction of the hanging wall relative to the footwall (rake angle) is indicated with arrows. (b) Surface projection of the slip (c) Moment Rate Function, describing the rate of the evolution of seismic moment after the origin time, relative to peak moment rate (maximum Mr = 4.48e+25 dyn-cm/s. (d) Modelling parameters of the USGS fine-fault model

1.4.2 Regional modeling

The mainshock was well recorded by the broadband seismic networks of Greece and Turkey, providing an excellent azimuthal coverage. 45 components were employed from stations, located in Greece and Turkey, at epicentral distances between 260 and 500 km to calculate a slip model. We adopted a non-negative least squares solver to determine the distribution of fault slip (Dreger and Kaverina, 2000; Kaverina et al., 2002). This inversion scheme has proved to provide finite source parameters that compare quite well with those obtained using local strong motion records. Original velocity waveforms were baseline corrected, tapered, corrected for the

instrument response, converted to displacement (cm), band pass filtered between 0.02 to 0.08 Hz, and re-sampled to 1 Hz. The frequency range is rather narrow and is a compromise between instrument limitations and the need to include long periods in the inversion, to limit the influence of the assumed velocity model on the inversion results. Green's functions were computed by the frequency-wave number method and the 1D velocity model of Novotný et al. (2001). This model has been found to be an appropriate representation of average crustal properties for the Aegean area, as it effectively describes regional wave propagation in the Aegean and accounts for the characteristics of the waveforms in the low frequencies used. The synthetic waveforms (Green's functions) were also filtered, between 0.02 and 0.08 Hz, similar to the real data. In the source model, the rupture propagates with constant velocity over a grid of point sources, each with constant dislocation rise time, and the Green's functions are shifted in time to account for relative hypocenter-subfault-station distances and the time for the passage of a circular rupture front. Because of the regional nature of the inversion procedure, the problem is simplified by considering only constant values of dislocation rise time and rupture velocity. We adopt the average fault strike 270° and dip 45°, while allowing the rake angle to vary between -45° and -135°. The initial fault model has dimensions that are 2 times larger from those scaled to the size of the seismic moment, to allow for bilateral rupture. Thus, a model of 65 km × 35 km was used, discretized into subfaults of 1 km × 1 km, along strike and dip, respectively. The dislocation rise time is assumed 10% of the approximate total duration, and in this parameterization, it was set equal to 1.8s. Grid searching indicated a rather low rupture speed, which was adopted equal to 1.7 km/s for the first time-window and 1.9 km/s for the second one.

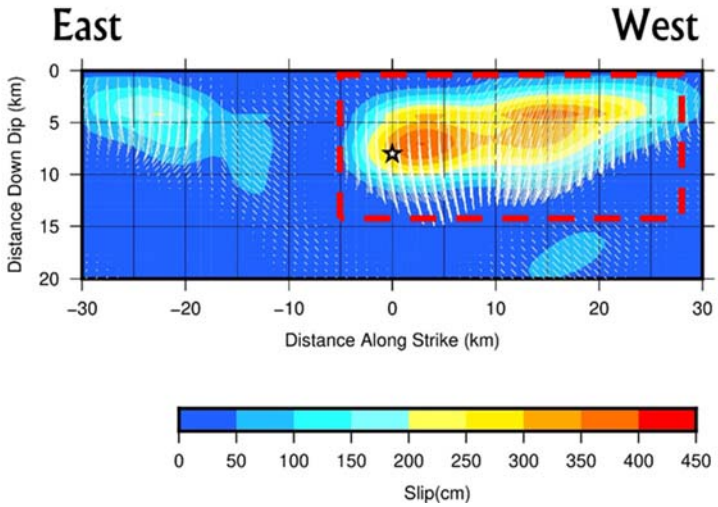

Figure 1.18. Slip distribution onto the fault plane striking N270°E and dipping 45° to the north. The largest slip is confined in a two-lobe asperity (dashed rectangle) updip from the hypocenter (asterisk) reaching very shallow depths, close to the sea-bottom surface. The white lines denote the motion direction of the hanging wall relative to the footwall (rake angle).

Figures 1.18 and 1.19 summarize the preferred slip model, using the regional waveform data. While this slip distribution should be considered as preliminary, as additional modeling and data,

(e.g. strong motion, geodetic) are required to better constrain its detailed features, the spatial distribution presented in Figure 1.19 shows an excellent anti-correlation with the spatial distribution of the largest relocated aftershocks (**M**≥3), and the epicenter where rupture initiated. More specifically, this model two major slip episodes to the west of the hypocenter, similar to the models in Figures 1.16 and 1.17, and in agreement with the aftershock "gap" (especially for the first 24h) previously presented (e.g. Figure 1.11). If any directivity is associated with this earthquake, then it is mainly towards west and less to the east, where a weak asperity is also observed.

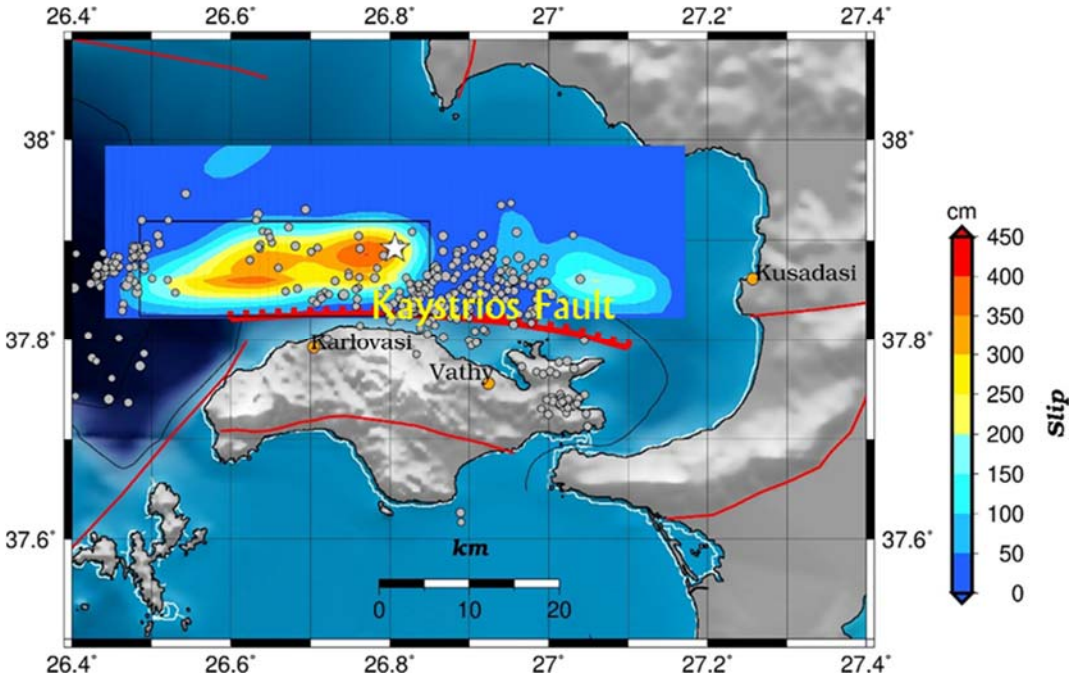

Figure 1.19. Surface projection of slip distribution, as obtained from the inversion of regional broadband waveforms. The main rupture is located to west of the epicenter, supporting directivity to the west (if any), while the easternmost asperity, a stable feature in all the inversions, probably indicates activation of secondary faults, during the propagation of the main rupture. Plotted grey circles are all aftershocks of the sequence up to 1 Dec 2020 with **M**≥3.0. The area that slipped during the mainshock remained depleted from seismicity, suggesting that the expected afterslip will be rather limited. The rectangle corresponds to the fault geometry as given in Table 1.2. From the spatial distribution of slip is evident that the inferred Kaystrios Fault extended more towards west, than it was originally considered.

1.4.3 Finite - fault model parameters based on the seismic data

Table 1.2 summarizes the main information on the geometry of the fault, based on seismic data interpretation. While several small-scale differences exist between all available models, the table presents a reliable working model that can be employed for further processing.

Table 1.2. Summary of the geometry of the fault based on seismic data. Upper left corner of fault is as viewed from hanging wall.

Parameter	Value
Hypocenter parameters (relocated AUTh)	Origin Time: 2020-10-30T11:51:25.20 Coordinates: 37.8919°N, 26.8066° E hypocenter depth = 8.2 km
Seismic Moment	4.01e19 Nm (GCMT)
Moment magnitude, M	7.0
Subsurface rupture length × Downdip rupture width	32 km ×15 km
strike/dip/rake of the fault (dips to N)	**270° / 45° /-89° (variable rake)**
Location of upper left corner of fault (east)	37.824°, 26.850°, 0.6 km
center top coordinates	37.82° / 26. 65°
coordinates of the fault rectangle as projected to the surface (32×15)	Upper (W) 37.824/26.485 Upper (E) 37.824/26.850 Bottom (W) 37.919/26.485 Bottom (E) 37.919/26.850
Z TOR	0.6 km (± 1 km)
Z BOT	11.2 km
rupture propagation	stronger propagation to the west, where the major slip patches are observed
Average displacement	1m (entire fault); 2.5 m (if Mo confined to the major asperity)
Maximum displacement	3-6m

1.5 Finite Fault Model: Geodetic Results

1.5.1 Sentinel-1 interferograms

We used the ascending and descending images acquired by the European satellites Sentinel-1 on October 24, October 30 and November 5, 2020 on the tracks 131 and 36. The initial co-seismic interferogram (Figure 1.20), was generated on the Geohazards Exploitation Platform (https://geohazards-tep.eu) using the online SNAP InSAR service (e.g., Foumelis et al. 2019), while the following interferograms (Figure 1.21) were generated using the GAMMA s/w package (Wegnüller et al., 2016). The digital elevation model (DEM) used for the processing is the Shuttle Radar Topography Mission (SRTM) 1 Arc-Second Global (Digital Object Identifier number: /10.5066/F7PR7TFT). We enhanced the signal to noise ratio by applying the adaptive power spectrum filter of Goldstein and Werner (1998) with a coherence threshold of 0.3. The quality of the interferograms is good, in terms of both coherence and tropospheric noise. There is consistency between independently generated interferometric measurements. The co-seismic differential interferogram, (Figure 1.20), shows six fringes corresponding to ground deformation onshore Samos. The absolute value (in mm) of the interferometric fringes is estimated by the tie to the permanent GNSS stations SAMO (Karlovasi) and SAMU (Vathy) that captured the co-seismic displacement (Ganas et al., 2020). All fringes correspond to motion towards the satellite (i.e. uplift of ground surface) except in one area located by the northern coast where the motion

is away from the satellite. The uplift is interpreted because of footwall co-seismic motion along an offshore normal fault, running E-W and dipping to the North. For the interferograms generated using scenes acquired 5 days after the event (on November 5, 2020), a slight increase of uplift was observed (Figure 1.21).

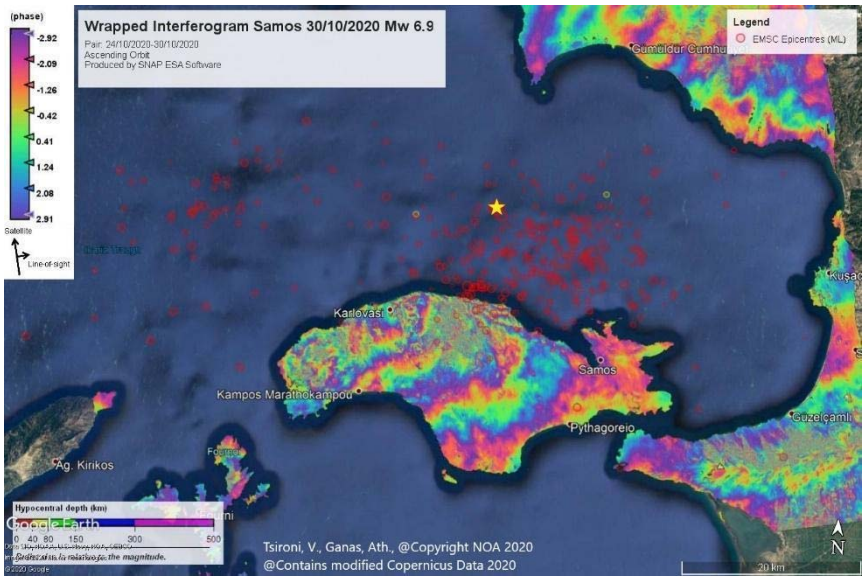

Figure 1.20. The coseismic differential interferogram (wrapped phase; cropped swath) over Samos Island. The image shows the image pair Oct. 24-Oct.30, 2020 (Sentinel-1 ascending orbit).

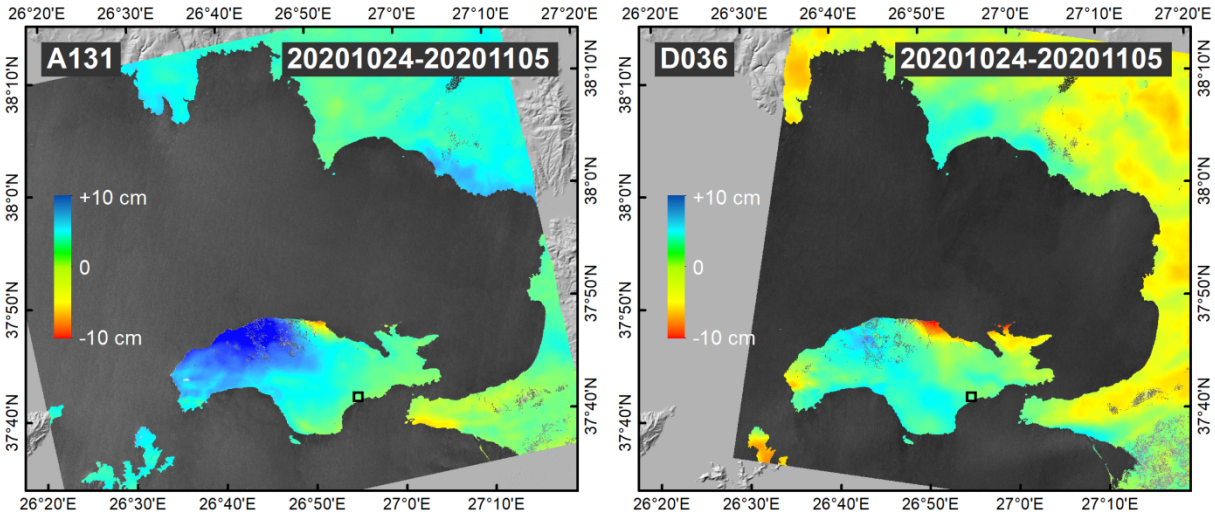

Figure 1.21. Sentinel-1 differential interferograms (unwrapped phases; cropped swath) over Samos Island, using Oct. 24 and Nov. 5, 2020 image pairs acquired at different timing (on 16:06 and 04:15 GMT for ascending 131 and descending 36 tracks, respectively). Local reference point is marked (black square).

1.5.2 GNSS data

Dual-frequency GNSS data from eighteen (18) permanent (continuously recording) GNSS stations were analyzed. The GPS data cover approximately one week before and after the earthquake (25 October 2020 to 11 November 2020; Table 1.3 and Figure 1.22). The stations belong to the NOANET (Ganas et al. 2008), and SmartNET networks of Greece and the Turkish National Permanent GNSS/RTK Network. The distribution of the GNSS stations is relatively optimal, as it extends mostly around the epicentral area but most of them are located about 50+ km away from the deformed area as mapped by InSAR (Figure 1.22). The sampling interval was 30-s, and the data were collected on a 24 h basis. All station records were complete (rejected epochs 0.00%), thus providing substantial observations for mapping the co-seismic displacement field and were included in our analysis. The daily positions are estimated in ITRF14 (epoch 2020.8) and converted to UTM (North) zone 35. The position uncertainties were converted onto the local geodetic frame, based on the given Cartesian (ECEF) sigma (95%) ones. The uncertainties on the vertical component exceeded by far the horizontal ones therefore there were disregarded from further analysis (with the exception of station SAMO).

Table 1.3. List of co-seismic offsets (North, East, Up) of GNSS time-series of positions determined by PPP processing (see Figure 1.22 for locations). S denotes uncertainties. Errors in U-component can reach one order of magnitude with respect to N, E.

STATION	LAT (°)	LON (°)	N (mm)	SN (mm)	E (mm)	SE (mm)	U (mm)	SU (mm)
CHIO	38.3679	26.1271	22.444	0.146	-7.884	0.252	1.035	4.406
CESM	38.3038	26.3725	53.621	0.144	-12.220	0.246	2.433	4.527
IZMI	38.3948	27.0818	34.957	0.151	12.735	0.242	1.234	4.557
IKAR	37.6282	26.2242	-33.440	0.055	-10.337	0.167	6.305	5.074
SAMO	37.7927	26.7053	-373.949	0.123	-61.901	0.202	91.903	4.778
DIDI	37.3721	27.2686	-10.135	0.134	0.577	0.214	2.490	4.557
KALY	36.9558	26.9761	-9.176	0.166	1.952	0.155	-8.413	4.988
MYKN	37.4416	25.3290	0.139	0.146	-0.678	0.230	0.519	5.048
ANDR	37.8863	24.7370	7.089	0.129	3.899	0.276	-16.100	4.632
ASTY	36.5451	26.3533	-5.917	0.126	-3.059	0.206	-3.724	6.843
LESV	39.1000	26.5537	10.427	0.186	0.088	0.158	-2.923	4.467
NAXO	37.0981	25.3811	-2.326	0.106	-1.733	0.229	-1.274	3.764
PRVK	39.2457	26.2650	7.560	0.238	-0.345	0.244	-5.350	4.668
RODO	36.2926	28.1616	0.198	0.135	0.737	0.184	-5.557	3.955
AYD1	37.8407	27.8378	1.664	0.204	-1.720	0.163	0.721	4.836
DATC	36.7085	27.6918	-3.388	0.067	-1.641	0.206	-6.037	5.128
MUG1	37.2142	28.3556	1.079	0.137	-1.397	0.196	0.116	4.591
SALH	38.4830	28.1235	3.068	0.232	-0.445	0.089	-3.335	4.931

Each station has been analyzed independently using the Precise Point Positioning (PPP) method, which computes the coordinates of each station separately (Zumberge et al., 1997). We used the

Canadian Spatial Reference System-PPP (CSRS-PPP) online processing tool. Elevation-dependent solutions have been obtained using an elevation mask of 7.5° and final precise orbits (IGS14) and clock data (sp3 and clk files) computed at the EMR IGS Analysis Centre daily, providing additional information compared to conventional final IGS products. The ionosphere-free linear combination was used for the elimination of the ionospheric influence. The tropospheric zenith delay was estimated using a dynamic filter, and these estimates are based on the Global Mapping Function derived from the European Centre for Medium-Range Weather Forecasts numerical weather model (Mireault et al., 2008). The static displacements (offsets) were obtained from the difference between trend lines -best fitting to time series of pre-seismic coordinates (5 days before) and of post-seismic coordinates from 9 to 12 days after (data from the day of the earthquake was ignored; see graph in Figure 1.23 for the case of station SAMO). The co-seismic uncertainties were calculated the same way as the displacements, following the propagation of error law (Taylor, 1997). The time series of station coordinates indicate significant, horizontal co-seismic displacements with a maximum of 37.3 cm at SAMO (motion towards south; location Karlovasi), 20 km away from the epicenter (Figures 1.22-1.23, and Table 1.3). Station IKAR (Ikaria Island) moved ~3.3 cm towards south and ~1 cm towards west while stations CESM and IZMI (in Turkey) moved ~5.3 cm and ~3.4 cm towards north, respectively. All displacements are compatible with surface deformation due to seismic slip along an E-W oriented, north-dipping normal fault embedded in an elastic medium.

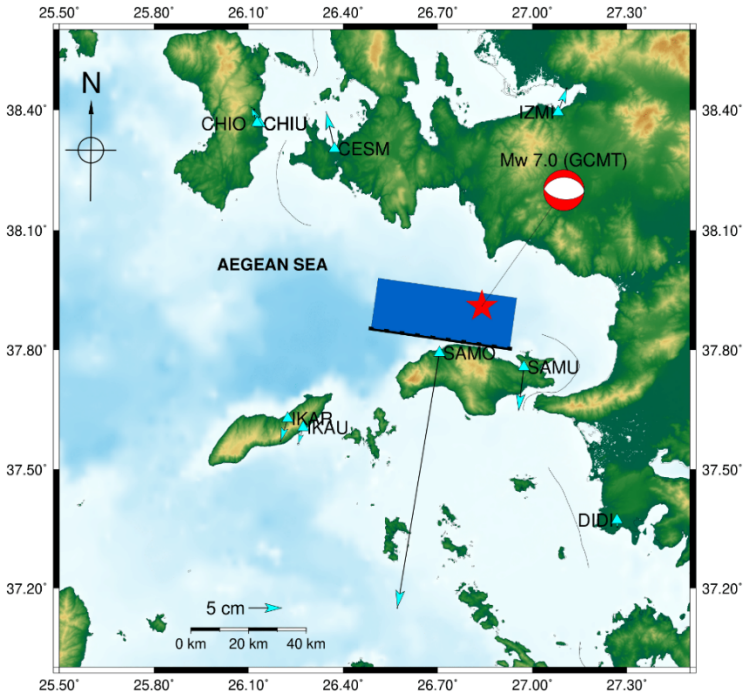

Figure 1.22. Location map showing the north-dipping seismic fault plane (shaded rectangle), the focal mechanism (beachball, compressive part in red; GCMT solution) and the EMSC epicenter of the Samos October 30, 2020 earthquake. Triangles indicate permanent GPS (GNSS) station locations. Blue vectors indicate co-seismic horizontal displacements (see 5-cm scale bar at lower right).

A **M**7.0 shallow earthquake is expected to cause permanent ground displacements of a few cm at distances up to 150-km from the epicenter (see Ganas et al. 2018 for ground displacement scaling with magnitude). The seismic fault parameters determined from the joint inversion of GNSS and InSAR data (Ganas et al. 2020) are given in Table 1.4. The upper edge of the fault is found 2.5 km north of the coast of Samos at a depth of 0.9 km.

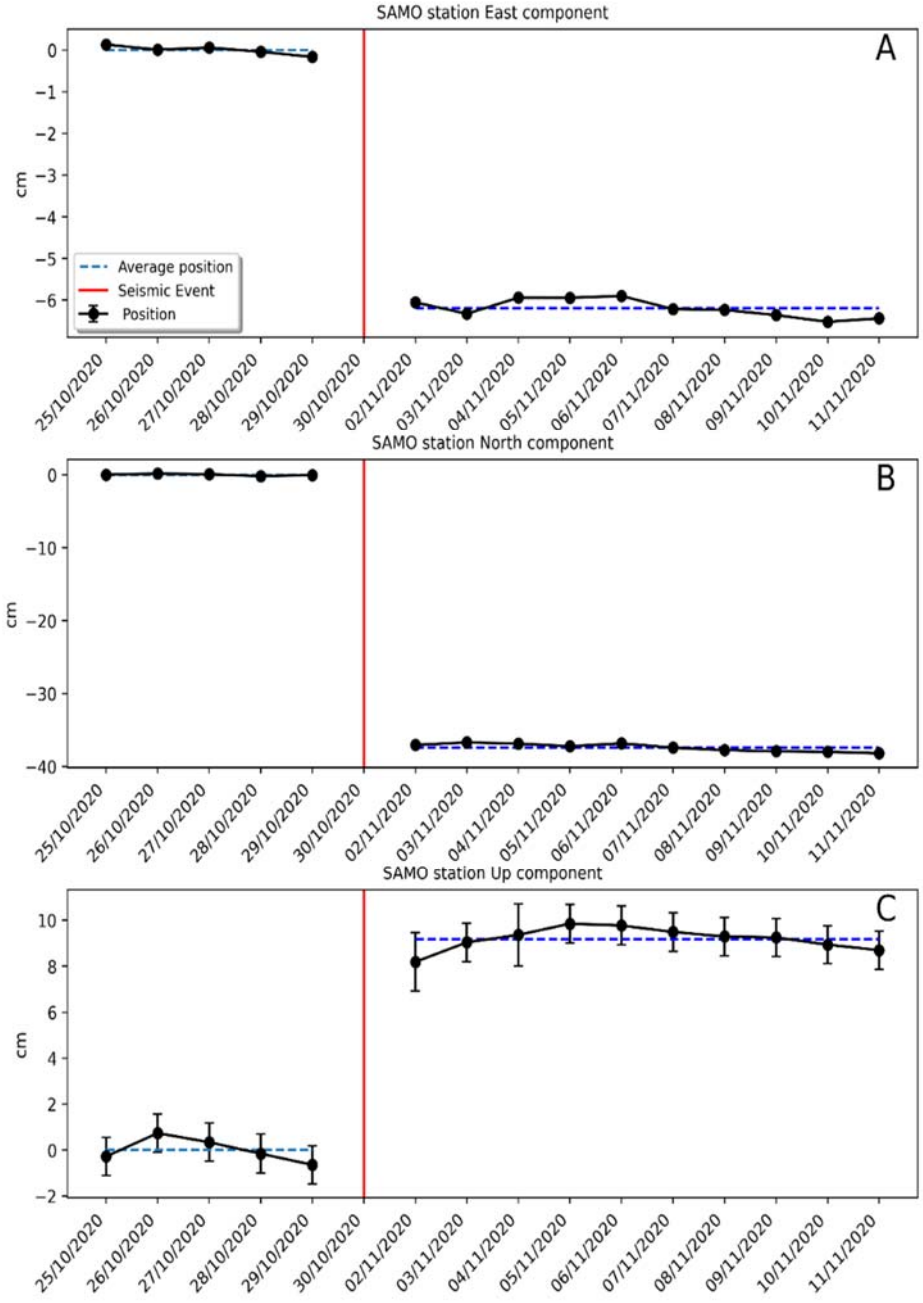

Figure 1.23. Position time series (E, N, Up) of station SAMO (see location in Figure 1.22). The co-seismic offsets are approximately dE = -6 cm, dN = -37 cm and dU = +9 cm. The red vertical lines indicate the day of the mainshock.

1.5.3 Finite-Fault model parameters based on geodetic analysis

Table 1.4 summarizes the main information on the geometry of the fault, based on geodetic (GNSS and InSAR) data interpretation. While some differences exist this model and the one based on seismic data (Table 1.2) models, the main 1st order fault features (fault strike and type, seismic moment, depth of top fault edge, average slip, etc.) are in very good agreement.

Table 1.4. Fault model for the Samos earthquake determined from geodetic data inversion.

M_o - geodetic	**3.49e+19Nm**
M	7.0
Centre of top fault edge - LON (°)	26.707
Centre of top fault edge - LAT (°)	37.827
Depth of top fault edge (km)	0.9
Location of upper left corner (east)	26.909°; 37.812°; 0.9 km
Length - km	36
Width - km	18
Strike (°)	N276E
Dip (°)	37
Normal slip (m)	1.8 (Uniform)
Strike slip (mm)	0

1.6 Stress Changes and Aftershock Activity Response

The **M**7.0 Samos mainshock is the largest earthquake in the eastern Aegean over the past 50+ years. Social concerns and scientific interest require an urgent evaluation of its implications and part of this evaluation is aftershock activity associated with stress transfer from the mainshock to neighboring regions. The clear increase of aftershocks in certain locations because of the Coulomb stress increase due to the coseismic slip is discussed here. The computed stress changes are predominantly positive in the areas accommodating most of the aftershock activity, with the largest stress increase of several bars, as estimated on the aftershock hypocenters.

The results imply that static stress driven activation of secondary faults in a local fault network should be anticipated in the case of a large earthquake occurrence, an implication suggesting that stress triggering must be considered for any seismic hazard assessment for the aftershock sequence and triggered postshocks.

1.6.1 Methods and data

Aftershock spatial and temporal distribution is controlled by the static stress changes produced by the slip of the main shock (King et al., 1994; Stein, 1990). The correlation between the increased positive static stress changes is remarkable with the off-fault aftershocks in particular (e.g. Papadimitriou et al., 2017). This influence is discernible in the postseismic seismic activity within the distance of static triggering, which corresponds to one or two source dimensions (Richards–Dinger et al., 2010). The closeness to failure is quantified by using the change in Coulomb Failure Stress (ΔCFS). This change depends upon both changes in shear stress, Δτ, and normal stress, Δσ, and for encountering the presence of pore fluid it takes the form:

$$\Delta CFS = \Delta\tau + \mu_f(\Delta\sigma + \Delta p) \tag{1.1}$$

where Δτ is the shear stress change (computed positive in the slip direction), Δσ is the normal stress change (positive for unclamping), Δp is the pore pressure change within the fault, and μ_f is the dimensionless friction coefficient, which for dry conditions takes values between 0.6 and 0.8 (Harris, 1998 and references therein). In our calculations we ignore the time–dependent changes in pore fluid pressure and consider only the undrained case (Beeler et al., 2000), meaning that Δp depends on the fault–normal stress whereas the fluid mass content per unit volume remains constant. Induced changes in pore pressure resulting from a change in stress under undrained conditions are calculated according to Rice and Cleary (1976) from:

$$\Delta p = -B\frac{\Delta\sigma_{kk}}{3} \tag{1.2}$$

where B is Skempton's coefficient ($0 \leq B < 1$), and $\Delta\sigma_{kk}$ the summation over the diagonal elements of the stress tensor. If air fills the pore space then B is nearly zero, whereas if water fills the pores, it is typically between 0.5 and 1.0 for fluid saturated rock and close to 1.0 for fluid–saturated soils. Sparse experimental determinations of B for rocks indicate a range from 0.5 to 0.9 for granites, sandstones, and marbles (Rice and Cleary, 1976). $\Delta\sigma_{kk}$ along with Δτ are calculated according to the fault plane solution of the target fault, whose triggering is inspected. A positive value of ΔCFS for a particular fault denotes movement of that fault towards shear failure (that is, likelihood that it will rupture in an earthquake is increased). The shear modulus and Poisson's ratio were fixed at 3.3×10^5 bar and 0.25, respectively, in the employed calculations.

The calculation of the static stress changes requires a well-constrained coseismic rupture, and accurate aftershock relocation for the spatial correlation between the spatial distribution of the static stress changes and aftershock spatial distribution. In this respect, we initially present results for a simple rupture (uniform coseismic slip) and later include results for a variable coseismic slip model, to better model the generation especially of on-fault aftershocks.

1.6.2 Uniform slip model

The finite fault model utilizing seismic recordings from regional distance (Section 1.3.2) revealed

that the main slip asperity is located to the west of the hypocenter. The simplified rupture model of uniform slip proposed from seismic data (Table 1.2) is utilized to model the change in Coulomb Failure Stress (ΔCFS) on the major asperity using the Coulomb 3.3 software (Toda et al., 2011). For this preliminary model, a fault with a length (L) of 32 km and down-dip width (W) of 15 km is assumed to rupture uniformly during **M**7.0 earthquake with an average slip within the asperity of 2.5 m and an effective coefficient of friction μ=0.4. An almost pure normal faulting mechanism is considered along a north-dipping rupture plane (ϕ_1=270°, δ_1=45°, λ_1=-89°). As mentioned before, both strike-slip and normal faults display seismic activity in the region. This trans-tensional regime may lead to highly variable maximum principle stress direction estimates and thus a regional stress tensor is not included in our calculation, which reflects ΔCFS for receiver faults with similar kinematics as that of the mainshock.

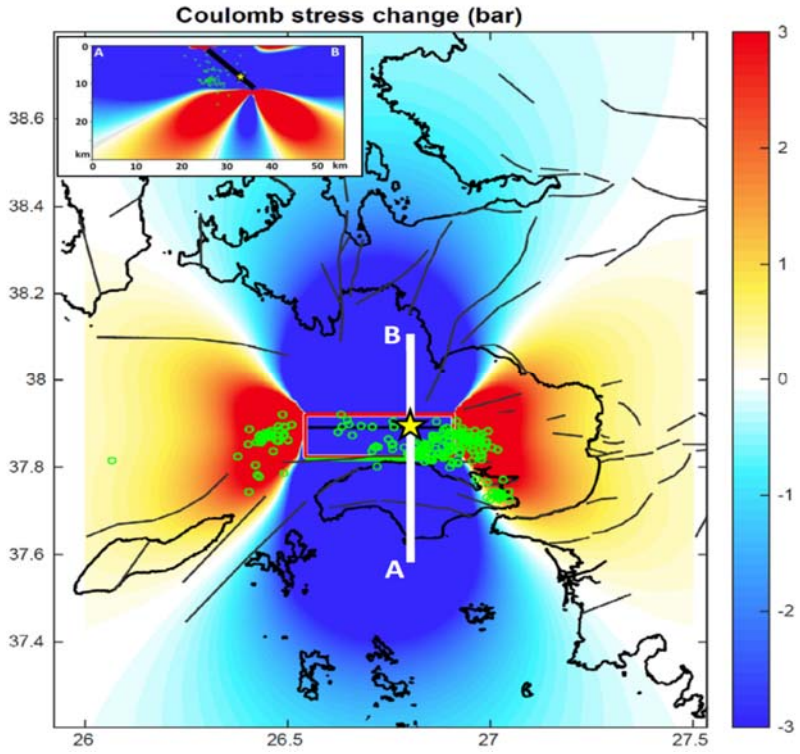

Figure 1.24. ΔCFS distribution for faults with mechanism similar to the mainshock at the depth of 8 km. The projected rupture plane is shown with red rectangle and surface trace of the fault with green line. Yellow star represents the relocated hypocenter of the mainshock. Active faults are shown with solid lines. Note that only relocated aftershocks (green circles) at depths between 6 km and 10 km are plotted in the map. Inset depicts the ΔCFS distribution along section AB (white line) cutting across the fault near the mainshock hypocenter in N-S direction.

The resultant ΔCFS distribution shows stress decrease towards north and south and stress loading towards west and east of the ruptured fault segment, which generally matches the spatial distribution of relocated aftershocks (Figure 1.11). This result indicates that active normal faults mapped between Gümüldür and Dilek Peninsula near Kuşadası towards coastal Turkey and active

faults on the west near the Ikaria Island and south of Chios Island and Çeşme are subjected to some degree of stress loading. Aftershock cluster in the western tip is located where static ΔCFS are highly elevated (exceeding 2 bars) and displays a strike-slip nature (Figure 1.14**;** Altunel and Pınar, 2020) which supports the possible activation of the NE-SW oriented neighboring strike-slip fault. On the other hand, the aftershock cluster located southeast of the Samos Island, is initiated after 2 days (Figure 1.12) which suggested a delayed seismic triggering at relatively more distant faults (Ozacar et al. 2020). At the eastern edge of the rupture, aftershocks are more widespread and display more complex spatial pattern that is likely linked to coseismic slip distribution. The section passing across the rupture illustrates the resultant ΔCFS at different depths near rupture plane (inset in Figure 1.24). It is worth noting that most of the relocated aftershocks are off plane, which may be due to multi-segmented rupture nature displaying noticeable variations in strike.

1.6.3 Variable slip model

The coseismic slip model of Karakostas et al. (2020; *submitted*) was used, determined with the inversion procedure described by Yagi and Kikuchi (2000), Yagi et al. (2004), and Tan and Taymaz (2006). This slip model is not presented in Section 1.4 and 1.5. 26 broadband teleseismic P-waveforms with high S/N ratio from the Incorporated Research Institutions for Seismology (IRIS) and the integrated seismograms from the 5 strong-motion stations of AFAD (Turkey) were used in the analysis. The final solution suggests a maximum displacement of 1 m, with the rupture extending westwards from the epicenter, with an area consistent with the relocated aftershock spatial distribution. While this peak displacement value is somewhat smaller than the results presented earlier, it is not critical for the overall stress change pattern.

The computed ΔCFS resolved for the faulting type of the main shock, adopted from the rapid global centroid moment tensor solution (GCMT), evidencing almost pure normal faulting, with the fault plane with strike=270^{o}, dip=37^{o}, and rake=-95^{o}. Given that the stress is a tensor that changes in space and time, it is clear that the change in the strike, dip and rake of the target fault plane and specifically the focal depth will considerably influence the spatial distribution of the ΔCFS in dip-slip faults. Here the ΔCFS are calculated at the depth of 10 km, which is considered as the mid-depth of the relocated aftershock seismicity, according to the same results (Karakostas et al., 2020). Values of μ=0.75 and B=0.5 were considered, which result in an apparent coefficient of friction $\mu' = \mu(1-B) = 0.375$.

Figure 1.25 shows the distribution of aftershock seismicity that occurred up to one month after the 2020 Samos earthquake. The on-fault aftershocks are close to areas with the higher positive ΔCFS values but not inside these areas on this map view. The off-fault seismicity is consistent with the stress-enhanced areas. At several locations, the seismicity density is remarkably higher than the rest of the aftershock area, mainly beyond the tips of the main rupture, where the positive ΔCFS obtains values between 1 and 10 bars. The good match for the eastern and western clusters indicates that the stress transfer imparted by the main shock promoted failure in

adjacent minor fault segments. For a detailed representation and a quantitative evaluation of the triggering mechanism, the ΔCFS values were calculated at each aftershock focus.

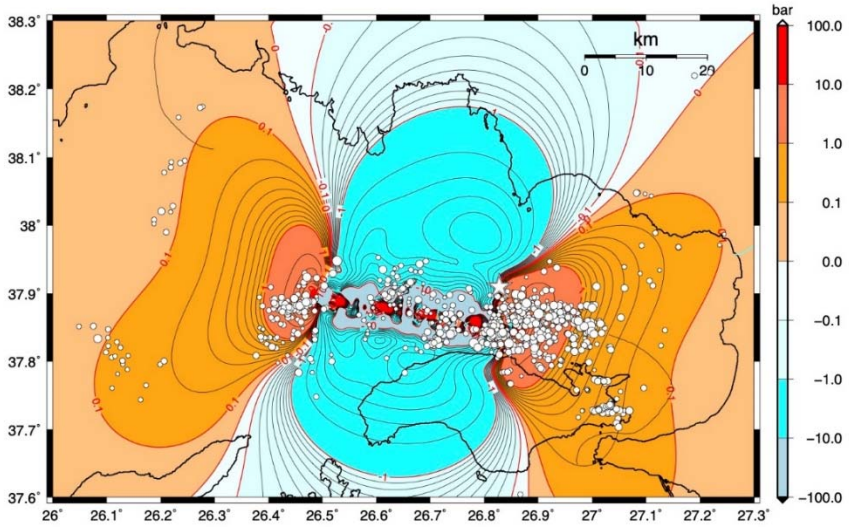

Figure 1.25. Coulomb stress changes due to the coseismic slip of the main shock calculated at a depth of 10 km. Changes are according to the color scale to the right (in bars) and by numbers in the contour lines. The main shock epicenter is depicted by a star and the aftershock epicenters by circles, scaled according to magnitude.

Figure 1.26 shows a histogram of these values for 1029 aftershocks, from which 770 (75% of the total number) correspond to positive stress changes, while 259 (25% of the total number) were generated at locations with negative Coulomb stress changes. The results presented here, based on a variable slip model for the main rupture and a relocated aftershock catalog, demonstrate that the static stress transfer plays an important role in the aftershock productivity. Off-fault aftershocks occurred in areas brought closer to failure by several bars, whereas the stronger of them occurred at short time lags.

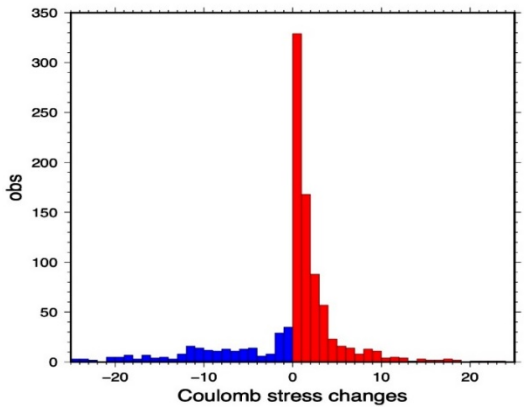

Figure 1.26. Number of aftershocks originating in areas of positive (red) and negative (blue) static stress changes (see Figure 1.25) calculated at the aftershocks' foci.

1.7 Field Observations

Field reconnaissance was undertaken to investigate possible surface rupture of regional faults and to document any evidence of tectonic uplift in coastal environments.

1.7.1 Turkish coast

Following the 30 October 2020 Samos earthquake, a two-day long field excursion took place. The main field observations points are shown in Figure 1.27.

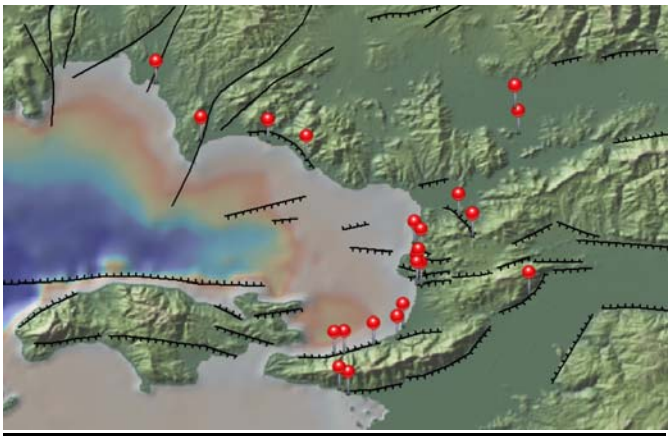

Figure 1.27. Map of field observations points with topography, bathymetry and active faults.

In the southern side of the Dilek Peninsula, young uplifted terraces are detected in the coast supporting a rapid tectonic uplift associated with active normal faulting (Figure 1.28). This location is near the Karina Lagoon, where different intercalations were deposited during tsunamis. To identify any coseismic ground deformation, in the Turkish side, the NE-SW oriented strike-slip Tuzla and Seferihisar, E-W oriented normal faults near Kuşadası, Gümüldür, Selçuk, Söke and Dilek Peninsula, were visited (Figure 1.27).

Figure 1.28. Photos taken at the southern side of Dilek Peninsula showing uplifted terrace deposits.

Figure 1.29 (a-e) shows the morphology of active Seferihisar strike-slip fault on land. At the Tuzla Fault site, geothermal alterations implying fault activity were detected. Moreover, the preserved striations identified on the fault scarp of the Tuzla fault revealed right lateral strike-slip motion, with a minor normal component (Figure 1.29c).

Figure 1.29. Photos of Seferihisar **(a)**, Tuzla **(b, c)** strike-slip faults and Söke **(d, e)** normal fault. Red arrows show the fault trace, while the yellow arrow points out to geothermal fluids coming from the fault zone.

Among normal faults, active fault scarp photos of Söke Fault are shown in Figure 1.29 (a-e), while Figure 1.30 (a-f) display the observed scarps in Kuşadası Bay and Gümüldür coast, respectively. Fault measurements collected on the normal faults revealed extension with occasional minor strike-slip component, similar to the ruptured normal fault during the 30 October 2020 **M**7.0 Samos earthquake. Some of these fault scarps were quite close to residential buildings, however, no structural damage was identified in the nearby structures.

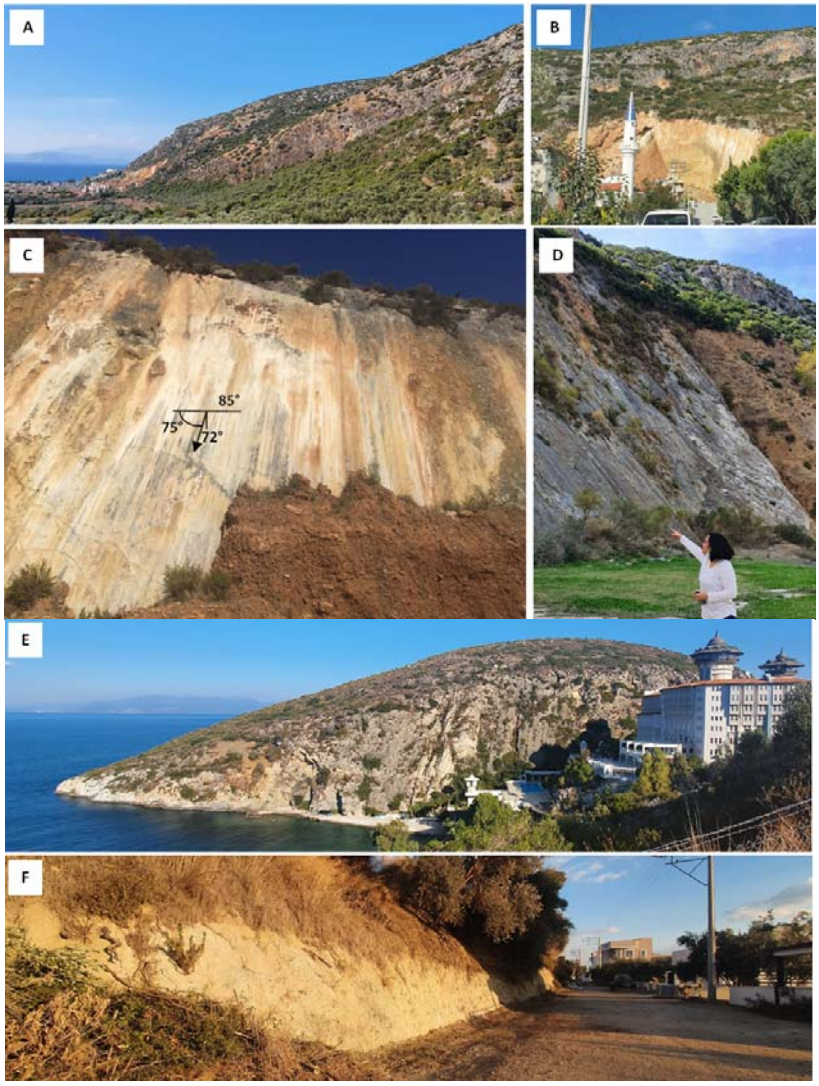

Figure 1.30. Active fault observations. Photos of south dipping normal faults near Kuşadası are given in **a, b,c** and **e;** Ephesus fault is in **d** and Gümüldür fault in **f**.

In all previously presented locations, *there is no field evidence indicating or implying coseismic surface deformation associated to the mainshock*. Thus, it is concluded that the 30 October 2020

M7.0 Samos earthquake rupture did not extend to the Turkish mainland and remained limited to the northern side of Samos Island.

1.7.2 Samos Island

The October 30, 2020, **M**7.0 Samos earthquake triggered primary and secondary environmental effects in Samos Island (Lekkas et al., 2020, Triantafyllou et al., 2020). The primary environmental effects comprise permanent surface deformation of tectonic origin, including uplift and subsidence, and coseismic surface ruptures (Figure 1.31). Secondary effects (landslides, liquefaction) are addressed in Chapter 5 of this report.

Figure 1.31. Google Earth map of Samos Island: Green triangles correspond to permanent uplift and yellow circles to surface ruptures (Lekkas et al., 2020).

Permanent surface deformation has been detected in the northwestern and southeastern parts of Samos Island. In the northwestern part of Samos, coastal uplift has been generated in the vessel shelter of Karlovasi, as well as along the Potami beach, the Punta promontory and Agios Isidoros beach located west of the Karlovasi area (Figure 1.32).

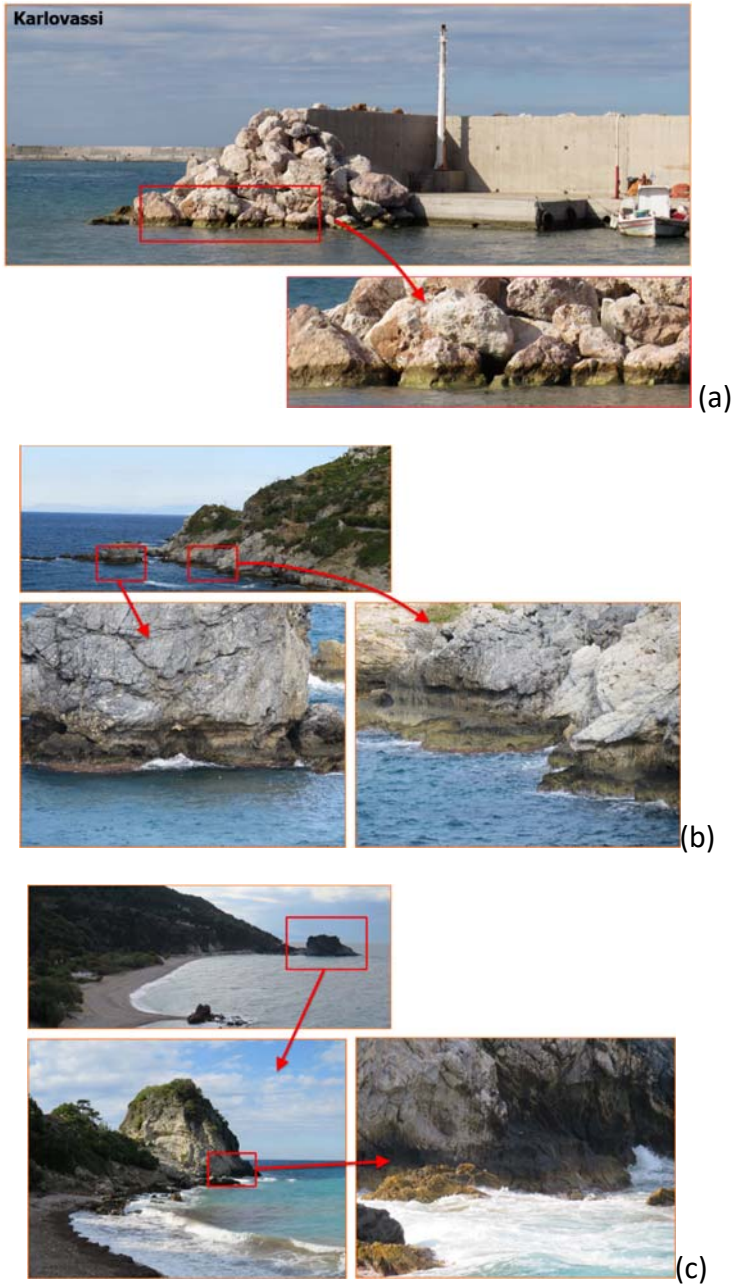

Figure 1.32. Permanent uplift (a) in the Karlovasi coastal area, imprinted not only on protection boulders, but also on the concrete jetty; (b) in the area west of the Karlovasi port imprinted on marbles of the Kerketeas nappe along the rocky promontory in Potami area; c) in the area west of the Karlovasi port imprinted on marbles of the Kerketeas nappe along Punta Promontory.

1.8 Conclusions

The information presented in this chapter attempts to provide a general overview of the seismotectonic setting and historical background, as well as of the generation of the 30 October 2020 11:51 UTC (13:51 local time) **M**7.0 destructive earthquake and the evolution of its aftershock seismic sequence. The information presented here incorporates preliminary

contributions from several research groups and establishes several robust features of the mainshock and its associated aftershocks. More specifically:

a) The earthquake occurred offshore the northern coast of Samos Island (Kuşadasi [Ephesus] gulf), along a known normal fault (named North Samos or Kaystrios fault), previously identified on the basis of morphotectonic evidence, and confirmed by the earthquake generation, as well as detailed sea bathymetry collected after the mainshock. The broader Samos area is located at a trans-tensional regime region, characterized by the presence of large E-W trending normal faults (like the one where the 2020 **M**7.0 fault occurred), as well as strike-slip (mainly dextral) NE-SW faults, that often link the normal fault bounded basins of the area.

b) The information from the available historical seismicity suggests that similar magnitude events have previously occurred in the area (47AD **M**~7.0, 1751 **M**~6.8, 1904 **M**6.8, 1955 **M**6.9). A similar magnitude earthquake (**M**7.0) has not occurred along the Kaystrios Fault during the last 270 years or so, though the 1873 **M**~6.5 earthquake may be associated with a rupture of the *eastern segment* of this fault.

c) The relocated aftershock sequence, waveform modelling (teleseismic and regional) results, preliminary geodetic data (InSAR and GNSS) interpretation and field data observations confirm the rupture of a 32-38km E-W trending (strike: 270-275^{o}), north dipping fault (dip angle 45° to 55^{o}) and almost pure normal-slip motion. The average slip is 1 to 2m, as loosely constrained by both seismic and geodetic information. While the models are not completely conclusive, they suggest that the rupture expanded towards but did not reach the surface (fault top constrained at ~0.5-1km beneath the sea bottom). The rupture initiated at the hypocenter, close to the fault's bottom-center area; however, the major slip episodes occurred at the western fault segment, as suggested by both regional and teleseismic waveform modelling, and confirmed by the complete lack of aftershocks in this large asperity, especially during the first 24 hours after the mainshock. The rupture velocity seems to be rather low (<2km/s) than typical values estimated for **M**7+ mainshocks (>2.5km/s), resulting in a source duration of almost 20s.

d) A rather subtle aftershock sequence followed the mainshock (until when this chapter was compiled), with a maximum aftershock of **M**5.1, and a handful of aftershocks with **M**>4.5. Though a **M**~6.0 would not be uncommon for such a mainshock, "quiet" aftershock sequences are also observed in the Aegean area e.g. the recent Kos and Lesvos 2017 sequences, or the similar magnitude 1955 southern Samos-Büyük Menderes river delta **M**6.9 mainshock in the same area. Most aftershocks occurred along off-fault edge splays of the main fault, often with more strike-slip than normal faulting mechanisms. Stress modeling suggests that their location is a result of stress loading/triggering from the mainshock on neighboring faults. Secondary fault activation on Samos Island and to the north of Ikaria Island also occurred at different times after the mainshock.

e) Several primary phenomena (e.g. coastal uplift ~10cm in the west Samos footwall, confirmed by InSAR, field and GNSS data) and secondary earthquake effects (described in Chapter 5) were observed on the Samos island, while no field evidence of coseismic surface deformation was identified on the Turkish coast.

f) The earthquake generated a significant tsunami, as described in Chapter 2. The tsunami generation should be attributed to the very shallow slip occurrence, the static deformation (subsidence) of the sea bottom, especially of the western fault segment or to the generation of subsurface landslides (for which evidence is available from the detailed sea bathymetry) or to a combination of these phenomena.

Besides the previous scientific conclusions, this earthquake has highlighted some well-known but often forgotten facts about the mainshocks of the eastern Aegean Sea:

1) While normal faulting events are usually associated with lower levels of strong seismic motions, they can have an important impact, even at large epicentral distances, especially when they affect large metropolitan complexes. The 2020 **M**7.0 Samos earthquake caused two fatalities in neighboring Samos but had devastating effects at a distance of >60km in Izmir, causing 116 fatalities. A similar impact has been observed even for smaller events, such as the 1978 **M**6.5 Mygdonia basin event (48 fatalities in Thessaloniki at an epicentral distance of ~30km) and the 1981 **M**6.7 Alkyonides event (20 fatalities and heavy damage impact in Athens, at a distance of ~60km from the epicenter).

2) The **M**7.0 2020 Samos Island (Kuşadasi [Ephesus] gulf) earthquake generation, as well as the rich seismic history of the broader Samos Island and the Izmir metropolitan area, due to the complex geotectonic setting of the region, suggest that we cannot neglect the seismic hazard factor in the long-term development planning of the eastern Aegean area. The major earthquake-major metropolitan area “weakness” link previously discussed and the amplification of primary and secondary earthquake effects in large cities like Izmir suggest that a careful and focused re-appraisal of the seismic risk mitigation policy is necessary. This is especially critical for Izmir, not only because of the effect of distant events, such as the 2020 **M**7.0 mainshock, but also considering the lack of strong events in the broader Izmir Bay area for the last ~150 years.

3) While earth data exchange has advanced in the recent years, there are still important obstacles that do not facilitate the efficient exploitation of the available scientific information after similar, hazardous events. For example, while InSAR data are readily available to all interested scientists though the ESA Copernicus program, GNSS data are mostly operated by government institutions and private companies in both countries (Greece and Turkey) and are often not freely available in the case of major earthquakes or other geohazard phenomena, unless commercially purchased. This is almost ironic, at least for the case of national networks (e.g. HEPOS in Greece), considering that they were

established through EU and national funding. Similarly, while the post-earthquake seismic waveform distribution has been facilitated through the recently built national EIDA nodes, or web-services available at several institutes, the collection of all available seismic data (e.g. strong-motion and broadband waveforms), metadata, and products (catalogues, phases, etc.) still remains a tedious task. This is verified by the results presented in this work, which often employ only a part of the data that could be potentially used for each study.

4) Eastern Aegean Sea mainshocks do not respect national and geophysical boundaries, killing people and destroying properties in both countries. Across-border cooperation at different levels (scientific, operational, etc.) is necessary for an efficient mitigation of the earthquake results. While this report is a preliminary effort in this direction, the scientific, engineering, and decision-making communities should work more closely together, in an attempt to develop an efficient, early-response policy in the case of similar geohazard phenomena. To this extent, we may all be inspired by the pioneering initiative observed in the art community, as demonstrated by the "Samir" painting (termed from the words Samos and Izmir) by Mikail Akar and Niko Nikolaidis.

1.9 Data and Resources

GNSS data were provided by NOANET and Hexagon SmartNET networks of Greece and the Turkish CORS network. The SAR images were provided through the free and open data policy adopted for the ESA Copernicus program.

Digital seismic waveforms were retrieved from the ORFEUS Eida-nodes (orfeus-eu.org), and AFAD [https://deprem.afad.gov.tr/] and are acquired from the following regional networks: HUSN (HL, doi:10.7914/SN/HL; HT, doi:10.7914/SN/HT; HA, doi:10.7914/SN/HA; HP, doi:10.7914/SN/HP; HI, doi:10.7914/SN/HI; HC, doi:10.7914/SN/HC); KOERI (KO, doi:10.7914/SN/KO), AFAD (TU, doi.org/10.7914/SN/TU). Catalogue and seismic phase data were collected from the following regional networks: HUSN (HL, doi:10.7914/SN/HL; HT, doi:10.7914/SN/HT; HA, doi:10.7914/SN/HA; HP, doi:10.7914/SN/HP; HI, doi:10.7914/SN/HI; HC, doi:10.7914/SN/HC), AFAD (TU, doi:10.7914/SN/TU) and KOERI (KO, doi:10.7914/SN/KO), obtained through the web services of the individual networks and the corresponding EMSC-CSEM online services.

Preliminary reports by various agencies and governmental institutions were also used here, and even though a number of them is referenced in the text, for a handy list (not complete probably) the reader can see Reports-Appendix.

A number of figures were drawn using the Generic Mapping Tools (GMT) software (Wessel & Smith, 1998).

Acknowledgements

We acknowledge the faculty and staff members of several Universities and research Institutes, both in Greece and Turkey, for the careful analysis of the data, the maintenance and operation of the networks. We additionally extend our thanks to our colleagues, from both countries, who participated in the installation and maintenance of the temporary stations, as well as those who participated in the field reconnaissance work. Without their unprecedented and continuous devotion, this report could not have been possible.

Special thanks are extended to our colleagues who undertook the initiative for this report, because they offered us the chance to cooperate, and appreciate the scientific excellence in both countries, Greece and Turkey.

Prof Emeritus Haluk Eyidogan and Prof Emeritus Konstantinos Makropoulos are gratefully acknowledged for providing feedback and comments, acting as expert external reviewers.

The Greek team acknowledges support by the project “HELPOS - Hellenic Plate Observing System” (MIS 5002697) which is implemented under the Action “Reinforcement of the Research and Innovation Infrastructure”, funded by the Operational Programme "Competitiveness, Entrepreneurship and Innovation" (NSRF 2014-2020) and co-financed by Greece and the EU (European Regional Development Fund). The Turkish team acknowledges Middle East Technical University that provided funding for fieldwork.

References

Aktar, M, Karabulut, H, Ozalaybey, S, and Childs, D, 2007. A conjugate strike-slip fault system within the extensional tectonics of Western Turkey. Geophysical Journal International, 171. 1363-1375.

Allen, TI, Wald, DJ, 2009. On the Use of High-Resolution Topographic Data as a Proxy for Seismic Site Conditions (VS30). Bull. Seismol. Soc. Am., 99, 935–943.

Altunel, E, Pınar, A, 2020. Tectonic implications of the Mw 6.8, 30 October 2020 earthquake in the frame of active faults of Western Turkey, Turkish Journal of Earth Sciences (under review).

Ambraseys, N, 1998. Engineering Seismology. Earthq. Engin. Struct. Dyn., 17, 1-105.

Ambraseys, N, 2009. Earthquakes in the Mediterranean and Middle East: a multidisciplinary study of seismicity up to 1900. Cambridge University Press. ISBN: 978-0-521-87292-8.

Avsar, U, 2019. Son 1500 Yıl Boyunca Ege Denizi’ndeki Tsunamilerin Sedimanter İzleri, (Karine Lagünü, B-Türkiye). Geological Bulletin of Turkey. 62. 199-220. 10.25288/tjb.545990.

Benetatos, C, Kiratzi, A, Ganas, A, Ziazia, M, Plessa, A, and Drakatos, G, 2006. Strike-slip motions in the Gulf of Sığacık (western Turkey): properties of the 17 October 2005 earthquake seismic sequence. Tectonophysics, 426, 263–279.

Biryol, CB, Beck, SL, Zandt, G, and Özacar, A, 2011. Segmented African lithosphere beneath the Anatolian region inferred from teleseismic P-wave tomography. Geophysical Journal International 184, 1037-1057.

Bohnhoff, M, Makris, J, Papanikolaou, D. and Stavrakakis, G, 2001. Crustal investigation of the Hellenic subduction zone using wide aperture seismic data. Tectonophysics, 343(3-4), 239-262.

Boore, DM, 2009. Comparing Stochastic Point-Source and Finite-Source Ground-Motion Simulations: SMSIM and EXSIM, Bull. Seism. Soc. Am, 99(6), 3202-3216.

Bouchon, M, 1979. Discrete wave number representation of elastic wave fields in three-space dimension. J. Geophys. Res, 84, 3609–3614.

Bouchon, M, 2003. A review of the discrete wavenumber method. Pure Appl. Geophys, 160, 445–465.

Bousquet, B. et Pechoux, PY, 1978. Recherches bibliographique sur la séismicité historique. Rapport Final D' ActivitéD'Activité Scientifique De L'EquipeÉquipe Du Laboratoire De Géologie Dynamique De L'Université Paris Sud Sur Le Résultat Des Etudes De Néotectonique en Grèce, 3, 47-65, 4, 93-126.

Briole, P. 2017. Modelling of earthquake slip by inversion of GNSS and InSAR data assuming homogenous elastic medium. Zenodo, http://doi.org/10.5281/zenodo.1098399

Byerlee, JD, 1978. Friction of rocks, Pure Appl. Geophys, 116, 615–626.

Caputo R, Pavlides, S, 2013. The Greek Database of Seismogenic Sources (GreDaSS), Version 2.0.0: A compilation of potential seismogenic sources (M>5.5) in the Aegean region, doi:10.15160/unife/gredass/0200. [http://gredass.unife.it/.]

Caputo, R, Chatzipetros A, Pavlides S. and Sboras S. 2012. The Greek Database of Seismogenic Sources (GreDaSS): state-of-the-art for northern Greece. Ann. Geophys, 55(5), 859-894.

Chatzipetros, A, Kiratzi, A, Sboras, S, Zouros, N, and Pavlides, S, 2013. Active faulting in the north eastern Aegean Sea Islands, Tectonophysics, 597-598, 106-122.

Coskun, S, Dondurur, D, Cifci, G, Aydemir, A, Gungor, T, and Drahor, M, 2017. Investigation on the tectonic significance of Izmir, Uzunada Fault Zones and other tectonic elements in the Gulf of Izmir, western Turkey, using high-resolution seismic data. Marine and Petroleum Geology. 83.

Dreger, DS, Kaverina, A, 2000. Seismic remote sensing for the earthquake source process and near-source strong shaking: a case study of the October 16, 1999 Hector Mine earthquake, Geophys. Res. Lett. 27, 1941–1944.

Duman, T.Y, Çan, T, Emre, Ö, Kadiroğlu, F.T, Başarır Baştürk, N, Kılıç, T, Arslan, S, Özalp, S, Kartal, R.F, Kalafat, D, Karakaya, F, Eroğlu Azak, T, Özel, N.M, Ergintav, S, Akkar, S, Altınok, Y, Tekin, S, Cingöz, A. and Kurt, A, 2017. Seismotectonic Map of Turkey with Explanations. General Directorate of Mineral Research and Explorations, Special Publication Series, 34, Ankara-Türkiye.

Emre, Ö, Duman, TY, Özalp, S, Şaroğlu, F, Olgun, Ş, Elmacı, H, and Can, T, 2018. Active fault database of Turkey. Bulletin of Earthquake Engineering, 16, 3229-3275.

Ergin, K, Güçlü, U. and Uz, Z, 1967. A catalog of earthquakes for Turkey and surrounding area (11 A.D. to 1964 A.D.), Publications of İstanbul Technical University, Istanbul-Turkey 24, 169 pp.

Evelpidou, N, Pavlopoulos, K, Vouvalidis, K, Syrides, G, Triantaphyllou, M, Karkani, A. and Paraschou, T, 2019. Holocene palaeogeographical reconstruction and relative sea-level changes in the southeastern part of the island of Samos. Geoscience, 351, 451-460.

Eyidoğan, H., U. Güçlü, Z. Utku ve E. Değirmenci, 1991, Türkiye büyük depremleri makrosismik rehberi (1900-1988), İstanbul Teknik Üniversitesi, İstanbul, 199 sayfa.

Faccenna, C, Bellier, O, Martinod, J, Piromallo, C. and Regard, V. 2006. Slab detachment beneath eastern Anatolia: a possible cause for the formation of the North Anatolian fault. Earth and Planetary Science Letters 242, 85–97.

Foumelis, M, Papadopoulou, T, Bally, P, Pacini, F, Provost, P, Patruno, J, 2019. Monitoring geohazards using on-demand and systematic services on ESA's geohazards exploitation platform, IEEE International Geoscience and Remote Sensing Symposium (IGARSS 2019), Yokohama, Japan, 28 July - 2 August, doi: https://doi.org/10.1109/IGARSS.2019.8898304.

Galanakis, G, Kontodimos, K. (2020). Mobilization of the emergency response team of the Hellenic Survey of Geology and Mineral Exploration (HSGME) after the 30/10/2020 earthquake in Samos Island. Report of HSGME. 5 p. Available at: https://www.igme.gr/index.php/enimerosi/deltia-typou/category/6-deltia-typou

Ganas, A, Andritsou, N, Kosma, C, Argyrakis, P, Tsironi, V, & Drakatos, G. 2018. A 20-yr database (1997-2017) of co-seismic displacements from GPS recordings in the Aegean area and their scaling with M and hypocentral distance. Bulletin of the Geological Society of Greece, 52, 98-130. doi: http://dx.doi.org/10.12681/bgsg.18070

Ganas, A, Drakatos, G, Rontogianni, S, Tsimi, C, Petrou, P, Papanikolaou, M, Argyrakis, P, Boukouras, K, Melis, N, Stavrakakis, G. 2008. NOANET: the new permanent GPS network for Geodynamics in Greece. European Geophysical Union, Geophysical Research Abstracts 10, EGU2008-A-04380.

Ganas, A, Elias, P, Briole, P, Tsironi, V, Valkaniotis, S, Escartin, J, Karasante, I, and Efstathiou, E, 2020. Fault responsible for Samos earthquake identified, Temblor, http://doi.org/10.32858/temblor.134

Ganas, A, et al, 2019. The July 20, 2017 M6.6 Kos Earthquake: Seismic and Geodetic Evidence for an Active North-Dipping Normal Fault at the Western End of the Gulf of Gökova (SE Aegean Sea), Pure and Applied Geophysics, 176 (10), 4177-4211

Ganas, A, Parsons, T, 2009. Three-dimensional model of Hellenic Arc deformation and origin of the Cretan uplift. J. Geophys. Res.: Solid Earth 114 (B6) https://doi.org/10.1029/2008JB005599

Ganas, A, Tsironi, V, Kollia, E, Delagas, M, Tsimi, C, Oikonomou, A, 2018. Recent upgrades of the NOA database of active faults in Greece (NOAFAULTs). 19th General Assembly of WEGENER, September 2018, Grenoble, sciences conf.org: 219400, https://doi.org/10.5281/zenodo.3483136

Gans, CR, Beck, SL, Zandt, G, Biryol, CB, and Ozacar, AA, 2009. Detecting the limit of slab break-off in Central Turkey: new high-resolution Pn tomography results, Geophys. J. Int, 179, 1566–1572.

Gök, E. & Polat, O. (2014). An assessment of the microseismic activity and focal mechanisms of the Izmir (Smyrna) area from a new local network (IzmirNET). Tectonophysics. 635. 10.1016/j.tecto.2014.08.003.

Goldstein, R. M.; Werner, C. L. 1998. Radar interferogram filtering for geophysical applications. Geophys. Res. Lett. 25(21), 4035-4038

Guidoboni, E, Comastri, A. and Traina, G. 1994. Catalogue of ancient earthquakes in the Mediterranean area up to the 10th century. SGA Storia Geofisica Ambiente, Bologna, pp. 504.

Harris, RA, 1998. Introduction to special section: stress triggers, stress shadows, and implications for seismic hazard, J. Geophys. Res, 103, 24 347–24 358.

Hartzell, SH, Heaton, T, 1983. Inversion of strong ground motion and teleseismic waveform data for the fault rupture history of the 1979 Imperial Valley, California, earthquake, Bull. Seism. Soc. Am. 73, 1553–1583.

Jeffreys, H. & Bullen, KE, 1958. Seismological tables/Brit. Assoc. for the advancement of Sci, London: Gray-Milne Trust, 65

Jolivet, L, Faccenna, C, Huet, B, Labrousse, L, Le Pourhiet, L, Lacombe, O, Lecomte, E, Burov, E, Denèle, Y, Brun, J.P, Philippon, M, Paul, A, Salaün, G, Karabulut, H, Piromallo, C, Monié, P, Gueydan, F, Okay, A.I, Oberhänsli, R, Pourteau, A, Augier, R, Gadenne, L. and Driussi, O. 2013. Aegean tectonics: progressive strain localisation, slab tearing and trench retreat. Tectonophysics 597-598, 1–33.

Kalogeras, I, Melis, N.S, Kalligeris, N, 2020. The earthquake of October 30th, 2020 at Samos, Eastern Aegean Sea, Greece. Report published at EMSC: https://www.emsc-csem.org/Doc/Additional_Earthquake_Report/915787/Samos_Preliminary_Report_EN.pdf (Last accessed: 12 December 2020)

Kapetanidis, V, Kassaras, I, 2019. Contemporary crustal stress of the Greek region deduced from earthquake focal mechanisms. J. Geodyn, 123, 55–82.

Karabulut, H, Paul, A, Özbakır, AD, Ergün, T. and Şentürk, S, 2019. A new crustal model of the Anatolia–Aegean domain: evidence for the dominant role of isostasy in the support of the Anatolian plateau. Geophysical Journal International, 218(1), 57-73.

Karadaş, A. 2012. Bornova Ovası ve Çevresinin Fiziki Coğrafyası. Doktora Tezi, Ege Üniversitesi

Karadaş, A. 2014. Bornova Ovası (İzmir) Holosen paleocoğrafyası ve kıyı çizgisi değişimleri. Ege Coğrafya Dergisi, 23, 37-52.

Karagianni. EE, Papazachos, CB, Panagiotopoulos, DG, Suhadolc, P, Vuan, A. and Panza, GF, 2005. Shear velocity structure in the Aegean area obtained by inversion of Rayleigh waves. Geophys. J. Int, 160, 127-143.

Karakonstantis, A, 2017. 3-D simulation of crust and upper mantle structure in the broader Hellenic area through Seismic Tomography. Ph.D. Thesis, Department of Geophysics-Geothermics, Faculty of Geology, University of Athens, Greece. (in Greek)

Karakostas, VG, Tan, O, Kostoglou, A, Papadimitriou, EE, and Bonatis, P, 2020. Seismotectonic implications of the 2020 Samos, Greece, M7.0 mainshock based on high–resolution aftershocks relocation, source slip model, and previous microearthquake activity. Acta Geophys. (Submitted).

Karnik, V, 1971. Seismicity of the European Area, Part II, 1801-1900. D. Reidel Publ. Comp. Dordrecht, Netherlands, 218 pp.

Kassaras, I, Kapetanidis, V, Ganas, A, Tzanis, A, Kosma, C, Karakonstantis, A, Valkaniotis, S, Chailas, S, Kouskouna, V, Papadimitriou, P, 2020. The New Seismotectonic Atlas of Greece (v1.0) and Its Implementation. Geosciences, 10(11), 447.

Kaverina, A, Dreger, D, Price, E, 2002. The Combined Inversion of Seismic and Geodetic Data for the Source Process of the 16 October 1999 M 7.1 Hector Mine, California, Earthquake, Bull. Seism. Soc. Am. 92, pp. 1266-1280.

Kikuchi, M, and Kanamori, H, 1991. Inversion of complex body waves—III, B SeismolSoc Am, 81(6), 2335-2350.

King, GCP, Stein, RS, and Lin, J, 1994. Static stress changes and the triggering of earthquakes, Bull. Seism. Soc. Am, 84, 935–953.

Kiratzi, A, 2002. Stress tensor inversions along the westernmost North Anatolian Fault Zone and its continuation into the North Aegean Sea, Geophysical Journal International, 151, 360–376.

Kiratzi, A, 2014. Mechanisms of Earthquakes in Aegean, in: Beer, M, Kougioumtzoglou, I.A, Patelli, E, Siu-Kui Au, I. (Eds.), Encyclopedia of Earthquake Engineering. Springer Berlin Heidelberg, pp. 1–22.

Kissling, E, Ellsworth, W.L, Eberhart-Phillips, D, Kradolfer, U, 1994. Initial reference models in local earthquake tomography. J. Geophys. Res, 99(B10), 19635-19646. https://doi.org/10.1029/93JB03138

Klein, FW, 2002. User's guide to HYPOINVERSE-2000: a FORTRAN program to solve for earthquake locations and magnitudes, U.S. Geol. Surv. Prof. Pap, rep. 02-17, 1-123.

Klimis, N. S, B. N. Margaris, and P. K. Koliopoulos, 1999. Site-Dependent Amplification Functions and Response Spectra in Greece, Journal of Earthquake Engineering, 3(2), 237-270, doi:10.1080/13632469909350346.

Klimis, N, Margaris, B, Anastasiadis, A, Koliopoulos P. and Em. Kirtas, 2006. Smoothed Hellenic Rock Site Amplification Factors, 5th Hellenic Congress of Geotechnical and Geoenvironmental Engineering, 2, 239-246, Xanthi, Greece [in Greek].

Lekkas, E, et al, 2020. The October 30, 2020, M 6.9 Samos (Greece) earthquake. Newsletter of Environmental, Disaster, and Crises Management Strategies, Issue No. 21, November 2020, ISSN 2653-9454. Available at: https://edcm.edu.gr/en/newsletter/newsletter-21-the-october-30-2020-M-6-9-samos-greece-earthquake (Last Accessed: 12 December 2020)

Lekkas, E, Mavroulis, S, Gogou, M, Papadopoulos, G.A, Triantafyllou, I, Katsetsiadou, K.-N, Kranis, H, Skourtsos, E, Carydis, P, Voulgaris, N, Papadimitriou, P, Kapetanidis, V, Karakonstantis, A, Spingos, I, Kouskouna, V, Kassaras, I, Kaviris, G, Pavlou, K, Sakkas, V, Karatzetzou, A. Evelpidou, N. Karkani, E. Kampolis, I, Nomikou, P, Lambridou, D, Krassakis, P, Foumelis, M, Papazachos, C, Karavias, A, Bafi, D, Gatsios, T, Markogiannaki, O, Parcharidis, I, Ganas, A, Tsironi, V, Karasante, I, Galanakis, D, Kontodimos, K, Sakellariou, D, Theodoulidis, N, Karakostas, C, Lekidis, V, Makra, K, Margaris, V, Morfidis, K, Papaioannou, C, Rovithis, E, Salonikios, T, Kourou, A, Manousaki, M, Thoma, T, Karveleas, N, 2020. The

October 30, 2020 M 6.9 Samos (Greece) earthquake. Newsletter of Environmental, Disaster and Crises Management Strategies, 21, ISSN 2653-9454, DOI: 10.13140/RG.2.2.13630.10561

Makropoulos, K, Drakopoulos, J, and J. Latousakis, 1989. A revised and extended earthquake catalogue for Greece since 1900. Geophysical Journal International, 98, 391-394.

Margaris, BN, and Boore, DM, 1998. Determination of Δσ and κ0 from response spectra of large earthquakes in Greece, Bull. Seism. Soc. Am, 88, 170-182.

Margaris, BN, and Hatzidimitriou, PM, 2002. Source spectral scaling and stress release estimates using strong-motion records in Greece. Bulletin of the Seismological Society of America, 92, 1040-1059.

Mascle, J, and Martin, L, 1990. Shallow structure and recent evolution of the Aegean Sea: A synthesis based on continuous reflection profiles, Marine Geology, 94, 4, 271-299.

McClusky, S, et al. 2000, Global Positioning System constraints on plate kinematics and dynamics in the eastern Mediterranean and Caucasus, J. Geophys. Res. 105, B3, 5695-5719, DOI: 10.1029/1999JB900351.

McKenzie, D, 1978. Active tectonics of the Alpine–Himalayan belt: the Aegean Sea and surrounding regions, Geophys. J. Roy. Astr. Soc. 55, 1, 217-254, DOI: 10.1111/j.1365-246X.1978.tb04759.x.

Mireault, Y, Tétreault, P, Lahaye, F, Héroux, P, Kouba, J, 2008. Online precise point positioning: A new, timely service from natural resources Canada. GPS World, 19, 59-64.

Motazedian, D, and Atkinson, GM, 2005. Stochastic Finite-Fault Modeling Based on a Dynamic Corner Frequency, Bulletin of the Seismological Society of America, 95(3), 995-1010, doi:10.1785/0120030207.

Mountrakis, D, Kilias, A, Vavliakis, E, Psilovikos, A, Karakaisis, G, Papazachos, C, Thomaidou, E, Seitanidis, G. (2006). Neotectonic Map of Greece, "Samos" sheet, scale 1:75.000, 78 p.

Mountrakis, D, Kilias, A, Vavliakis, E, Psilovikos, A. and Thomaidou, E, 2003. Neotectonic map of Samos Island (Aegean Sea, Greece): implication of geographical information systems in the geological mapping, Proc. of the 4th European Congress on Regional Geoscientific Cartography and Information Systems, Bologna, Italy, pp. 11-13.

Mourtzas, N, Stavropoulos, X, 1989. Recent tectonic evolution of the coast of the islands of Samos (E. Aegean). Bull. Geol. Soc. Gr. 23/1, 223-241.

Novotný O, Zahradník J, Tselentis GA (2001). North-Western Turkey earthquakes and the crustal structure inferred from surface waves observed in Western Greece, Bull. Seismol. Soc. Am, 91, 875-879.

Ozacar A.A, Uzel, B, Sopacı, E, Gulerce, Z, 2020. Chapter 2: Geological and Seismological Observations on the 30October 2020 Samos (İzmir, Şeferihisar) Earthquake. EERC Report, METU.

Ozacar, A, 2011. Present-day Stress Pattern of Turkey from Inversion of Updated Earthquake Focal Mechanism Catalogue. AGU Fall Meeting Abstracts.

Pamuk, E, Akgün, M, Özdağ, Ö.C. and Gönenç, T, 2017. 2D soil and engineering-seismic bedrock modeling of eastern part of Izmir inner bay/Turkey. Journal of Applied Geophysics, 137, 104-117.

Papadimitriou, E, Karakostas, V, Mesimeri, M, Chouliaras, G, and Kourouklas, Ch, 2017. The M6.7 17 November 2015 Lefkada (Greece) earthquake: structural interpretation by means of aftershock analysis. Pure Appl. Geophys, 174, 3869–3888, DOI 10.1007/s00024–017–1601–3, 2017.

Papadimitriou, P, Chousianitis, K, Agalos, A, Moshou, A, Lagios, E, Makropoulos, K, 2012. The spatially extended 2006 April Zakynthos (Ionian Islands, Greece) seismic sequence and evidence for stress transfer. Geophys. J. Int, 190, 1025–1040.

Papadimitriou, P, Kapetanidis, V, Karakonstantis, A, Spingos, I, Kassaras, I, Sakkas, V, Kouskouna, V, Karatzetzou, A, Pavlou, K, Kaviris, G, Voulgaris, N, 2020. First results on the M=6.9 Samos earthquake of 30 October 2020. Bull. Geol. Soc. Greece, 56(1), 251-279. https://doi.org/10.12681/bgsg.25359

Papanikolaou, D, 1979. Unités tectoniques et phases de déformation dans l'ile de Samos, Mer Égée. Bull. Soc. Geol. Fr, 7 (21), 745-752.

Papazachos BC, and Papazachou C, 2003. The earthquakes of Greece. Ziti publications, Thessaloniki, Greece, 286 pp. (in Greek).

Papazachos, B, Papaioannou, Ch, Papazachos C, and Savvaidis, A.S, 1997. Atlas of isoseismal maps for strong (M≥5.0) shallow (h<60km) earthquakes in Greece and surrounding area, 426 BC-1995, Ziti Publ, 176pp.

Papazachos, BC, Papaioannou, CA, Papazachos, CB, & Savvaidis, AS, 1997. Atlas of Isoseismal Maps for Strong Shallow Earthquakes in Greece and Surrounding Area (426BC-1995): Thessaloniki. Technical books Editions.

Papazachos, C. and Papaioannou, Ch. 1997. The macroseismic field of the Balkan area. Journal of Seismology, 1, 181–201, https://doi.org/10.1023/A:1009709112995

Pavlides, S, Tsapanos, T, Zouros, N, Sboras, S, Koravos, G, Chatzipetros, A. 2009. Using Active Fault Data for Assessing Seismic Hazard: A Case Study from NE Aegean Sea, Greece. Earthquake Geotechnical Engineering Satellite Conference, XVIIth International Conference on Soil Mechanics & Geotechnical Engineering, 2-3/10/2009, Alexandria, Egypt.

Pınar, N. and Lahn, E, 1952. Türkiye'de zelzelelere müteallik etüdler. Publications of General Directorate of Mineral Research and Explorations B (5), 5–21.

Rice, J, and Cleary, M, 1976. Some basic stress diffusion solutions for fluid saturated elastic porous media with compressible constituents. Rev. Geophys, 14, 227–241.

Richards–Dinger, K, Stein, RS and Toda, S, 2010. Decay of aftershock density with distance does not indicate triggering by dynamic stress. Nature, 467, 583–588.

Ring, U, Laws, S, Bernet, M, 1999. Structural analysis of a complex nappe sequence and late-orogenic basins from the Aegean Island of Samos, Greece. Journal of Structural Geology 21, 1575-1601.

Ring, U, Okrusch, M, Will, T. 2007. Samos Island, Part I: metamorphosed and non-metamorphosed nappes, and sedimentary basins. In: Lister, G, Forster, M, Ring, U. (Eds.), Inside the Aegean Metamorphic Core Complexes, Journal of the Virtual Explorer, Electronic Edition, ISSN 1441-8142, volume 27, paper 5. https://doi.org/10.3809/jvirtex.2007.00180

Roche, V, Jolivet, L, Papanikolaou, D, Bozkurtf, E, Menant, A, Rimmelé, G, 2019. Slab fragmentation beneath the Aegean/Anatolia transition zone: Insights from the tectonic and metamorphic evolution of the Eastern Aegean region. Tectonophysics 754, 101-129.

Sakellariou, D, Tsampouraki-Kraounaki, K, 2019. Plio-Quaternary Extension and Strike-Slip Tectonics in the Aegean. In: Transform Plate Boundaries and Fracture Zones, (Ed) João C. Duarte, Springer, 339-374.

Sboras S. 2012. The Greek Database of Seismogenic Sources: Seismotectonic implications for North Greece. PhD Thesis, University of Ferrara, Ferrara, 252 pp.

Schmidt, J. A treatise on the earthquake of December 26, 1861 in Aegio. National Printing Office, Athens, 52 pp, 1867.

Shebalin, N.V. (editor), 1974. Catalogue of earthquakes. Part 1, 1901-1970, Part 2, prior to 1901. UNDP/UNESCO Survey of the Seismicity of the Balkan Region, Skopje.

Sieberg, A, 1832b. Untersuchungen uber Erdbeben und Bruchschollenbau im ostlichen Mittelmeergebiet. Velag von Gustav Fisher, Jena.

Sieberg, A, 1932a. Erdbebengeographie. Handbuch der Geophysik, Berlin, 4, 687-1005.

Skarlatoudis, AA, Papazachos, CB, Margaris, BN, Theodulidis, N, Papaioannou, C, Kalogeras, Scordilis, E, and Karakostas, V, 2003, Empirical peak ground-motion predictive relations for shallow earthquakes in Greece. Bull. Seism. Soc. Am, 93, 2591-2603.

Sodoudi, F, Kind, R, Hatzfeld, D, Priestley, K, Hanka, W, Wylegalla, K, Stavrakakis, G, Vafidis, A, Harjes, H.P. and Bohnhoff, M, 2006. Lithospheric structure of the Aegean obtained from P and S receiver functions. Journal of Geophysical Research: Solid Earth, 111(B12).

Soysal, H, Sipahioğlu, S, Kolçak, D. and Altınok, Y, 1981. Türkiye ve Çevresinin Tarihsel Deprem Kataloğu (M.Ö. 2100-M.S.1900). Technical Report, TÜBİTAK Project No: TBAG-341.

Sözbilir, H, Sümer, Ö, Uzel, B, Ersoy, Y, Erkül, F, İnci, U, Helvacı, C. and Özkaymak, Ç, 2009. The Seismic geomorphology of the Sığacık Gulf (İzmir) earthquakes of October 17 to 20, 2005 and their relationships with the stress field of their Western Anatolian region. Geological Bulletin of Turkey, 52 (2), 217–238.

Stein, R, 1999. The role of stress transfer in earthquake occurrence, Nature, 402, 605–609.

Stewart, JP, Klimis, N, Savvaidis, A, Theodoulidis, N, Zargli, A, Athanasopoulos, G, Pelekis, P, Mylonakis, G, and Margaris, B, 2014. Compilation of a Local VS Profile Database and Its Application for Inference of VS30 from Geologic- and Terrain-Based Proxies, Bull. Seism. Soc. Am, 104(6), 2827-2841.

Tan, O, and Taymaz, T, 2006. Active tectonics of the Caucasus: earthquake source mechanisms and rupture histories obtained from inversion of teleseismic body waveforms. Post-collisional Tectonics and Magmatism in the Mediterranean Region and Asia. Geol. Soc. Am. Bull, Special Paper, 409, pp. 531–578. doi:10.1130/2006.2409.

Tan, O, Papadimitriou, E.E, Pabucçu, Z. et al. 2014. A detailed analysis of microseismicity in Samos and Kusadasi (Eastern Aegean Sea) areas. Acta Geophysica, 62, 1283–1309.

Tan, O, Tapırdamaz, C. and Yörük, A, 2008. The Earthquake catalogues for Turkey. Turkish Journal of Earth Sciences, 17, 405–418.

Taylor, JR, 1997. An Introduction to Error Analysis, in a series of Books in Physics, Commins, Eugene, D, Editor University Sciences Books, Mill Valley, California.

Taymaz, T, J. Jackson, and D. McKenzie 1991. Active tectonics of the north and central Aegean Sea, Geophys. J. Int. 106, 2, 433-490.

Theodoropoulos, D, 1979a. Geological map of Greece, Vathy sheet. Institute of Geology and Mineral Exploration of Greece scale 1:50.000.

Theodoropoulos, D, 1979b. Geological map of Greece, Neon Carlovassi sheet. Institute of Geology and Mineral Exploration of Greece scale 1:50.000.

Toda, S, Stein, R.S, Sevilgen, V, Lin, J, 2011. Coulomb 3.3 Graphic-rich deformation and stress-change software for earthquake, tectonic, and volcano research and teaching-user guide. U.S. Geological Survey Open-File Report 2011-1060, pp. 63. http://pubs.usgs.gov/of/2011/1060/

Triantafyllou, I, Gogou, M, Mavroulis, S, Katsetsiadou, K.-N, Lekkas, E, Papadopoulos, G.A, . (2020). The tsunami caused by the 30 October 2020 Samos (Greece), East Aegean Sea, M 6.9 earthquake: impact assessment from post-event field survey and video records (v2, 16 Nov. 2020). Joint Scientific Report of the National and Kapodistrian University of Athens, the Postgraduate Program "Environmental, Disaster, and Crisis Management Strategies", AGITHAR COST tsunami project, Safe Greece, International Society for the Prevention and Mitigation of Natural Hazards. DOI: 10.13140/RG.2.2.13938.12487, Available at: https://www.researchgate.net/publication/345977238_Samos2020-TSUNAMI-REPORT-FINALv2

Triantafyllou, I, Gogou, M, Mavroulis, S, Katsetsiadou, K.-N, Lekkas, E, Papadopoulos, G.A, 2020. The tsunami caused by the 30 October 2020 Samos (Greece), East Aegean Sea, M6.9 earthquake: impact assessment from post-event field survey and video records. Report published at EMSC: https://edcm.edu.gr/images/docs/2020/Samos2020-TSUNAMI-REPORT.pdf (Last Accessed: 12 December 2020)

Tur H, et al, 2015. Pliocene-Quaternary tectonic evolution of the Gulf of Gökova, southwest Turkey. Tectonophysics, 638, 158-176.

Türkelli, N, Kalafat, D. and Gündoğdu, O, 1995. Field observations and focal mechanism solution of November 6, 1992 İzmir (Doğanbey) Earthquake. Jeofizik Dergisi, 9 (10), 343–348.

USGS, 2017. ShakeMap – Earthquake Ground Motion and Shaking Intensity Maps: U.S. Geological Survey, https://doi.org/10.5066/F7W957B2.

Uzel, B, Sözbilir, H, Özkaymak, Ç, Kaymakçı, N, Langeris, C.G, 2013. Structural evidence for strike-slip deformation in the İzmir-Balıkesir Transfer Zone and consequences for late Cenozoic evolution of western Anatolia (Turkey). Journal of Geodynamics, 65, 94–116.

Vadaloukas, G, Vintzilaiou, E, Ganas, A, Giarlelis, C, Ziotopoulou, K, Theodoulidis, N, Karasante, E, Margaris, V, Mylonakis, G, Papachristidis, A, Repapis, K, Psarropoulos, P, Sextos, A., 2020. Samos earthquake, 30 October 2020 - Preliminary Report. Hellenic Association of Earthquake Engineering, 65 p. Available at: https://www.eltam.org/images/nltr/newsletters/20201125/etam_report_samos2020earthquake.pdf

Vamvakaris, DA, Papazachos, CB, Papaioannou, CA, Scordilis, EM, and Karakaisis, GF, 2016. A detailed seismic zonation model for shallow earthquakes in the broader Aegean area. Natural Hazards and Earth System Sciences, 16(1), p.55.

Van Hinsbergen, D.J, Kaymakci, N, Spakman, W, Torsvik, T.H, 2010. Reconciling the geo-logical history of western Turkey with plate circuits and mantle tomography. Earth Planet. Sci. Lett, 297 (3-4), 674–686.

Vernant, P, Reilinger, R, McClusky, S, 2014. Geodetic evidence for low coupling on the Hellenic subduction plate interface, Earth and Planetary Science Letters, 385, 122-129.

Wald, D. J, and T. I. Allen, 2007. Topographic Slope as a Proxy for Seismic Site Conditions and Amplification, Bulletin of the Seismological Society of America, 97(5), 1379-1395.

Waldhauser, F, 2001. HypoDD-A Program to Compute Double-Difference Hypocenter Locations, U.S. Geol. Surv. Open File Rep. 01-113, 25 p. Wessel, P, Smith, W.H.F, 1998. New, improved version of generic mapping tools released, Eos. Trans. Am. Geophys. Union, 79, 579.

Wegnüller, U, Werner, C, Strozzi, T, Wiesmann, A, Frey, O, Santoro, M, 2016. Sentinel-1 support in the GAMMA Software, Proc Compu Sci 100:1305–1312.

Wessel, P, Smith, WHF, 1998. New, improved version of generic mapping tools released, Eos. Trans. Am. Geophys. Union, 79, 579.

Wortel, MJR, Spakman, W, 2000. Subduction and slab detachment in the Mediterranean–Carpathian region. Science, 290, 1910–1917.

Yagi, Y, & Kikuchi, M. 2000. Source rupture process of the Kocaeli, Turkey, earthquake of August 17, 1999, obtained by joint inversion of near-field data and teleseismic data. Geophysical Research Letters, 27(13), 1969-1972.

Yagi, Y, Kikuchi, M, & Nishimura, T. 2003. Co-seismic slip, post-seismic slip, and largest aftershock associated with the 1994 Sanriku-haruka-oki, Japan, earthquake. Geophysical research letters, 30(22).

Yagi, Y, Mikumo, T, and Pacheco, J, 2004. Source rupture process of the Tecoman, Colima, Mexico earthquake of January 22, 2003, determined by joint inversion of teleseismic body wave and near–field data. Bull. Seismol. Soc. Am, 94 (5), 1795–1807.

Yoshida, S, Koketsu, K, Shibazaki, B, Sagiya, T, Kato, T. & Yoshida, Y, 1996. Joint inversion of near- and far-field waveforms and geodetic data for the rupture process of the 1995 Kobe earthquake, J Phys Earth, 44, 437–454.

Zhu, L, Akyol, N, Mitchell, BJ, and Sözbİlİr, H, 2006a. Seismotectonics of western Turkey from high-resolution earthquake relocations and moment tensor determinations. Geophysical Research Letters 33, L07316, doi: 10.1029/2006GL025842.

Zhu, L, Mitchell, BJ, Akyol, N, Cemen, I. and Kekovali, K, 2006b. Crustal thickness variations in the Aegean region and implications for the extension of continental crust. Journal of Geophysical Research: Solid Earth, 111(B1).

Zumberge, JF, MB. Heflin, DC. Jefferson, MM. Watkins, and FH. Webb, 1997. Precise point positioning for the efficient and robust analysis of GPS data from large networks, J. Geophys. Res, 102(B3), 5005–5017.

APPENDIX

Table S1-Electronic Appendix (TableS1.cat)

Table S1 Catalogue of relocated sequence from AUTh of the period 30 Oct 2020 – 1 Dec 2020

Available at https://www.dropbox.com/s/o4y70nknb62cn39/Samos2020.cat?dl=0

Table S2. Moment tensor solutions for the major aftershocks (SL-NKUA determinations).

YYYYMMDD	hh:mm:ss.ss	Latitude	Longitude	Depth (km)	**M**	strike	dip	rake	Mo (dyn-cm)
20201030	11:51:24.850	37.8822	26.7887	13	6.9	27	50	-81	2.81E+26
20201030	13:00:43.890	37.8756	26.8598	12	4.7	294	41	-72	1.43E+23
20201030	14:46:04.790	37.8408	26.8570	11	4.0	91	51	-89	1.38E+22
20201030	15:14:57.140	37.8433	26.8596	15	5.0	264	37	-126	3.90E+23
20201030	16:18:27.820	37.6703	27.3073	12	3.9	79	38	-75	7.89E+21
20201030	17:16:04.440	37.8502	26.9720	11	3.8	114	45	-118	6.57E+21
20201030	20:35:24.640	37.8065	26.4794	13	4.1	165	57	-20	1.62E+22
20201030	21:46:25.460	37.8336	26.8172	11	3.7	111	47	-113	4.57E+21
20201030	22:53:21.400	37.8185	26.7353	10	3.8	93	42	-97	7.01E+21
20201030	23:05:30.480	37.8334	26.8610	8	4.0	119	47	-116	1.30E+22
20201031	00:20:52.000	37.8140	26.9465	12	3.9	99	47	-107	8.48E+21
20201031	01:40:31.950	37.8574	26.4510	12	4.1	140	20	-20	1.69E+22
20201031	02:10:28.700	37.8625	26.9123	8	4.1	91	42	-77	1.55E+22
20201031	05:31:30.540	37.8424	26.8249	12	4.8	285	61	-113	1.87E+23
20201031	08:41:51.730	37.8718	26.9184	11	3.8	105	33	-87	6.90E+21
20201031	08:46:59.520	37.8532	26.4470	13	4.1	126	35	-30	1.59E+22
20201031	14:42:43.800	37.8637	26.4483	12	4.2	121	27	-41	2.14E+22
20201031	19:31:31.480	37.7743	27.0160	12	3.9	89	49	-113	7.98E+21
20201101	07:05:13.470	37.8486	26.9920	12	4.2	89	39	-111	2.81E+22
20201101	07:33:08.130	37.8276	26.8831	11	4.4	297	74	-61	5.18E+22
20201101	08:33:13.700	37.8470	26.8631	9	3.7	100	42	-116	5.30E+21
20201102	11:58:03.990	37.8609	26.8869	11	4.0	109	33	-105	1.27E+22
20201102	15:09:07.440	37.7261	27.0480	13	3.9	83	50	-81	7.82E+21
20201102	19:16:39.540	37.8495	26.4245	13	4.2	121	40	-13	2.16E+22
20201103	20:35:36.820	37.8601	26.4132	13	4.1	125	28	-42	1.64E+22
20201103	23:17:07.440	37.7292	27.0050	13	3.9	281	25	-103	9.49E+21
20201104	02:24:17.330	37.7330	27.0199	11	3.8	249	55	-113	7.32E+21
20201109	20:30:59.510	37.8471	26.9344	10	4.1	271	54	-97	2.06E+22
20201111	06:49:46.470	37.8852	26.9707	12	4.3	92	51	-98	4.16E+22

Table S3. Centroid Moment Tensor (CMT) solutions for the **M**7.0 2020 Samos (Kusadasi bay) aftershock sequence, during the period from October 30, 2020 to November 11, 2020. The source parameters have been retrieved using the broadband stations operated by KOERI.

No	Date	Time	Latitude	Longitude	CMT Depth	Strike°	Dip°	Rake°	**M**
1	30.10.2020	13:00	37.84	26.79	8	226	65	-177	4.9
2	30.10.2020	15:14	37.84	26.85	8	286	52	-78	5.1
3	30.10.2020	15:19	37.83	26.91	8	230	68	-151	4.7
4	30.10.2020	16:18	37.64	27.14	5	37	63	174	4.2
5	30.10.2020	16:28	37.80	26.83	4	306	67	-59	4.0
6	30.10.2020	16:37	37.92	26.48	4	85	82	-106	3.9
7	30.10.2020	16:40	37.85	26.96	12	230	74	-173	3.8
8	30.10.2020	16:47	37.89	26.92	8	236	51	-148	3.7
9	30.10.2020	17:16	37.87	27.00	9	261	38	-96	4.1
10	30.10.2020	17:47	37.89	26.95	6	267	39	-113	3.7
11	30.10.2020	18:47	37.88	26.98	6	256	40	-123	3.7
12	30.10.2020	18:59	37.88	26.39	6	353	48	-11	3.7
13	30.10.2020	19:08	37.86	26.45	6	86	86	-106	4.3
14	30.10.2020	20:35	37.79	26.52	6	42	83	178	4.3
15	30.10.2020	21:41	37.87	26.99	6	293	43	-66	4.0
16	30.10.2020	21:46	37.81	26.80	12	43	88	178	3.9
17	30.10.2020	22:37	37.81	26.89	6	276	51	-93	3.9
18	30.10.2020	22:53	37.82	26.75	4	273	31	-98	4.1
19	30.10.2020	23:05	37.79	26.86	6	287	58	-65	4.1
20	30.10.2020	23:09	37.89	26.92	12	247	55	-166	4.0
21	30.10.2020	23:33	37.85	26.86	4	242	61	-125	4.0
22	30.10.2020	23:45	37.85	26.86	4	241	57	-123	3.6
23	31.10.2020	00:20	37.81	26.96	12	323	82	-29	4.0
24	31.10.2020	01:40	37.86	26.44	4	329	69	22	4.0
25	31.10.2020	01:59	37.83	27.01	6	287	48	-72	3.7
26	31.10.2020	02:10	37.85	26.90	5	270	43	-112	4.2
27	31.10.2020	02:39	37.89	26.49	3	96	89	-110	3.7
28	31.10.2020	02:41	37.88	26.49	6	252	79	174	3.8
29	31.10.2020	04:12	37.86	26.46	3	248	78	150	3.9
30	31.10.2020	04:28	37.80	26.90	12	254	81	179	3.5
31	31.10.2020	05:22	37.82	26.80	6	296	57	-70	3.8
32	31.10.2020	05:31	37.84	26.81	6	285	48	-82	5.0
33	31.10.2020	06:34	37.84	26.93	10	265	81	-112	3.8
34	31.10.2020	12:37	37.90	26.59	8	273	83	-119	3.9
35	31.10.2020	14:42	37.88	26.47	3	96	86	-110	4.3
36	31.10.2020	16:06	37.89	26.67	2	271	87	40	4.0
37	1.11.2020	02:21	37.84	26.42	8	295	32	-88	4.0
38	1.11.2020	07:05	37.83	26.99	12	239	84	-178	4.4

39	1.11.2020	07:33	37.81	26.88	5	299	54	-71	4.6
40	2.11.2020	11:58	37.88	26.91	2	244	29	-174	4.0
41	2.11.2020	19:16	37.88	26.51	3	252	72	155	4.2
42	2.11.2020	19:39	37.72	27.05	6	257	75	-166	3.9
43	3.11.2020	18:03	37.88	26.45	5	83	80	-127	3.9
44	3.11.2020	23:17	37.70	26.99	6	20	38	146	4.1
45	3.11.2020	23:56	37.74	27.02	6	60	86	-166	3.7
46	4.11.2020	00:00	37.72	27.02	3	70	61	-168	3.9
47	4.11.2020	13:21	37.60	26.87	15	239	73	-162	3.8
48	5.11.2020	22:19	37.84	26.88	6	262	45	-101	3.9
49	6.11.2020	15:31	37.87	26.87	8	237	72	-150	3.8
50	6.11.2020	20:57	37.75	26.01	12	252	41	139	3.9
51	8.11.2020	17:56	37.87	26.60	8	277	32	-5	3.6
52	9.11.2020	04:20	37.86	26.76	6	273	43	-102	3.7
53	9.11.2020	20:30	37.89	27.00	6	296	38	-79	4.2
54	10.11.2020	02:25	39.01	27.16	6	289	57	-92	3.9
55	11.11.2020	06:49	37.88	27.00	10	245	44	-127	4.5

Reports-Appendix

List of available reports for the 2020 Samos earthquake (not a complete list)

- AFAD(2020). "30 Ekim 2020 EGE DENİZİ, SEFERİHİSAR (İZMİR) AÇIKLARI (17,26 km) Mw 6.6 DEPREMİNE İLİŞKİN ÖN DEĞERLENDİRME RAPORU"
- Eyidoğan H (2020). “Report on the seismological characteristics and effects of the 30 October 2020 Samos-Kuşadası Bay earthquake (Mw7.0) in the western Aegean Sea”
- GÜ (2020). “SEFERİHİSAR AÇIKLARI (İZMİR) DEPREMİ ÖN DEĞERLENDİRME RAPORU”
- İÜ-CERRAHPAŞA (2020). "İZMİR (KUŞADASI-SİSAM) DEPREMİ ÖN İNCELEME RAPORU MW 7.0 (EMSC)
- KOERI (2020). "30 EKİM 2020 EGE DENİZİ DEPREMİ"
- KOERI-INGV-NOA (2020). “Serious tsunami hits Greece and Turkey after 7.0 earthquake”
- İTÜ (2020). “30.10.2020 İZMİR DEPREMİ DEĞERLENDİRME RAPORU
- METU (2020). “October 30, 2020 Aegean Sea Samos-Seferihisar Izmir Earthquake (Mw=6.9) Reconnaissance Report”
- Kalogeras et al. (2020). "The earthquake of October 30th, 2020 at Samos, Eastern Aegean Sea, Greece"
- Lekkas et al. (2020). The October 30, 2020, Mw 6.9 Samos (Greece) earthquake, EMSC Report
- AÜ (2020). "2020.10.30 (Mww=7.0) Sisam depremi ve artçılarının Ege’nin neotektonik çerçevesinin anlaşılmasına katkıları"
- Seyitoğlu et al. (2020). “2020.10.30 (Mww=7.0) Sisam depremi ve artçılarının Ege’nin neotektonik çerçevesinin anlaşılmasına katkıları”
- Yalçıner et al. (2020). “THE 30 OCTOBER 2020 (11:51 UTC) IZMIR-SAMOS EARTHQUAKE AND TSUNAMI; POST-TSUNAMI FIELD SURVEY PRELIMINARY RESULTS
- ITSAK (2020). The Earthquake of Oct. 30, 2020, Mw7.0 (11:51GMT) North of Samos Island (Greece): Observed strong ground motion on Samos island, - Preliminary Report ITSAK v3.0, Thessaloniki pp. 9.
- DEÜ (2020). “30 EKİM 2020 SİSAM (SAMOS) DEPREMİ (Mw: 6,9) DEĞERLENDİRME RAPORU”
- MTA (2020). "30 EKİM 2020 EGE DENİZİ DEPREMİ (Mw=6,9) SAHA GÖZLEMLERİ VE DEĞERLENDİRME RAPORU"
- Papadimitriou et al. (2020). “Preliminary report on the Mw=6.9 Samos earthquake of 30 October 2020”
- Eyidoğan H (2020). "7.0 büyüklüğündeki İzmir depreminin özellikleri, tsunami ve ağır hasarın nedenleri"

2.0 Tsunami Effects and Performance of Port Structures

Turkish Authors: Gözde Güney Doğan, Ahmet Cevdet Yalçıner, Yalçın Yüksel, Orhan Polat, Işıkhan Güler, Ergin Ulutaş, Cihan Sahin, Berguzar Ozbahceci, Öcal Necmioğlu, Utku Kanoğlu

Greek Authors: Nikos Kalligeris, Marinos Charalampakis, Vassilios Skanavis, Nikolaos Melis, Costas Synolakis

2.1 Introduction

On October 30th, 2020, a **M**7.0 earthquake struck the eastern Aegean Sea, with the epicenter ~10 km offshore, north of the coast of Samos Island. The earthquake prompted the Tsunami Service Providers (TSPs), operating in the Eastern Mediterranean under the umbrella of the North-Eastern Atlantic, Mediterranean and Connected Seas (NEAM) Tsunami Warning System of IOC/UNESCO, to issue tsunami warning messages. These were disseminated to the national Civil Protection Authorities and other Member States that have subscribed to the TSP services.

The tsunami arrived within about ten minutes to the NW coast of Samos Island and within 20 min to the coast of Turkey, where one person died due to the tsunami and significant damage was caused to coastal infrastructure (TUBITAK, 2020). The short arrival time left a very narrow window for the coastal population to evacuate and move to higher ground, not to mention an impossibly small window for TSP messages to be delivered and acted upon by local authorities.

The tsunami resulting from the Samos Island (Aegean Sea) earthquake was yet another reminder of the tsunami threat on coastal communities in the Eastern Mediterranean. The region has numerous tsunamis in its documented history (Ambraseys and Synolakis, 2010), including the 365 and 1303 A.D. tsunamis that impacted the whole eastern Mediterranean basin (England et al., 2015), and the Amorgos 1956 tsunami with 20 m maximum runup documented on the south coast of Amorgos (Okal et al., 2009).

Since 2012 when the NEAM region started to be operationally monitored, five tsunamis have been recorded. The most recent events that resulted in tsunami inundation are the 2 May 2020 Ierapetra and the 20 July 2017 Bodrum-Kos (Dogan et al., 2019) tsunamis. The latter had similar characteristics with the Samos-Aegean tsunami: both had associated runup less than 10m, and the first wave arrived on the nearest coast within minutes. Such near-field tsunamis pose significant challenges to TSPs which have to issue timely warnings. Tsunami education and awareness of local populations remains the cornerstone of any effective tsunami emergency plan; self-evacuation of the population at risk after ground shaking that lasts more than 15 sec or after unusual shoreline motions can save lives.

In this chapter, we present the findings of post-tsunami reconnaissance field campaigns in the impacted areas and provide quantitative measurements of tsunami intensity, as well as

observations of the tsunami runup and impact on coastal infrastructure, ports and utilities. The objective is to allow the tsunami community to better understand the dynamics of tsunami generation, the timeline and intensity of tsunami impact, and provide data to validate hydrodynamic modeling results. We also present tide gauge records of the tsunami, information on tsunami warning messages issued during the event, tsunami source models published before this report was drafted, and hydrodynamic modeling results.

Our objective is to contribute to our ongoing quest for wisdom to reduce tsunami impacts. This chapter is dedicated to the people who lost their lives due to the earthquake and the tsunami, with our condolences for the casualties and property lost in Turkey and Greece.

2.2 Observed Runup and Flow Depth

The generated tsunami mostly affected the north coast of Samos Island, Greece, and the central Aegean coast of Turkey, from the Alacati locality in Cesme district in the north, to the Gumuldur coast in the Menderes district of Izmir province in the south. Immediately after the event, post-tsunami reconnaissance teams were deployed in Turkey (Sections 2.2.1-2.2.6) and Greece (Sections 2.2.7-2.2.8). The teams collected quantitative measurements of tsunami impact along the coast, documented the tsunami effects and interviewed eyewitnesses.

2.2.1 *Overview of field observations along the Turkish coast*

In Turkey, a first field reconnaissance campaign took place between October 31 - November 01 to collect quantitative data before cleanup. On November 04-06, a second field survey was held for more detailed measurement and investigation. The surveyed coast in Turkey consisted of: i) Alacati and Zeytineli regions in the Northwest, ii) Sigacik Bay, Akarca and Tepecik regions in the North, and iii) Gumuldur region in the Northeast with respect to the earthquake epicenter (Figure 2.1).

The survey team collected flow depth, inundation height, runup and inundation distance measurements along the surveyed coastline. The teams aimed to document the tsunami effects along the coast, take pictures and video recordings before the traces were cleaned, and interview eyewitnesses. Table 2.1 presents a list of the surveyed locations and measurements, including explanatory notes.

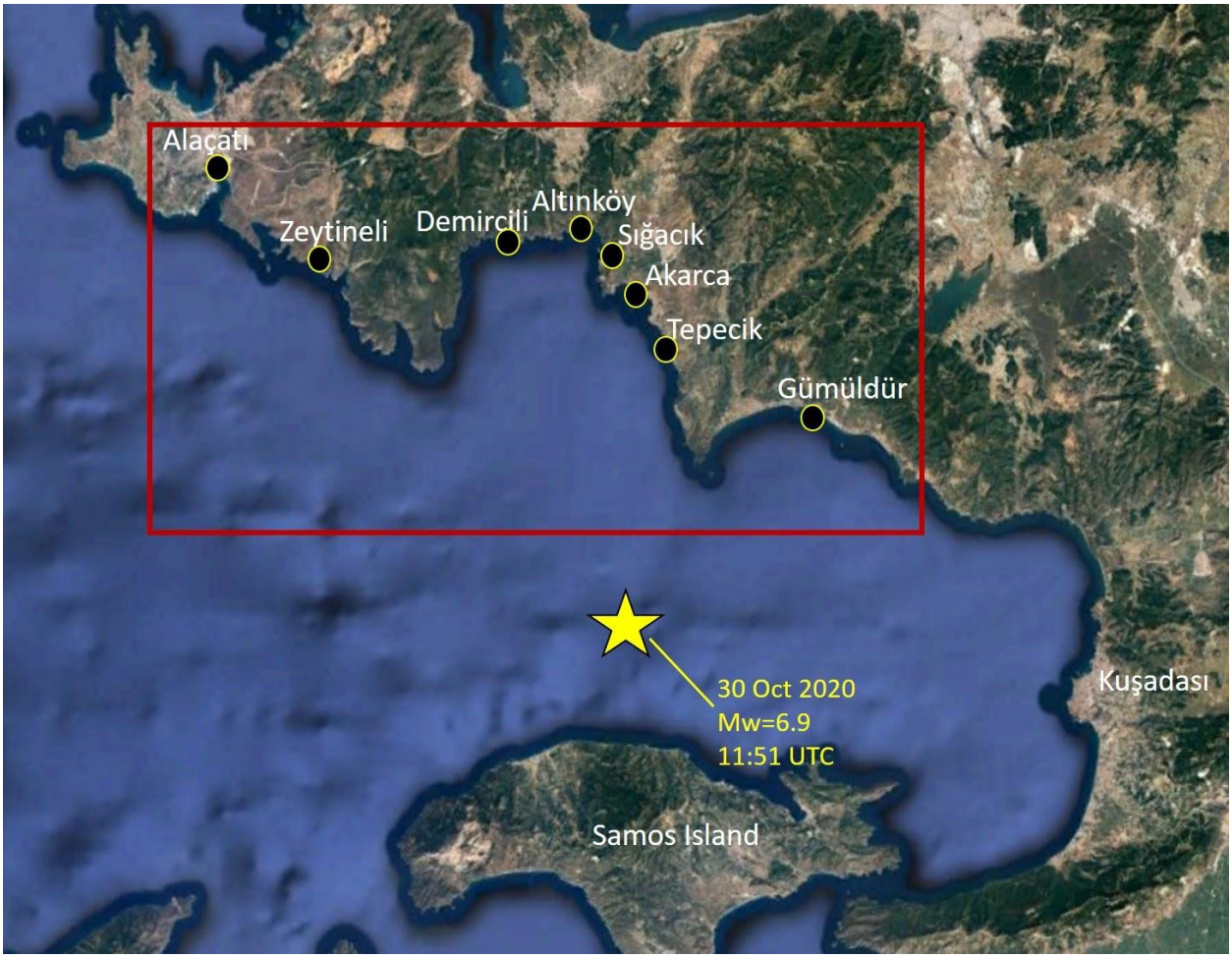

Figure 2.1. Post-tsunami field survey areas where observations of tsunami effects were obtained from eyewitnesses, debris or traces identified along the Turkish coast of Aegean Sea in İzmir Province.

Table 2.1. The post-tsunami survey measurements.

ID	Label/Place	Region	Lon. °E	Lat. °N	Notes	Measure-ment (m)	Measurement Type
Z1	Palm Tree-1	Zeytineli	26.48859	38.19600	Traces on the palm tree	1.9	Flow depth
Z2	Summer House	Zeytineli	26.49027	38.19587	Traces on the wall of a house	1.5	Flow depth
Z3	House-3	Zeytineli	26.49296	38.201206	**707 m**, maximum inundation at Zeytineli	-	
Z4	Road/pavement	Zeytineli	38.197321	26.493027	Maximum inundation 265	0.63	Runup height
Z5	Summerhouse	Zeytineli	38.195093	26.491905	-	2.43	Inundation height
AL1	Boat	Alacati	26.377520	38.265709	A boat was dragged to this point along the stream ~1160 m		

AL2	Port Alacati Houses-1	Alacati	26.37427	38.26370	water level increased and overtopped the garden wall up to 1.7 m		
AL3	Azmak Bridge	Alacati	26.37684	38.27061	1.0 km far from coast	0.3	Flow depth
AL4	Port Alacati Houses-2	Alacati	26.37304	38.26346	water level increased and overtopped the garden wall up 1.7 m		
AL5	Stream	Alacati	26.392672	38.276917	Maximum tsunami penetration **~2490 m at Alaçatı**		
AL6	Fishery Port	Alacati	26.381979	38.255867	72 m inundation distance	1.00	Runup height
D1	Beach	Demircili	26.676901	38.211628	45 m inundation		
D2	Southeastern narrow beach	Demircili	26.686378	38.207508	Significant damage, 1.8m sea receded. More than 1m water level increase inside the port		
D3	Denizyildizi Beach	Demircili	26.694419	38.210438	15 m inundation	0.7	Runup height
ALT1	Altinkoy Beach	Altinkoy	26.721817	38.212994	230 m inundation	-	
ALT2	Streambed	Altinkoy	26.721487	38.214794	600 m inundation	0.15	Flow depth
S1	Keyf-i Kahya Lounge Cafe	Sigacik	26.785155	38.191387		0.22	Flow depth
S2	Local park	Sigacik	26.784490	38.191601	A wall in the local park	0.8	Flow depth
S3	Teos Marina	Sigacik	26.783164	38.191170	a garden fence surrounding the port	0.86	Flow depth
S4	Kumsal Cafe	Sigacik	26.786701	38.195445	@ entrance: 0.6 @ inside: 0.86	1.22	Flow depth
S5	House	Sigacik	26.787424	38.19560	trace on a wall of a white colored house	0.88	Flow depth
S6	House	Sigacik	26.79003	38.19578	a trace on a house wall	0.1	Flow depth
S7	Shop- Kaleiçi	Sigacik	26.78609	38.19488	trace on the walls of shops	0.4	Flow depth
S8	Shop-Kaleiçi	Sigacik	26.786443	38.195027	trace on the walls of shops	0.4	Flow depth
S9	Vuslat Restaurant	Sigacik	26.785967	38.201305	trace on the windows of the restaurant	1.86	Runup height
S10	Building	Sigacik	26.788412	38.195615	trace on the garden wall of a building	0.6	Flow depth
S11	Beach	Sığacık	26.780158	38.203886	tsunami deposits	1.51	Runup height
S12	Building	Sığacık	26.785291	38.194144	Watermarks/traces	1.38	Inundation

							height
S13	Kaleiçi	Sığacık	26.785409	38.195129	Maximum inundation height	**2.31**	Inundation height
S14	-	Sığacık	38.199234	26.792919	**415 m,** maximum inundation distance at Sığacık	1.35	Runup height
A1	Fishery port	Akarca	38.1647	26.8146	A wire fence next to coast	1.3	Flow depth
A2	House	Akarca	38.164393	26.814826	Trace on the walls of the closest house to the shoreline	1.9	Splash height
A3	Diving center area	Akarca	26.813511	38.168288	**285 m**, maximum inundation distance at Akarca	1.04	Runup height
A4	Southeastern part	Akarca	26.825079	38.155888	Traces on the wall, sweeps on the road	0.8	Flow depth
A5	Cafe	Akarca	26.821295	38.161486	Trace on the steps of a cafe	0.2	Flow depth
A6	Okeanos Beach Bungalows	Akarca	26.821212	38.161753	100 m inundation		
A7	Stream	Akarca	26.821461	38.162223	150 m inundation		
A8	Fishery Port Area	Akarca	26.814925	38.164035	Trace on the wall of a house at 40 m distance from shore	0.5	Flow depth
A9	Garden	Akarca	26.810972	38.166476	Trace on the wall of a garden	0.55	Flow depth
A10	Diving Center Area	Akarca	26.811804	38.166841	112 m inundation	0.2	Flow depth
A11	House/Diving Center Area	Akarca	26.812036	38.166436	The eyewitness cleaned the wall; he said that it was 1 meter, the veranda was all covered by sweeps	0.8	Flow depth
A12	Northwestern part	Akarca	26.807888	38.168139	80 m inundation		
A13	Northwestern part	Akarca	26.803827	38.171062	20 m inundation		
A14	Northwestern part	Akarca	26.811287	38.168131	250 m inundation		
A15	Northeastern part	Akarca	26.820431	38.16152	45 m inundation		
A16	Northeastern part	Akarca	26.818972	38.162938	80 m inundation		
A18		Akarca	38.167196	26.809288		2.30	Inundation Height
A19		Akarca	38.168056	26.809219		1.15	Runup Height
A20		Akarca	38.165614	26.813773		2.35	Inundation Height
A21		Akarca	38.165683	26.813717		**2.88**	Inundation Height

G1	Beach	Gumuldur	27.013597	38.056631	Only traces on the beach		
G2	Yali Resort Beach	Gumuldur	26.999167	38.065173	25 m inundation		
G3	Yali Resort Beach	Gumuldur	26.998755	38.065219	Trace on an object	0.5	Flow depth
G4	Harbour	Gumuldur	26.995283	38.067702	Minor damage on the boats. No trace of water on walls, etc.		
G5	Rafael Boutique Hotel	Gumuldur	26.949292	38.075673	25 m inundation only at the beach		
G6	Beach	Gumuldur	26.949218	38.075688	15 m inundation, sweeps next to beach valley line, inundation only at the beach		
T1	Central part	Tepecik	38.145829	26.820073	Inundation 12 m, only sweeps		
T2	Stream	Tepecik	38.139539	26.831444	Penetration 120 m along a small stream		
T2a	Cafe	Tepecik	38.138961	26.83055	Inundation 20 m No flow into the cafe. Café next to the stream		
T3	Beach area/summer houses	Tepecik	38.135566	26.833051		1.5	Flow Depth
T4		Tepecik	38.111374	26.844436	24 m inundation, only sweeps		

2.2.2 *Field observations in Alaçatı and Zeytineli localities*

Alaçatı Locality. In Alaçatı maximum tsunami penetration reached ~2490 m along the "Alaçatı Azmak" local stream. According to the observations and eyewitness reports, the tsunami inundation mainly followed the topographical features. The tsunami impact was apparent, starting from the river's beginning, Alacati Azmak (Figure 2.2-Figure 2.3). A flow depth of 0.3 m was measured in the Alacati Azmak bridge located at the North (near the Izmir-Cesme highway viaduct) and 1.0 km away from the coast (38.27061N 26.37684E).

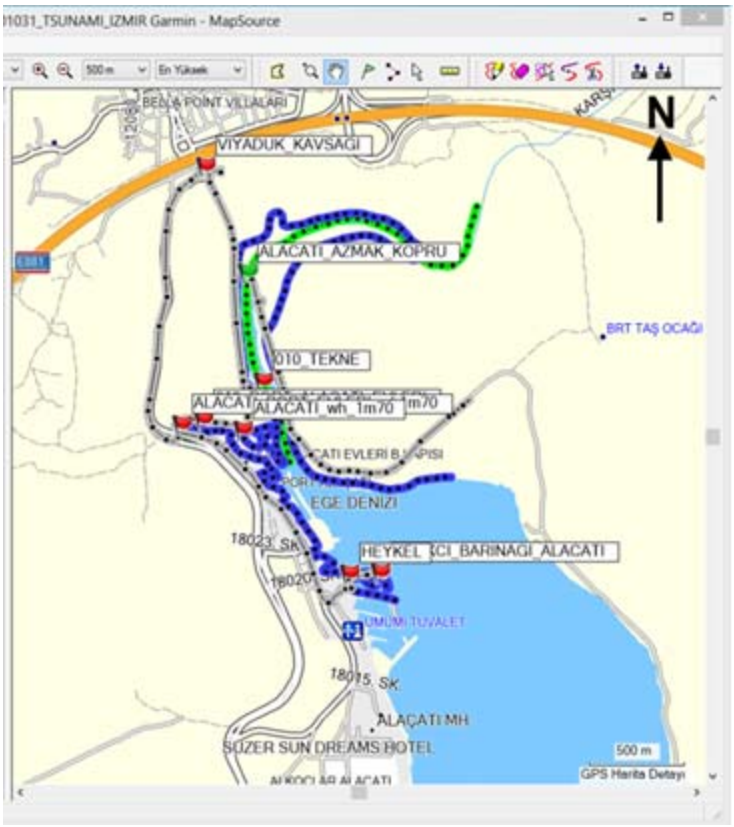

Figure 2.2. View of the stream bed (green line) and the tsunami inundation zone (blue line) as of GPS records for Alacati. Gray lines denote track records.

Figure 2.3. View of the stream bed and the tsunami inundation zone in Alacati (photo view from W to E). The boat was dragged ~1160 m from the shore, slightly visible at the right extremity of the photo.

The water level increased and overtopped the garden wall of Port Alacati Houses up to 1.70 m (38.26346N 26.37304E and 38.26320N 26.37654E) (Figure 2.4). Here, the sea receded up to a depth of 1.5 m, 28 minutes after the earthquake, as seen in a security video recording.

Figure 2.4. Water level rise at the garden wall of Alacati Port Houses according to the house owner (38.26370N 26.37427E).

Zeytineli Locality. In the Zeytineli locality, a 760 m maximum inundation distance was measured along the NNE-SSW direction from the coastline. The tsunami mainly followed the stream bed (Zeytineli Azmak), clearly showing that the tsunami inundation directly followed the topographic features, as there are steep slopes on both sides (mountainside). The tsunami impact was mostly observable in an area bracketed between two main roads at the beginning of the valley heights in the East and West (Figures 2.5 and 2.6).

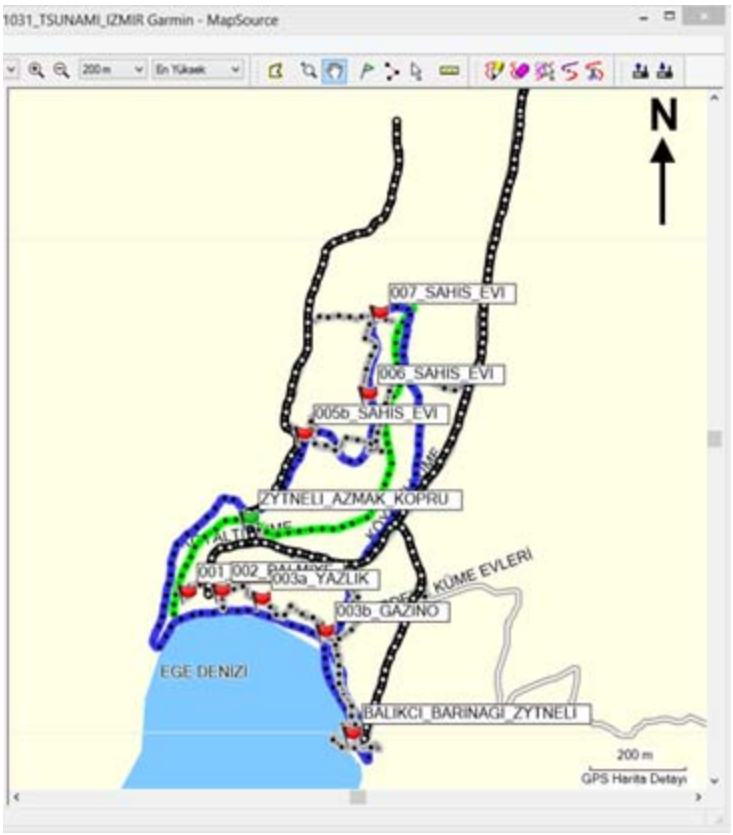

Figure 2.5. View of the stream bed (green line) and the tsunami inundation zone (blue line) as of GPS records for Zeytineli. Main roads (black line) are located at the E and W part of the valley heights. Gray lines denote track records.

Figure 2.6. View of the stream bed and the tsunami inundation zone in Zeytineli (photo view from E to W).

A 1.9m flow depth was measured on the palm trees, about 50 m away from the coastline (38.19600N 26.48859E and 38.19602N 26.48936E), and from debris materials accumulated at the outer wall of a house (38.19587N 26.49027E) (Figure 2.7). The abandoned summer houses along the shore were severely damaged, and debris materials accumulated on both outer walls and inside them. Additionally, tsunami boulders of concrete material (30x50x300 cm), weighing approximately 1 ton, were found transported 20-25 m inland.

Figure 2.7. (Left) Wave traces on the palm tree (1.90 m) near the coastline (38.19600N 26.48859E), and (Right) trace of debris materials accumulated at the outer wall (1.50 m) of a house (38.19587N 26.49027E).

2.2.3 *Field observations in Demircili and Altınköy localities*

In the Demircili locality, 45m inundation was measured at the beach (38.211628N 26.676901E) on the northwestern side of the bay (Figure 2.8). However, significant damage was observed by the local people and fishermen in a narrow beach site in the southeastern part of the bay (Figure 2.9, 38.207508N 26.686378E). According to the eyewitness statements, the sea receded almost 20 min after the earthquake, and came back in 3-4 minutes. They observed this cycle of ebb and tide for about five hours. A boat moored at a depth of 1.8 m was grounded when the sea receded during the leading-depression wave (Tadepalli and Synolakis, 1994). The water level increased more than 1 m inside the local fishery port.

Figure 2.8. Demircili locality, small inundation (45 m) in the northwestern part.

Figure 2.9. Highly damaged boats in a small fishery port in the Demircili locality.

In Denizyildizi Beach, the bay next to Demircili Beach in the eastern direction, the runup was measured as 0.7 m, and the inundation distance was 15 m (38.210438N 26.694419E, Figure 2.10).

Figure 2.10. Denizyıldızı Beach inundation Denizyıldızı beach inundation extent; the tsunami inundation limit was identified through the accumulated sweeps.

In the Altinköy locality, the tsunami inundated up to ~230 m towards the beach. On the other hand, the tsunami penetration along the streambed reached ~600 m with a 0.15 m flow depth (Figure 2.11).

Figure 2.11. Inundated areas in Altınköy. (left) view of the seawater along an initially dry streambed that accumulated during the largest tsunami inundation; (center) a closer view of the streambed after the tsunami; (right) view of the coastline just after the sea receded back following the largest inundation.

2.2.4 *Field observations in Sığacık, Akarca, and Tepecik localities*

Sığacık Locality. Sığacık locality was the most impacted area among the surveyed coastline, being a low-lying bay-shaped area with several local streambeds. Figure 2.12 shows the locations where maximum tsunami parameters were measured, and severe damage was observed. Eyewitnesses described how Teos Marina was damaged by cycling waves lasting 4-5 hours with an amplitude of 0.7 m. Four pontoons (out of six) were moved from their locations, and more than 200 boats were damaged. Near the pedestrian entrance of Teos Marina (38.191379N 26.783131E), the flow depth was measured as 0.86 m on the port's garden fence (Figure 2.13). The sea level increased 1.45 m from the stream level, overflowing the small bridge according to the eyewitnesses at a stream located towards the East direction from Teos Marina (38.192722N 26.784206E). The inundation distance here reached up to 260 m (Figure 2.14).

Figure 2.12. Summary of tsunami parameters measured in Sigacik.

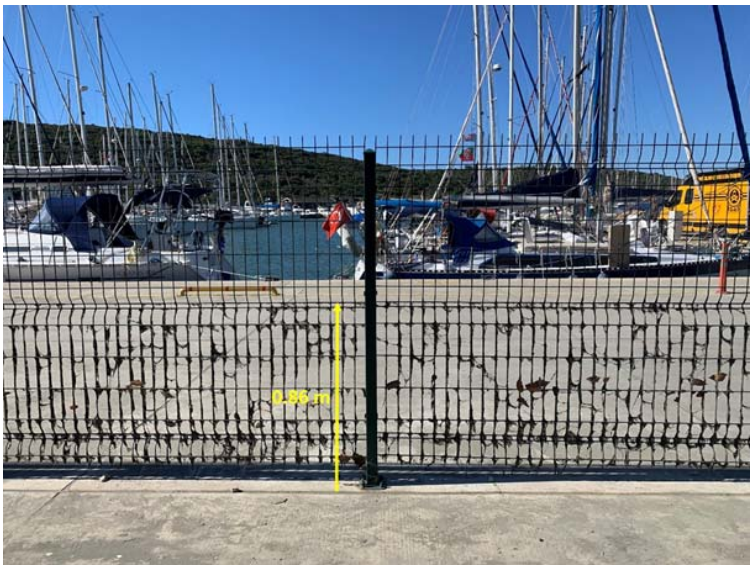

Figure 2.13. Tsunami traces on the garden fence of Teos Marina corresponding to a flow depth of 0.86 m. Classic presentation of debris "escalator" showing maximum flow depth.

Figure 2.14. Azmak river in the East direction from Teos Marina where the tsunami overflowed the small bridge.

All cafés and restaurants along the beachside in Sığacık Bay (Kaleiçi region) were severely damaged from the tsunami (Figure 2.15). The overland flow depth was measured as 0.6 m at the entrance of Kumsal Café (38.195445N 26.786701E). It increased to 0.86 m on the walls inside, and to 1.22 m at the back garden (landside) of the café since there is a reverse slope (the

elevation is decreasing) from the landslide entrance. The inundation distance in this part of Sigacik Bay was measured as ~70 m at 38.195248N 26.787168E. A paddleboat was transported 136 m inland to 38.196150N 26.789420E. When moving to the northern part inside Sigacik Bay, the flow depth was measured as 0.88 m from the trace on the wall of a white house (38.195600N 26.787424E). The maximum inundation distance in Sığacık was measured as 415 m along a streambed at 38.199234N 26.792919E. The maximum inundation height was found in the Kaleiçi region as 2.31 m at 38.195129N 26.785409E. The maximum runup height was measured as 1.86 m at 38.201539N 26.785637E.

Figure 2.15. Damage on properties and tsunami traces in cafes and shops in Sigacik.

Akarca Locality. The coast in the Akarca region from 38.171062N 26.803827E to 38.168131N 26.811287E was highly impacted by the tsunami, whereas a significant reduction of impact was observed in the region after the small V shape cape in the northwestern direction. In a small fishery port in the small cape (38.164666N, 26.814649E), 20 boats sank. A boat was dragged inland by the strong currents 90 m from the shoreline (Figure 2.16). A water storage tank (half full) and a car were also dragged towards land at 38.164526N 26.814808E. A 1.9 m splash height was measured on a vertical wall of a house located just near the shore (38.1646660N 26.8146490E, Figure 2.17).

Figure 2.16. A boat dragged 90 m from the shoreline.

Figure 2.17. A damaged house located just near the shoreline where a 1.9 m splash height was measured in Akarca.

In Seferihisar Diving Center (Figure 2.18, 38.165560N 26.813708E), located in Akarca, the sea receded up to a depth of 4m and ~180m in the horizontal direction, 10 minutes after the earthquake, according to the owner of the center, Mr. Aydın Tunca. He observed the first wave arrival between 10-15 minutes. He stated that he jumped on a sofa and drifted ~200-250 m inland on the sofa until the foot of the sofa was locked on the land. He observed 4-5 waves, about 8-10 minutes apart. The inundation distance measured was 279 m and the flow depth 2.19 m.

Figure 2.18. Tsunami damage on Seferihisar Diving Center (38.165683N 26.813717E).

Tepecik Locality. In the Tepecik locality, the team observed localized tsunami effects in several small bay-shaped areas. However, there was an overall decrease in the tsunami impact, after Akarca in the south-eastern direction. Only small inundation was inferred from the sweep deposits on the beaches at 38.145829N 26.820073E and 38.111393N 26.844270E (Figure 2.19). The maximum inundation distance reached 120 m along a small stream (38.139539N 26.831440E), where 20 m inundation was measured on the beach (238.138977N 26.830576E). A flow depth of 1.5 m was measured at point 38.135566N 26.833051E, where the ground elevation was ~0.5m above sea level.

Figure 2.19. Sweep deposits found in small beaches in Tepecik locality. The red dashed line indicates the estimated inundation border according to the sweep deposits.

2.2.5 *Field observations in Gümüldür locality*

Minor tsunami impact was observed in Gümüldür locality, where the tsunami effects were mainly limited to narrow beach areas. The inundation distance ranges between 15-25 m at different locations, with a maximum value measured as 25 m at Rafael Boutique Hotel beach (Figure 2.20, 38.075673N 26.949292E). At one location in Gümüldür, we found a trace on a small pier, suggesting a flow depth of 0.5 m at 38.065219N 26.998755E.

Figure 2.20. Tsunami inundation observed at Rafael Boutique Hotel beach and measured as 25 m.

2.2.6 *Summary of field observations on the Turkish coast*

According to the findings in this field survey and eyewitness reports, the most impacted areas were the Sigacik Marina, Sigacik Bay and the Akarca locality, about 30 km from the epicenter in the northern direction. In Sigacik locality, the maximum inundation distance reached 415 m, whereas it was 285 m in Akarca, where 20 boats sunk in a small fishery port. The maximum penetration reached 2490 m in Alacati Azmak Region. In the ancient Teos City, the inundation distance was 552 m.

The 2.31 m maximum inundation height was measured in Sığacık Bay in the Kaleiçi Region. The maximum runup height measured was 3.82 m in Akarca, about 90 m from the shore. Splash traces were found 1.9 m above the ground level on the wall of a highly damaged residence located nearshore, built at 0.89 m elevation. There was almost no significant inundation or water motion after Gümüldür locality. The tsunami impacts rapidly decreased after the cape of the "V" shaped peninsula between Tepecik and Gumuldur. Northward, the flow depth was measured as 1.9 m on the palm trees 50 m away from the coastline in Zeytineli Region.

To summarize, our findings show that in small bay-shaped areas with narrow entrances, the tsunami was highly amplified, and the impact on these coasts was more severe than elsewhere. The region contains many streams (Azmak in local language), which increases the potential of tsunami inundation and damage as first reported by Okal et al. (2002) who noted how far further tsunamis travel inland along riverbeds compared to the surrounding topography. Another important point is the remarkable increase in the awareness of the people, who mostly moved away from the shore after noticing the initial sea withdrawal, which suggested a leading depression N-wave. However, a woman in the Kaleiçi region of Sığacık locality could not resist the strong tsunami current and perished.

2.2.7 *Field observations in the island of Samos*

The day after the earthquake (October 31, 2020), a post-tsunami reconnaissance team from the National Observatory of Athens (NOA) and the Academy of Athens (AA) visited the island of Samos to collect quantitative measurements of the tsunami impact and interview eyewitnesses of the tsunami per established methods (Synolakis and Okal, 2005; UNESCO, 2014). From the eyewitness interviews, and collected photos and videos, information can be extracted regarding the arrival time of the first wave, its polarity (whether the water level rises or drops with the arrival of the first wave), as well as the time sequence of subsequent floods.

The survey focused on three coastal areas of Samos Island, on Karlovasi, Vathi and Pythagorion. The quantitative data collected is given in Table 2.2 and the findings from each of the three visited sites are given below. Tsunami eyewitness observations from the island of Chios, where the tsunami had a smaller impact, are summarized in the following section.

Table 2.2. Tsunami field measurement collected in the island of Samos.

ID	Site	Lat (deg)	Lon (deg)	Measurement (m)	Measurement type	Description
GR1	Pythagorion	37.68867	26.94287	0.53	Runup	The water just reached the top of the harbor quay at this location.
GR2	Pythagorion	37.68844	26.94319	<-0.46	Rundown	A fishing boat touched the seabed during rundown. The seabed at this location is rocky; measurement is approximate.
GR3	Pythagorion	37.69010	26.94309	-0.56	Rundown	Along the quay wall of the harbor as indicated by an eyewitness.
GR4	Pythagorion	37.69010	26.94309	0.57	Runup	Along the quay wall of the harbor as indicated by an eyewitness.
GR5	Karlovasi	37.79646	26.68700	0.99	Tsunami elevation	Flow depth water mark on the side of a structure.
GR6	Karlovasi	37.79492	26.68650	1.84	Runup	Water pond; eyewitness confirmed.
GR7	Vathi	37.75503	26.97700	1.70	Tsunami elevation	Stairs of the Bank of Greece branch; confirmed through eyewitness footage.

Karlovasi - Ag. Nikolaos. Karlovasi is a coastal town located on the NW side of the island, and therefore very close to the upper dip edge of the fault ruptured by the earthquake on October 30th, 2020. The tsunami reached Karlovasi within minutes after the earthquake. An eyewitness video from the area posted on Facebook live (reliable time information) shows that the sea level in the port of Karlovasi had already dropped significantly by 11:55 UTC and had begun rising again. At 11:57 UTC (~ 6 minutes after the earthquake), the risen sea level had reached the boat maintenance area (Figure 2.21a) on the western part of the harbor. At 11:59 UTC, the sea level had dropped again below the height of the quay. On the eastern part of the harbor, where the small craft marina is located, the flow depth over the quay, although not significant (of the order of 5-20 cm), was enough to suspend a mobile structure of the Greek Rescue Team and displace it from its base (Figure 2.21b). An eyewitness indicated that tsunami inundation reached an empty lot south of the marina and past the coastal road, where a water pond had formed (Figure 2.21c). This point corresponds to a wave runup of 1.84 m and 100 m of horizontal inundation.

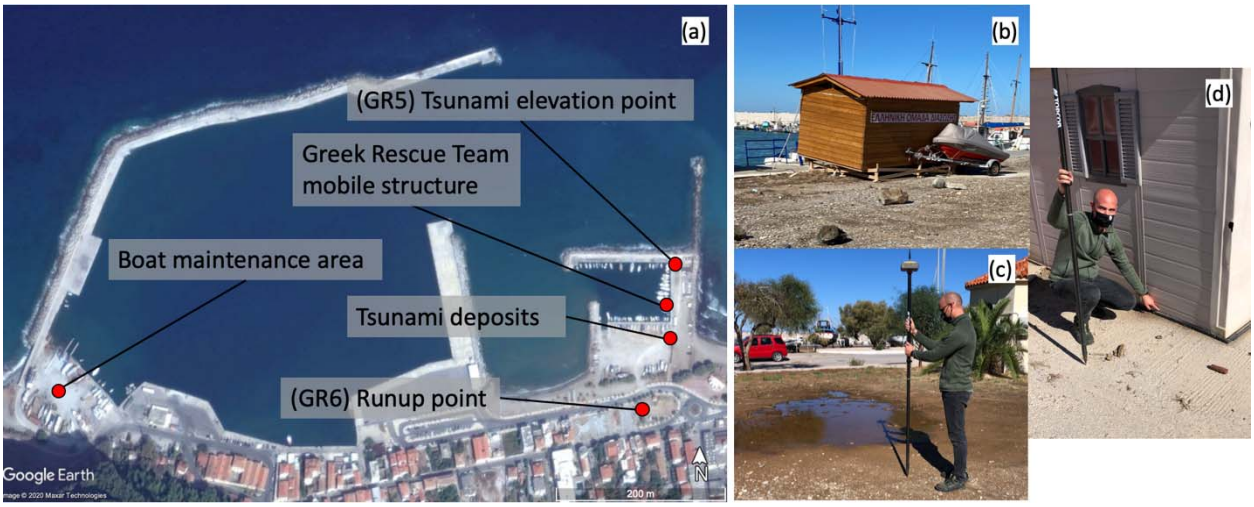

Figure 2.21. (a) Google Earth satellite picture of the harbor of Karlovasi and the locations of tsunami observations. (b) The mobile structure of the Greek Rescue team that was displaced by the tsunami. (c) The maximum runup point location. (d) The flow depth mark on the side of a structure where tsunami elevation was measured.

The very short arrival time of the first wave on the NW coast of Samos Island was confirmed through another video made available on social media. The CCTV footage from a coastal residence in the town of Ag. Nikolaos (~ 4 km ENE of Karlovasi) includes accurate timestamps on the video frames (Figure 2.22). It shows that the shoreline started receding between 11:52:32 and 11:53:08 UTC, reaching its minimum at 11:53:45 UTC and the first wave violently impacted the residence starting at 11:55:36 UTC. This footage is a testament of the very short arrival time of the first flood which left little time for evacuation, let alone for a timely tsunami warning to reach the local population.

Figure 2.22. Frames from a CCTV video shared on social media. The coastal residence is located in Ag. Nikolaos, Samos Island.

Vathi. The town of Vathi and the port of Samos are located on the edge of Vathi Bay. The bay is ~ 5 km long, and the depth at its entrance is 40 m, hardly a "bathy" bay, a word which in Greek means deep. The shallow bay and the distance to the fault rupture resulted in delay of the first wave arrival in Vathi (with respect to the NW coast of Samos Island). The damage from the tsunami was limited to the flooding of the ground floor and basement of buildings located close to the waterfront, as well as cars and bikes being swept away by the flood.

Eyewitnesses that were interviewed reported that the water level dropped ~ 20 minutes after the earthquake and that the first flood in Vathi started ~ 12 minutes later. However, a video recording from a security camera showed that the first flood started at 12:04 UTC, reaching its maximum height within a minute, and another, more powerful flood arrived at 12:24 UTC (Triantafyllou et al., 2020). Perhaps the eyewitnesses remember the second and more powerful flood more vividly than the first flood, and thus reported an arrival time of ~32 minutes. Two eyewitness videos shared on Facebook Live show two more powerful floods (> 1.5 m tsunami elevation) reaching their maximum height at 13:29 and 14:04 UTC.

Field measurements focused on the area landward from the marina of Vathi and Pythagoras Square (Figure 2.23). An eyewitness indicated the maximum level the water reached at the entrance steps to the Bank of Greece branch, which was confirmed through videos shared on social media. This datapoint, located 62 m inland from the marina (Figure 2.23b), corresponds to a tsunami overland flow depth of 1.0 m and 1.7 m tsunami height. A flow depth of 0.95 m was measured along Tobazis St. at the side of the Bank of Greece branch that runs normal to the shoreline (Figure 2.23c). The inundating water traveled through the narrow street and

reached the commercial street of Cpt. Stamatis, where a flow depth of 0.5 m was observed (Figure 2.23d). The water entered the stores and flooded the basements of the buildings. Further north, the inundating water traveled through Pythogoras Square and reached the pavement next to Ag. Nikolaos Square (Figure 2.23e).

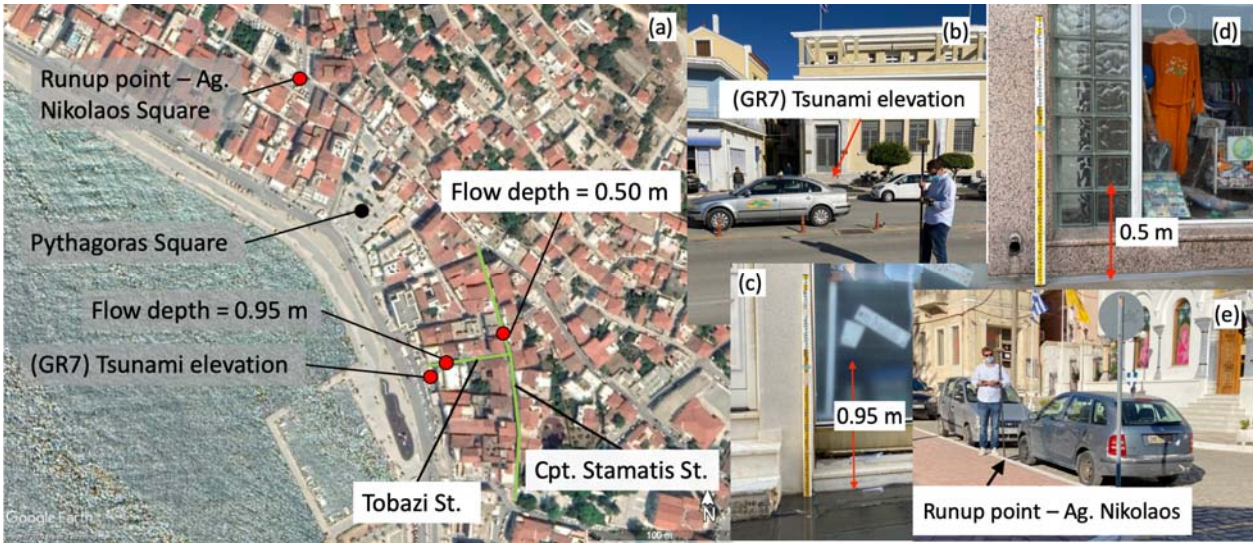

Figure 2.23. (a) Google Earth satellite picture of Vathi and the locations of tsunami observations. (b) The steps at the entrance to the Bank of Greece branch where tsunami elevation was measured. (c-d) Flow depth marks on store windows along Tobazi. (c) and Cpt. Stamatis (d) streets. (e) The runup location at Ag. Nikolaos Square.

Pythagorion. Pythagorion is located in southeastern Samos. Here, the tsunami waves arrived through the Strait of Mykali. On the south part of the harbor, eyewitnesses indicated that the wave just reached the height of the quay (0.53 m above W.L.) but did not exceed it, as the waves did not reach the shops along the waterfront. A fisherman mentioned that a boat moored in shallow water (~ 0.46 m deep) near the runup point touched the seabed during the withdrawal of the sea. Further north along the waterfront, two eyewitnesses who were on their sailing boat during the tsunami indicated the maximum runup (0.57 m) and minimum rundown (-0.56 m) of the waves along the quay wall.

2.2.8 *Eyewitness observations in the island of Chios*

A virtual reconnaissance mission was organized for the islands of Chios and Ikaria through telephone interviews of local authorities. A number of predefined questions were asked to the authorities, namely the local fire service, police, port police and the local civil protection office. In the island of Chios, located about 70 km north of the epicenter, tsunami waves were observed along its southeastern coast. Local authorities reported that in the coastal town of Komi, the first wave arrived about one hour after the earthquake (~13:00 UTC). It was a leading

depression wave per Tadepalli and Synolakis (1994), and the shoreline withdrew ~15 m at the beach adjacent to the small craft harbor of Komi.

About 3 minutes later, the water level started rising again, and about an hour after the arrival of the first wave, the water level rose to ~1.10 m. above mean sea level. The water level fluctuations were intense for about 3 hours after the 1st wave arrival. Small boats that were docked in the small harbor of Komi were swept ashore along the breakwater (Figure 2.24). The eyewitness estimated the maximum horizontal inundation at the beach to be ~20 m.

Figure 2.24. Small boats were swept away and put ashore along the breakwater of the harbor of Komi, Chios (https://15minutes.gr/).

2.3 Damage to Ports, Harbors and Coastal Utilities

Post-tsunami field surveys have also documented the effects of tsunami impact on coastal structures in Turkey. The coastal stretch of Izmir province between the districts of Güzelbahçe and Kuşadası, which hosts marinas, fishery harbors, and one commercial and cruise port is the closest Turkish coastal region to the earthquake epicenter. Some of them were visited during the post-earthquake survey. While only ground shaking impacted the ports and harbors at the northern coast of the Peninsula, shelters and marinas at the southern coast were affected by both the earthquake and the tsunami.

During the post-earthquake survey, no damage on the rubble mound breakwaters, i.e., settlement or damage on the armor layer of any rubble mound protection, was observed (Figures 2.25 and 2.26).

Figure 2.25. Rubble Mound Breakwater with the crown wall in Urla Fishery Harbor.

Figure 2.26. Rubble Mound Breakwater without crown wall in Guzelbahce Fishery Harbor.

For the berthing and mooring inside the harbors, gravity-type quay walls composed of concrete blocks were constructed in fishery harbors, and commercial and cruise ports. Visual observations show that there was no significant damage, no major cracks, no sliding or overturning in the quays.

Contrary to the concrete block type, piers composed of floating pontoons in Teos Marina were the most damaged mooring structures. The damage was not due to the earthquake shaking but entirely due to tsunami hydrodynamic forces. Two dramatic photos of the floating piers shared on social media are shown in Figures 2.27 and 2.28.

Figure 2.27. Floating Piers in Teos Marina after tsunami attack.

Figure 2.28. Drift of floating piers in Teos Marina after tsunami attack.

The pontoons of Teos Marina were constructed using floaters under an aluminum frame (Figure 2.29). The pontoon length and width were 20 and 2.5 m, respectively. The pontoons were connected to the gravity type anchorage at the seafloor by both steel chains and ropes. Apparently, strong tsunami currents broke the moorings, and the pontoons were dragged and detached. Moreover, aluminum pontoons and the moored ships were damaged. During the survey, the detached pontoons were moored to another location, as can be seen in Figure 2.30; these photos also show buckling in the rings at the fairlead. The ropes and the chains were broken off. In contrast to the aluminum pontoons, the concrete floating pontoon was not damaged (Figure 2.31).

Figure 2.29. One of the pontoons used in Teos Marina (floaters are at the bottom).

Figure 2.30. Damages in the pontoons and rings at the fairleads.

Figure 2.31. Undamaged concrete pontoon in Teos Marina.

Similar observations were made for concrete pontoons in other marinas. For example, in Alacati Marina, the sea level rose by 1.5-2 m, but the pontoons sustained no damage (Figure 2.32).

Figure 2.32. Concrete Pontoons in Alacati Marina.

In addition to the ports and harbors previously described, the small fishery port in Akarca locality also suffered substantial damage, as all of the floating piers used for berthing and

mooring, including other seafront port facilities, were destroyed or became unusable (Figure 2.33). More than 20 boats sunk in this location, as reported by the president of Seferihisar fishery cooperative (Mr. Mustafa Gul).

We also examined serious tsunami damage in another small fishery shelter in the Zeytineli locality (Figure 2.34). The non-engineered mooring and berthing structures and all boats in the shelter were destroyed, requiring a reconstruction. The parked cars on the shore drifted to the sea and the boats that sank also required rescue operations.

Figure 2.33. Observed damage in the floating piers used for berthing and mooring and the seafront harbor facilities in Akarca fishery shelter.

Figure 2.34. Photos showing the heavy damage and rescue operation of a car which was dragged into the water by the tsunami in Zeytineli fishery shelter (38.19336N 26.49233E); all of the boats and mooring facilities were unusable after the tsunami.

2.4 Tsunami Records at Tide Gauges

The tsunami generated by the main shock was recorded by tide gauges belonging to various institutions. The records of the tide gauges nearest to the earthquake epicenter publicly accessible through the SLMF/IOC web page are shown in Figure 2.35. All tide gauges are radar-type, except Syros (pressure sensor) and Bodrum (acoustic echo sounder).

The Syros tide gauge operated by the Hellenic Navy Hydrographic Service was the nearest tide gauge to the epicenter. It registered ~ 0.10 m as the highest wave amplitude for the first three waves. The first wave arrived at 12:37 UTC as leading depression. The next closest tide gauges of Plomari (Lesvos Island) and Kos (Kos Island), operated by NOA and JRC, and the tide gauge of Bodrum (Turkish coast), operated by the General Command of Mapping and KOERI, picked up smaller amplitude waves for the first three waves; the polarity of first-wave arrival is not clearly distinguishable due to the low signal/noise ratio. As evident in the time series presented here, the tsunami excited the Aegean and Cretan Sea basins and the tide gauge oscillations continued for at least 7 hours after first-wave arrival.

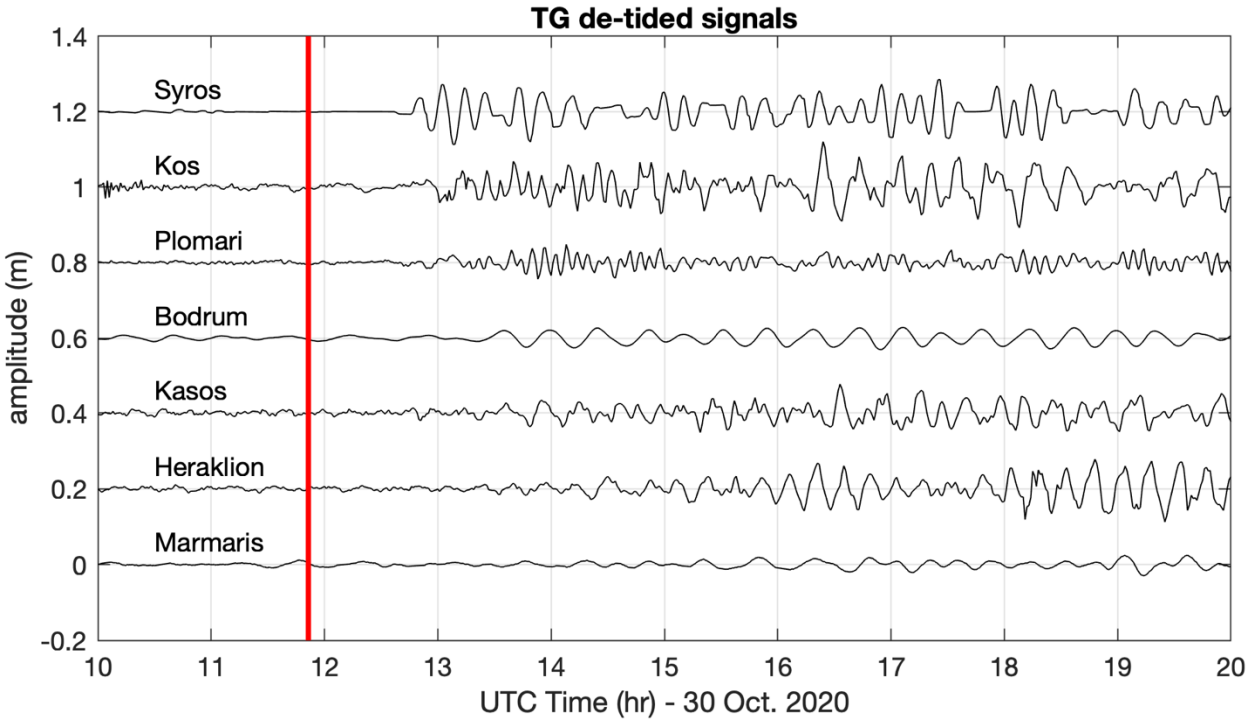

Figure 2.35. Records of the Samos-Aegean tsunami at the tide gauges (TG) nearest to the earthquake epicenter; the original records were low-pass filtered using a cutoff frequency of 1/3600 Hz to remove tidal oscillations. The red line indicates the time of earthquake occurrence.

2.5 Tsunami Warning

Following the **M**7.0 Samos-Aegean earthquake on 30 October 2020 11:51 UTC, all three Tsunami Service Providers (TSPs) operating in the Eastern Mediterranean under the North-

Eastern Atlantic, Mediterranean and connected seas Tsunami Warning System (NEAMTWS) of UNESCO issued Tsunami Warning Messages. CAT-INGV-TSP disseminated a local WATCH 8 minutes after the earthquake, while KOERI-TSP and HLNTWC-NOA-TSP disseminated a regional WATCH message 11 min after the earthquake origin time. The KOERI-TSP initial message, which included enhanced products (Figure 2.36), was delivered to the AFAD (Civil Protection Authority of Turkey) within the same minute.

Figure 2.36. Enhanced products disseminated by KOERI-TSP during the 30 October 2020 11:51 UTC **M**7.0 Samos-Aegean earthquake. Threat Level Zones Map (left), TFP Threat Level Map (center), Tsunami Travel Time Map (right).

The initial messages of the TSPs were followed by ONGOING messages. CAT-INGV-TSP issued two ongoing messages, one at 13:13 and a second one at 14:43 UTC, reporting wave amplitudes from Syros (GR) / 8 cm, Kasos (GR) / 3 cm, Mugla (TR) / 2 cm & Heraklion (GR) / 3 cm. HLNTWC-NOA-TSP issued one ongoing message at 13:23, reporting wave amplitudes from Kos (GR) / 6 cm, & Plomari (GR) / 2 cm, plus a statement that tsunami waves have been observed in Samos, Pythagorion and Izmir.

KOERI-TSP also disseminated one ongoing message at 14:32 UTC, which did not include instrumental sea-level observations, but a statement that sea level readings and eyewitness observations indicate a tsunami was generated. This was mainly due to the fact that detailed instrumental observations were already provided by INGV and NOA earlier, with wave heights of < 10 cm in distant locations, which were naturally not representing the actual scene in the near-field, as available through social and mass media.

Near-field measurements were not reported because tide-gauge records were not available, leading to a pragmatic warning approach during the course of the event to avoid any possible confusion for end-users, due to mismatch between actual observations and instrumental readings. KOERI-TSP's post-event assessment concluded that a better way would have been to include instrumental observations in the ONGOING message and to add a statement that higher wave-heights have been observed by eyewitnesses and communicated out via social-media. This practice was applied by NOA during the 21 July 2017 Bodrum-Kos event in their ONGOING message #002.

Finally, END messages were disseminated about 9 hours after the earthquake. The relative delay in issuing the END messages is attributed to the prolonged excitation of the tide gauge recordings across the Aegean and Cretan seas (Section 2.3). KOERI-TSP issued the END message at 20:55 UTC in consultation with both HLNTWC-NOA-TSP and AFAD (Civil Protection Authority of Turkey), while HLNTWC-NOA-TSP and CAT-INGV-TSP issued the END messages at 20:56 and 21:25 UTC, respectively.

One person died in Turkey due to the tsunami. A total of 45 homes, 195 workplaces and 54 vehicles were damaged, 17 boats sank, and 34 boats ran aground. No public warning messages were disseminated by the Civil Protection of Turkey (AFAD). Self-organized evacuations were likely triggered by the social media posts and need to be further analyzed, in close cooperation with social scientists.

An interview with the TEOS Marina Manager in Sığacık (İzmir-Turkey) clearly demonstrated the unawareness of the local stakeholders of the tsunami hazard and risk in the region. Disaster and Emergency Response Plans did not account for tsunamis. Yet, it was also acknowledged that, even if a tsunami warning would have been available to the Marina as shortly as 1 min after the EQ origin time, there would have been no realistic opportunity to prevent any of the material damage experienced.

On the Greek Islands, no casualties were reported by the tsunami, while damages were mostly limited to cars and flooded basements in the buildings along the waterfront of Vathy, in Samos. The national Civil Protection Authority (CPA) disseminated a message on the possibility of tsunami waves being generated by the earthquake to all cell phones in the geographical area between the islands of Kos, Ikaria and Chios.

That message was disseminated through Greece's 1-1-2 Emergency Communications Service. This is bidirectional and equivalent to 9-1-1 in the US. Mobile phone data show it was received about half an hour after the earthquake. This left 2 to 5 minutes before what video evidence suggests was the second and bigger flood in Vathy. According to the eyewitnesses and local authorities, the message disseminated had a positive impact, and triggered self-evacuation of the local population in Vathy, apparently that small first wave had not sufficiently alarmed residents, who had no prior knowledge of tsunamis. Early indications suggest that this technology should be examined for future events.

This event shed light – once again – on the complexity of providing warnings for locally generated tsunamis, whose rapid onset challenges the ability of local authorities and communities at risk to take preventive early action. It is a bitter reminder after the wake-up call on 20 July 2017 Bodrum-Kos tsunami to increase tsunami preparedness through enhanced sea-level detection networks, education, as well as international cooperation.

2.6 Tsunami Generation - Published Source Models

Published finite fault models used in this chapter as initial conditions for tsunami generation include USGS (2020) and Okuwaki (2020), and the uniform slip fault model of Ganas et al. (2020) (the Okuwaki and Ganas et al. models are different from the models presented in Chapter 1). The finite fault sources of USGS (2020) were derived using waveforms, and the slip history was constrained using the finite fault inversion algorithm of Ji et al. (2002). Two nodal planes were tested: a north-dipping (strike = 270 deg, dip = 32 deg) and a south-dipping (strike = 93 deg, dip = 53 deg) plane. The finite fault sources of Okuwaki (2020) were derived using the inversion algorithm of Shimizu et al. (2020) and the two nodal planes of the USGS W-phase moment tensor (Table 1.1). As described in Sections 1.3-1.4, the finite fault models show bilateral propagation of rupture from the point of nucleation, with most slip concentrated in the western part of the fault rupture area.

The co-seismic surface vertical deformations produced by the Ganas et al. (2020) uniform slip model, and the USGS (2020) and Okuwaki (2020) finite fault models are shown in Figure 2.37. The finite fault sources of USGS (2020) and Okuwaki (2020) consider the seismic waveforms and moment tensors but fail to reproduce the uplift observed in western Samos. Moreover, the maximum deformation of the USGS north-dipping finite fault falls on land, and both USGS sources are relatively deep (30.3 and 28.4 km at the down-dip edge for the south- and north-dipping sources, respectively), and as a result, the tsunami-generation potential of the USGS finite fault models is limited.

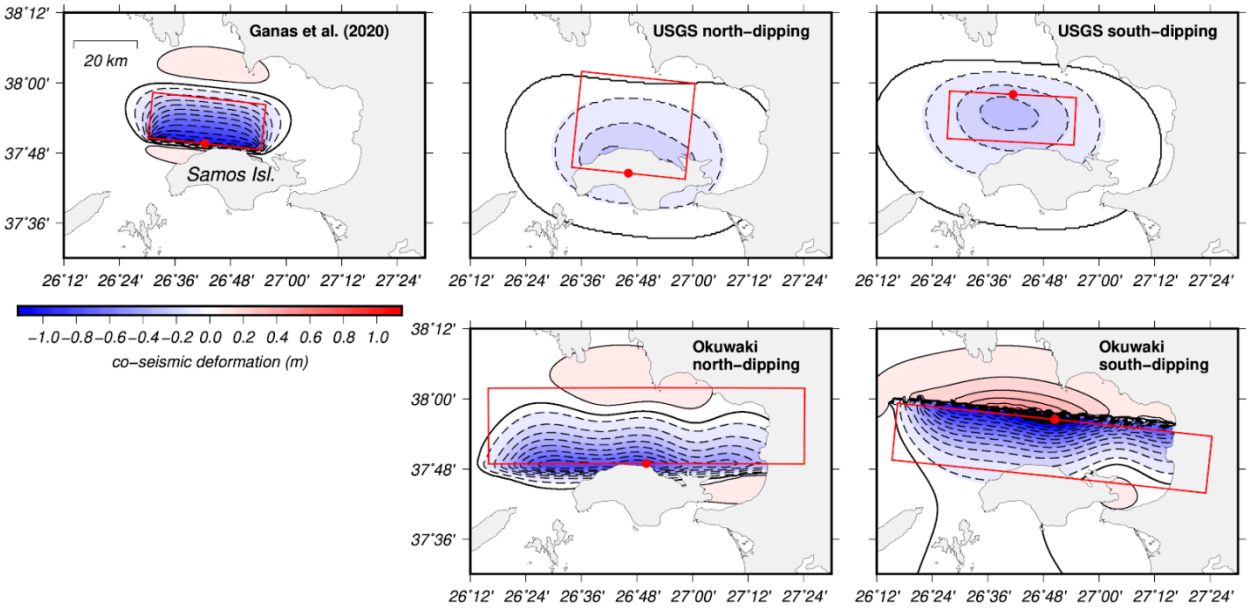

Figure 2.37. Co-seismic (vertical) surface deformation produced by the Ganas et al. (2020) uniform-slip source, and the north- and south-dipping USGS (2020) and Okuwaki (2020) finite fault sources. 0.1 m contours show deformation (dashed = negative, black = positive, thick black = zero). The fault rupture areas are shown with the red rectangles; red circles correspond to the center of the up-dip edge.

The Okuwaki (2020) finite fault models, while having more tsunami-generation potential compared to the USGS (2020) models, they fail to reproduce the uplift observed in NW Samos. The uniform slip model of Ganas et al. (2020) on the other hand was developed based on the earthquake moment tensor (fixed dip angle of 37 deg) and available surface deformation data, assuming a rake angle of 270 deg (normal faulting). The best-fitting source has a fault rupture length of 36 km, width of 18 km and a strike of 276 deg (north-dipping), while the possible range for the down-dip edge depth and slip magnitude are 10-13 km and 1.5-2.2 m, respectively. Using a down-dip edge depth of 11.3 km and a slip magnitude of 1.8 m, the co-seismic surface deformation reaches values of -1.04 m near the up-dip edge (Figure 2.37a).

2.7 Tsunami Hydrodynamic Simulation Results

We present tsunami simulation results for two numerical models: MOST (Section 2.7.1) and NAMI DANCE (Section 2.7.2). Both models are used to study the propagation of the tsunami waves in the Aegean Sea. MOST and NAMI DANCE are also used to study tsunami inundation in Vathi (Samos Island) and Sığacık and Akarca (Turkish coast), respectively. All hydrodynamic simulations were initialized using the Ganas et al. (2020) source model (see Section 2.6).

2.7.1 *Setup of Numerical Models*

MOST. The Method Of Splitting Tsunamis (MOST, Titov and Synolakis, 1995, 1998; Titov et al., 2018), solves the nonlinear shallow water equations (NSWE) by splitting the conservation and momentum equations in the two horizontal dimensions through the method of fractional steps (Yanenko, 1971). The resulting two systems of equations are advanced sequentially at each time step using an explicit finite difference scheme of Godunov (1972). A moving shoreline algorithm simulates wave inundation over land (Titov and Synolakis, 1995). Wave energy is attenuated through wave breaking (inherently modeled in the NSWE) and for inundation computations through a bottom friction term added in the momentum equations applied to the finest-resolution nested grid.

Two sets of simulations were performed with MOST: a wave propagation simulation in the Aegean Sea and a high-resolution inundation simulation for the town of Vathi. For the wave propagation simulation, the bathymetric grid of GEBCO (2020) with a 15 arc-sec cell size is utilized; computations stop at 10 m depth, where a solid boundary condition is imposed. For the inundation simulation, three nested grids of increasing resolution are used to numerically capture the increasing nonlinearity of the waves as they move to shallower water (Figure 2.38). Nested grid A is extracted from the EMODnet (2018) bathymetric 115m grid, whereas grids B and C, with cell sizes of 40 m and 10 m, respectively, are seamless Digital Elevation Models (DEMs) created by merging the digitized (and gridded) bathymetric charts (1:50,000 and 1:5,000 scale) issued by the Hellenic Navy Hydrographic Service and a 5 m cell-size Digital Terrain Model (DTM) produced by the Hellenic Cadaster. A Manning's coefficient of 0.03 $s/m^{1/3}$ was used for the MOST inundation results presented.

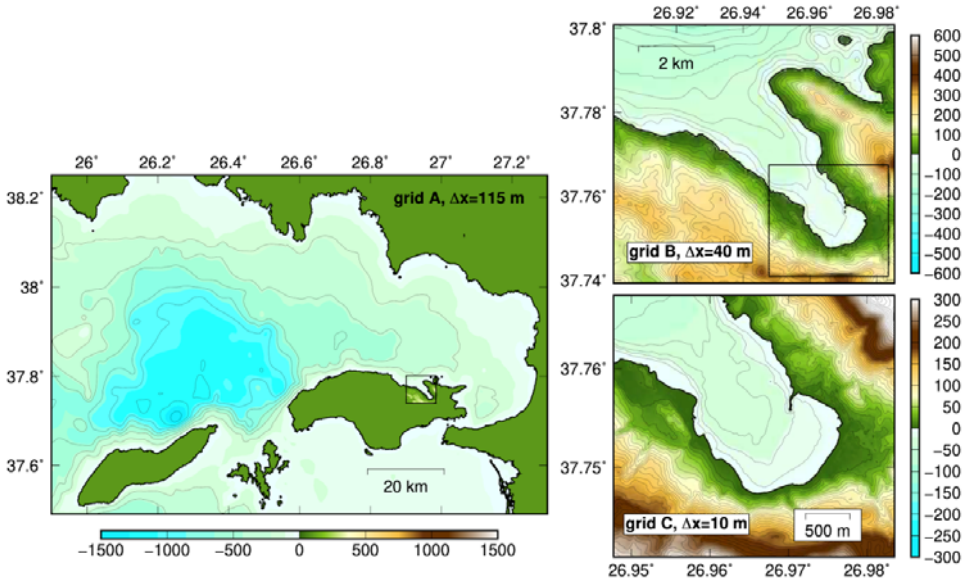

Figure 2.38. Numerical relief grids used for the inundation simulation with MOST for the town of Vathi (Samos Island). Contours for grids A, B and C drawn every 200, 20 and 10 m, respectively. Color bars show relief values in meters.

NAMI DANCE. NAMI DANCE solves the nonlinear form of shallow water equations using the water surface disturbances as the inputs and simulates propagation and coastal amplification of long waves. The nonlinear forms of long-wave equations are solved using a staggering leapfrog scheme numerical solution procedure in nested domains with rectangular structured mesh. NAMI DANCE has been developed from TUNAMI N2 to model the hydrodynamics of tsunamis (Yalciner et al., 2002, 2004; Zahibo et al., 2003; Yalciner et al., 2014; Aytore et al., 2016; Cankaya et al., 2016; Kian et al., 2016; Velioglu et al., 2016, Zaytsev et al., 2016, 2019, 2020). Later it was upgraded to a new version, which uses a Graphical Processor Unit (GPU) and achieved high-speed processing capability (Yalciner and Zaytsev, 2017). The upgraded version of the code, which solves tsunamis and tropical cyclones related to long oceanic waves, is called NAMI DANCE SUITE. It also visualizes the 3D view of the wave propagation on the screen during a simulation. NAMI DANCE has been applied to specific long wave benchmark problems (Yalciner et al., 2008; Lynett et al., 2017; Dilmen et al., 2014; Sogut and Yalciner, 2019) and several tsunami events have also been reproduced by implementing NAMI DANCE (Sozdinler et al., 2015; Tufekci et al., 2018).

Two different simulation approaches are employed for the far-field propagation and the near-field amplification and inundation of the October 30 tsunami. In the far-field propagation part of the simulations, a large single grid (including the Eastern Aegean) is used with 200 m grid size where the source of the data is GEBCO (2020). In the second part of the simulations, the coastal amplification and inundation part, a nested grid approach is employed, with two domains of 25 m (parent grid B) and 5 m (child grid C) grid sizes (Figure 2.39). The bathy/topo data source of

these two grids is the EMODnet Bathymetric grid (2018) and the national navigation charts. For the first part of the simulations, the distribution of maximum water elevations computed in the Eastern Aegean is presented in Figure 2.43. For the second part, the computed maximum water surface elevations in Sığacık and Akarca regions (Domain C) is given in Figure 2.44. The tide gauge comparison for the stations Bodrum, Kos, Syros and Plomari are also provided in Figure 2.45.

2.7.2 *Far-field Propagation Simulation Results*

The wave propagation simulations using MOST (Figure 2.40) and NAMI DANCE (Figure 2.41) show that tsunami impact is most prominent along the northern coast of Samos Island, and along the most impacted areas observed in the field along the Turkish coast, namely Zeytineli, Sığacık, and Akarca, are well captured in the simulations. However, there are some other areas with low observed tsunami impact where the simulations predict high wave amplitudes. Smaller wave amplitudes can be observed on the SE coast of Chios Island, the N coast of Ikaria and Fourni, and the E coast of the islands of Mykonos and Andros.

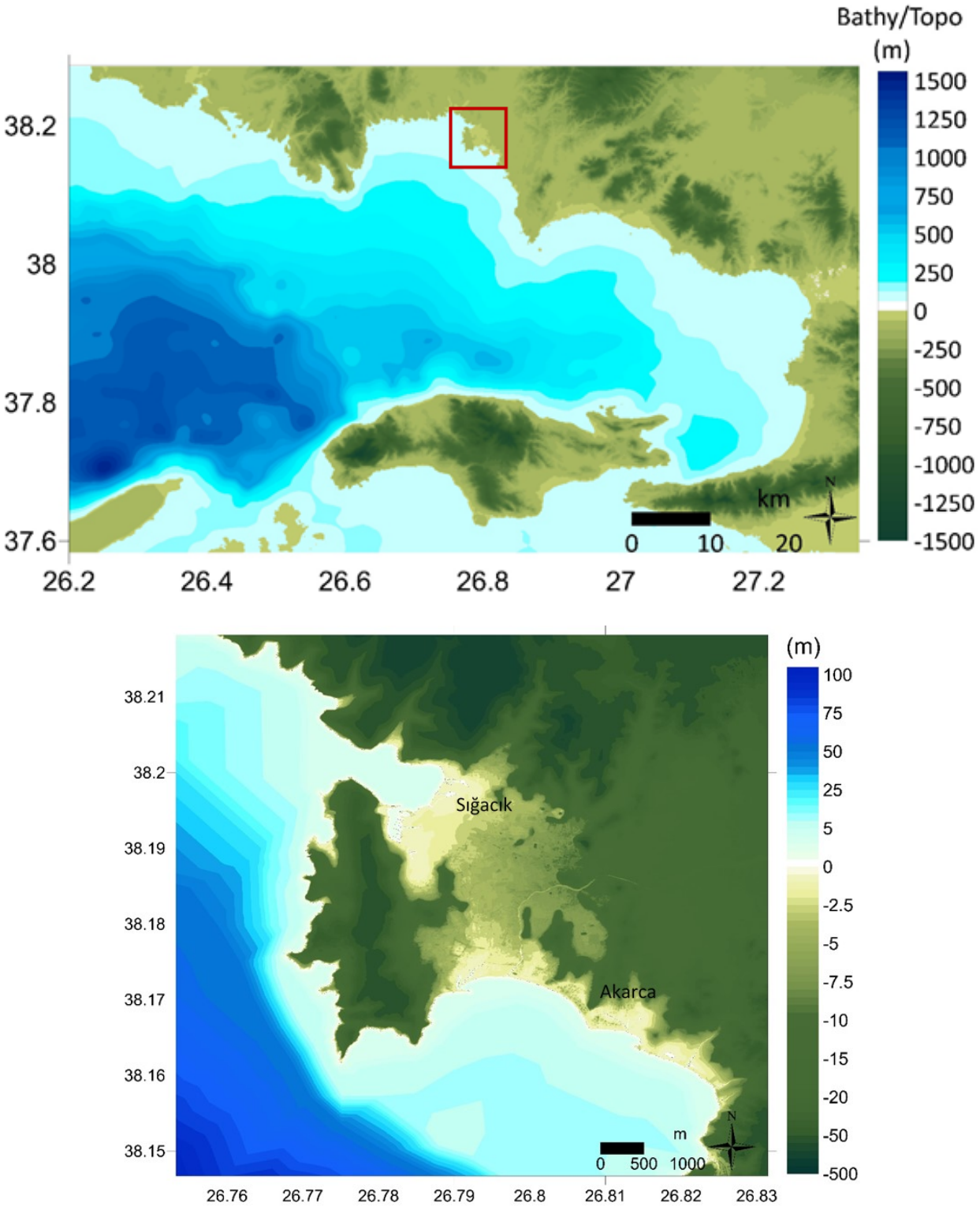

Figure 2.39. Maps showing the grids B (Kuşadası Bay) with 25m grid size (top) and C with 5 m grid size (bottom) employed in the near-field simulations via NAMI DANCE for Sığacık and Akarca localities

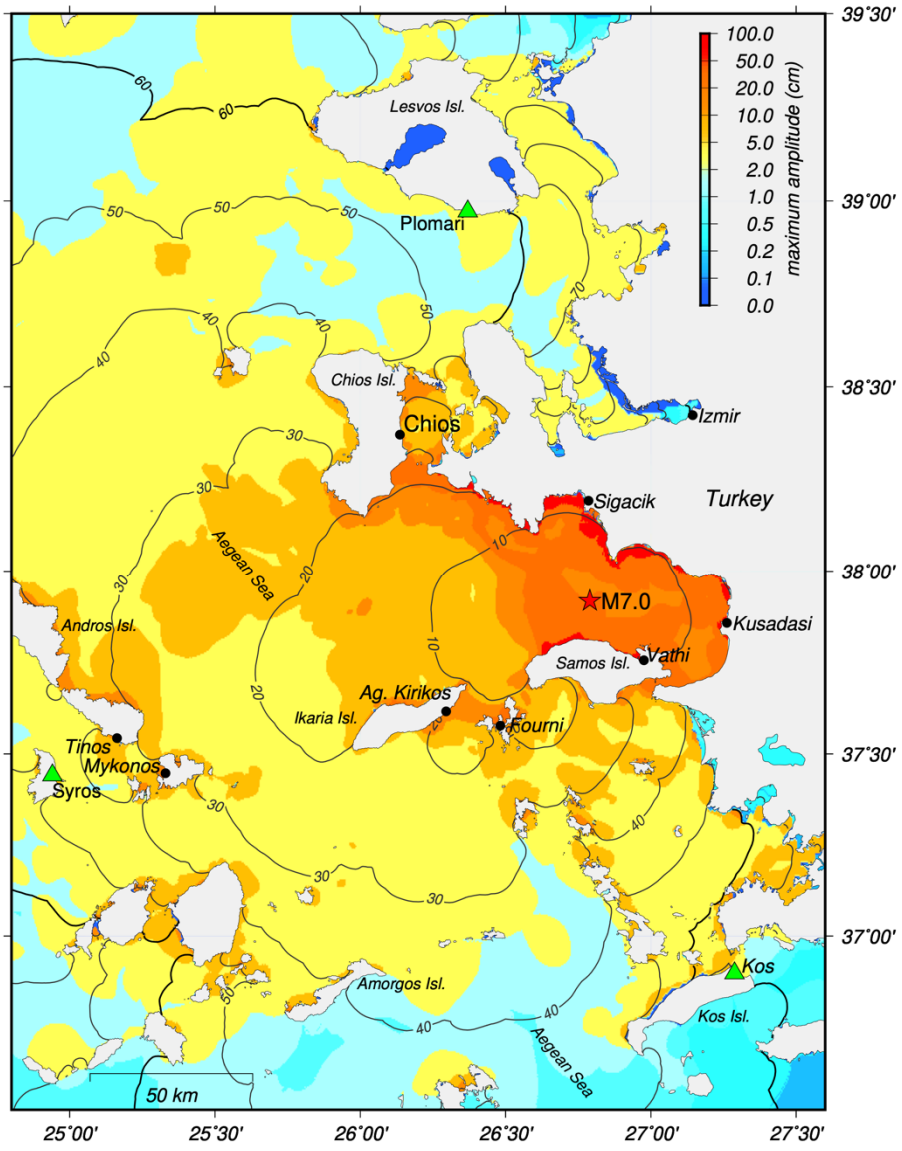

Figure 2.40. Maximum amplitude map using MOST, the Ganas et al. (2020) source model and GEBCO (2020) bathymetry; contours show wave arrival times in minutes, assuming the waves propagate from the earthquake epicenter (point source), and the green triangles show the locations of the tide gauges plotted in (a).

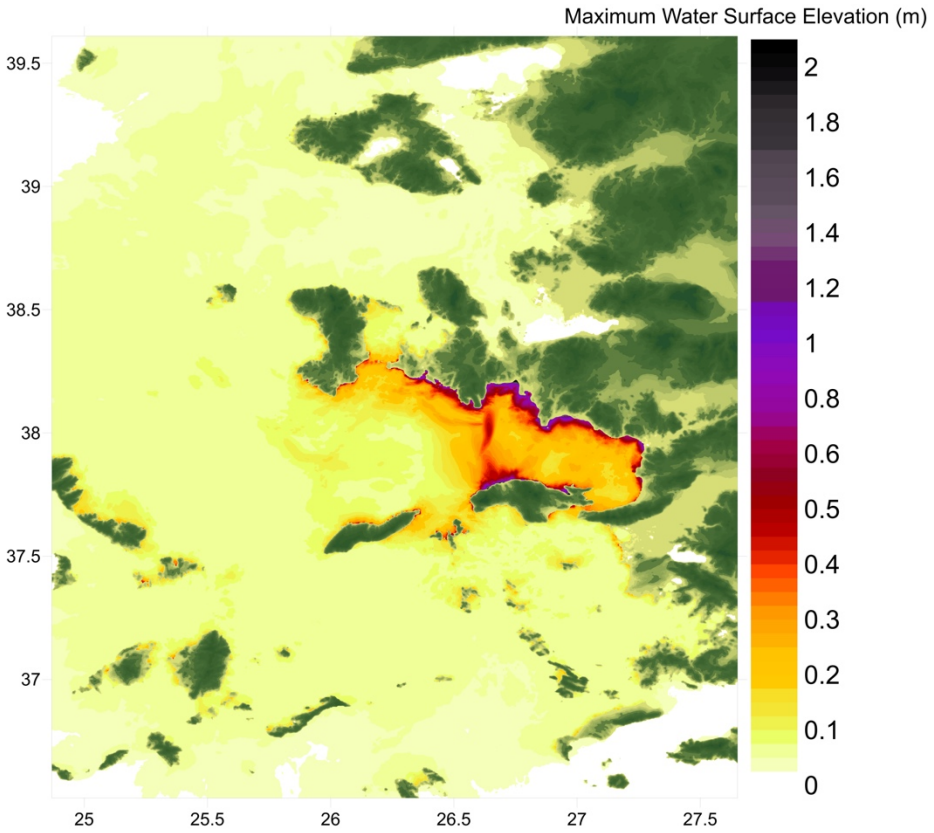

Figure 2.41. Distribution of maximum water surface elevations in Eastern Aegean computed in the far-field simulations via NAMI DANCE

Comparison to tide gauge records. The tide gauges installed in the Aegean Sea were not optimally positioned to timely detect the generated tsunami. In the nearest tide gauge of Syros, the first tsunami wave arrived 46 min after the earthquake in the form of a leading depression after propagating between the islands of Mykonos and Tinos. The first wave in the MOST and NAMI DANCE time series extracted from the offshore nodes nearest to the Syros tide gauge (at 19 and 23 m depth, respectively) arrived ~8 min earlier and with a more pronounced leading depression compared to the recording (Figure 2.42). The amplitudes of the first peak and second trough match the recording well, but the models produce smaller amplitudes compared to the peak of the second and largest wave of the recording. The phases and amplitudes of subsequent recorded waves are better matched by the NAMI DANCE simulation compared to MOST.

The amplitudes of the MOST and NAMI DANCE time series extracted from the offshore nodes nearest to the Kos tide gauge (at 13 and 15 m depth, respectively) compare well with the recording but miss the amplitude of the higher-frequency fluctuations recorded. On the other hand, the amplitudes of the NAMI DANCE time series extracted from the offshore node nearest to the Plomari tide gauge (at 37 m depth) compare well with the recording and the NAMI DANCE time series capture the amplitudes of the recorded high-frequency fluctuations to a

certain extent. Last, the phases and amplitudes of the waves recorded by the Bodrum tide gauge are better captured by MOST (extracted at a depth of 29 m) compared to the NAMI DANCE simulation (extracted at a depth of 6 m).

For both the Kos and Plomari tide gauge records, the long-frequency component of the MOST time series matches that of the NAMI DANCE time series, but the MOST time series miss the higher-frequency components of NAMI DANCE. A possible explanation for this observation is the inclusion of the higher resolution grid (grid B) around the source region and the use of a smaller time step in the NAMI DANCE simulation (0.75 and 2 s time steps were used with NAMI DANCE and the far-field propagation simulation of MOST, respectively), which allows to reproduce the higher-frequency fluctuations in the source region. Simulations using nested grids in which the high-resolution grid includes the geometry of the harbors - where the tide gauge are installed - should yield higher quality time series that would allow to identify the source of the high-frequency fluctuations.

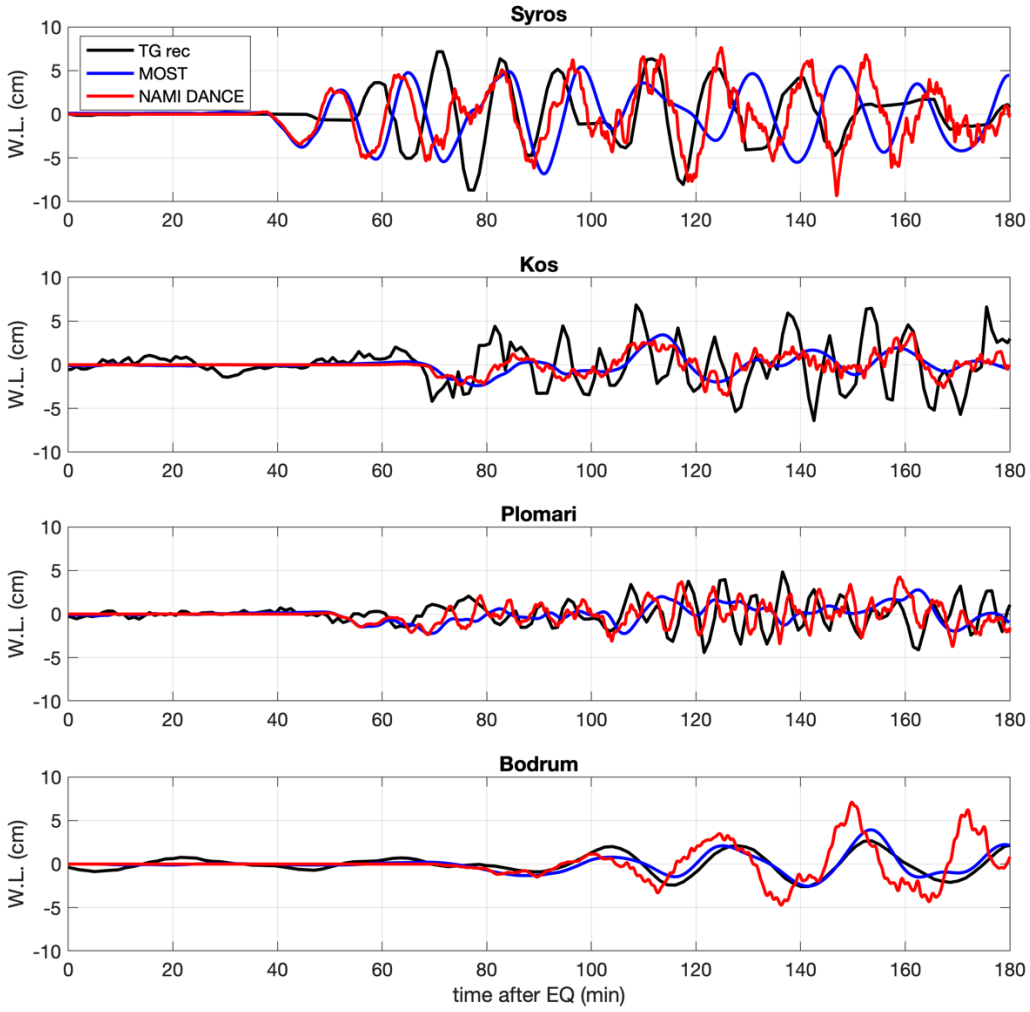

Figure 2.42. Comparison of tide gauge records at four stations in the Aegean Sea and the simulation results of MOST and NAMI DANCE.

2.7.3 *High-resolution inundation results*

Inundation simulation results for Vathi, Samos Island using MOST. The inundation simulation focusing on the town of Vathi allows us to examine the timing and intensity of the tsunami waves generated by the Ganas et al. (2020) source in the near field. The maximum wave amplitude predicted by the MOST simulation inside the bay of Vathi (Figure 2.43a) ranges between 0.8 m at the entrance of the bay and 2 m near the waterfront of the town of Vathi at the end of the bay. The simulation yields wave inundation along the SW flank of the bay, but inundation is most extensive along the waterfront of the town, where the wave amplitude is the highest. The maximum wave runup in the simulation is 2.5 m, at the north end of Pythagoras square; Triantafyllou et al. (2020) have reported a wave runup of 2.0 m at this location. Landward of the Vathi marina, where the tsunami height datapoint of 1.7 m was collected, the simulation produces a wave runup of 2.0 m. Overall, the runup and inundation model predictions are a bit higher than observed. A possible explanation is that the Hellenic Cadaster 5 m resolution DTM used is a bare earth model of the topography without building blocks. The use of a higher Manning's friction coefficient would be justified to mimic the attenuation effect of buildings as the waves advance through the urban environment (e.g., Baba et al., 2014).

The timing of tsunami impact in the town of Vathi can be examined through numerical time series of free surface elevation extracted just offshore of the Pythagoras square and the timing recorded through CCTV footage (Triantafyllou et al., 2020) and eyewitness videos (Figure 2.43b). The peak of the first flood is predicted at 12:05 UTC in the simulation, which matches the timing of the first flood captured through CCTV footage. The peak of the second flood that occurred between 12:24 and 12:25 UTC according to CCTV footage arrives 1-2 min late in the simulation. The second flood was reportedly higher than the first (Triantafyllou et al., 2020), which is not predicted in the simulation; the model predicts floods of similar intensity. A subsequent peak flood captured on an eyewitness video in front of the Bank of Greece branch at 13:29 UTC arrives 2 min late in the simulation, however the model accurately captures the non-decaying intensity of the flood compared to the first two floods.

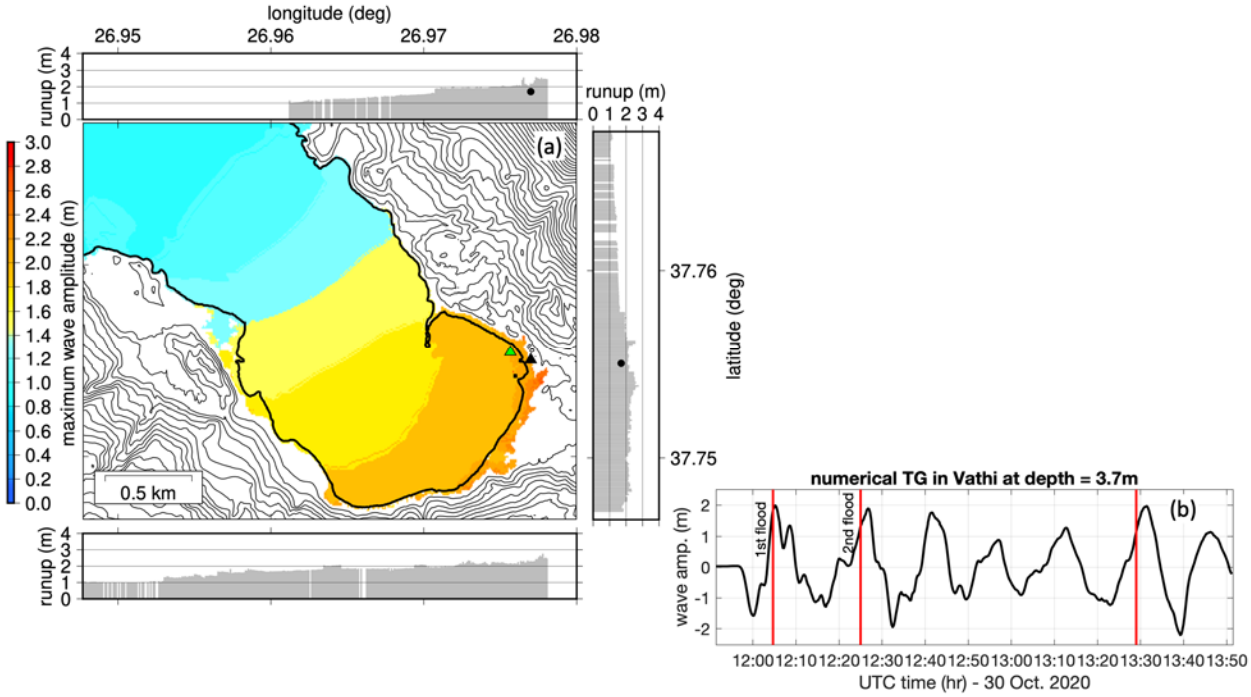

Figure 2.43. (a) Maximum wave amplitude map for the bay and town of Vathi. Horizontal bars and vertical bars at the right, top and bottom show the projected wave runup values along the coastline. The black triangle shows the location of the tsunami height field measurement; the measurement is projected to the side plots using black circles. (b) Numerical time series of wave amplitude extracted at the location shown with the green triangle in (a). The red lines designate peak flood times extracted from CCTV (Triantafyllou et al., 2020) and eyewitness videos.

Inundation simulation results for Kuşadası Bay and Sığacık locality using NAMI DANCE. the nearshore maximum amplitudes for Kuşadası Bay and Sığacık locality computed through the nested (higher resolution) simulations (Figure 2.44) reproduce the large inundation and amplitudes observed in Sığacık fairly well. However, the computed arrival times of the first sea withdrawal and the incoming wave are 10 min late compared to the observations. More source models will be tested in the future as they become available to determine the source model that reproduces the tsunami impact field measurements and observations the best.

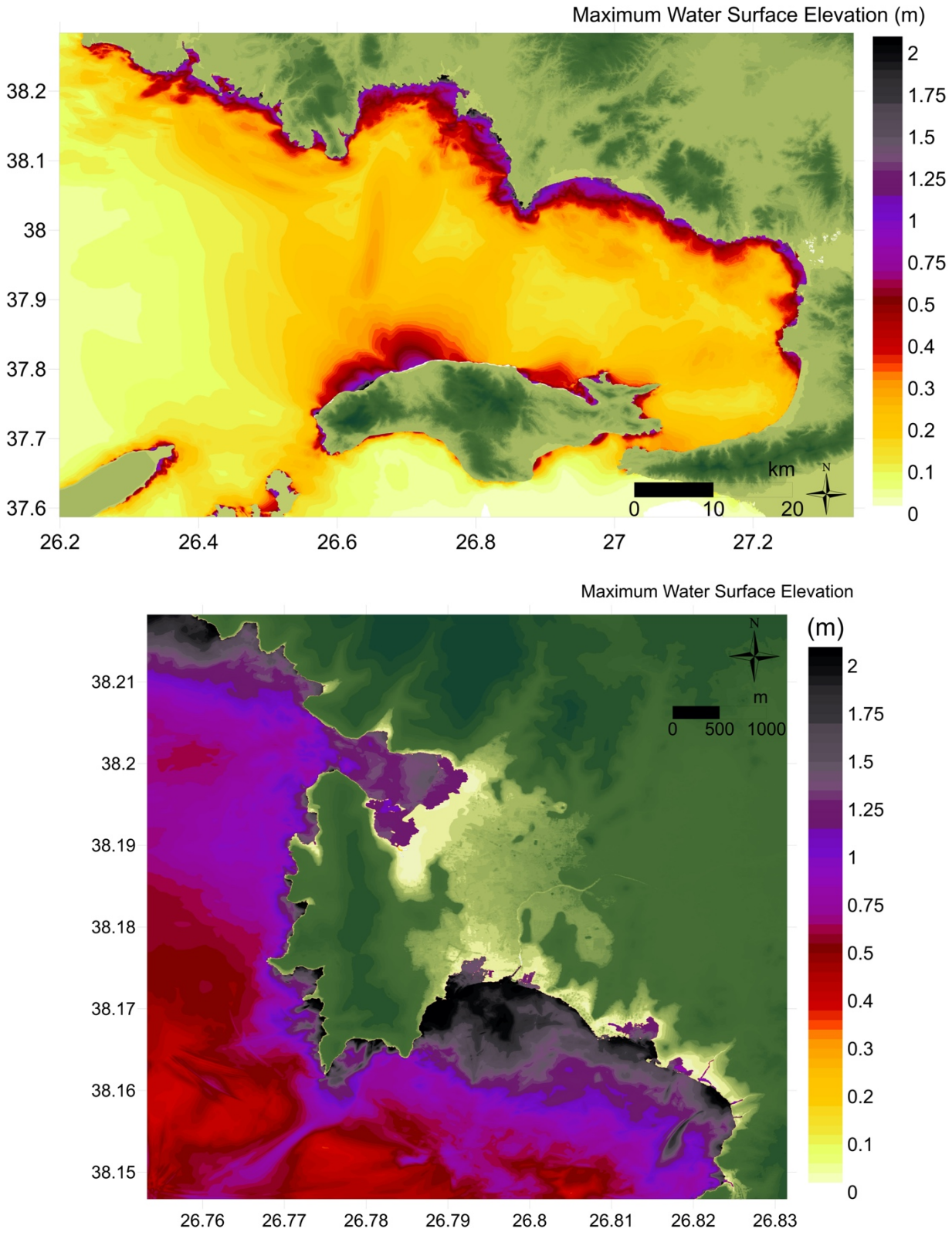

Figure 2.44. Distribution of maximum water surface elevations in Domains B, Kuşadası Bay (top) and C near-field simulations for Sığacık and Akarca localities (bottom) using NAMI DANCE.

Conclusions

The Samos-Aegean earthquake on October 30th, 2020, produced a tsunami that within a few minutes struck the NW coast of Samos Island, with wave runup measured at 1.8 m just inland of Karlovasi harbor. Wave arrival in the town of Vathi, which is located at the end of a narrow bay on the NE coast of Samos Island was delayed compared to Karlovasi, with the first inundation being captured through CCTV footage 13 min after the earthquake (Triantafyllou et al., 2020); Vathi experienced a series of floods every ~20-30 min that lasted at least until 14:04 UTC (2 hr and 13 min after the earthquake). In Pythagorion on the southern coast of Samos, wave runup reached 0.5 m and did not inundate the waterfront of the harbor. At the harbor of Komi in the island of Chios, the water level rose to +1.1 m and tsunami inundation reached 20 m according to an eyewitness.

Along the Turkish coast, the most impacted areas were Sigacik Marina, Sigacik Bay and the Akarca locality, about 30 km from the epicenter in the northern direction. The tsunami was amplified in small bay-shaped areas with narrow entrances, maximum inundation distance reached 415, 285 and 552 m in the Sigacik locality, Akarca, and Teos Ancient City, respectively. The maximum tsunami penetration of 2490 m was observed along the Alacati Azmak stream. The maximum inundation height (2.31 m) was measured in the Kaleiçi Region of Sığacık Bay and maximum wave runup (3.82 m) was measured in Akarca. In the Kaleiçi region of the Sığacık locality, a woman could not resist the strong tsunami current and perished. Floating pontoons of Teos Marina were heavily damaged by the tsunami; the hydrodynamics forces broke the pontoon mooring lines and the pontoons drifted with the tsunami-induced currents. A 1.9 m flow depth was measured in the Zeytineli Region. Non-engineered mooring and berthing structures and all boats in the fishery shelter of Zeytineli were destroyed. A significant decrease in tsunami impact was observed after the “V” shaped peninsula between Tepecik and Gümüldür in the southeast direction. Almost no significant inundation or water motion was observed further east of the Gümüldür locality.

Far-field propagation and high-resolution inundation simulations using the NAMI DANCE and MOST hydrodynamic models shed light on the dynamics of tsunami impact; the simulations with both models were initialized using a uniform slip source model by Ganas et al. (2020). The far-field tsunami propagation simulations correctly identified the high-impact areas on the north coast of Samos and the Turkish coastal stretch between Sigacik and Gümüldür. The comparison between the tsunami recordings at the three tide gauges nearest to the earthquake epicenter with numerical time series extracted from the simulations showed that the recorded tsunami amplitude was captured well by the models, however, the simulations predicted an early arrival time and a more pronounced leading depression wave at the Syros tide gauge compared to the recording. The high-resolution inundation simulation using MOST that focused in the town of Vathi in Samos Island accurately captured the arrival of the first two floods but predicted a slightly higher maximum wave runup and inundation extent that observed in the field. The nearshore maximum amplitudes for Kuşadası Bay and Sığacık locality computed

through the high-resolution inundation simulations using NAMI DANCE reproduce the large inundation and amplitudes observed in Sığacık fairly well. However, the computed arrival times of the first sea withdrawal and the incoming wave are 10 min late compared to the observations. As more source models for the Samos earthquake become available, the field data will provide the benchmark to determine the source model that reproduces the tsunami impact observations the best.

The tsunami posed operational challenges for the Tsunami Service Providers (TSPs) operating in the Eastern Mediterranean under the NEAM Tsunami Warning System of IOC/UNESCO. All TSPs issued initial tsunami warning messages based on the preliminary earthquake parameters within 11 min after the earthquake. However, the tsunami had already arrived on the NW coast of Samos Island and reached the Turkish coast within 20 min from the earthquake requiring a very efficient message dissemination mechanism to reach the local population. The Greek national Civil Protection Authority disseminated a message through Greece's 1-1-2 Emergency Communications Service on the possibility of tsunami waves being generated by the earthquake to all cell phones in the geographical area between the islands of Kos, Ikaria and Chios. It left 2 to 5 minutes before what video evidence suggests was the second and bigger flood in Vathy occurred, and according to the eyewitnesses and local authorities, the message had a positive impact and triggered self-evacuation of the local population in Vathy. TSP operations were further challenged by the absence of tide gauges near the epicenter to timely confirm tsunami generation following the earthquake; the first wave arrived at the nearest tide gauge of Syros 46 min after the earthquake. With the tide gauges being positioned far away from the tsunami generation region and with the waves traveling through the Aegean Sea that is populated with numerous islands, the wave amplitudes of tide gauge recordings reported by two of the three TSPs were relatively small (8 cm amplitude waves reported by INGV-TSP for the Syros tide gauge), and not representative of the impact potential of the tsunami in the near-field.

This event once again shed light on the complexity of providing warnings for locally generated tsunamis, whose rapid onset challenges the ability of local authorities and communities at risk to take preventive early action. It is a bitter reminder after the wake-up call on 20 July 2017 Bodrum-Kos tsunami to increase tsunami preparedness through enhanced sea-level detection networks, education, as well as international cooperation.

Acknowledgments

The Turkish authors acknowledge Yüksel Proje International Co. for major and invaluable support, which enabled the field survey to be quick, secure, safe, and effective under the critical pandemic conditions. The authors also acknowledge EMAY International Engineering Co. for considerable support to the expenses for the effective survey. Acknowledgements are extended to several institutions and the numerous individuals for their supports at different

phases of post-tsunami field survey works. The institutions and/or entities are, TUBITAK (Project No: 119Y419 and Project No: 5200101), METU, Yıldız Technical University, Kocaeli University, İstanbul Metropolitan Municipality, Dokuz Eylül University, İzmir Metropolitan Municipality, Çeşme Municipality, Seferihisar Municipality and Dolfen Consultancy and Engineering Company. The distinguished individuals are, Prof. Dr. Lütfi Süzen, Res. Assist. Duygu Tüfekçi Enginar, General Manager Mr. Faruk Günlü and Technical Director Özgür Ugan of Sığacık Teos Marina, General Manager Ms. Deniz Şahin of Port Alaçatı Marina, General Manager Mr. Can Akalkan of Çeşme Marina, Dr. Hasan Gökhan Güler, Civil Engineer MSc. Cem Bingöl, Civil Engineer MSc. Mehmet Sedat Gözlet, Geomantic Engineers Özgür Şahin Sarı and Seçkin Demirel, Geology Engineer Evrens Yapar and Geophysical Engineer MSc. Evrim Yavuz, Civil Engineer Yurttabir Özel,Mapping Technicians Mr. Erhan Yükselen and Mr. Ömer Mede. The eyewitnesses, Temel Okyar, Mehmet Ali Okyar, Nejat Demirkıran, Aydın Tunca, Mehmet Yarar, Zuhal Karabey, Mustafa Gül, Cengiz Özkan are also acknowledged for their close cooperation.

The Greek authors would like to acknowledge Mr. Vorias (local civil protection office in Chios), Mr. Koutras (police office in Samos) and Mr. Tsaparikos (port police office in Samos) for the valuable information they provided regarding the timing, response and impact of the tsunami in Chios and Samos.

References

Ambraseys, N, and Synolakis, C, 2010. Tsunami catalogs for the Eastern Mediterranean, revisited. *Journal of Earthquake Engineering*, 14(3), 309-330.

Aytore, B, Yalciner, AC, Zaytsev, A, Cankaya, ZC, and Suzen, ML, 2016. Assessment of tsunami resilience of Haydarpaşa Port in the Sea of Marmara by high-resolution numerical modeling. *Earth, Planets and Space*, 68(1), 139.

Baba, T, Takahashi, N, Kaneda, Y, Inazawa, Y, and Kikkojin, M, 2014. Tsunami inundation modeling of the 2011 Tohoku earthquake using three-dimensional building data for Sendai, Miyagi Prefecture, Japan. In *Tsunami events and lessons learned: Environmental and Societal Significance;* Kontar, Y., Santiago-Fandino, V., Takahashi, T., Eds.; Springer, Dordrecht, The Netherlands; 89-98.

Cankaya, ZC, Suzen, ML, Yalciner, AC, Kolat, C, Zaytsev, A, and Aytore, B, 2016. A new GIS-based tsunami risk evaluation: MeTHuVA (METU tsunami human vulnerability assessment) at Yenikapı, Istanbul. *Earth, Planets and Space*, 68(1), 133.

Caputo, R, and Pavlides, S, 2013. The Greek Database of Seismogenic Sources (GreDaSS), version 2.0.0: A compilation of potential seismogenic sources (Mw > 5.5) in the Aegean Region. https://doi.org/10.15160/unife/gredass/0200.

Dilmen, DI, Kemec, S, Yalciner, AC, Düzgün, S, and Zaytsev, A, 2014. Development of a Tsunami Inundation Map in Detecting Tsunami Risk in Gulf of Fethiye, Turkey. *Pure and Applied Geophysics*, 1-9.

Dogan, GG, Annunziato, A, Papadopoulos, GA, Guler, HG, Yalciner, AC, Cakir, TE, Sozdinler, CO, Ulutas, E, Arikawa, T, Suzen, ML, and Guler, I, 2019. The 20th July 2017 Bodrum–Kos Tsunami Field Survey. *Pure and Applied Geophysics*, 176(7), 2925-2949.

EMODnet Bathymetry portal, 2018. http://www.emodnet-bathymetry.eu.

England, P, Howell, A, Jackson, J, and Synolakis, C, 2015. Palaeotsunamis and tsunami hazards in the Eastern Mediterranean. *Philosophical Transactions of the Royal Society A: Mathematical, Physical and Engineering Sciences*, 373(2053), p. 20140374.

European-Mediterranean Seismological Centre, 2020. https://www.emsc-csem.org/Earthquake/mtfull.php?id=915787&year=2020;INFO. Last accessed on Dec. 6, 2020.

Ganas, A, Tsironi, V, Tsimi, C, Delagas, M, Konstantakopoulou, E, Kollia, E, Efstathiou, E, and Oikonomou, A, 2020. NOAFaults: a digital database for active faults in Greece, version 3.0. https://arcg.is/04Haer.

Ganas, A, Elias, P, Briole, P, Tsironi, V, Valkaniotis, S, Escartin, J, Karasante, I, and Efstathiou, E, 2020. Fault responsible for Samos earthquake identified, Temblor, http://doi.org/10.32858/temblor.134.

GEBCO Bathymetry portal, 2020. http://www.gebco.net.

Godunov, SK, 1973. Finite-difference schemes. Nauka, Moscow, U.S.S.R.

Ji, C, Wald, DJ, and Helmberger, DV, 2002. Source description of the 1999 Hector Mine, California, earthquake, part I: Wavelet domain inversion theory and resolution analysis. *Bulletin of the Seismological Society of America*, 92(4), 1192-1207.

Kian, R, Velioglu, D, Yalciner, AC, and Zaytsev, A, 2016. Effects of Harbor Shape on the Induced Sedimentation; L-Type Basin. *Journal of Marine Science and Engineering*, 4(3), 55. http://www.mdpi.com/2077-1312/4/3/55/htm

Lynett, PJ, Gately, K, Wilson, R, Montoya, L, Arcas, D, Aytore, B, Bai, Y, Bricker, JD, Castro, MJ, Cheung, KF, David, GC, Dogan, GG, Escalante, C, González-Vida, JM, Grilli, ST, Heitmann, TW, Horrillo, J, Kânoglu, U, Kian, R, Kirby, JT, Li, W, Macías, J, Nicolsky, DJ, Ortega, S, Pampell-Manis, A, Park, YS, Roeber, V, Sharghivand, N, Shelby, M, Shi, F, Tehranirad, B, Tolkova, E, Thio, HK, Velioglu, D, Yalciner, AC, Yamazaki, Y, Zaytsev, A, and Zhang, YJ, 2017. Inter-model analysis of tsunami-induced coastal currents. *Ocean Modelling*, 114, 14–32, http://dx.doi.org/10.1016/j.ocemod.2017.04.003

NASA Earth Applied Sciences, 2020. Aegean Sea Earthquake October 2020. https://appliedsciences.nasa.gov/what-we-do/disasters/disasters-activations/aegean-sea-earthquake-october-2020. Last accessed on Dec. 6, 2020.

Okada, Y, 1985. Surface deformation due to shear and tensile faults in a half-space. *Bulletin of the seismological society of America*, 75(4), 1135-1154.

Okal, EA, Synolakis, CE, Fryer, GJ, Heinrich, P, Borrero, JC, Ruscher, C, Arcas, D, Guille, G, and Rousseau, D, 2002. A field survey of the 1946 Aleutian tsunami in the far field. *Seismological Research Letters,* 73(4), 490-503.

Okal, EA, Synolakis, CE, Uslu, B, Kalligeris, N, and Voukouvalas, E, 2009. The 1956 earthquake and tsunami in Amorgos, Greece. *Geophysical Journal International*, 178(3), 1533-1554.

Okuwaki, R, 2020. rokuwaki/2020Greece: Preliminary tele-seismic finite-fault models of the 2020 Greece earthquake (Version v2, 1 November 2020). Zenodo. http://doi.org/10.5281/zenodo.4175289.

Sea Level station Monitoring Facility (SLMF), Intergovernmental Oceanographic Commission (IOC). http://www.ioc-sealevelmonitoring.org.

Shimizu, K, Yagi, Y, Okuwaki, R, and Fukahata, Y, 2020. Development of an inversion method to extract information on fault geometry from teleseismic data. *Geophysical Journal International*, 220(2), 1055-1065.

Sogut, DV, and Yalciner, AC, 2019. Performance Comparison of NAMI DANCE and FLOW-3D® Models in Tsunami Propagation, Inundation and Currents using NTHMP Benchmark Problems. *Pure and Applied Geophysics*, *176*(7), 3115-3153.

Sozdinler, CO, Yalciner, AC, Zaytsev, A, Suppasri, A, and Imamura, F, 2015. Investigation of Hydrodynamic Parameters and the Effects of Breakwaters During the 2011 Great East Japan Tsunami in Kamaishi Bay. *Pure and Applied Geophysics*, 1-19.

Synolakis, CE, and Okal, EA, 2005. 1992-2002: Perspective on a decade of post-tsunami surveys. In: Tsunamis: Case studies and recent developments, ed. by K. Satake, *Advances in Natural and Technological Hazards*, 23, 1-30.

Tadepalli, S, and Synolakis, CE, 1994. The run-up of N-waves on sloping beaches. *Proceedings of the Royal Society of London. Series A: Mathematical and Physical Sciences*, 445(1923), 99-112.

Titov, VV, and Synolakis, CE, 1995. Modeling of breaking and nonbreaking long-wave evolution and runup using VTCS-2. *Journal of Waterway, Port, Coastal, and Ocean Engineering*, 121(6), 308-316.

Titov, VV, and Synolakis, CE, 1998. Numerical modeling of tidal wave runup. *Journal of Waterway, Port, Coastal, and Ocean Engineering*, 124(4), 157-171.

Titov, VV, Kânoğlu, K, and Synolakis, CE, 2018. Development of MOST for Real-Time Tsunami Forecasting, *Journal of Waterway, Port, Coastal, and Ocean Engineering*, 142(6), 03116004.

Triantafyllou, I, Gogou, M, Mavroulis, S, Katsetsiadou, KN, Lekkas, E, and Papadopoulos, G, 2020. The tsunami caused by the 30 October 2020 Samos (Greece), East Aegean Sea, Mw6.9 earthquake: impact assessment from post-event field survey and video records. Report published at EMSC: https://edcm.edu.gr/images/docs/2020/Samos2020-TSUNAMI-REPORT.pdf (Last Accessed: 30 December 2020)

TUBITAK, 2020. Turkey Emergency Disaster Monitoring Project Field Survey Report. TUBITAK Project No: 5200101

Tufekci, DE, Suzen, ML, Yalciner, AC, and Zaytsev, A, 2017. Revised MeTHuVA method for assessment of tsunami human vulnerability of Bakirkoy district, Istanbul, *Natural Hazards*, 90, 943–974. https://doi.org/10.1007/s11069-017-3082-1

UNESCO, 2014. International Tsunami Survey Team (ITST) Post-Tsunami Survey Field Guide. 2nd Edition. IOC Manuals and Guides No.37, Paris: UNESCO 2014 (English).

US Geological Survey, 2020. https://earthquake.usgs.gov/earthquakes/eventpage/us7000c7y0/ finite-fault. Last accessed on Dec. 6, 2020.

Velioglu, D, Kian, R, Yalciner, AC, and Zaytsev, A, 2016. Performance Assessment of NAMI DANCE in Tsunami Evolution and Currents Using a Benchmark Problem. *Journal of Marine Science and Engineering*, 4(3), 49. http://www.mdpi.com/2077-1312/4/3/49/htm

Wells, WL, and Coppersmith, KJ, 1994. New empirical relationships among magnitude, rupture length, rupture width, rupture area, and surface displacement. *Bulletin of the Seismological Society of America*, 84(4), 974-1002.

Yalciner, AC, Alpar, B, Altinok, Y, Ozbay, I, and Imamura, F, 2002. Tsunamis in the Sea of Marmara: Historical Documents for the Past, Models for Future. *Special Issue of Marine Geology, 190*(1-2), 445-463.

Yalciner, AC, Pelinovsky, E, Talipova, T, Kurkin, A, Kozelkov, A, and Zaitsev, A, 2004. Tsunamis in the Black Sea: Comparison of the historical, instrumental, and numerical data, *Journal of Geophysical Research,* 109, C12023. https://doi.org/10.1029/2003JC002113

Yalciner, AC, Imamura, F, and Synolakis, C, 2008, Amplitude evolution and eunup of long waves; Comparison of experimental and numerical data on a 3D complex topography. In *Advanced Numerical Models for Simulating Tsunami Waves and Runup*, 243-247.

Yalciner, AC, Zaytsev, A, Aytore, B, Insel, I, Heidarzadeh, M, Kian, R, and Imamura, F, 2014. A Possible Submarine Landslide and Associated Tsunami at the Northwest Nile Delta, Mediterranean Sea. *Oceanography*, 27(2), 68-75.

Yalciner, B, and Zaytsev, A, 2017. Assessment of Efficiency and Performance in Tsunami Numerical Modeling with GPU. *EGU General Assembly,* 1246.

Yanenko, NN, 1971. The method of fractional steps. translated by M. Holt, Springer, New York, Berlin, Heidelberg.

Zahibo, N, Pelinovsky, E, Yalciner, A, Kurkin, A, Koselkov, A, and Zaitsev, A, 2003. The 1867 Virgin Island tsunami: observations and modeling. *Oceanologica Acta*, 26(5-6), 609-621.

Zaytsev A, Kostenko I, Kurkin A, Pelinovsky E, and Yalciner AC, 2016. The depth effect of earthquakes on tsunami heights in the Sea of Okhotsk. *Turkish Journal of Earth Sciences*, 25(4), 289-299.

Zaytsev, AI, Pelinovsky, EN, Yalciiner, A, Susmoro, H, Prasetya, G, Hidayat, R, Dolgikh, GI , Dolgikh, SG, Kurkin, AA, Dogan, G, Zahibo, N, and Pronin, PI, 2019. Generation of the 2018 Tsunami on Sulawesi

Island: Possible Sources. *Doklady Earth Sciences*, 486(1), 588–592, Pleiades Publishing. https://doi.org/10.1134/S1028334X19050295

Zaytsev, A, Dogan, GG, Dolgikh, G, Dolgikh, S, Yalciner, AC, and Pelinovsky, E, 2020. The 25 March 2020 Tsunami At The Kuril Islands: Analysis and Numerical Simulation. In *SCIENCE OF TSUNAMI HAZARDS*, *Journal of Tsunami Society International*, 39(4). http://www.tsunamisociety.org/STHVol39N4Y2020.pdf

3 Strong Ground Motion

Coordinators: Sinan Akkar, Ayşegül Askan, Zeynep Gülerce, Basil Margaris, Nikolaos Theodulidis, Ioannis Kalogeras, Nikolaos Melis

Contributors:

METU, Turkey: Abdullah Altındal, Burak Akbaş, Eyüp Sopacı, Dr. Shaghayegh Karimzadeh, Dr. A. Arda Özacar, Prof. K. Önder Çetin

Ted University, Turkey: Assoc. Prof. Özkan Kale

ITSAK Greece: Dr. Dimitris Sotiriadis, Mrs. K. Konstantinidou

Univ. of PATRAS GREECE: Assist. Prof. Zafeiria Roumelioti.

3.1. Introduction

The October 30th, 2020 Samos mainshock was recorded by numerous recording stations located at epicentral distances up to 600 km. The broader area around the epicenter is characterized by the continental part of Asia Minor to the East and the Aegean Sea to the West. Both, raw and processed versions of these records are available at the following websites:

- https://tadas.afad.gov.tr
- http://www.itsak.gr/uploads/data/SamosOct2020/Greek_SMdata_Others.zip
- https://accelnet.gein.noa.gr/2020/11/09/the-earthquake-of-october-30th-2020-at-samos-eastern-aegean-sea-greece-preliminary-report/.

Within this report, two subsets of strong motion recordings are used. The first subset that includes 35 records at stations located up to 100km from the epicenter is used for the demonstration of recorded acceleration-time histories, Fourier amplitude spectra and acceleration response spectra with 5% damping. Among these 35 stations, two are located on the Samos Island; one is operated by the Institute of Engineering Seismology & Earthquake Engineering (ITSAK) and the other one by the Institute of Geodynamics (NOA-IG). These two stations are installed in the Vathi town of Samos in different geological conditions. Their 30 meters-averaged shear wave velocities (V_{S30}) were measured after the earthquake using the MASW geophysical method. The remaining 33 strong motion stations are located in the surroundings of Aydın and İzmir provinces in Turkey and are operated by AFAD (Disaster and Emergency Management Presidency). The V_{S30} values and site classes for 27 stations in Turkey were assigned after geotechnical and geophysical site investigations, while for the rest of the stations the respective values were assigned based on the surface geology. The second subset of ground motions (located within 200 km) is utilized for the evaluation of recorded strong

ground motion values in comparison with a set of ground motion prediction models (GMMs) in Section 3.5.

3.2. Processing and Filtering of the Recordings

A uniform data processing procedure was applied to the Greek strong motion data recorded by the national networks (ITSAK and NOA-IG). This approach is applied to compile processed strong motion accelerograms with minimum interference of noise effects in a predefined frequency band, especially if the examined records produce unexpected results for different reasons (Margaris et al., 2021; Boore et al., 2021). The basic steps of this procedure are:

1. Visual screening to identify records with "non-standard errors" that should be screened out (not used) or should be subjected to a specific treatment by subsequent processing.
2. Windowing of records to identify the time intervals containing the acceleration traces.
3. Mean removal and low-cut filtering to reduce noise effects.

Visual screening of raw (uncorrected) accelerograms is applied to find out records with various issues (Douglas 2003; Boore and Bommer 2005), such as low resolution in the digitizer relative to the signal amplitude, artificial cut-off of the records at the beginning, the anomalous spikes along the time history, etc. (Douglas 2003; Boore and Bommer 2005). The component windowing is used to capture the time interval containing a measurable signal from the event (e.g. including multiple events). This screening and windowing procedure is implemented by AFAD (Paolucci et al., 2011) to the strong motion recordings before disseminating the unprocessed records to public; therefore, this procedure is not repeated in this report.

After the screening and windowing application, the mean over the pre-event portion of the record, if it exists, or the mean over the whole record length, if pre-event portion does not exist, was removed and a low-cut filtering procedure was used. A specific procedure is adopted to guide the operators towards selecting an optimal low-cut corner frequency (Flc) for each component of the record. The procedure was presented by Boore (2001; 2005) and applied with some revision in the NGA projects (e.g., Ancheta et al. 2014). As an example, the processing procedure on the SMG1 record is shown in Figure 3.1**.** The procedure begins by plotting the uncorrected acceleration time series over the window length, along with integrations to velocity and displacement. To remove possible afore-mentioned issues, the windowed accelerogram is zero-padded at the beginning and at the end to include the filter transient (length of the zero-pad depends on the filter corner frequency) and to achieve time steps with powers of two (e.g., 1024, 2048, 4096, etc.). Acausal, low-cut Butterworth filters of sufficient order are then applied to achieve a specified asymptotic behavior at low frequencies (usually f^8 per recommendations in Boore, 2005) for 10 discrete cut-off frequencies (f_c-values) equally spaced in log scale in three groups: 0.05-0.5 Hz, 0.1–1 Hz, and 0.5–5Hz. The filtered accelerograms are then double integrated for displacement, the results of which are shown for the 0.05-0.5 Hz group in Figure 3.1**.** The results are visually inspected to select an f_c value that produces a stable displacement time series (without baseline drift) and with the minimal

possible reduction in amplitudes. This procedure uses several of the programs in the TSPP suite of time-series processing routines (Boore, 2012). Above defined filtering procedure is automatized in AFAD's website; the user can choose the low-cut and high-cut filters and download the processed recordings. For the strong ground motions compiled from AFAD, the common filter values of 0.1–25 Hz (default values defined by AFAD for this event) are utilized.

3.3. Preliminary Analyses of Strong Ground Motion Records

Figure 3.2 shows the spatial distribution of the recordings in the first subset and the orientations of the two sensors located on Samos Island which recorded the closest strong motion data from this earthquake. Peak ground motion amplitudes, significant duration and Arias as well as Housner intensity values of these recordings are provided in Table 3.1. In Table 3.1, PGA, PGV and PGD are the peak ground acceleration, velocity and displacements, respectively. The significant duration is calculated as the time between 5% and 95% of the cumulative Arias Intensity. The horizontal components listed on this table match the sensor orientations.

The strong ground motion records of the Samos mainshock show variability in terms of azimuth, source-to-site distances and site classes. Acceleration time histories, Fourier amplitude spectra and the 5%-damped acceleration response spectra of the recorded accelerations at these stations are displayed in Figure 3.3. The 5%-damped acceleration response spectra in Figure 3.3 are compared against the design spectra defined in the current and previous seismic codes of Turkey (TBDY, 2019) and Greece (EAK, 2000, EC8), respectively.

Among the stations located in Turkey, the one with the shortest distance from the epicenter is the station #0905 which is located on a stiff soil site (V_{S30}=369 m/s) in the town of Kuşadası, (Aydın province) and has the highest recorded peak ground acceleration (PGA) value of 0.18 g. Fourier amplitude spectra (FAS) and acceleration response spectra of this record indicate a short-period peak within 0.2-0.3 seconds range (3-5 Hz range in frequency domain), yet no significant structural damages are reported near this site. Station #3528, located in the town of Çeşme Ilıca, is also on stiff soil (V_{S30}=532 m/s), has a PGA value of 0.15 g and shows short-period amplification. Two stations, Stations #3519 and #3521 are located in the Karşıyaka district, İzmir on soft soil sites with Site Class E (V_{S30}=131 m/s and 145 m/s, respectively). The records at these stations display long-period peaks up to 1 s and 1.5 s, respectively. Stations #3513 and #3514 are both in the Bayraklı district close to the structural failures and are located on soft soil (V_{S30}=196 m/s) and rock (V_{S30}=836 m/s) sites with Site Classes of D and B, respectively. At the Station #3513, despite a low PGA level of 0.1 g, clear long-period amplification is observed up to 1.5 sec. We note that at the rock station in the Bayraklı district, Station #3514, no similar amplifications are observed.

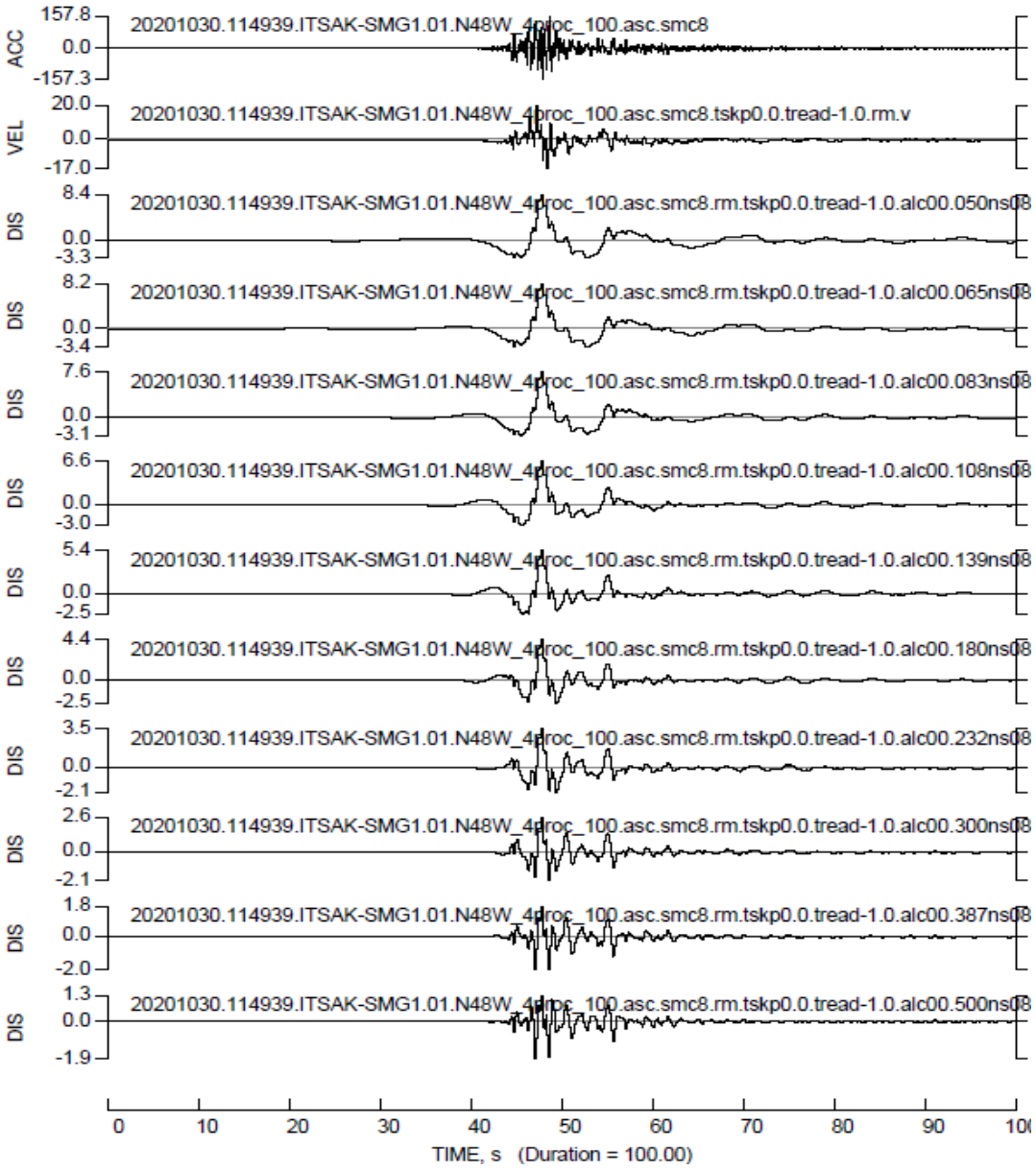

Figure 3.1. Time histories of the N48W horizontal component record at SMG1 station (Samos Vathi ITSAK). Presented is acceleration and velocity time series of the unfiltered record (top 2 plots), as well as the displacement time series after implementing the low-cut filters at various Flc values (equally spaced in log scale) from 0.05- 0.5 Hz.

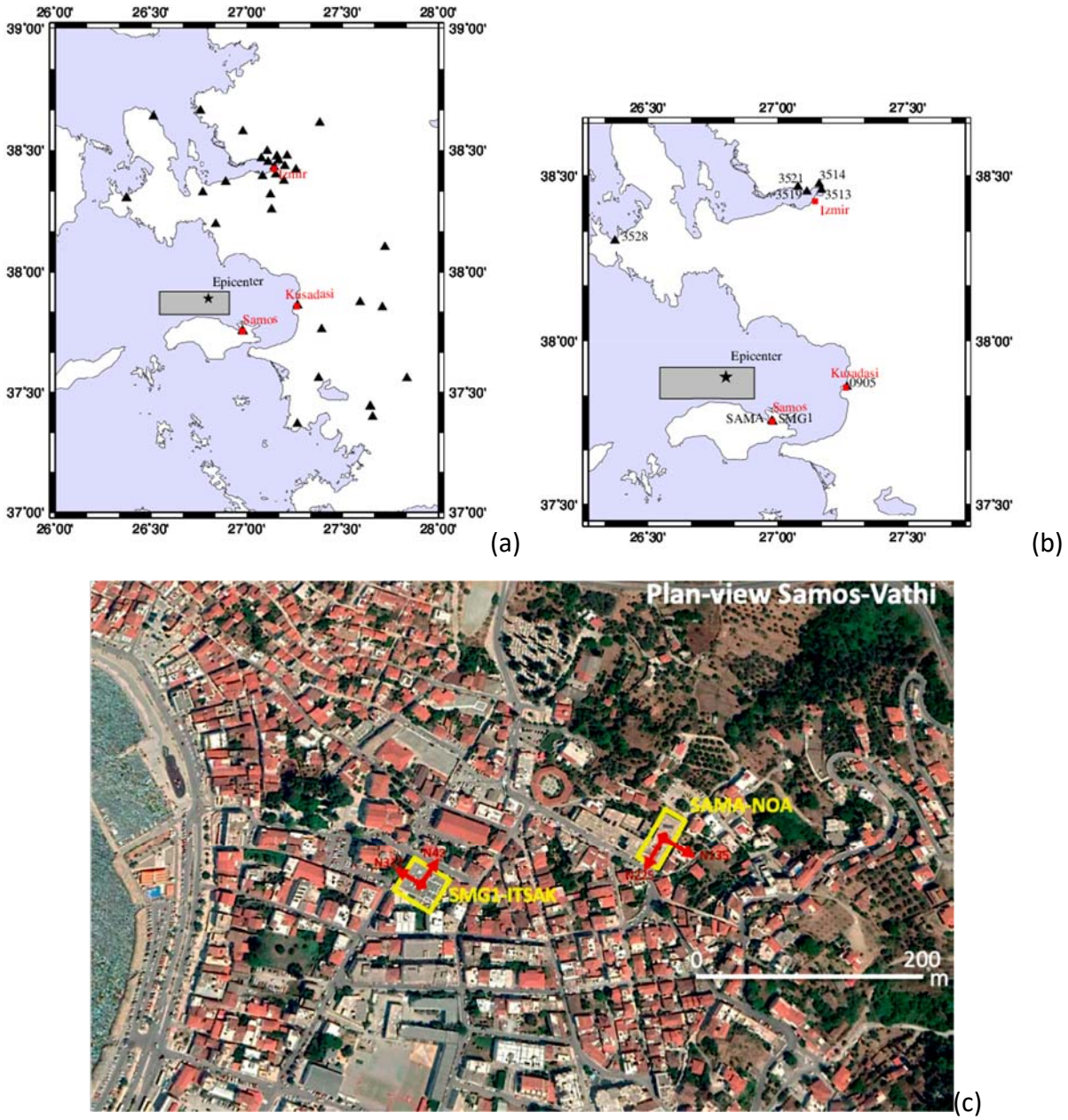

Figure 3.2. Locations of strong ground motion stations in the first subset (black triangles) with respect to the relocated epicenter (star symbol) and surface projection of the rupture plane (gray area) (a) within 100 km epicentral distance, (b) selected for close investigation in this report, and (c) sensor orientations of the stations on Samos Island (station code and agency in yellow and the orientation axes in red). Town names are written in red, whereas station codes (in b) are written in black.

Table 3.1. Information on Recorded Strong Ground Motions of Samos earthquake for stations within 100 km epicentral distance

Station Code	Name	Lat.	Long.	Rjb (km)	Rrup (km)	Repi (km)	Vs30 (m/s)	Site Class*	Comp.	PGA (cm/s²)	PGV (cm/s)	PGD (cm)	Significant Duration (s)	Arias Intensity (cm/s)	Housner Intensity (cm)
SMG1	Vathi	37.7561	26.9762	9.59	9.60	23.23	550	B*	N42N	227.30	21.49	8.38	12.09	36.49	53.80
									48N31	157.80	19.88	5.96	12.26	55.82	57.92
									U-D	134.02	11.16	5.51	15.12	14.24	23.24
SAMA	Vathi	37.7537	26.9806	10.03	10.05	22.38	840	A*	N225	166.31	16.00	2.84	10.29	34.81	51.70
									135N1	120.32	17.37	3.78	11.38	23.05	48.79
									U-D	99.68	6.77	2.28	14.16	10.82	21.26
905	Aydın Kuşadası Meteoroloji Müdürlüğü	37.8600	27.2650	31.52	31.69	42.95	369	C	E-W	144.02	8.93	2.26	16.61	20.37	35.60
									N-S	179.31	7.85	1.50	15.43	21.81	32.61
									U-D	79.84	4.56	1.35	17.88	8.38	20.13
911	Aydın Söke Yenikent	37.7621	27.3909	42.90	42.91	55.71	307	D	E-W	66.66	4.54	1.84	25.56	7.51	21.34
									N-S	48.01	4.31	1.06	23.88	7.64	20.93
									U-D	47.47	2.78	1.61	25.55	4.55	10.09
918	Aydın Didim Hükümet Konağı	37.3697	27.2643	59.43	59.43	71.86	630	C	E-W	30.99	4.98	2.15	29.21	4.56	21.65
									N-S	38.19	5.99	3.06	29.91	5.05	27.23
									U-D	20.96	4.09	1.19	37.79	2.62	21.58
919	Aydın Karpuzlu Halk Eğitim Merkezi	37.5595	27.8355	86.67	86.67	100.01	986	B	E-W	17.95	1.03	0.75	30.74	0.54	4.09
									N-S	21.40	1.22	0.70	26.59	0.65	4.53
									U-D	14.86	1.21	0.92	32.28	0.33	4.80
920	Aydın Sarıkemer Belediye	37.5604	27.3749	50.39	50.40	63.98	894	B	E-W	30.69	2.71	1.27	19.57	1.54	11.37
									N-S	25.68	3.00	1.95	21.70	1.45	12.45
									U-D	21.98	1.99	1.06	24.58	0.55	5.37
921	Aydın Germencik Devlet Hastanesi	37.8747	27.5922	60.15	60.33	71.56	None	None	E-W	70.85	8.47	3.23	30.85	13.14	37.22
									N-S	55.03	4.94	1.37	36.60	8.35	27.61
									U-D	23.06	3.11	1.06	38.76	3.07	16.04
922	Aydın İncirliova Spor Lisesi	37.8537	27.7082	70.26	70.32	81.83	None	None	E-W	58.60	5.17	2.62	40.15	11.20	24.81
									N-S	60.05	4.93	3.11	46.91	9.68	22.94
									U-D	56.46	1.84	0.86	32.09	5.00	9.60

Station Code	Name	Lat.	Long.	Rjb (km)	Rrup (km)	Repi (km)	Vs30 (m/s)	Site Class*	Comp.	PGA (cm/s^2)	PGV (cm/s)	PGD (cm)	Significant Duration (s)	Arias Intensity (cm/s)	Housner Intensity (cm)
3506	İzmir Konak Güzelyalı Meteoroloji Müdürlüğü	38.3944	27.0821	54.99	56.12	62.30	771	B	E-W	41.04	3.17	0.92	20.33	3.43	16.17
									N-S	43.88	3.39	0.91	20.44	3.89	12.91
									U-D	23.59	2.07	0.91	26.69	1.66	9.55
3511	İzmir Pınarbaşı Bornova	38.4213	27.2563	63.57	64.55	72.61	827	B	E-W	41.29	5.98	1.51	22.11	2.03	23.03
									N-S	29.11	3.96	1.08	21.36	2.48	17.60
									U-D	18.90	1.87	0.65	30.41	0.82	10.09
3512	İzmir Buca Gürçeşme Zübeyde Hn Huzurevi	38.4009	27.1516	57.63	58.71	65.76	468	C	E-W	56.75	3.90	1.14	25.59	8.21	18.16
									N-S	57.54	3.31	1.16	24.99	7.93	17.01
									U-D	28.16	1.58	0.78	26.28	2.60	8.36
3513	İzmir Bayraklı ÇŞB İl Müd	38.4584	27.1671	64.08	65.05	72.00	196	D	E-W	94.67	14.42	3.15	20.16	35.30	84.81
									N-S	106.28	17.11	2.90	20.59	33.17	79.76
									U-D	44.19	4.48	0.80	30.84	6.42	23.29
3514	İzmir Bayraklı Sağlık Evi	38.4762	27.1581	65.67	66.62	73.39	836	B	E-W	56.02	6.41	1.31	23.75	4.58	28.26
									N-S	39.42	4.23	1.44	25.90	3.52	22.39
									U-D	25.15	1.94	0.73	27.17	2.10	10.91
3516	İzmir Güzelbahçe Belediye Spor Salonu	38.3706	26.8907	50.22	55.75	54.57	460	C	E-W	48.36	3.63	1.30	20.67	5.35	17.35
									N-S	47.29	4.84	1.19	21.65	4.85	20.13
									U-D	32.08	2.44	1.05	24.15	2.49	9.72
3517	İzmir Buca DEU	38.3756	27.1936	56.54	57.64	65.32	695	C	E-W	36.14	3.50	1.28	25.69	2.73	16.94
									N-S	40.10	3.95	1.11	24.67	2.86	16.15
									U-D	19.82	2.11	0.79	34.71	1.69	11.45
3518	İzmir Konak Fuar Kulturpark Tenis Kulubu	38.4312	27.1435	60.53	61.56	68.36	298	D	E-W	91.45	10.65	2.70	18.81	31.94	67.85
									N-S	106.10	11.33	1.61	25.03	23.66	56.05
									U-D	31.14	8.33	5.16	19.06	4.52	23.47
3519	İzmir Karşıyaka Orman İl Müdürlüğü	38.4525	27.1112	61.90	62.91	69.23	131	E	E-W	109.98	14.48	3.24	23.17	35.95	76.79
									N-S	150.09	22.53	3.93	20.58	45.60	92.24
									U-D	34.17	4.33	1.05	31.06	6.00	22.86
3520	İzmir Manavkuyu Halk Kütüphanesi	38.4780	27.2111	67.53	68.46	75.78	875	B	E-W	58.55	8.37	2.04	19.73	5.21	36.08
									N-S	36.11	4.65	1.13	20.11	3.60	24.21
									U-D	19.37	2.68	0.70	26.80	1.33	13.63

Station Code	Name	Lat.	Long.	Rjb (km)	Rrup (km)	Repi (km)	Vs30 (m/s)	Site Class*	Comp.	PGA (cm/s^2)	PGV (cm/s)	PGD (cm)	Significant Duration (s)	Arias Intensity (cm/s)	Housner Intensity (cm)
3521	İzmir Mavişehir Karşıyaka Bel	38.4679	27.0764	62.76	63.76	69.58	145	E	E-W	93.99	12.29	3.14	26.06	29.47	66.66
									N-S	110.84	16.17	4.08	22.61	35.19	87.41
									U-D	40.31	3.86	1.14	30.03	6.49	23.70
3522	İzmir Çamdibi Sağlık Ocağı	38.4357	27.1987	62.79	63.78	71.18	249	D	E-W	63.94	14.81	2.77	24.49	13.37	55.71
									N-S	73.72	9.92	2.56	20.55	19.25	49.83
									U-D	24.65	3.72	0.71	30.13	2.32	18.42
3523	İzmir Urla Kapalı Spor Salonu	38.3282	26.7706	45.50	51.14	48.94	414	C	E-W	63.57	4.99	1.43	22.08	10.38	22.26
									N-S	80.32	5.73	1.93	20.46	10.91	30.20
									U-D	36.90	4.11	1.97	26.85	4.30	17.62
3524	İzmir Yamanlar Müyesser Turfan Güçsüzler Evi	38.4969	27.1073	66.55	67.49	73.59	459	C	E-W	68.34	5.90	0.98	16.98	9.24	24.91
									N-S	64.71	4.74	0.94	18.91	7.29	19.38
									U-D	29.83	1.93	0.62	24.94	2.55	7.71
3526	İzmir-Menemen-Seyrek	38.5782	26.9795	73.56	74.41	78.75	205	D	E-W	81.50	10.45	2.27	31.43	20.33	53.04
									N-S	88.77	10.82	3.19	24.44	25.36	61.01
									U-D	29.15	3.41	0.86	38.81	3.83	18.82
3527	İzmir-Karaburun-Halk Eğitim	38.6390	26.5128	80.11	80.89	86.63	207	D	E-W	56.57	7.03	1.76	13.75	6.68	38.13
									N-S	80.93	8.85	2.62	15.07	10.66	47.62
									U-D	46.65	6.07	1.03	17.25	4.15	22.87
3528	İzmir Çeşme Ilıca Meteoroloji Müdürlüğü	38.3039	26.3726	45.38	46.75	58.23	532	C	E-W	149.31	8.36	1.89	12.90	31.26	40.95
									N-S	117.57	7.57	2.26	14.77	14.33	32.67
									U-D	77.00	3.63	1.49	16.82	6.75	14.52
3533	İzmir Menderes Sağlık Grup Başkanlığı	38.2572	27.1302	42.29	43.75	51.38	415	C	E-W	45.90	5.95	1.89	25.16	7.53	26.11
									N-S	73.64	5.52	2.31	27.21	8.49	27.29
									U-D	37.46	3.39	1.14	29.36	3.81	18.20
3534	İzmir-Foça-Reha	38.6624	26.7586	82.66	87.77	86.11	328	D	E-W	92.48	4.91	0.94	19.00	14.52	20.58
									N-S	73.16	5.09	0.68	17.00	16.09	23.37
									U-D	38.31	2.63	0.69	24.42	2.39	10.09

Station Code	Name	Lat.	Long.	Rjb (km)	Rrup (km)	Repi (km)	Vs30 (m/s)	Site Class*	Comp.	PGA (cm/s^2)	PGV (cm/s)	PGD (cm)	Significant Duration (s)	Arias Intensity (cm/s)	Housner Intensity (cm)
3536	İzmir Seferihisar Hükümet Konağı	38.1968	26.8384	30.89	37.02	34.75	1141	B	E-W	79.14	8.71	2.13	17.48	8.06	27.31
									N-S	50.22	5.32	1.88	19.42	5.12	21.51
									U-D	31.32	3.57	1.12	22.07	2.56	11.37
3538	İzmir Gaziemir Toplum Sağlık Merkezi	38.3187	27.1233	48.24	49.52	56.67	None	None	E-W	76.95	6.08	1.24	22.00	15.44	29.66
									N-S	85.48	5.48	1.11	23.88	12.36	27.32
									U-D	39.26	2.66	0.83	25.76	5.18	15.53
3539	İzmir Tire Devlet Hastanesi	38.1023	27.7211	74.01	74.85	86.09	None	None	E-W	27.02	1.94	0.52	28.38	1.67	9.57
									N-S	37.63	2.68	1.43	27.03	2.44	11.40
									U-D	22.25	1.75	0.93	30.93	1.05	8.84
4501	Manisa-Merkez-ÇŞB Müd	38.6126	27.3814	87.46	88.17	96.31	340	D	E-W	40.00	6.81	1.78	23.61	4.68	29.15
									N-S	34.89	7.06	1.41	21.83	4.31	30.71
									U-D	24.36	3.54	1.16	36.12	2.25	20.10
4814	Muğla Selimiye Orman İşletme	37.3991	27.6567	81.05	81.06	94.63	694	C	E-W	23.23	1.09	0.64	22.72	0.35	4.35
									N-S	25.33	1.63	1.09	20.54	0.58	7.05
									U-D	10.22	1.30	0.64	26.01	0.21	4.11
4822	Muğla Milas Derince Barajı-Crest	37.4417	27.6460	77.58	77.58	91.18	None	None	E-W	80.06	5.39	0.97	19.05	12.46	20.70
									N-S	32.52	1.68	0.82	38.61	2.87	6.79
									U-D	37.98	2.04	0.76	27.76	2.46	7.77
4823	Muğla Milas Derince Barajı-Bedrock	37.4418	27.6440	77.43	77.43	91.03	None	None	E-W	25.77	1.60	0.86	22.95	1.17	8.17
									N-S	22.77	1.38	0.79	25.57	0.86	4.76
									U-D	18.57	1.66	0.74	26.15	0.58	5.63

*Site classes are given according to Eurocode 8 (EC8; CEN, 2004) site classification for stations in Greece (SMG1 and SAMA) and according to the site classification of the 2019 edition of earthquake code in Turkey (TBDY, 2019) for stations in Turkey.

On the basis of comparisons with median response spectra from ground motion models, it is noted that relatively long period (0.5-1.5 sec) high energy is also present in the rock motions (e.g.: 3506, 3411, 3514, 3517 and 3520) recorded in Izmir Bay. Moreover, this elevated unexpected energy signature of the event at spectral period range of (0.5-1.5 sec) is again present at rock motions recorded at stations closer to the fault rupture (e.g.: 3536, 3518). Hence, it is attributed to the source rather than path effects. These already rich intensity rock shaking levels in the period range of 0.5 to 1.5 seconds, are further amplified with deep alluvial sites of Izmir Bay (e.g: at Konak and Bayrakli districts) which happen to exhibit natural periods falling in the same period range, leading to resonance of these soil sites. As also described in Chapters 4 and 7, the long-period content at Station #3513 in Bayraklı could help to explain the structural damage in 7-9 story structures as a combination of basin effects in the bay and site amplifications. The long significant durations also support this explanation. Considering the entire set of records, elevated long-period content and overall longer significant durations are observed at softer sites, particularly at those located within the İzmir Bay, implying the emergence of significant basin effects. These and more are discussed in Chapter 5 Site Effects.

The two stations on Samos island (SMG1, SAMA) - the closest stations to the causative fault- recorded the highest PGA≈0.23g and PGV= 24cm/s (at SMG1). The surface geology of the SMG1 station consists of alluvial deposits of Quaternary age with a measured (using MASW method) average V_{S30}≈550m/sec. It is installed at the basement of a 3-story reinforced concrete (RC) building. The geological conditions of the SAMA station consist of metamorphic formations (marble) of Paleozoic are with a measured average V_{S30}≈840m/sec. It is also installed at the basement of a 3-story R/C building.

At all Turkish stations, the observed spectra lie below the design spectra defined in the current seismic code of Turkey (Turkey Building Earthquake Code - TBDY, 2019). The same observation holds for the 2007 and 1975 editions of the design spectra provided by same national code. Yet, at Stations #0905 and #3528, within short period range below 0.25 seconds, the response spectra are above the equivalent elastic spectra obtained from the inelastic design spectra of the 1975 edition of the Turkish seismic code with load reduction factors of R=4, 6 and 8. However, no structural collapses have been reported nearby these stations. Response spectra and Fourier amplitude spectra of the recordings at both stations of the Samos Island, SMG1 and SAMA, indicate amplification within a period range of 0.3-0.7 seconds. By comparing the observed and the elastic design spectra of the seismic codes, which are currently in use (EAK2000, Eurocode 8 – EC8), it is observed that the latter satisfactorily covers the observed data almost for the entire period range, except for a narrow band of periods between 0.5 and 0.7 seconds.

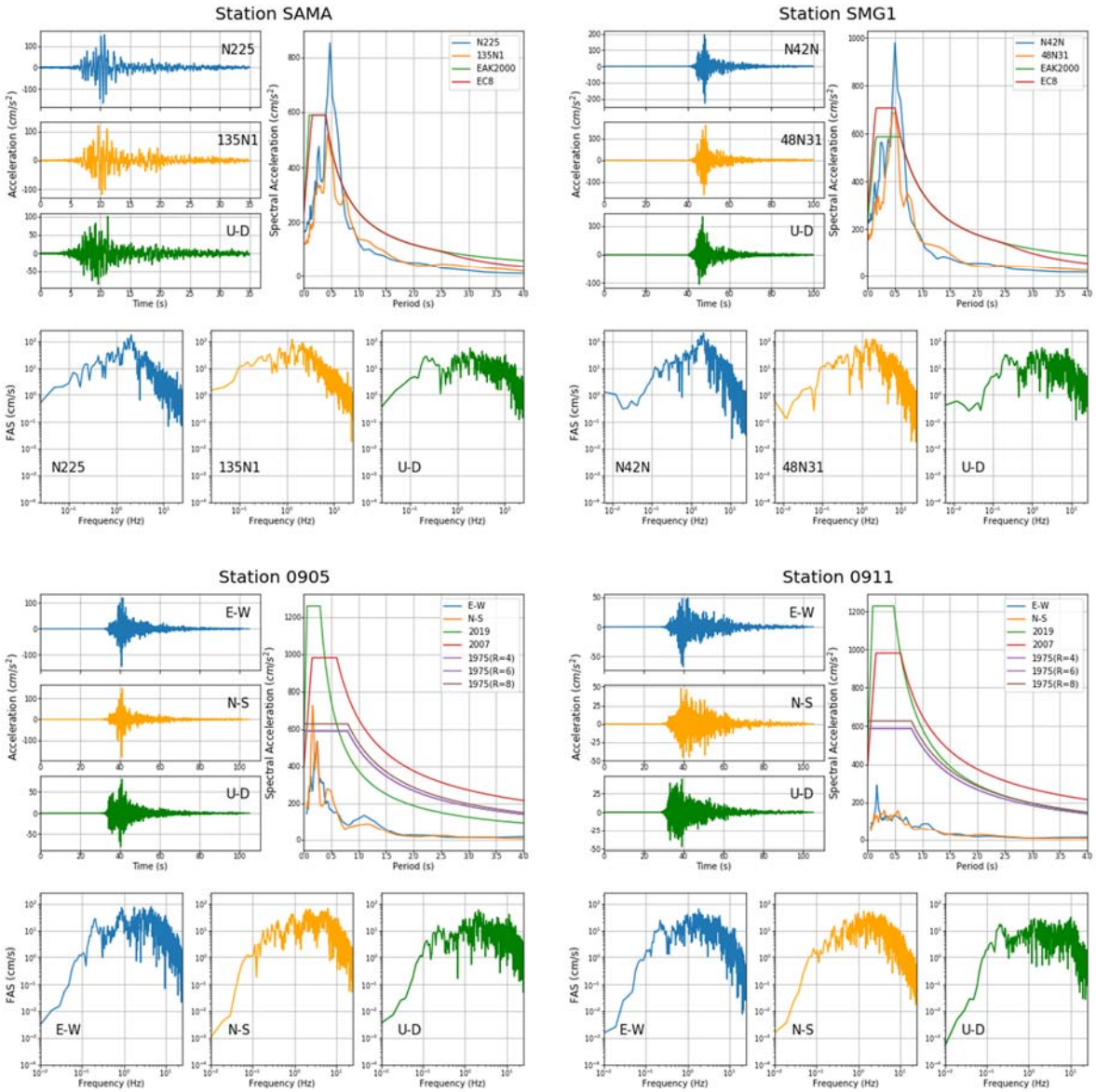

Figure 3.3 Acceleration time histories, Fourier amplitude spectra and 5%-damped response spectra of records at stations located within 10 km epicentral distance. To the right of acceleration waveform plots, acceleration response spectra are compared to the design spectra of current and previous versions of the Turkish (TBDY, 2019) and Greek (EAK, 2000) national building codes.

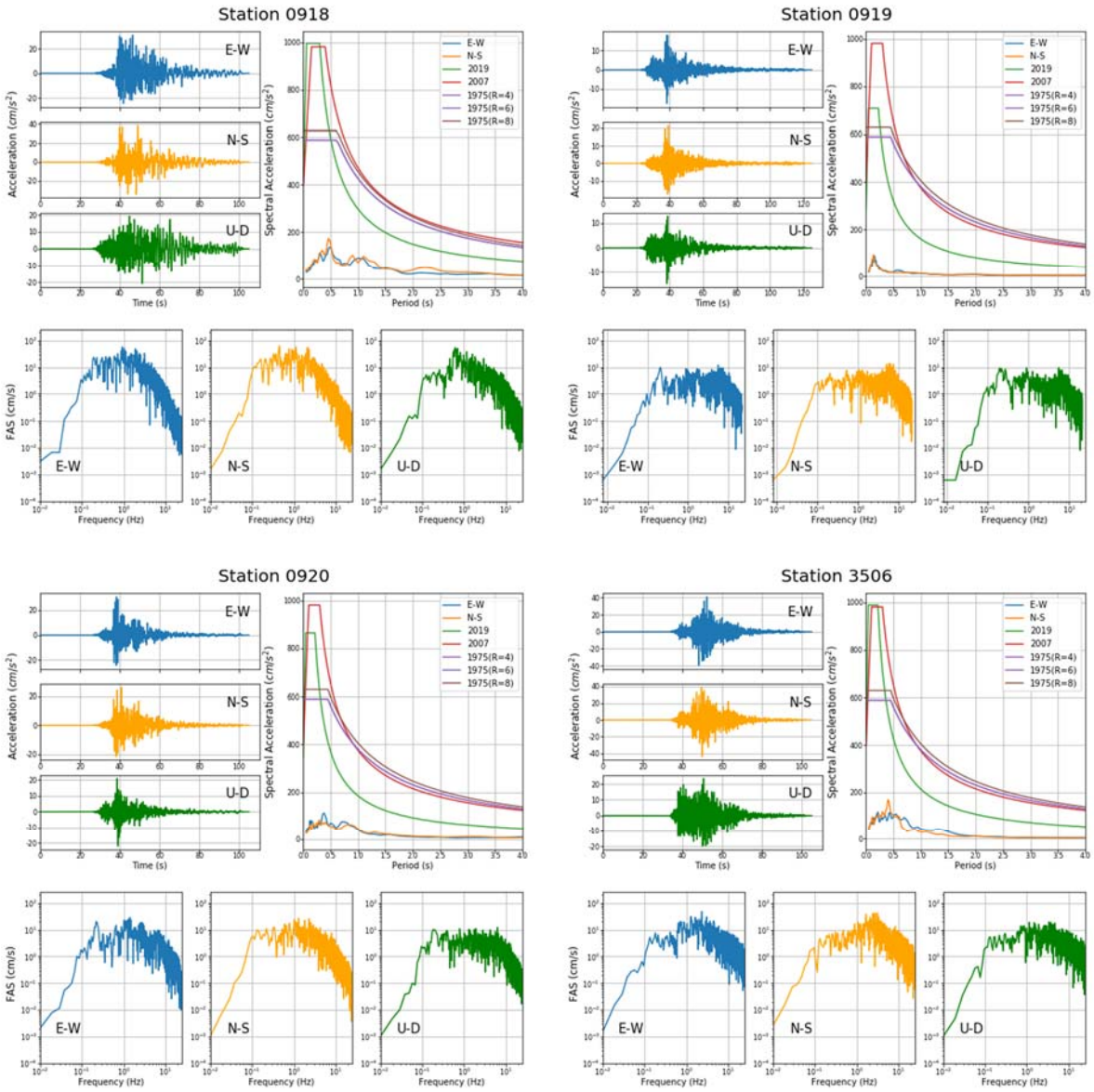

Figure 3.3 (Continued)

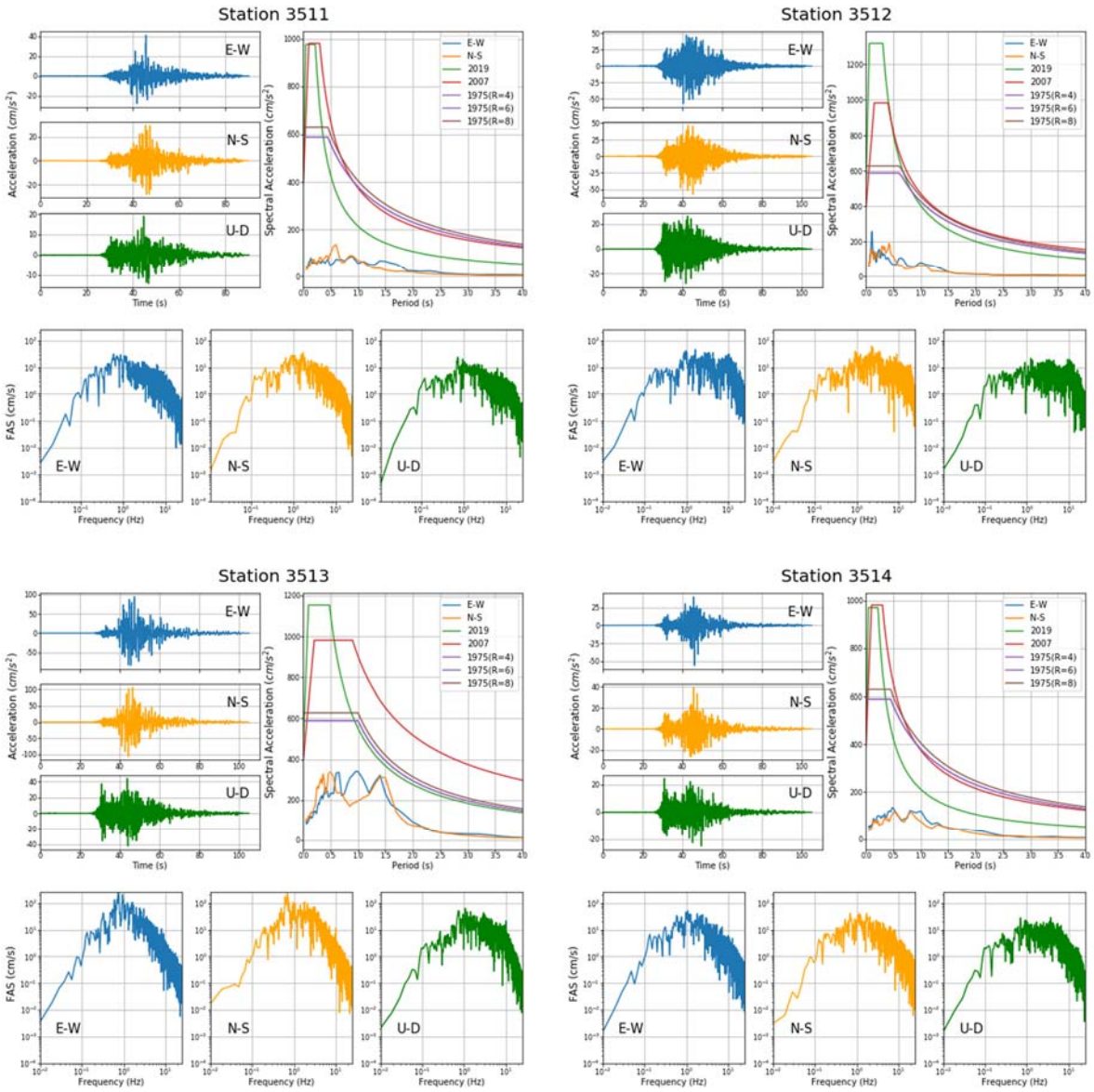

Figure 3.3 (Continued)

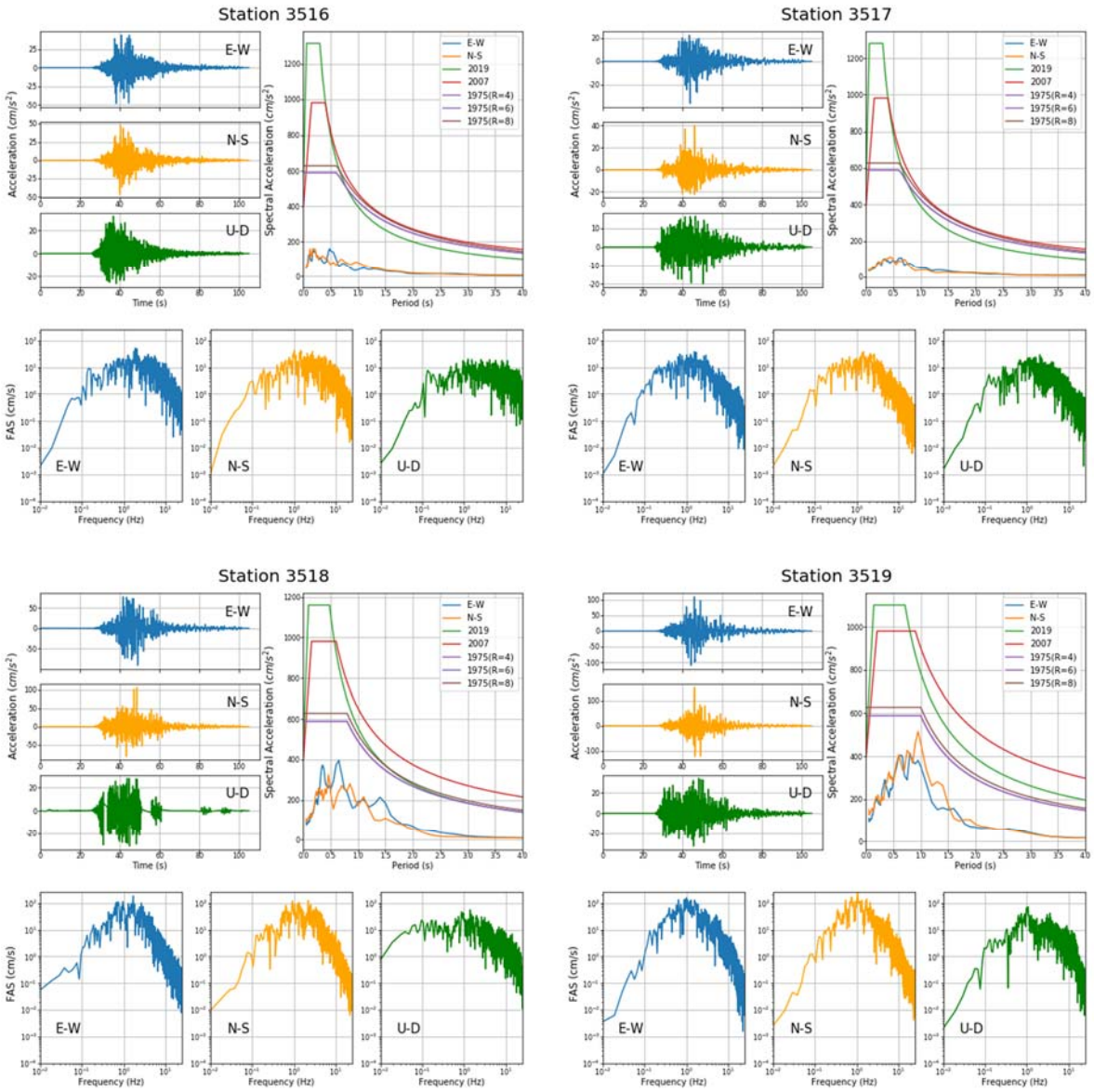

Figure 3.3 (Continued)

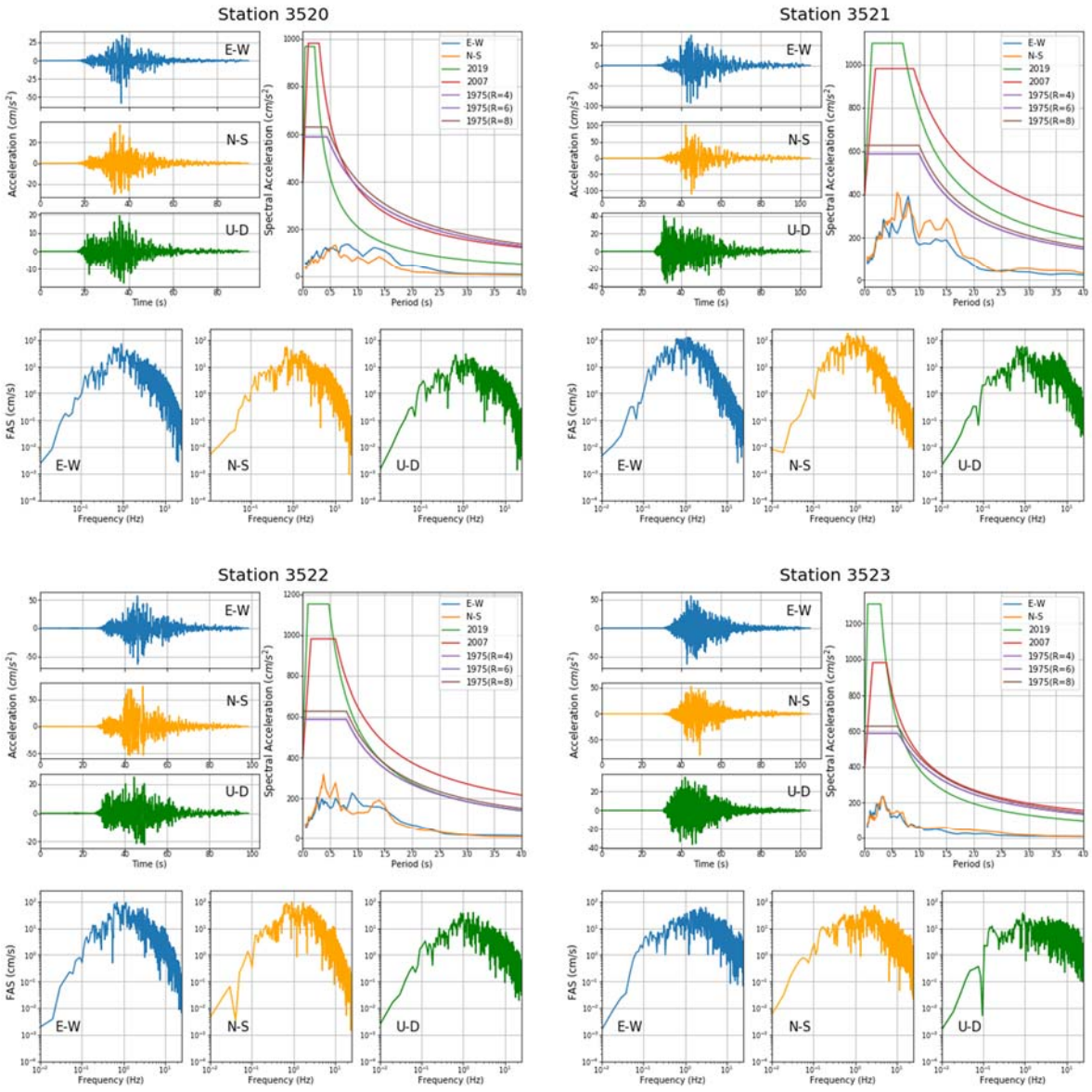

Figure 3.3(Continued)

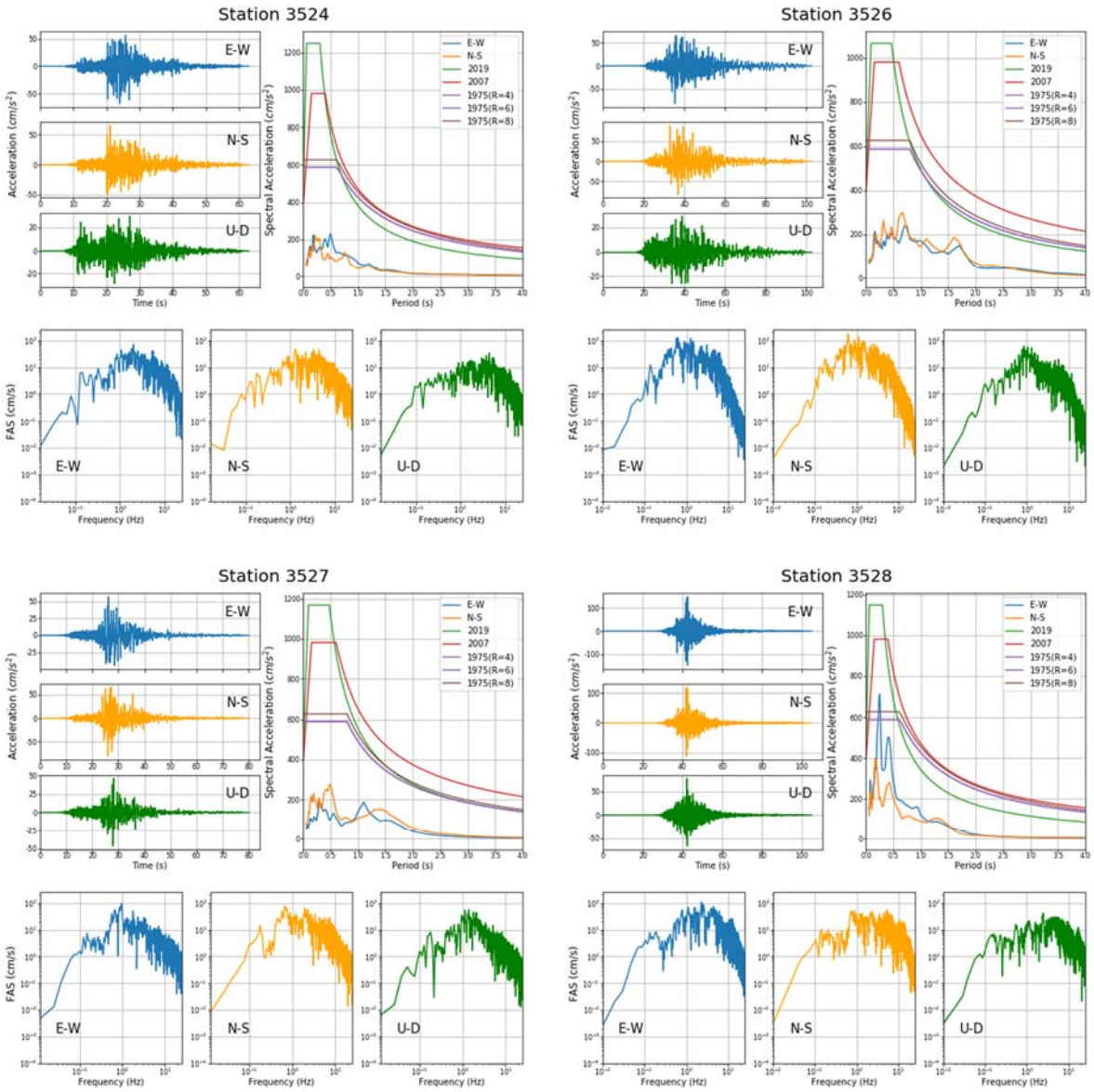

Figure 3.3 (Continued)

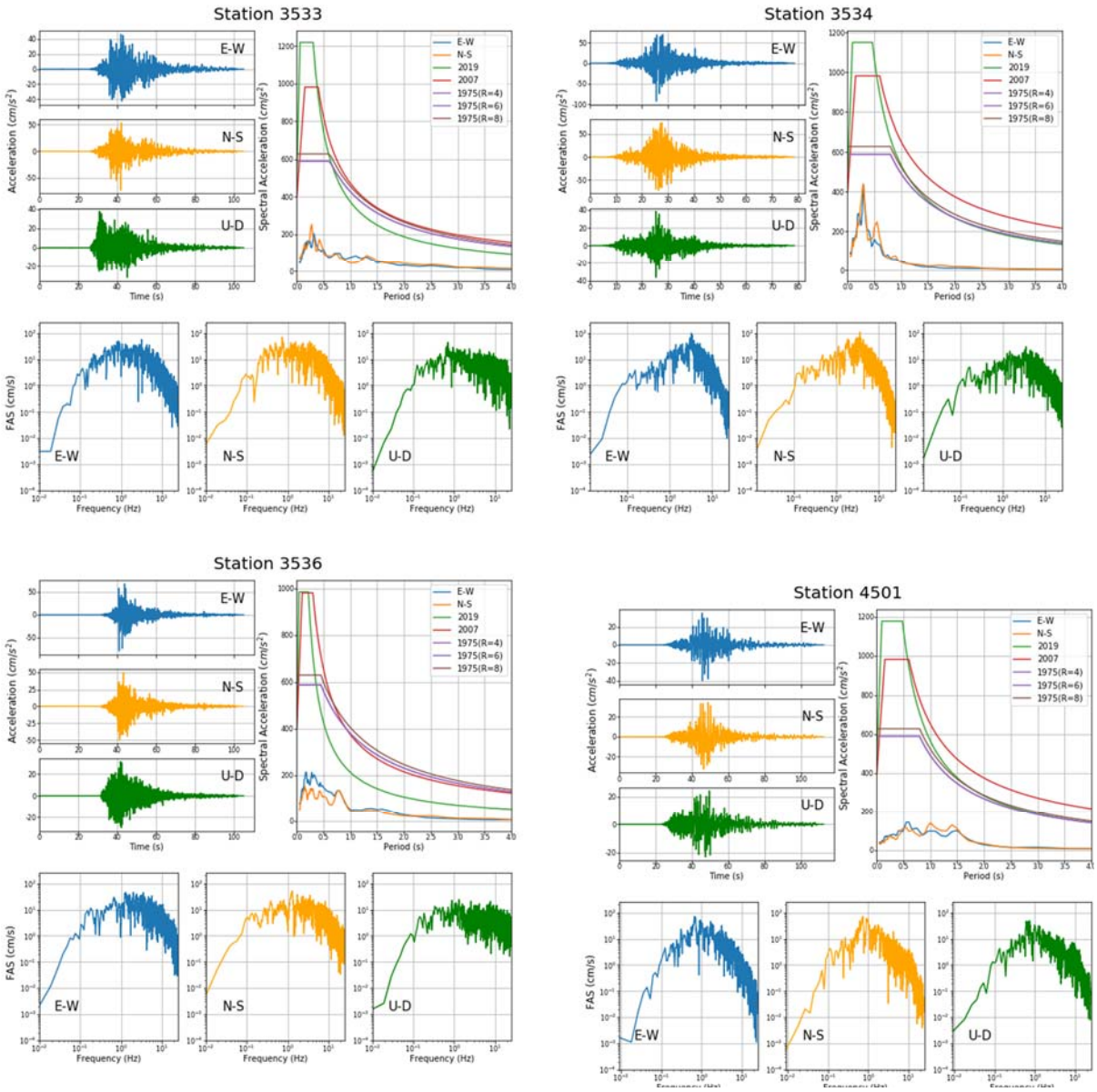

Figure 3.3 (Continued)

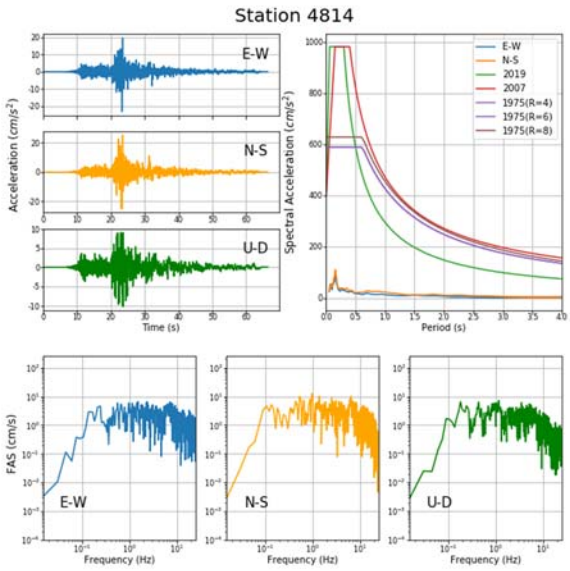

Figure 3.3 (Continued)

3.4. Assessment of Macroseismic Intensity Distributions

Among alternative intensity measures of seismic effects, macroseismic intensity distributions are commonly employed to rapidly identify locations with varying ground shaking levels. Along with instrumental ground motion parameters, seismic intensity has been used extensively after large events. Despite the subjectivity involved in the estimation of intensity values, they provide valuable information regarding the distribution of seismic effects. Computed intensity distributions are used to rapidly estimate the areas of relatively high and maximum levels of ground shaking. Within the scope of this report, a Modified Mercalli Intensity (MMI) map has been prepared for the region affected by the earthquake. The empirical equations of Bilal and Askan (2014) are employed herein where MMI values are obtained not only from citizens' reports and field observations, but also from the actual peak ground motion values recorded at the 35 stations within 100 km epicentral distance. For the stations on Samos Island, MMI-PGA correlations have been preferred against MMI-PGV as the building stock on the island comprises basically typical low rise buildings mostly prone to damage from high-frequency shaking, which is better correlated with PGA. In Turkey, however, PGV is preferred, as it is well known to be a better indicator of damage in reinforced concrete structures. The following relationships are employed to compute MMI values from observed PGA (in cm/s^2) and PGV (in cm/s), in Greece and Turkey respectively (Bilal and Askan, 2014):

$$MMI = 0.132 + 3.884 \log(PGA) \tag{3.1}$$

$$MMI = 2.673 + 4.340 \log(PGV) \tag{3.2}$$

Figure 3.4 shows that the computed instrumental MMI on the Samos Island are in the order of VII to VIII and are in agreement with the observations reported by EMSC. In addition, damages observed at the various sites on the island by the reconnaissance teams indicate MMI values near VIII. The coastal Gümüldür-Tepecik-Seferihisar-Sığacık regions (in the southeast of the Anatolia peninsula) which were hit by the earthquake induced tsunami; MMI values of VI to VII are estimated. The majority of the Aegean inland region exhibits MMI values of V and VI. However, the Bayraklı district in İzmir, where severe structural damages are observed, has an estimated MMI value of VII. Use of recorded PGA and PGV values in estimating MMI values yields a clear understanding of regions with larger levels of shaking and damage.

3.5. Evaluation of the Predictive Performance of the Ground Motion Models

Figure 3.5 shows the spatial distribution of 77 strong motion recording stations in the second subset (located within 200km of the rupture plane), which are used for evaluating the predictive performance of the ground motion models (GMMs). The source-to-site-distance metrics of the recording stations are computed using the finite fault model given in Table 1.2. Distance parameters provided include the Joyner-Boore distance (R_{JB}), rupture distance (R_{RUP}), and other site-specific distance measures that depend on the source-to-site azimuth (Rx and Ry0). All of these distance metrics are calculated and added to the flatfile. The finite fault parameters used in calculating the distance metrics (and the parameters used in estimating the

prediction performance of GMMs) are summarized in Table 3.2 (please refer to Section 1.4 of this report for further details about the selected finite fault model, FFM).

The site parameters required for GMMs, such as the basin depth terms, which are defined as the depths to the 1.0 and 2.5 km/s shear wave velocity horizons in the soil profile (denoted by $Z_{1.0}$ and $Z_{2.5}$) are estimated using Equations 3.3 (Abrahamson and Silva, 2008) and 3.4 (Campbell and Bozorgnia, 2008):

$$\ln(Z_{1.0}) = \begin{cases} 6.745 & for\ V_{s30} < 180\ m/s \\ 6.745 - 1.35 * \ln\left(\frac{V_{s30}}{180}\right) & for\ 180 \leq V_{s30} \leq 500\ m/s \\ 5.394 - 4.48 * \ln\left(\frac{V_{s30}}{500}\right) & for\ V_{s30} > 500\ m/s \end{cases} \quad (in\ meter) \qquad (3.3)$$

$$Z_{2.5} = 0.519 + 3.595 * Z_{1.0} \qquad (3.4)$$

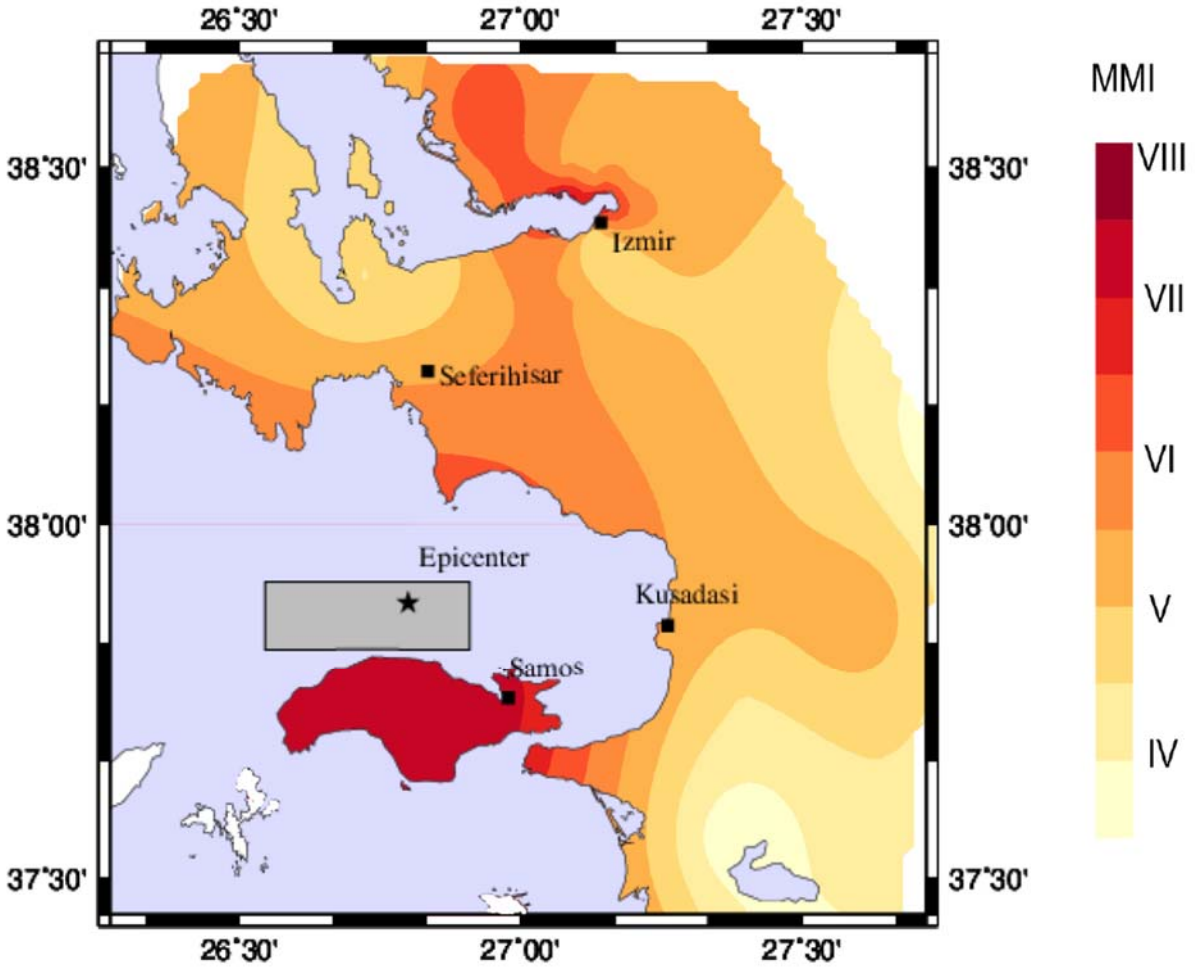

Figure 3.4. MMI map for the 30 October Samos earthquake based exclusively on recorded peak ground motions

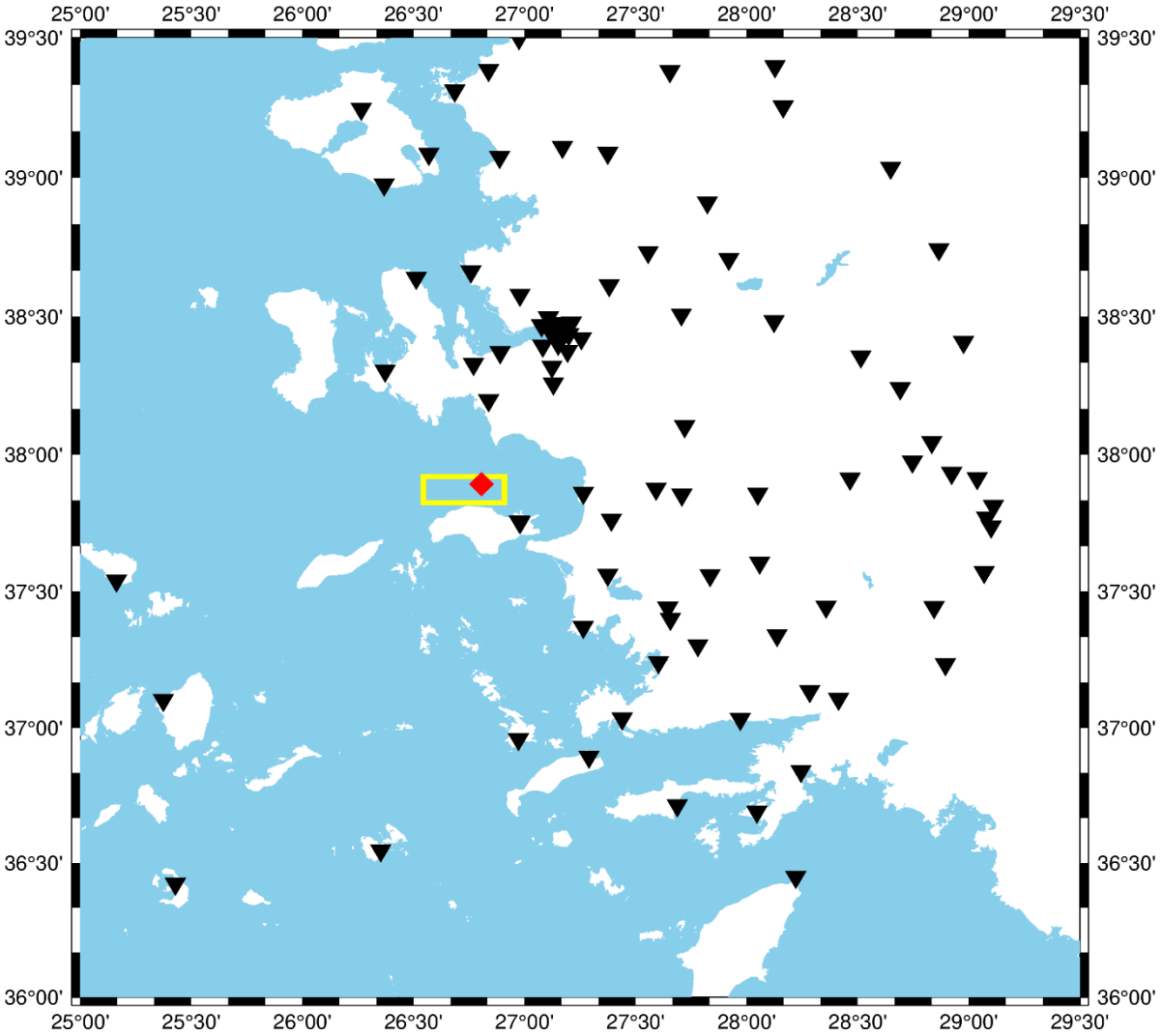

Figure 3.5. Spatial distribution of the strong motion stations in the joint database that is located within 200km of the rupture plane. Surface projection of the preferred rupture plane is given by the yellow rectangle and the epicenter of the event is denoted by the red point.

Table 3.2. Fault plane parameters used in calculating the source to site distance metrics

Parameter	**Value**	**Explanation/reference**
Rupture length Rupture width	32 km 15 km	Chapter 1
Rupture center	37.892° 26.807°	Stronger propagation to the west, where the strongest slip patch was observed
Strike / Dip	270°/ 45°	Chapter 1
Z_{TOR}	0-2 km	Z_{TOR}= 0.6 km is used for distance metrics and 1 km resolution in computations is given in Chapter 1.
Max. rupture depth	11.2 km	Chapter 1

Figure 3.6 presents the R_{RUP}-V_{S30} distribution of the strong motion stations in the joint database. A majority of the stations are classified in Site Class D and Site Class C according to TBDY (2019) and classified as Site Class C and B according to EC8 (2004). Only 13% of the stations have V_{S30}>800 m/s or V_{S30}<180 m/s. The number of near-fault stations is very limited; more than half of the recording stations are located at distances more than 100 km to the rupture plane. Approximately 15% of the strong motion stations are located within 60-70 km to the rupture (more specifically, located in the İzmir metropolitan area) where the structural damage is observed.

The horizontal component spectral values in terms of RotD50 (Boore, 2010) for 111 spectral periods between 0.01 and 20 seconds are calculated for consistency with the evaluated global GMMs.

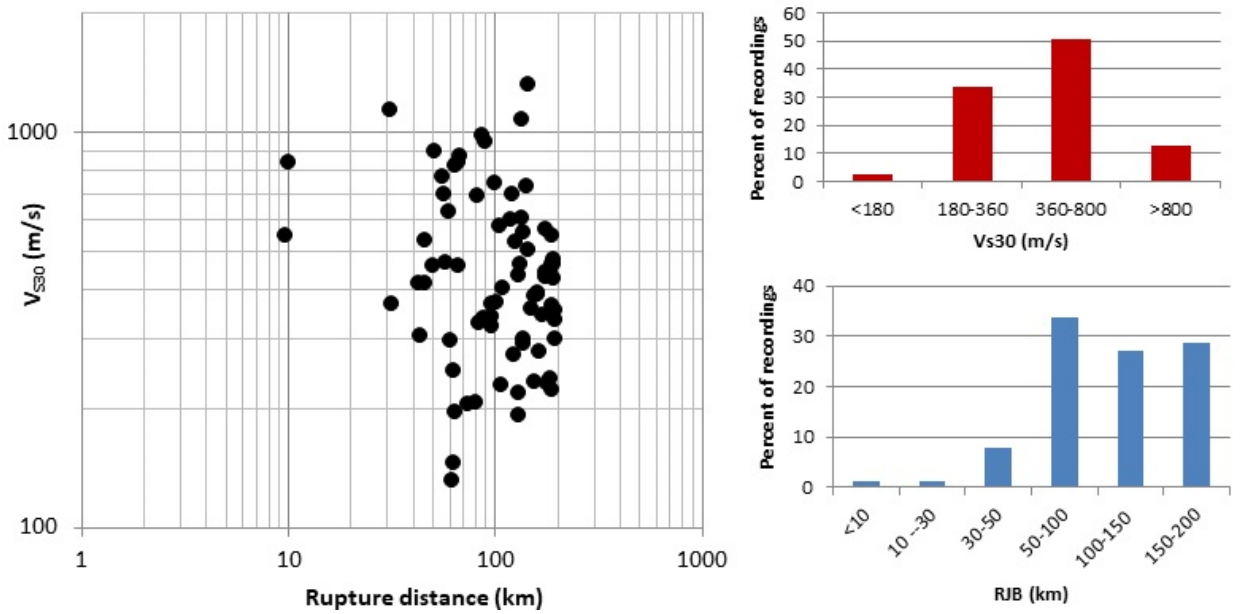

Figure 3.6. R_{RUP} -V_{S30} distribution of the stations in the joint database (left). Percentages of recording stations in each site class defined in TBDY19 and EC8 (top, right) and percentages of recording stations in each distance bin (bottom, right).

A recent study by Kale (2019) utilized several ranking methods for comparing the predictive performance of several GMMs for shallow crustal and active tectonic regions with the Turkish strong motion database. The GMMs that were tested by Kale (2019) and the GMMs that were used in recent large-scale projects (e.g. site licensing reports of new NPP sites in Turkey) are in good agreement. In essence, these recent studies suggest that the global Next Generation Attenuation (NGA) West 2 models developed by Abrahamson et al. (2014, ASK14), Boore at al. (2014, BSSA14), Campbell and Bozorgnia (2014, CB14) and Chiou and Youngs (2014, CY14), the most recent local GMM developed from a Turkish strong motion dataset (Kale et al., 2015, KAAH15) and the Turkey-adjusted versions of the global NGA-W1 models by Gülerce at al.

(2016) (TR-Adjusted AS08, TR-Adjusted BA08, TR-Adjusted CB08 and TR-Adjusted CY08) performed well under several subsets of Turkish ground-motion data.

A representative suite of GMMs is selected to evaluate their distance attenuation by using the mainshock ground motion data of the Samos earthquake. The two NGA West-2 predictive models (BSSA14 and CY14) that yield comparable predictions with the observed ground motions recorded in Turkey as well as the local model KAAH15 developed from a database consisting of records from Turkey (for reflecting the regional effects) are members of this suite to discuss the distance attenuation features of the subject earthquake. Among the Turkey-adjusted global GMMs, the TR-Adjusted AS08 and TR-Adjusted CY08 models are also selected as members of the GMM suite because the adjustments applied to the large distance scaling of these models can capture the distance attenuation between 100-200 km. The discussions made by Kale (2019) through different ranking methods, residual trends, etc. agree with the selected GMMs in this part.

The latest attempt for deriving a GMM for shallow (focal depth ≤ 30km) crustal earthquakes in Greece is carried out by Boore et al. (2021). In this GMM, a database of uniformly processed strong motion data have been utilized (Margaris et al., 2021) for predicting horizontal-component peak ground velocity, peak ground acceleration, and 5%-damped pseudo-acceleration response spectra at 105 periods ranging from 0.01 s to 10 s. Some specific effects related to rapid attenuation and weaker magnitude scaling in the Greek ground motions that are not captured in the global GMMs were captured by modifying the BSSA14 global model. This ground motion predictive model is calibrated for Greek data of a magnitude range 4.0 – 7.0 and V_{s30} from 150 to 1200 m/s. Specific features are included in this new GMM by developing a magnitude scaling that extends the range of magnitude applicability to M_w 8.0 and nonlinear site response. During the development of the new GMM, another interesting characteristic of the Greek strong motion data was revealed, which is also observed in Italian data: the Greek strong ground motions are substantially over-predicted by the global GMMs, which may be a regional feature, but may also be consequence of soil-structure interaction at the recording stations.

To evaluate the distance attenuation of the recorded strong motions with the distance scaling of selected GMMs, the distributions of RotD50-component PGA, PSA at T=0.2 sec., and PSA at T=1 sec. with R_{RUP} or R_{JB} (depending on the distance metric used by the GMM) are shown in Figures 3.7 to 3.12. The median estimates of BSSA14 (global, low-Q and high-Q options) and CY14 for V_{S30}=270 m/s (center V_{S30} of the Site Class D in TBDY-2019 and Site Class C in EC8) and V_{S30}=800 m/s (proxy of B/C boundary of TBDY-2019 and A/B boundary of EC8) are presented in Figures 3.7, 3.9, and 3.11. Median predictions of the regional models (Boore et al., 2021, KAAH15, TR-adjusted AS08 and TR-adjusted CY08) for V_{S30}=270 m/s and V_{S30}=800 m/s are shown in Figures 3.8, 3.10, and 3.12.

Figures 3.7 to 3.12 show that:

- There are a couple of far-field stations that have systematically lower ground motions than the median estimates of the tested GMMs at all spectral periods. This overestimation indicates faster attenuation after ≈120 km (lower Q) in accordance with the observations from previous studies (e.g. Akkar et al., 2011).
- At longer periods (T=1sec plots), recorded ground motions at several stations in İzmir (marked by red) are systematically higher than the median estimates of the tested GMMs. This underestimation can be explained by significant site amplifications at long periods (please refer to Chapter 4 of this report for further discussions).
- When the slower attenuation option of BSSA14 model (developed for China and Turkey) is implemented, the large-distance scaling of this model is less consistent with the recorded data when compared to the Average-Q (global) and Low-Q options.
- Future work will compare ground motion attenuation trends for rupture distances larger than 80 km for Greece and Turkey. This is of interest because prior results for Greece show relatively fast attenuation, whereas prior results for Turkey show slower attenuation. By comparing results for a common event, we can investigate whether they are actually different.

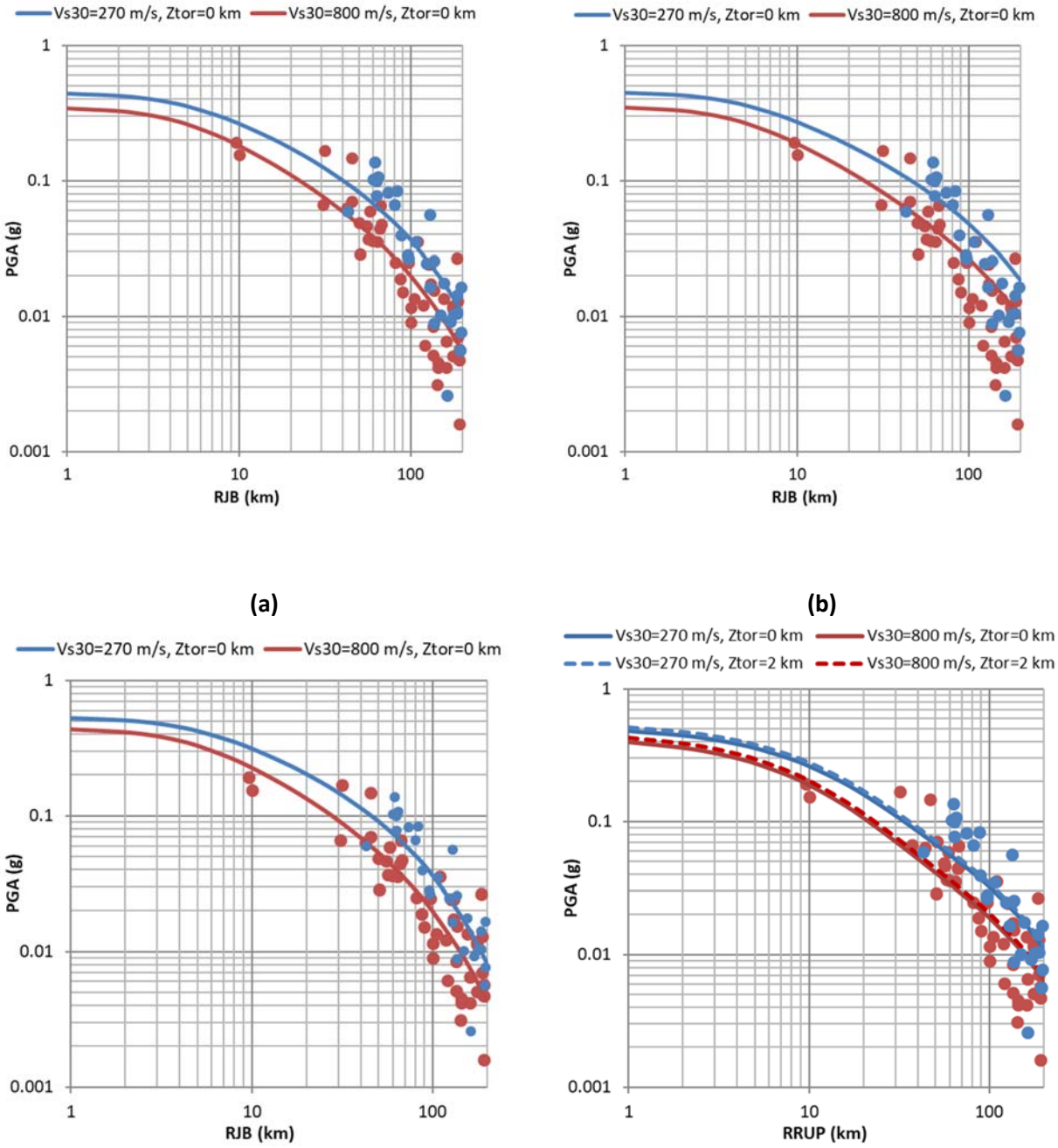

Figure 3.7. Comparison of the distance attenuation of global ground motion models with recorded strong motion data for PGA. Blue and red curves are the median predictions for V_{S30}=270 m/s and V_{S30}=800 m/s, respectively. Blue and red points belong to the stations with V_{S30}<360 m/s and V_{S30}≥360 m/s, respectively. Plots in (a) for BSSA14 model, global anelastic attenuation, (b) for BSSA14 model, anelastic attenuation for China and Turkey (c) for BSSA14 model, anelastic attenuation for Japan and Italy (d) for CY14 model.

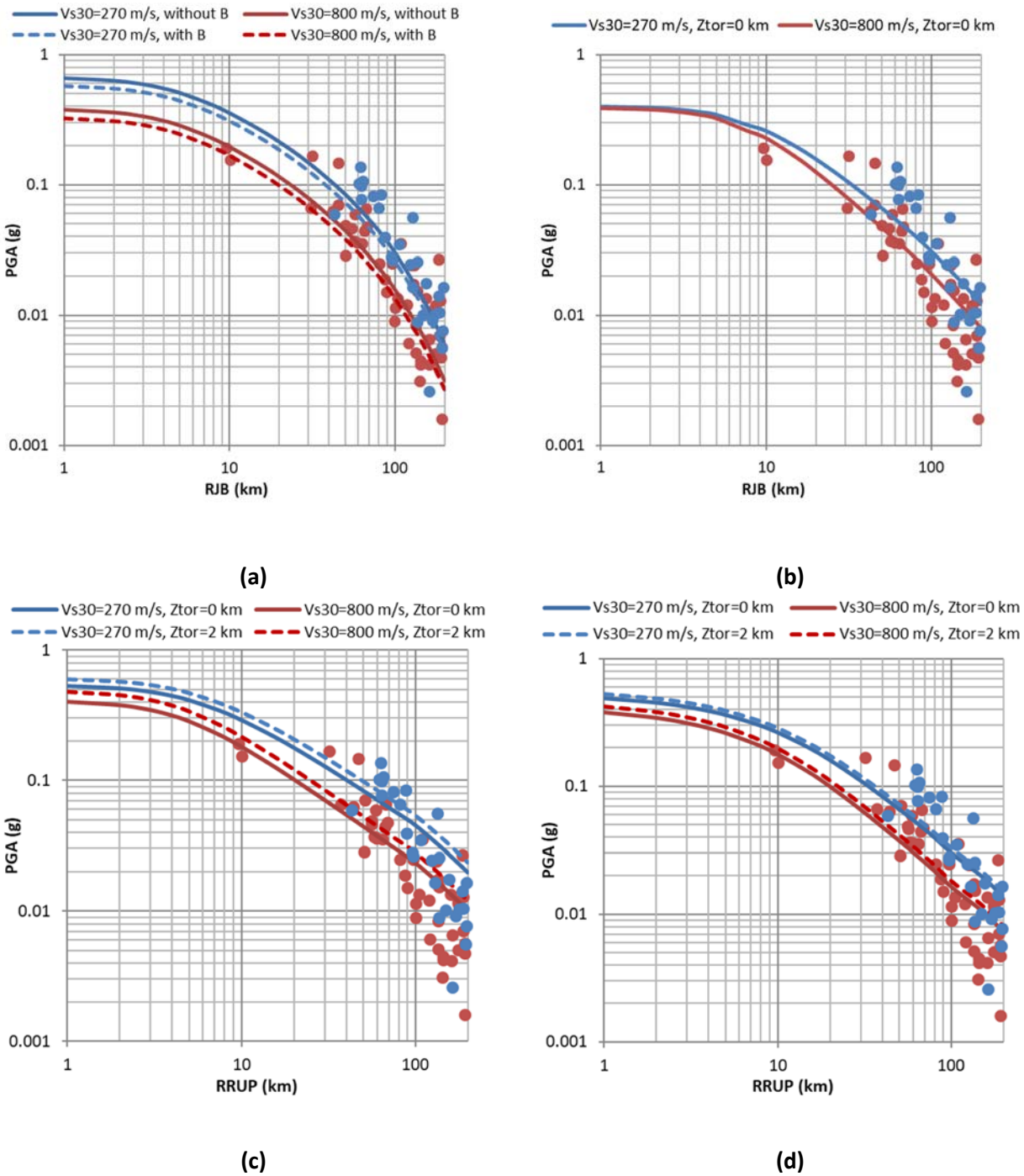

Figure 3.8. Comparison of the distance attenuation of regional ground motion models with recorded strong motion data for PGA. Blue and red curves are the median predictions for V_{S30}=270 m/s and V_{S30}=800 m/s, respectively. Blue and red points belong to the stations with V_{S30}<360 m/s and V_{S30}≥360 m/s, respectively. Plots in (a) for Greek Boore et al. (2021) model, (b) for Turkish KAAH15 model, (c) for Turkey-adjusted AS08 model, (d) for Turkey-adjusted CY08 model.

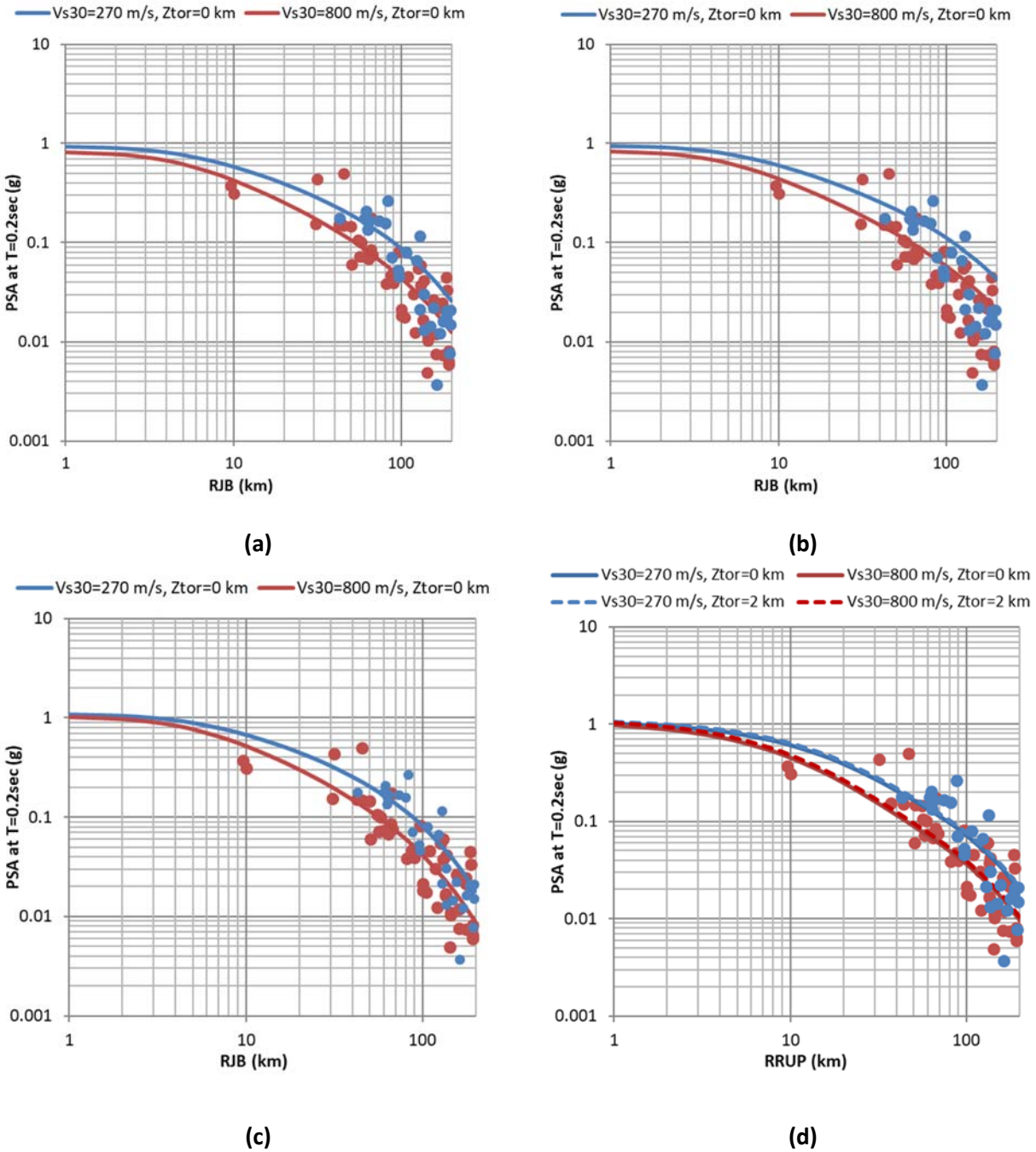

Figure 3.9. Comparison of the distance attenuation of global ground motion models with recorded strong motion data for PSA at T=0.2 sec. Blue and red curves are the median predictions for V_{S30}=270 m/s and V_{S30}=800 m/s, respectively. Blue and red points belong to the stations with V_{S30}<360 m/s and V_{S30}≥360 m/s, respectively. Plots in (a) for BSSA14 model, global anelastic attenuation, (b) for BSSA14 model, anelastic attenuation for China and Turkey (c) for BSSA14 model, anelastic attenuation for Japan and Italy (d) for CY14 model.

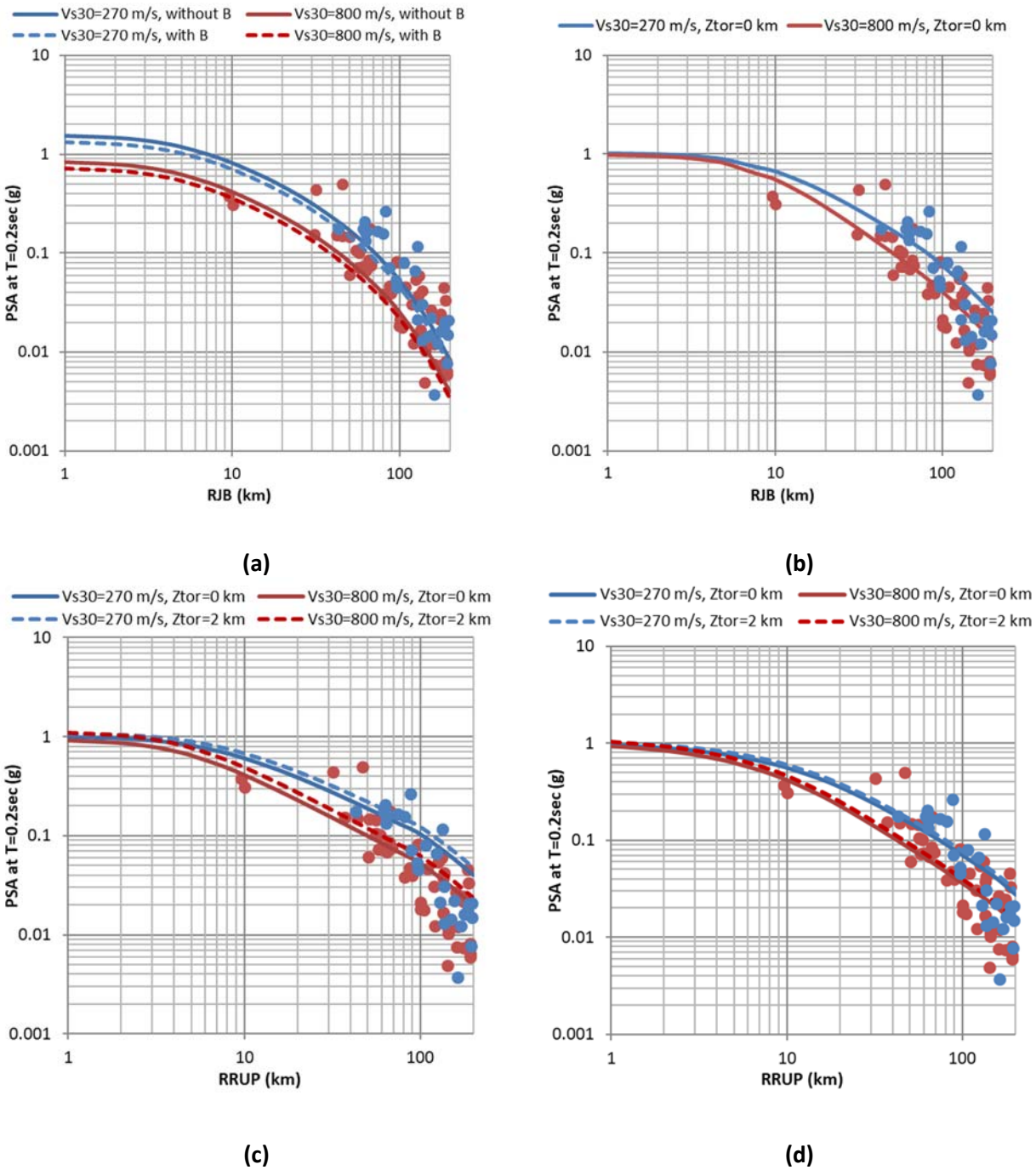

Figure 3.10. Comparison of the distance attenuation of regional ground motion models with recorded strong motion data PSA at T=0.2 sec. Blue and red curves are the median predictions for V_{S30}=270 m/s and V_{S30}=800 m/s, respectively. Blue and red points belong to the stations with V_{S30}<360 m/s and V_{S30}≥360 m/s, respectively. Plots in (a) for Greek Boore et al. (2021) model, (b) for Turkish KAAH15 model, (c) for Turkey-adjusted AS08 model, (d) for Turkey-adjusted CY08 model.

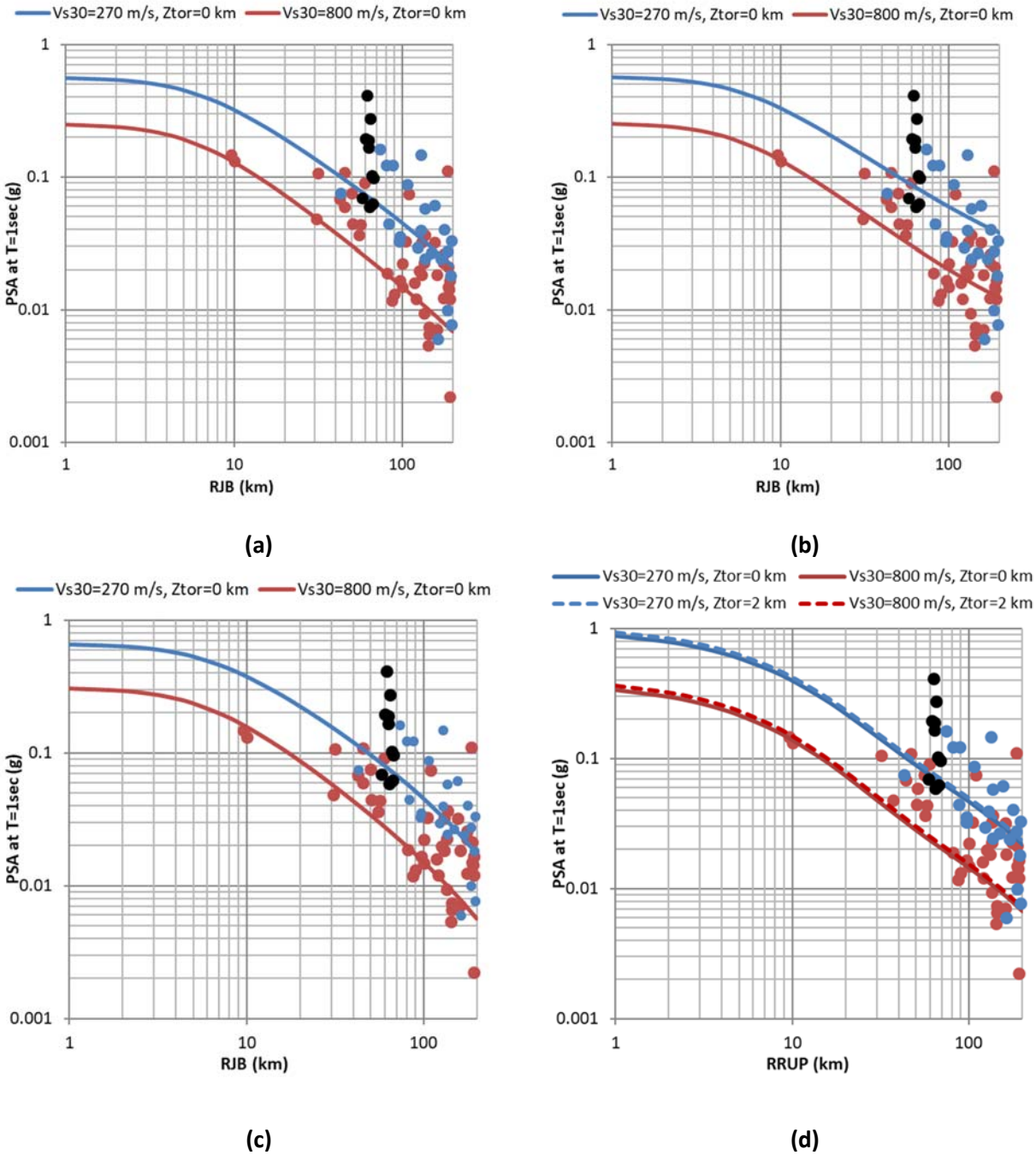

Figure 3.11. Comparison of the distance attenuation of global ground motion models with recorded strong motion data for PSA at T=1 sec. Black dots represents the recordings stations in the İzmir Metropolitan Area. Blue and red curves are the median predictions for V_{S30}=270 m/s and V_{S30}=800 m/s, respectively. Blue and red points belong to the stations with V_{S30}<360 m/s and V_{S30}≥360 m/s, respectively. Plots in (a) for BSSA14 model, global anelastic attenuation, (b) for BSSA14 model, anelastic attenuation for China and Turkey (c) for BSSA14 model, anelastic attenuation for Japan and Italy (d) for CY14 model.

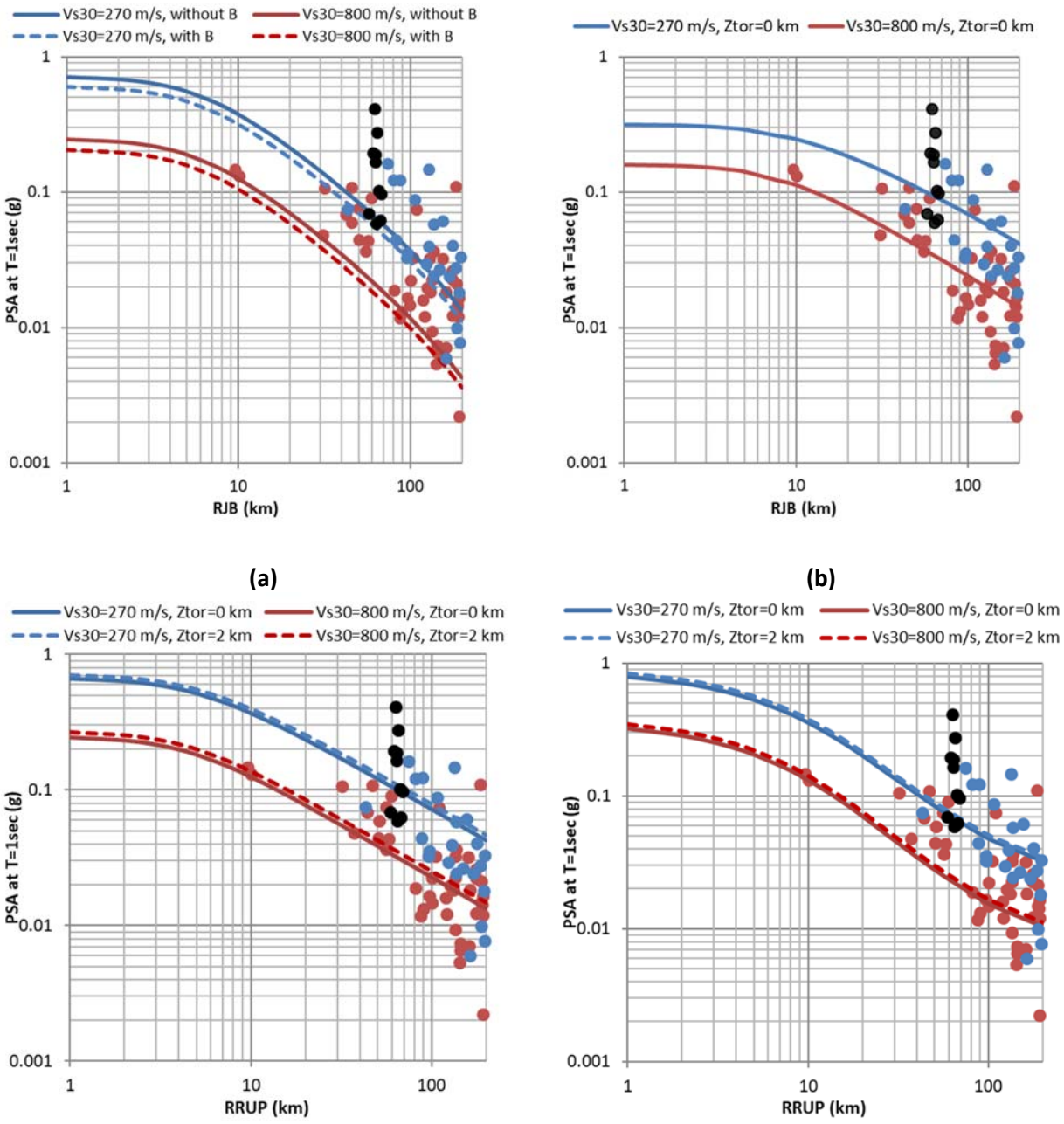

Figure 3.12. Comparison of the distance attenuation of regional ground motion models with recorded strong motion data PSA at T=1 sec. Black dots represents the recordings stations in the İzmir Metropolitan Area. Blue and red curves are the median predictions for V_{S30}=270 m/s and V_{S30}=800 m/s, respectively. Blue and red points belong to the stations with V_{S30}<360 m/s and V_{S30}≥360 m/s, respectively. Plots in (a) for Greek Boore et al. (2021) model, (b) for Turkish KAAH15 model, (c) for Turkey-adjusted AS08 model, (d) for Turkey-adjusted CY08 model.

3.6. A Summary of Major Findings and Conclusions

This chapter intends to convey preliminary information about the strong ground motion features of the 30 October 2020 Samos Earthquake. Uniform data processing was implemented to the raw accelerograms and some of the important period-independent ground-motion intensity measures (PGA, PGV and PGD) as well as the strong-motion durations were computed and are listed along with 5%-damped spectral acceleration comparisons of the Turkish, Greek and Eurocode 8 design codes. The provided information also includes the V_{S30} site parameter for the strong-motion stations as well as the frequently used source-to-site distance metrics in GMMs. The computed distances rely on the rupture plane discussed in Chapter 1 of this reconnaissance report. The Fourier acceleration spectra of the recorded accelerograms and macroseismic intensity distributions of the region struck by the earthquake compliment the conveyed information. Some local GMMs from Greece and Turkey as well as the global and Turkey-adjusted GMMs are evaluated for PGA and 5%-damped PSA at T = 0.2s and 1.0s to observe their behavior in the intermediate-to-long distance range (confined to the spatial distributions of the strong-motion stations listed in this chapter).

The preliminary observations from the analyses presented in this chapter are as follows:

1. The spectral values computed from the ground motions of this earthquake are mostly lower than those provided by the design codes.
2. Long-period spectral amplifications at some stations located on soft to very soft soil sites (Vs30 < 200 m/s) are significant suggesting the dominant site-amplifications. In addition, stations located in Izmir on stiffer site conditions also exhibit large long-period spectral amplitudes when compared to GMM estimations. Overall, these observations indicate potential basin effects in the Izmir bay which require further investigation.
3. Regional effects control the ground-motion attenuation towards long source-to-site distances. Such effects require better modeling of regional Q in future GMMs.

References

Abrahamson, N. A., Silva, W. J. (2008). Summary of the Abrahamson and Silva NGA ground motion relations. Earthquake Spectra, 24(1), 67–97, http://dx.doi.org/10.1193/1.2924360.

Abrahamson, N. A., Silva, W. J., Kamai, R. (2014). Summary of the ASK14 ground-motion relation for active crustal regions. Earthquake Spectra, 30(3), 1025–1057, http://dx.doi.org/10.1193/070913EQS198M.

Ancheta, T.D., R.B. Darragh, J.P. Stewart, E. Seyhan, W.J. Silva, B.S.-J. Chiou, K.E. Wooddell, R.W. Graves, A.R. Kottke, D.M. Boore, T. Kishida and J.L. Donahue (2014). NGA-West 2 database, Earthquake Spectra, 30, 989-1005.

Akkar, S., Aldemir, A., Askan, A., Bakır, S., Canbay, E., Demirel, İ. O., ... & Prakash, S. (2011). 8 March 2010 Elazıg-Kovancılar (Turkey) earthquake: Observations on ground motions and building damage. Seismological Research Letters, 82(1), 42-58.

Bilal, M. and Askan, A. (2014). Relationships between Felt Intensity and Recorded Ground-Motion Parameters for Turkey, Bulletin of the Seismological Society of America, 104 (1), 484–496. (DOI: 10.1785/0120130093)

Boore D.M. (2001). Effect of baseline corrections on displacement and response spectra for several recordings of the 1999 Chi-Chi Taiwan, earthquake, Bull. Seism. Soc. Am., 91, 1199-1211.
Boore D.M. (2005). On pads and filters: Processing strong-motion data. Bull. Seism. Soc. Am., 95, 745-750.
Boore DM (2010). Orientation-independent, non geometric-mean measures of seismic intensity from two horizontal components of motion, Bulletin of the Seismological Society of America, 100, 1830-1835.

Boore D.M. (2012). TSPP---A Collection of FORTAN Programs for Processing and Manipulating Time Series, U.S. Geological Survey Open File Report 2008-1111, V4.3, 09 Oct. 2012, 47pp.

Boore, D.M. and J.J. Bommer (2005). Processing of strong-motion accelerograms: Needs, options and consequences, Soil Dyn. Earthquake Eng., 25, 93–115.

Boore D., Stewart J.P., Skarlatoudis A., Seyhan E., Margaris B., Theodoulidis N., Scordilis E., Kalogeras I., Klimis N., and Melis N. (2021). A Ground-Motion Prediction Model for Shallow Crustal Earthquakes in Greece. Bull. Seism. Soc. Am. (accepted for Publication).

Boore, D. M., Atkinson, G. M. (2008). Ground-motion prediction equations for the average horizontal component of PGA, PGV, and 5%-damped PSA at spectral periods between 0.01s and 10.0s. Earthquake Spectra, 24(1), 99–139, http://dx.doi.org/10.1193/1.2830434.

Boore, D. M., Stewart, J. P., Seyhan, E., Atkinson, G. A. (2014). NGA-West 2 equations for predicting PGA, PGV, and 5%-damped PSA for shallow crustal earthquakes. Earthquake Spectra, 30(3), 1057–1087, http://dx.doi.org/10.1193/070113EQS184M.

Campbell, K. W., Bozorgnia, Y. (2008). NGA ground motion model for the geometric mean horizontal component of PGA, PGV, PGD and 5% damped linear elastic response spectra for periods ranging from 0.01 to 10 s. Earthquake Spectra, 24(1), 139–173, http://dx.doi.org/10.1193/1.2857546.

Campbell, K. W., Bozorgnia, Y. (2014). NGA-West2 ground motion model for the average horizontal components of PGA, PGV, and 5%-damped linear acceleration response spectra. Earthquake Spectra, 30(3), 1087–1117, http://dx.doi.org/10.1193/062913EQS175M.

Chiou, B. S. J., Youngs, R. R. (2008). Chiou-Youngs NGA ground motion relations for the geometric mean horizontal component of peak and spectral ground motion parameters. Earthquake Spectra, 24(1), 173–217, http://dx.doi.org/10.1193/1.2894832.

Chiou, B. S. J., Youngs, R. R. (2014). Update of the Chiou and Youngs NGA model for the average horizontal component of peak ground motion and response spectra. Earthquake Spectra, 30(3), 1117–1155, http://dx.doi.org/10.1193/072813EQS219M.

Douglas, J. (2003). What is a poor quality strong-motion record? Bull Earthquake Eng 1, 141–56.

Gülerce, Z., Kargıoğlu, B., Abrahamson, N. A. (2016). Turkey-adjusted NGA-W1 horizontal ground motion prediction models. Earthquake Spectra, 32(1), 75-100, https://doi.org/10.1193/022714EQS034M.

Kale, Ö. (2019). Some Discussions on Data-Driven Testing of Ground-Motion Prediction Equations under the Turkish Ground-Motion Database. Journal of Earthquake Engineering, 23(1), 160-181, https://doi.org/10.1080/13632469.2017.1323047.

Kale O, Akkar S, Ansari A and Hamzehloo H (2015). “A ground-motion predictive model for Iran and Turkey for horizontal PGA, PGV, and 5% damped response spectrum: Investigation of possible regional effects,” Bulletin of the Seismological Society of America, 105(2A), 963-980.

Margaris B., Scordilis E, Stewart J.P., Boore D.M., Theodoulidis N., Kalogeras I., Melis N., Skarlatoudis A., Klimis N., and Seyhan E. (2020). Hellenic Strong-motion Database with Uniformly Assigned Source and Site Metadata for the Time-Period 1972-2015. Seism. Res. Lett. (submitted for publication).

Paolucci R., Pacor F., Puglia R., Ameri G., Cauzzi C., Massa M. (2011) Record Processing in ITACA, the New Italian Strong-Motion Database. In: Akkar S., Gülkan P., van Eck T. (eds) Earthquake Data in Engineering Seismology. Geotechnical, Geological, and Earthquake Engineering, vol 14. Springer, Dordrecht. http://doi-org-443.webvpn.fjmu.edu.cn/10.1007/978-94-007-0152-6_8.

4. Site Effects

Chapter Coordinators: Kemal Onder Cetin, Achilleas Papadimitriou, George Mylonakis and Katerina Ziotopoulou

Authors:

Middle East Technical University: Kemal Onder Cetin, Aysegul Askan Gundogan, Makbule Ilgaç, Gizem Can, Elife Çakır, Berkan Söylemez, Ahmed Al-Suhaily, Alaa Elsaid, Moutasem Zarzour

University of Bristol: George Mylonakis

Ege University: Selim Altun, Alper Sezer

University of California Davis: Katerina Ziotopoulou

Hacettepe University: Berna Unutmaz

University of Patras: Panagiotis Pelekis

Dokuz Eylül University: Mustafa Akgun, Cem Kıncal

Institute of Engineering Seismology and Earthquake Engineering, Greece: Emmanouil Rovithis

National Technical University of Athens: Achilleas G. Papadimitriou, Prodromos Psarropoulos

Democritus University of Thrace: Nikos Klimis

4.1 Introduction

This chapter presents the findings regarding the site effects on recorded strong ground motion intensities and duration, along with the resulting induced-structural damage. These issues will be separately discussed for Izmir Bay and Samos Island, respectively.

4.2 Izmir Bay

The city of İzmir is located around the inner İzmir Bay (Fig. 4.1). Northern, eastern and southern coasts of Inner İzmir Bay is the most densely populated areas of the city of Izmir. All these coastal areas are situated over deep alluvial sediments.

Figure 4.1. Eastern part of Izmir Bay showing densely populated and highly-affected districts and the location of strong ground motion stations

Although located at about 65-70 km to the N-NE of the earthquake epicenter, the city of Izmir was rather heavily affected by the earthquake (M_w = 7.0), which occurred in the eastern Aegean Sea on October 30 2020, with hundreds of buildings either collapsed or heavily damaged and 118 lives lost (116 in Turkey and 2 in Samos Island). Figure 4.2 shows the location of these moderate to heavily damaged buildings, mostly concentrated in Bayraklı district.

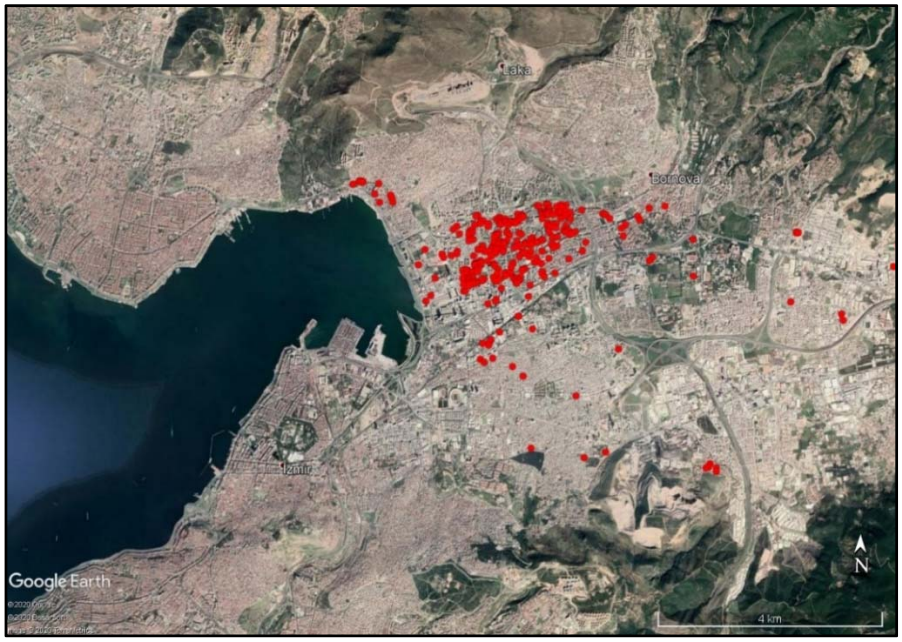

Figure 4.2. The scatter of moderate to heavily damaged structures in the east of Izmir Bay (Bayrakli)

Additionally, as will be discussed later in this chapter, strong ground motion records on soil sites from Izmir Bay, had significantly larger intensities (0.05 g < PGA_{soil} < 0.15 g) as compared with those of rock sites (0.03 g <PGA_{rock} < 0.06 g), clearly revealing these unique site amplifications, reaching to a factor of 2-4 from peak ground acceleration point of view. Significant differences in the frequency content, as well as in the duration of the records are also observed. The differences are mostly attributed to the variability in geological, morphological and geotechnical setting of the regions, which will be briefly discussed next.

4.3 Geological, Morphological and Geotechnical Settings of Izmir Bay

Yunt Mountain volcanic rocks are widespread in and around the northern part of Izmir Bay. The Upper Miocene volcanic rocks, which lie on top of the Neogene aged sedimentary rocks were formed by several volcanic activities in this region. The majority of Karsiyaka and Cigli districts is located on a typical alluvial delta in front of the Yamanlar Mountain blocks. The old Gediz River Delta, which is in the north-western part of Karsiyaka and Bostanlı districts, was formed by sedimentation of alluvial deposits transported by the Gediz River in the Quaternary Era.

As shown in Figure 4.3, Bayrakli, the most affected district from the earthquake, is located on a very deep alluvial basin, which is bordered to the north and south by hills. While most of the district is founded on quaternary alluvial sediments of the basin, the outskirts of which extend over the rising slopes of the rock outcrop to the north and south. The bedrock of north side descends tending south, and reaches a depth of about 1000 m beneath the alluvium underlying the Bayraklı district. The composition and characteristics of alluvium are spatially variable in horizontal and vertical directions. The detailed geological and geophysical investigations conducted in the Bayraklı district revealed the underground soil and rock characteristics in the alluvial basin as illustrated in Figures 4.3 and 4.4.

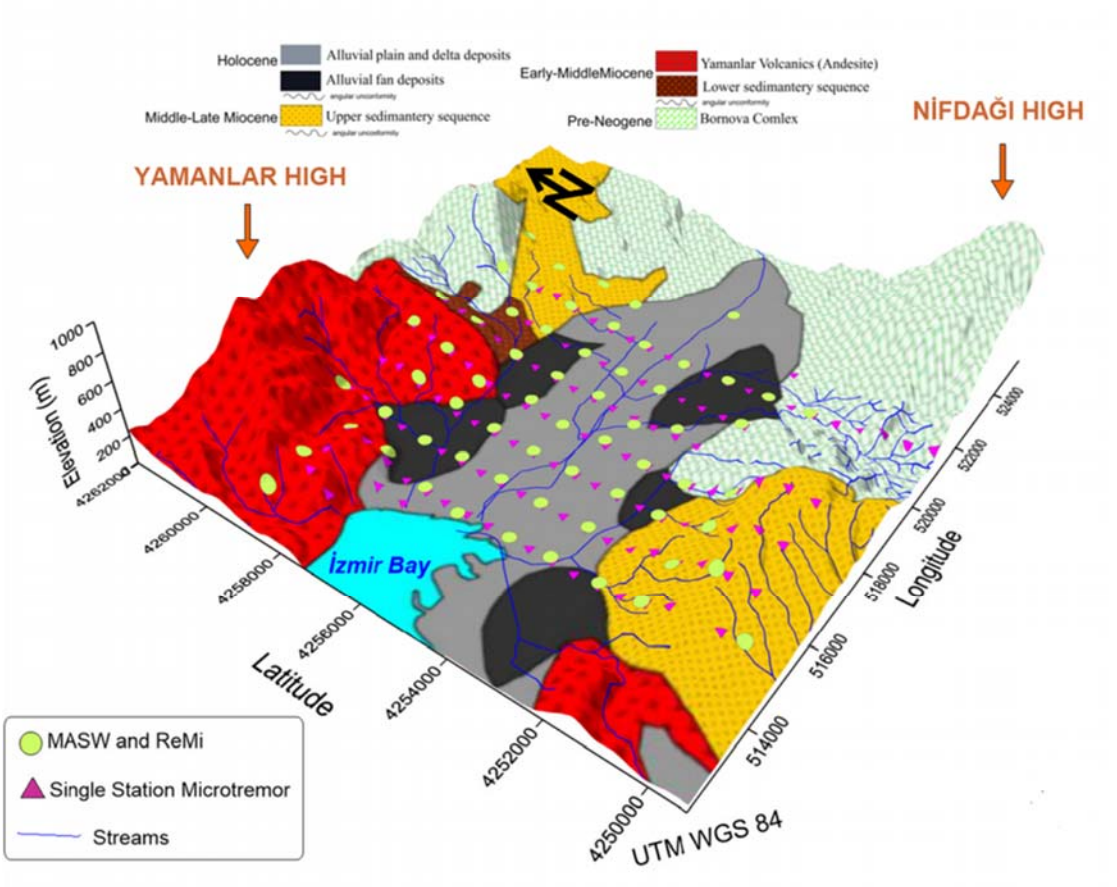

Figure 4.3. Geological map of the study area indicating the location of geophysical studies performed in Bayrakli and Bornova districts (Pamuk et al. 2019)

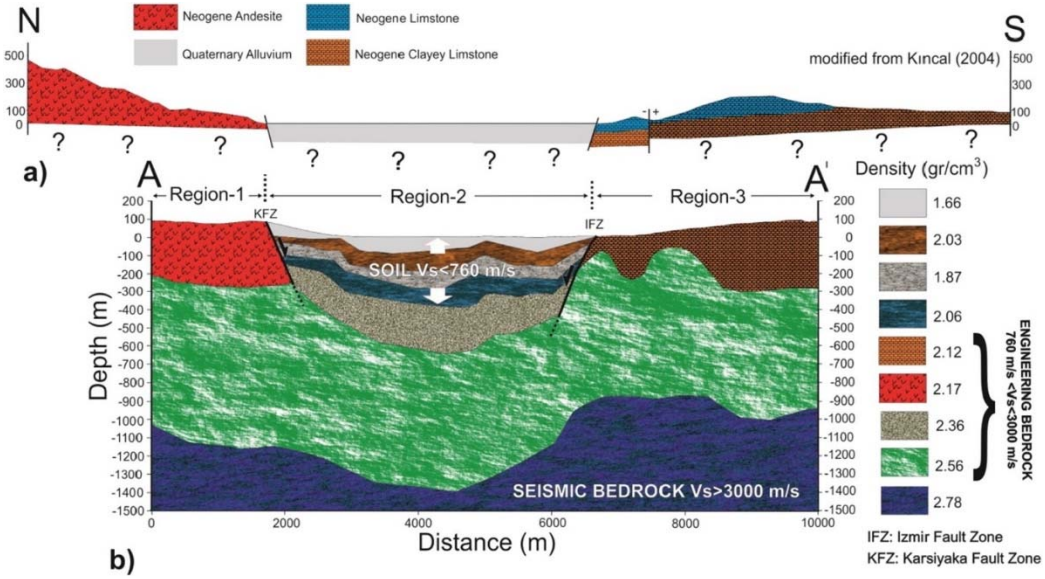

Figure 4.4. Geological cross-section of the Inner Izmir Bay developed based on geophysical measurements (Pamuk et al. 2017)

The basins of Bayraklı and Bornova districts are bordered to the north and south by active E-W extending normal faults as shown with red lines in Figure 4.1. The young (Holocene) alluvium, several river delta and shallow marine deposits, are confined by İzmir Fault in the south and by Karsiyaka-Bornova fault in the north. As illustrated in Figure 4.4., it constitutes the uppermost soft sediments in the basin reaching to 300 m depth by the inner bay. The groundwater level is located at a maximum of 5 m depth by the shoreline. The very soft sediments and basin edge geometry and structure itself played a significant role in amplifying the ground shaking.

For the purpose of illustrating the differences in local soil site conditions, Figure 4.5 is prepared, which presents typical borelogs, compiled for selected residential districts. Deep alluvial soil layers underlie residential structures at Bayrakli, Bornova, Mavisehir and Karşıyaka Districts. These, very deep (>200 m) soft, mostly low plasticity clayey soil profiles with interbedded silt, sand and gravel are judged to be the governing factor behind these pronounced site effects.

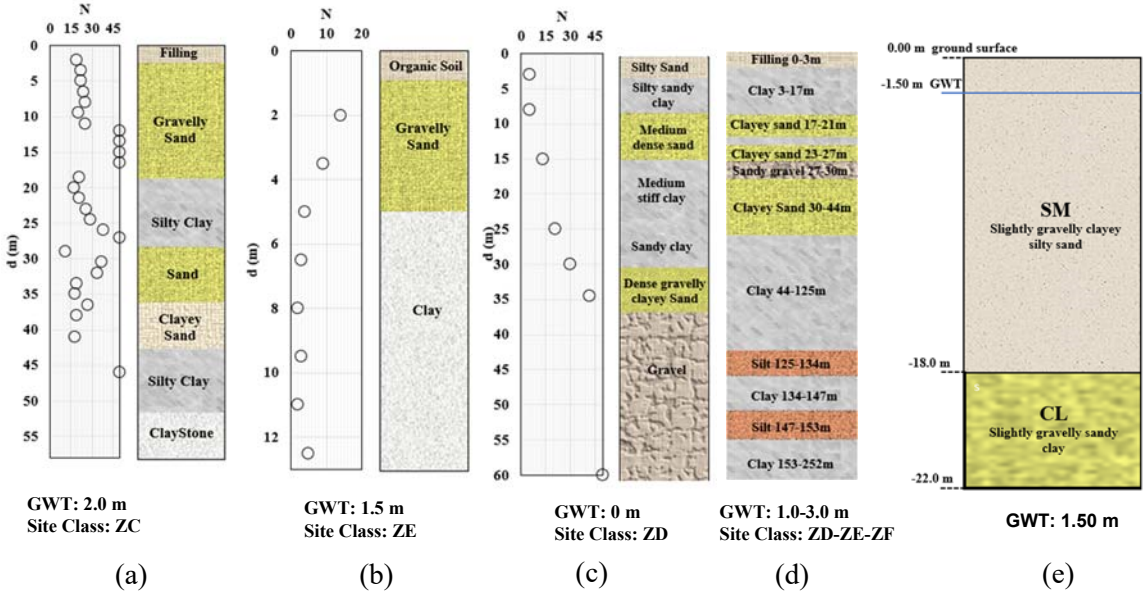

Figure 4.5. Typical borelogs from selected residential districts a) Gumuldur (DTA Proje, Personnel communication 2020), b) Sigacik-Seferihisar (Akbug 2019), c) Mavisehir (Kubilay 2012) and d) Bayrakli (Pamuk et al. 2018a), e) Karşıyaka Semikler (Ecemiş 2020)

4.4 Comparative Assessment of Available Rock and Soil Motions Recorded in Izmir Bay

For the purpose of quantitatively assessing the effects of site conditions on strong ground motion characteristics, the response spectra are given in Figures 4.6 and 4.7, respectively separately for soil and rock sites. Same scale was used in both figures to enable visual comparison between soil and rock spectra. On the same figures, mean and ±1 standard deviation of recorded ground motions' response spectra values are also shown, which are estimated simply by taking the average of soil or rock spectra. As clearly revealed by these figures, peak ground accelerations at Izmir Bay soil sites, vary in the range of 0.05 g to 0.15 g, as compared to those of rock varying in the range of 0.03 g to 0.06 g. This simple comparison revealed that peak ground acceleration

intensities are amplified by a factor of 2 to 4. Similarly, and more importantly, spectral acceleration values at 0.5 to 1.5 second period range reaches 0.4-0.5 g levels at soil sites, as compared to 0.1 to 0.2 g levels at rock sites. When these 5 to 6 times amplified spectral acceleration values at 0.5 to 1.5 second period range, are jointly considered with the seismic response of 7-9 story reinforced concrete buildings of Izmir Bay (more specifically Bayrakli) with natural period of 0.6 to 1 second, the resonance of the soil-structure system is inevitable. The concentrated damage on 7 to 9 story buildings located in Bayraklı region is attributed to these site effect-induced amplifications and resonance along with other structural engineering factors, which will be discussed in Chapter 7.

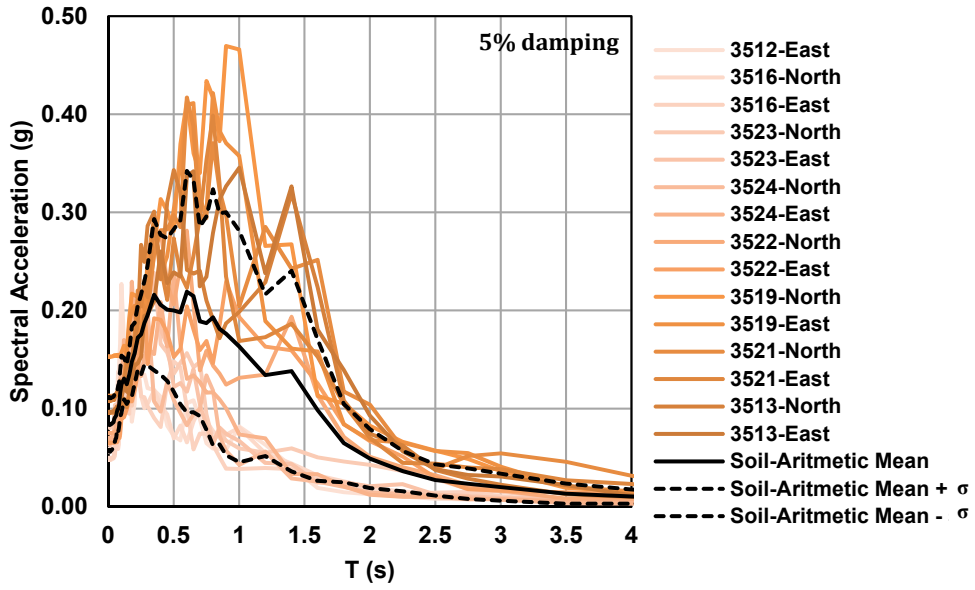

(a)

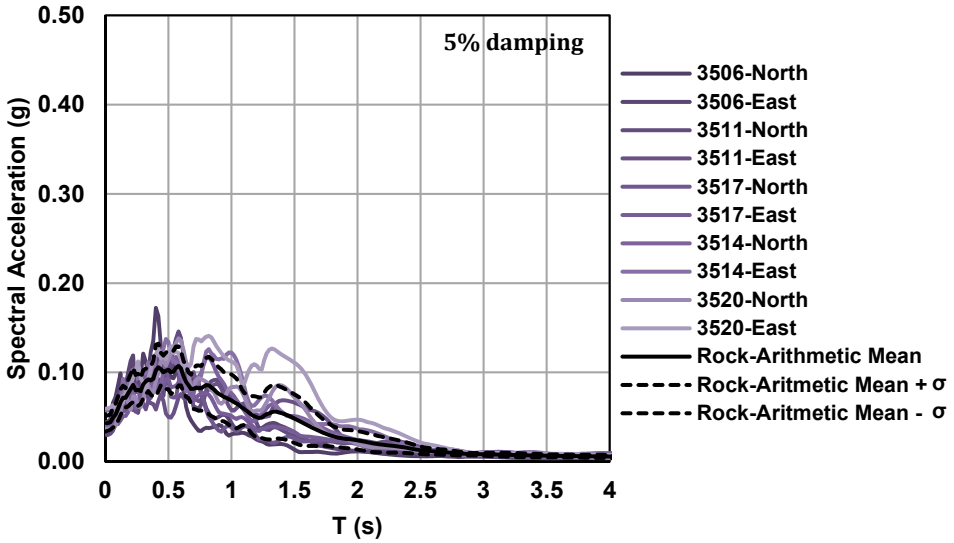

(b)

Figure 4.6. Elastic response spectra of strong ground motions on a) soil and b) rock sites in Izmir Bay

With the intend of assessing if the amplified seismic demand levels exceed design basis earthquake intensities, they are comparatively presented in Figure 4.7, with those of 475 year- and 72- year return period events, as suggested by recent Turkish Earthquake Design Code (2018). It is concluded that despite unusual amplifications, the seismic demand was observed to be lower than that of design basis level (i.e.: 475-year return period event) and comparable with a 72-year return period event.

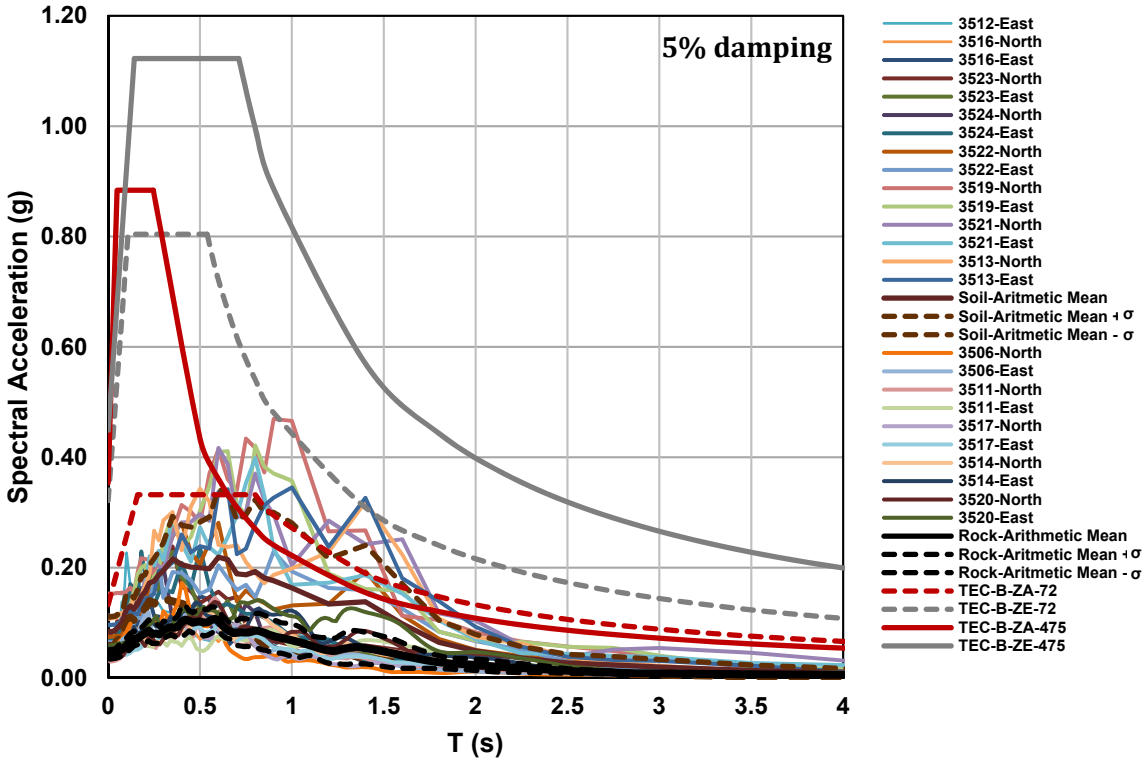

Figure 4.7. Comparisons of recorded strong ground motion stations with design basis (475 year-return period) and 72-year return period response spectra.

For the purpose of better understanding the site effect-induced amplifications, soil spectral acceleration values were normalized with those of nearest rock sites. Estimated amplification response spectra were plotted as given in Figure 4.8. This figure clearly illustrates unusually large amplifications reaching to a maximum of 14 to 16 in the east-west direction at Bayraklı station. Again, elevated amplifications at the period range of 0.5 to 1.5 seconds are observed. The top three soil sites, where amplifications were observed to be the most pronounced (also the locations where site effects are predominant) are listed as Konak, Karsiyaka, Bayrakli, consistent with the geological, morphological and geotechnical setting discussed earlier. Among them, Konak station was speculated as not being a free field due to the presence of an underground

parking lot in the immediate vicinity of the station. Hence, its use and interpretation require further careful advance assessments.

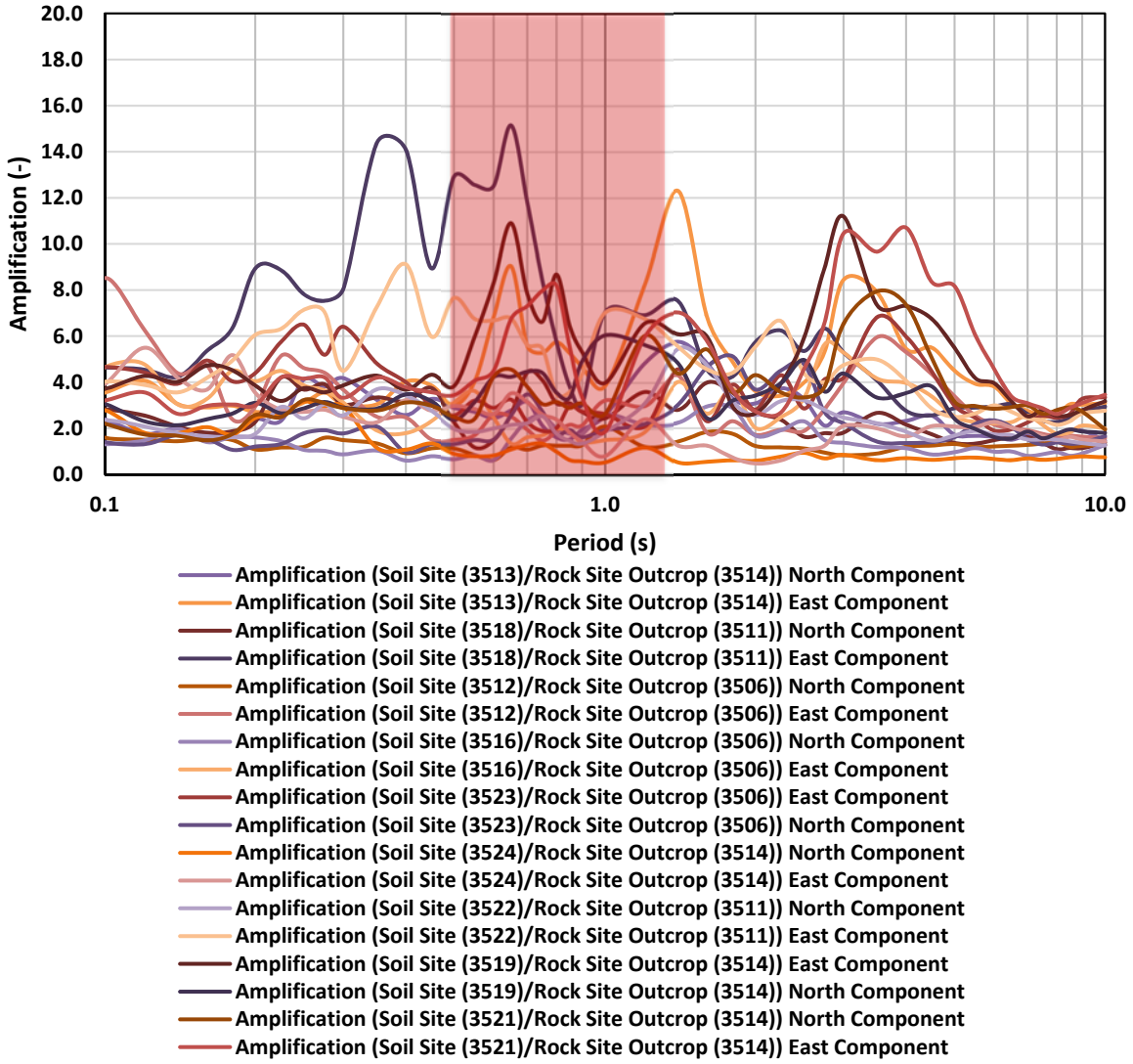

Figure 4.8. The amplification spectra, estimated by normalizing the spectral soil accelerations with those of the nearest rock sites.

4.5 Preliminary Site Response Assessments for Bayrakli Station

With the intend of better understanding site effects, preliminary 1-D total stress-based equivalent linear site response assessments were performed for Bayraklı station 3513. As shown in Figure 4.9, nearby rock motions were de-convolved to 1500 m depth, where the seismic bedrock was reported to be located (Pamuk et al. 2018b). The representative site profile is tailored by jointly assessing available shallow and deep borelogs along with available deep Vs profiles. More specifically, the soil profile in Bayrakli consists of deep alluvial deposits of

alternating thin gravel, silty sand, silty clay, and clay layers, with field (raw) SPT-N values less than 30 blows/30 cm in the upper 200 m. The groundwater table in Bayrakli is located at 1-3 m depth. As stated earlier, the depth to the engineering bedrock (V_S>3000 m/s) layer is documented to vary in the range of 1100 m to 1200 m (Pamuk et al. 2018 b), and may reach up to 1500 m. Modulus degradation and damping relationships of Seed and Idriss (1970), Vucetic and Dobry (1991), Rollins et al. (2020), Schnabel (1973) were used as part of preliminary site response analyses to assess the individual response of sand, low plasticity clay, gravel and rock layers, respectively. Site-response estimated outcrop response spectra were comparatively shown with the one of the recorded in the upper left corner of Figure 9. Relatively reasonable match with the recorded motion validated the developed preliminary 1-D model. The amplification response spectra are also shown in Figure 10, revealing again unusually large amplifications at the period range of 0.5 to 1.5 seconds.

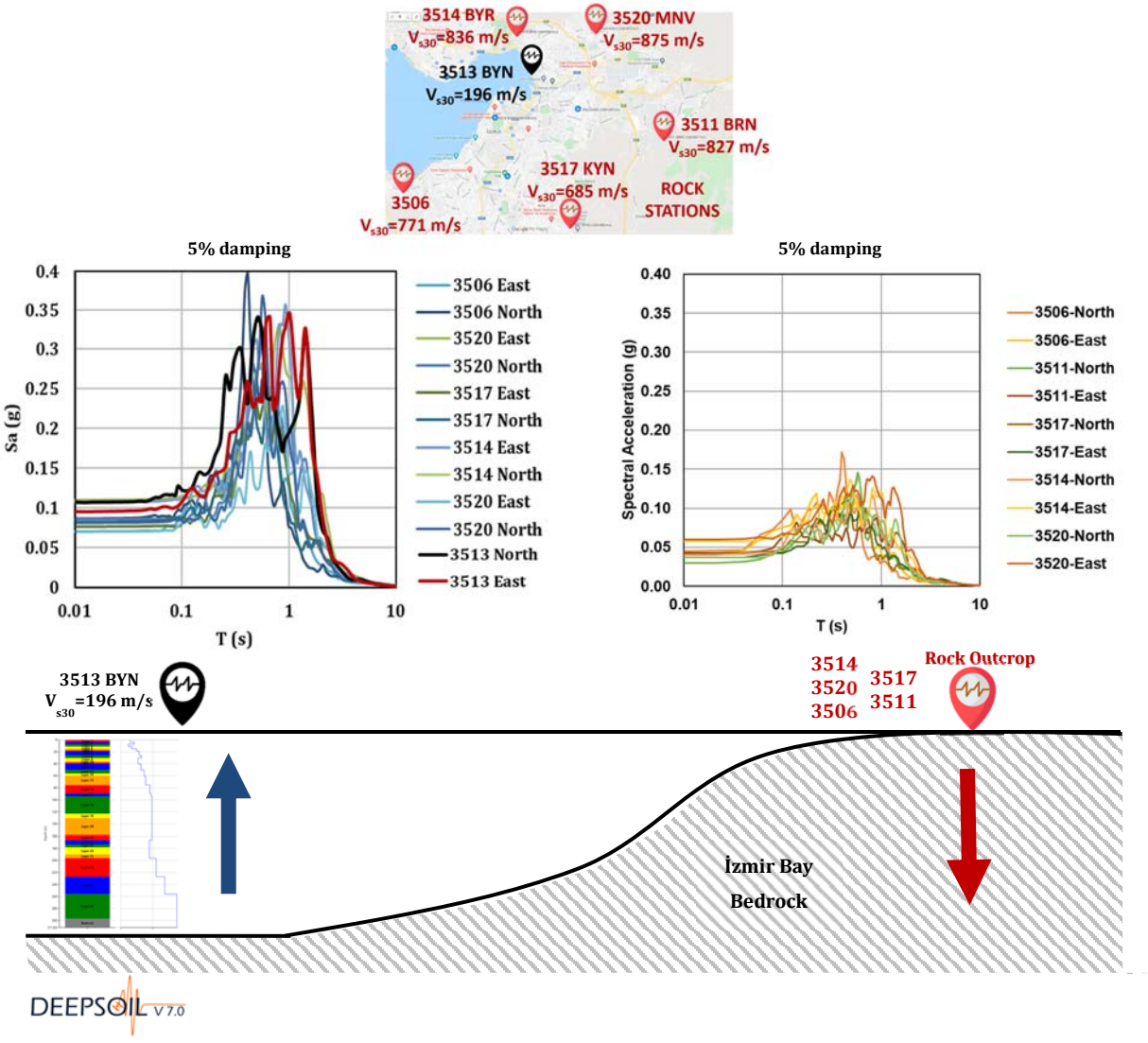

Figure 4.9. Preliminary 1-D site response model and analysis results for Bayrakli Station 3513

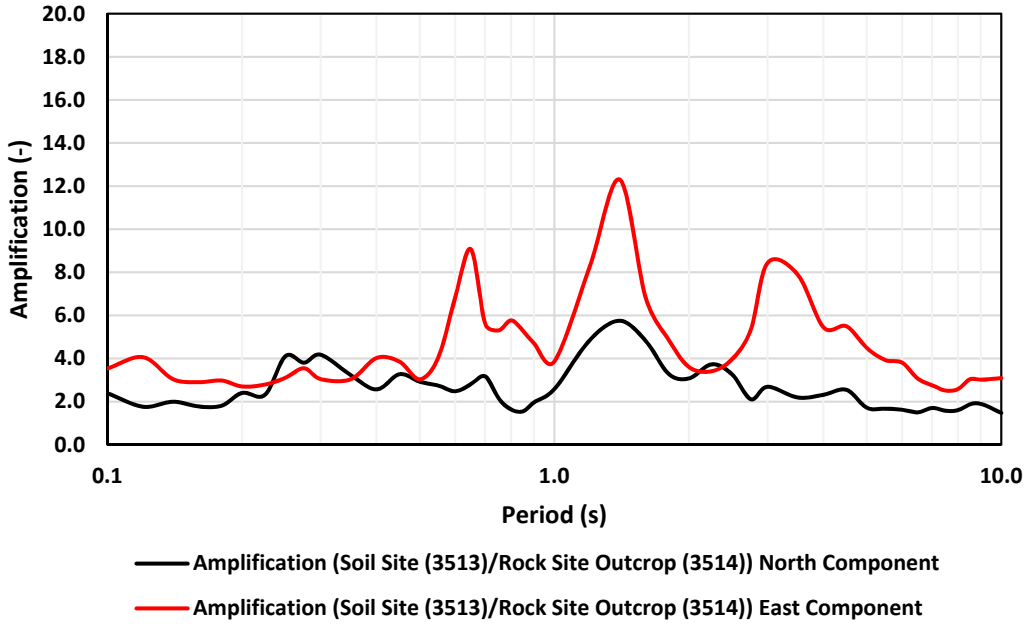

Figure 4.10. Amplification spectra estimated by 1-D Site Response Analyses for Bayrakli Station

4.6 Comparisons with Code-based Amplification Factors

The amplification spectra are given in Figure 4.10 is also compared with the amplification factors presented in Turkish Earthquake Design Code (2018), as shown in Figure 4.11. It should be noted that TEDC (2018) suggests similar intensity-dependent amplification factors with those of NEHRP (2015) and Eurocode 8. It is clearly seen that due to unique soil and site conditions in Izmir Bay, amplifications in the excess of code based recommended values, are observed. This observation clearly addresses the need for region specific seismic zonation for Izmir Bay, and more specifically, for Bayraklı and Karsiyaka districts. It should be noted that occasionally, such region-specific assessments may be needed to overcome the limitations of overly generalized earthquake design codes. A vivid example of such a region, where site effects are similarly and unusually pronounced, is Mexico City, which is founded on very deep, soft, high plasticity clays of lake deposit origin.

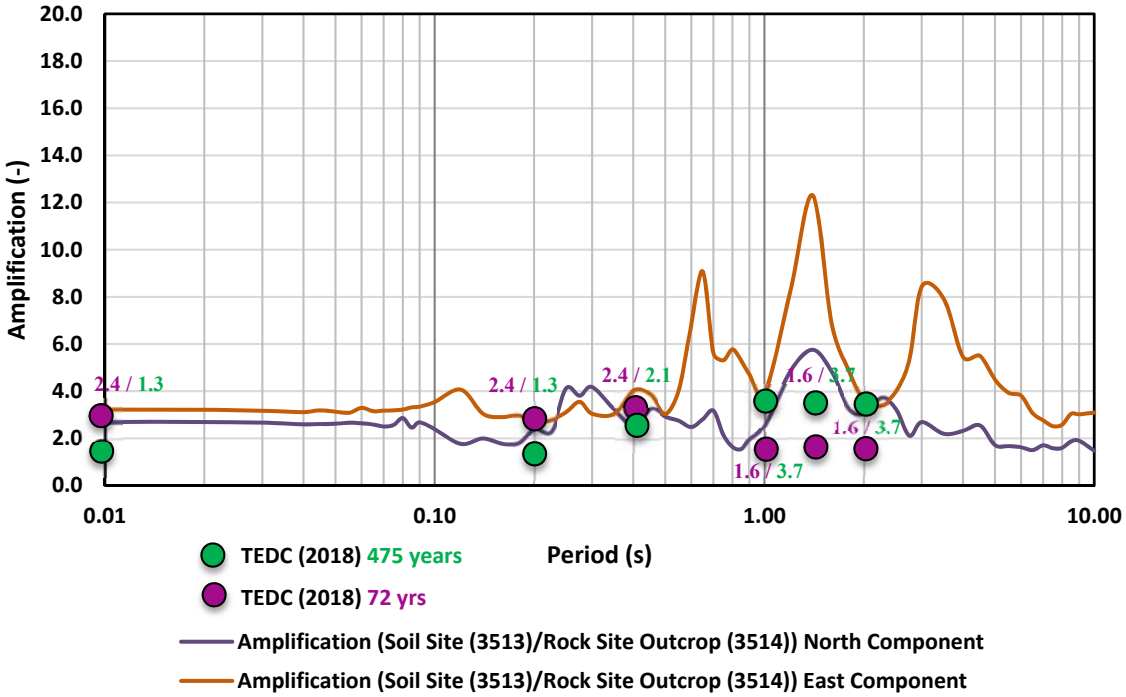

Figure 11. The amplification spectra for Bayrakli as compared with the amplification factors recommended by TEDC (2018)

4.7 The Effects on Observed Structural Damage in Bayrakli

As discussed earlier, deep to very deep soil sites of Izmir Bay, and more specifically of Bayrakli and Karsiyaka with natural periods varying in the range of 0.5 to 5 seconds, amplified the spectral accelerations at the period range of 0.5 to 1.5 seconds. The amplification ratios as high as 14 to 16 were observed at these periods. However, these soil site specific amplifications were not the only reason behind concentrated structural damage in these deep alluvial soil sites. When response spectra of rock motions of Izmir Bay are compared with ground motion prediction equations, one of which is illustrated in Figure 4.12, it is clearly seen that relatively long period (0.5-1.5 sec) high energy is also present in rock motions.

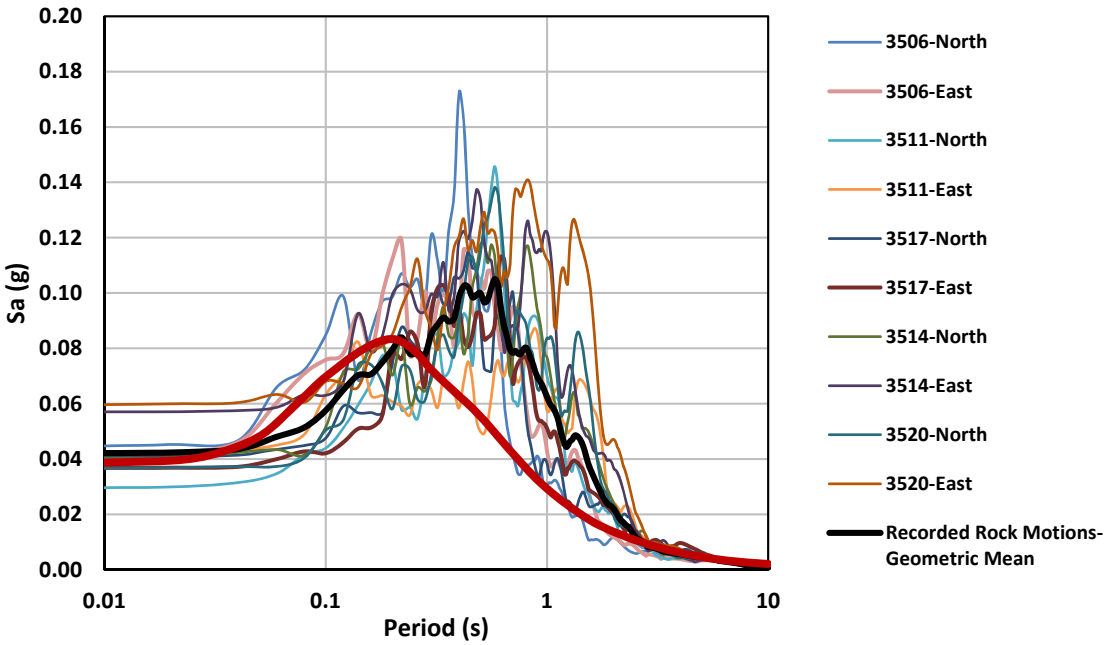

Figure 4.12. The comparison of rock motion response spectra with the predictions of Abrahamson et al. (2014)

Moreover, it should be noted that this relatively long period energy is also present in the records closer to the fault rupture, as shown in Figures 13 (a) through (c). Hence this relatively long period energy cannot be attributed to path effects but to the source mechanism, which is thought to produce an anomalously rich spectral energy in the period range of 0.5 to 1.5 s.

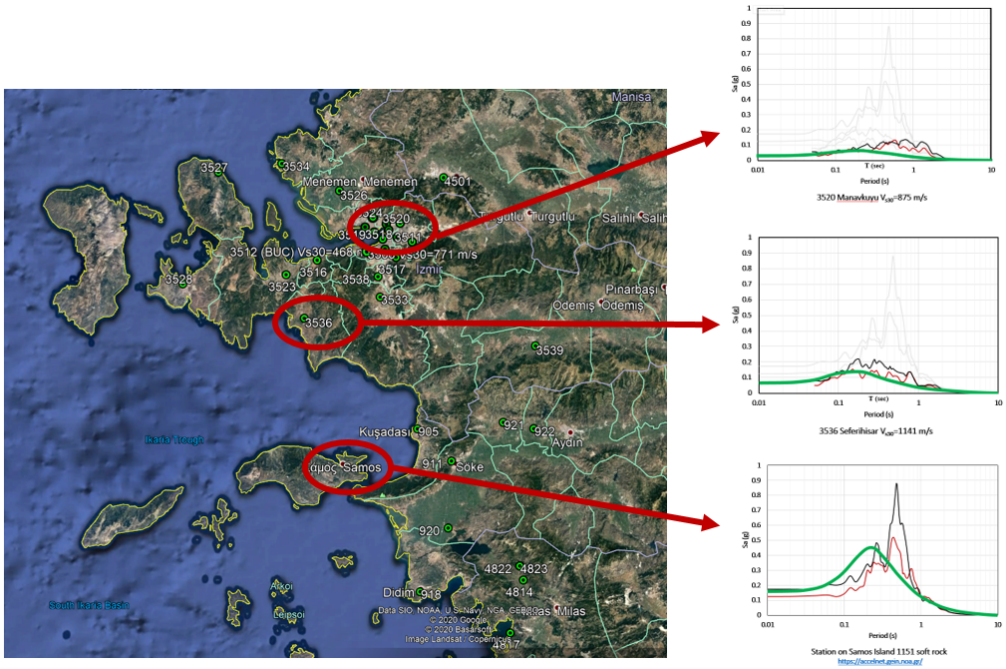

Figure 4.13. The rock motion response spectra of rock stations closer to fault rupture as compared with the predictions of Abrahamson and Silva (2014)

Hence, as the concluding remark, the bedrock excitation with anomalously rich spectral energy (due to most likely source effects) at the period range of 0.5 to 1.5 seconds, is further amplified by the resonating responses of long period, soft, deep soil sites. These already amplified soil outcrop motions were then resonated again by 7-9 story residential structures of Bayrakli district, leading to a double resonating system, which in turn produce unusually amplified seismic demands. Moreover, soil site effects are also observed to extend the duration of significant shaking. Figure 4.14 presents two strong ground motion records obtained at a rock and a soil site, which were drawn on the same plot to enable visual inspection of durational effects.

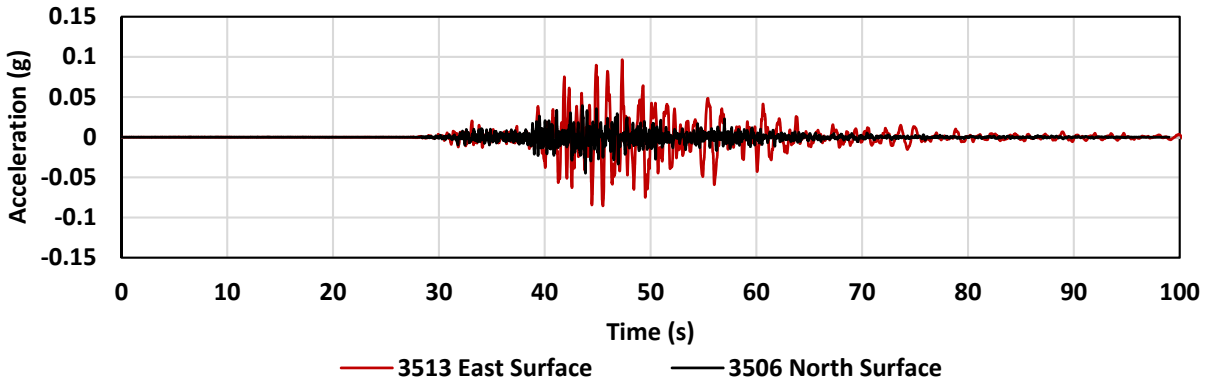

Figure 4.14. Two accelerograms obtained at a soil (Bayraklı 3513) and a rock site (Guzelyali 3506) drawn on top of each other to illustrate durational differences

However, even these unusually amplified and prolonged seismic demand, was below the design basis response spectra. The recent event is not classified as a design basis event, but more of a 72 year return period event, and is not expected to cause structural damage, not to mention hundreds of collapsed or heavily damaged buildings, one of which is shown in Figure 4.15. There, poor structural design and detailing, along with construction practices come into the picture, which are discussed thoroughly in Chapter 7.

Figure 4.15. Doganlar residential building, fully collapsed after the event (courtesy of Ali Aksoyer)

4.8 Samos Island

The island of Samos is situated in the meizoseismal area, right south of the rupture zone, at the footwall of the normal fault. Only the northern part of the island was significantly affected from the earthquake. Except for some coastal areas, the island is covered by stiff soil formations and outcropping rock.

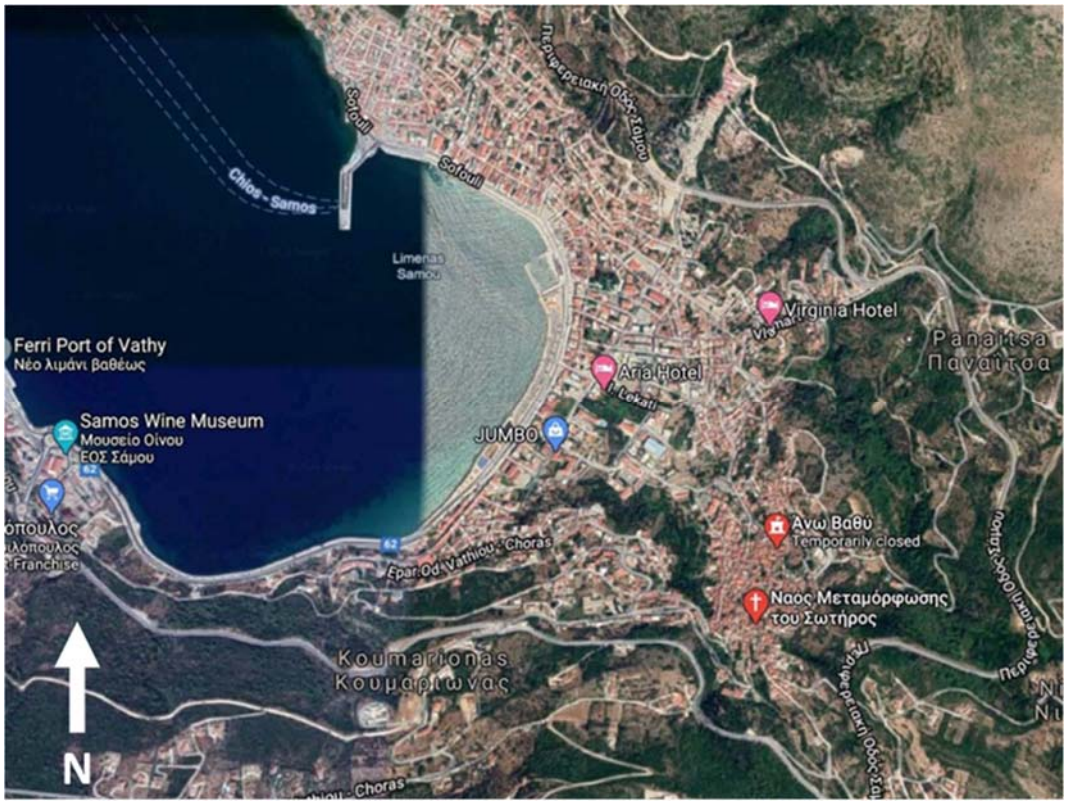

Figure 4.16. Town of Vathy, at the northeastern side of Samos island

Although located only about 10 km from the ruptured area (22 km away from the epicenter), in the near fault zone, the seaside town of Vathy (Figure 4.16, from Google Earth) at the northeastern part of the island was rather lightly affected by the earthquake. Despite the tragic death of 2 high school students in Vathy, the collapsed or heavily damaged buildings were relatively few considering the magnitude of the event and the proximity to the source. Figure 4.17 shows the area of concentrated damage in the Ano Vathy district.

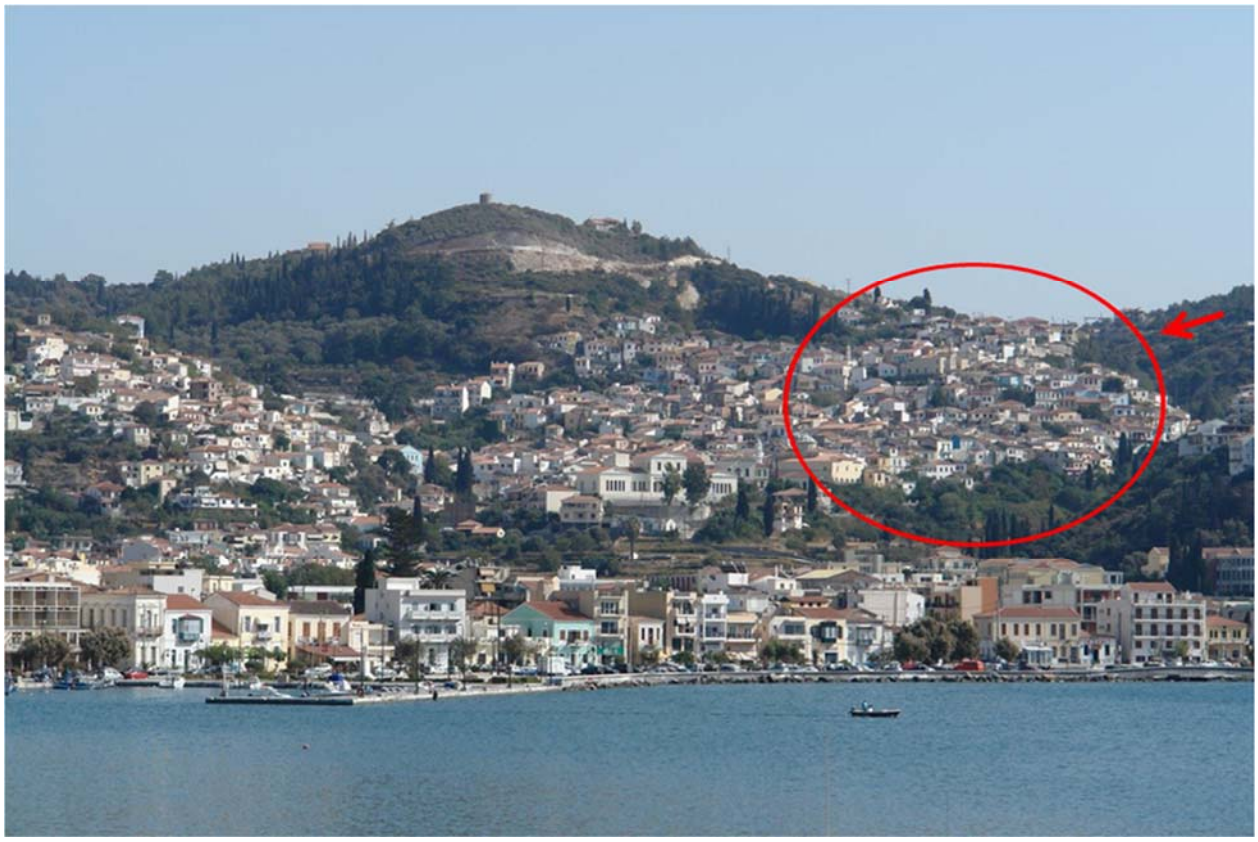

Figure 4.17. Ano Vathy hill (at the southeastern side of Vathy) highlighting the area of potential topographic and valley effects (Photo by Christos Giarlelis, HAEE Team).

As discussed in Chapter 3, strong ground motion recordings on stiff sites in the town of Vathy had relatively modest PGA and PGV values, of about 0.23 g and 22 cm/s respectively, with predominant periods of 0.4 – 0.6 s and significant durations between 10-15 s. The geology of the region together with some site (i.e., topographic and valley) effects will be briefly discussed in the following.

4.9 Geological and Geotechnical Setting of Samos Island

With reference to the pre-Neogene metamorphic setting, the geological succession on Samos island consists mainly of four distinct units, as shown in the simplified geological map published by Roche et al. 2019 (Figure 4.18). These refer to: (i) the Kerketeas marbles in the western part of the island, (ii) the Ampelos unit, which outcrops over the central part of the island, (iii) the Selçuk nappe, which crops out in the center area of the island as well, and (iv) the Vourliotes nappe which crops out in the eastern part of Samos. More recent Neogene deposits form the Karlovasi and the Mytilini basins, where the dominant geological formations are lacustrine, travertine-like or marly, medium-to-thick limestones and hard marls, with intercalations of clays, sandy marls, breccia with components from the Neogene sediments and conglomerates. Recent

Quaternary deposits are mainly present in the Northern-Western and the Southern-Eastern part of the Island, close to Karlovasi and Pythagorio, respectively. Part of the Samos Capital city (Vathy) is also founded in such alluvial sediments, which are composed of clayey-sandy materials, sands and gravels. The detailed geological map of Samos Island published by the Hellenic Survey of Geology and Mineral Exploration (HSGME) is shown in Figure 4.19.

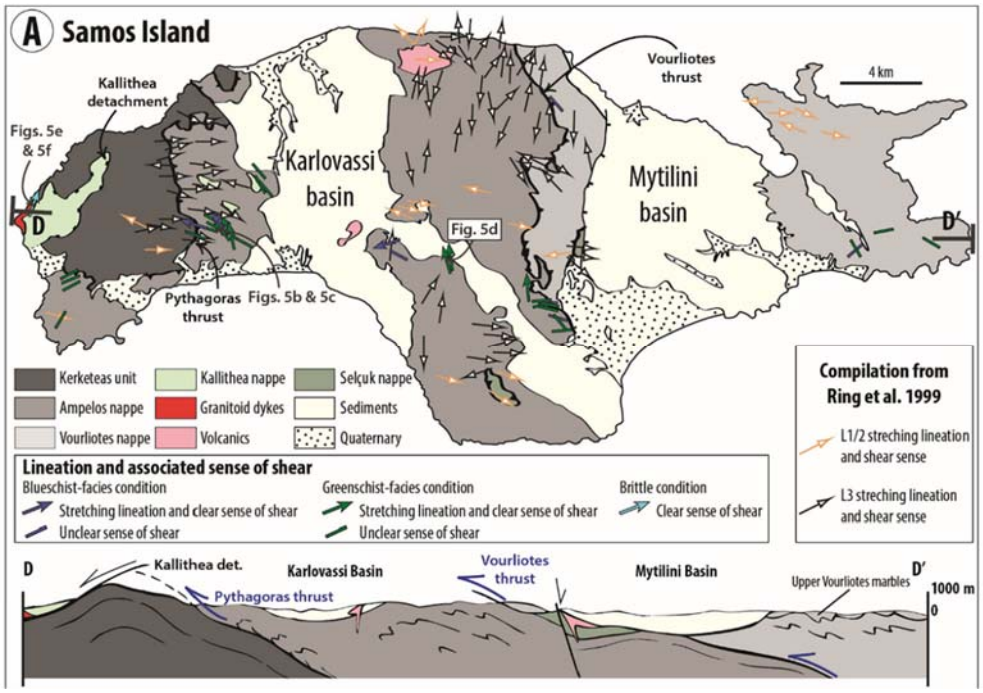

Figure 4.18. Simplified geological map of Samos Island, indicating the dominant geological units (Roche et al. 2019).

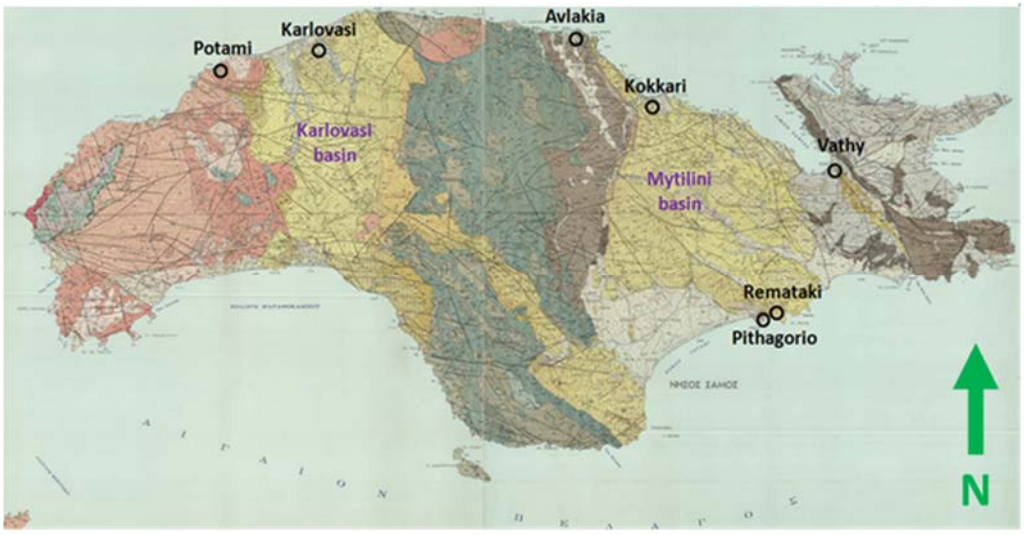

Figure 4.19. Detailed geological map of Samos Island, published by the Hellenic Survey of Geology and Mineral Exploration (HSGME 1979).

Selected sites of the island of Samos are also marked onto the geological map in Figure 4.19. A short description of the main geological formations in these areas is provided below given their relevance to the observed damage:

- **Vathy (capital of Samos):** Mainly Quaternary plain deposits of clayey-sandy material, loam, sand and gravels. Such types of recent sediments are also met at the west of Pithagorio on the southern shore and at the north of the Karlovasi basin.
- **Along the Vathy – Karlovasi provincial road:** Mainly marly and travertine-like lacustrine limestones with intercalations of low-cohesion marls.
- **Potami (west of Karlovasi):** Dolomitic thin to medium-bedded marbles of Kerketeas unit and schist overlaying Kerketeas marbles.
- **Rematakι:** Lacustrine, medium-to-thick bedded, travertine-like limestones and thin-bedded marls. The above geological formations dominate the broader area of Pythagorio.
- **Avlakia:** Vourliotes marbles with intercalations of schist and they are met mainly in the eastern side mountainous block of the central island.

Table 4.1 and Figure 4.20 summarize a first collection of geotechnical data with reference to the town of Vathy (the capital of Samos).

Table 4.1. Summary for geotechnical boreholes available in the area of Vathy, location and source.

BH Notation	Site Description	Location		Type	Depth (m)	Source
		LAT.	LONG.			
BH1	Old Port of Vathy	37.757144°	26.970566°	BH	23.2	Milionis G. Geologist
BH2	Municipal Cultural Center “Epikourio”	37.753649°	26.979372°	BH	15	Milionis G. Geologist
BH3	Municipal Nursing Home (Vathy)	37.753731°	26.978154°	BH	15	Milionis G. Geologist
BH4	New Port of Vathy	37.751489°	26.960249°	BH	20	Milionis G. Geologist
BH5	New Port of Vathy	37.754001°	26.957913°	BH	21	Ministry for the Environment, Physical Planning and Public Works of Greece

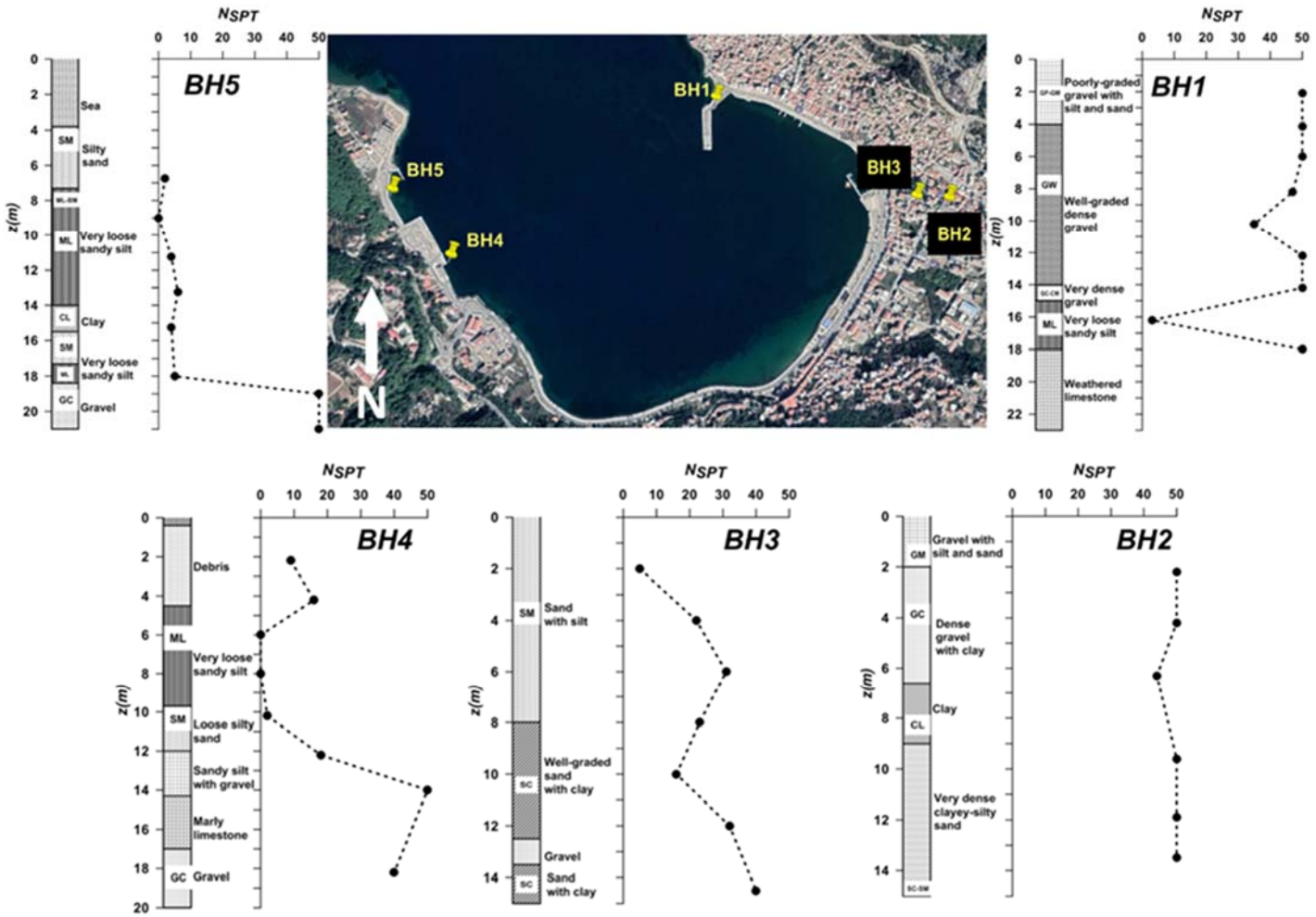

Figure 4.20. Selected borehole locations and geotechnical information in the area of Vathy.

4.10 Basin/Topography Effects in Ano Vathy

The reconnaissance efforts in the greater area of Vathy depicted a concentration of damage in the low-rise buildings of Ano Vathy, an area of about 0.1 km^2 resting in the southeastern side of Vathy (at a distance of 600 to 1000 m from the coastline), at an elevated location (altitude ranging from 50 to 120 m). The building stock includes several structures dating from the 19th (possibly even the 18th) century, built at a high elevation to protect the inhabitants from pirates. Examples of the observed damage are depicted in Figure 4.21 and Figure 4.22.

Figure 4.21. Ano Vathy hill: Red circles denote damaged buildings. (Photo by Christos Giarlelis, HAEE/ETAM Team).

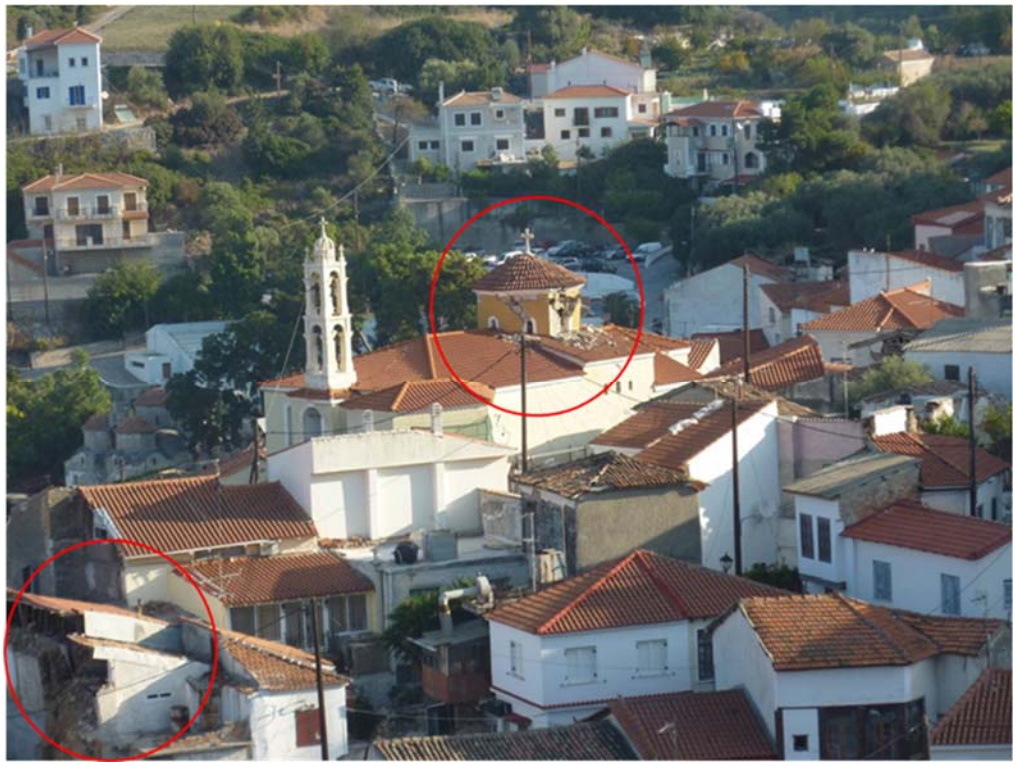

Figure 4.22. Ano Vathy: Close view of the damaged dome of the Church of Metamorphosi Sotiros and neighboring building. (Photo by Christos Giarlelis, HAEE/ETAM Team).

Figure 4.23 shows a (scaled) Google Earth image of the greater Vathy area, where the area of Ano Vathy is depicted by purple shading. This figure also includes two (2) cross sections: the red section having a NW-SE orientation and the yellow section with a SW-NE direction, which will be used to depict the topography of the area in the sequel. It also shows with red pins the two recording locations of the main shock (ITSAK and NOA, with the former being the one closest to the sea front).

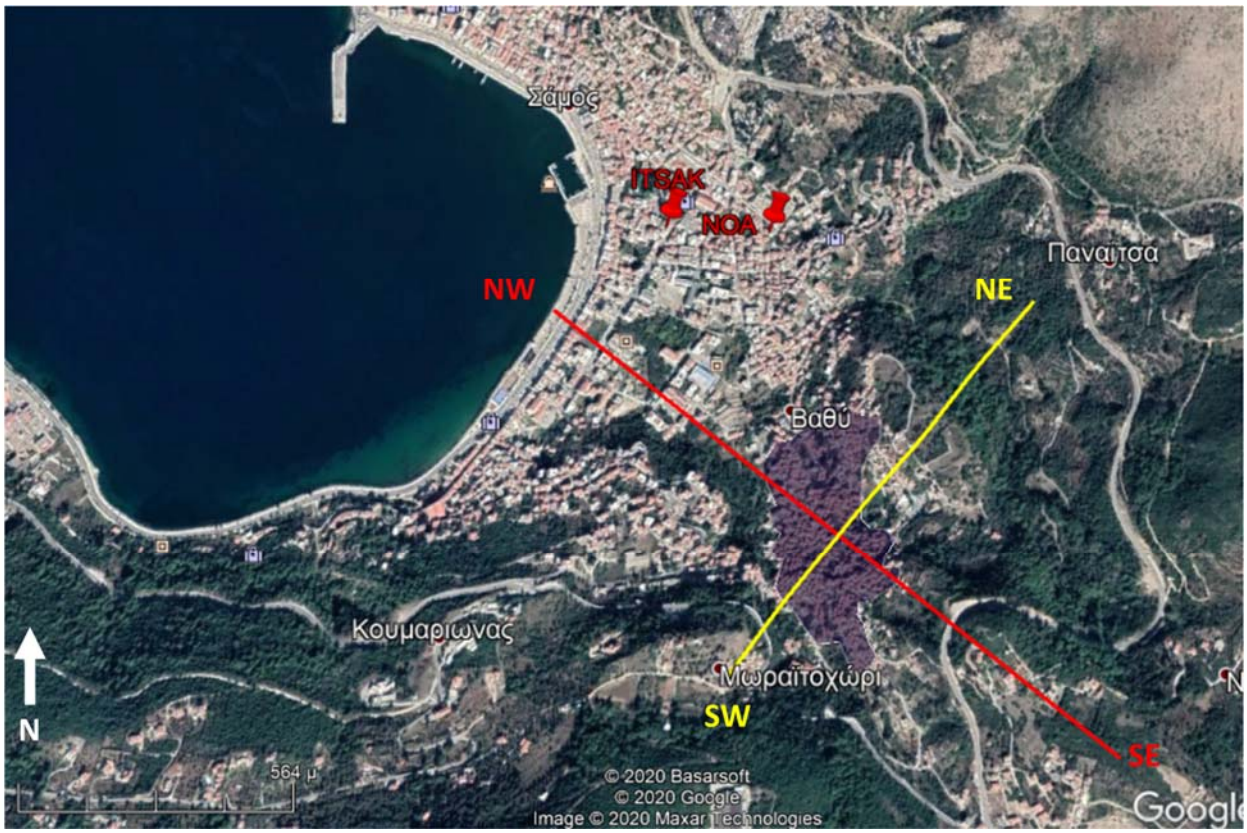

Figure 4.23. Location of Ano Vathy (highlighted purple) at the southeastern side of the seaside town of Vathy and depiction of two cross sections and two recording locations of main shock (ITSAK and NOA)

The map of Figure 4.24 depicts the geology of the area, with reference to the two aforementioned cross sections. This figure shows that the sea front flat area of Vathy is built on alluvial deposits, namely plain deposits of clayey-sandy material, loam, sand pebbles, gravels. However, Ano Vathy (the area around the crossing point of the two sections; see Figure 4.23) is built mostly on the northern-western end of medium-to-thick bedded travertine-like limestones (of probable Miocene age), with intercalations of marls and loose, fine materials, of maximum depth of 80 m. This geological unit lies over the bedrock of the greater area, i.e., medium-to-thick bedded marbles, of a maximum thickness of 500 m, which outcrops towards the SW and NE of Ano Vathy. Of interest is also a probable or covered geologic fault that has an NNW-SSE direction at the western side of Ano Vathy, which may affect the thickness of the marly limestone layer under Ano Vathy. The outcropping limestones at the western part of Vathy gulf, are similar to

those of Ano Vathy but of younger (pliocene) age. At the east of Ano Vathy, there is a narrow outcrop of schists (running in parallel to the NW-SE cross section), that surfaces in between marbles, all being metamorphic strata of similarly large stiffness.

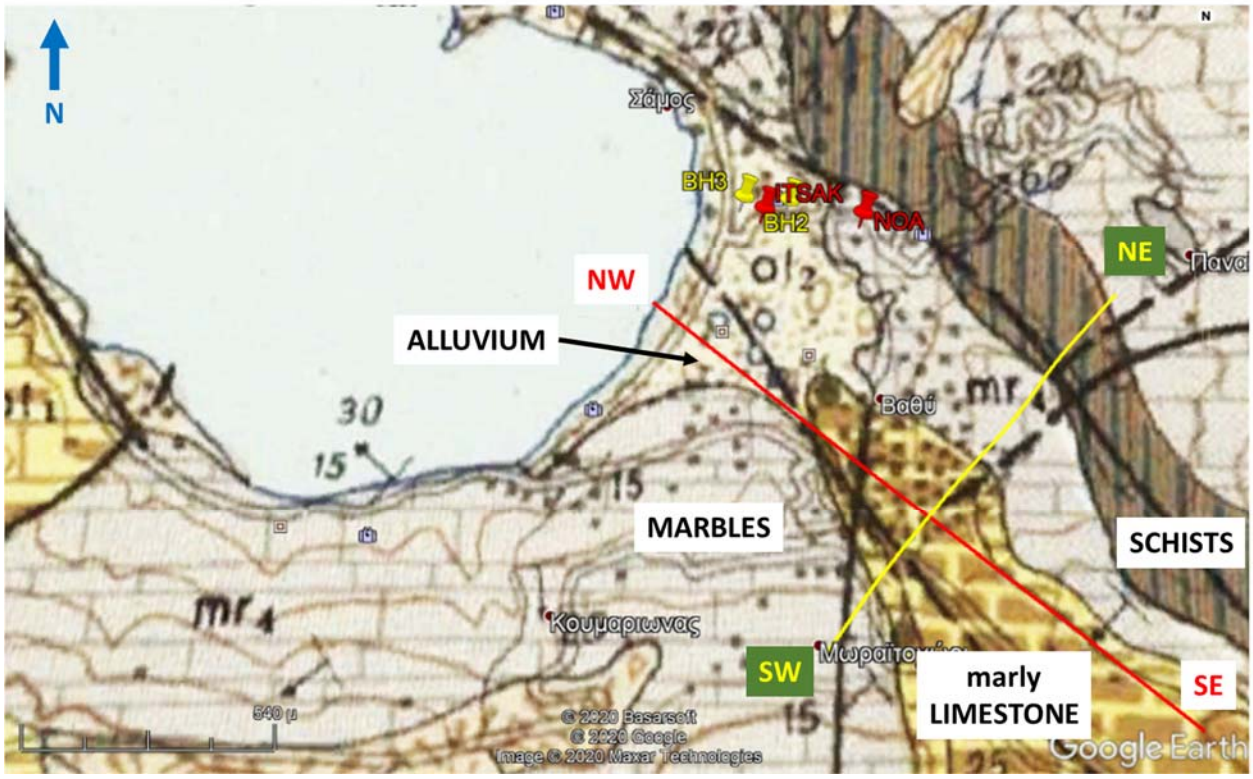

Figure 4.24. Geological map of the greater area of the seaside town of Vathy and locations of boreholes (BH2, BH3), recording sites (NOA, ITSAK) in Vathy, as well as NW-SE and SW-NE cross sections running through the damaged area of Ano Vathy; Geological info from HSGME (1979) map.

Figure 4.25 shows the ground surface elevation and the (approximate) geological layers that are to be found along the NW-SE section running through the urban area of Ano Vathy. This figure also includes an idealization of the ground surface topography, which shows that Ano Vathy is situated at about the mid height of an H = 170 m tall slope with a mild average inclination angle i = 13°. Geologically, Ano Vathy sits on top of the (marly) limestone formation which has a thickness ranging approximately from 5 to 30 m along this cross section and lays over the stiffer bedrock of marbles. The figure also depicts the existence of a thick alluvium layer near the sea front, while it includes the projection of the two recording stations (ITSAK, NOA) on the NW-SE section, as well as the location of the second SW-NE section of interest.

This type of ground surface topography may be marginally considered a cause of increased seismic ground motion at Ano Vathy. Specifically, according to EC8, this is possible for slopes having a height H > 30 m, as that shown in Figure 4.25. However, the same code prescribes that topography effects may be neglected if the inclination angle is i < 15°. Disregarding this notion, EC8 also mentions that for ridges with crest width significantly less than the base width, a

topography factor S > 1.2 should be used near the top of the slopes with angles i < 30° (as this one). Furthermore, this S factor may be assumed to decrease as a linear function of height above the base of the cliff or ridge, and to become unity at the base. Hence, for the Ano Vathy area a factor of S = 1.1 may be assumed, as the average of S = 1.2 at H = 170 m and S = 1 at the base, given that it is located at mid-height of the slope.

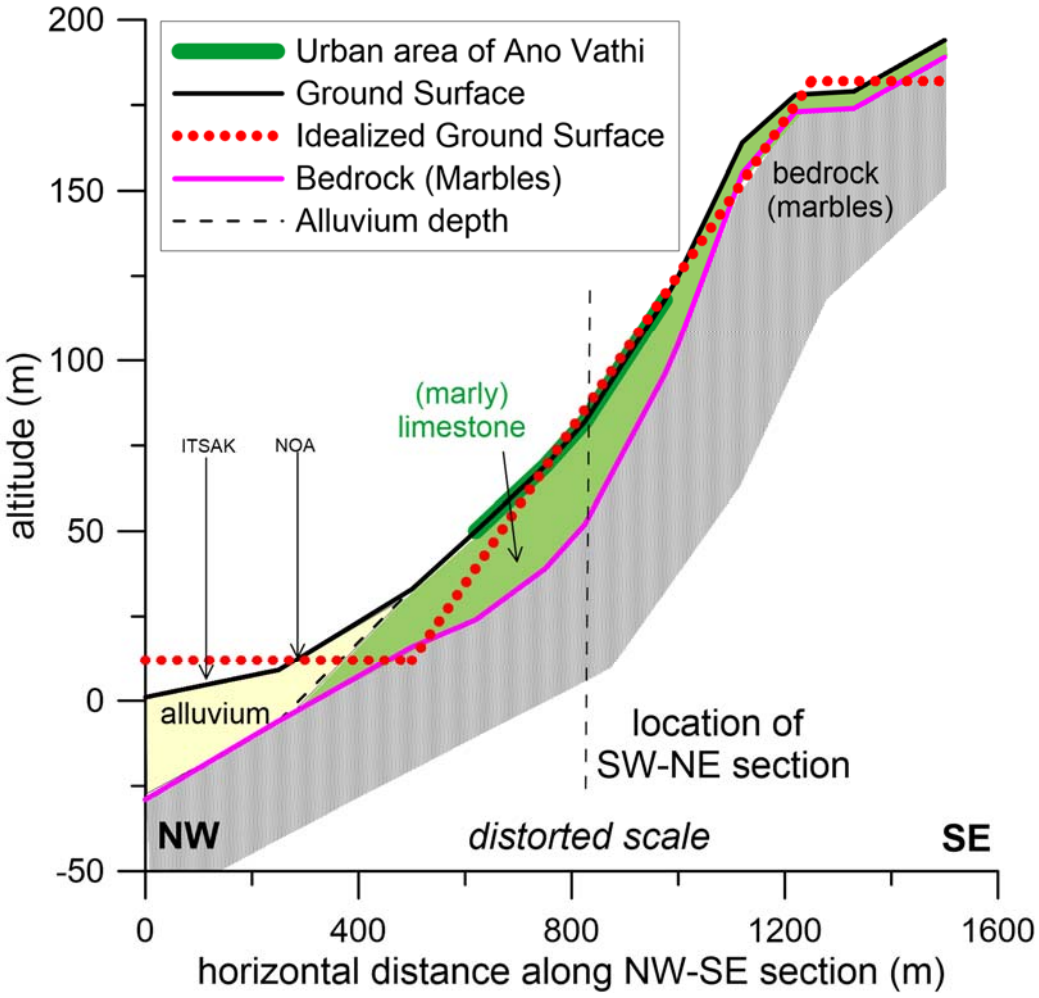

Figure 4.25. Ground surface elevation and approximate geological cross section along the NW-SE section running through the damaged area of Ano Vathy. Average (idealized) inclination is 13°.

From another point of view, one may estimate the topographic amplification on the basis of the approximate relations of Bouckovalas and Papadimitriou (2005). Considering the seismic excitation as having a predominant period of T_e = 0.5 sec (on the basis of the 2 recordings at Vathy), and by assuming that the inclined ground has an average shear wave velocity of V_s (m/s) = 500 (near the weathered surface of the marly limestone) to significantly more than 800 (marble bedrock) but a relatively small damping ratio (ξ = 2%), the idealized cross section with H = 170 m and i = 13° shown in Figure 4.25 is expected to be characterized by S = 1.16 at its crest. Therefore, for the Ano Vathy area that lies at the mid-height of the slope, the S = 1.08, on average, which is

in good agreement with the EC8 provision. On top of this, Bouckovalas and Papadimitriou (2005) prescribe parasitic vertical accelerations whose peak values are in the order of 14-20% of the horizontal acceleration. This vertical acceleration has the low-frequency content of the horizontal motion and is considered additionally to the vertical acceleration of the earthquake itself, which has a high frequency content (predominant period of 0.1 s). This parasitic vertical acceleration is disregarded by EC8.

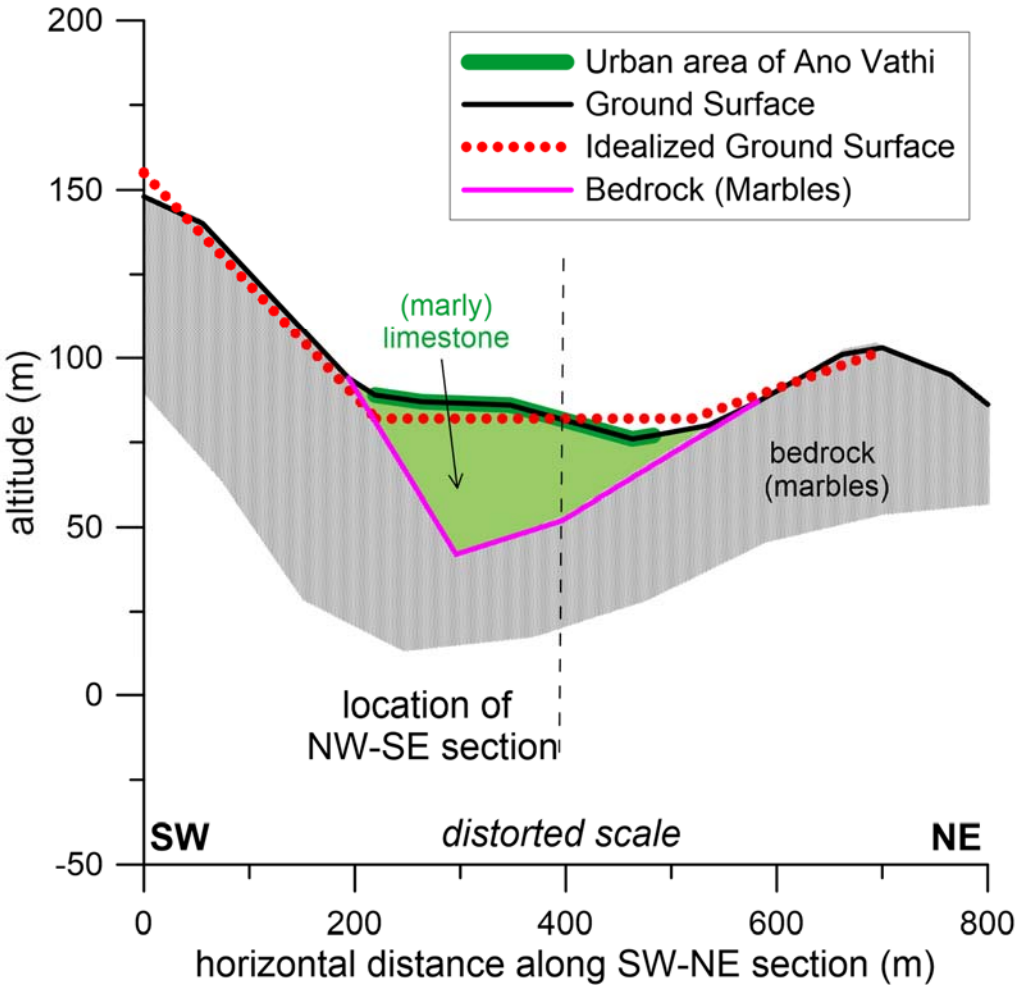

Figure 4.26. Ground surface elevation and approximate geological cross section along the SW-NE section running through the damaged area of Ano Vathy.

Figure 4.26 shows the ground surface elevation as well as the (approximate) geological layers that are to be found along the SW-NE cross section running through the urban area of Ano Vathy (see location in Figure 24). This figure also includes an idealization of the ground surface, which shows that Ano Vathy sits roughly at the top of an (approximately triangular) valley with surface width B = 300 m and maximum thickness H = 40 m at the location where the probable or covered geological fault (with a NNW-SSE direction) lies (see also Figure 4.24) at the western side of Ano Vathy. This western side of Ano Vathy exhibits the steepest bedrock inclination (i = 28^{o}) and

tallest outcropping bedrock (73 m with i = 18^o), whereas at the eastern side the bedrock inclination is milder (i = 14^o) and the outcropping bedrock is quite shorter (30 m with i = 7^o).

In this cross section, (ground surface) topography effects alone give negligible amplification at Ano Vathy, since it lies at the base of the canyon shaped topography where seismic strong motion is generally not significantly amplified (Papadimitriou 2019). However, the valley-shaped stratigraphy of the underlying layers may be considered a cause of increased seismic ground motion at Ano Vathy, concurrently with that due to surface topography effects that was depicted along the NW-SE direction (see Figure 4.25). It may be assumed here that the role of "soft" soil should be attributed to the marly limestone with a V_s > 500 m/s, that overlies the bedrock (marbles with V_s > 800 m/s), and consequently this valley-shaped structure is not expected to have an intense impedance contrast. Unfortunately, there are no code provisions for valley effects on seismic ground motion and any approximate estimation may only be based on the literature. For example, according to Vessia et al. (2011), this valley has a thickness over half-width shape ratio SR = 40/(300/2) = 0.27 (intermediate-depth valley), leading to an amplification of at least 35%, on top of ordinary 1D soil amplification. In this case, this value should be considered an upper limit, since the valley material is not soft alluvium and the horizontal acceleration has a low frequency content (predominant period 0.5 sec), thus increasing the predominant shear wavelength to values comparable with the valley width and much larger than the valley thickness (Papadimitriou 2019). However, the aforementioned 35% amplification may be considered an appropriate value if one also considers any 1D soil amplification (Ground Category B as per EC8), as well as the enhanced amplification effect due to the outcropping bedrock slopes (Papadimitriou 2019). This is especially so at its western side where the bedrock slopes are relatively tall (73m). In addition, this valley configuration may have also created low frequency (predominant period 0.5 sec) parasitic vertical accelerations, that should be in the order of 10% of the horizontal acceleration (Papadimitriou et al. 2018).

Hence, overall, Ano Vathy seems to lie at an unfavorable location in terms of its ground surface topography and its bedrock geomorphology. This must have led to coupled topography-valley amplification phenomena, and a possible amplification (over the outcropping bedrock motion) in the order of 45% in the horizontal acceleration (≈ 1.08 x 1.35) at the western side of Ano Vathy and less so (e.g., 1.25) at its eastern side. These horizontal amplifications apply to the low period components of the horizontal acceleration (for structural periods up to 0.5 sec) and diminish for larger periods (e.g., for structural periods larger than 1 s; Papadimitriou 2019). In addition, this geomorphology must have created low frequency (predominant period 0.5s) parasitic vertical acceleration (in the order of 20% of the horizontal component), which adds to the high frequency (predominant period 0.1s) vertical acceleration of the bedrock motion itself. These coupled amplification effects may explain, partly at least, the increased structural damage observed at Ano Vathy during the October 30th 2020 earthquake.

4.11 Soil Effects in Vathy

The seismic recordings of the main shock of the October 30th 2020 event in Samos were recorded within the relatively flat area of the seaside town of Vathy (see Figure 4.23). The ITSAK recording was closer to the sea front, while the NOA recording was obtained 235m to its east, at an elevation 11m higher (there is a mild average inclination of 4.5% towards the west, i.e., toward the see front). Both recordings have been presented in full detail in the reports of the referenced Institutes. Of interest here is to combine the information from the recordings with the currently available geological and geotechnical data, in an effort to ascertain whether there are any site effects that have affected the recordings. Figure 4.27 presents a comparative evaluation of the elastic response spectra (5% structural damping) of all (horizontal and vertical) components of acceleration from the two recordings of the October 30th 2020 earthquake at Vathy, i.e., the records from NOA (Kalogeras et al. 2020) and the records from ITSAK (ITSAK-EPPO, 2020). The blue curves present the spectral information along an approximately NE-SW direction, while the red curves do the same along the (perpendicular) NW-SE direction. The legends of the various subplots depict the exact orientations of the instruments at the two recording stations.

Particularly, Figure 4.27a and Figure 4.27b compare directly the elastic response spectra at the 2 recording stations. It is shown that the main event is characterized by a relatively low-frequency content, since at both recordings the predominant period of the horizontal acceleration is in the order of 0.5sec. This is anticipated given the length of the rupture. Another interesting finding is that the NOA recording is characterized by relatively lower values of spectral acceleration [approximately 20-40% lower for structural periods of practical interest (T = 0 to 0.8 sec)], without significant alterations in spectral shape. Given the close proximity of these recording stations, as compared to the average of about 10 km (epicentral distance of about 22 km) distance from rupture zone, this differentiation is a manifestation of site effects on the seismic ground motion within the flat area of Vathy. Concurrently, the vertical acceleration has a significantly lower predominant period of 0.1 sec and a much smaller amplitude than the horizontal components, without any noteworthy differentiation in the two recording stations. To further explore these findings, Figure 4.27c and Figure 4.27d compare the horizontal to vertical spectral ratios at the two recording sites. These ratios underline that the NE-SW horizontal components were generally larger than their NW-SE counterparts. They also show predominant peaks at periods around 0.6 sec, however these peaks are significantly more pronounced in the ITSAK recording. Moreover, both recordings depict a similar secondary peak in the large period region (around 1.5 sec). Finally, Figure 4.27e presents the standard spectral ratio of the two recordings employing the NOA site as the “reference” (bedrock) site. It is deduced that the peak ground acceleration is relatively amplified by 40% on average, higher amplifications appear at intermediate periods 0.1 – 0.6s, while the amplification diminishes at periods higher than 1 sec.

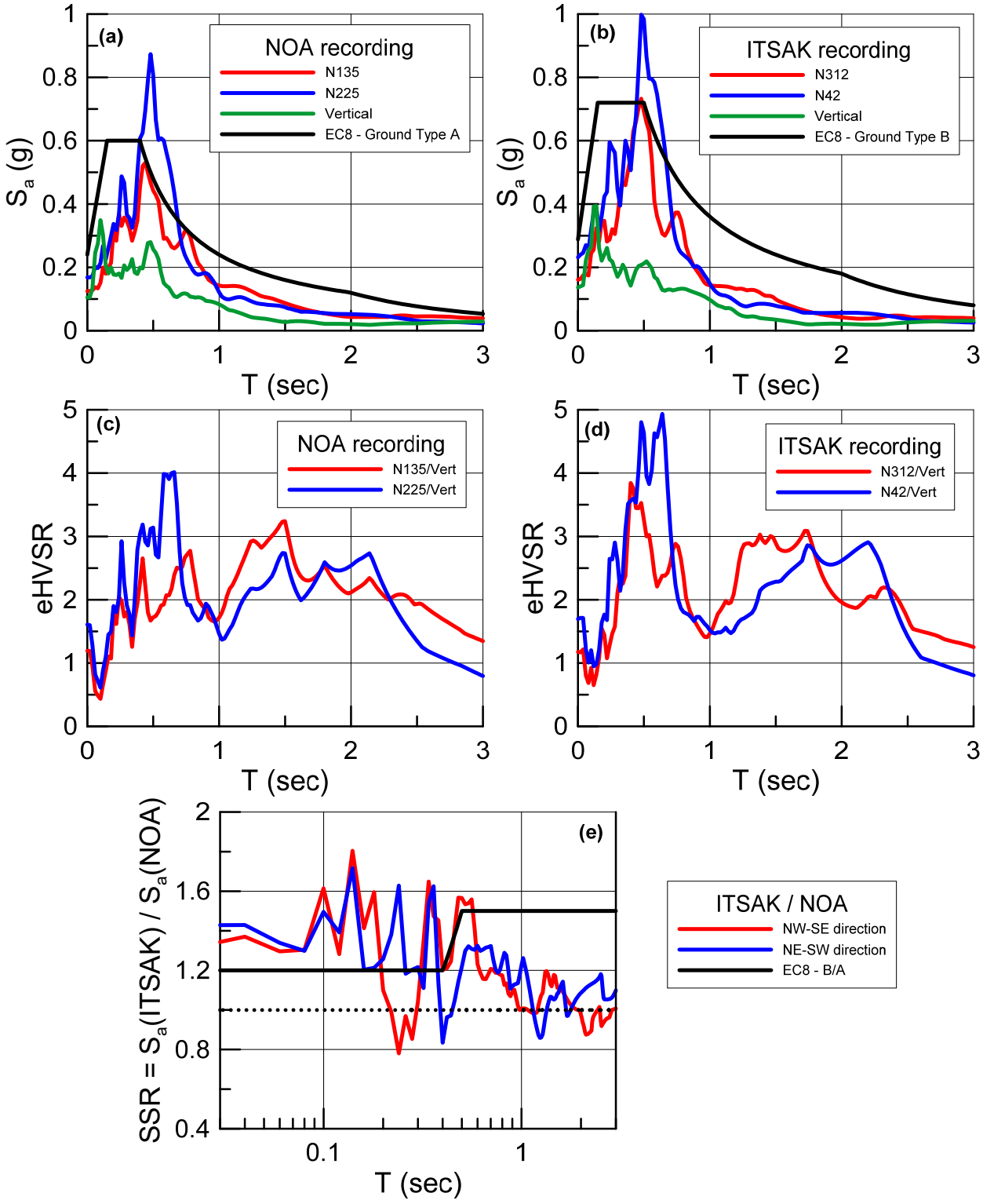

Figure 4.27. Comparison of elastic response spectra (5% structural damping) of acceleration records of the October 30th 2020 earthquake at NOA (Kalogeras et al. 2020) and ITSAK (ITSAK-EPPO, 2020) at Vathy: (a, b) Spectral accelerations; (c, d) horizontal to vertical spectral ratios; (e) standard spectral ratios.

Careful examination of the locations of the two recording sites versus the surface geology in Figure 4.28 reveals that the ITSAK recording (Figures 4.27b, 4.27d) was obtained at an alluvium site closer to the sea front, whereas the NOA recording (Figure 4.27a, 4.27c) was performed at a location where the marbles outcrop. Obviously, this geological differentiation needs to be verified by geophysical and geotechnical investigation. This process is ongoing and the only currently available geotechnical investigations in this particular area of Vathy are two (2) sampling boreholes of 15 depth, namely BH3 closer to the sea front than the ITSAK recording and BH2 approximately in between the two recording sites, as also shown in Figure 4.28. The geotechnical profile with depth (stratigraphy and SPT blow count) of the two boreholes in question is presented in Figure 4.29. It is shown that alluvium is found within the first 15m of both borehole locations (in agreement with the geological map), however the stiffness of these geomaterials is quite different. In particular, the SPT blow counts are well below 45 at the western borehole BH3 (downstream of ITSAK recording site), but are approximately equal to 50 (or more) at all depths in the eastern borehole BH2 (in between the two recording sites). The geological bedrock has not been reached at neither of the two boreholes. However, it is expected to be shallower in the eastern direction (see approximation in Figure 4.25).

In closing, one may consider the ITSAK and NOA recording sites as being a “stiff soil” and a “bedrock” site, respectively. This approximation is backed by in-situ geophysical measurements performed by Prof. P. Pelekis (HAEE/ETAM Member and co-author of this report). These measurements give preliminary estimates of predominant site frequencies (via HVSR microtremor technique) that are well below and above 12 Hz for the ITSAK and NOA recording sites, respectively. These measurements also give preliminary estimates of V_{s30} (via MASW) at these sites that equal 550 m/s (“stiff soil”) and 840 m/s (“bedrock”) at the ITSAK and NOA recording sites, respectively. Note that these values are different from preliminary estimates based on proxies developed by Stewart et al (2014). On the basis of this approximation, the 1D soil amplification (versus the acceleration at outcropping bedrock) is found to be significant within the town of Vathy, i.e., on the order of 30% on average, which is clearly higher than the EC8 soil factor of 1.2 (Ground Category B in EC8 for the ITSAK site).

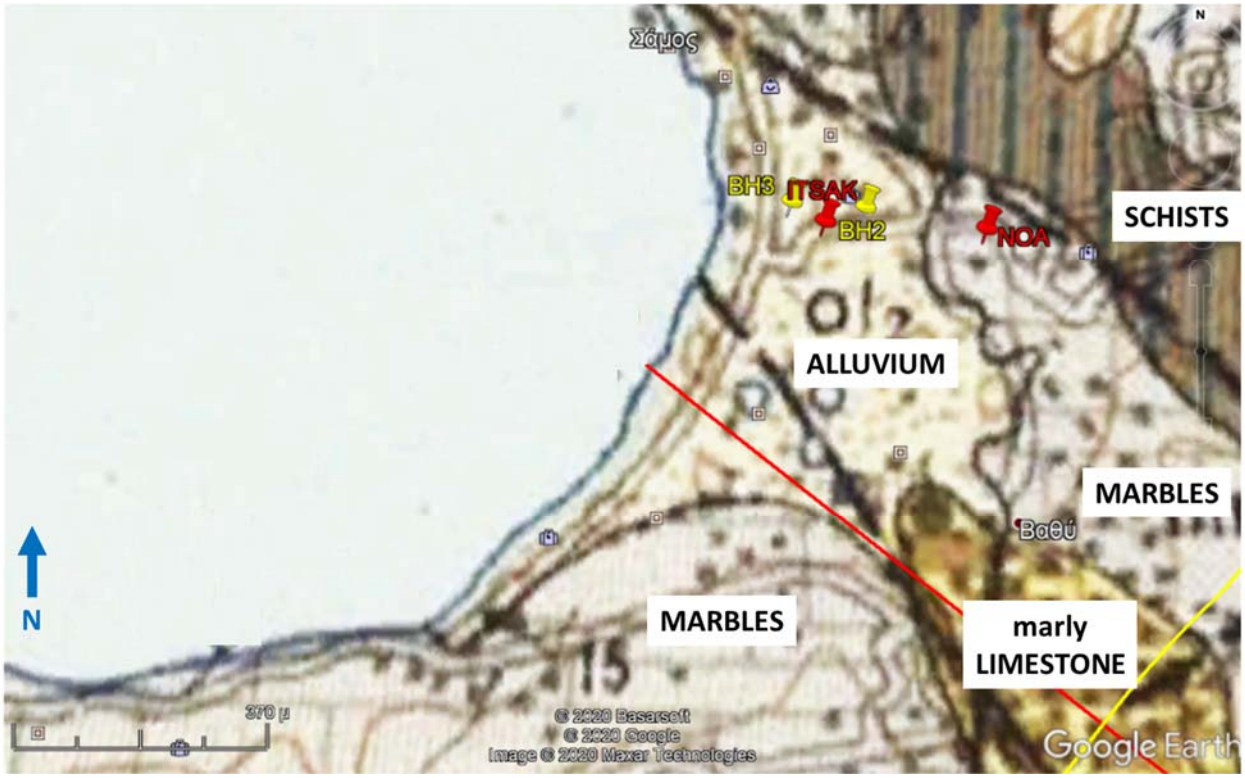

Figure 4.28. Detail of geological map of the area of the two recording sites (ITSAK and NOA) at Vathy, as well as locations of two available boreholes (BH3 and BH2); Geological info from HSGME (1979) map.

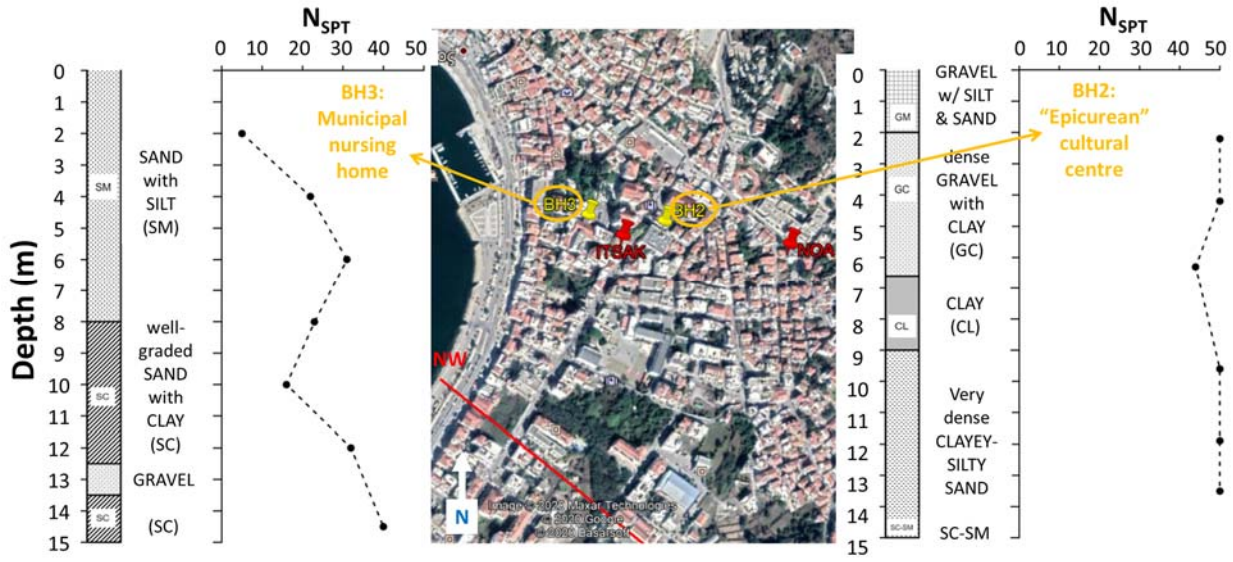

Figure 4.29. Geotechnical profile (stratigraphy and SPT blow count) with depth at borehole locations BH2 and BH3 in close proximity of the recording sites (ITSAK and NOA) at Vathy (see also Figure 4.28).

4.12 Major Findings and Conclusions

With reference to site effects at Izmir, the amplifying and prolonging effects of site conditions on seismic demand have been widely known and discussed in geotechnical earthquake engineering literature. The response of Mexico City basin subjected to 1985 Mexico City Earthquake of M_w = 8.0 is a well-known case on how site effects can be the source of structural damage due to amplified and prolonged seismic demand. This event and the response of Izmir Bay has once again reminded us the importance of site effects. Followings are the major reminders of this event:

i) This event produced anomalously rich long period rock spectral accelerations in the period range of 0.5 - 1.5 seconds, which is attributed to source mechanism and magnitude of the event.

ii) Deep soils sites of Izmir Bay, and more specifically Bayraklı, which have natural periods of 0.5 to 5 seconds, amplify further these already-relatively-long-period-rich rock excitations.

iii) Overlying 7-9 story reinforced concrete buildings, which happen to have natural periods also falling in this already amplified longer period range of 0.7-1 seconds resonated, which again further amplified the seismic demand.

iv) These double resonance effects (rock and soil resonance, and soil and superstructure resonance) unusually amplified the overall response.

v) Additionally, these site effects have also prolonged the seismic shaking duration.

vi) However, these unusually amplified and prolonged excitations should not have triggered failure of structures, since they are shown to be below design basis earthquake levels.

vii) There, poor structural design, detailing and construction practices come into the picture.

viii) Code based amplification factors for Izmir Bay and especially Bayrakli, are shown to be exceeded by this relatively distant event and low intensity seismic shaking, clearly addressing the need to re-visit them, and to develop region specific zonation, when general code practices are proven to be inadequate to assess such unusual site effects.

With reference to site affects in Samos island (greater Vathy area), following are some preliminary findings:

i) The event produced rather long period rock spectral accelerations on hard ground/soft rock in the town of Vathy, in the period range 0.4 - 0.6 s and significant durations between 10 - 15 s. This, again, can be attributed to the size of the rupture.

ii) Although located only about 10 m from rupture (22km from the epicenter), within the near fault zone, the town of Vathy was rather lightly affected by the earthquake, with

relatively few collapsed or heavily damaged buildings. This can be partially attributed to the low height / low weight of structures in the area (see Chapter 7).

iii) The strong ground motion recordings on stiff sites close to shore in the town of Vathy had relatively modest horizontal PGA and PGV values, of about 0.23 g and 22 cm/s, respectively. Moreover, one may consider the ITSAK and NOA recording sites as being a "stiff soil" (V_{s30} = 550 m/s) and a "bedrock" site (V_{s30} = 840 m/s), respectively. On the basis of this approximation, 1D soil amplification is found to be significant within the town of Vathy, i.e., on the order of 30% on average.

iv) Concentration of damage in low-rise buildings in the old town of Vathy (Ano Vathy), at a distance of 600 to 1000 m from shore and an elevation of 50 to 120 m (having an approximate area of 0.1 km^2), is indicative of a combination of coupled valley and topography phenomena. Such effects have been observed in other recent earthquakes in Greece (e.g. Margaris et al 2008, Nikolaou et al 2014)

v) Ano Vathy seems to lie at an unfavorable location in terms of its ground surface topography and bedrock geomorphology. This combination may have led to a possible amplification of the horizontal acceleration (over that of the outcropping bedrock motion) in the order of 25-45%, especially for low structural periods.

vi) In addition, the geomorphology of Ano Vathy may have created low frequency (predominant period 0.5s) parasitic vertical acceleration (in the order of 20% of the horizontal component), which adds to the high frequency (predominant period 0.1s) vertical acceleration of the bedrock motion itself (e.g., as recorded at NOA site).

Acknowledgements

The authors are indebted to Professor George Bouckovalas of the National Technical University of Athens, Prof. Dr. Atilla Ansal of Ozyegin University, Istanbul, Prof. Dr. Ayfer Erkin of Istanbul Technical University, Prof. Dr. Bilge Siyahi of Gebze Technical University, Istanbul for their valuable review of the Chapter, and their insightful comments that significantly improved many of the discussions presented herein, particularly those pertaining to site effects in the town of Vathy and city Izmir.

The authors would also like to deeply thank external contributors who kindly provided data and assistance with carrying out field measurements included in this Chapter. In this regard, George Milionis, Geologist, provided the boreholes log data for BH1, BH2, BH3 and BH4 shown in Figure 4.20 and Figure 4.29, while the borehole log data for BH5 shown in Figure 4.20 was provided by Peggy Sechioti, employee of the Greek Ministry of Infrastructure and Transport. A number of photographs and information about structural damage in Ano Vathy were provided by HAEE/ETAM members Christos Giarlelis and Prof. A. Sextos, respectively. Information about the orientation and polarity of the strong motion instruments at Vathy was provided by Drs Ioannis Kalogeras, Vassilis Margaris and Nikos Theodulidis of NOA and ITSAK-EPPO. MASW and HVSR field measurements by Prof. P. Pelekis were supported by Vasilis Christopoulos, laboratory member, and Paraskevi Paliatsa, postgraduate student, of the Civil Engineering Department, University of

Patras. Additionally, a number of photographs and information about structural damage in Izmir Bayrakli were provided by Ali Aksoyer. Their valuable contribution is gratefully acknowledged.

The members of Middle East Technical University, Ankara were partially funded by reconnaissance funds of METU, which is greatly appreciated. Financial support to the U-Patras team was provided by HAEE/ETAM. Prof Katerina Ziotopoulou's field reconnaissance and participation was supported by the NSF-sponsored Geotechnical Extreme Events Reconnaissance (GEER) association. The work of the GEER Association, in general, is based upon work supported in part by the National Science Foundation through the Geotechnical Engineering Program under Grant No. CMMI-1826118. Any opinions, findings, and conclusions or recommendations expressed in this material are those of the authors and do not necessarily reflect the views of the NSF. Any use of trade, firm, or product names is for descriptive purposes only and does not imply endorsement by the U.S. Government. The GEER Association is made possible by the vision and support of the NSF Geotechnical Engineering Program Directors: Dr. Richard Fragaszy and the late Dr. Cliff Astill. GEER members also donate their time, talent, and resources to collect time-sensitive field observations of the effects of extreme events.

Last but not least, thanks to EduPro Civil Systems Inc., the ProShake software licence was freely provided for the assessment of site response analyses, which is acknowledged.

References

Akbuğa, E. (2019). "Seferihisar (Izmir) Bolgesinde Sivilasma Analizi ve Haritalandirilmasi". Manisa Celal Bayar Üniversitesi, Master Thesis (in Turkish).

Bouckovalas, GD, and Papadimitriou AG, 2005. Numerical Evaluation of Slope Topography Effects on Seismic Ground Motion. Soil Dynamics and Earthquake Engineering, 25(7-10), 547 – 555

Building Seismic Safety Council (BSSC), 2015. NEHRP Recommended Seismic Provisions for New Buildings and Other Structures, FEMA P-1050, Washington, D.C., 515 pp., available at https://www.fema.gov/media-library/assets/documents/107646.

Demirtaş, R. 2019. İzmir İli, Menderes İlçesi, Değirmendere, Gümüldür ve Özdere Mahallelerinin Paleosismolojik Ve Yüzey Faylanması Tehlike Zonu Açısından Değerlendirilmesi. DOI:10.13140/RG.2.2.14234.70087

DTA Proje, Personal communication 2020.

Ecemiş N., Personal communication 2020.

EN 1998-1, 2004. Eurocode 8: Design of Structures for Earthquake Resistance. 1st ed. Brussels: BSi.

HAEE – Vadaloukas, G., Vintzileou, E., Ganas, A., Giarlelis, C., Ziotopoulou, K., Theodoulidis, N., Karasante, I., Margaris, B., Mylonakis, G., Papachristidis, A., Repapis, C., Psarropoulos, P. N., and Sextos, A. G. (2020). Samos Earthquake of 30th October, 2020. Preliminary Report of the Hellenic Association for Earthquake Engineering, Athens, Greece. https://doi.org/10.13140/RG.2.2.22609.76644

Hellenic Survey of Geology and Mineral Exploration (H.S.G.M.E) (2020) Immediate response of HSGME after the 30 October 2020 Samos earthquake. Short note released on 31/10/2020 (in Greek).

Hellenic Survey of Geology and Mineral Exploration 1979. Geological Map of Samos Island (Scale 1:50,000).

ITSAK- EPPO (2020) "The Earthquake of Oct. 30, 2020, Mw7.0 (11:51GMT) North of Samos Island (Greece): Observed strong ground motion on Samos island, -Preliminary Report ITSAK v3.0, Thessaloniki pp.9."

Kalogeras I., Melis N.S., Kalligeris N. 2020. The earthquake of October 30th, 2020, at Samos, Eastern Aegean Sea, Greece. Preliminary Report v2., National Observatory of Athens, Institute of Geodynamics, Greece.

Kubilay, K. (2012)."Deprem Dalgalarinin Zemin Büyütmesi Üzerine Örnekler." TÜBAV Bilim Dergisi 5:4, 17-32.

E. Lekkas, S. Mavroulis, M. Gogou, G.A. Papadopoulos, I. Triantafyllou, K.-N. Katsetsiadou, H. Kranis, E. Skourtsos, P. Carydis, N. Voulgaris, P. Papadimitriou, V. Kapetanidis, A. Karakonstantis, I. Spingos, V. Kouskouna, I. Kassaras, G. Kaviris, K. Pavlou, V. Sakkas, A. Karatzetzou, N. Evelpidou, E. Karkani, I. Kampolis, P. Nomikou, D. Lambridou, P. Krassakis, M. Foumelis, C. Papazachos, A. Karavias, D. Bafi, T. Gatsios, O. Markogiannaki, I. Parcharidis, A. Ganas, V. Tsironi, I. Karasante, D. Galanakis, K. Kontodimos, D. Sakellariou, N. Theodoulidis, C. Karakostas, V. Lekidis, K. Makra, V. Margaris, K. Morfidis, C. Papaioannou, E. Rovithis, T. Salonikios, A. Kourou, M. Manousaki, T. Thoma, N. Karveleas (2020). The October 30, 2020 Mw 6.9 Samos (Greece) earthquake. Newsletter of Environmental, Disaster and Crises Management Strategies, 21, ISSN 2653-9454.

Makra K., Rovithis E., Riga E., Raptakis D. & Pitilakis, K. (2020). A note on the strong ground motions recorded in Izmir (Turkey) during the October 30th, 2020 M 7.0 Aegean Sea earthquake: The role of basin effects. A non-peer reviewed preprint uploaded to ResearchGate (November 29, 2020), DOI: 10.13140/RG.2.2.34517.65762

Margaris V, C. Papaioannou, N. Theodoulidis, A. Savvaidis, N. Klimis, K. Makra, C. Karakostas, V. Lekidis, T. Makarios, T. Salonikios, M. Demosthenus, G. Athanasopoulos, G. Mylonakis, C. Papantonopoulos, V. Efthymiadou, P. Kloukinas, I. Ordonez, V. Vlachakis, and J. P. Stewart (2008)."Preliminary report on the principal seismological and engineering aspects of the Mw = 6.5 Achaia-Ilia (Greece) earthquake on 8 June 2008" GEER Association Report No. GEER-013, Web report

Nikolaou et al, “Geotechnical Aspects of the M = 6.1 January 27 and February 03, 2014, Cephalonia, Greece, Earthquakes” GEER Association Report No. GEER-034 Web report

Pamuk, E., Akgün, M., Özdağ, Ö., Gönenç, T. (2017). 2D soil and engineering-seismic bed-rock modeling of eastern part of Izmir inner bay/Turkey. J. Appl. Geophys. 137,104–117.https://doi.org/10.1016/j.jappgeo.2016.12.016.

Pamuk, E., Gönenç, T., Özdağ, Ö.C. et al. (2018a). 3D Bedrock Structure of Bornova Plain and Its surroundings (İzmir/Western Turkey). Pure Appl. Geophys. 175, 325–340 https://doi.org/10.1007/s00024-017-1681-0

Pamuk, E., Özdağ, Ö.C. & Akgün, M. (2018b). Soil characterization of Bornova Plain (Izmir, Turkey) and its surroundings using a combined survey of MASW and ReMi methods and Nakamura's (HVSR) technique. Bull Eng Geol Environ 78, 3023–3035. https://doi.org/10.1007/s10064-018-1293-7

Pamuk, E., Özdağ, Ö. C., & Akgün, M. (2019). Soil characterization of Bornova Plain (Izmir, Turkey) and its surroundings using a combined survey of MASW and ReMi methods and Nakamura's (HVSR) technique. Bulletin of Engineering Geology and the Environment, 78(4), 3023-3035

Papadimitriou, AG, 2019. An engineering perspective on topography and valley effects on seismic ground motion", Theme Lecture, 7th International Conference on Earthquake Geotechnical Engineering, June 16-19, Rome, Italy

Papadimitriou, AG, Paraskevopoulos, SA, and Lamprakopoulos, AN, 2018. Aggravation of spectral acceleration along 2D symmetrical trapezoidal valleys, Proceedings, 16th European Conference on Earthquake Engineering, Thessaloniki, Greece, Paper ID 11491

Roche V., Jolivet L., Papanikolaou D., Bozkurtf E., Menant A., Rimmelé G. (2019) Slab fragmentation beneath the Aegean/Anatolia transition zone: Insights from the tectonic and metamorphic evolution of the Eastern Aegean region, Tectonophysics 754: 101-129.

Rollins K. M., Singh M., Roy J. (2020). Simplified Equations for Shear-Modulus Degradation and Damping of Gravels, Journal of Geotechnical and Geoenvironmental Engineering, 146(9). DOI: 10.1061/(ASCE)GT.1943- 5606.0002300

Schnabel, P. B. (1973). Effects of Local Geology and Distance from Source on Earthquake Ground Motions, PhD Thesis, University of California, Berkeley, California.

Seed H.B., Idriss I.M. (1970). Soil Moduli and Damping Factors for Dynamic Analysis, EERC Report No. 10-70, University of California

Stewart, J. P, N. Klimis, A. Savvaidis, N. Theodoulidis, E. Zargli, G. Athanasopoulos, P. Pelekis, G. Mylonakis, and B. Margaris, 2014. Compilation of a Local VS Profile Database and Its Application for Inference of VS30 from Geologic- and Terrain-Based Proxies, *Bull. Seism. Soc. Am*,104(6), 2827-2841.

TEC (2018). "Turkish Earthquake Code: Specifications for Building Design Under Earthquake Effects.

Vessia G, Russo S, Lo Presti D (2011). A new proposal for the evaluation of the amplification coefficient due to valley effects in the simplified local seismic response analyses. Rivista Italiana di Geotecnica, 4: 51-77

Vucetic, M. and Dobry, R. (1991). Effect of Soil Plasticity on Cyclic Response. Journal of Geotechnical Engineering, 117, 89-107.

5. Geotechnical Reconnaissance Findings

Chapter Coordinators: Kemal Onder Cetin, Katerina Ziotopoulou, George Mylonakis and Nikos Klimis

Authors:

Middle East Technical University: Kemal Onder Cetin, Mustafa Tolga Yılmaz, Zeynep Gülerce, Gizem Can, Makbule Ilgaç, Elife Çakır, Berkan Söylemez, Ahmed Al-Suhaily, Alaa Elsaid, Moutasem Zarzour

University of Bristol: George Mylonakis

Ege University: Selim Altun, Alper Sezer

University of California Davis: Katerina Ziotopoulou

Izmir Institute of Technology: Nurhan Ecemis

University of Patras: Panagiotis Pelekis

Hacettepe University: Berna Unutmaz, Mustafa Kerem Kockar

Institute of Engineering Seismology and Earthquake Engineering, Greece: Emmanouil Rovithis

Dokuz Eylül University: Mustafa Akgun, Cem Kıncal

National Technical University of Athens: Achilleas G. Papadimitriou, Prodromos Psarropoulos

Democritus University of Thrace: Nikos Klimis

Istanbul Technical University: Ece Eseller Bayat

Yildiz Technical University: Pelin Ozer Tohumcuoglu

5.1 Introduction

This chapter presents the findings of geotechnical field and desk reconnaissance studies performed after the earthquake, and discusses major conclusions drawn based upon these. Both Turkish and Greek geotechnical reconnaissance teams were mobilized to the field to collect and document perishable geotechnical data immediately after the event. On the Anatolian side, the route followed by these teams, and sites visited are shown in Figure 5.1, along with a summary of major geotechnical findings. In response to this event, the members of the Middle East Technical University, Earthquake Engineering Research Center (METU-EERC) along with several other research teams from Ege and 9 Eylul Universities, and Izmir Institute of Technology have visited the region to investigate the effects of the earthquake. The reconnaissance study had covered a large area, starting from Dilek Peninsula in the southwest, all the way up to Izmir Bornova in the northeast. METU research teams mobilized to the area as of 3rd of November to

collect and document perishable data in the form of ground deformations, liquefaction manifestations, possible failure or non-failure performances of soil and rock slopes, retaining structures. On the island of Samos, geotechnical reconnaissance was conducted on two separate phases: Firstly, geotechnical engineers (Professor Katerina Ziotopoulou and Dr. Prodromos Psarropoulos) were deployed between 7th and 9th November 2020 as part on the HAEE/ETAM reconnaissance effort. Secondly, a team of geotechnical engineers and geophysical testing experts (Professor Panagiotis Pelekis accompanied by Vasilios Christopoulos, Special Teaching Staff, and Vivian Paliatsa, postgraduate student) was deployed between the 19th and 21st December 2020.

Discussions presented in this Chapter will focus on the documentation and the preliminary assessment of i) performance of building foundations, ii) seismic soil liquefaction and induced ground failures, iii) performance of slopes and deep excavations, and iv) performance of retaining structures and quay walls.

It is noted that with the exception of Bayrakli region, where significant site effects were observed (leading to several building collapses and significant loss of life – see Chapter 4), no major geotechnical effects in the form of foundation failures, surface manifestation of liquefaction and lateral soil spreading, rockfalls/landslides, failures of deep excavations, retaining structures, quay walls and subway tunnels, were observed on the Anatolian side.

On the Samos island, evidence of liquefaction, lateral spreading and damage to quay walls in ports were observed on the northern side. However, despite the proximity to the fault (about 10 km), and the significant amplitude / duration of shaking, the associated liquefaction phenomena were not pervasive, which suggests marginal liquefaction. Also, it is unclear if the damage to quay walls was due to liquefaction of the underlying soil, or merely due to the inertia of those structures, in conjunction with presence of soft (yet not necessarily liquefied) foundation soil. A number of rockfalls / landslides were observed; yet, again, the relevant phenomena were not particularly severe. Like in the Anatolian side, no failures of engineered retaining structures and major infrastructure such as dams, bridges, viaducts, tunnels were observed. This can be mostly attributed to the lack of such infrastructure on the island.

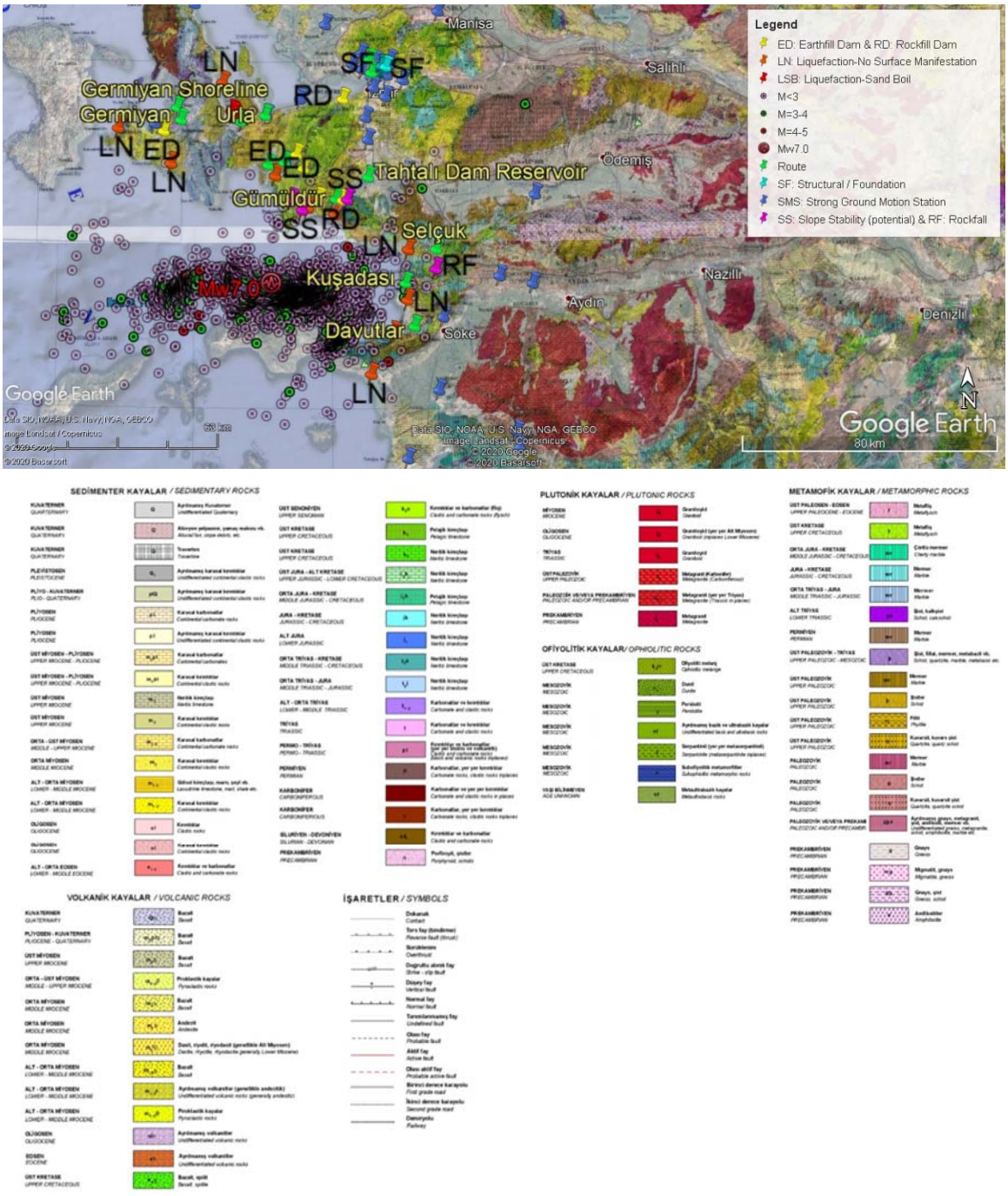

Figure 5.1. Geological map of the region, showing the locations of major reconnaissance findings (Google Earth, 2020) LN: Potentially liquefiable site with no evidence of surface manifestation; LSB: Potentially liquefiable site with sand boils; ED or RD: Earthfill or Rockfill Dam; SF: Structural (Foundation) Performance; SMS: Strong Motions Station; SS: Slope Stability (Instability) Performance; RF: Rock Fall

5.2 Performance of Foundation Systems

Many residential buildings have been investigated in the center of Urla, Cesme, Kusadasi, Gumuldur, Izmir-Konak, Izmir-Bayrakli regions, which are further detailed in Chapter 7. In this chapter, the foundation performances of these residential structures will be discussed. Among them, no foundation-induced failures, evident by excessive total or differential settlement or tilting, or bearing capacity exceedance, were mapped. A sample set of pictures illustrating these satisfactory foundation performances, is shown in Figures 5.2 (a) through (f).

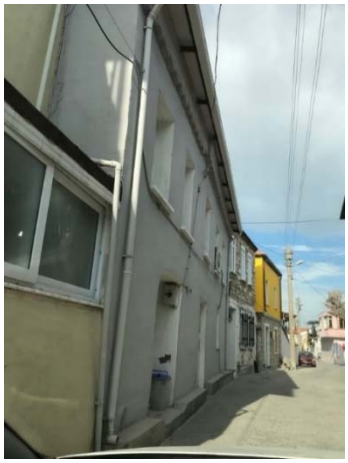

(a) Urla

(b) Cesme

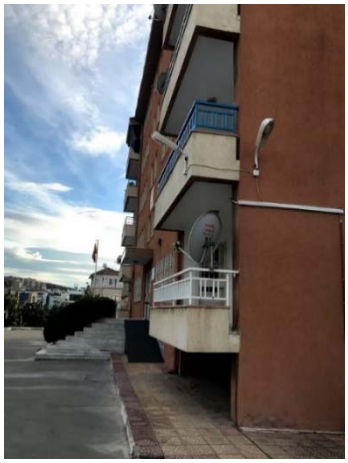

(c) Kusadasi

(d) Gumuldur

(e) Izmir Konak

(f) Izmir Bayrakli

Figure 5.2. Illustrative pictures of satisfactory foundation performances after the event

Moreover, no foundation-induced structural failure mechanisms were observed or reported for the collapsed or heavily damaged buildings in Bayrakli and Bornova districts. For residential structures up to 7-9 stories, foundation systems were mostly selected as two-way combined footings or individual footings with strap beams. Mat foundations are not very commonly used

as foundation elements of these low to mid-rise buildings belonging to pre-1995 period, despite the soft nature of underlying foundation soils. Figure 5.3 presents the foundation system of one of the fully collapsed buildings in Bayrakli.

Figure 5.3. Two-way combined footing system of a heavily damaged building in Bayrakli

However, as part of recent development of high-rise buildings (Figure 5.4), piled raft systems are commonly used. Barrette (rectangular pile) elements have been used in the foundation of these high-rise buildings. Additionally, in recent residential development in Mavisehir, ground improvement applications in the form of jet grout and rammed aggregate piers have been widely used.

Figure 5.4. 200 m high Twin Folkart Towers in Bayrakli

In Samos, no foundation failures were observed in the areas visited by the HAEE reconnaissance team, with the possible exception of structural damages due to lateral spreading (to be discussed later in the present Chapter). Figure 5.5 illustrates the Port authority building at the Eastern port of Vathy, where the observed damage patterns indicate a satisfactory piled foundation performance. Indeed, despite cracks and settlements around the building, the structure per se remained intact and was operating normally eight days after the earthquake when the HAEE team visited. At this point, it is unknown whether these settlements are related to liquefaction, dynamic compaction, or failure of the retaining wall and an associated overall displacement of the backfilled soil. For more information regarding the performance of the quay wall at the same site, the reader is referred to Section 5.5.2.

Figure 5.5. Damage observed around the Port authority building in Vathy, Samos (location: 37°45'27.0"N 26°58'15.4"E). The cracks indicate soil settlement/distortion around the building which remained intact and functioning 8 days after the earthquake (8th November 2020) [photos taken by the HAEE reconnaissance team]

5.3 Seismic Soil Liquefaction Manifestations and Induced Ground Failures

In this section, observations regarding the presence or lack of surface manifestations of earthquake-induced soil liquefaction in the form of sand boils and ejecta, excessive settlement, and lateral spreading, are presented. Along the Aegean coasts of Anatolia and inland, except in Gulbahce, no surface manifestation of seismic soil liquefaction triggering was observed or reported. As shown in Figure 5.6, evident by the USGS susceptibility map released for this event, there are liquefaction susceptible regions at which no surface manifestation of soil liquefaction

was observed. On the other hand, extensive liquefaction phenomena were observed on the island of Samos (and possibly in the port of the island of Chios) and its nearshore alluvial deposits in particular, despite the fact that the accompanying effects were not destructive.

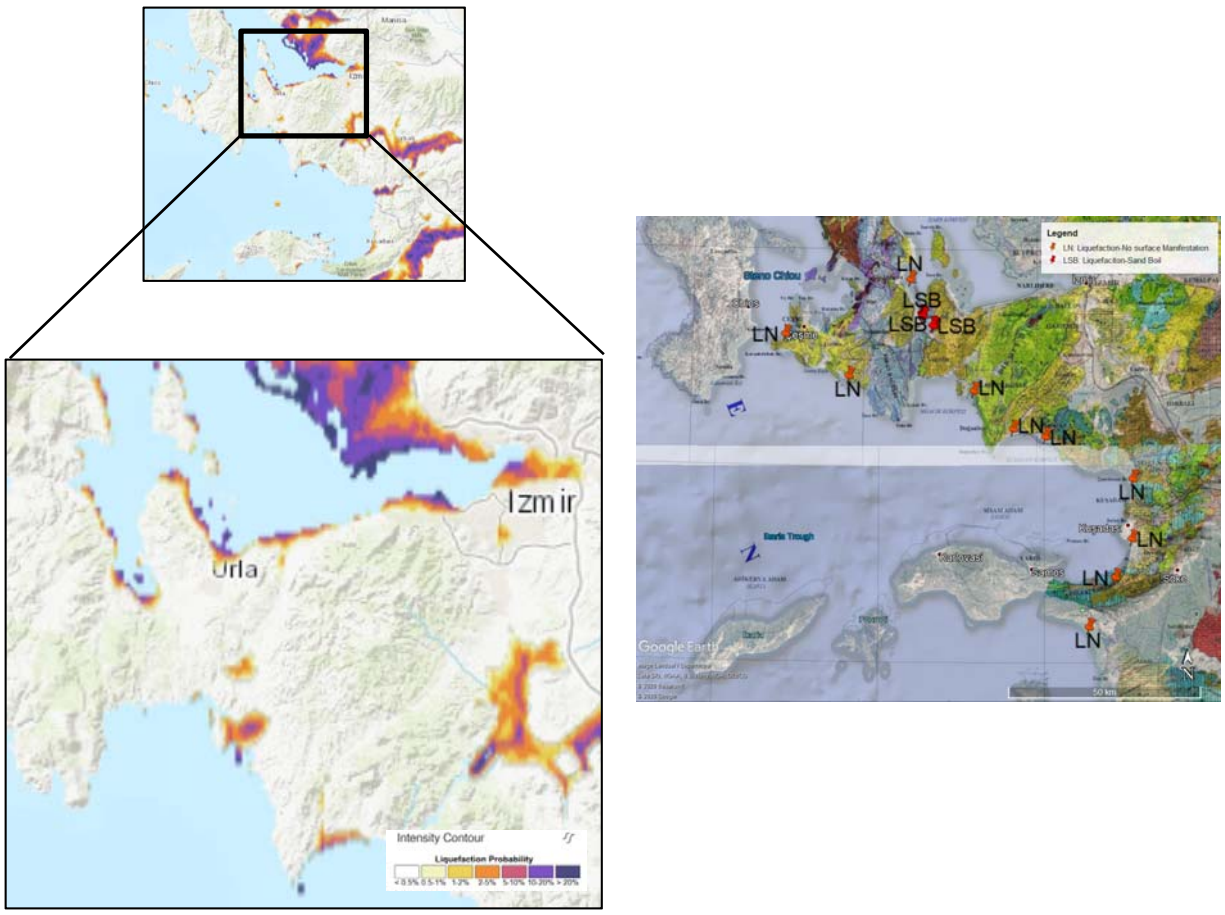

(a) (b)

Figure 5.6. a) USGS liquefaction susceptibility map released after the event showing liquefaction probability and b) sites visited during the reconnaissance showing the major reconnaissance finding (LN: No Liquefaction Observed, LSB: Sand Boil Observed)

As presented in Figures 5.7 through 5.10, potentially liquefiable sites and shores were visited, and the lack of surface manifestation of soil liquefaction triggering was documented.

Figure 5.7. No seismically-induced soil liquefaction manifestation was observed at the shores of Gumuldur city (38°04'30.9"N 26°58'32.7"E/ November 3rd 2020/ 11:03)

Figure 5.8. No seismically-induced soil liquefaction manifestation was observed at the shores of Cesme (38°20'54.5"N 26°27'07.6"E/ November 3rd 2020 / 09:54)

Figure 5.9. No ground failure was observed at the shores of Gumuldur city (38°03'30.6"N 27°00'38.3"E/ November 3rd 2020/ 10:30)

Figure 5.10. No liquefaction manifestation was observed on the shore of the Seferihisar district (38°05'11.5"N 26°51'39.7"E / November 3rd 2020/ 11:31)

However, a number of surface evidences were documented indicating the triggering of soil liquefaction in Gulbahce-İzmir and Samos Island, which will be discussed next.

5.3.1 Gulbahce/Izmir

Consistent with USGS predictions, at 45-50 km away from the rupture, along the shores of Icmeler and Gulbahce districts, sand boils were observed, as shown in Figure 5.11 (a) through (d). These sites were close to Gulbahce fault zone, and artesian pressures along with hot water springs are known to be present, which are also believed to have contributed to the observed

soil ejecta formation. The soil samples were retrieved from sand ejecta, and sieve analyses were performed on these samples, the results of which are presented in Figures 5.12 (a) and (b).

(a)

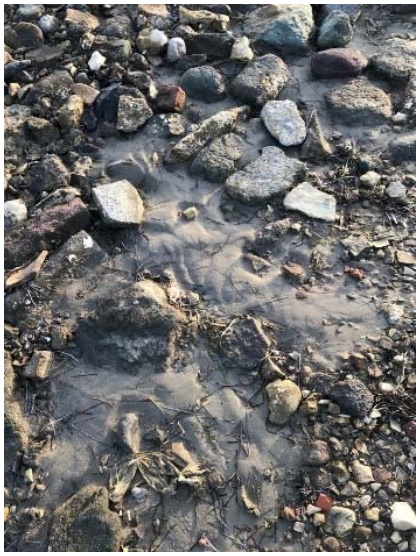

(b)

(c)

(d)

Figure 5.11. Surface manifestations of earthquake-induced soil liquefaction in the form of sand boils at a) 38°20'18.4"N 26°38'51.0"E and b) 38°18'37.3"N 26°40'47.1"E, c) and d) 38.338088 N, 26.647763E

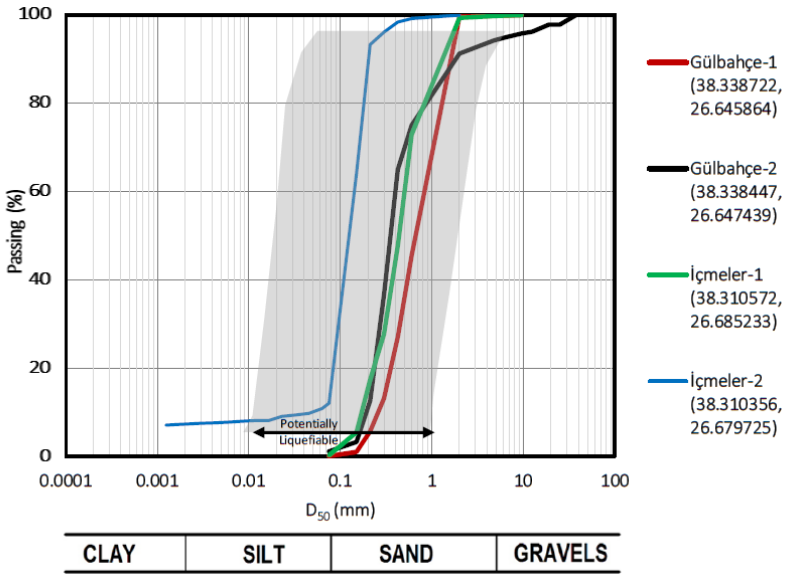

Figure 5.12. Grain size distribution curves of sand ejecta obtained from Gulbahce

5.3.2 Samos Island

Liquefaction has been historically manifested in various locations in Greece, particularly in many of its islands (Papathanasiou et al. 2005, 2010 – Figure 5.13). In the eastern Aegean Sea, the most recently recorded case of liquefaction was the one in Kos during the Bodrum-Kos **M**=6.6 earthquake of 2017 (Papathanasiou et al. 2018). No liquefaction case histories have been recorded for Samos prior to this earthquake. The reconnaissance team visited several locations along the northern and southern shores of the island. No liquefaction-related damages were observed along the southern coasts visited. In the north, liquefaction-induced sand boils and ejecta, as well as lateral spreading was observed in one location (Malagari), while liquefaction is also suspected to be the leading cause behind the failure of some quay walls in the ports of Vathy and Karlovasi. Structural damages compatible with a lateral spreading mode of failure were observed in three buildings in the location of Vyrsodepsia in Karlovasi.

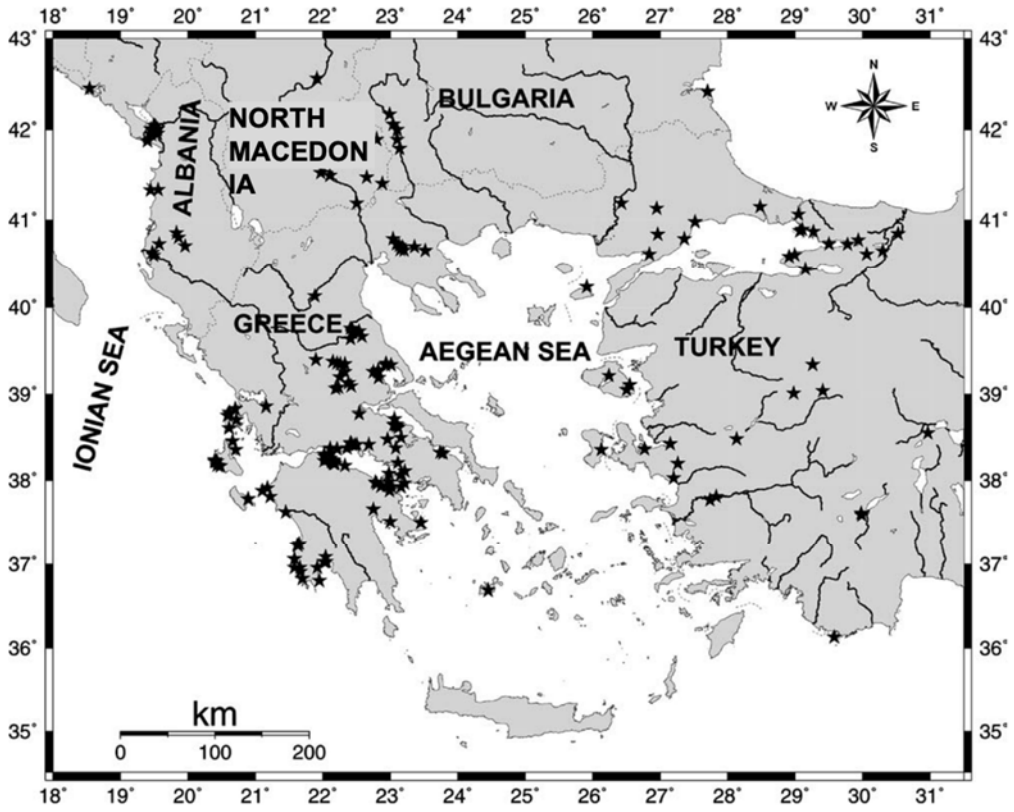

Figure 5.13. Map of historical liquefaction occurrences in the broader Aegean region from 1509 AD to 2008 AD (after Papathanassiou et al., 2005, 2010).

Manifestation of earthquake-induced liquefaction in the free field was observed in the area of Malagari, north-west from the town of Vathy, capital of the island of Samos. Specifically, the reconnaissance team located nearshore surface manifestations of liquefaction in the form of sand ejecta of grey color. As can be seen in Figure 5.14 below, by the time the HAEE team visited the site of interest (8 days after the earthquake), the ejecta had been slightly distorted due to the passage of vehicles. Nevertheless, the sand boils and their ejecta alongside with their broader extent, were still easily visible and distinguishable.

Figure 5.14. Surface manifestations of earthquake-induced soil liquefaction in the form of sand boils in Malagari (location: 37°45'24.6"N 26°57'28.8"E) [photos taken by the HAEE reconnaissance team and Dr. A. Ganas from NOA]

In the same area, ground cracks compatible with a lateral spreading mode of failure were observed and are emphasized in the inset of Figure 5.14. The combination of the aforementioned with a free face to water like in Malagari eases the process, but lateral spreading has been manifested also in case histories with no free face (e.g. Balboa Boulevard failure during the 1994 Northridge earthquake – e.g. Stewart et al. 1996, Pretell et al. 2021).

Professor Panagiotis Pelekis performed trenching and soil sampling at two locations at the Malagari site, which yielded two rough cross-sections and three grain size distributions for samples at three distinct depth intervals at the site illustrated in Figures 5.15 and 5.16 respectively. The fines portion in all three samples was found to be non-plastic.

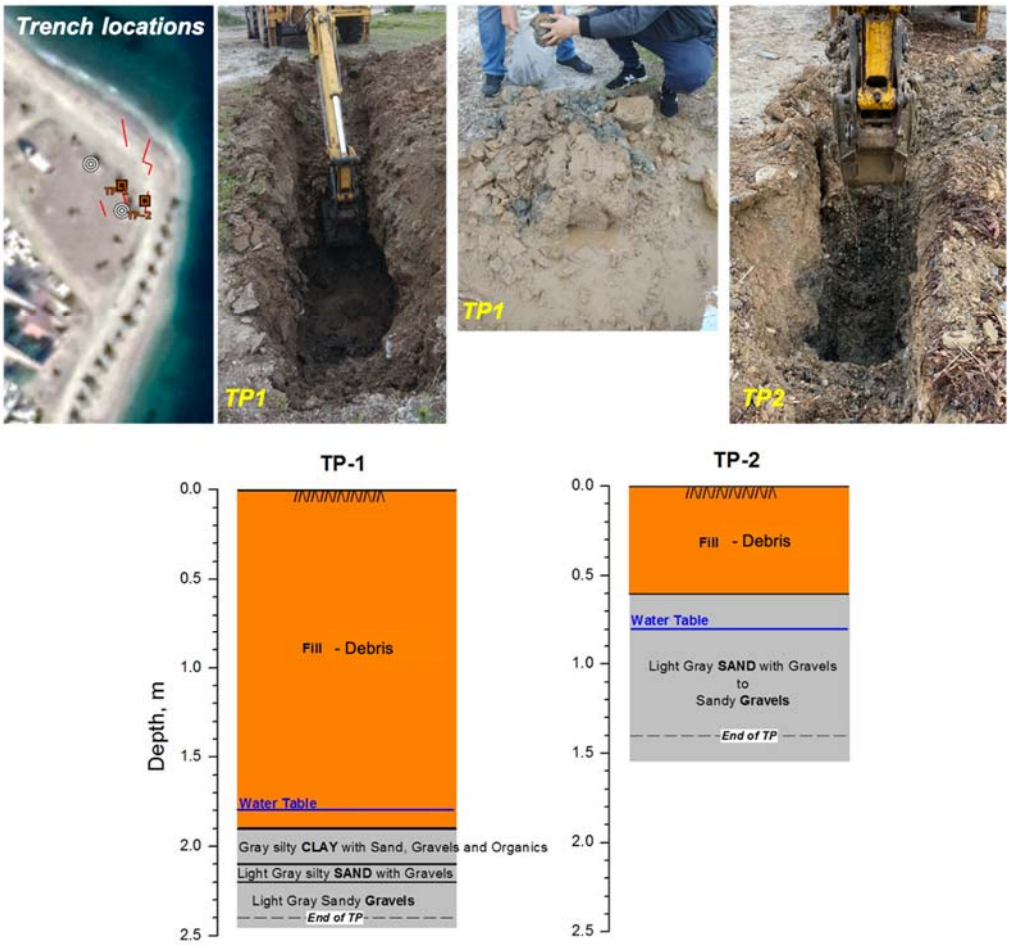

Figure 5.15. Trenching at the Malagari liquefaction site and rough stratigraphy resulting from it (courtesy of Professor P. Pelekis).

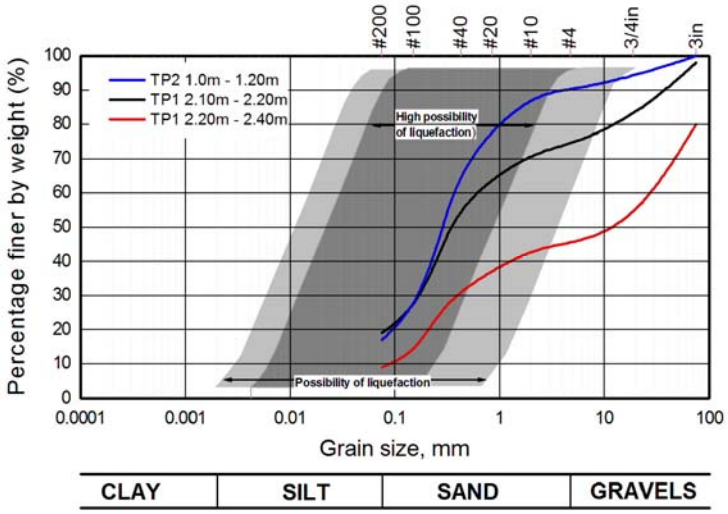

Figure 5.16. Grain size distributions of three samples retrieved from different depths at the two trenching locations at the Malagari liquefaction site. The fines were found to be non-plastic (NP).

Shear wave velocity measurements performed after the earthquake by Professor Panagiotis Pelekis on 20th December 2020 (see introduction on HAEE-deployed teams) in the Malagari area that was affected by liquefaction gave a time-averaged shear-wave velocity in the upper 30 m of the site, V_{s30}, of 215 m/sec. The distribution of shear wave velocity V_s with depth is shown in Figure 5.17. There are no borehole SPT or CPT data available at this site and the only relevant information is that from the Port of Malagari (West side of Vathy gulf) and borehole BH5 (Figure 4.20 – Chapter 4) in particular. The geologic map of Samos (Figure 4.19 – Chapter 4) indicates that the Malagari site has alluvial deposits featuring plain deposits of clayey-sandy material, loam, sand, pebbles and gravels, which are potentially liquefiable when saturated. This particular site, where liquefaction was undoubtedly manifested, can be studied as a case history of either True Negative or True Positive liquefaction manifestation after more data are obtained and processed.

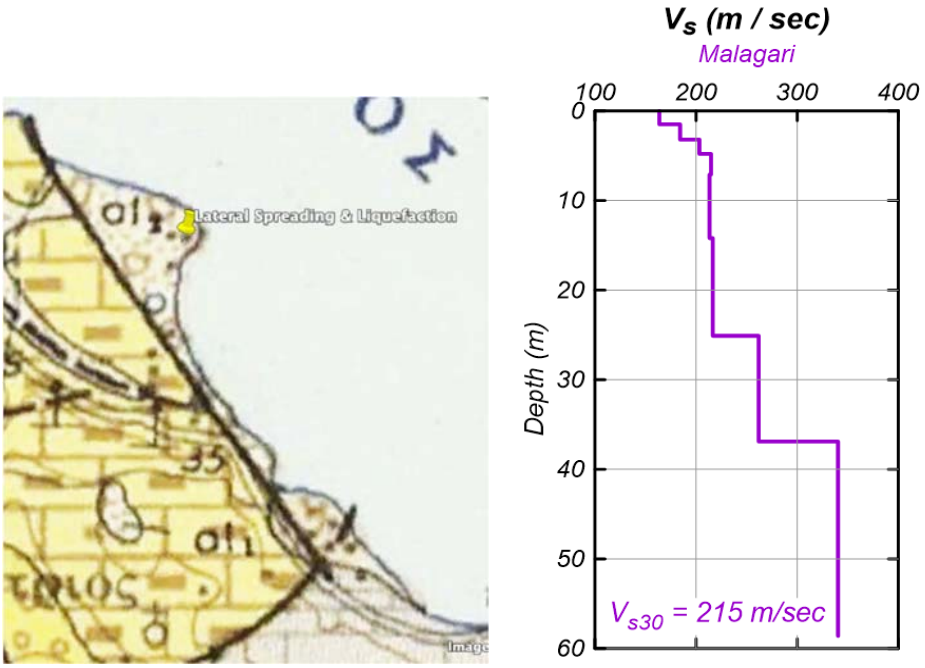

Figure 5.17. Geologic map of Malagari indicating alluvial deposits and shear wave velocity distribution at Malagari and time-averaged shear wave velocity in the upper 30 m of the site [data courtesy of Professor Panagiotis Pelekis].

Structural damages at some nearshore locations were compatible with a lateral spreading failure mechanism. Specifically, Figures 5.18 and 5.19 illustrate three buildings and their location close to the north shore of the island, in the neighborhood Vyrsodepsia in Karlovasi. No surface manifestation of liquefaction was identified nearby, but the ground cracking crossing the street pavement and running through the buildings (the two in Figure 5.18 are about 70 m inland and the one in Figure 5.19 is about 20 m inland), in combination with the level/mildly sloping ground, the shallow water table, and the free face to the sea are all compatible with the hypothesis of lateral spreading.

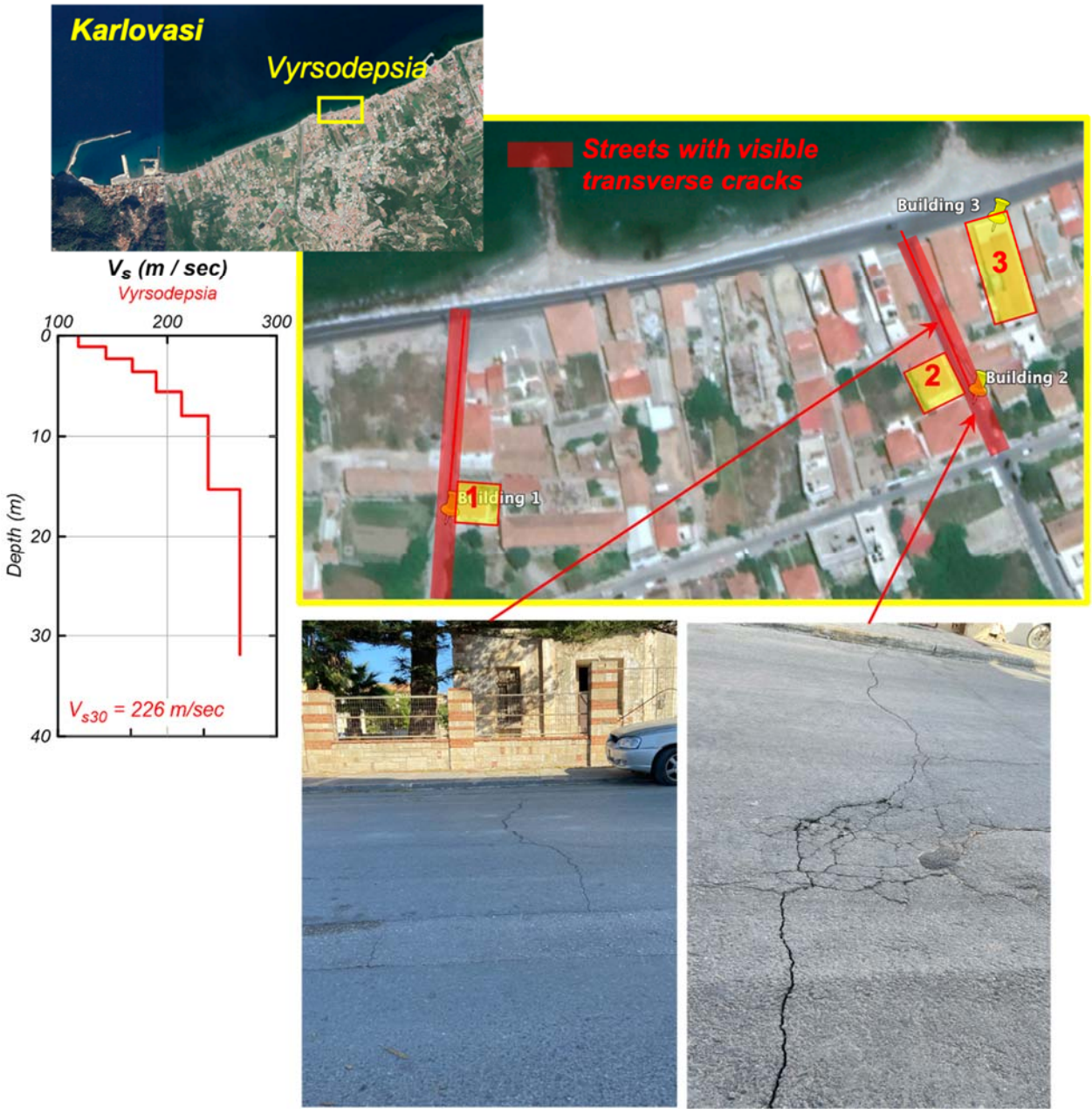

Figure 5.18. Plan view of Karlovasi and Vyrsodepsia neighborhood with buildings likely affected by lateral spreading towards the seafront alongside with shear wave velocity profile of the area [data courtesy of Professor Panagiotis Pelekis]. The enumerated buildings are individually shown in Figures 5.20 and 5.21.

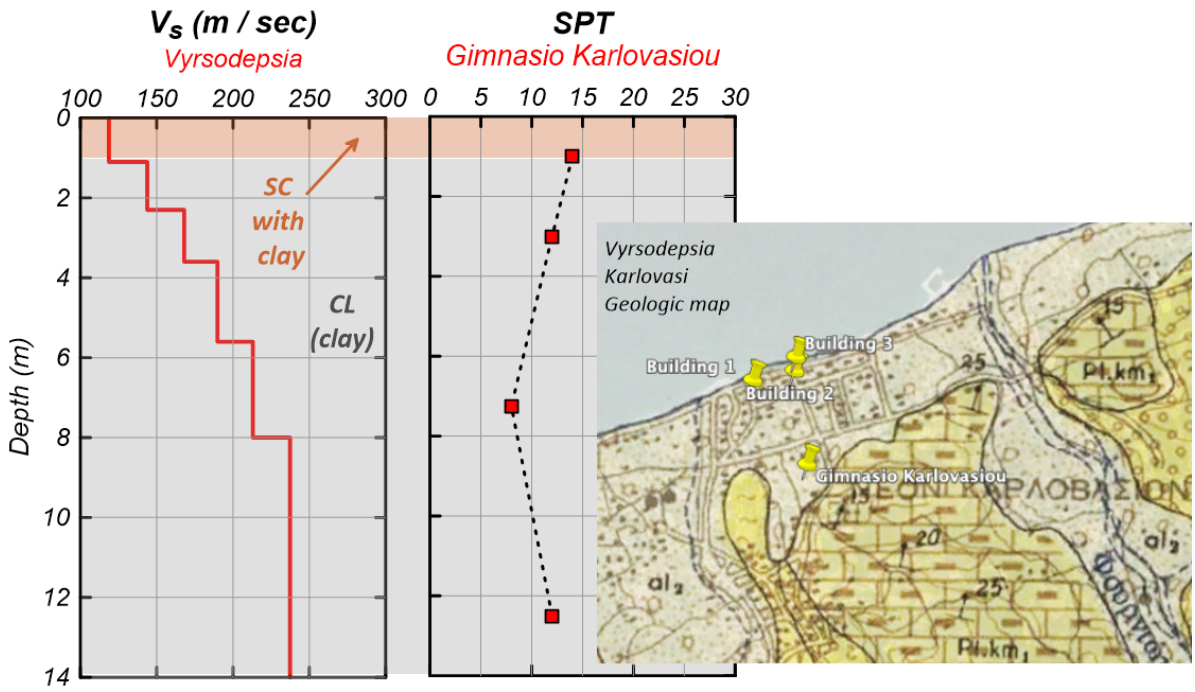

Figure 5.19. Shear wave velocity profile down to a depth of 14 m alongside with SPT blow count information from the nearest borehole at the Gymnasium (middle school) of Karlovasi (Gimnasio Karlovasiou). Locations shown in inserted geologic map.

Figure 5.20. Buildings likely affected by lateral spreading towards the seafront in the neighborhood of Vyrsodepsia in Karlovasi (left: 37°47'57.6"N 26°42'12.5"E and right: 37°47'59.3"N 26°42'20.0"E) [photos taken by the HAEE reconnaissance team]

Figure 5.21. Building affected by lateral spreading towards the seafront in the neighborhood of Vyrsodepsia in Karlovasi (37°48'01.1"N 26°42'20.6"E). The cracks observed running across the building indicate 3-5cm of movement. [Photos courtesy of Prof. K. Antonopoulos]

5.4 Performance of Slopes and Deep Excavations

5.4.1 Performance of slopes in Anatolia

A limited number of rockfalls were observed by the benches of highways, one of which is illustrated in Figure 5.22. Some potential and existing landslide sites were also visited, but no signs of seismically induced movements were documented, one of which is shown in Figure 5.22 (b).

(a) (b)

Figure 5.22. a) Fallen rock blocks (37°53'50.4"N 27°22'06.2"E, b) A view from a highway cut with potential for slope instability (38°17'31.6"N 26°40'14.6"E)

The highways were also investigated; no proof of any seismically induced damage both on the highways or on the shoulder slopes was found, as shown in Figure 5.23.

Figure 5.23. Views from a highway cuts with no signs of slope instability (38°17'31.6"N 26°40'14.6"E)

5.4.2 Performance of slopes in Samos

A series of minor-to-moderate slope failures and rockfalls were identified during the earthquake reconnaissance, mainly on the northern part of the Island. The areas with nearby slope failures which are marked in a Google Earth map (Figure 5.24) were imprinted mainly by the reconnaissance team of the Hellenic Association of Earthquake Engineering (HAEE).

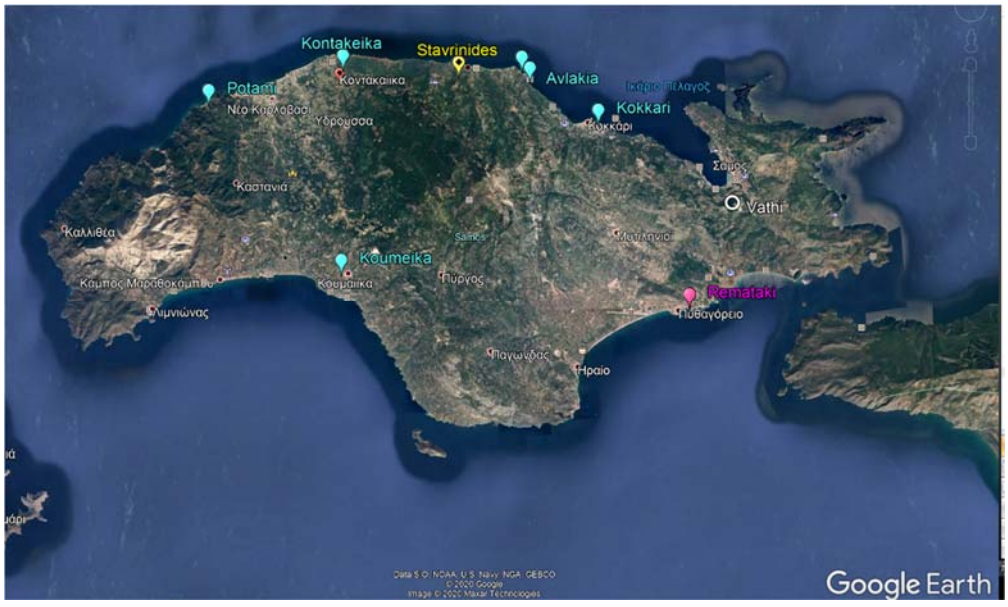

Figure 5.24. Geographical distribution of slope-type failures imprinted by the Hellenic Association of Earthquake Engineering (HAEE) reconnaissance team during in-situ visit on 7th November, 2020 (cyan points). Additional sites with light slope failures recorded by Lekkas et al. (2020) (magenta point) and HSGME (2020) (yellow point) are also shown.

The exact coordinates of these failures are listed in Table 5.1, while some additional cases reported in Lekkas et al. 2020 and HSMGE (2020) are also shown. A brief description and representative photos are given below for some of these cases.

Table 5.1. Locations of the slope failures recorded by the Hellenic Association of Earthquake Engineering (HAEE) reconnaissance team during in-situ visit on 7th November, 2020

Region with nearby slope failure	**Coordinates of the inspected slope failure**	
	Latitude (°)	Longitude (°)
Avlakia	37°47'48.0"N	26°51'27.7"E
Potami (close to Karlovasi)	37°47'17.6"N (approx)	26°40'00.5"E (approx.)
Tsampou beach (close to Avlakia)	37°48'08.0"N	26°51'17.2"E
Kokkari	37°46'49.9"N	26°53'35.0"E
Koumeika (south Samos)	37°42'33.7"N	26°44'52.9"E
Kontakeika	37°48'01.6"N	26°44'29.5"E

A weathered rock slide was recorded at a steep slope close to Avlakia region (Figure 5.25), which caused a temporary closure of the road. It is reiterated that the main geological formations in the above area are marbles with intercalations of schist (see Chapter 4). However, the road access was quickly recovered after a few days by temporary restraining measures with large concrete blocks placed at the slope toe (Lekkas et al. 2020). Detachments of sandy marls and marly limestones were recorded very close to a residential building in Kokkari region (Figure 5.26), while lighter failures referring to rockfalls and detachments of limestones, were observed close to the villages Potami (Figure 5.27 – left) and Koumeika (Figure 5.27 – right). Slope failures of similarly low intensity were also recorded by other reconnaissance teams. These include limestone segments falls at the area of Remataki (next to Pythagorio – Figure 5.28) or rockfalls close to the village Stavrinides (Figure 5.29).

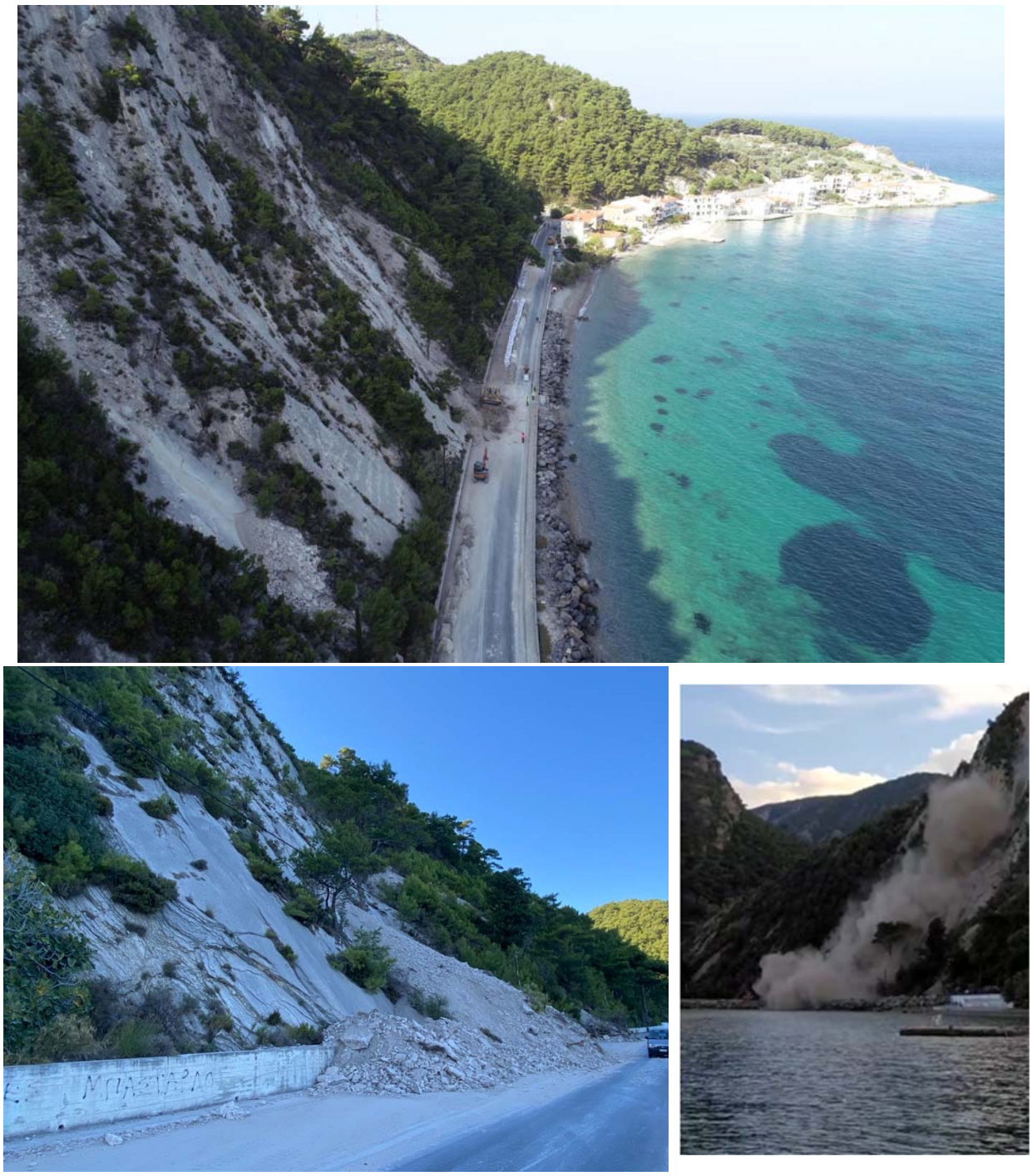

Figure 5.25. Up: A rock slide close to Avlakia region (aerial photograph courtesy of I.N. Spyrou and Prof. K. Ziotopoulou – *to not be reproduced without permission from Prof. Ziotopoulou*, 37°47'48.0"N, 26°51'27.7"E), Bottom – left: a closer view of the above rockslide reported illustrating the rock formation more clearly (picture by HAEE reconnaissance team), Bottom – right: Snapshot from a video recorded during the failure (source: https://www.cnn.gr/ellada/story/240726/seismos-samos-vinteo-apo-katolisthisi-sta-aylakia)

Figure 5.26. Detachment of sandy marls and marly limestones recorded very close to a residential building in the Kokkari region (photos taken by the HAEE reconnaissance team, 37°46'49.9"N, 26°53'35.0"E). Vertical open cracks are visible, clearly susceptible to detachment and overturning.

Figure 5.27. Left: Rockfalls recorded at the road network close to the village Potami (37°47'17.6"N, 26°40'00.5"E), Right: Detachment of limestone segments close to the village Koumeika (photos taken by the HAEE reconnaissance team, 37°42'33.7"N, 26°44'52.9"E).

Figure 5.28. Limestone segments falls to a provincial road in Rematakі region (photo reported in Lekkas et al. 2020).

Figure 5.29. Slope failures close to the village Stavrinides (photo reported in HSGME 2020).

In the village of Kontakeika, extended ground cracks (openings of about 10 – 20 cm) were observed that were compatible with the mobilization of a larger, albeit very mild, slope or could be more broadly characterized as seismically-induced secondary ground failures. The HAEE team did not locate other similar indications of ground cracking in the near or extended vicinity of Kontakeika so it is hard to draw conclusions regarding the nature of this observation. (According to local engineers, the Municipality of Samos had repaired the pavement in that particular location several times in the past, which suggests a pre-existing creeping landslide that got reactivated by the earthquake.) The cracks were extending from soft soil formations, crossing the street and extending to soil formations across.

Figure 5.30. Ground and pavement cracks in the village of Kontakeika (Samos), indicative of the mobilization of an extended but mild slope or more broadly characterized as seismically-induced secondary ground failures. The cracks extended on both sides of the street through soft soil formations.

5.4.3 Deep excavations

The new downtown district (Bayraklı-Bornova) of Izmir is raised on the sedimentary basin, where the heavily affected region from the earthquake is situated. Numerous high-rise buildings are constructed on that soft soil conditions. Many of them have multi-story basements, thus deep excavation systems need to be designed reaching 20 m. Due to shallowly located ground water levels, and proximity to the shoreline, the shoring system contains mostly diaphragm walls laterally supported by pre-stressed anchors.

In the sedimentary district, two well-monitored deep excavation systems, which were under construction in the last three months before the earthquake, were shaken. Both of these systems reached a depth of about 9 m; their (satisfactory) performance was recorded by instruments. (Fig. 5.31). No failure or relaxation of pre-stressing loads on anchors was measured/observed. These observations are also supported by inclinometer measurements taken before and after the earthquake. The measurements suggest that the lateral displacements accumulated during the earthquake are less than 2 mm. These displacements are illustrated in Fig. 5.32.

(a) (b)

Figure 5.31. a) A picture taken earlier from the shored deep excavation located in the “new downtown” district (37°53'50.4"N 27°22'06.2"E, b) Plan view of the site

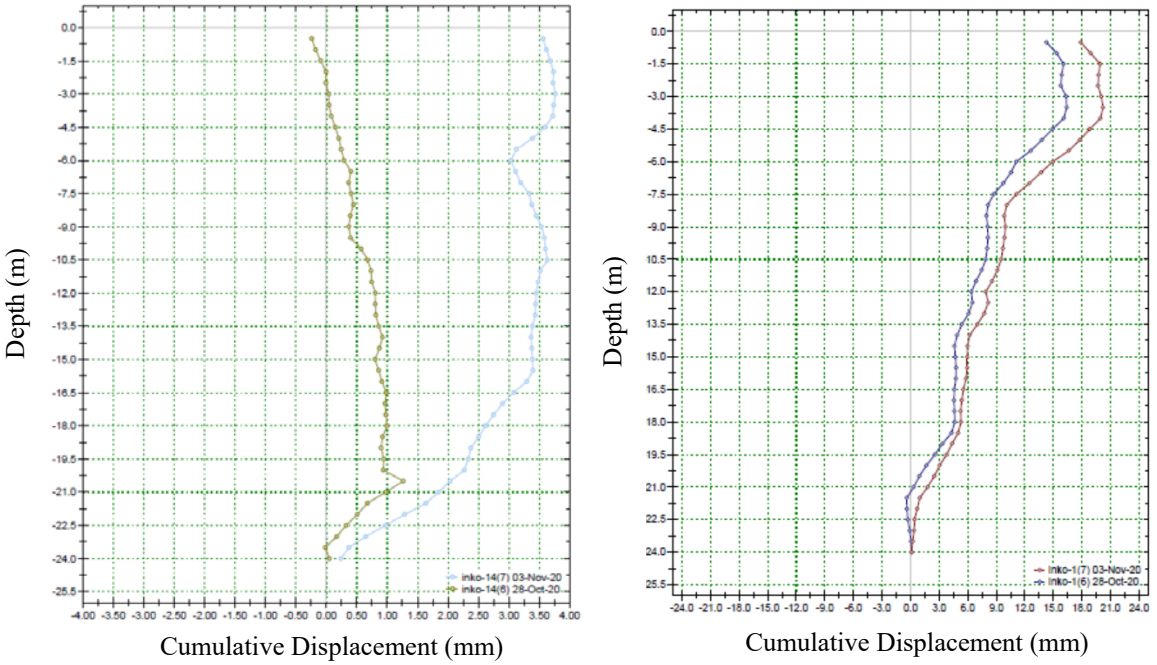

Figure 5.32. Inclinometer data covering the period of earthquake shaking, at a 9m-deep excavation, supported by diaphragm walls.

No relevant data are available from Samos and Chios islands.

5.5 Performance of Retaining Structures and Quay Walls

5.5.1 Retaining structures

There are no reported failures of engineered retaining structures in Turkey. During the reconnaissance studies, a limited number of tilted and/or partially collapsed safety walls were observed, as documented in Figures 5.33 through 5.35.

Figure 5.33. No signs of soil liquefaction. Tilted and partially collapsed very poor safety walls (38°27'24.6"N 27°10'53.1"E/ 11:10/ 04.11.2020).

Figure 5.34. Deformed and cracked safety wall 38°11'40.93"N 26°47'3.47"E /14:16/ 31.10.2020

Figure 5.35. Deformed and cracked safety wall 38°11'40.34"N 26°47'3.22"E /14:22 / 31.10.2020

Additionally, no damage on retaining walls due to seismic shaking was likewise encountered during the reconnaissance inspections of the sites in the south of İzmir province, as shown in Figure 5.36. These stone walls are generally used to provide a buffer area between the cut slopes and highway to obstruct or retard the shallow failures to reach the highway. Regardless of the height of these stone walls, no seismically-induced deformations or failure was observed on the highway connecting Menderes to Gumuldur.

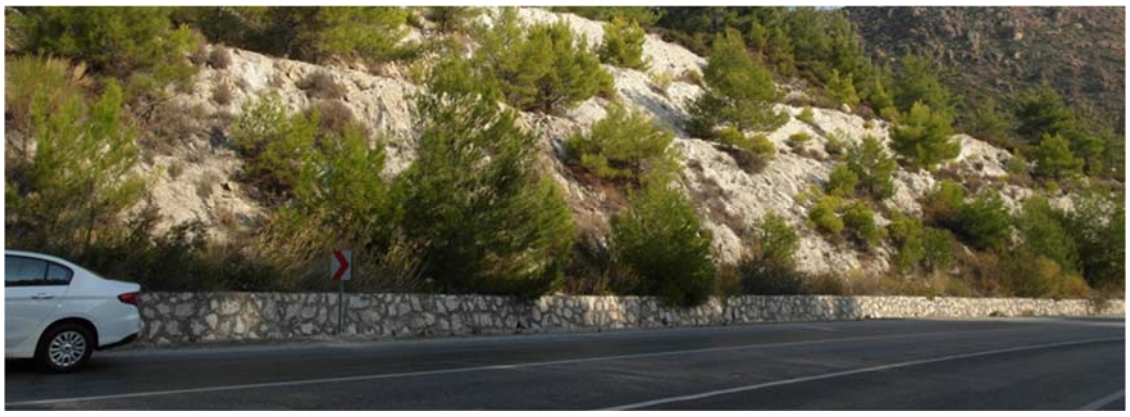

Figure 5.36. Short, stoned retaining walls on the toe of the highway cuts between Menderes and Gumuldur in the south of İzmir city center.

Figure 5.37 shows the sides of the spillway channels of the dams in the region. No sign of any structural damage was likewise observed on these walls.

(a) (b)

(c) (d)

Figure 5.37. (a) Wall on the end of spillway chute of Kavakdere Dam, and side walls of spillways of (b) Urkmez Dam, (c) Tahtalı Dam, and (d) Gumuldur Dam

Figure 5.38 shows the sidewalls of the river canal in Sıgacık Marina, hit by the tsunami after the earthquake. No structural distress can be observed on these walls, which suggests that the severity of shaking was modest despite its proximity to the rupture. Additionally, no signs of liquefaction or permanent deformations were reported.

Figure 5.38. Sidewalls of the river canal in the Sıgacık Marina (Photo: Courtesy of Gurel Özdemir). (38°11'33.86"N 26°47'4.07"E 14:16 / 31.10.2020)

The lack of failed or damaged retaining systems is not surprising, since this event produced less severe shaking intensities than the design basis levels. More specifically, in general, the seismic stability of retaining walls has been analyzed in design assessments by considering a seismic coefficient (k_h) equal to half of peak ground acceleration (PGA), or 20% of spectral acceleration for a short period range (or, for a period of 0.2 sec) of the design spectrum. Hence, for İzmir, a seismic coefficient value of 0.2 (k_h=0.2) has been generally presumed in seismic analysis and design considering a seismic hazard level expressed by the return period of 475 years for being exceeded, due to the seismic hazard map of Turkey that took effect after the year 1996. The recorded PGA during the seismic event and spectral amplitudes on response spectra of accelerograms point out a less severe shaking intensity than that considered for seismic design of the retaining walls.

No relevant data are available for the Samos and Chios islands.

5.5.2 Quay walls

Performance of Quay Walls at Samos and Chios ports. This part focuses on the performance of the main ports of Samos island, and to a lesser extent on the performance of the main port of Chios island, where a member of the Greek reconnaissance team happened to be present when the earthquake struck.

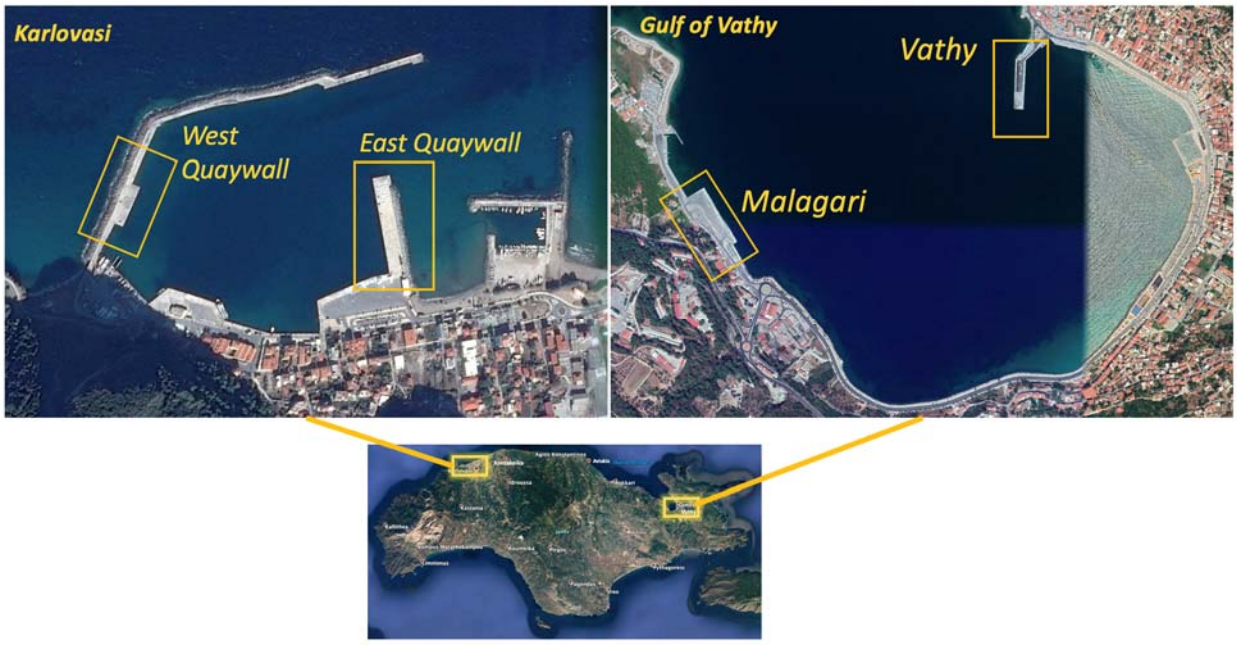

Figure 5.39. Overview of ports of interest in Samos where significant earthquake damage was observed. Annotations indicate the names assigned for ease of reporting herein.

The ports of Vathy and Karlovasi (Figure 5.39) are the two main gates of ferry connection between Samos and the mainland, as well as the rest of the islands in NE Aegean Sea and the Dodecanese islands. Both ports are situated at the northern part of Samos and suffered damage due to the earthquake. There is also a smaller port, Kokkari, which is located in-between the Vathy and Karlovasi ports. That port was also affected by the earthquake; however, the economic impact of the damage was less important relative to that of the other two ports. At the southern part of the island, there are some other ports, at Pythagorio, Iraion, and Marathokampos bay, that were less affected by the earthquake (EAEE).

Ports of Vathy. In Vathy (Figure 5.39 top right), port installations are split between two facilities: the eastern (old) port and the western (new) port - also known as the "Malagari" port, due to its proximity to the Malagari area that is situated about 1 km northwest. (For liquefaction effects at Malagari, see Section 5.3.2).

The eastern (old) port is founded on alluvial deposits consisting mainly of clayey-sandy materials, sands, gravels and pebbles. This is shown in Figure 5.40, where part of the geological map of Samos published by HSGME, is presented. In the same Figure, a number of boreholes on the specific geology are superimposed.

Although all boreholes have been drilled through the same alluvial deposits, there is a clear pattern that can be observed as one moves alongshore, from east (BH 1) to west (BH 4 and BH 5): If continuous, the layer of sandy silt or silty sand (ML-SM) emerges at shallower depths and also gets thicker (Fig. 5.41). However, given the distance between Vathy and Malagari as well as the relative depth and thickness of the ML-SM layer in each location, it is also possible that this is not the same layer across the sites. The associated SPT blow counts are extremely low (essentially zero), which indicates very low strength and high compliance. As the associated materials are non-plastic and saturated, this provides evidence of susceptibility to liquefaction.

Figure 5.40. Detail of the geological map of Samos, according to the Hellenic Survey of Geology and Mineral Exploration (HSGME). A number of boreholes are shown, carried out on the same geology (al2).

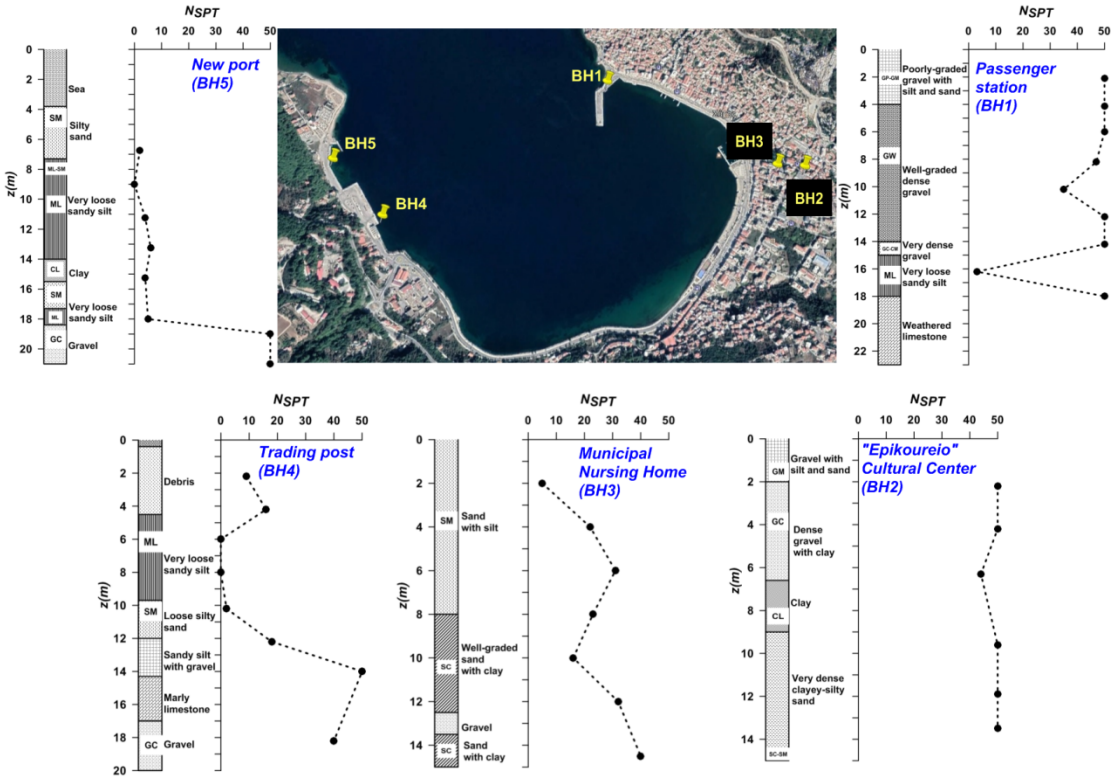

Figure 5.41. Four geotechnical borehole logs (BH1, BH2, BH3, BH4) alongshore from the eastern (old) port to the western (new) port at Vathy *(courtesy of G. Milionis – modified by Em. Rovithis).* One offshore borehole (BH5) at the NW edge of the new port (*kindly provided by the Ministry for the Environment, Physical Planning and Public Works of Greece – modified by Em. Rovithis)*.

The jetty of the eastern (old) port experienced extensive longitudinal and transverse open cracks - several centimeters wide - whilst the backfill behind the quay wall experienced a subsidence that locally exceeded 50 to 60 cm (Fig 5.42). In the upper part of the figure, traces of gravels and sand are visible behind the quay wall. These might be remnants of ejecta partially washed out by the tsunami. The presence of ejecta could be the result of liquefaction of a very loose sandy silt layer located 15 to 18 m deep, right beneath the backfill material (Fig. 5.42). Similar observations of ejecta behind quay walls have been made in many previous earthquakes (Professor G. Bouckovalas – *personal communication*), even in the absence of any native liquefiable soil layer. As such, any observed ejecta may be due to liquefaction and wash out of a loosely deposited fine silty-sand phase which fills the voids of a typically much coarser backfill gravel skeleton that does not participate in the load-carrying capacity of the wall (Professor G. Bouckovalas – *personal communication*). This could explain the lack of excessive displacements and rotations of the wall towards the sea. Construction records from the said ports and further investigations can elucidate this further.

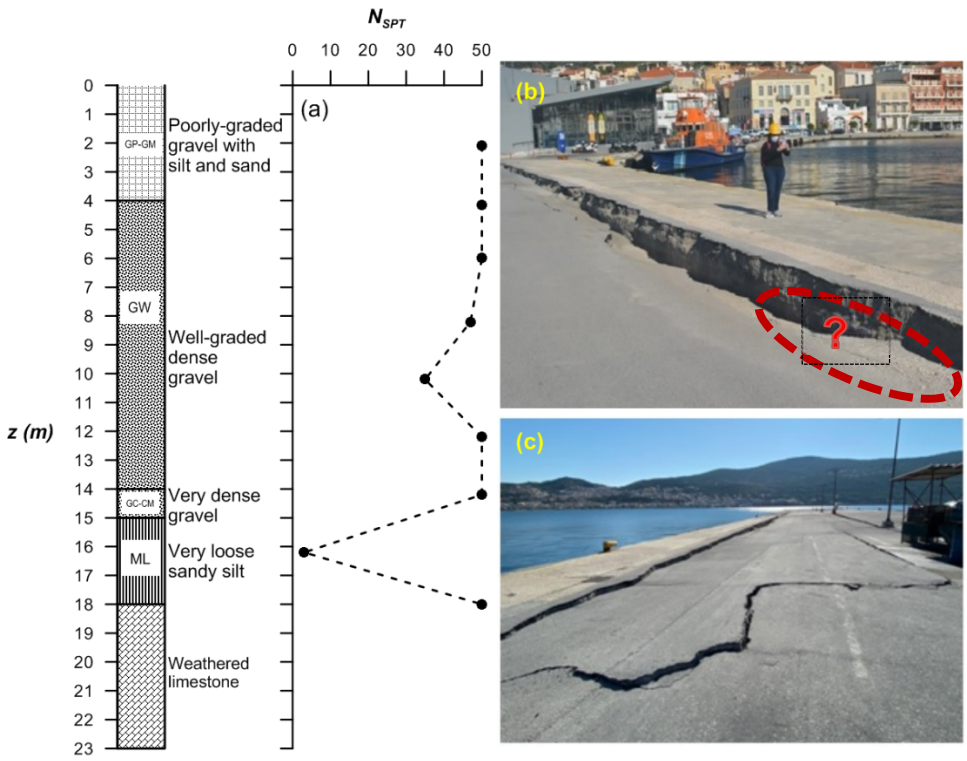

Figure 5.42. Top right (b): subsidence of backfill material behind the quay wall at the eastern (old) port, measuring up to 60 cm. Down right (c): 10 – 15 cm wide longitudinal and transversal open cracks, located on the pavement over the backfill material, in contact with the quay wall. Left part: a crude log of borehole S-1 located at the jetty of the old port where the liquefiable layer of the very loose sandy silt layer is located at a depth of 15 m (*borehole kindly provided by G. Milionis - elaboration by Em. Rovithis)*

The previous observations and arguments are further strengthened by the magnitude of the recorded accelerations. It is indeed questionable whether the accelerations recorded on that site were strong enough to force the liquefiable loose sandy silt get ejected from a depth of 15 to 18m to the surface. These doubts are reinforced by information from the opposite side of the port, i.e. the western (new) port where the very loose to very soft layer of silty sand to sandy silt (SM-ML) does not provide any evidence of severe/extensive liquefaction. This seems to be the case, despite the layer at hand being thicker and shallower, as well as similar to that in the Malagari site (situated about 400 m NW from the new port – see Section 5.3.2).

On the basis of the above data, it is possible that the upper 15 m of borehole BH1 is material that has been superimposed over the layer of very loose sandy silt, which most likely is the preexisting natural layer (often found in ports and bays). This material appears highly deformable, with very low bearing capacity, so that cracks and deformations might have already existed. Discussions with the local port engineers, revealed that the pavement was mildly cracked prior to the earthquake (pers. communication with Mrs. Sechioti). If this is indeed the case, then most probably the cracks might have simply further opened/intensified after the earthquake. Also, it

needs to be verified whether the traces of sand and gravel shown in Fig. 5.42 are 1) ejecta from a distinct layer that liquefied, 2) ejects from a finer sand portion in the coarser skeleton of the backfill, or 3) just a natural product of friction and bouncing between the backfill material and the quay wall following their detachment. Given the preliminary observations and the experience for other earthquakes in the broader area and their effects on similar infrastructure, it is more likely that the latter two explanations are the most plausible ones.

The western (new) port of Vathy, is the commercial port, where passenger and car ferries are mainly serviced, as well as smaller ships. The total length of the coastal quay wall is about 500 m along the NW-SE direction. Some basic geological features and relevant geotechnical data have already been presented in Figures 5.40 and 5.41. Based on these data, a remediation study and the quay wall and the port infrastructure was put together on December 2017 (Triton Consulting Engineers, 2017). Figure 5.43 shows the quay walls, as part of the recent rehabilitation project (Triton, 2017).

According to Triton (2017), the jetty of Malagari is a gravity structure made of overlapping layers of artificial boulders (5 in each column). On the crown there is an in-situ cast superstructure. The quay wall is founded on a rockfill prism, whose external side along the seaside is protected by natural boulders. A representative sketch of a typical cross-section of the quay wall is depicted in Figure 5.44 (Triton, 2017). The technical issues encountered before the earthquake mainly relate to scouring of the quay walls which can be attributed to leakage of the relief prism and upstream backfill material, leading to substantial subsidence behind the quay walls, opening of cracks parallel and transversely to the sea front, and a mild rotation of some quay wall columns towards the sea. The remedial measures outlined in the 2017 report were probably in progress (yet, not completed) when the earthquake struck.

Figure 5.43. Satellite view over infrastructures of the western (new, Malagari) port, Vathy (Triton, 2017)

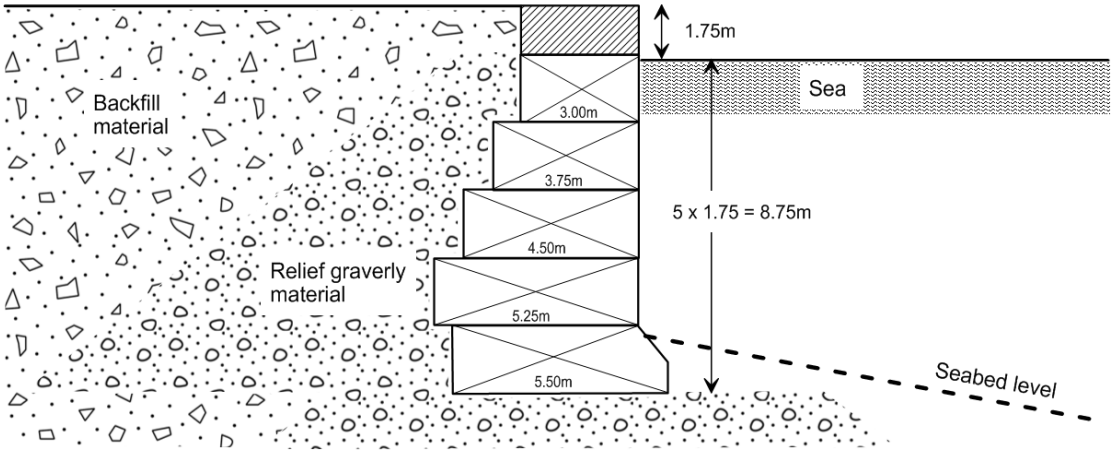

Figure 5.44. Typical cross-section of the quay wall of the new (Malagari) port of Vathy in section A - B of Figure 5.43. (Out-of-scale drawing, modified after Triton, 2017)

Figure 5.45 illustrates (a) a view of the pre-existing open joints between the quay wall and the backfill material and the subsidence of the backfill material behind the quay wall about 3 years ago (Triton, 2017), and its comparison to (b) its condition immediately after the earthquake (HAEE reconnaissance report, 2020). Interestingly, the earthquake damage observed are quite similar but most probably intensified by the earthquake. At the time the site was visited by the HAEE team, the construction operations in response to the Triton (2017) study were ongoing.

Hauled construction materials did allow the team to delineate between those and any potential liquefaction-induced ejecta at the site. Nevertheless, given the geotechnical data (see Fig. 5.41) liquefaction might have taken place on a rather limited scale and probably worsened the already existing damages. In addition, the quay walls at this particular site are massive and consequently subject to large inertia forces mostly due to their own mass and not due to seismic earth pressures from the backfill. Consequently, it is likely that the quay walls at the Malagari port rotated somewhat outwards during the earthquake, thus widening any pre-existing gaps (Triton 2017) and also leading to some settlement of the backfill next to the wall. As such, it is rather unlikely that the present picture of the quay wall damages can be attributed entirely to liquefaction and dynamic settlement.

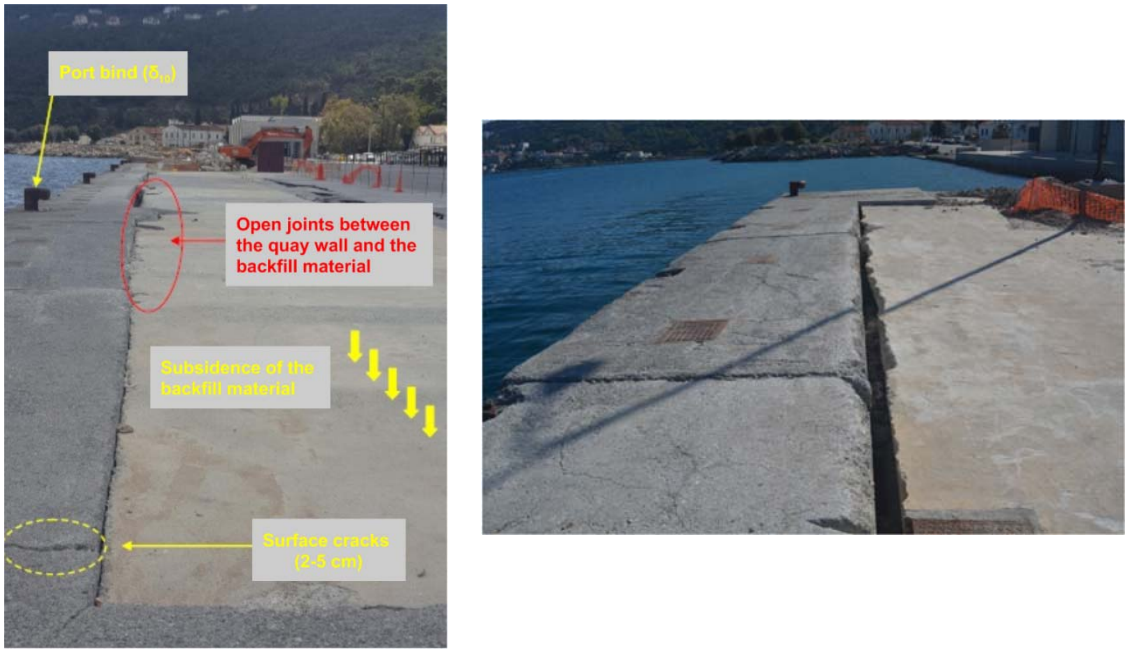

Figure 5.45. View of the quay wall at new (Malagari) port, Vathy, from NW to SE direction: (left) photo taken 3 years before the earthquake (Triton, 2017); (right) photo taken a few days after the earthquake (HAEE reconnaissance report, 2020)

Port of Karlovasi. The Karlovasi port is second only to that of Vathy for the commercial and economic life of the island. In Fig. 5.46, a satellite view of the port is presented showing both east and west quay walls.

Karlovasi is founded on the same geological structure as Vathy, al2 i.e. alluvial deposits consisting mainly of clayey-sandy materials, sands, gravels and pebbles. This is shown in Figure 5.47, where part of the detailed geological map of Samos Island published by the Hellenic Survey of Geology and Mineral Exploration (HSGME), is presented.

Figure 5.46. Satellite view of east and west quay walls of Karlovasi port.

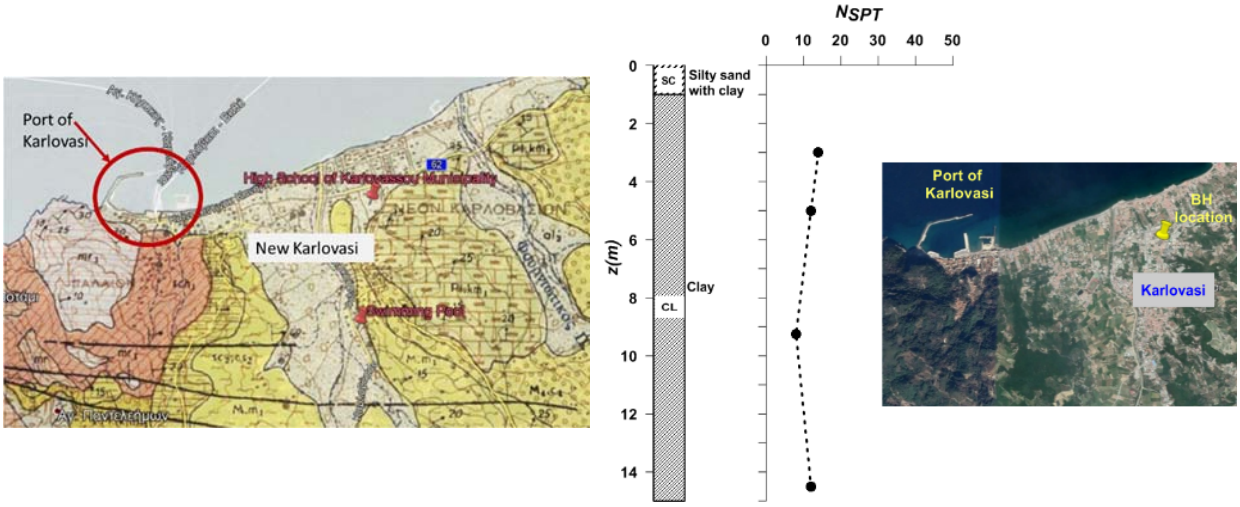

Figure 5.47. (left) Part of the detailed geological map of Samos Island, published by the Hellenic Survey of Geology and Mineral Exploration (HSGME) with the location of two (2) geotechnical boreholes on the same geological formation (al2). (right) Borehole log next to the High School of Karlovasi (Gymnasion), at a distance of about 2 km from the east quay wall of the port and 550 m from the seafront.

Available data from a borehole close to the high school of Karlovasi, indicates that the soil consists of grey to grey-brownish medium stiff to stiff sandy clay of medium plasticity (excluding the top 1m that consists of silty sand with a few gravels). The distance to the closest part of Karlovasi port (east quay wall) is about 2 km; therefore, it is difficult to extrapolate as to the subsoil in the port. However, based on the soil layering at Vathy, there is a possibility that the surficial layer of silty sand gets thicker near the seashore. This however, albeit generally true, cannot be reliably deducted without geotechnical data.

The port of Karlovasi suffered damage to both jetties, namely: subsidence of the backfill material (or the subsoil), mild tilting and displacement of the quay walls towards the sea, cracks (both transversely and parallel) to the quay walls. Also, grey-brown ejecta of sand-gravel mixture was found on the west quay wall, which possibly emerged through the cracks. Even in the absence of sufficient data to substantiate the occurrence of liquefaction, it appears that liquefaction is a reasonable scenario. This possibility is reinforced considering that the surface layer of grey-brownish silty sand identified at the high school area, seems to be continuing and getting thicker close to the sea shore. However, without more extensive geotechnical data, it is impossible to draw conclusions and this is only a hypothesis is in accordance to the subsurface structure at Vathy. Last but not least, the construction details of each port need to be accounted for since the placement of a backfill under “wet” or “dry” conditions can severely affect its dynamic response in later

Figure 5.48 illustrates both jetties (east and west), as well as ejecta observed on the western quay wall. Nevertheless, it is hard to tell whether the cracks and subsidence/tilting patterns are earthquake induced, or merely preexisting gravity-induced effects.

Figure 5.48. (top left) east quay wall of Karlovasi port, (top right) west quay wall of Karlovasi port, (bottom left) ejecta on the west quay wall, presumably product of liquefaction occurrence, and (bottom right) a detailed view of the ejecta, brownish to grey color, mostly sandy and silty with some gravels (aerial photographs courtesy of I.N. Spyrou and Prof. K. Ziotopoulou – *to not be reproduced without permission from Prof. Ziotopoulou*).

Port of Kokkari. Kokkari is a small village in the northern part of Samos, situated about 10 km NW from Vathy. It has a small port mainly serving fishing boats and small yachts. The reconnaissance team of HEAA visited Kokkari and observed that the quay wall had suffered severe subsidence, 10 to 20 cm wide open cracks alongside the sea front, and mild tilting towards the sea, as shown in Figure 5.49. It is unclear whether the deformations were preexisting i.e. due to the low quality of the quay wall construction and the lack of protection of its underwater part from scour. Problems related to low bearing capacity and differential settlements due to a soft and compressible surface soil layer at the foundation of the jetty cannot be excluded. However, no clear traces of liquefaction were detected following the earthquake.

Figure 5.49. (left) clear trends of differential subsidence of the quay wall of Kokkari port with wide open cracks alongside and transversely, (right) close view of an open crack of 10 to 15cm alongside the sea front (HAEE *reconnaissance report, 2020*).

Port of Chios Island. Earthquake-induced failures were observed in the port of Chios island, situated approximately 80 km from fault, referring mainly to surface cracks of considerable width and depth (Fig. 5.50a), as reported in the post-earthquake preliminary report by Pelekis and Roumelioti (2020). At specific locations these cracks were about 10-15 cm wide and about 40 cm deep (Fig. 5.50b). Such type of failures in the port of Chios may indicate soil liquefaction that was marginally triggered during the earthquake, and ensuing lateral spreading effects towards the shoreline, as suggested by Pelekis and Roumelioti (2020). The existence of inclined strata below the filling material of the quay walls and pre-earthquake damage due to gravity loads (e.g. scour of its foundation) should be considered when interpreting the observed seismic behavior.

The possibility of marginal triggering of soil liquefaction was reinforced following a series of MASW field tests, which revealed the existence of soft/low-strength surficial soil layers with shear wave propagation velocity at about 100 m/s. A preliminary Vs-based assessment of the safety factor against soil liquefaction revealed a potential triggering of the phenomenon during the M_w=7.0 event for PGA's above approximately 0.12g (Fig. 5.51). Details may be found in the above reference.

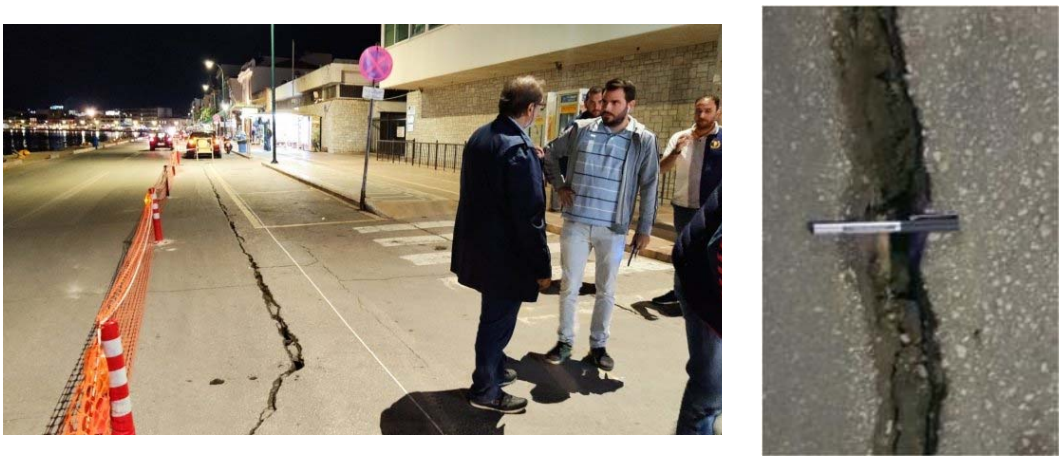

(a) (b)

Figure 5.50. (a) Earthquake-induced surface cracks parallel to the quay wall front in the port of Chios; (b) Close view of 10-15 cm wide and 40 cm deep surface cracks.

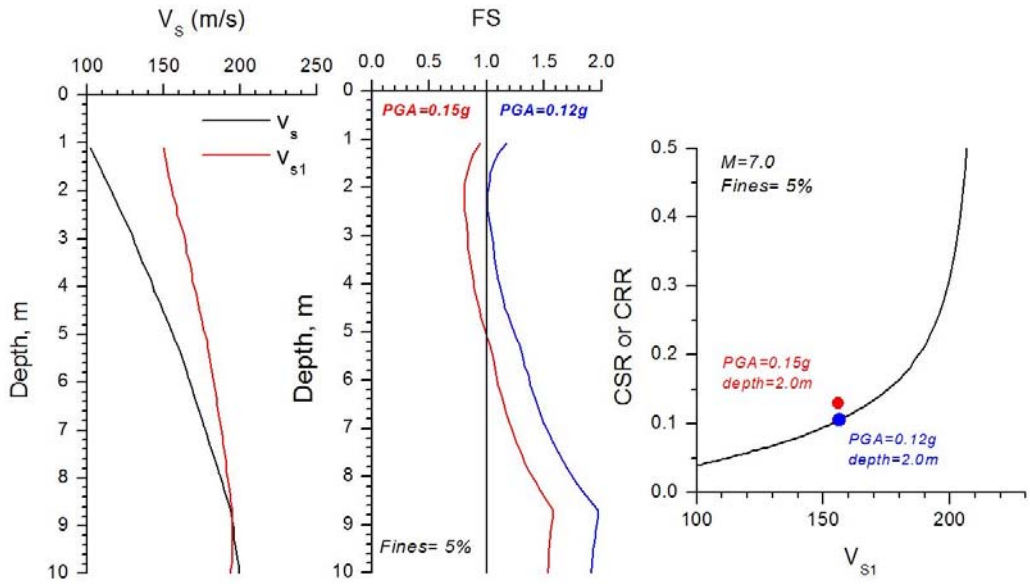

Figure 5.51. Preliminary Vs-based assessment of the safety factor against soil liquefaction at the depth of 2.0m for PGA at (a) 0.15g and (b) 0.12g (Pelekis and Roumelioti, 2020).

As discussed in more detail in Chapter 2, during the post-earthquake survey, no excessive settlement or induced-damage on the rubble mound breakwaters, or on the armor layer of any rubble mound protection, was observed along the Anatolian coastal line. Additionally, for the berthing and mooring inside the harbors, gravity-type quay walls, composed of concrete blocks and constructed in fishery harbors and commercial and cruise ports, and floating piers in the

Marinas, were inspected. Although these port structures are relatively old, visual observations have again confirmed the lack of seismic shaking- and geotechnical-induced damages.

5.6 Geotechnical Performance of Metro Tunnels, Bridges, Viaducts and Highways

Metro tunnels, most of which were located within 10-20 m depths, occasionally in soil formations or weathered rock were reported to be in uninterrupted service after the event. Additionally, although Naldoken and Zafer Payzın viaducts, and Turan and Egemak bridges are located on relatively soft and/or potentially liquefiable soils, no geotechnical or foundation-induced damages were reported at these bridges, viaducts, along with highways. The structural performance details of these are presented later in Chapter 7.

Due to lack of relevant infrastructure, no such effects were observed in Samos and Chios islands.

5.7 Major Findings and Conclusions

From a geotechnical engineering point of view, consistent with the proximity to the source and elevated intensity levels, the majority of the documented permanent ground deformation, liquefaction, and slope failure cases are concentrated in Samos Island. However, equally importantly, their lack was also documented on the Anatolian side. While this can be mainly attributed to the distance from the source, more research is needed to identify the relevant factors of safety.

Followings are the major geotechnical performance observations from the Anatolian side after this event:

i) Many residential buildings have been investigated in the center of Urla, Cesme, Kusadasi, Gumuldur, Izmir-Konak, Izmir-Bayrakli regions. No foundation-induced failures, evident by excessive total or differential settlement or tilting, or bearing capacity exceedance, were mapped or reported.
ii) Along the Aegean coasts of Anatolia and inland, no surface manifestation of seismic soil liquefaction triggering was observed or reported, despite the presence of liquefaction susceptible alluvial basins.
iii) However, at 45-50 km away from the rupture, along the shores of Icmeler and Gulbahce districts, sand boils were observed. These sites were close to Gulbahce fault zone, and the presence of artesian pressures along with hot water springs are believed to contribute to the observed soil ejecta formation.
iv) A few rockfalls were observed by the benches of highways. Some potential and existing landslide sites were visited, but no signs of seismically induced movements were documented. Similarly, deep excavation support systems in Izmir were reported to have performed well.

v) There are no reported failures of engineered retaining structures in Turkey. During the reconnaissance studies, a limited number of non-engineered tilted and/or partially collapsed safety walls were observed.
vi) Similarly, despite tsunami-induced damage in port facilities, no geotechnical engineering related permanent ground deformations or failures are reported for quay walls.
vii) Metro line in Izmir were reported to be in uninterrupted service after the event, and no permanent deformations or failures were reported.

The geotechnical performance observations from the Samos and Chios islands after the earthquake event of the 30th of October, 2020 are:

i) Although located only about 10 km from rupture, the towns of Vathy and Karlovasi in Samos were rather lightly affected by the earthquake, with relatively few collapsed or heavily damaged buildings. With the possible exception of a small set of structures (e.g. at Vyrsodepsia near Karlovasi) which were damaged due to lateral soil spreading, no earthquake-induced damage was observed on foundations.
ii) Several manifestations of liquefaction were observed along the north coast of Samos, including Vathy (Malagari site), Karlovasi (Vyrsodepsia), and possibly the ports. Nevertheless, the associated phenomena were not spectacular, which may suggest marginal liquefaction. This is remarkable given the intensity (PGA's > 0.2g) and duration (> 10 s) of ground motion.
iii) A number of landslides and rockfalls (6 are documented in this Chapter) occurred in the north part of Samos. Again, the relevant phenomena were not particularly severe and probably relate to precariously standing rocks and slopes. Such effects have been observed in other recent earthquakes in Greece (Margaris et al 2008, Nikolaou et al 2014)
iv) There are no reported failures of engineered retaining structures and other infrastructure (e.g. dams, bridges, viaducts, tunnels) in Samos or Chios. This can be mostly attributed to the lack of such infrastructure in the islands.
v) Port facilities in Vathy, Karlovasi and Kokkari were significantly affected by the earthquake, with considerable displacements/rotations of quay walls towards the water, pavement cracks and backfill settlements behind the walls, and some signs of ejecta associated with liquefaction. Nevertheless, it is unclear if the primary source of those movements is soil liquefaction – or simply the significant inertia of those structures, in combination with the cyclic mobility of soft (mostly cohesive) soil layers under the walls, and the unilateral nature of loading and ensuing response.
vi) Significant movements, including cracks on the pavement, were observed on the quay wall in the port of Chios island, about 80 km from fault. Again, it is unclear if the movement can be attributed soil liquefaction or the inertia of the quay walls per se.

Acknowledgements

The authors are indebted to Professor George Bouckovalas of the National Technical University of Athens, Prof. Dr. Atilla Ansal of Ozyegin University, Istanbul, Prof. Dr. Ayfer Erkin of Istanbul Technical University, Prof. Dr. Bilge Siyahi of Gebze Technical University, Istanbul for their valuable review of the Chapter, and their insightful comments that significantly improved many of the discussions presented herein, particularly those pertaining to the seismic performance of foundation systems and seismic response of port facilities.

The authors would also like to deeply thank external contributors who kindly provided data and assistance with carrying out field measurements included in this Chapter. In this regard, George Milionis, Geologist, provided the boreholes log data for BH1, BH2, BH3 and BH4 shown in Figure 5.39 while the borehole log data for BH5 shown in the same figure was provided by Peggy Sechioti, employee of the Greek Ministry of Infrastructure and Transport. MASW field measurements by Prof. P. Pelekis were supported by Vasilis Christopoulos, laboratory member, and Paraskevi Paliatsa, postgraduate student, of the Civil Engineering Department, University of Patras. The members of Middle East Technical University, Ankara were partially funded by reconnaissance funds of METU, which is greatly appreciated.

The authors are also thankful to Professor K. Antonopoulos and Gurel Ozdemir for sharing photographs from local earthquake damages. Their valuable contribution is gratefully acknowledged. Financial support to the U-Patras team was provided by HAEE/ETAM. Prof Katerina Ziotopoulou's field reconnaissance and participation was supported by the NSF-sponsored Geotechnical Extreme Events Reconnaissance (GEER) association. The work of the GEER Association, in general, is based upon work supported in part by the National Science Foundation through the Geotechnical Engineering Program under Grant No. CMMI-1826118. Any opinions, findings, and conclusions or recommendations expressed in this material are those of the authors and do not necessarily reflect the views of the NSF. Any use of trade, firm, or product names is for descriptive purposes only and does not imply endorsement by the U.S. Government. The GEER Association is made possible by the vision and support of the NSF Geotechnical Engineering Program Directors: Dr. Richard Fragaszy and the late Dr. Cliff Astill. GEER members also donate their time, talent, and resources to collect time-sensitive field observations of the effects of extreme events.

References

E. Lekkas, S. Mavroulis, M. Gogou, G.A. Papadopoulos, I. Triantafyllou, K.-N. Katsetsiadou, H. Kranis, E. Skourtsos, P. Carydis, N. Voulgaris, P. Papadimitriou, V. Kapetanidis, A. Karakonstantis, I. Spingos, V. Kouskouna, I. Kassaras, G. Kaviris, K. Pavlou, V. Sakkas, A. Karatzetzou, N. Evelpidou, E. Karkani, I. Kampolis, P. Nomikou, D. Lambridou, P. Krassakis, M. Foumelis, C. Papazachos, A. Karavias, D. Bafi, T. Gatsios, O. Markogiannaki, I. Parcharidis, A. Ganas, V. Tsironi, I. Karasante, D. Galanakis, K. Kontodimos, D. Sakellariou, N. Theodoulidis, C. Karakostas, V. Lekidis, K. Makra, V. Margaris, K. Morfidis, C. Papaioannou, E. Rovithis, T. Salonikios, A. Kourou, M. Manousaki, T. Thoma, N. Karveleas (2020). The October 30, 2020 Mw 6.9 Samos (Greece) earthquake. Newsletter of Environmental, Disaster and Crises Management Strategies, 21, ISSN 2653-9454.

HAEE – Vadaloukas, G., Vintzileou, E., Ganas, A., Giarlelis, C., Ziotopoulou, K., Theodoulidis, N., Karasante, I., Margaris, B., Mylonakis, G., Papachristidis, A., Repapis, C., Psarropoulos, P. N., and Sextos, A. G. (2020). Samos Earthquake of 30th October, 2020. Preliminary Report of the Hellenic Association for Earthquake Engineering, Athens, Greece. https://doi.org/10.13140/RG.2.2.22609.76644

Hellenic Survey of Geology and Mineral Exploration (H.S.G.M.E) (2020) Immediate response of HSGME after the 30 October 2020 Samos earthquake. Short note released on 31/10/2020 (in Greek).

Makra K., Rovithis E., Riga E., Raptakis D. & Pitilakis, K. (2020). A note on the strong ground motions recorded in Izmir (Turkey) during the October 30th, 2020 M 7.0 Aegean Sea earthquake: The role of basin effects. A non-peer reviewed preprint uploaded to ResearchGate (November 29, 2020), DOI: 10.13140/RG.2.2.34517.65762

Margaris V, C. Papaioannou, N. Theodoulidis, A. Savvaidis, N. Klimis, K. Makra, C. Karakostas, V. Lekidis, T. Makarios, T. Salonikios, M. Demosthenus, G. Athanasopoulos, G. Mylonakis, C. Papantonopoulos, V. Efthymiadou, P. Kloukinas, I. Ordonez, V. Vlachakis, and J. P. Stewart (2008)."Preliminary report on the principal seismological and engineering aspects of the Mw = 6.5 Achaia-Ilia (Greece) earthquake on 8 June 2008" GEER Association Report No. GEER-013, Web report

Nikolaou et al, “Geotechnical Aspects of the M = 6.1 January 27 and February 03, 2014, Cephalonia, Greece, Earthquakes” GEER Association Report No. GEER-034 Web report

P. Pelekis and Z. Roumelioti (2020), “Preliminary results of an autopsy at Chios port”, Technical report of Patras University for TEE of Chios island, Section of NE Aegean

Papathanasiou, G., Pavlides, S., Christaras, B., Pitilakis, K. (2005) Liquefaction case histories and empirical relations of earthquake magnitude versus distance from the broader Aegean region, Journal of Geodynamics 40 (2005) 257–278, doi:10.1016/j.jog.2005.07.007

Papathanasiou, G., Valkaniotis, S., Chatzipetros, Al., Pavlides, S. (2010) Liquefaction susceptibility map of Greece. Bulletin of the Geological Society of Greece, Vol. 43, 10.12681/bgsg.11314

Papathanasiou, G., Valkaniotis, S., and Pavlides, S. (2018) The July 20, 2017 Bodrum-Kos, Aegean Sea M_w= 6.6 earthquake; preliminary field observations and image-based survey on a lateral spreading site. Soil Dynamics and Earthquake Engineering Vol. 116, pp. 668-680.

Pretell, R. A., Ziotopoulou, K., and Davis, C. (2020). Numerical modeling of ground deformations at Balboa Blvd. in the Northridge 1994 Earthquake. ASCE Journal of Geotechnical and Geoenvironmental Engineering, doi.org/10.1061/(ASCE)GT.1943-5606.0002417

Stewart, J. P., R. B. Seed, and J. D. Bray. 1996. “Incidents of ground failure from the 1994 Northridge earthquake.” Bull. Seismol. Soc. Am. 86 (1): 300–318.

Triton, Consulting Engineers (2017), “Damage repair and reinforcement of the superstructure of the port of Malagari Samos” Final study of port infrastructures, Technical Report, Athens, December 2017.

U.S. Geological Survey (2020). Earthquake Hazards Program accessed November 11, 2020, at URL https://earthquake.usgs.gov/earthquakes/eventpage/us7000c7y0/executive

6. Performance of Hydraulic Structures, Lifelines and Industrial Structures

Chapter Coordinators: Kemal Onder Cetin

Authors:

Middle East Technical University: Kemal Onder Cetin, M. Tolga Yılmaz

Gebze Technical University: Selçuk Toprak

Boğaziçi University, KOERI: Eren Uçkan

State Hydraulic Works (DSI), The General Directorate: Faik Cüceoğlu

Yıldız Technical University: Mustafa Ümit Gümüşay

Pamukkale University: Engin Nacaroglu

Alanya University: Ercan Serif Kaya, Murat Aksel

6.1 Seismic Performance of Hydraulic Structures (Dams)

A group of engineers assembled by the Izmir Regional Directorate of State Hydraulic Works (DSI) (on October 31st) and a reconnaissance team from METU (on November 6) visited dam sites to document the performance of earthfill and rockfill dams, shaken by the event. Figure 6.1 represents the location of Samos Earthquake epicenter and the locations of these dams. This chapter summarizes the findings of these reconnaissance studies on hydraulic structures (dams).

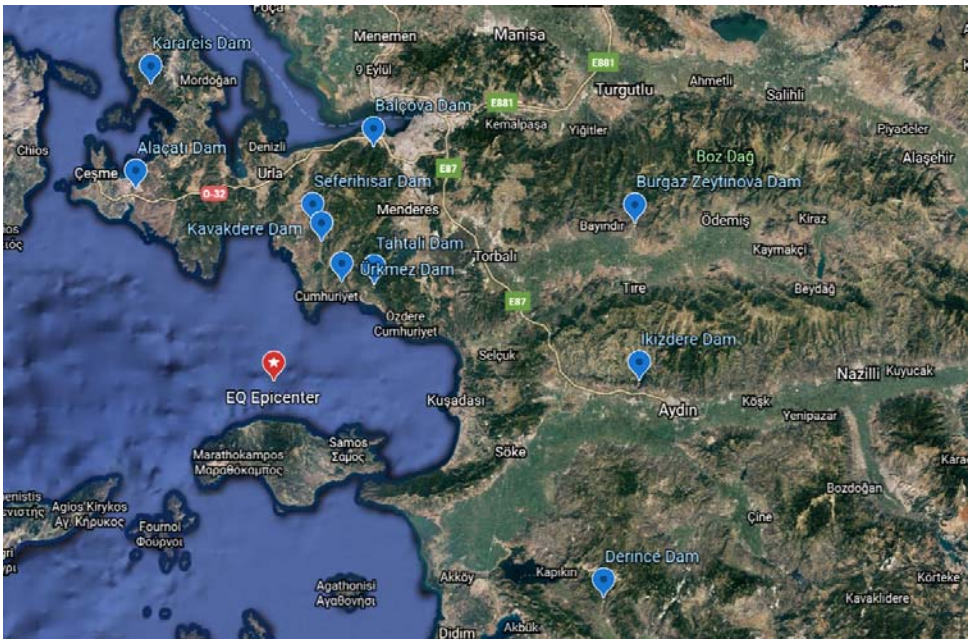

Figure 6.1. The location of dams, close to the epicenter of the Samos-Seferihisar Earthquake

6.1.1 Characteristics of hydraulic structures

Reconnaissance teams visited Urkmez, Tahtali, Kavakdere, Seferihisar, Alacati, Balcova dams, and Menderes-Gumuldur reservoir constructed for drinking/domestic water and irrigation purposes in Kucuk Menderes Basin. Some major characteristics of these dams are summarized in Table 6.1.

Table 6.1. List of inspected dams by DSI reconnaissance team

	Urkmez Dam	**Tahtali Dam**	**Kavakdere Dam**	**Seferihisar Dam**	**Alacati Dam**	**Balcova Dam**
Location (District)	Izmir (Seferihisar)	Izmir (Menderes)	Izmir (Seferihisar)	Izmir (Seferihisar)	Izmir (Alacati)	Izmir (Balcova)
Purpose	Irrigation	Drinking Water	Irrigation	Irrigation	Drinking Water	Drinking Water
Construction Completion (year)	1991	1996	2006	1994	1997	1980
Dam Type	Zoned Earthfill	Clay Core Rockfill	Zoned Earthfıll	Zoned Earthfıll	Zoned Earthfıll	Clay Core Rockfill
Dam Volume (10^3 m^3)	981	-	2,100	1,485	275	1,011
Height from Foundation (m)	44.5	54.5	42	59	17.3	73.4
Total Reservoir Capacity (hm^3)	7.92	-	13.88	29.10	16.61	8.1
Active Storage (hm^3)	7.57	306	13.6	28.18	16.11	7.94
Reservoir Area (km^2)	0.61	25	0.96	1.79	42	0.69
Distance from EQ Epicenter (km)	26.7	32.2	33.9	37.5	54.6	58.5

6.1.2 Strong ground motion records from dam sites

Derince Dam located on Derince River in Muğla is about 91 km from the Samos Earthquake epicenter. In 2015, two accelerometer devices, one on the right abutment bedrock and one on the crest, as shown in Figure 6.2, were installed to monitor the structural behavior and performance of the dam.

The largest recorded peak accelerations during the main shock of Samos Earthquake were 0.080 g and 0.026 g at crest and right abutment, respectively. Strong ground motion acceleration records and pseudo acceleration response spectra (5% damping) taken from these instruments are plotted in Figure 6.3 to 6.5. The significant duration of these records was approximately 19 seconds. Based on these, it was concluded that crest accelerations at Derince Dam were amplified by a factor of 3.

Figure 6.2. Accelerometer configuration on Derince Dam, Muğla (modified from Ateş et al. 2019)

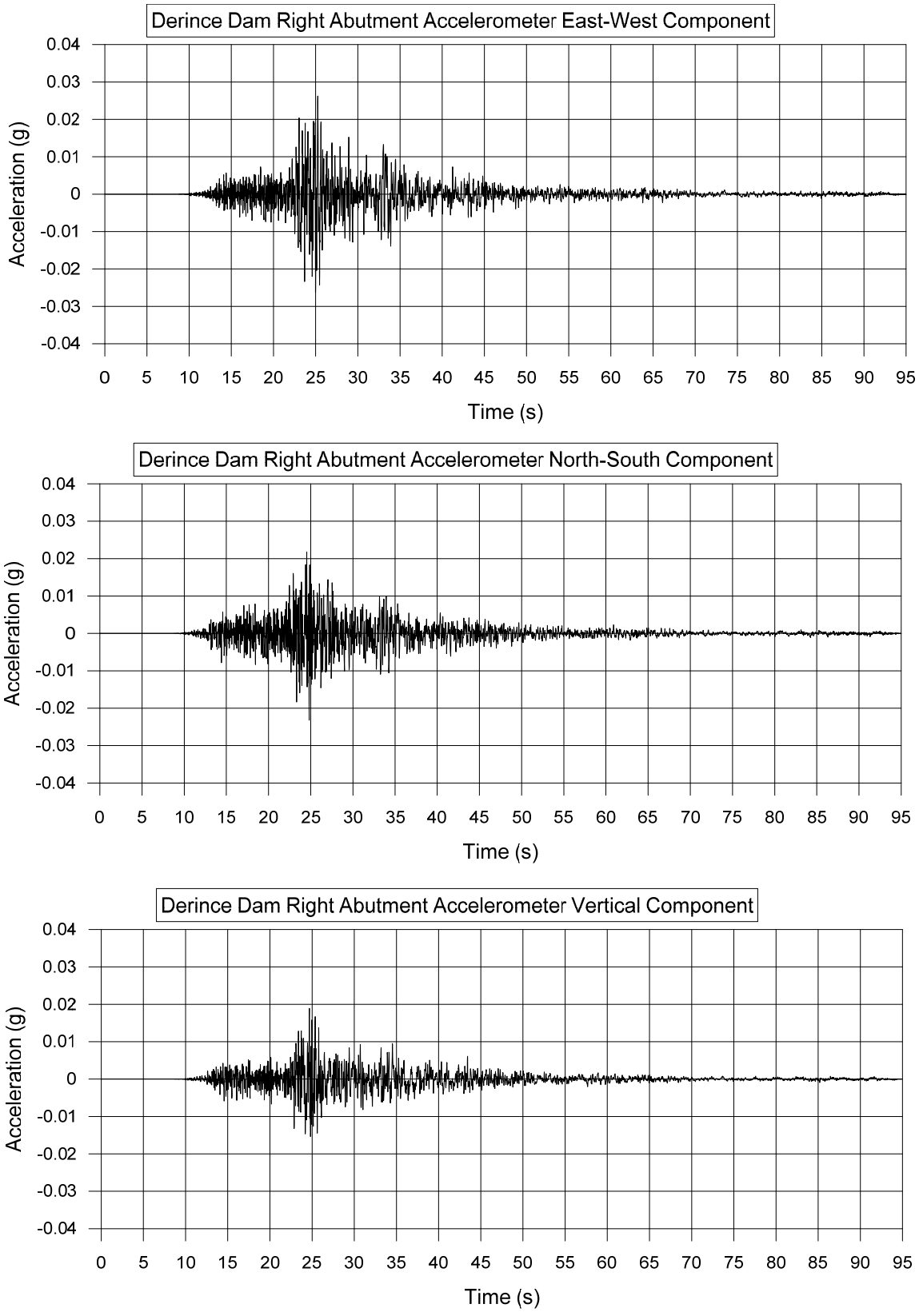

Figure 6.3. Accelerograms from Derince Dam right abutment

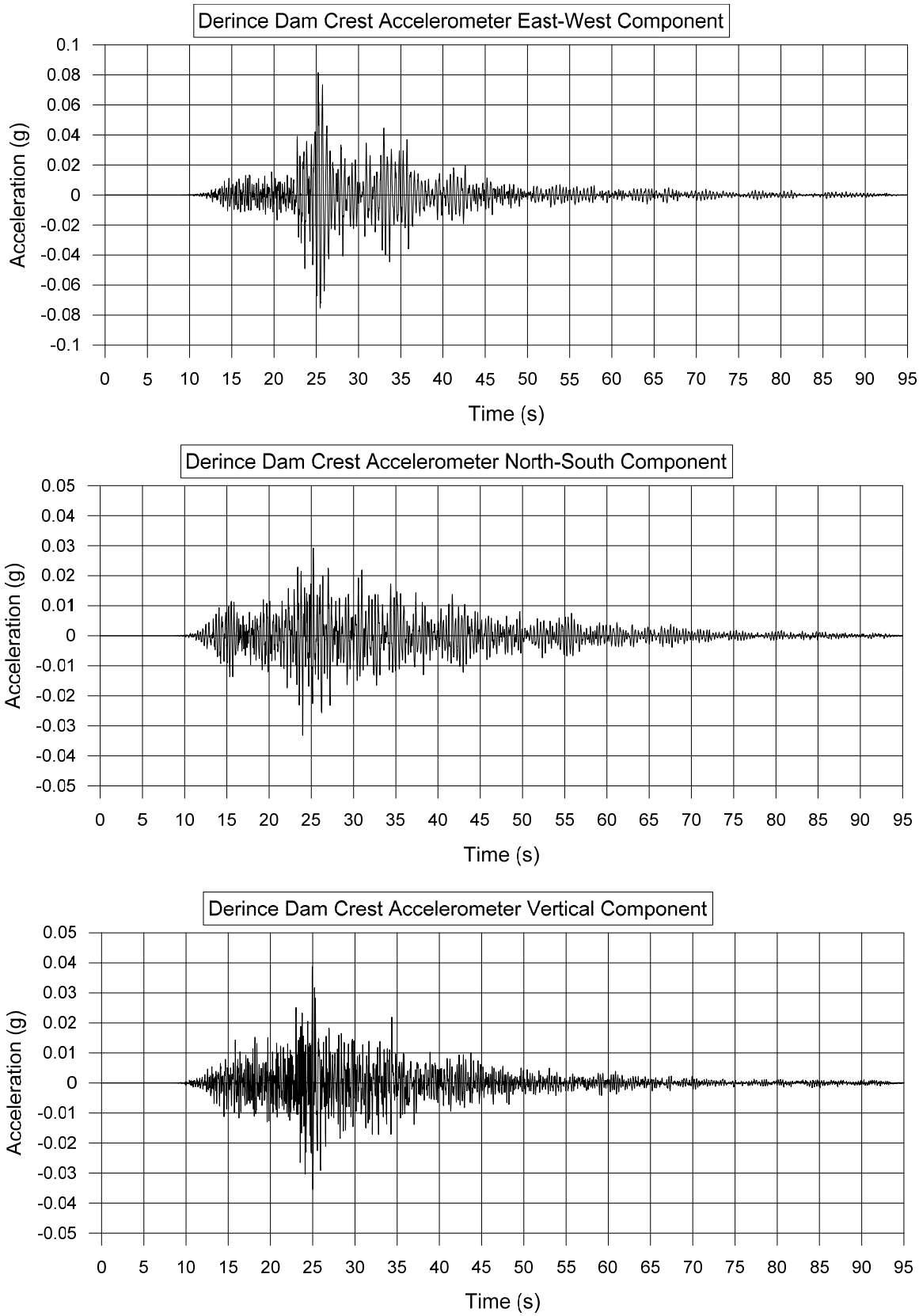

Figure 6.4. Accelerograms from Derince Dam crest

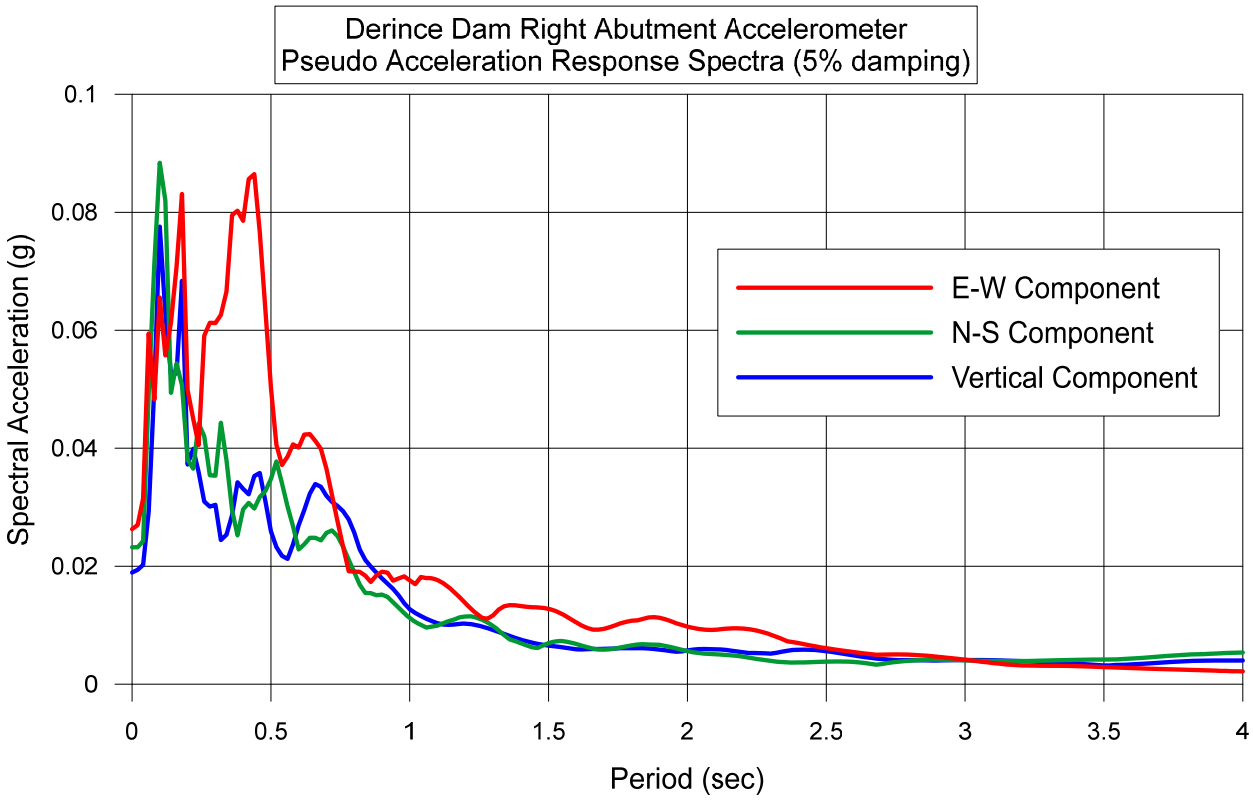

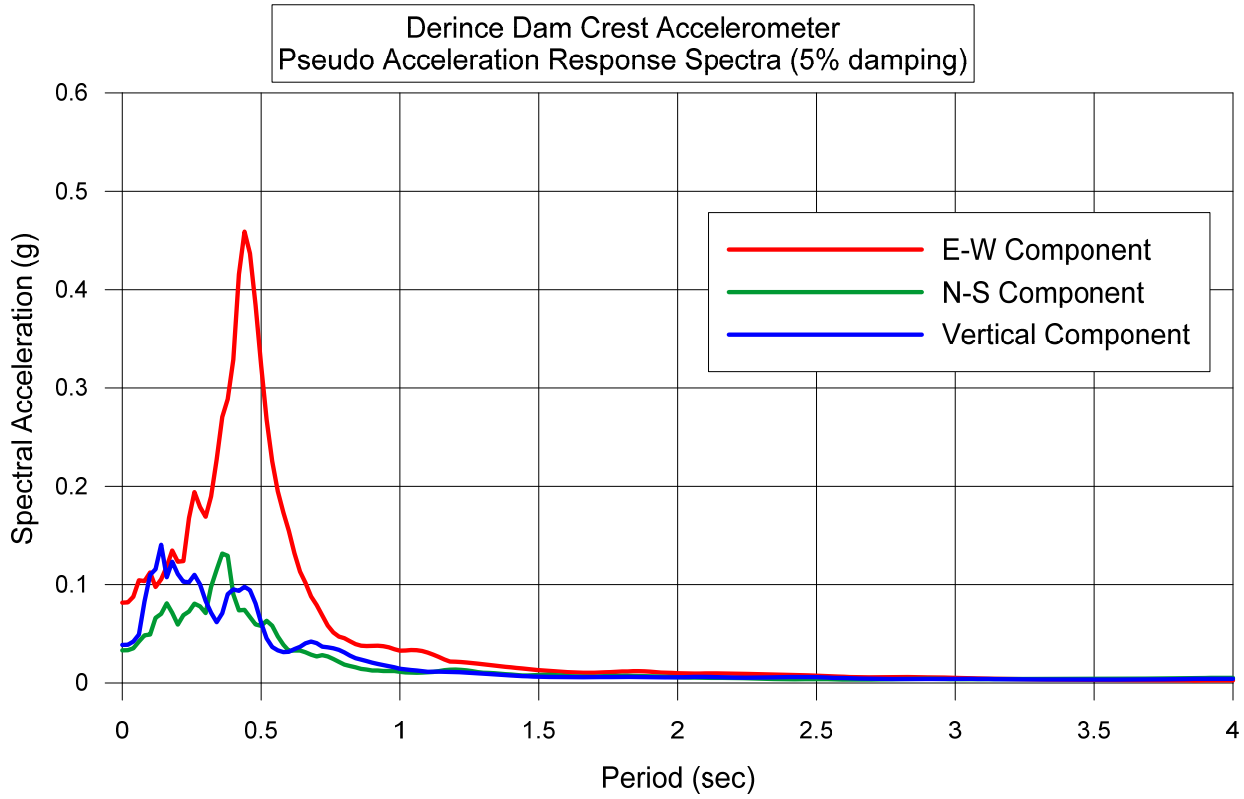

Figure 6.5. Pseudo acceleration response spectra of Derince Dam accelerometer records

6.1.3 Seismic performance of hydraulic structures

During the reconnaissance, the dam body, crest, abutments, upstream and downstream slopes of the dam, as well as auxiliary structures (inlet, spillway, etc.), were investigated along with the evaluation of instrumental and visual inspection data.

Typical cross-sections of Urkmez, Kavakdere, Seferihisar, Alacati, Balcova dams are shown in Figure 6.6 - 6.10. In addition, the views from the crest and spillway of Urkmez, Kavakdere, Seferihisar dams are presented in Figure 6.6 – 6.8. Moreover, the reservoir site, crest, and spillway views belonging to Tahtali Dam can be seen in Figure 6.11 and the Menderes-Gumuldur reservoir view after the event can be seen in Figure 6.12.

After the event, no damage or settlement was observed on the lightning poles and bollards located on the crests. Any falling rocks, bulge, or settlements were observed over the both upstream and downstream slopes. No signs of seismically induced permanent deformations along the dam crests and at the abutments.

Seismic design of the dam was carried out to the DSI design standards; a horizontal peak ground acceleration of 0.11 g at the dam site was reported for Alacati and Urkmez Dam (DSI, 2020). They were tested by equivalent or slightly lower levels than the design basis event ($PGA_{design} \approx 0.11$ g), they performed elastically during the earthquake.

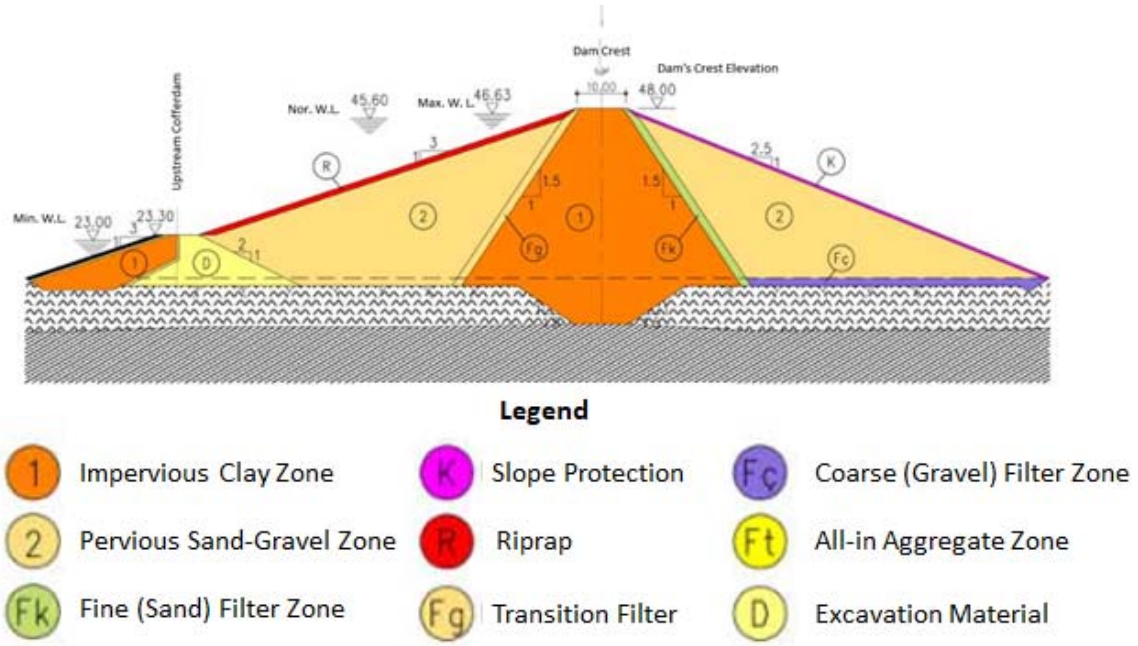

(a)

(b)

Figure 6.6. Urkmez Dam a) typical cross-section (Courtesy of DSI), b) crest and spillway view on November

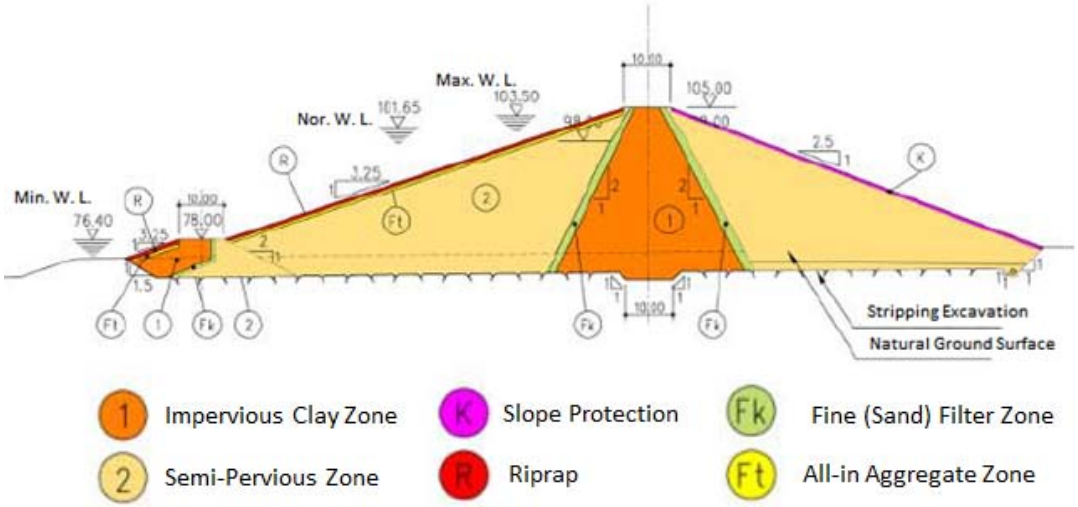

(a)

(b)

Figure 6.7. Kavakdere Dam a) typical cross-section (Courtesy of DSI), b) crest and spillway view on November 6

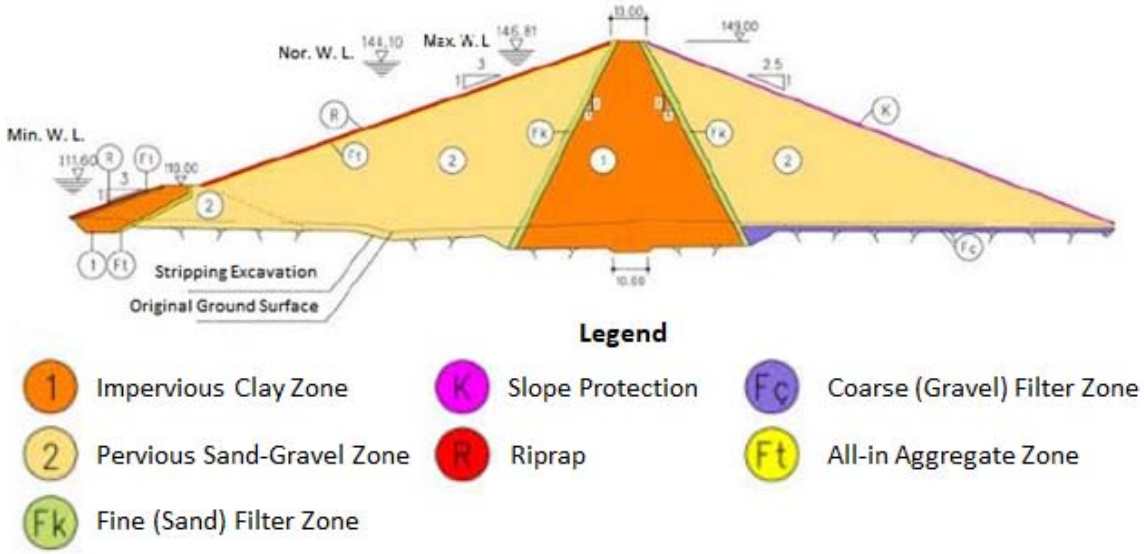

(a)

(b)

Figure 6.8. Seferihisar Dam a) typical cross-section (Courtesy of DSI), b) crest and spillway view on November 6

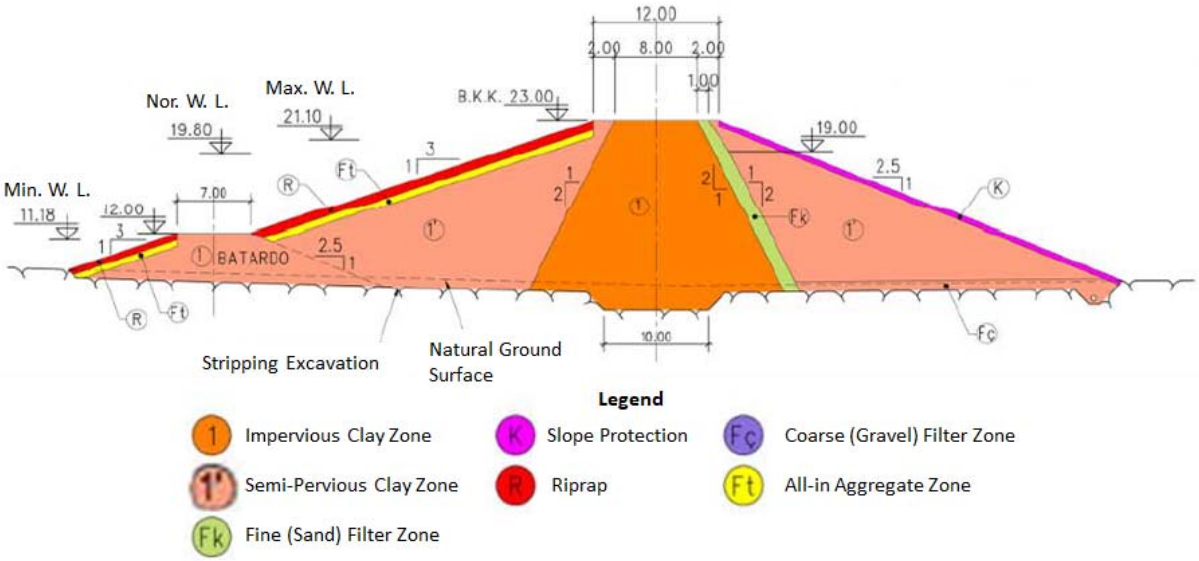

Figure 6.9. Alacati Dam Typical Cross-section (Courtesy of DSI)

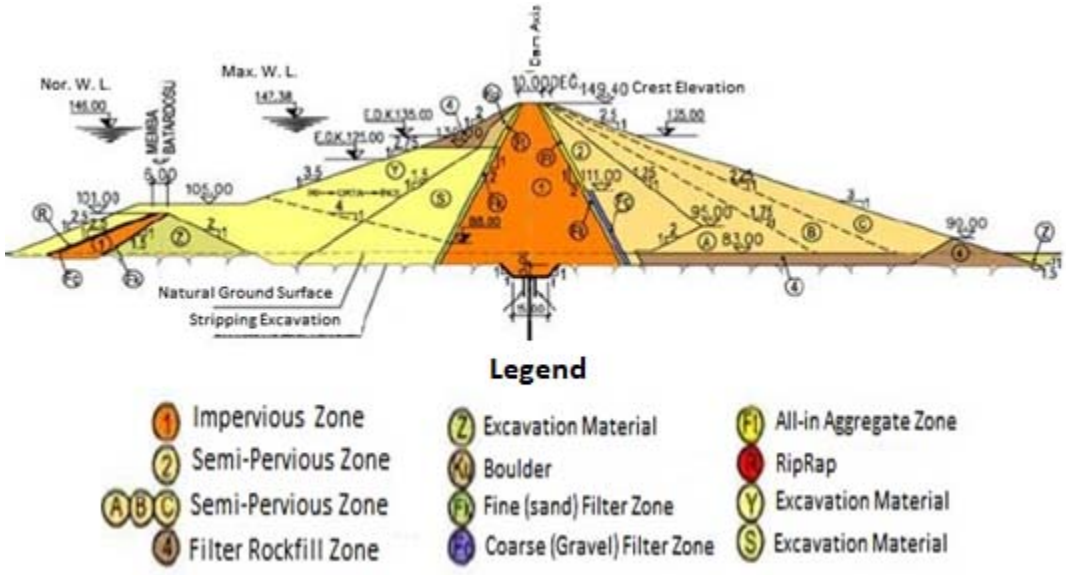

Figure 6.10. Balcova Dam typical cross-section (Courtesy of DSI)

(a)

(b)

Figure 6.11. Tahtali Dam a) reservoir site, no damage observed (38°07'48.7"N 27°06'13.3"E/ 18:34/ 04.11.2020) b) crest and spillway view on November 6

Figure 6.12. Menderes-Gumuldur dam crest and spillway view on November 6

6.1.4 Interim conclusion

In general, the dams, which were higher than 30 meters and consisted of clay cores with shells ranging from the semipervious zone to rockfill, performed significantly well under Samos Earthquake seismic loading. After a detailed inspection of six small to medium size earthfill and rockfill dams, no apparent damage was reported at these dams by reconnaissance teams.

6.2 Lifelines/Pipelines Performance

The October 30, 2020 earthquake affected one of the most populated and industrial areas of Turkey. The largest city in the affected area is Izmir with a population of about 4.5 million. Figure 6.16 shows the area most affected by the earthquake within the boundaries of Izmir and Aydın. This area covers many different large lifeline systems including water, wastewater, natural gas, and electricity. There was no reported sign of ground failure in the region (Chapter 5). Further investigations by using remote sensing systems (e.g. satellites, air photo) can be beneficial for detecting any ground deformations as these systems can be quite effective for evaluating pipeline damage performance (Toprak et al., 2018). At this stage, wave propagations effects rather than the permanent ground deformations appear to be the only sources of seismic demands for the lifeline systems. We contacted several municipalities, utility companies, and industrial organizations to gather and report information about the performance of the lifeline systems during the earthquake.

6.2.1 Potable and Wastewater Distribution Systems

Water is supplied from dams located approximately 30 km north and south of Izmir city center. The route of the transmission line extends from Gordes and Guzelhisar dams in the north, from Tahtali dam in the south to the city center (Figure 6.13). In addition, there are 53 water tanks and 4 treatment plants (Figure 6.14) in 11 districts. Water is transported to the tank area by pumps (Figure 6.15) and distributed to the city by gravity flow. The potable water network consists of about 8565 km pipes. Tables 6.2 and 6.3 provide the length of the pipelines with respect to pipe diameter and material.

The wastewater and storm water systems of Izmir consist of about 3585 and 650 km segmented pipes of various sizes, respectively. Tables 6.2 and 6.4 provide the length of the pipelines with respect to pipe diameter and material. In addition, there are 22 large scale wastewater treatment plants in İzmir and its surroundings (Figure 6.16).

The potable water network of Aydin consists of about 1771 km pipelines (ASKI, 2020). The wastewater and storm water systems of Aydin have about 856 and 167 km segmented pipes of various sizes, respectively.

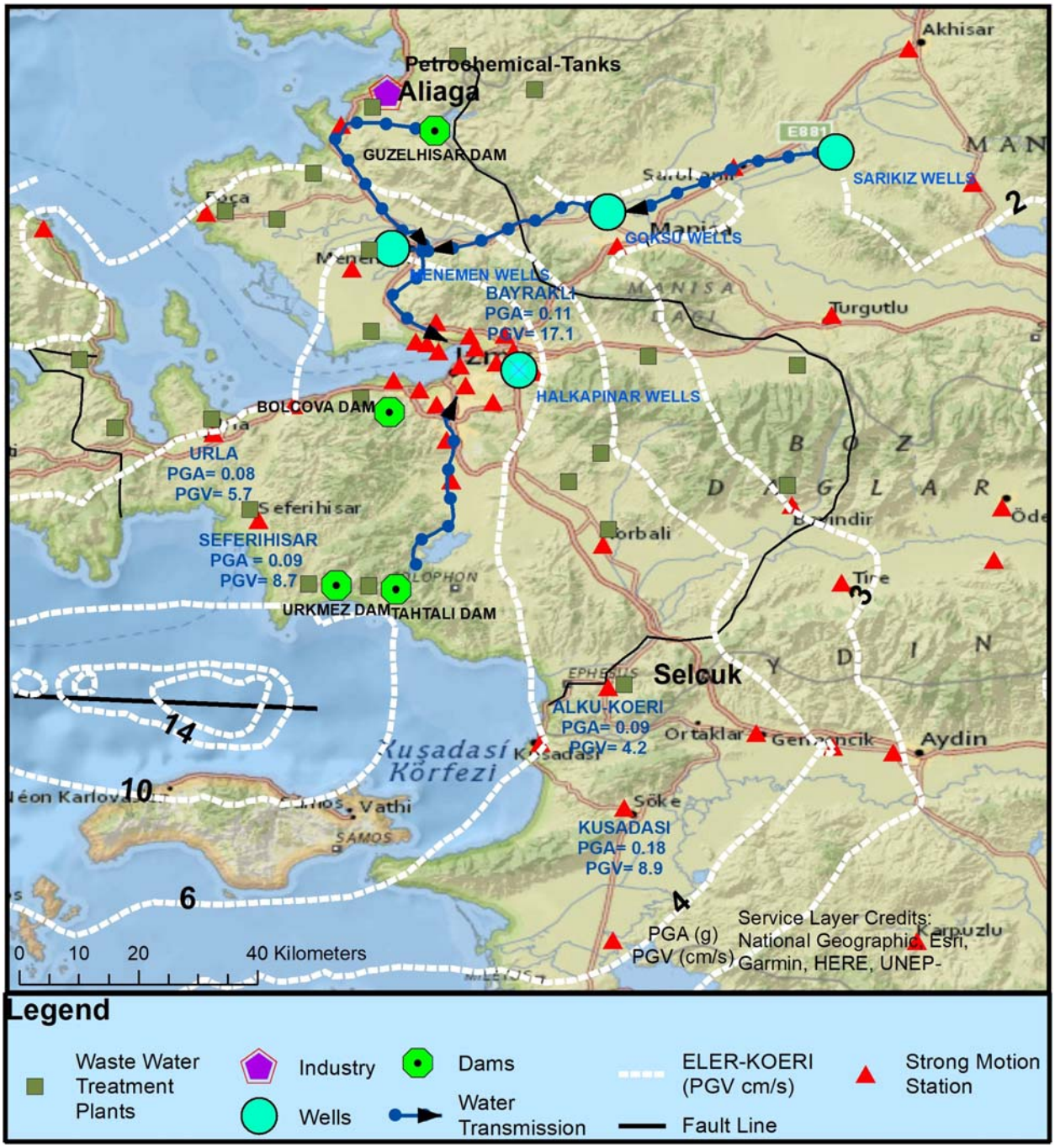

Figure 6.13. The distribution of the SM stations, water transmission system, water sources, water and waste water treatment plants, and large industry overlaid on the PGV iso-seismal maps developed by the ELER software (PGV source: KOERI)

Past investigations regarding pipeline damage relationships showed that the independent shaking hazard parameter for the pipe damage is the peak ground velocity (PGV) which is also correlated to transient ground strain. Predicted isoseismal PGV maps just following the earthquake (KOERI) and PGV values observed at strong ground motion stations (AFAD, KOERI,

ALKU) are shown in Figure 6.16. Note that the PGV contour values involve, region specific ground motion prediction equations, using shear wave velocity distributions and strong ground motion data for the improvement and bias adjustment of theoretical estimations (KOERI) which may not include local variations associated with different site responses. However, it is reported that site amplification was observed in Izmir (Chapter 4). The maximum PGV values, obtained from the stations of AFAD, in portions of Izmir with site response effects in Karşiyaka and Bayrakli, are 22 cm/s and 17 cm/s, respectively.

According to the information provided by the Izmir and Aydin Municipalities, no damage was reported in the water and waste water systems after the earthquake (Oral communication, IZSU and ASKI). Existing pipeline damage correlations (e.g., O'Rourke and Ayala, 1993; ALA, 2001; O'Rourke and Deyoe, 2004; O'Rourke et al., 2014) predict between 70-100 pipe repairs for Izmir potable pipelines, by using the average seismic values and pipe lengths given in Tables 6.2 and 6.3. Any break or leak in the pipeline is defined as a pipe damage which require a pipe repair. The discrepancy between observed and predicted values may be due to the reliability of the damage identification techniques used by site crews. For example, unless there is a strong shaking around waste water pipelines, leakage may not be observed on the ground surface. A detailed investigation, for example by pipeline inspection robots, could not be performed until the time of this report preparation. Also, no pressure drop was observed in the SCADA system of IZSU for the water transmission and distribution system (Oral communication, IZSU). However, whether there is a latent damage or weakening of the network will likely be revealed after the next earthquake, during long-term operation of the system or after comprehensive investigations. For example, after the earthquake in Van in 2011, there was no water interruption or leakage in the pipeline system. Therefore, the system was initially reported to be undamaged. However, careful investigations after the earthquake revealed that many leaks occurred especially after the second earthquake. Hence the damages were cumulative (Uckan, 2012). Another way of determining the effect of earthquake on the water distribution system for such cases will be the comparison of the repair rates per day and daily rate (e.g., total repairs for each week divided by seven days) by using the regular repair records of the utility companies in the earthquake stricken area for pre-earthquake and post-earthquake periods as applied by O'Rourke et al. (2014) in Christchurch water distribution system damages.


Figure 6.14. The Gordes Dam Kavaklidere (left) and Karaburun Mordogan Potable Water Treatment Facilities in İzmir (Izsu, 2020)


Figure 6.15. The Goksu (left) and Yahselli (right) pump stations in İzmir (Izsu, 2020)

Figure 6.16. The Cigli Waste Water Treatment Plant (Izsu, 2020)

Table 6.2 Potable water and wastewater pipeline lengths with respect to pipe diameter

Diameter (mm)	Potable Water Length (m)	Wastewater Length (m)
0-110	4744100	301891
110-200	2761636	395750
200-300	451888	2222501
300-400	148838	237257
400-600	159404	208802
600-800	38479	71535
800-1000	70668	51757
1000-1200	40901	21812
1200-1400	15138	14375
1400-1600	7562	5773
1600-1800	3201	-
1600-2200	-	18473
1800-2000	44709	-
2000-2500	80213	-
2200-2400	-	22416
Total	**8566737**	**3584825**

Table 6.3 Potable water pipeline lengths with respect to pipe material

Material	Steel	DI	HDPE	PVC	Others	Total
Length (m)	166635	3422963	3310673	270776	1395691	8566737

Table 6.4 Wastewater pipeline lengths with respect to pipe material

Material	Reinforced Concrete	Rubber Gasketed Concrete	HDPE	PE	Others	Total
Length (m)	2220272	399372	280736	39799	644646	3584825

6.2.2 Large scale industry

Significant large-scale industry exists around Aliaga, approximately 40 km north of İzmir, where most of the petrochemical facilities are located. Liquid storage tanks containing dangerous substances are among the most critical equipment, as their failure can result in leakage, environmental pollution and fire. Damages observed in such structures can be related to the high (impulsive) and low frequency (shaking) vibrations of the tank.

Possible forms of damage to these elements include elastic and plastic buckling of the tank wall, anchorage damage, sliding, baseplate damage due to the base uplift and sloshing damage in fixed and floating roof tanks. There was no reported damage in these facilities (Oral communication).

6.2.3 Natural gas and electric distribution systems

Following the earthquake, the electric and gas service to about 74500 and 3000 subscribers, respectively, stopped (ETKB, 2020). Intense gas restoration works resulted in providing service to most of the customers in about 3 days. However, as the inspection of damaged buildings started immediately after the earthquake and continued for several weeks, Izmirgaz and Disaster and Emergency Agency (AFAD) coordinated their efforts in providing service to selected inspected buildings. Izmirgaz reported that gas service discontinued to about 160 building which collapsed or planned for demolition as of 26.11.2020 (Izmirgaz, 2020).

Electric service interruptions just after the earthquake affected a much larger area, especially three nearby cities, Izmir, Aydin and Mugla. Nevertheless, electric services were restored much faster than the gas system. However, electric services could not be restored entirely in short time at certain parts of Izmir like Bayrakli where several buildings collapsed and there were many damaged buildings. Also, electricity could not be restored in a short time in Seferihisar where a small scale tsunami was observed and transformer substation got damage after inundation.

6.3 Concluding Remarks

In conclusion, existing dams, shaken by peak ground rock acceleration levels varying in the range of 0.01 g to 0.05 g did not experience any apparent damage. The crest amplifications are monitored to be as high as 3, also consistent with current state of knowledge.

Similarly, no significant damage in lifeline systems and large industrial facilities was reported by utility companies and industrial organizations. As there were no observed permanent ground deformations in the area and shaking levels were relatively low, these results were not surprising. However, based on the experience in previous earthquakes for the similar seismic intensities, some damages in water and waste water systems are expected to be determined sometime after the earthquake. The studies to determine these possible effects should be performed to develop methodologies against undetected damages after earthquakes. As tsunami effects are real around Turkey as shown by this particular earthquake, protection against electric and other infrastructure facilities along the sea borders should be taken.

Acknowledgements

The authors are indebted to DSI field engineers, who have collected perishable data after the event and shared with us. The members of Middle East Technical University, Ankara were partially funded by reconnaissance funds of METU, which is greatly appreciated.

References

AFAD-Earthquake Department of Disaster & Emergency Management Authority, http://www.deprem.gov.tr

ALA2001-American Lifeline Alliance, Seismic Fragility Formulations for Water Systems

Ateş, E., Kuru, T., & Aydın, R. K. (2019). Deprem Kayıtları Kullanılarak Muğla-Milas Derince Barajının Dinamik Özelliklerinin Belirlenmesi . Çanakkale Onsekiz Mart Üniversitesi Fen Bilimleri Enstitüsü Dergisi , 5 (2) , 319-338 . DOI: 10.28979/comufbed.542314

ASKI (2020), http://www.aydinaski.gov.tr/

DSI, Personal communication 2020 through Faik Cüceoğlu and Seçkin Aydın.

ETKB (2020) https://www.enerji.gov.tr/

KOERI (2000), http://www.koeri.boun.edu.tr/

Izmirgaz (2020), https://www.izmirgaz.com.tr/

IZSU (2020), https://www.izsu.gov.tr/

O'Rourke, M.J., Ayala G. (1993) "Pipeline Damage Due to Wave Propagation,"Journal of Geotechnical Engineering, ASCE, September, Vol. 119, No. 9, pp.1490-1498.

O'Rourke M., Deyoe E. (2004) "Seismic damage to segmented buried pipe",Earthquake Spectra, Vol.20, No:4, pp. 1167-1183.

O'Rourke TD, Jeon SS, Toprak S, Cubrinovski M, Hughes M, Ballegooy S, Bouziou D.Earthquake response of underground pipeline networks in Christchurch. NZ. Earthquake Spectra 2014;30(1):183–204.

Toprak, S., Nacaroglu, E., Koc, A. C., O'Rourke, T.D., Hamada, M.; Cubrinovski, M., Ballegooy, S., "Comparison of horizontal ground displacements in Avonside area, Christchurch from air photo, LiDAR and satellite measurements regarding pipeline damage assessment", Bulletin of Earthquake Engineering, (2018), https://doi.org/10.1007/s10518-018-0317-9

Uckan E "Lifeline Damage Caused In the 23 October (Mw=7.2) 2011 and 9 November (M=5.6) 2011, Van Earthquakes in Eastern Turkey" Sixth China-Japan-US Trilateral Symposium on Lifeline Earthquake Engineering- ASCEOctober 23 - 27, 2012, Chengdu, China.

7.0 Building and Bridge Performance

Turkish Authors: Ahmet Yakut, Erdem Canbay, Barış Binici, Halûk Sucuoğlu, Alper İlki, Cemalettin Donmez, Alp Caner, Ozan Cem Celik, Bekir Özer Ay

Greek Authors: Elizabeth Vintzileou, Maria Kleanthi, George Vadaloukas, Aristidis Papachristidis, Christos Giarlelis, Constantinos Repapis, Vasiliki Koussi, Vassilis Lekidis, Anastasios Sextos

As described in Chapter 1, the earthquake of October 30, 2020 occurred along the Samos Fault under the Aegean Sea, with an epicenter lying 9 km north of the coast of Samos; 14 km SE from the closest coast of Turkey; 34 km south of Seferihisar and 58 to 76km SW from the metropolitan area of Izmir. Although the epicenter was closer to Samos, most of the structural damage occurred in İzmir, the third largest city of Turkey with a population around 4 million. The impact of the earthquake on structures is discussed in this chapter, jointly for the İzmir area and the Samos Island.

7.1 Characteristics of Building Stock in İzmir

The physical characteristics and geographical distribution of buildings in İzmir have been investigated in this section. Similar to other large urban areas in Turkey (and Greece), reinforced concrete (RC) buildings constitute about 70% of the inventory in İzmir. The data compiled and presented in this section is taken from the 2000 Building Census and the Building Occupancy Permit Statistics (post-2000 buildings) disseminated by the Turkish Statistical Institute (TSI). According to the TSI data for İzmir, about 670,000 buildings (TSI data does not include the buildings without permits in sub districts and villages and squatter houses) contain 1,710,000 dwellings by the end of 2018. 88.5% of these buildings are used for residential, or mostly residential purposes, whereas 11.5% are non-residential buildings such as office buildings, hotels, industrial buildings, museums, etc. Figure 7.1 shows the number of buildings (left panel) and dwellings (right panel) in İzmir at the district level.

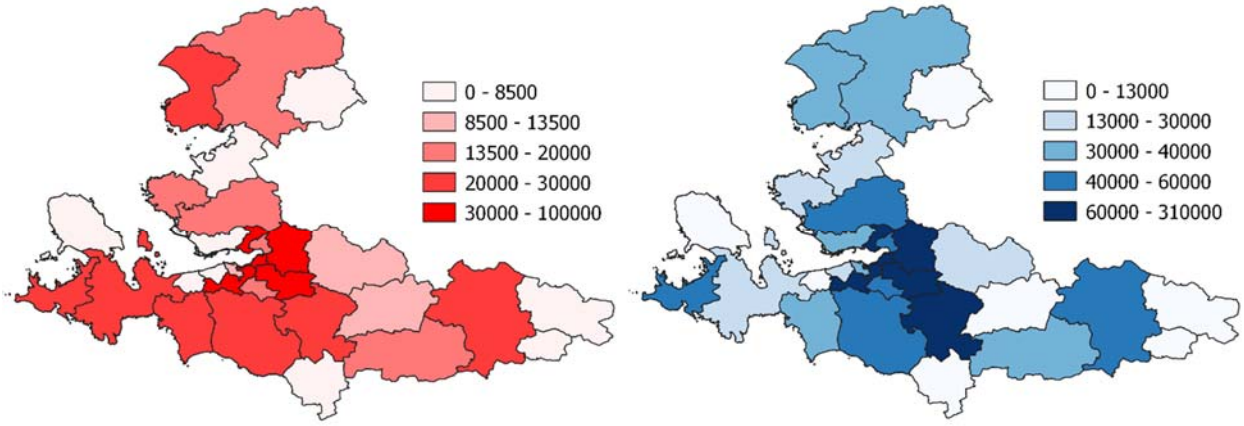

Figure 7.1. The number of buildings (left panel) and dwellings (right panel) in districts of İzmir

The buildings in İzmir can be classified into three construction types: RC (frame, wall, and dual), masonry (load-bearing walls made of stone, clay brick, concrete block, etc.), and others (structural steel, wood frame, etc.) buildings. The statistics show that RC and masonry buildings constitute 69% and 30% of the entire inventory, respectively, where the proportion of other buildings is not more than 1%.

Considering the resolution of TSI data in terms of the construction year and the structural design regulation that was in effect at the time of construction, RC buildings in İzmir can further be classified into three types, as pre-1980 buildings, buildings constructed between 1980 and 2000, and post-2000 buildings. The number of story information can also be used as a primary classification parameter since it strongly influences the vulnerability of buildings, particularly that of existing RC structures. The number of stories of RC buildings in İzmir can be investigated in three groups; as 1-3 story (low-rise), 4-8 story (mid-rise), and 9+ story (high-rise). Figure 7.2 displays the percentages of RC buildings with respect to the construction year and the number of stories.

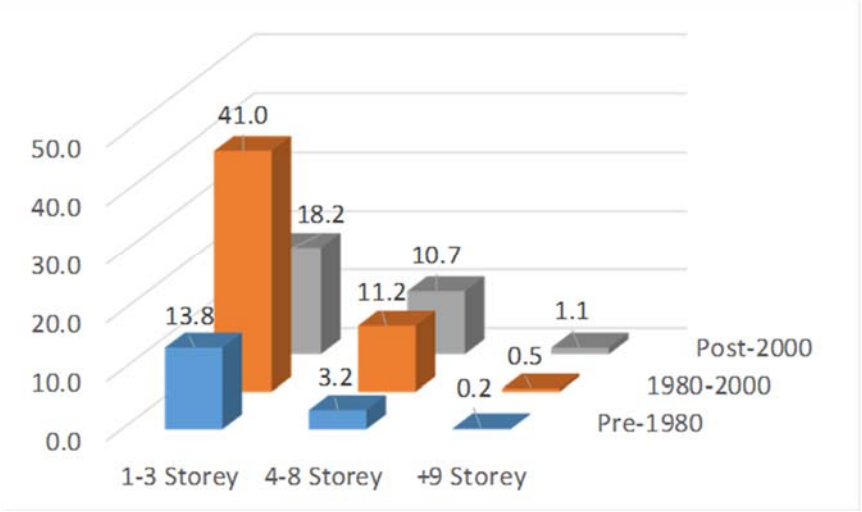

Figure 7.2. The percentages of low-rise (1-3 story), mid-rise (4-8 story), and high-rise (+9 story) reinforced concrete buildings with respect to their time of construction

Figure 7.3 compares the number of buildings constructed within approximately ten-year time intervals. The results clearly show the rapid increase in the number of new buildings which have been constructed between 1980 and 2000. More than 40% of the buildings in İzmir have been constructed within this 20-year period, and presumably according to the 1975 earthquake code, as will be discussed in detail in the following sections. The reconnaissance studies showed relatively poor seismic performance of these buildings not only in İzmir but also throughout Turkey. However, post-earthquake damage observations (see Section 7.2.2) also highlighted the remarkably different damage levels of similar buildings which were very close to each other and have been constructed according to the same code. The statistics presented in Figure 7.3 indicate that more than almost half of the buildings in İzmir have been constructed after 1980.

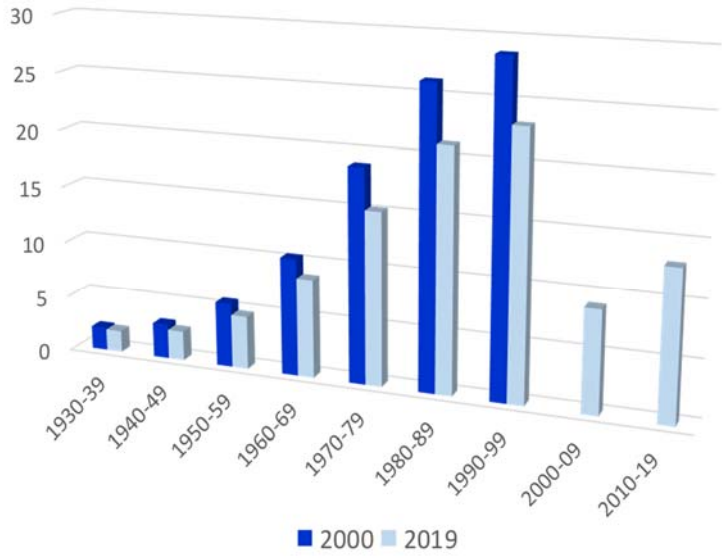

Figure 7.3. The percentages of buildings constructed from 1930 to 2019 in approx. ten year intervals (2000 census versus 2019 TSI)

7.2 Performance of Buildings in Izmir

7.2.1 Damage Distribution

According to data received in December 2020 from Disaster and Emergency Management Presidency (AFAD) and Ministry of Environment and Urbanization, the total number of damaged buildings in İzmir is 9,444. With an assumption based on the report prepared my METU (2020), the total number of buildings at the time of the earthquake could be around 700,000. Therefore, the percentage of damaged buildings (relative to the total number of buildings) in İzmir is approximately 1.3%. It should be noted that the damage inspectors do not examine all the buildings in the affected area. They inspect the buildings only upon request from a resident. Therefore, the buildings for which damage inspection is not conducted may be assumed to be undamaged.

Among the damaged buildings, 795 (8%) were assessed as heavily damaged (including collapsed ones), 804 (9%) were moderately damaged, and 7,845 (83%) were slightly damaged. Considering the overall building population in İzmir, the percentages of heavily, moderately and slightly damaged buildings are approximately 0.11%, 0.11% and 1.12%, respectively. Accordingly, the percentage of buildings that sustained the earthquake without damage is approximately 98.7%.

The structural damage was mostly concentrated in the Bayraklı, Bornova, Karşıyaka and Konak Districts of İzmir. These are among the most densely populated, central regions of the city. The distribution of damage in these districts as obtained from AFAD and the Ministry of Environment and Urbanization are shown in map form in Figures 7.4-7.7. It should be noted that green, yellow,

orange and red colors indicate buildings with no, slight, moderate and heavy damage, respectively, in these maps. The black and pink indicators show the buildings which were totally or partially collapsed during the earthquake.

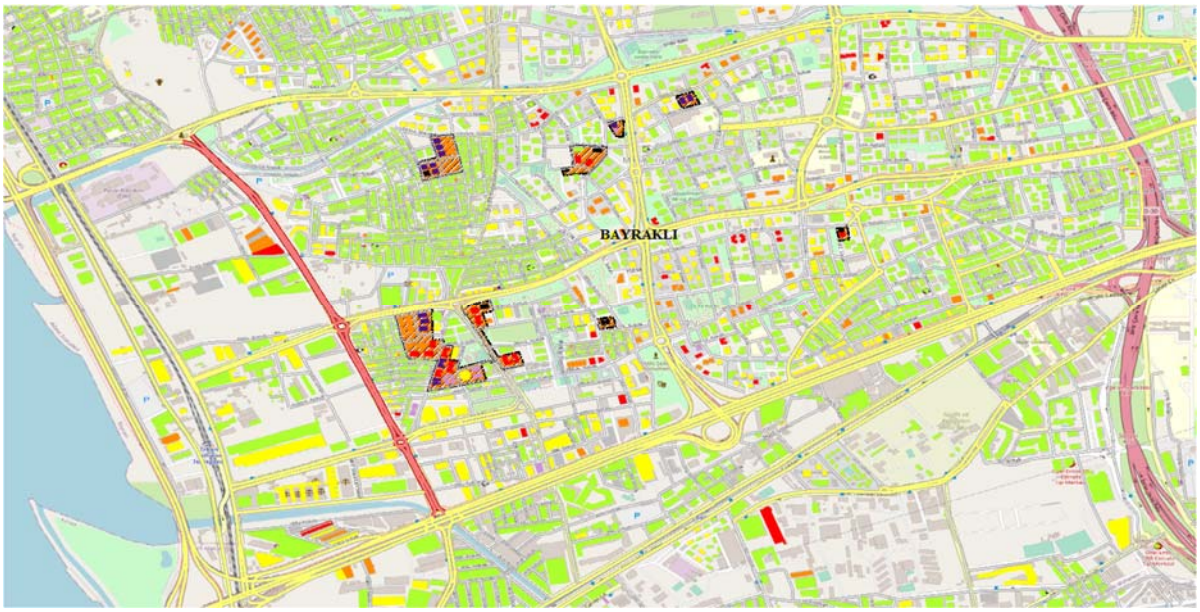

Figure 7.4. Damage distribution in the Bayraklı district of Izmir (green, yellow, orange and red colors indicate buildings with no, slight, moderate and heavy damages, respectively. The black and pink indicators show the buildings that have totally or partially collapsed during the earthquake)

Figure 7.5. Damage distribution in the Bornova district of Izmir

Figure 7.6. Damage distribution in the Karşıyaka district of Izmir

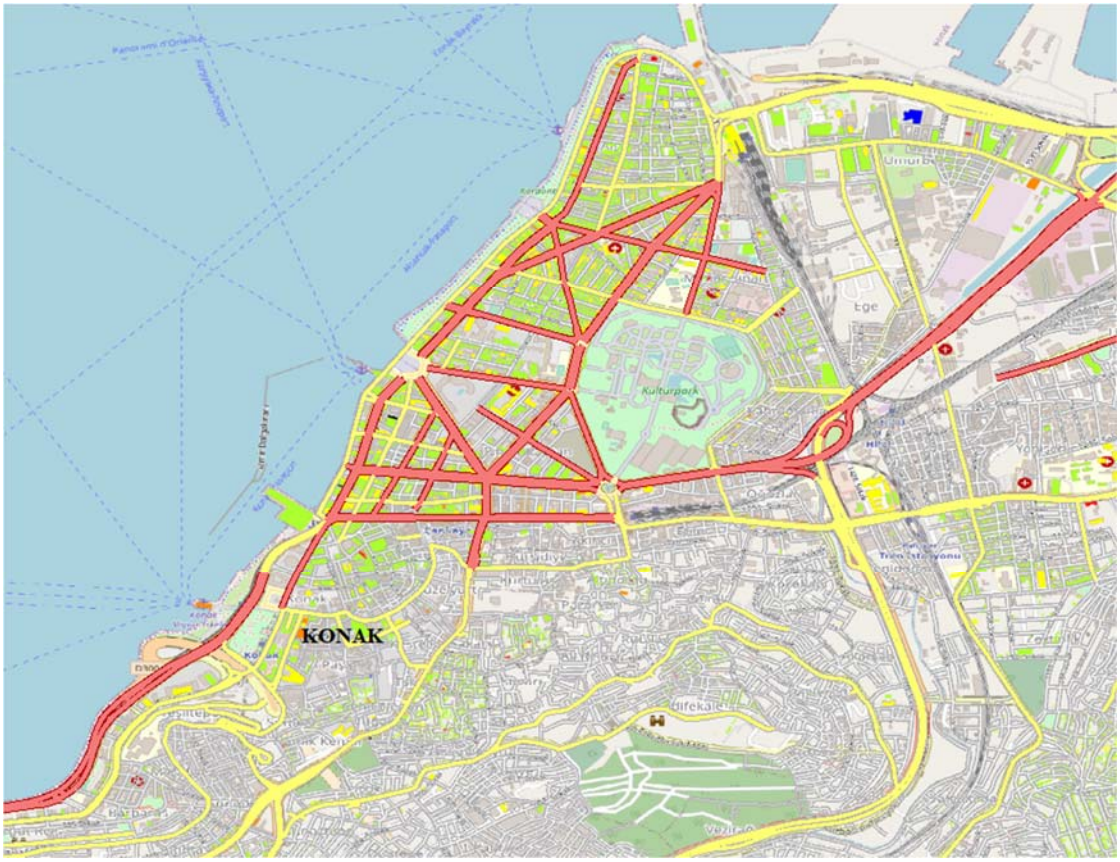

Figure 7.7. Damage distribution in the Konak district of Izmir

The statistical distribution of structural damage within these districts is separately presented in Figure 7.8, which shows that the largest number of damaged buildings are in the Bayraklı district. In addition, the ratio of the number of heavily damaged buildings to the number of buildings with different levels of damage is again the highest in Bayraklı.

The distribution of structural damage as a function of construction period is presented in Figure 7.9a, which shows, somehow interestingly, a remarkable portion of the damaged buildings was constructed between 1990 and 2000. The structural damages are significantly less in buildings constructed after 2010. Quite unexpectedly, a large number of buildings constructed between 2000 and 2010 have also suffered damage to different extents, including heavy damage. This data suggest that the number of damaged buildings is correlated with the changes in urban zoning plans and with the volume of construction.

The distribution of damages classified by the building height (number of stories) is shown in Figure 7.9b. Interestingly in this figure, no buildings with more than 10 stories are identified as heavily damaged. Nevertheless, quite a large number of such buildings were slightly damaged, most of which are deemed to stem from damage to non-structural infill walls. Again, interestingly and unexpectedly (considering the presented response spectra in this report), many buildings with three stories or less have also been assessed as damaged by the inspectors. Furthermore, a significant number of these one to three story buildings (558) are designated as heavily damaged. It is observed that rather than actual structural damages, the urban transformation plans may have played an important role in the damage assessment decisions for these one to three story buildings, which are relatively old, poorly constructed/maintained, and located in slum areas where it may be possible to conduct urban transformation projects. Few examples of such buildings designated as heavily damaged by the inspectors are shown in Figure 7.10. It should be noted that the structural systems of most of these buildings are composed of irregular masonry walls and there are only few reinforced concrete buildings among them. It is also important to note that, in agreement with the spectral accelerations obtained particularly for the stations located in areas with poor ground conditions, seven to ten story buildings seem to be damaged in a more pronounced way.

For the first time in Turkey, the damage assessors (mostly civil engineers and architects serving for the Ministry of Environment and Urbanization, and other public institutions) have been trained through an online education system to carry out seismic damage assessment before the earthquake. The online training was organized and coordinated by the Ministry of Environment and Urbanization. More than 40,000 individuals were trained through this remote education system in addition to face-to-face trainings in İstanbul, Kocaeli and İzmir, which included several thousands of technical staff with potential to work in the field for damage assessment in case of an earthquake. The rational damage distribution and very limited amount of inconsistent damage assessment decisions clearly demonstrated the success of the damage assessment training and use of a simple and robust damage assessment methodology. The damage assessment training is based on the damage assessment methodology developed by Ilki *et al.* (2020a, 2020b), which

can be considered as an extensively modified version of the damage assessment methodology proposed by Boduroglu *et al.* (2013) earlier. Since the damage assessors of Turkish Compulsory Insurance Pool (TCIP) also used the same methodology and received similar training, the assessments made by the staff of Ministry of Environment and Urbanization and TCIP were also in good agreement.

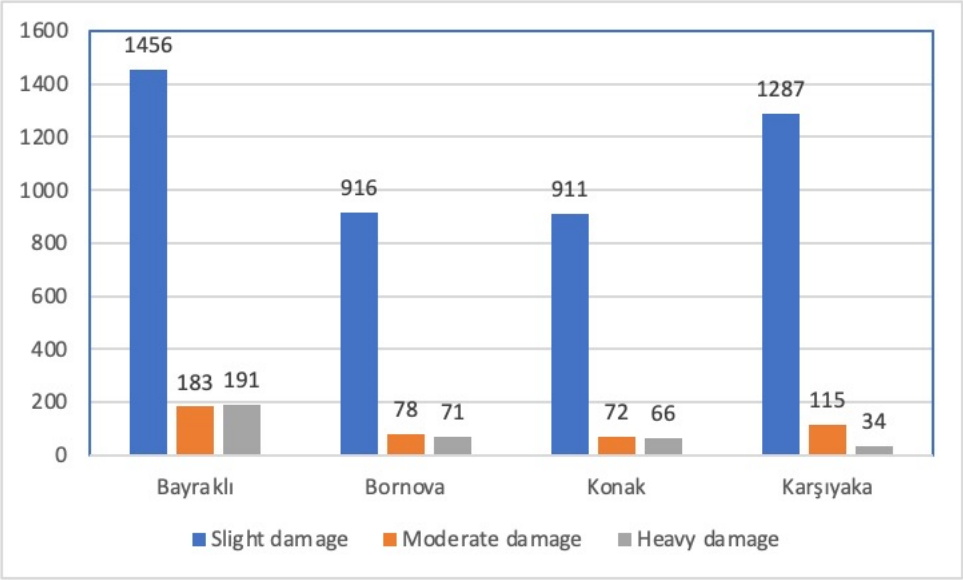

Figure 7.8. Damage distribution in Bayraklı, Bornova, Konak and Karşıyaka Districts (vertical axis shows the number of buildings)

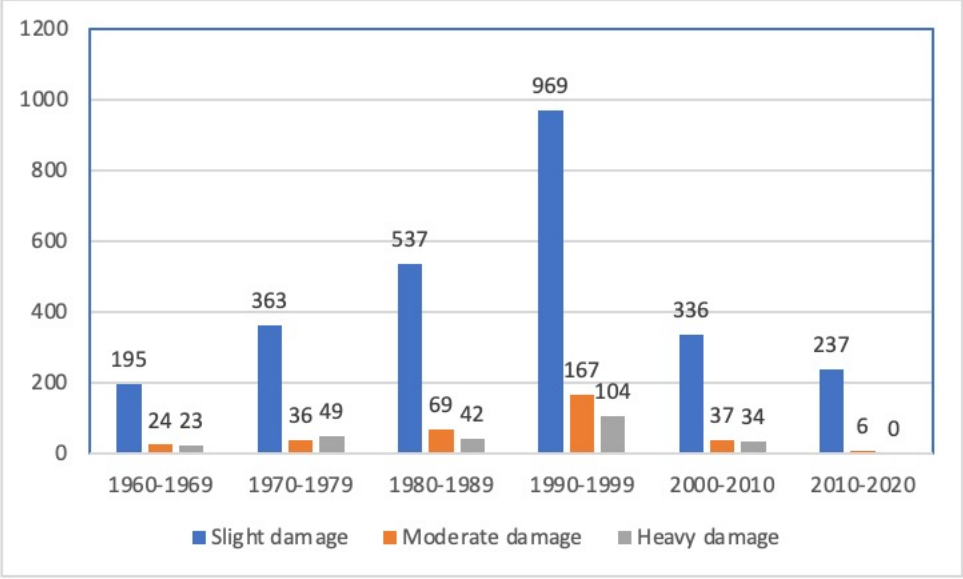

Figure 7.9a. Damage distribution in terms of building age (vertical axis shows the number of buildings)

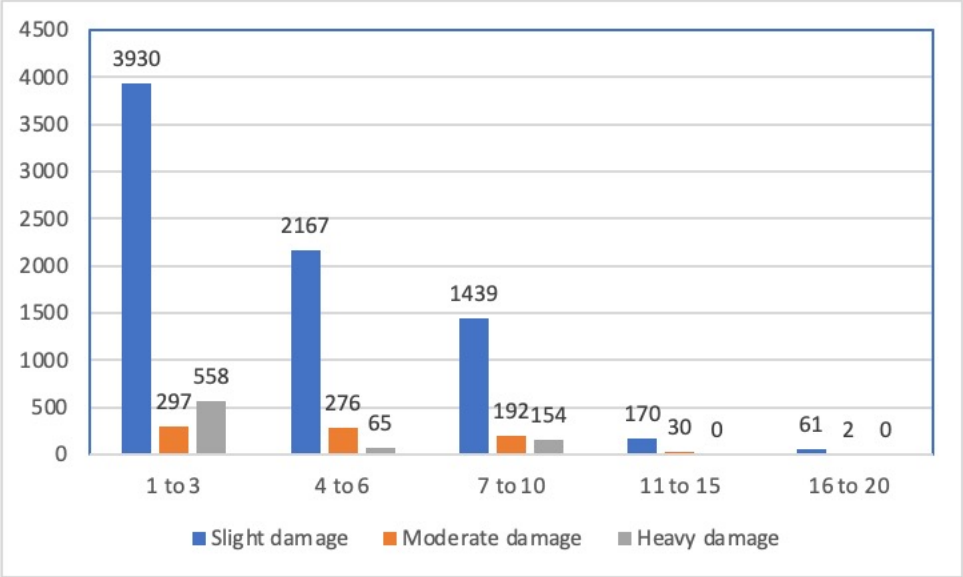

Figure 7.9b. Damage distribution in terms of the number of stories (vertical axis shows the number of buildings)

Figure 7.10. Examples of one- and two-story buildings designated as heavily damaged even though the damages due to earthquake are not severe

7.2.2 Observations on Reinforced Concrete Building Performance

This section summarizes the observations of the reconnaissance surveys performed after the October 30 earthquake. In these reconnaissance surveys, reinforced concrete buildings, which constitute a significant portion of the building inventory, were investigated. Table 7.1 summarizes the general damage assessment of the İzmir province on a district basis (https://webdosya.csb.gov.tr/db/izmir/haberler/2020_20201121031632.pdf). It is worth noting that the data in this table is older than that given in the previous section, hence the numbers may be slightly different. It can be observed that the number of collapsed and heavily damaged buildings was around 650 despite their locations being more than 60 km away from the epicenter. Examination of the ground motion records presented earlier in this report shows that the spectral acceleration measured on the soft soils in Bayraklı was around $0.35g$ in the period range of 0.6-

1.5 seconds. According to Turkey's current seismic hazard map, these values are close to spectral accelerations corresponding to the ground motion level of a service-level earthquake (72-year return period). They approximately correspond to 30-40 percent of the design-level earthquake ground motion (with 475-year return period). The expected level of structural performance for the service level earthquake is Immediate Occupancy. Accordingly, it can be interpreted that the collapses and heavy damages observed at the 7-10 story buildings constructed between 1990-1994, were due to major structural inadequacies. The remaining part of this section is organized based on the type of deficiencies leading to the observed damage.

Soft / Weak Story Damage. A number of buildings have suffered damage or partial collapse at their first stories. A typical feature of the buildings in Turkish city centers is the presence of shops at the ground levels. In order to create wider space, infill walls are generally removed in those stories where the seismic demands are maximum (Figure 7.11). In addition, poor beam-column connections and the presence of weak columns are the key reasons for the development of soft-story mechanisms. Due to the soft/weak stories, building collapses occur partially in the ground story in some cases, whereas total collapse was observed in some other buildings.

Infill Wall Damage. The most widespread damage type observed in İzmir is infill wall damage. The most common infill material was hollow-core clay bricks in the Bayraklı Region. Infill wall damage consisted of interface cracking at frame-boundary interfaces, diagonal cracking, and crushing (Figure 7.12). The structural benefits and weaknesses of the infill walls were similar to those observed in previous earthquakes such as Kocaeli 1999, Bingöl 2002, Van 2011, and Elazığ 2020. In some buildings, the infill walls appeared to stiffen the building and reduce the lateral deformation demands. In one of the eight-story apartment complexes comprised of four buildings, the benefit of infill walls was clearly observed. In one of those buildings, there were extensive infill walls in the first story (Figure 7.13). In the other buildings, this floor had no infill walls at all (Figure 7.11, top row). Three of the buildings without infill walls were either heavily damaged or collapsed, resulting in nine fatalities. The one with the infill walls in the first story, on the other hand, experienced moderate infill wall damage without any significant structural damage (Figure 7.13). It can be viewed as a striking example of the "unintended" benefit of infill walls contributing to lateral stiffness, strength, and axial capacities. Our assessments revealed that the presence of infill walls and the difference in the quality of construction might have increased the building base shear capacity, also reducing soft/weak story irregularity. The past observation on the effect of infill walls to help the buildings survive small to medium-sized earthquakes by contributing to their lateral load-carrying capacity was confirmed.

Table 7.1a. General damage assessment of İzmir provinces (as of 20 November 2020): General, b) Public buildings

İzmir Province General Damage Assessment Table																
District	Collapsed		Urgent Demolition		Severe		Moderate		Slight Damage		No Damage		Total # of Assessment		Total # of Urgent+ Severe+ Collapsed	
	Bldg	Ind. Units	Bldg	Ind. Units	Bldg	Ind. Units	Bldg	Ind. Units	Bldg	Ind. Units	Bldg	Ind. Units	Bldg	Ind. Units	Bldg	Ind. Units
Bornova	7	7	2	2	59	105	72	508	894	7420	55,612	212,993	56,646	221,035	68	114
Bayraklı	9	136	30	795	127	1,922	170	3,305	1,372	16659	29,785	121,733	31,493	144,550	166	2,853
Seferihisar	2	2	0	0	23	47	33	49	235	471	6,805	13,425	7,098	13,994	25	49
Aliağa	2	2	0	0	11	71	20	178	107	1,127	1,629	12,845	1,769	14,223	13	73
Buca	1	1	1	35	28	180	49	431	428	4,311	9,588	53,031	10,095	57,989	30	216
Karabağlar	2	2	1	1	21	95	33	358	345	3,922	4,766	34,001	5,168	38,379	24	98
Karşıyaka	6	7	0	0	25	392	105	1,638	1,239	16,607	15,512	135,099	16,887	153,743	31	399
Kemalpaşa	0	0	0	0	10	11	2	111	42	77	1,134	2,015	1,188	2,114	10	11
Konak	3	6	1	15	40	231	55	858	642	6,975	5,504	29,152	6,245	37,237	44	252
Menderes	1	2	0	0	23	94	29	129	192	941	1,745	4,730	1,990	5,896	24	96
Other	17	18	0	0	214	402	120	915	1,187	7,801	18,004	75,543	19,542	84,679	231	420
Total	50	183	35	848	581	3,550	688	8,380	6,683	66,311	150,084	694,567	158,121	773,839	666	4,581

Table 7.1b. General damage assessment of İzmir provinces (as of 20 November 2020): public buildings

Damage Assessment of Public Buildings			
	School	Mosque	Other Public Buildings
Total Assessment #	1810	517	1919
# of Severely Damaged Buildings	18	10	20
# of Moderately Damaged Buildings	33	18	23

a. Before the earthquake b. After the earthquake

Figure 7.11. Soft / weak story failure (without infill walls)

Figure 7.12. Infill wall damages

a. Before the earthquake b. After the earthquake

Figure 7.13. Infill wall contribution

Overhang Induced Damage. The footprint of buildings and the upper floor plan areas were significantly different in some of the buildings due to the presence of overhangs. The upper floors are enlarged in plan with cantilever overhangs to gain additional space. These cantilever overhangs can be excessive, on the order of few meters, and prematurely cracked under the weight of the exterior walls bearing on overhangs. Figure 7.14 shows wall cracking, and severe damage at the corners of heavy overhangs. Damage in heavy overhangs is not only limited to the partition walls, but also exists in the structural system. Flexural and shear cracks (residual crack widths above 1mm) were observed in the structural members connected to these overhangs (Figure 7.14). It is interesting to note that such localized damage in the overhangs resulted in irreparable damage due to residual lateral and vertical deformations reaching substantial cantilever tip settlement; hence these buildings could not be re-occupied. In short, it can be stated that the damage observed in overhangs, cantilever connections, and ground floor columns in some buildings did not lead to structural collapse, but prevented re-occupation, hence leading

to demolition. The effect of these overhangs on the continuity of frames and lateral load path needs to be considered as part of the design.

Figure 7.14. Overhang damages

Damage to Vertical Load Bearing Members. Heavy damage was observed in some of the building columns of the heavily damaged buildings. The observed damage patterns were mainly concrete spalling, shear cracking, and buckling of longitudinal reinforcement (Figure 7.15). It is well-known that these damage types are associated with detailing deficiencies such as insufficient transverse reinforcement, use of smooth bars, absence of 135-degree hooks, and low concrete compressive strength. One of the two identical buildings collapsed at its lower two stories, whereas the other building had almost no damage observed during street survey (Figure 7.15). The assessment from inside revealed heavy shear damage and significant corrosion in columns. This observation clearly shows that damage assessment based on building examination without entering inside may lead to misleading results.

Figure 7.15. Severe column damages

Corrosion induced damage. Our investigations showed that corrosion in reinforcement is a widespread problem in İzmir (Figure 7.16). Excessive corrosion was especially observed at the bottom of columns in the basement or ground floors. The loss in the cross-sectional area of reinforcement due to corrosion was significant in some instances, reaching ratios of 25 to 65 percent. The critical problems associated with corrosion in building columns are reduced moment and shear capacities, loss of bond strength, and concrete spalling leading to premature rebar buckling. Hence, addressing problems related to corrosion detection and protection remains critical for seismic risk reduction.

Figure 7.16. Corrosion damages

Design Problems. The aforementioned damage occurred mainly in buildings constructed in the 1990's, before the publication of TEC 1997 (CSCDA 1997) and before the Kocaeli and Düzce Earthquakes (1999), which increased awareness of the importance of construction quality and control. However, some examples of design errors leading to heavier non-structural damage than expected were encountered. The widespread non-structural damages that were observed in a recently constructed commercial center reveals some noteworthy design mistakes. Figure 7.17 shows a 10-story commercial center with a shear wall core and a large opening in the center of the slab. All offices are located around the opening. Although no damage was observed in the shear wall, wide shear cracks were observed in the infill walls. It is surprising to see such heavy infill wall damage in a recently constructed building under an earthquake ground motion with intensity well below the design earthquake level. It is believed that due to the lack of diaphragm action, the core wall was unable to limit the inter-story drifts. It appears that improper modeling due to lack of diaphragm action and poor design led to excessive drift of office areas, and the infill walls around offices suffered heavy damage. This observation emphasizes the importance of slab openings (slab discontinuity) and ways for developing proper load transfer mechanisms to the shear walls.

Figure 7.17. Non-structural damage due to large openings in slabs

Another major drawback observed in the buildings was the discontinuity of frames in plan. Continuous and regular frame lines that provide uniform distribution of forces and proper transfer of earthquake load do not exist in many cases. The beams and columns were simply oriented and arranged according to the architectural plan. Hence, the beams are generally discontinuous and supported by girders. Thus, discontinuous and zigzagged beam lines were observed, resulting in poor seismic performance.

It is noteworthy that widespread staircase damage was also observed in RC buildings (Figure 7.18).

Figure 7.18. Observed staircase damages

Concluding Remarks. The following remarks summarize our field observations in Bayraklı after the October 30 Aegean Sea earthquake:

1- The strong motion accelerations measured in the center of İzmir after the earthquake are generally very low, reaching higher values in Bayraklı due to its special site conditions (see Chapters 3 and 4). However, the relatively high spectral accelerations, recorded at the mid-to-long period (0.6s-1.5s) range due to soil amplification, are well below the design basis values. Soil amplification resulted in heavy damage in inadequately designed and/or constructed 7-10 story reinforced concrete buildings in Bayraklı. Thus, in the design of multi-story buildings in Bayraklı and similar regions, site amplification should be taken into account in the design.

2- Infill wall damage observed in many buildings resulted in significant property loss and played an essential role in the earthquake aftermath psychology of people. Even if no structural damage was observed, it caused a perception of excessive damage to the buildings.

3- It was observed that those buildings that appear to have no damage from a street survey might have experienced significant damage when examined from inside.

4- Infill walls that do not experience out-of-plane failure may have a beneficial contribution to the vertical and lateral load-carrying capacity of deficient buildings, reducing the drift demands and thus preventing the collapse of buildings under low- and medium-intensity earthquakes.

5- Inadequate stiffness and strength of slabs and tie-beams, which transfer the lateral loads to shear walls, led to high drift demands in some buildings, resulting in a concentration of damage in non-structural members.

6- In most of the damaged buildings, it was observed that a regular structural system and continuous frame system required for a proper earthquake load transfer, was not established.

7- Excessive corrosion was observed in the bottom ends of columns located at the basement and ground floors of the examined buildings in Bayraklı, İzmir (similar effects are anticipated elsewhere). Corrosion levels accelerate the loss of bond, cover spalling and deformation capacity of RC columns.

8- Local overhang-column connection and ground floor column damage observed at the cantilevers of 7-10 story buildings are so high that the retrofit and re-occupation of the buildings was deemed impossible.

9- The damage observed is due to inadequacies and deficiencies present in the buildings; the fact that the levels of ground motions measured are less than the design levels is a clear indication of this phenomenon. Therefore, this earthquake should not be considered as the design level earthquake. Consequently, the impression that the buildings suffering no damage have adequate seismic capacity would be quite misleading.

7.2.3 Observations on Masonry Buildings

Masonry buildings also suffered damages during the October 30 earthquake. Observations show that except for two regions, damage to masonry structures are very limited and do not show a geographic concentration in terms of sub-districts. Konak district of İzmir and Kösedere village in Karaburun peninsula are the two locations where damage to masonry buildings was observed.

Konak is the central district of Izmir with a long historical existence. Therefore, there are many masonry structures in the region, most of which are registered as historical structures. Observations show that even though some of these structures responded to the earthquake satisfactorily, others had structural damage. There exists a ground motion record in the region with the acceleration response spectra given in Figure 7.19. Spectra show that the maximum

spectral accelerations reached at the typical period ranges of the masonry structures (shown by dashed vertical lines) are in the interval of 0.1g to 0.4g.

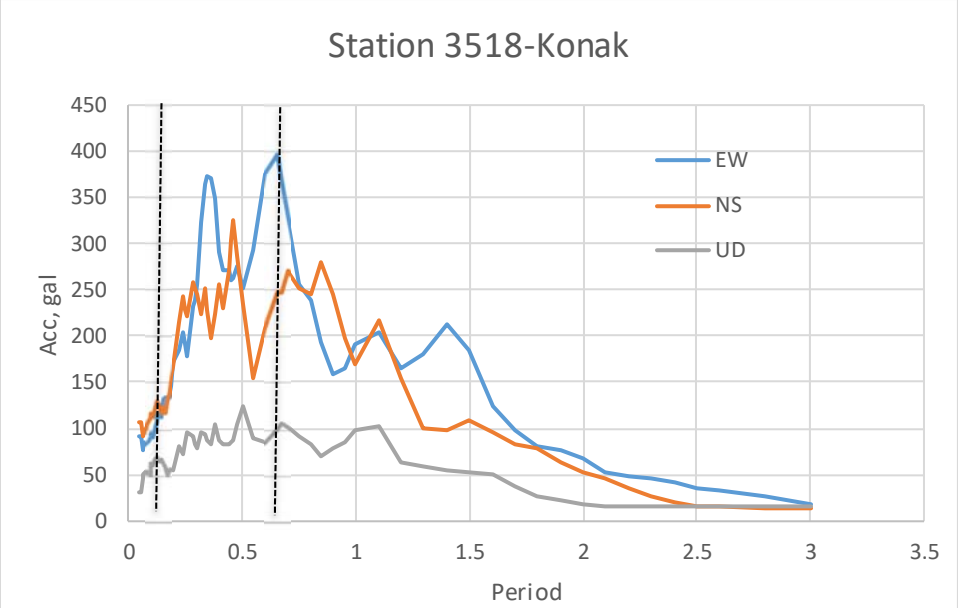

Figure 7.19. Acceleration response spectra of October 30th motion for the Konak Station record. The vertical dashed lines show the approximate period range of masonry structures

Renovated historic structures typically performed adequately. There are some with damage, though. The first impression from the damaged historic structures indicates that a renovation/modification that creates disruption of the original structural system could be the main reason for the damages sustained in some structures. Some early 20th century structures and historical mosques are in this class.

The İzmir Commerce Building is a basement plus three floor structure that originates from the 1920s. It is originally a mixed masonry and RC structure. The exterior façade of the building was built with stone-brick mix masonry walls, and the internal spaces were supported with a RC frame. Later in its history, internal partial stories were added to the system with structural steel framing. An overview of the building is presented in Figure 7.20. The detailed information about the building and its damages are adopted from Alkan (2020).

Figure 7.20. İzmir Commerce Building, a general view

The building suffered both structural and nonstructural damage. It is reported that the disruption of the original frame due to the partial stories added by dividing the stories with high headspace inside the building is the root cause of the damage. The plan of the ground story is presented in Figure 7.21. Some structural damage observed in the structure is presented in Figures 7.22 and 7.23.

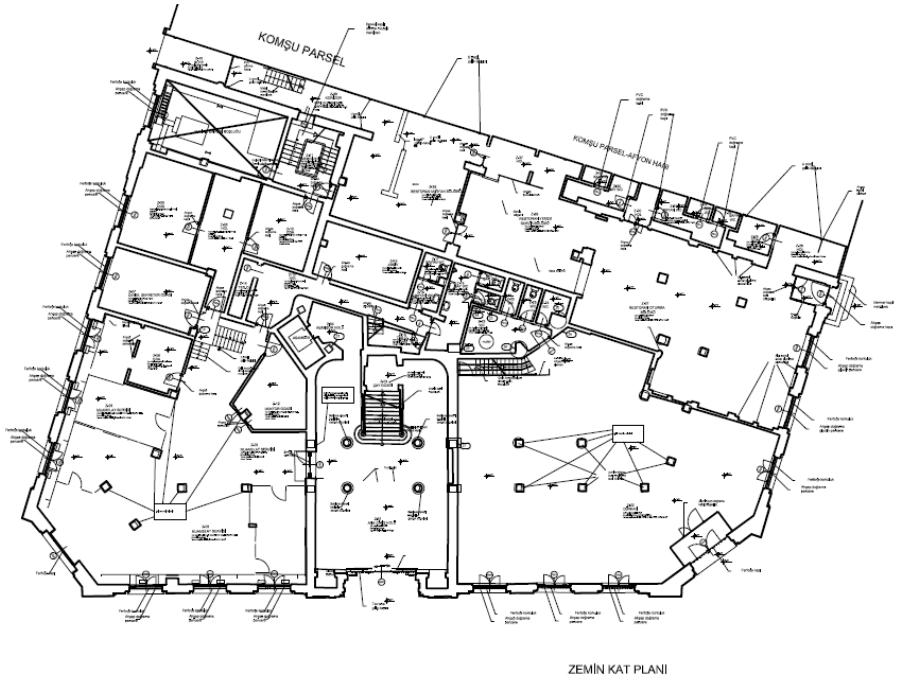

Figure 7.21. Ground floor plan of İzmir Commerce Building

Figure 7.22. İzmir Commerce Building, observed damages; both outside and inside

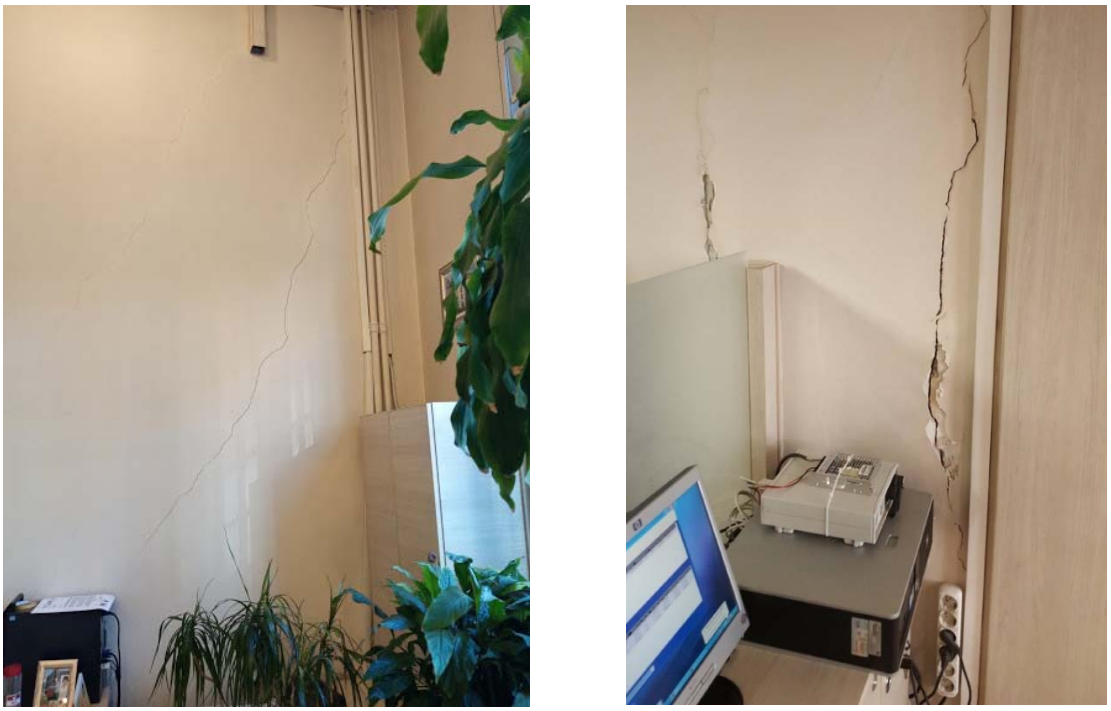

Figure 7.23. İzmir Commerce Building. Observed damages from inside the structure

Another example in the Konak district is a school building. It is a two-story masonry structure. Detailed information about the structure is not available yet. The observed damages clearly show that the structure reached its capacity levels, as evidenced in Figures 7.24 and 7.25.

Figure 7.24. Perimeter wall damages in the school building

About 40 masonry buildings in the Kösedere village, Mordoğan, suffered structural damage (Figure 7.26). The village is about 75 km away from the epicenter. These are traditional, old rubble stone masonry structures in the age range of 60-80 years. Typically, lime mortar is used for the walls, most with plaster on both sides. Almost all structures have two stories with wooden floors and roof trusses. The floor and the roof framing of the structures are observed to be very light, and the perimeter walls of the buildings provide the main resistance.

It should be noted that the neighboring villages with very similar construction type and quality did not experience comparable damage. There exists either none or very few damaged masonry structures in the rest of the peninsula. The cause of the concentration in Kösedere village deserves further investigation.

Figure 7.25. Interior wall damages in the school building

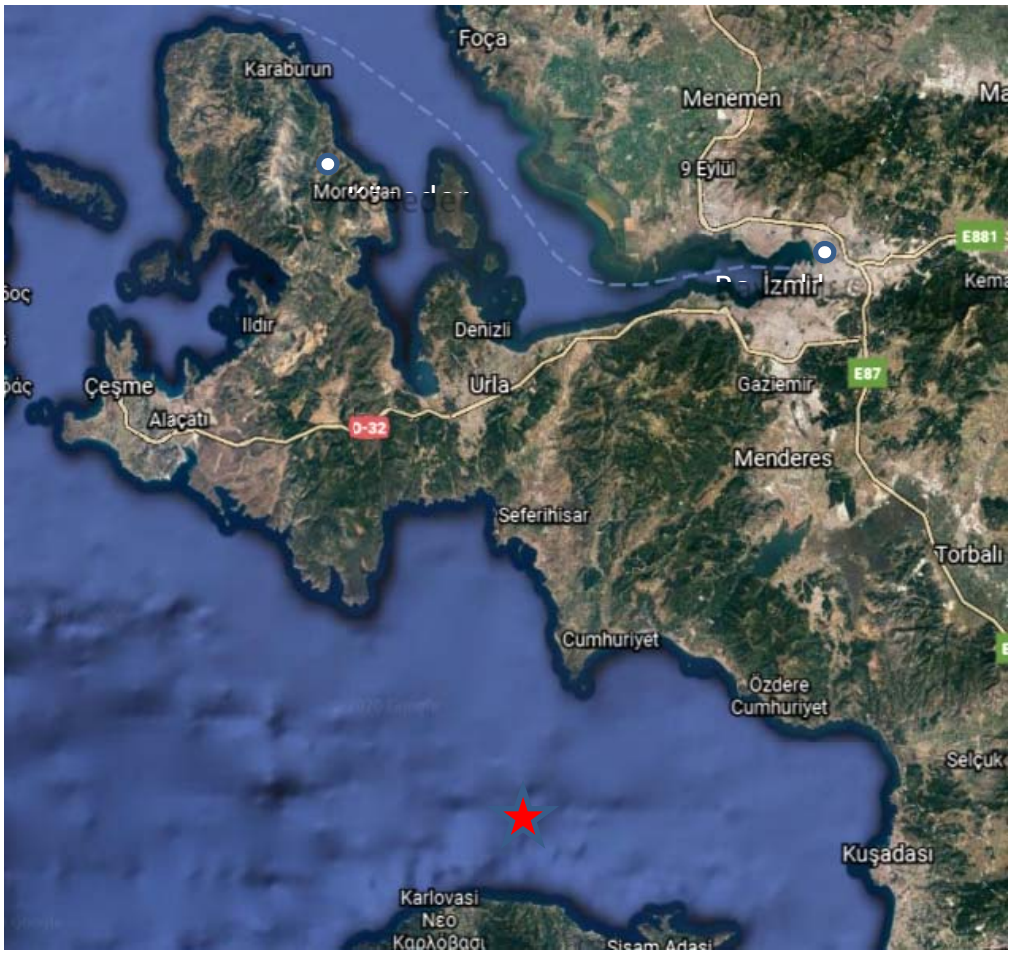

Figure 7.26. Location of Kösedere Village and Alaçatı with respect to epicenter of the earthquake

Masonry walls in Kösedere are rubble mount walls, and a view of the typical construction technique is presented in Figures 7.27 and 7.28. Wall thicknesses vary from 40 to 60 cm.

Figure 7.27. Typical wall construction

Figure 7.28. Collapsed portion of a wall

Wall damage developed as separations at the wall-to-wall connections (Figure 7.29), cracks in wall bodies (Figure 7.30), and at the window/door openings (Figure 7.31). Due to cracking, the

structures are on the verge of losing the box behavior, which is the key mechanism to provide the out-of-plane stability of masonry walls and overall lateral structural strength.

There are individual masonry structures that sustained damage during the earthquake. There is a police station building in the Alaçatı neighborhood of Çeşme. The building is about 55 km away from the epicenter, and about 2 km to Alaçatı strong motion station of AFAD. It is again a two-story structure with a wooden floor and roof framing. Walls are composed of two layers of stone with rubble infill. Soft Alaçatı stone is the wall material. This structure was originally constructed as a mill, later converted to a school, and finally became a police station. It is estimated as 70-80 years old. It suffered shear cracks in the interior and exterior wall bodies (Figures 7.32 and 7.33).

Figure 7.29. Separation at a wall-to-wall connection

Figure 7.30. Cracking in the body of a wall

Figure 7.31. Cracking at the door opening

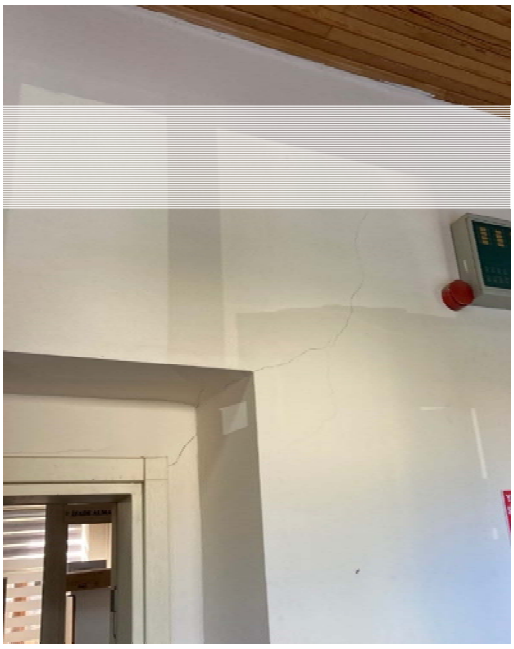

Figure 7.32. Cracking at the door opening

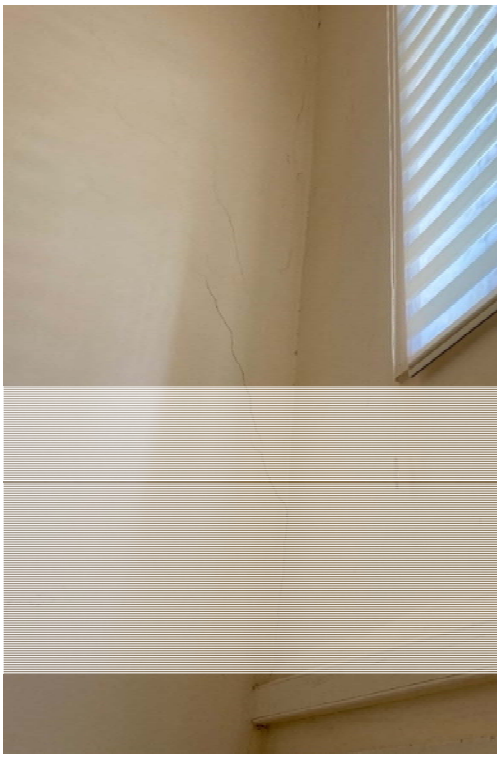

Figure 7.33. Interior to exterior wall connection

Masonry structures in İzmir, fortunately, did not collapse during the October 30th earthquake. But there exist many structures with heavy damage. Considering the level of earthquake demand, it could be said that the damaged structures do not provide the safety levels needed by the current seismic regulation. Therefore, the earthquake could be viewed as an indicator of the weakest structures. The lessons learnt by the earthquake should be taken seriously, and these structures should be strengthened to provide safety in future events.

7.3 Implications of Recorded Strong Ground Motions and Site Effects on the Seismic Performance of Buildings in Izmir

Strong motions from the earthquake were recorded by several stations operated by AFAD and KOERI, which are shown on the topographical maps of İzmir bay area in Figures 7.34 and 7.35. Figure 7.34 also shows the major active faults in the İzmir region as well as the epicenter of the main shock of the October 30 earthquake. The map in Figure 7.35 shows İzmir Bay at a larger scale, and the close-up view of the ground motion stations in the most severely stricken region.

Basic properties of five selected stations and peak recorded ground motion values are presented in Table 7.2. Epicentral distances of all five stations are quite similar. BAY 3514 is on a stiff site, at the edge of an outcrop (Yamanlar Hill), while all other stations are located on soft alluvial soil deposits. These five strong motion stations are shown on a larger aerial view of the Bay in Figure 7.36.

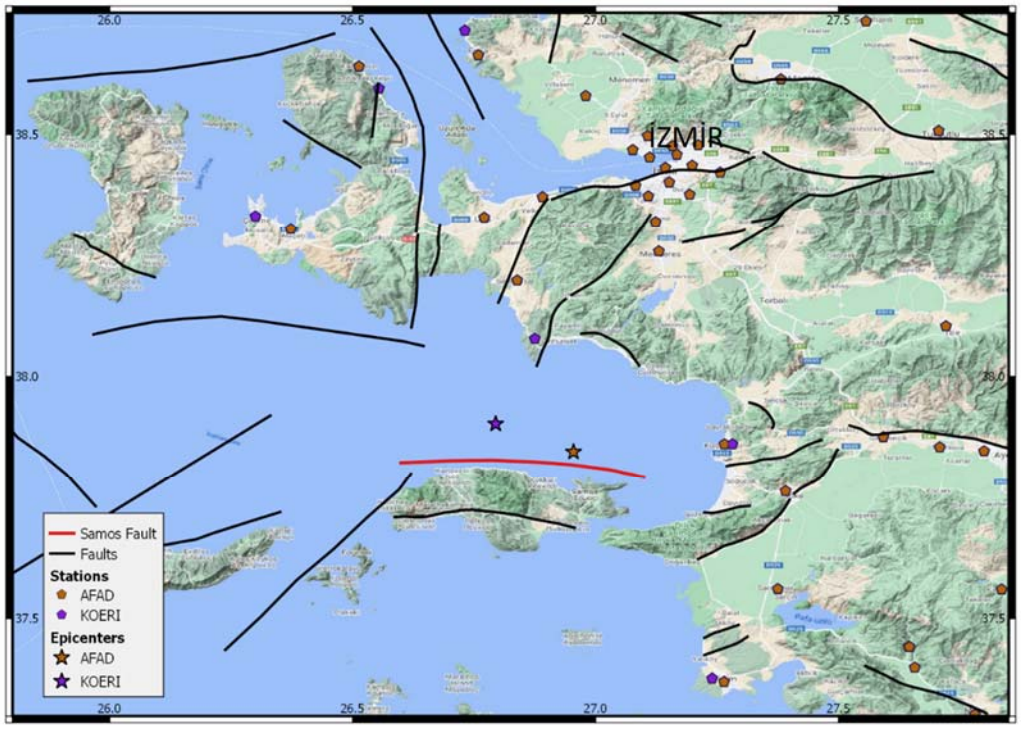

Figure 7.34. Topographical map of Izmir Bay, active faults, Samos fault, epicenter of the main shock, and locations of strong motion stations (Courtesy of Özkan Kale). İzmir urban area is distributed around the tip of the shoe.

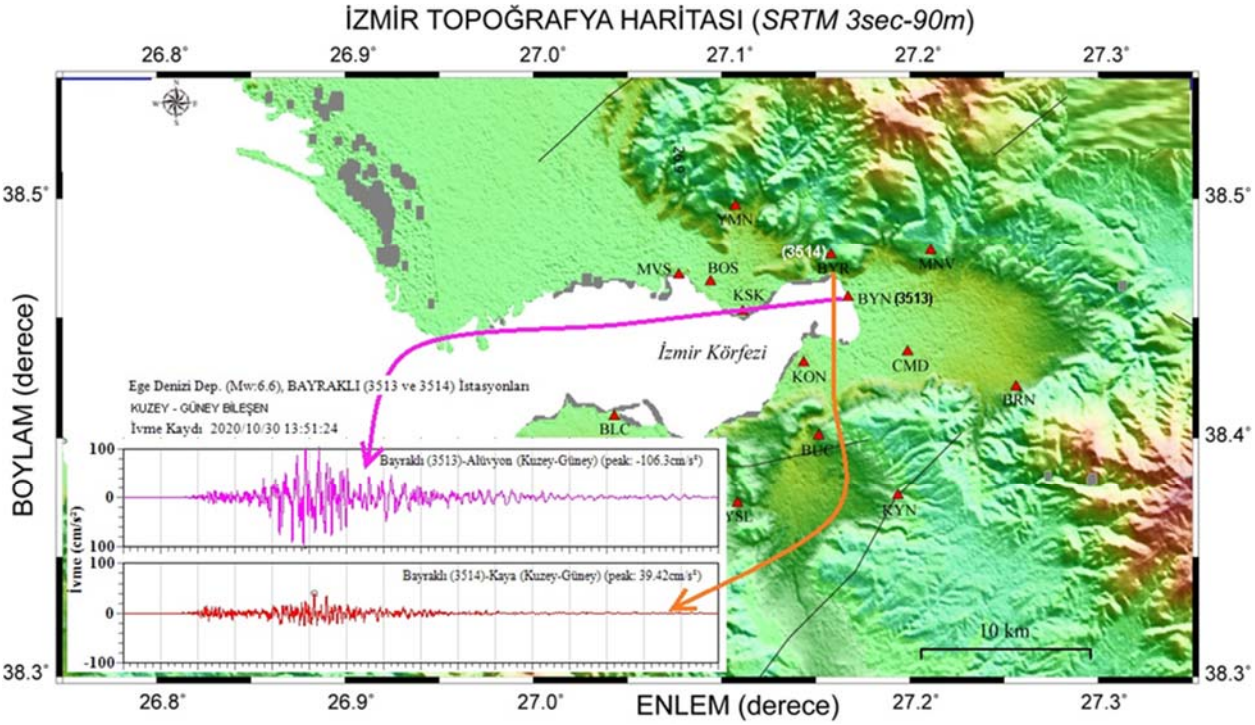

Figure 7.35. Topographical relief map of Izmir Bay, locations of strong motion stations and NS components of ground motions recorded at the BYN 3513 and BYR 3514 stations (Courtesy of Ulubey Çeken, AFAD)

Table 7.2. Properties of the strong motion stations and the peak recorded values.

Location	**Station code**	**V_{S30}** (m/s)	**Repi** (km)	**PGA** (cm/s^2)	**PGV** (cm/s)
Bayraklı	BYN 3513	196	72.0	106.3	17.1
Bayraklı	BYR 3514	836	73.4	39.4	4.2
Alsancak	KON 3518	298	68.4	106.1	11.3
Karsıyaka	KSK 3519	131	69.2	150.1	22.5
Bostanlı	BOS 3521	145	69.6	110.8	16.2

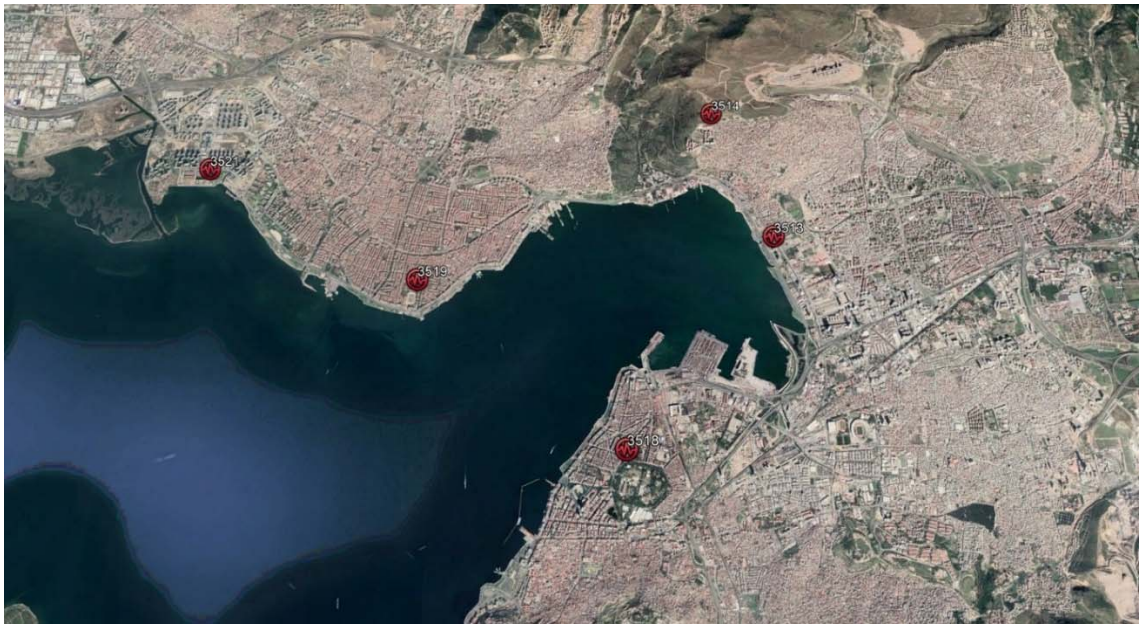

Figure 7.36. Aerial view of the tip of Izmir Bay and the locations of strong motion stations.

A satellite photo of the Northern shore of the inner bay is shown in Figure 7.37, which includes stations 3513 and 3514. The regions of heavily damaged buildings are enveloped with a yellow ellipse, where the red spots are indicating the collapsed building blocks. Yellow and green spots in the photo mark heavily and moderately damaged buildings, respectively. Station 3513, marked in orange, is very close to the region of heavy damage.

Figure 7.37. Satellite view of Izmir Bay, and the region of heaviest damage.

Station 3514 is the only stiff soil station among the five stations shown in Figure 7.36 and in Table 7.2. Since it is quite close to Station 3513, we compare the ground motions from these two stations recorded during the main shock. The NS components of the horizontal ground motions are compared at the inset of Figure 7.35 and in Table 7.2. Response spectra of both horizontal components and their geometric mean are presented in Figure 7.38. It is evident that the site properties played a strong influence on the intensity of ground motions recorded by these two stations, as discussed in detail in Chapters 3 and 4. Soft soil deposits amplified spectral response accelerations almost three times on average compared to the stiff soil site over the period range of 0.5 to 1.5 seconds. However, it should be considered that this amplification may be less under stronger ground shaking due to nonlinear site and soil response.

The long period portion ($T > 1$ s for stiff soil, $T > 1.6$ s for soft soil) of spectra from both stations match reasonably well with the 72-year (DD3) design spectra. However, the shorter period regions ($T < 0.5$ s) fall significantly below the design spectra. This is understandable, because the seismic waves from the October 30 earthquake arrive from 70km distance, and high frequency components in seismic waves were filtered out along this long travel path. Long period waves however retain their energy and dominate the response spectra, both at the stiff and soft soil recording sites. In fairness, it is not consistent to compare the response spectra from a single recorded event and the design spectra obtained by PSHA in the seismic hazard map. Seismic hazard maps account for all causative faults shown in Figure 7.34 in estimating spectral design accelerations at these stations. The faults closer to the strong motion stations will perhaps produce seismic waves that are richer in high frequencies, which will eventually increase the spectral response accelerations at shorter periods. Nevertheless, the two sets of spectra displayed in Figure 7.38 clearly reveal that the medium period structures with the fundamental period range of 0.5-1.5 seconds (approximately 7-12 story RC buildings) are affected more heavily compared to similar buildings on stiff soil sites. This observation has been ratified by the associated building damages (Section 7.2), although the observed spectral accelerations were less than half of the spectral design accelerations. If seismic strengths of buildings in the region are uniform over stiff and soil sites, which seems likely, amplified ground accelerations on soft soil sites played a major role in the localization of building damages shown in Figure 7.37.

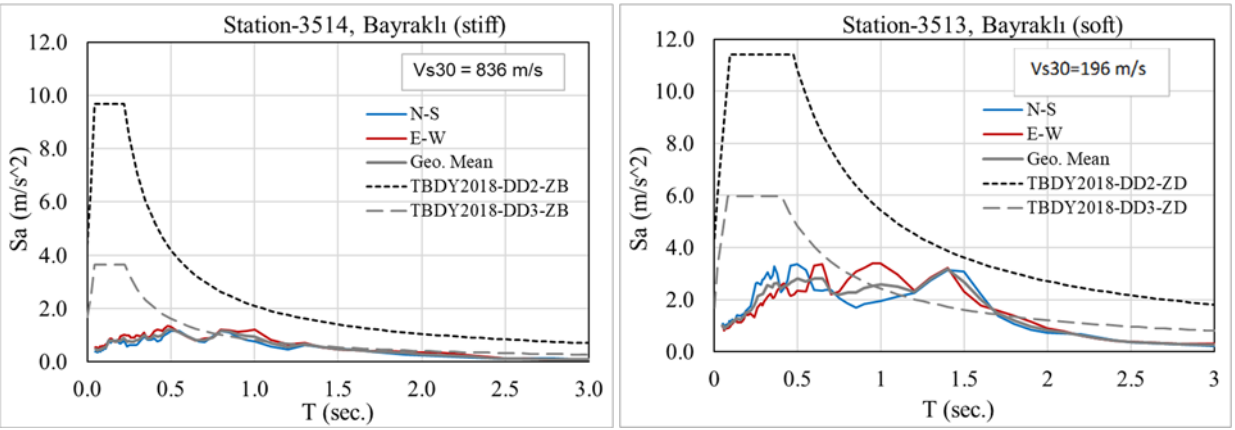

Figure 7.38. Response spectra of the recorded ground motions in stations 3514 and 3513, and the 475-year (DD2) and 72-year (DD3) design spectra obtained from the 2018 Turkish Seismic Hazard map for the corresponding in-situ soil properties.

Although soft soil sites along the margins of İzmir bay were subjected to higher intensity ground motions during the October 30 earthquake than in inland areas, this does not solely explain the non-uniform distribution of damage across the region. The response spectra of recorded ground motions from all four strong motion stations on soft soils are shown in Figure 7.39. All of these stations are located at regions of densely populated buildings. Spectral accelerations are quite similar for buildings of 5-10 stories, which dominate the RC building stock. However, heavy damage is only observed in the Bayraklı region. There are damages observed also in Karşıyaka, Bostanlı and Alsancak, but to a much lesser extent. The damage level dispersion can be explained by the differences in the quality of building stock to some extent. The distribution of damage in these regions in connection with the structural quality of buildings as well as the local site effects requires further investigation. But the information gathered on urban development in Section 7.1 reveal that Bayraklı region has developed much later compared to the other regions, and the region served to settle the surging population in İzmir after the 1980's. Substantial damage despite seismic demands lower than the requirements of the 1975 seismic code, discussed in the following section, indicates that design of these buildings in Bayraklı were not code-conforming, leading to inadequate seismic force capacity. Damage observations presented in Section 7.2 reveal that seismic detailing required by the 1975 Turkish Earthquake Code (in effect from 1975 to 1997) was not always applied. This area was developed during a period of intensive migration from small rural settlements to large urban centers.

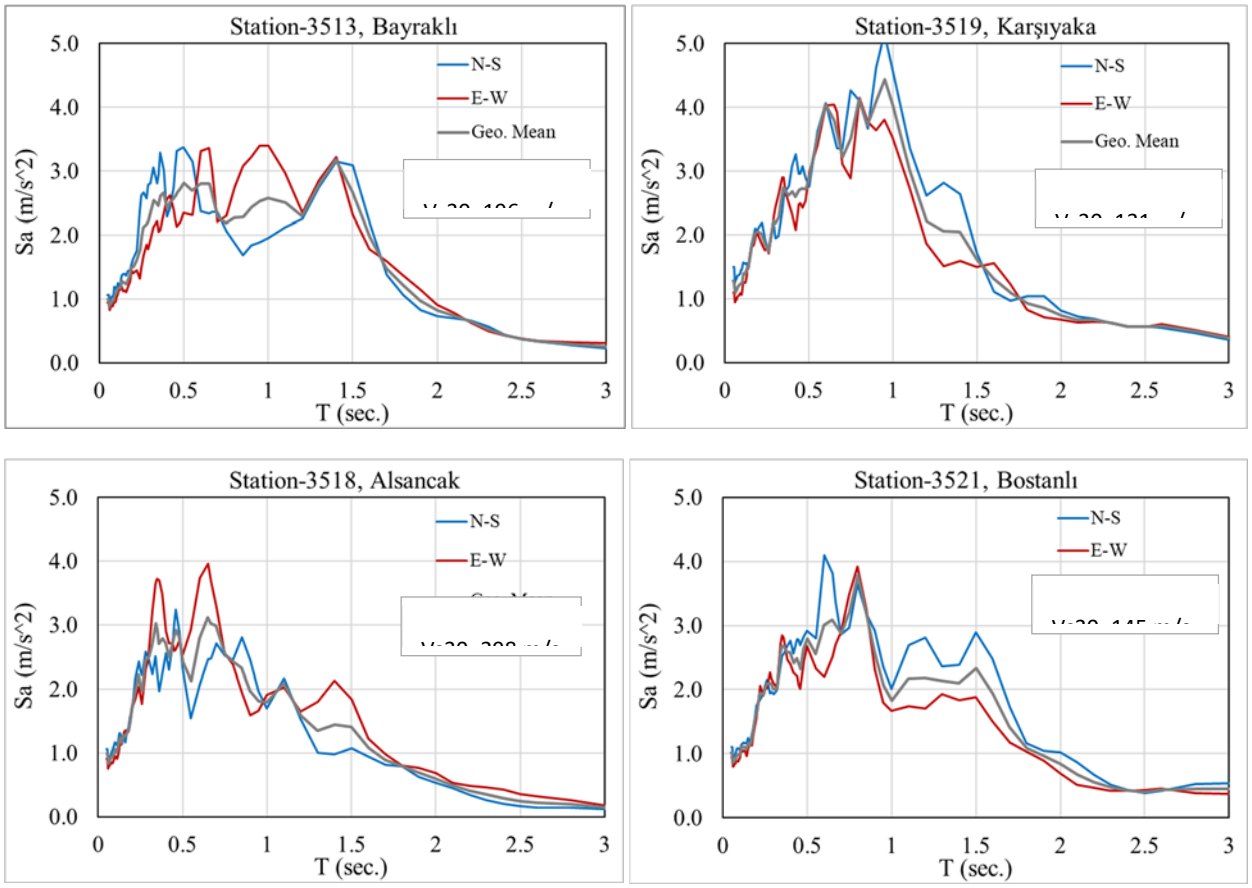

Figure 7.39. Response spectra of the recorded ground motions at stations 3513, 3518, 3519 and 3521, all on soft soil sites.

7.4 Review of Turkish Seismic Codes

The history of seismic design codes dates back to the 1940s, after which many revisions and updates have been published. As alluded to in the previous sections, most of the heavily damaged buildings were designed using recommendations given in the 1975 code i.e. *Code for Structures to be Constructed in Disaster Areas* (CSCDA 1975). The buildings constructed after 1997 and 2007 were designed according to the 1997 code (CSCDA 1997), or the 2007 code, *Code for Buildings to be Constructed in Seismic Areas* (CBCSA 2007), respectively. Few buildings are encountered in the region that were designed according to the 2019 code, *Turkish Building Earthquake Code* (TBEC 2019). We briefly summarize here the requirements of the 1975 code and highlight major changes introduced thereafter.

In CSCDA (1975), response modification factors were not provided explicitly, and the inelastic spectrum was directly specified for the design of structures. The dimensionless spectrum shape was described by the following equation;

$$S = \frac{1}{|0.8 + T - T_0|} \leq 1.0 \tag{7.1}$$

where T is the fundamental period of the structure in s and T_0 is the predominant period of soil in s. The average values suggested for T_0 range from 0.25 s (stiff soil, Vs>700 m/s) up to 0.80 s (soft soil, Vs<200 m/s). The 1975 code employs an equivalent static lateral load procedure for calculating internal forces, which relies on the base shear force calculated as

$$\begin{aligned} F &= CW \\ C &= C_0 \times K \times S \times I \end{aligned} \tag{7.2}$$

Here, W is the weight, C is the seismic coefficient, C_0 is the seismic zone coefficient representing earthquake forces, K represents the type of structural system and I is the building importance factor. Seismic zone dependence is imposed through C_0 for four earthquake zones according to the seismic hazard map published in 1972 (MPWS 1972). It is noteworthy to mention that K varies for ductile systems (as ductile and non-ductile) and structural systems (as RC frame, RC dual, Steel, Masonry, etc.) between 0.6 and 1.5, hence it serves as a relative measure of ductility between different building systems and ductility levels. A lower K is assigned to more ductile systems. There is no direct use of any force reduction factor in order to convert an elastic spectrum to the inelastic spectrum. Therefore, one should be careful about interpreting the CSCDA (1975) design spectrum.

The 1975 code can be viewed as a sufficient code for its time (it was similar to the US code), incorporating some general ductile design requirements for RC structures including confinement zones, reinforcement detailing, minimum reinforcement and size requirements for all structural members. Our past experience has indicated that, in general, the buildings designed and constructed according to the 1975 code performed satisfactorily after the earthquakes.

After approximately 22 years, the Turkish seismic design code was updated with significant changes in 1997, including more stringent requirements for ductile design and detailing, incorporating irregularities in more detail, including capacity design concepts, and using a more rational seismic hazard map displaying effective peak ground acceleration (A_0). The elastic code spectrum amplitude ($S_{ae}(T)$) was described based on A_0, specified for four seismic zones by using the following equation.

$$Sae(T) = A_0 \times I \times S(T) \tag{7.3}$$

$S(T)$ in Equation 7.3 denotes the shape of the spectrum as shown in Figure 7.40. The influence of soil on the spectrum is reflected through the changes in corner periods (T_A, T_B) given for four different soil types. In softer soil types both a shift in T_A and a wider range for T_A-T_B (i.e. wider constant acceleration region) are introduced with no direct amplitude amplification of the spectrum shape. An inelastic spectrum obtained by dividing the elastic spectrum with the

earthquake force reduction coefficient (Ra(T)) is used in the seismic design of structures. In addition to equivalent static lateral load analysis, mode superposition and response history analyses were also included in the CSCDA (1997).

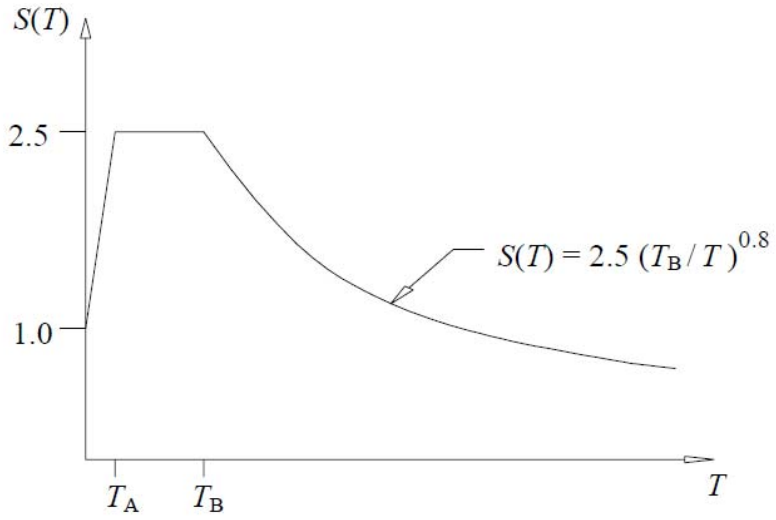

Figure 7.40. The shape of design spectrum in the 1997 and 2007 codes

The 2007 code retained all contents of the 1997 code with the addition of a new chapter for the seismic assessment and rehabilitation of existing buildings. The most recent and current code that has been promulgated in 2019 (TBEC 2019) includes almost similar general design principles of the previous code, but also included some new sections focusing on different structures (tall buildings, seismically isolated buildings, light steel buildings, wood buildings etc.). The 2019 code also introduces performance-based design approach in addition to the force-based design by using nonlinear analysis methods. One of the major changes introduced in this code is the definition of design spectrum. It is a uniform hazard spectrum that is based on a new and rational seismic hazard map, which provides spectral amplitudes (S_S and S_1) at different return periods for a reference rock soil class in geographical coordinate basis. The soil amplification in the code is similar to the NEHRP approach that modifies spectral amplitudes using amplification coefficients given for different soil types to obtain the design spectral amplitudes (S_{DS}, S_{D1}). The horizontal design spectrum is shown in Figure 7.41.

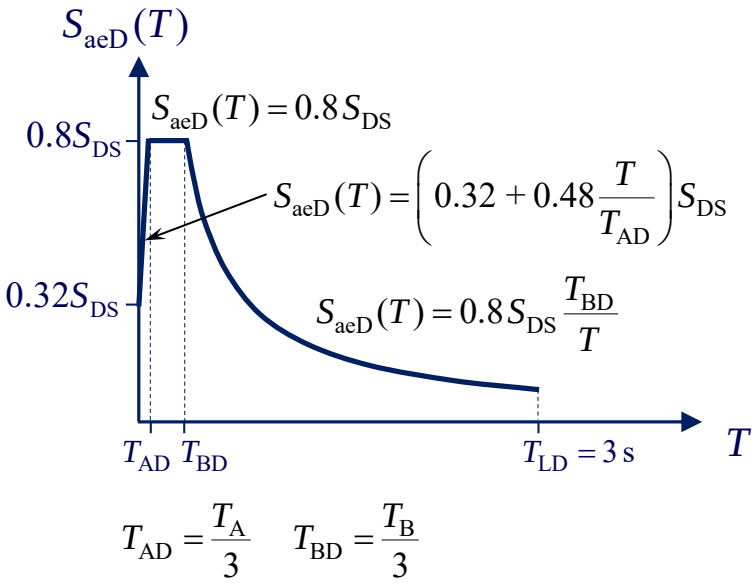

Figure 7.41. Design response spectrum defined in TBEC 2019

The elastic response spectra of all four codes are compared for soft and stiff soil sites of Bayraklı station in Figure 7.42. The 1975 code spectra are converted to elastic spectra by assuming a moderate ductility level. Although there is no explicitly specified R factor in the 1975 code, the requirements given for detailing, reinforcement and sizes imply an inherent R factor in the buildings designed per the code. Thus, a value of R=6 that corresponds to moderate ductility defined in the recent codes is assumed to be reasonable. The relative ductility factor K is taken as 1.0. As mentioned before, all code spectra are above the recorded values, even in the 0.6-1.5 second period range where significant amplification is observed. Figure 7.42 reveals clearly that corner periods of TBEC 2019 are shorter than in the other codes implying that it is less conservative in the period range of 0.6-1.5 second as compared to the 1997 and 2007 codes.

Turkish seismic design codes appear to define design force levels and other requirements that would suffice for earthquake resistant design as revealed by the past earthquakes including the October 30, 2020 earthquake. The 1997, 2007 and 2019 codes include the most recent knowhow, up-to-date approaches, advanced methods and requirements of modern seismic design codes. Despite its limited coverage of ductility, irregularity, detailing and capacity design principles, the buildings designed and constructed properly according to the 1975 code are expected to sustain limited damage during this event.

A pronounced effect of the 30 October earthquake is the significant damage in Bayraklı, some 70 km away from the epicenter. There is consensus that this is due to site amplification at mid-to-long periods. However, the amplified ground motion acceleration levels observed are still lower than the design values.

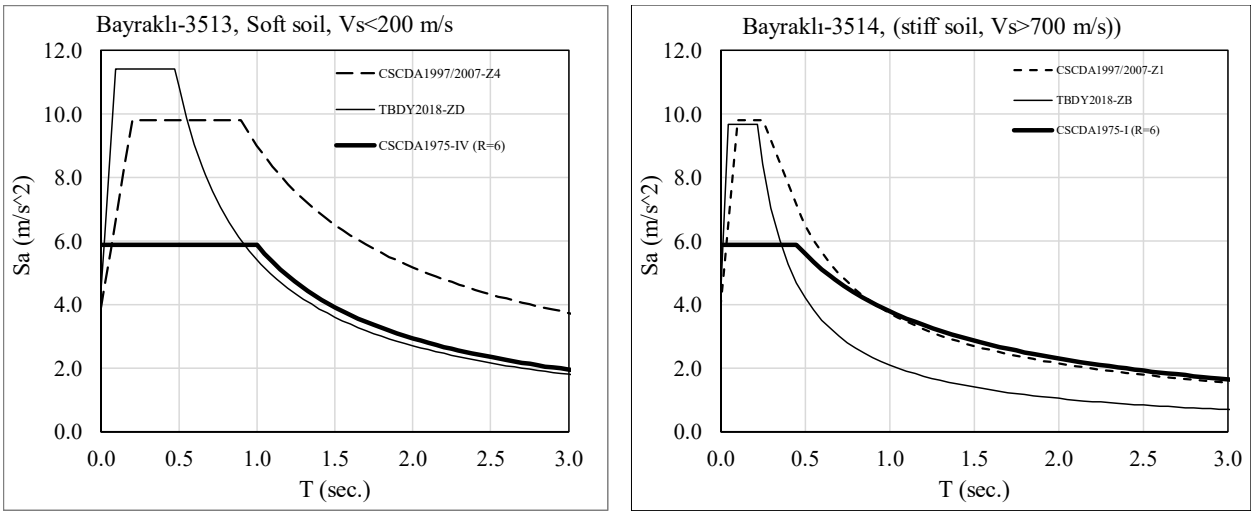

Figure 7.42. Comparison of Design Spectra

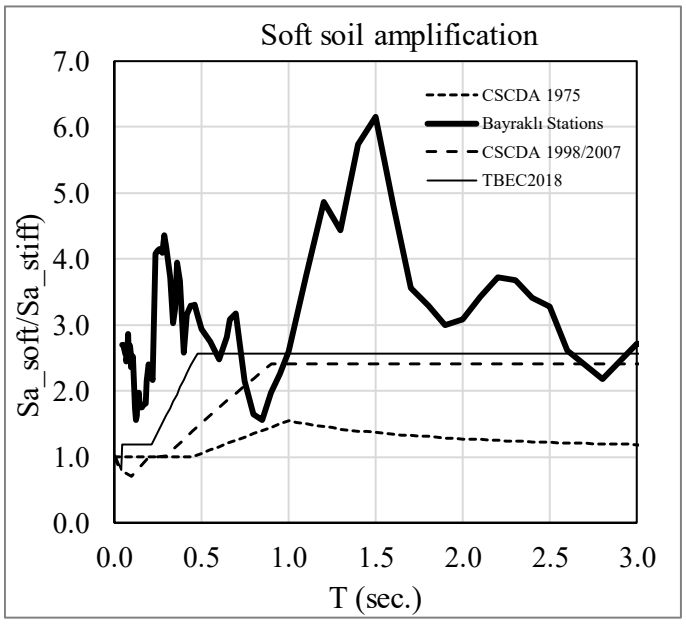

Figure 7.43. Soft-to-stiff soil amplifications based on Bayraklı Stations

This implies that not only soil amplification, but also some major drawbacks and deficiencies of the buildings played an important role in the poor building performance. The observed site spectrum compared to the design spectra indicates that for the mid-to-long period range, the code spectrum shape may be improper and unconservative for such sites. The spectral ordinates obtained for station 3513 (soft soil) are divided with the ones determined for 3514 (rock) to obtain the soil amplification coefficients, which are compared in Figure 7.43. This figure clearly shows that the code amplifications are below the measured amplification levels in Bayraklı. Therefore, site-specific response spectra for such areas have to be considered and necessary modifications in the current code should be undertaken. Aside from this exception, TBEC (2019) appears to address the requirements for earthquake resistant building design adequately.

7.5 Response of Tall Buildings in Izmir

The tallest building in Izmir, the 216 m tall 48-story Mistral Izmir Office Tower in the Konak district, has been monitored since January 27, 2019 within the scope of a research project entitled “Guidelines for Structural Health Monitoring Systems on Tall Buildings and a Case Study”. The project is undertaken by METU and funded by the Disaster and Emergency Management Presidency of Turkey (AFAD) under its National Earthquake Research Program. The building was permanently instrumented with a 27-channel structural health monitoring system (Figure 7.44) and vibration records from the building and seven AFAD strong motion stations in the vicinity of the building have been streamed in real time to METU (Gumus and Celik, 2019). Recorded floor accelerations and calculated floor displacements during the mainshock are presented in Figure 7.45. The maximum floor acceleration is 0.28 g at the 48th floor and 0.11 g at the second basement while the maximum displacement is 16 cm at the 48th floor. No damage was reported, and the building is in continued use following the earthquake.

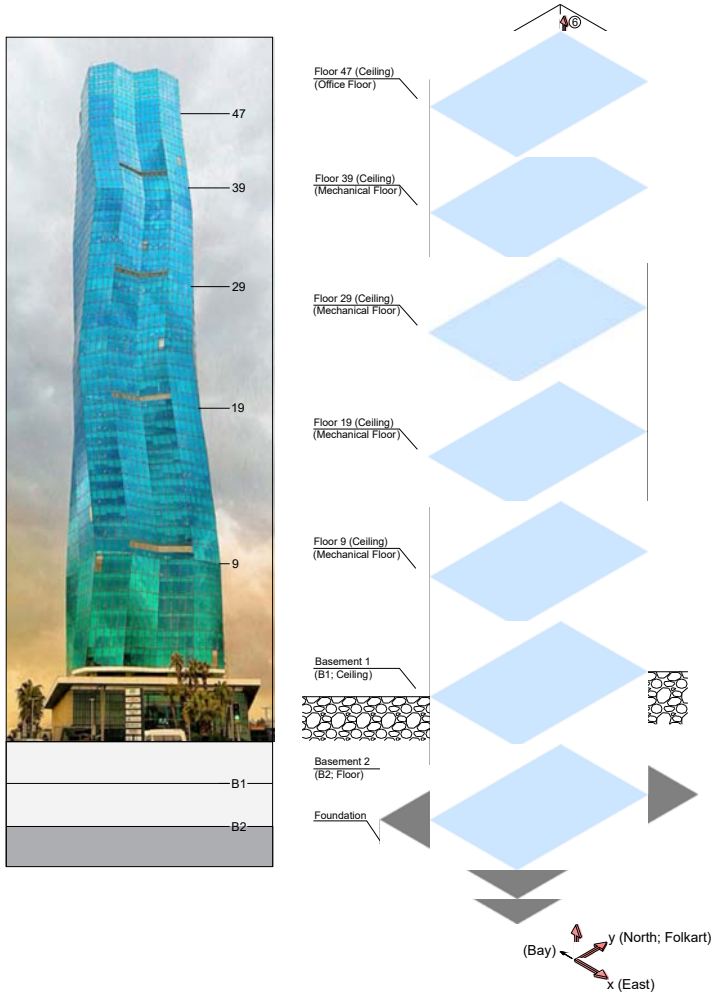

Figure 7.44. The instrumentation scheme

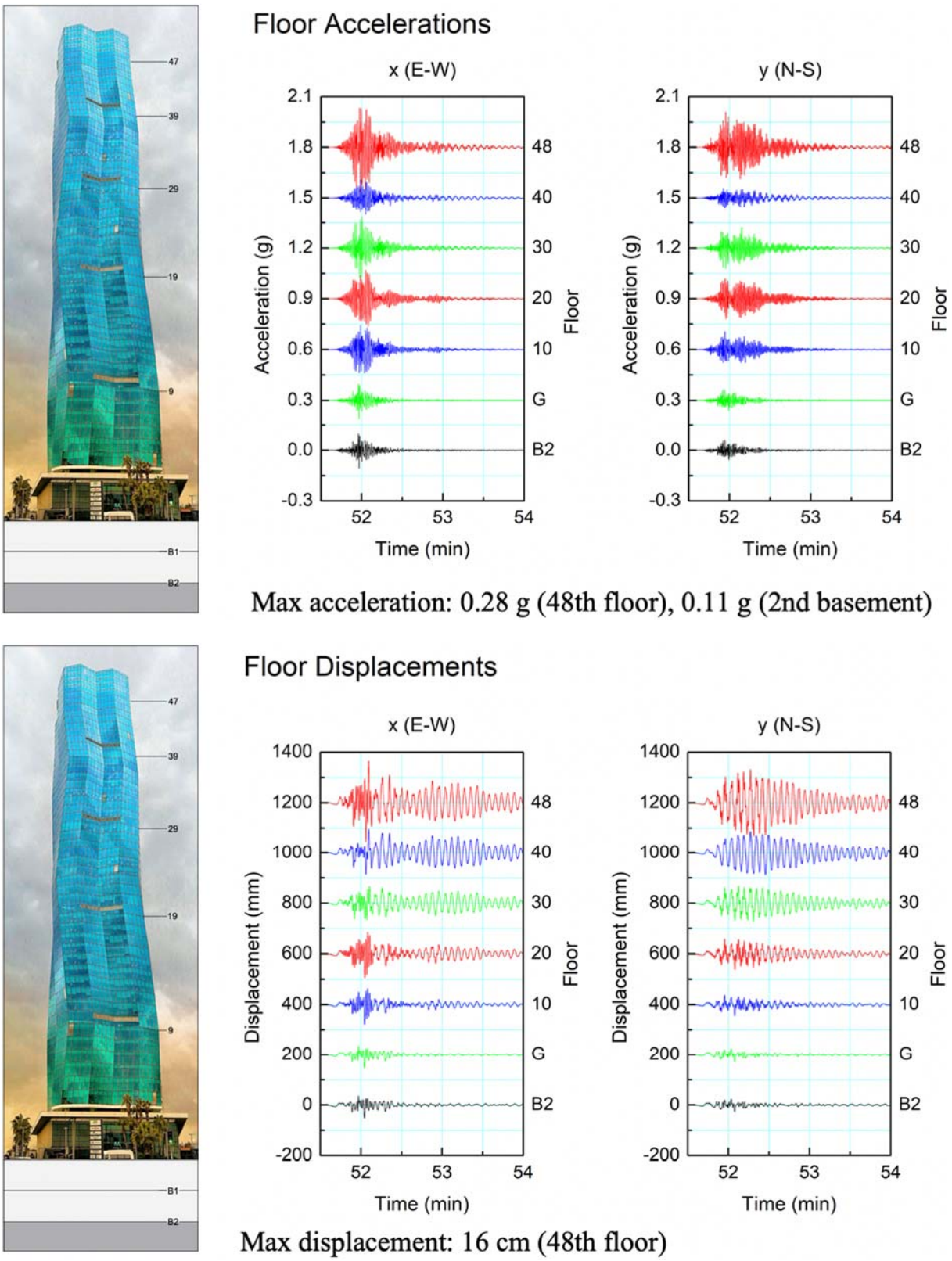

Figure 7.45. Floor accelerations and displacements

Figure 7.46 compares the 5% damped elastic response spectra for the building base motion recorded during the earthquake with the spectra defined in the Earthquake Code for Railway, Harbor and Airport Structures (RHA; Ministry of Transportation, 2008), Turkish Earthquake Code at the time of construction (TBEC 2007; Ministry of Public Works and Settlement), and the current Turkish Building Earthquake Code (TEC 2019; AFAD). Although the building base motion contains kinematic interaction, the comparison is given to have an idea about the level of ground motion measured at the base with respect to the code spectra. Spectral acceleration amplitudes for the building base motion are less than those for the design earthquake (return period, T_r = 475 years) at all periods. The mainshock can at most be considered as frequent/service earthquake (T_r = 72/43 years) given that the natural periods of the building are around 4 s and 1 s for the first and second modes, respectively, along both the E-W and N-S axes (Gumus and Celik, 2019). Hence, the nearby tall buildings would not be anticipated to suffer structural damage during the earthquake.

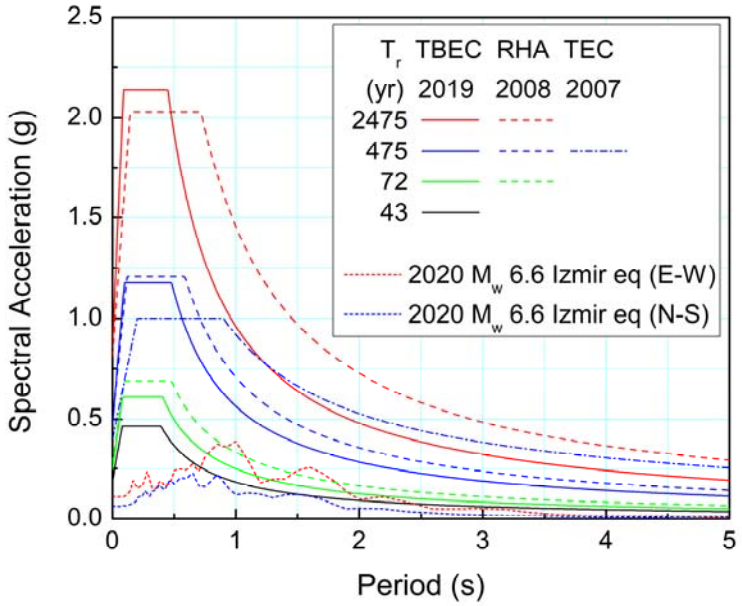

Figure 7.46. Building base motion versus code spectra

7.6 Performance of Bridges

The bridges along Mürselpaşa - Zafer Payzın highway line were investigated in detail after the October 30, 2020 mainshock. The visited line and bridges are marked in Figure 7.47.

Figure 7.47. Inspected line & bridges

The investigated bridges are approximately 70 km away from the earthquake epicenter. No permanent movement has been observed in the superstructure beams and supports. The bending or shear capacity of the bridge columns and foundations has not been exceeded and no cracks have been observed due to the recent earthquake. There were no settlements on the foundations over soft soil. No movement was observed at the bridge expansion joints. No loss of function such as rupture or fracture has been observed in non-structural bridge elements (precast panels, pedestrian railings, lighting poles, etc.). The earthquake performance of longitudinal joints between twin bridges was adequate as expected, and some small concrete pieces not more than 2-3 cm fell on the ground only at some local zones. After the examination of the superstructure and infrastructure of the bridges, no earthquake-related damage was detected.

A structural modal analysis has been performed on two segment of bridges, one curved and the other straight. The periods ranged from 0.65 seconds to 1.55 seconds. These analyzed bridges are in the close vicinity of the Bayraklı region and close to the seismic recording station 3513. Most likely, they have been subjected to spectral accelerations around 0.3 g at their corresponding vibration periods (Figure 7.48-7.49).

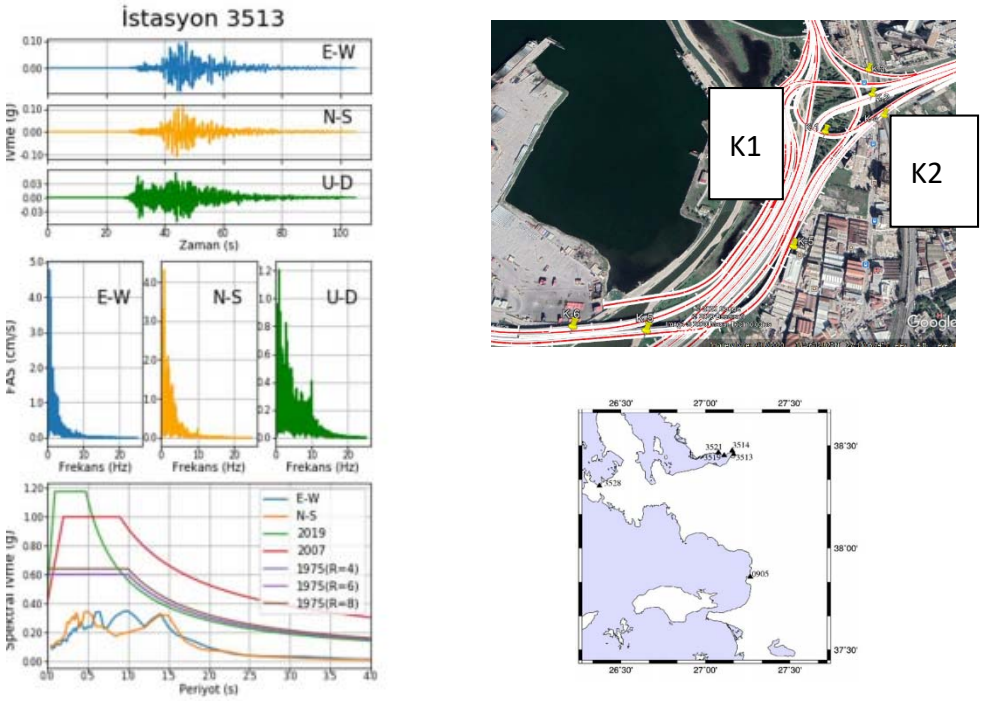

Figure 7.48. Bridges in the Vicinity of the Bayraklı 3513 Station. (taken from DMAM report 2020)

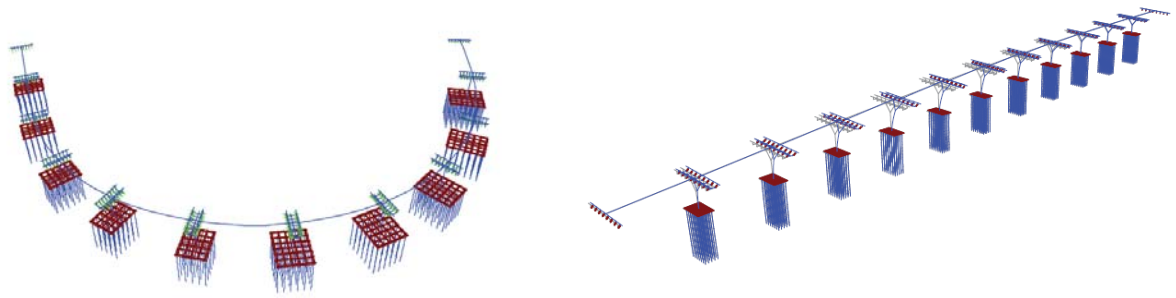

(a) (b)

Figure 7.49. a) Curved Bridge, Long Axis of Bridge Path: Mode Period = 0.85 sec, Transverse Axis of Bridge Path: Mode Period = 0.65 sec, b) Straight Bridge , Long Axis of Bridge Path: Mode Period = 1.55 sec, Transverse Axis of Bridge Path: Mode Period = 1.25 sec (taken from draft seismic bridge evaluation report submitted to Izmir Municipality on August 24, 2020)

The structural history of the bridges cannot be traced after the transfer of ownership from KGM to İzmir municipality. Mürselpaşa-Zafer Payzın highway line rehabilitation project began in September 2019, and includes the maintenance, repair and identification of seismic performance of the bridges, highway, connection and roads. Improvement and strengthening studies continue within the scope of the strengthening projects. Most of the cracks observed since the beginning of the project were caused by rainwater and are ASR (Alkali-Silica Reaction) cracks, which are the result of a chemical reaction that occurred years ago in the bridge elements. These chemical

cracks did not grow after the earthquake. The repair of these cracks will be carried out within the scope of the related project (Figure 7.50).

Figure 7.50. ASR based cracks (non-seismic) and general view

Bridges were available for use right after the earthquake. As a result, it was determined that bridges that performed successfully during the earthquake were serviceable without a need of emergency intervention (Figure 7.51).

Figure 7.51. A typical before-and-after earthquake photo (December 2019 and November 2020)

Bridge girders, which were started to be built 20 years ago and discontinued because of a plan change, fell during the earthquake because their lateral stability has not been provided for the last 20 years (Figure 7.52). These bridges were not on the highway line for service.

Figure 7.52. An incomplete bridge construction 20 years ago without providing a lateral girder stability at the site (10 years ago and now)

No seismic induced damage has been observed on bridges under service, even the bridges that had some prior deterioration due to the ASR problems developed over the last 30 years. The analysis of spectral accelerations obtained from a close-by station indicate that the bridges are most likely subjected to 0.3g at their fundamental vibration modes. Similar observations have also been made after three major earthquakes in Turkey, even for the very old bridges, most probably not designed for seismic events. The flexible supports between the superstructure and substructure levels are believed to facilitate this successful seismic performance. Bridge construction is usually under strict supervision of the governmental agencies, which also contributed to obtain this satisfactory level of performance.

7.7 Seismic Damage Observations on the Island of Samos, Greece

7.7.1 Overview of the structural portfolio

Samos island (Greek: Σάμος [ˈsamos]) is located in the eastern Aegean Sea, south of Chios, north of Patmos and the Dodecanese, and off the coast of western Turkey. It is the 9th most populous island in Greece with a population of 33,814 people. Given its proximity to the epicenter (see Chapter 1), Samos suffer extensive structural damage, however, the earthquake impact on buildings and infrastructure was not as devastating as that observed in Izmir due to the different structural typologies, building stock exposure (Izmir being 100 times larger in terms of population) and the frequency content of ground motion.

The buildings in Samos can by classified in four major typologies in terms of their load bearing system and use:

- *Reinforced concrete buildings:* Located sparsely throughout the island, the majority of these buildings has been constructed according to the 1959 and 1985 seismic codes (more details are provided in section 7.7.3). With very few exceptions, they are low-rise buildings (i.e., 1-3 storys), with a Moment Resisting Frame (MRF) or Dual RC load bearing system (Section 7.7.4).

- *Masonry buildings:* One or two-story residential and school buildings that are constructed by clay, stone or concrete blocks, typically with high quality mortar, or in case of small villages,

residential buildings by rubble stones and low-strength lime or clay mortar (Section 7.7.5). Tanneries are also included in this category (Section 7.7.6).

- *Timber buildings:* constructed partly of wood or timber framed masonry located in some of the villages.
- *Listed buildings* (*i.e., of special architectural, religious and historical importance) and other cultural heritage masonry buildings:* including churches (Section 7.7.7), the Castle of Lykourgos Logothetis, and the Heraion (Section 7.7.8).
- *Reinforced concrete and stone bridges*: small (length<50m) bridges part of the island roadway network. Stone bridges are also part of the network (Section 7.7.9).

7.7.2 Seismic codes and recorded spectra

The first Greek Seismic Code (*Αντισεισμικός Κανονισμός*, ΑΚ) was issued in 1959 prescribing, as in most countries at that time, a seismic coefficient for horizontal loads that was taken as constant, independent of the dynamic properties and the type of the buildings. For Samos Island, the base shear seismic design coefficient was set equal to ε = 0.06, 0.08 and 0.12, for firm, medium and soft soils, respectively. This code was revised considerably in 1985 introducing several new provisions including more closely spaced stirrups in joints and the requirement for using frame analysis for multi-story buildings instead of the one-storey-model analysis prescribed in the 1959 code. Also, the 'weak beam – strong column' concept was adopted with a simplified capacity design. The seismic code was further revised in 1995 (ΝΕΑΚ1995) and then again in 2000 (ΕΑΚ2000), after the major earthquakes in Greece and Turkey in 1999. The lattest upgraded version, adopted the Eurocode philosophy of earthquake-resistant design and it was enriched with a new seismic hazard map in 2003. It is still in use in Greece in parallel with Eurocode 8. Differences between the two codes (ΕΑΚ2000 – EC8) are not major and the performance of structures designed to them is expected to be similar.

Figure 7.53 compares the 5%-damped elastic acceleration response spectra of the earthquake record at the SMG1 station in Vathy, Samos with those of the Greek Seismic Code (ΕΑΚ2003). Note that the comparison is made for two different soil classes, namely, "Β"/"Γ" (i.e., medium and soft) given an estimate of the V_{S30} value (equal to 380 m/sec) at the location of the accelerometric station. Because that design to the 1959 Code was based on allowable stresses, the seismic coefficient is multiplied by 1.7 to correspond to ultimate strength and to facilitate comparison with the modern code (straight lines referring to ε' = 0.10, 0.14 and 0.21) for firm, medium and soft soils, respectively.

It is seen that the spectral accelerations of the recorded motions do not exceed those of the elastic spectra of ΕΑΚ2000 or the Eurocode 8 (Figure 7.54) except for the frequency range of 0.5-0.7sec, which is beyond the elastic periods of the vast majority of the building stock in Samos. However, seismic demands exceed the design level of buildings designed to the older versions of the code. A similar comparison is performed in Figure 7.54 between the spectra of the recorded

motion and the elastic spectra of Eurocode 8. Again, two code spectra are plotted for Soil Classes "B" and "C".

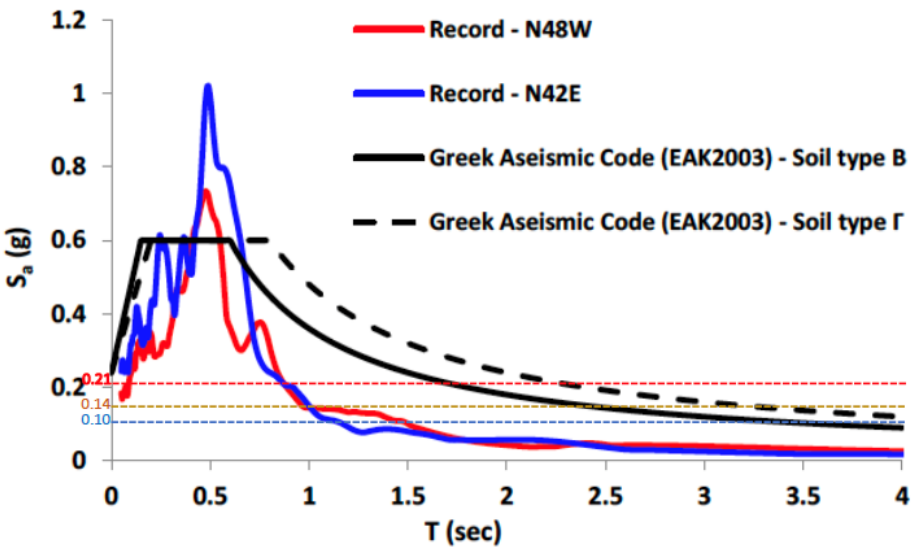

Figure 7.53: Comparison of the 5%-damped elastic acceleration response spectra between the earthquake record at Vathy, Samos and the Greek Seismic Code (EAK2003) - horizontal components of seismic motion. The horizontal lines anchored at 0.10, 0.14, 0.21g correspond to the base shear coefficients according to 1959 Greek Seismic Code for ultimate strength design.

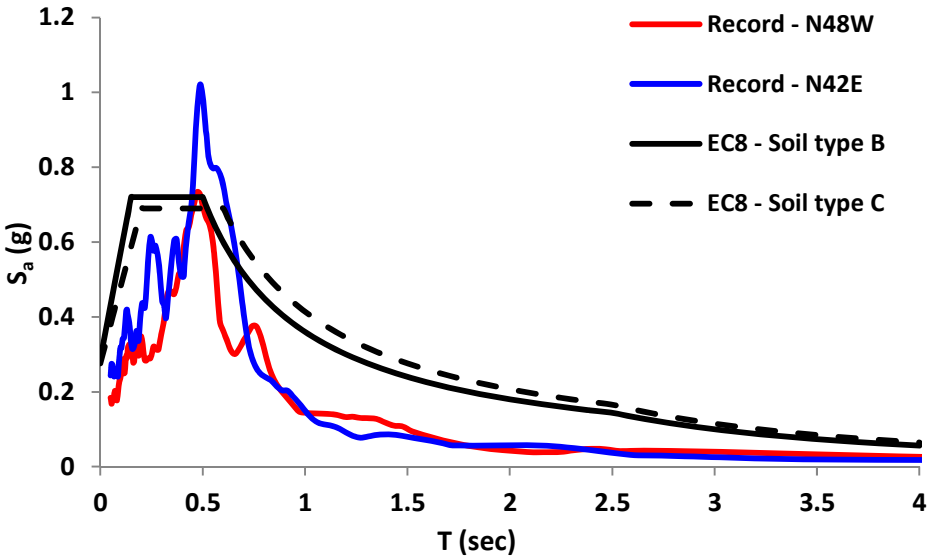

Figure 7.54: Comparison of the 5%-damped elastic acceleration response spectra between the earthquake record at Vathy, Samos and Eurocode 8 - Horizontal components of seismic motion.

From both Figures 7.53 and 7.54 and the elastic spectra plotted, it is evident that the seismic demand over capacity ratio, though considerable, matches well the lack of collapses building response during the 30/10/2020 earthquake even if, for the sake of comparison a behaviour factor q of 3.5 and 1.5 is assumed for the (limited number of) reinforced concrete buildings and the majority of masonry buildings, respectively. It also explains to a great extent the good performance of newly constructed buildings and the (varying) degree of damage of older, under designed, masonry ones. Overall, the performance of buildings designed following the respective provisions of the code enforced at the time of construction as well as basic principles of structural configuration (in terms of regularity in plan and height, allocation of infill panels, quality control) was quite satisfactory, despite the severity of the shaking, even for buildings designed to the 1985 and 1959 seismic codes.

Another important aspect to note is damage to non-structural elements, such as infill walls, as well as heavy equipment movement that was observed on several occasions posing a potential threat, particularly in schools, for the lives of students. Fortunately, schools were just closed at the time of the earthquake, however, the above observations demonstrated the importance of pre-earthquake assessment of potential non-structural damage and the need for mitigating measures. It is expected that for all schools in the island, a second-level inspection of their seismic capacity, which is currently ongoing, will contribute to their restoration and retrofit, where needed, including the inspection and repair of the non-structural elements.

7.7.3 Structural damage distribution in Samos island - rapid visual inspection

Immediately after the earthquake, the General Secretariat of Infrastructure authorities and services was mobilized to deal with the impacts of the earthquake on the island. A few hours after the event, the Secretary General of Public Infrastructure, the Director General of Natural Disasters Rehabilitation (GDAEFK) and the First Response Team of engineers arrived in Samos, according to emergency planning protocols. Upon their arrival, engineers of GDAEFK carried out inspections of several critical buildings. At the same time, the Director General of GDAEFK met with the Vice Governor and the island Mayors and was briefed about the impacts of the earthquake. After the coordination meeting outside the City-Hall of Vathy, phone calls with the presidents of the local administrative districts, the General Director and the executive engineers of GDAEFK, immediate inspections were planned for buildings and ports around the island affected by the earthquake and tsunami. It is noted herein that the Directorate General of Natural Disasters Rehabilitation (GDAEFK) is the State Authority for damage assessment and rehabilitation after natural disasters and is responsible for the inspections of buildings as well as for implementing the foreseen measures at the affected area. In this context, a total of 90 engineers were deployed on the island and classified buildings as “safe”/”unsafe to use”, as well as identified those requiring temporary support.

Figure 7.55. Engineers of GDAEFK in duty

Post-Earthquake Building Inspections. As shown in Figure 7.56, post-earthquake assessments of building damage and usability were performed by means of visual inspection and expert's judgement in three phases: Phase A (first degree) Rapid Damage Inspection, Phase B (second degree - reinspection), and Phase C (third and final inspection by three civil engineers, only for buildings with extensive damage).

The above assessments were recorded on official technical documentation, leading to rehabilitation or repair. The purpose of post-earthquake inspections was to inform citizens whether their houses could be used, identify and register primarily dangerously high-risk buildings so that they can be demolished by the authorities, as well as assessing, as soon as possible, the number of buildings that are not usable. It was further aimed to identify the households needing emergency shelter and estimate the cost of repairs of the damaged buildings before taking the necessary measures. The above analysis of these data further assisted the government to prioritize the actions for faster recovery, policymaking and disaster preparedness in light of future events. Next, compensation was provided for the losses incurred, in order to rebuild or restore properties (Figure 7.56). Structural rehabilitation can then be performed by implementing either Eurocode 8 – Part 3 (CEN, 2004) or the Greek Code for Seismic Interventions (ΚΑΝ.ΕΠΕ., ΕΡΡΟ, 2012).

The whole program will last several years given the lack of insurance policies in the region and the fact that citizens rely on the state for funding.

Building Inspection Data. Rapid Damage Inspections started the same day of the earthquake, on October 30th and ended on November 15th. Engineers of GDAEFK performed inspections on the islands of Samos, Ikaria, Chios and Fourni. The number of inspections performed per municipality and per municipal unit is shown in Figure 7.57. During Phase A, a total of 4,245 inspections of buildings were performed and 57% of buildings were classified as "unsafe to use" (Figure 7.58). The assessments were performed as part of a door-to-door inspections of damaged buildings, or upon people's request. The rather high proportion of "safe" buildings among those inspected is a consequence of the fear of people for another strong earthquake and the need of inspection of their buildings by experts. Ultimately, the entire building stock was inspected. The majority (87%) of the "unsafe" buildings, was masonry and only 6% was RC (Figure 7.59). It is also reported that among the total building stock inspected in Samos, 647 were RC, out of which 136 buildings were tagged as unsafe for further use. However, only 20 exhibited significant damage on the load bearing system.

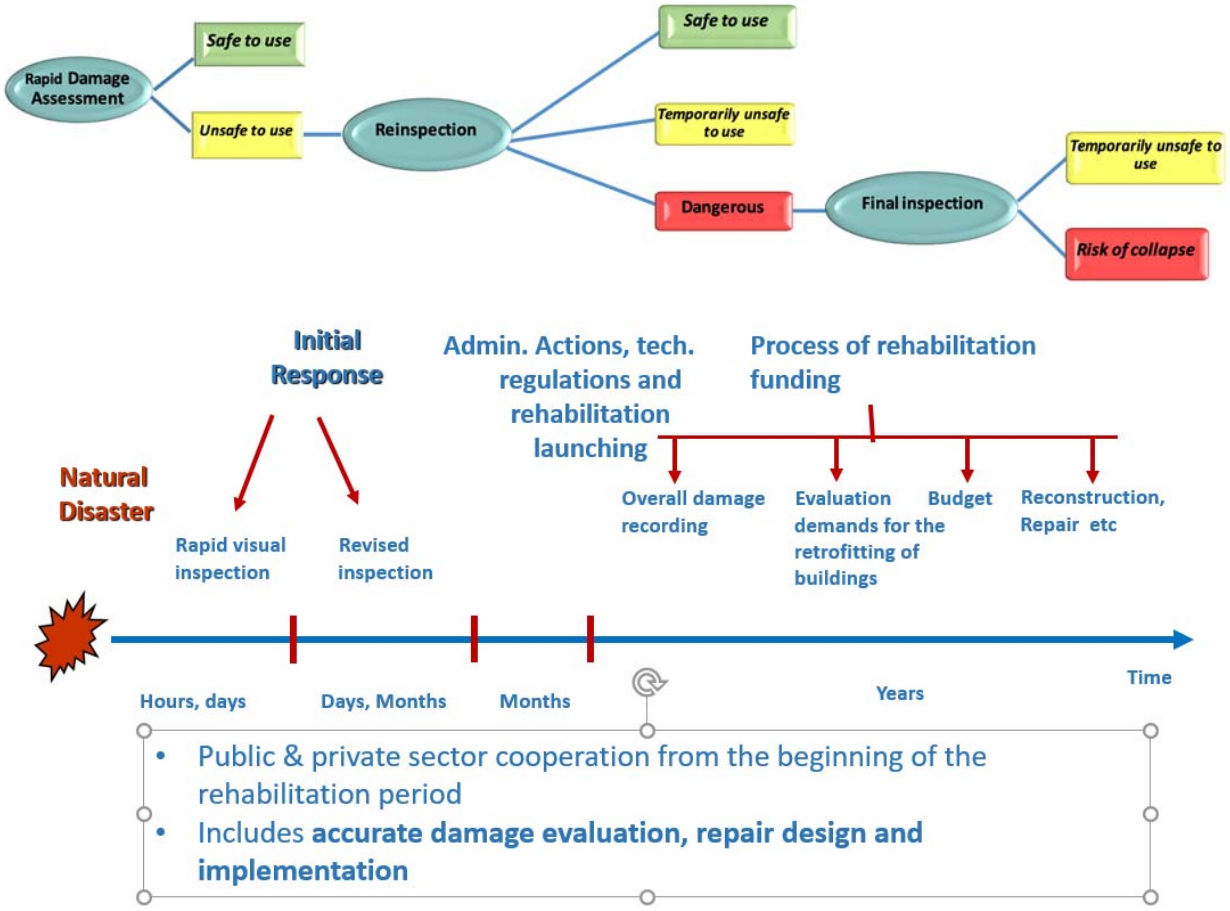

Figure 7.56. Action sequence of post-earthquake building inspection.

Table 7.3 summarizes the outcomes of the Phase A inspections. The majority of inspections concerned residential buildings; 1,992 of them (53%) were classified as "unsafe to use", while 138 buildings were deemed as collapse hazards. Buildings at risk of collapse required immediate measures, including issuing a special permission for immediate demolition. Table 7.4 summarizes the outcomes of Phases B and C inspections. The corresponding numbers of residential buildings that needed repair ("unsafe to use") was reduced to 1,593, with an increased amount of 303 buildings tagged for demolition.

Structural characteristics of Samos building stock. For completeness, the profile of the building stock in the island of Samos is provided in Table 7.5 as provided by the Hellenic Statistic Authority in 2011. It is noted that the census figures listed in the table refer to apartments and not statically independent buildings, hence, they can only be used in relative sense and with caution. It is a good indication, however, of the period of construction of buildings in Samos, as they reveal that 44% of the buildings were constructed before 1960, that is, without seismic provisions (see Section 7.7.2). It is also interesting to note that 54% of the buildings are masonry or composite structures.

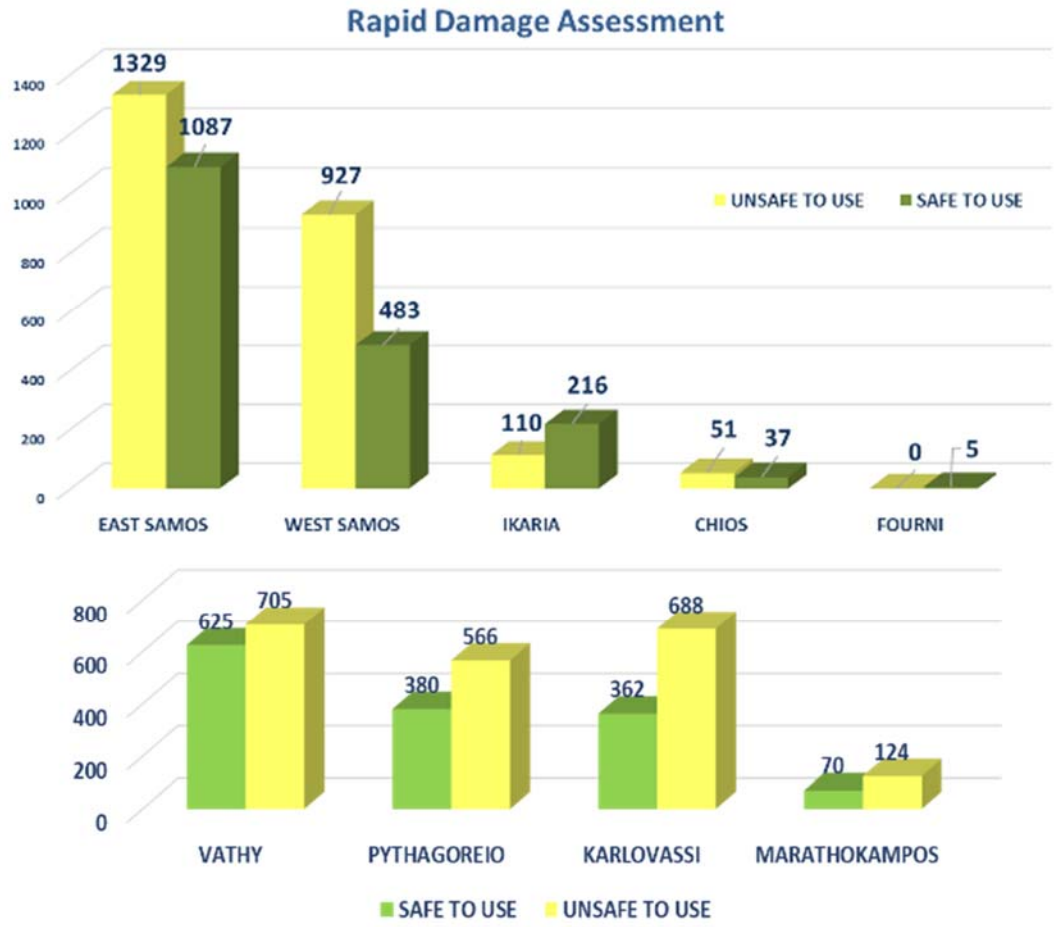

Figure 7.57. Number of assessments and classification per municipality and per municipal unit in the islands of Samos, Ikaria, Chios and Fourni.

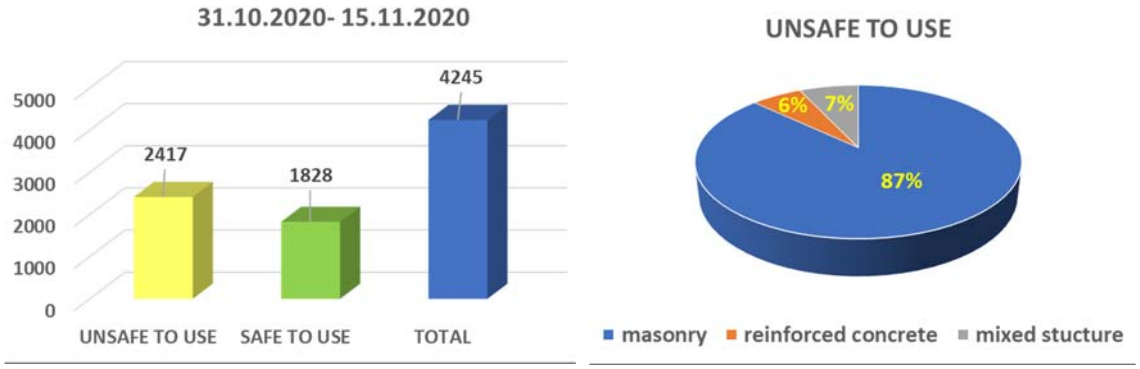

Figure 7.58. Number of assessments per classification (left) and distribution of structural typology for buildings tagged as “unsafe to use” (right).

Table 7.3. Rapid Damage Assessment: Number of assessments classified per usage for the islands of Samos, Ikaria, Chios and Fournoi (Phase A).

	HOUSES			PREMISES- STORES			CHURCHES - PUBLIC BUILDINGS			WAREHOUSES- STABLES ETC			TOTAL			
MUNICIPALITY	UNSAFE TO USE	RISK OF COLLAPSE	SAFE TO USE	UNSAFE TO USE	RISK OF COLLAPSE	SAFE TO USE	UNSAFE TO USE	RISK OF COLLAPSE	SAFE TO USE	UNSAFE TO USE	RISK OF COLLAPSE	SAFE TO USE	UNSAFE TO USE	RISK OF COLLAPSE	SAFE TO USE	TOTAL
EAST SAMOS	1114	33	895	46	3	107	80	0	54	89	1	31	1.329	37	1.087	2.453
WEST SAMOS	748	105	403	44	0	34	50	0	40	85	6	6	927	111	483	1.521
IKARIA	86	0	190	0	0	1	20	0	22	4	0	3	110	_	216	326
CHIOS	44	0	31	0	0	4	6	0	2	1	0	0	51	_	37	88
FOURNOI	0	0	0	0	0	0	0	0	5	0	0	0	0	_	5	5
TOTAL	*1.992*	*138*	*1.519*	*90*	*3*	*146*	*156*	*0*	*156*	*179*	*7*	*40*	*2.417*	*148*	*1.828*	4.393
	3.649			*239*			*312*			*226*			*4.393*			

Table 7.4. Rapid Damage Assessment: Number of assessments classified per usage for the islands of Samos, Ikaria, Chios and Fournoi (Phases B & C).

	HOUSES			PREMISES-STORES			CHURCHES- PUBLIC BUILDINGS			WAREHOUSES-STABLES ETC			TOTAL			
MUNICIPALITY	GREEN	YELLOW	RED	GREEN	YELLOW	RED	GREEN	YELLOW	RED	GREEN	YELLOW	RED	GREEN	YELLOW	RED	TOTAL
WEST SAMOS	496	540	181	37	15	5	13	48	0	22	60	62	568	663	248	1.479
EAST SAMOS	477	920	120	29	32	10	20	65	1	17	90	29	543	1.107	160	1.810
IKARIA	18	58	1	1	2	0	2	7	0	0	5	0	21	72	1	94
CHIOS	106	75	0	4	1	0	3	11	0	2	2	0	115	89	0	204
TOTAL	1.097	1.593	302	71	1	0	38	131	38	41	157	91	1.247	1.931	409	3.587
	2.992			136			207			289			3.587			

Table 7.5 Building stock in Samos classified by period of construction[1]

Construction period			
Municipality Unit	Before 1960	Before 1985	Before 2000
Vathy	44%	72%	90%
Karlovassi	47%	74%	91%
Marathokampos	37%	73%	93%
Pythagorio	46%	79%	95%
Total	**44%**	**74%**	**92%**

[1] https://www.statistics.gr/census-buildings-2011

Table 7.6 Percentage of RC buildings per Municipality Unit [2]

Municipality Unit	Total	R/C	%
Vathy	9,345	4,038	43%
Karlovassi	7,588	3,178	42%
Marathokampos	3,552	1,583	45%
Pythagorio	6,903	3,195	46%
Total	**27,388**	**74%**	**44%**

7.7.4 Reinforced concrete buildings

As already reported, the damage observed in RC buildings was rather limited, and no collapse occurred. Typical damage was related to soft (open) ground floors, in buildings designed and constructed before 1985. The lack of adequate stiffness at the ground floor, combined with scarcity of shear reinforcement, led to shear failures of columns, walls and beam-column joints, as shown in Figure 7.59, where buckling of longitudinal reinforcement is also visible. Short column failures were also observed (e.g., Figure 7.60), while diagonal cracking of shear walls occurred, especially in soft stories (Figure 7.61). The tallest RC building on the island, a seven-story residential building, did not experience any damage, despite its irregularities (Figure 7.62). Quite common was the damage in non-structural elements, mainly in infill walls made of brickwork (Figure 7.63). The most common types of damage observed was: (a) separation of the infill wall from the concrete frame and in some cases overturning, (b) out-of-plane movement and cracking due to out-of-plane bending (Figure 7.64).

[2] https://www.statistics.gr/census-buildings-2011

Figure 7.59. Soft-story failure of a five-story residential building in Karlovasi.

Figure 7.60. Short column (top) and beam-column joint failure of a 4-story building.

Figure 7.61. Shear failure of a shear wall in a soft story.

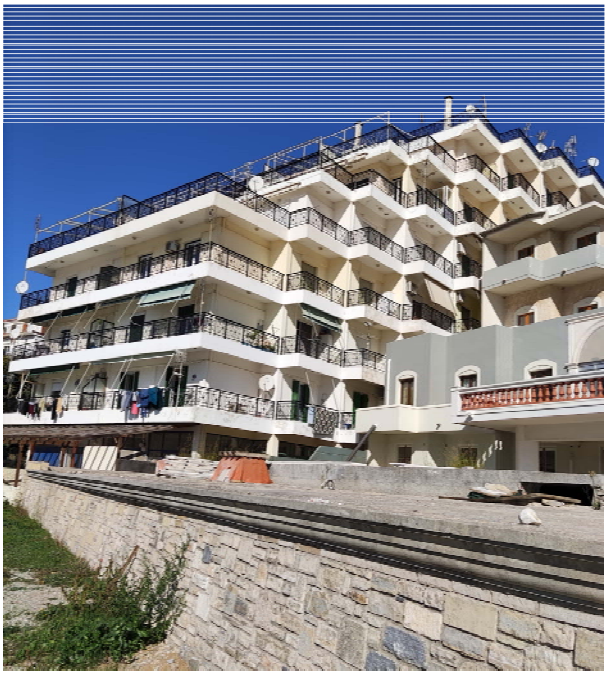

Figure 7.62. Irregular 7-story residential building without any damage.

Figure 7.63. Separation and overturning of infill walls.

Figure 7.64. Cracking of infill walls due to out-of-plane bending.

7.7.5 Masonry buildings

Unreinforced masonry buildings constitute a significant percentage of the building stock of Samos island. Those structures are typically found in small villages. They can be classified in four main categories, namely: residential buildings, public buildings (e.g. town halls, schools, etc.), industrial buildings (e.g. tanneries) and religious buildings (churches and monasteries). Buildings belonging to those categories present differences depending on the dimensions, the structural system, the quality of materials, as well as the construction details. It should be noted that the preliminary interpretation of typical damage presented in this report is based on the pattern of cracks, dislocations and local collapses observed mainly from the exterior of the buildings, since access to the interior of the buildings was, in general, not allowed thus hampering a more accurate identification of the structural system and its state.

Residential Buildings. They are single or, more frequently, two-story buildings made of poor-quality (two- or three-leaf) rubble stone masonry. In some cases, three-story buildings were also found.

Figure 7.65. Poor-quality, three-leaf stone masonry building.

An important detail in the construction of masonry structures is the corners, and we encountered different construction styles and different levels of performance (Figure 7.66). Openings (doors and windows) represent on average one fourth to one third of the buildings' perimeter (Figure 7.67). Their lintels are either horizontal (supposedly, made of timber) or arched (Figure 7.68). In several cases the arches were rather squat.

Figure 7.66. Connection of transverse walls.

Figure 7.67. Typical dimensions of openings.

Figure 7.68. Horizontal and arched lintels. Presence of steel ties (right).

Floors are typically made of timber joists, covered with timber flooring (wooden planks), whereas roofs are made of timber trusses covered with ceramic roof tiles. Residential buildings typically suffered structural damage regardless of whether they belonged in the past to wealthy families or not. However, the extent of damage differs from building to building and from location to location. Typical diagonal or bi-diagonal cracks occurred, frequently extending to the, vulnerable in shear, lintels (Figure 7.68). The lack of stiff in-plane diaphragms at the floor and the roof level, as well as the poor quality of the, typically used, three-leaf masonry led to out-of-plane damage. The observed damage varies in extent and severity, ranging from simple cracks at mid-length of the walls and close to the corners of the building (Figure 7.69) to collapse (Figure 7.70).

Figure 7.69. In-plane shear damage to walls and lintels.

Figure 7.70. Shear cracks at mid-length of the walls and corner failures.

Figure 7.71. Partial collapse of residential masonry buildings.

In some town neighborhoods and several villages, there are buildings of a masonry ground floor and an upper story made of timber-framed masonry or of timber walls. In those buildings, part of the upper story façade is cantilevered (Figure 7.72). Apparently, the majority of those buildings were uninhabited. They were found at an advanced decay stage and hence it is not possible to identify possibly pre-existing damage that deteriorated due to the earthquake.

Figure 7.72. Buildings in which the ground floor is made of masonry and the upper story is made either of timber-framed masonry or timber walls.

Figure 7.73. Masonry building with extensive damage adjacent to a concrete building with no damage.

School Buildings. School buildings are characterized by their large dimensions, their symmetry, as well as by their high-quality construction details, such as the connections between transverse walls, the perimeter of openings, etc. (Figure 7.74). The damage observed in school buildings follows the typical damage typology for masonry structures, but in this case, the extent and the severity of damage was less than that of residential buildings (Figures 7.74-7.75). However, significant non-structural damage was observed in many schools (Figure 7.76-7.77). It is noted that assessment of non-structural potential hazards of school buildings is envisaged in the framework of the pre-earthquake rapid visual assessment programme of the Organization of School Buildings, however, it was not implemented in the reported cases.

Figure 7.74. School buildings at Vathy. Limited damage was observed.

Figure 7.75. Damage to the primary school at Vathy.

Figure 7.76. Primary school at Chora: Shear failure of masonry wall.

Figure 7.77. Primary school at Kontakeika: Major shear failure at the masonry walls, delamination of coating and overturning of equipment.

Figure 7.78. Primary school at Karlovassi (Porphyriad School): damage to the triangular metope and the perimeter eaves, damage to the roof, and cracks inside the building.

Figure 7.79. Out-of-plane masonry wall failure and corner detachment at the Lyberi building of the University of Aegean (School of Sciences).

Tanneries. Until the second World War tanneries were the most important economic activity of the island. More than 50 tanneries existed at the time, while today several out-of-use buildings can be found standing next to the sea. They are typical industrial buildings (Figure 7.80) that date to the end of 19th to early 20th century, with one or two stories, and have been subjected to varying levels of alterations during their lifetime.

The buildings exhibited typical damage, mainly out of the plane of their long walls. For the tanneries closer to the sea, some of the damage observed could also be attributed to the lateral spreading of the soil, as further discussed in Chapter 5.

Figure 7.80. Typical tannery buildings at Karlovassi. Temporary out-of-plane support (top left).

Figure 7.81. Typical damage in tannery buildings at Karlovassi.

Churches. There is always special interest in the behavior of religious establishments following a damaging earthquake. These structures are not only the places of worship and religious education but they are also the centers of social activities for the local communities and play an important role in humanitarian efforts following a devastating seismic event.

From a structural point of view, religious buildings are usually challenging structures due to their architecture and hence their dynamic response is interesting to study. Most of the churches of the island are characterized by well-constructed walls (Figure 7.82) that suffered significant, but repairable damage. On the contrary, arches and cupolas—some of which are of significant span/diameter—are rather poorly constructed and not well connected (Figure 7.83) to the body of the main structure. Thus, the well-known vulnerability of the dome-and-arches system is further accentuated by poor construction which in, several cases, led to catastrophic consequences (Figure 7.84).

In cases where interventions were applied and the dome-and-arches system was provided with steel ties (Figure 7.85), collapse was avoided, although significant damage was not prevented. Of special interest is the seismic response of bell towers. These structures generally exhibit seismic behavior dissimilar to other masonry structures, because of their unique characteristics such as the slenderness and the shape. Damage in bell towers is shown in Figures 7.86, 7.91 and 7.92.

Figure 7.82. Perimeter walls of churches and damage observed.

Figure 7.83. Poor construction of the dome-and-arches system.

Figure 7.84. Severe damage of dome-and-arches roofs

Figure 7.85. Steel ties were installed to alleviate the effect of the thrust of dome-and-arches roofs.

Figure 7.86. Cathedral of the Assumption of the Virgin Mary in Karlovasi. Heavy damage observed in both bell towers which were not built at the same time as the main part of the temple but were added afterwards.

Figure 7.87. Roof failure on the west side of the Cathedral of the Assumption of Virgin Mary in Karlovasi.

Figure 7.88. Out-of-plane failure of the south lateral wall which supports the dome of the Cathedral of the Assumption of Virgin Mary in Karlovasi. In this particular temple there was a collapse of the roof on the west side of the Temple.

Figure 7.89. Extensive failures at the Church of Agios Nikolaos in Kokkari, the largest Church of Samos. Failure in arches, in the keystone of the two main entrances, cracks and complete failures in domes as well as damages in the bell tower.

Figure 7.90. Out-of-plane failure of the gable below the roof of the Church of Genesis of Virgin Mary at Konteika, which dates back to the 19th century.

Figure 7.91. Shear failure at the bell tower of the Agios Spyridon Cathedral at Bathi.

Figure 7.92. Shear failure at the bell tower of the Agia Paraskevi Church at Chora.

7.7.6 Structures and non-structural objects of cultural interest

In Samos there is a large number of cultural buildings, archeological sites, monuments and museums with important exhibits. The earthquake caused failures, some of which led to irreparable damage. In the Archaeological Museum of Pythagorion city, ancient vessels suffered damage due to overturning, while in some sculptures the welds were broken (Figure 7.94). Close to Pythagorion city, segments of the perimeter walls of the Castle of Lycurgus Logothetis collapsed (Figures 7.95-7.96). Furthermore, in the same area, columns of the Early Christian Basilica of the Castle overturned as shown in Figure 7.97. On the other hand, the Castle of Lykourgos Logothetis survived the earthquake suffering no damage due to fact that it was recently seismically rehabilitated (Figure 7.98). At the Archaeological Museum of Vathy, a crack was formed at the thigh of the famous oversized marble sculpture of Kouros, which dates back to 570 BC (Figure 7.99). At the archaeological site of Heraion of Samos (dedicated to the goddess Hera during the 6th century BC) no displacement was observed in the single upright multidrum column (Figure 7.100) that survives today. However, contemporary structures that are part of the archaeological site, suffered some minor damage.

Figure 7.93. Breaking of ancient vessels in the Archaeological Museum of Pythagorion in Samos due to overturning.[3]

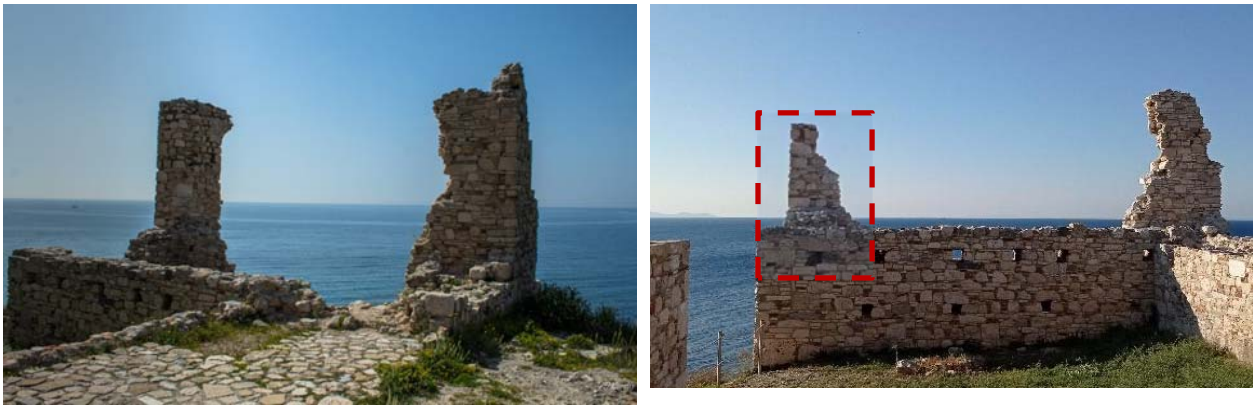

Figure 7.94. The Castle of Lykourgos Logothetis (a) before the earthquake[4], (b) after the earthquake of the October 30th 2020, showing the partial collapse of the perimeter walls into the sea.

Figure 7.95. Partial collapse of the perimeter walls of the Castle of Lykourgos Logothetis.

[3] www.skai.gr/news/greece/samos-seismos-zimies-se-mouseia-kai-mnimeia-se-samo-ikaria-xio
[4] Google Earth

(a) before the earthquake[5] (b) after the earthquake of the October 30th 2020

Figure 7.96. The Early Christian Basilica Church of the Castle of Lykourgos Logothetis before and after the earthquake of the October 30th 2020 respectively. Probable overturned column are circled in red.

[5] http://whc.unesco.org/en/list/595
http://visit.samos.gr/index.php/things-see/sightseeing/archaeological-sites/?lang=EL
https://www.arthro-13.com/news/i-vyzantini-samos-meros-v/

Figure 7.97. The Castle of Lykourgos Logothetis. No damage was observed; the seismic behavior of the structure was very good due to fact that it has been recently seismically rehabilitated.

Figure 7.98. Overview of the sculpture of Kouros at the Archaeological Museum of Vathy in Samos (the largest Kouros in Greece) before the earthquake (left) and crack in the thigh of the sculpture as a result of the recent earthquake (right)[6]

[6] www.mononews.gr/politismos/ti-esose-ton-kouro-tis-samou-apo-ton-katastrofiko-sismo

Figure 7.99. Archaeological site of Heraion of Samos. No evident displacement was observed on the single upright multidrum column (though minor displacements could be possible).

Figure 7.100. Stone and reinforced concrete bridges along the roadway network of Samos

7.7.7 Bridges

Given the size and the topography of the island of Samos, the number of bridges is limited. No damage was observed or has been reported to any of the bridge structures.

7.8 Conclusions

The earthquake of 30/10/2020 resulted in considerable structural damage in Samos but had a stronger impact on Izmir (including several collapses) despite the relatively lower peak ground accelerations recorded in the latter. This can be attributed to (a) the different frequency content of the ground motions with evident high spectral accelerations in Izmir, particularly within the mid-to-long period (0.6s-1.5s) range due to soft soil amplification, (b) the different structural typologies and height of structures (low-story masonry versus high story RC buildings in Samos and Izmir, respectively) as well as (c) the considerably higher degree of exposure of Izmir, with a population of 4 million, more than 100 times higher than that of Samos island.

Quality control in construction and adoption of fundamental design principles have also played a significant role in both cases; where such measures are lacking, disproportionate damage for the intensity of shaking was observed. It was also evident that buildings designed to modern seismic codes and constructed with a professional standard of care performed very well. However, structural performance should be assessed with caution. In fact, given that the ground motion intensity was lower compared to the current design level (particularly in Izmir) the impression that the buildings suffering no damage have adequate seismic capacity is quite misleading. On the contrary, this earthquake has highlighted the importance of improving the site factors used to develop design spectra and enforcement of code provisions for structural design and detailing. It is also quite important to emphasize that there are still many buildings located in other parts of İzmir, that have not experienced damage because they were subjected to lower ground motions compared to the heavily damaged or collapsed ones in Bayraklı. These deficient buildings are exposed to high risk. The issue of quality control and the large percentage of buildings designed to previous versions of the code (estimated approximately 60% in Greece as well) is deemed a major issue for both countries and other parts of the world.

Acknowledgments

The Turkish authors wish to express their gratitude to AFAD, Ministry of Environment and Urbanization and their administrators for sharing the damage data with us. The assistance provided by graduate students İsmail Ozan Demirel, S. Selin Aktaş, Beyazıt Bestami Aydın and Batu Türksönmez during the field surveys is gratefully acknowledged. They also wish to thank Dr. Soner Alıcı for preparing some of the graphs. The research on the Tall Building monitoring is supported by the Disaster and Emergency Management Presidency of Turkey under grant UDAP-G-17-04. This support is gratefully acknowledged. The Turkish authors thank Mistral Izmir Management for authorizing the deployment of the structural health monitoring system, Ozan

Caglar Inac for coordinating all these efforts and Suleyman Tunc for setting up the structural health monitoring system.

References

Boduroglu, H., Ozdemir, P., Binbir, E., Ilki, A. "Seismic damage assessment methodology developed for Turkish Compulsory Insurance System", *The 9th Annual Conference of the International Institute of Infrastructure Renewal and Reconstruction*, Brisbane, 2013.

CEN (2004) European Standard EN 1998-1. Eurocode 8: Design of structures for earthquake resistance, Part 1: General rules, seismic actions and rules for buildings", *European Committee for Standardization*, Brussels, Belgium

CEN (2004) European Standard EN 1998-3. Eurocode 8: Design of structures for earthquake resistance - Part 3: Assessment and retrofitting of buildings", *European Committee for Standardization*, Brussels, Belgium.

Ministry of Public Works and Settlement (1997) *Code for Buildings Constructed in Earthquake Areas (CBCEA)*, Ankara, Turkey.

Ministry of Public Works and Settlement, (1975) Code for Structures Constructed in Disaster Areas (CSCDA), Ankara, Turkey.

Ministry of Public Works and Settlement (1997) Code for Structures Constructed in Disaster Areas (CSCDA), Ankara, Turkey.

Earthquake Protection and Planning Organization – EPPO/OASP (1995) New Greek Seismic Code (NEAK1995), Athens, Greece

Earthquake Protection and Planning Organization – EPPO/OASP (2000) Greek Seismic Code (ΕΑΚ2000), Athens, Greece

Earthquake Protection and Planning Organization – EPPO/OASP (2012) Greek Code for Seismic Interventions (ΚΑΝ.ΕΠΕ.), Athens, Greece

Greek Organization for Standarization - ELOT (2008) Greek National Annex to Eurocode 8, Athens, Greece

Gumus O and Celik OC (2019) Structural Health Monitoring System on a 216 m Tall Building in Izmir per the New Turkish Building Earthquake Code, *Proceedings of the Fifth International Conference on Earthquake Engineering and Seismology*, October 8–11, Ankara, Turkey.

Ilki, A., Halici, O., Kupcu, E., Comert, M., Demir, C. “Modifications on seismic damage assessment system of TCIP based on reparability”, *17th World Conference on Earthquake Engineering*, 17WCEE, Sendai, Japan, 2020.

Ilki, A., Halici, O.F., Comert, M., Demir, C. “The modified post-earthquake damage assessment methodology for TCIP (TCIP-DAM-2020)”, in *Advances in Assessment and Modeling of Earthquake Loss*, eds. S. Akkar, M. Erdik, A. Ilki, Springer, in press, 2020.

Institute of Earthquake Engineering and Engineering Seismology - Earthquake Protection and Planning Organization – EPPO/OASP (2020) The Earthquake of Oct. 30, 2020, Mw7.0 (11:51GMT) *North of Samos Island (Greece): Observed strong ground motion on Samos island*, Preliminary Report ITSAK v3.0, Thessaloniki, Greece

İzmir Ticaret Odası Gözlemsel İnceleme Raporu, İnş. Yük. Müh. Deniz Alkan, Aralık 2020

METU (2020) Earthquake Engineering Research Center, 30 Ekim 2020 Mw 6.6 Sisam Adası (İzmir-Seferihisar açıkları) Depremi Sismik ve Yapısal Hasara İlişkin Saha Gözlemleri, Report No: ODTÜ/DMAM 2020-03, November.

Ministry of Public Works - Υ.ΠΕ.ΧΩ.Δ.Ε. and Earthquake Protection and Planning Organization – EPPO/OASP (2000) *Greek Seismic Code* (Υ.Α. Δ17α/116/4/ΦΝ 429, ΦΕΚ 1329Β΄/ 6-11-2000)

Ministry of Public Works (1984) *Amendments to the Royal Decree of 1959 on the Seismic Provisions for Building Projects*, Athens, Greece

Ministry of Public Works and Settlement, MPWS (1972) *Earthquake Zone Map*. Published by Law No. 7/5551 on 23.12.1972.

Ministry of Transportation (2008) *Seismic Code for the Constructions of Harbor and Coastal Structures, Railways and Airports*, General Directorate for Construction of Railways, Harbors and Airports, Ankara, Turkey.

Royal Decree (1959) on the Seismic Provisions for Building Projects, Government Gazette 36/A/19.2.1959, Athens, Greece

Turkish Building Earthquake Code (TBEC) (2018). *Disaster and Emergency Management Presidency*, Ankara, Turkey.

Vadaloukas, G., Vintzileou, E., Ganas, A., Giarlelis, C., Ziotopoulou, K., Theodoulidis, N., Karasante, I., Margaris, B., Mylonakis, G., Papachristidis, A., Repapis, C., Psarropoulos, P. N., & Sextos, A. G. (2020) *Samos Earthquake of 30th October, 2020. Preliminary Report of the Hellenic Association for Earthquake Engineering*, Athens, Greece, https://doi.org/10.13140/RG.2.2.22609.76644

8.0 Emergency Response and Societal Impact/Recovery

Former Mayor of Konak: Muzaffer Tunçağ
National and Kapodistrian University of Athens: Efthymios Lekkas, Spyridon Mavroulis
Turkish Earthquake Foundation: Seyhun Püskülcü
Earthquake Planning and Protection Organization: Efthymios Lekkas, Asimina Kourou, Maria Manousaki, Thekla Thoma, Nikolaos Karveleas
Middle East Technical University: Kemal Onder Cetin, Makbule Ilgaç, Gizem Can
University of Bristol: Anostasios Sextos

8.1. Civil Protection in Greece

8.1.1 *"Enceladus" – National action plan for earthquake disaster management in Greece*

The General Secretariat for Civil Protection, aiming mainly to coordinate bodies involved in disaster risk management, prepared a document entitled "General Plan for emergency response and immediate/short-term management of earthquakes effects" (hereafter the General Plan), with codename "Enceladus" on February 2020 (GSCP, 2020). The General Plan was sent to all the involved bodies, which are mentioned below.

The aim of the General Plan is the immediate and coordinated actions of the authorities involved at national, regional and local levels for the effective response to effects caused by earthquakes. One of the key aims of the document is management of the immediate post-disaster situation, including to protect life, health and property of citizens as well as the protection of the natural environment, the wealth-producing resources and infrastructures. The requirement for achieving this aim is the synergy, cooperation and interoperability of the authorities involved.

The authorities involved in the frame of Enceladus are the following: (a) All administrative regions, regional units and municipalities, (b) the Ministry of Citizen Protection including the General Secretariat of Civil Protection, the Hellenic Fire Service, the Hellenic Police, (c) the Ministry of Infrastructures and Transport comprising the General Directorate of Natural Disaster Recovery, the General Secretariat of Infrastructures, the Earthquake Planning and Protection Organization, the Building Infrastructure SA (former School Buildings Organization S.A.), the General Directorate of Transport Infrastructure, the General Directorate of Hydraulic, the Port and Building Infrastructure, the Dam Administrative Authority, the Airport Administrations (Hellenic Civil Aviation Authority, the Athens International Airport SA, the Fraport Regional Airports of Greece SA), the Water Supply and Sewerage Company, (d) the Ministry of Shipping and Island Policy including the Headquarters of the Coast Guard - Hellenic Coast Guard, port administration and operation bodies (port organizations, port funds, municipal port funds, etc), (e) the Ministry of National Defense including Hellenic National Defense General Staff, (f) the Ministry of Health comprising General Directorate of Public Health & Quality of Life, National Center For Emergency Assistance, Hellenic National Public Health Organization, (g) the Ministry of Environment & Energy comprising supervised bodies of the Ministry of Environment and Energy and the Hellenic Survey of Geology and Mineral

Exploration, (h) the Ministry of Education, Research and Religious Affairs including Department of Emergency Policy Planning, Geodynamic Institute of the National Observatory of Athens, (i) the Ministry of Culture & Sports, (j) the Presidency of the Government, (k) the Ministry of Labor and Social Affairs comprising General Directorate of Social Solidarity, National Center for Social Solidarity and (l) the Ministry of Development and Investment including General Secretariat of Industry / Directorate of Industrial Policy.

8.2. Planning and Preparedness before the Earthquake

In Greece, a national policy is in place to mitigate earthquake impacts and enhance preparedness at national, regional, local, workplace and family levels. This includes pre-earthquake inspection of critical infrastructure (i.e., schools and public buildings) and prioritization for strengthening based on relative risk scoring. The Earthquake Planning and Protection Organization (EPPO) is a Legal Entity of Public Law and operates under the supervision of the Hellenic Ministry of Infrastructure and Transport as the competent authority to develop and design the national policy on earthquake protection. EPPO, among other actions, contributes substantially to build an earthquake safety culture in order to protect the citizen's life, health and property from earthquakes. EPPO organizes and/or participates in training exercises designed to help users plan and implement effective earthquake mitigation strategies, in collaboration with the involved local authorities.

In Samos Island, prior to the October 2020 event (on March 2017), EPPO implemented the following:

- Training Seminar at Samos' prefecture, to educate and train school directors and teachers responsible for earthquake planning. The teachers were trained to follow specific documented preparedness and evacuation procedures in case of an earthquake and to teach basic safety concepts to students, including drills. The seminar took place in collaboration with the Samos' Divisions of the Ministry of Education.
- Training Seminar targeting municipal childcare centers' personnel. EPPO provided education to the childcare providers by utilizing a mix of brief information along with discussion, to expand their knowledge and to improve their skills on earthquake management to the specific settings (Figure 8.1).

In addition, the following earthquake exercises were performed in Samos Island:

Table-top-exercise in 2015: On April 30, 2015, a table-top-exercise took place in Samos, with the code name «Efpalinos 2015». Efpalinos is the name of the great architect of the ancient time, who constructed a water tunnel on the island. The exercise was planned and organized by the Prefecture of Samos with the collaboration of EPPO. In the exercise, the following agencies also participated: the Municipalities of Samos and Ikaria, the Hellenic Armed Forces, the Hellenic Police, the Hellenic Fire Service, the Hellenic Coast Guard, the National Centre for Emergency Assistance, the General Hospital of Samos, volunteer teams, etc. (Figure 8.2).

Field Exercise in 2017 – Efpalinos 2017: On March 15, 2017, the field exercise of «Efpalinos 2017» was organized by the Prefecture of Samos, under the coordination of EPPO. The scenario magnitude was a 6.4 event at a focal depth 11km. Its epicenter was located 8km SSE of Samos Island. The local authorities that participated in the exercise were the Regional Unit of Samos (Department of Civil Protection), the Municipality of Samos, the 79th Senior National Guard Battalions Command, the Police Directorate, the Fire Department, the Port Authority, the National Center For Emergency Assistance, the General Hospital, the Hellenic Electricity Distribution Network Operator, the Samos Amateur Radio Association, volunteer organizations and teams of the island as well as a 4-member Special Team for Special Missions from Ikaria. Among the exercises were evacuation of buildings, decision-makers meetings, search and rescue operations, triage (for the injured), communication problems, camp management and food distribution by the Hellenic Armed Forces, organized evacuation of population and inspection of building (Figure 8.3). The level of the drill was characterized as "excellent" and "very good" by the majority of the participants.

Figure 8.1. EPPO's Seminars for Directors of primary and secondary schools of Samos in March 2017.

Figure 8.2. Table-top-exercise «Efpalinos 2015». The teams of decision makers and volunteers.

Figure 8.3. The "Efpalinos 2017" field exercise comprised decision-makers meetings, search and rescue operations practice and food distribution.

8.3. Emergency Response Phase of the 2020 Samos Earthquake

Following the Samos mainshock, emergency response activities were undertaken including: (a) search and rescue operations, (b) first-aid treatment and medical care, (c) mitigation of the impact of the induced phenomena, (d) provision of essential emergency supplies, (e) provision of emergency shelters and procedures of housing restoration, (f) post-earthquake building inspection and (g) immediate financial relief measures. As needed, these activities can also rehabilitate and replace water and wastewater utilities and services, transport and communication infrastructure etc., essential for normal existence.

8.3.1 *Initial notification of the earthquakes, earthquake alerts and announcements*

The staff of the local police departments in cooperation with the staff of the fire agencies officially notified the General Secretariat of Civil Protection (GSCP) and especially the Civil Protection Operations Centre (CPOC) that the earthquake had occurred. These staff also notified senior administration police officers and the decentralized Civil Protection Agencies regarding the situation in the earthquake affected area. Acting on the orders of the Prefect, the Mayor, and the presidents of the local administrative districts, the staff of the local Civil Protection agency collected data from the local police departments and fire agencies according to pre-determined contingency plans. That data collection had the aim of further informing the Prefect, the Mayor, the presidents of the local administrative districts, the Civil Protection Agencies of the Region of the Ionian Islands and the CPOC / GSCP. The above actions were possible because the information and communication technology infrastructures and services were not damaged and were fully operational after the earthquake. The GINOA was responsible for the earthquakes announcement and the official notification of the GSCP and the EPPO.

8.3.2 *First assessment of the impact – Mobilization and response of the state authorities*

The October 30, 2020, **M**=7.0, Samos (Aegean Sea) earthquake disrupted the normal functioning of the island society directly through fatalities and injuries, and indirectly through damage to building stock, infrastructure networks, and facilities, as well as economic losses. The island society resilience in the face of an earthquake disaster mainly depends on the level of preparedness of competent agencies and critical facilities at the central, regional and local levels of administration and on the capacity of the population to cope with the disaster and recover to the normal condition.

Immediately after the earthquake, the Greek government mobilized to assist and provide relief to the affected local population. All earthquake response plans for saving and safeguarding life and health, and for protecting natural environment and properties, were applied in accordance with the General Plan.

According to the General Plan, during the emergency response begins with an official announcement of the earthquake characteristics and updates on the effects of the earthquake in the eastern part of Aegean. The Minister of Citizen Protection went to the operational center of the Hellenic Fire Service, where management of the earthquake disaster was coordinated and monitored.

The Deputy Minister for Civil Protection and Crisis Management visited Samos together with governmental staff comprising the Deputy Minister of Interior, the Directors of the 1st and the 2nd Regional Healthcare Authorities of the Ministry of Health, staff of the Planning and Crisis Management Directorate of the General Secretariat of Civil Protection and the First Response Team of the General Secretariat for Civil Protection (Figure 8.4). They assessed the effects of the earthquake on the population and on the natural and built environments. These assessments were very important for the implementation of the planned actions to deal with the adverse effects of the earthquake. Due to the Samos airport remaining not operational until inspections couple be completed, the aforementioned officials visited the earthquake-affected island by helicopters.

By mandate of the Chief of the Hellenic Fire Service, all the Disaster Management Special Units (E.M.A.K. – D.M.S.U.) of the Hellenic Fire Service were put on increased alert. A team of the 1st EMAK set up in Elefsina with rescue search dog capabilities to located trapped victims. Moreover, rescuers from the Special Department of Disaster Medicine of the National Center for Emergency Assistance and civil engineers of the Ministry of Transport and Infrastructure visited Samos with special flights organized by the General Secretariat of Civil Protection. A second team of the 1st EMAK followed along with a second team of the Special Department of Disaster Medicine.

It is important to highlight the constant readiness of the aforementioned disaster management units. They were ready to visit not only the earthquake affected area of Samos, but also the worst affected coastal parts of the neighboring Turkey, in order to assist the

search and rescue operations conducted by the respective disaster management units of Turkey.

Regarding the actions of the North Aegean Region, its Civil Protection mechanisms in all of its islands were activated. A quick assessment of damage to buildings and infrastructures was implemented mainly in the regional unit of Samos, which was severely affected by the earthquake.

The European Union (EU) and the North Atlantic Treaty Organization (NATO) expressed their readiness to provide assistance to Greece and Turkey after the strong earthquake that shook the Eastern Aegean Sea. The President of the European Council also expressed the readiness of the EU to provide assistance to the areas affected by the earthquake, while the European Commissioner for Crisis Management stated that the European Emergency Coordination Center is in close contact with the civil protection authorities in order to assist if necessary.

Early in the afternoon after the earthquake, a coordination meeting was held among mayors and other authorities at the City Hall of Karlovassi town, located at the northwestern part of Samos Island (Figure 8.4). It was decided that if affected residents have to stay away from their damaged houses, they would stay in hotels, tourist facilities and tents in order to comply with the protection measures for the limitation of the transmission of the new virus SARS-CoV-2 amid pandemic. Also, the municipal authorities remained at the disposal of residents throughout the night in order to record effects and mitigate difficult situations from the earthquake. During the coordination meeting, the emergency shelters were announced. Tents were set up in these sites for the safe accommodation of residents, whose houses were damaged by the earthquake.

The Prime Minister of Greece chaired a meeting with the participation of the Deputy Minister for Civil Protection and Crisis Management, the Deputy Minister of Interior, the General Secretary of Infrastructure, the General Secretary of Reception of Asylum Seekers, the Regional Governor of Attica and First Vice President of the Union of Regions of Greece, the Deputy Regional Governor of Samos, the Mayor of Eastern Samos and Professors of Disaster Management from the National and Kapodistrian University of Athens and the Technical University of Crete (Figure 8.4). During this meeting, the authorities expressed their satisfaction for the immediate mobilization of the state mechanism and discussed the damage to infrastructure and businesses by both the earthquake and the subsequent tsunami.

Figure 8.4. First meeting of the Deputy Minister for Civil Protection and Crisis Management with local authorities for the assessment of the post-earthquake situation and the coordination of the emergency response phase in Karlovassi, capital town of the Municipality of Western Samos. Second meeting the day after the earthquake in Vathy, the capital town of the Municipality the Eastern Samos, with the Prime Minister of Greece.

The Municipalities of Eastern and Western Samos submitted a request to declare a state of emergency in order to address the emergencies and to manage the adverse effects of the October 30, 2020, Samos earthquake. By mandate of the Deputy Minister of Civil Protection and Crisis Management and the General Secretary of Civil Protection, the request was accepted and the Municipalities of Eastern and Western Samos of the Samos Regional Unit of the North Aegean Region were declared in a State of Civil Protection Emergency. This declaration is valid from the occurrence date of the earthquake (October 30, 2020) and for the next 6 months (until April 30, 2021).

As regards the Hellenic Armed Forces, their response and mobilization were immediate under the command of the Chief of the General Staff of National Defense (GEETHA). They assisted the management of the earthquake disaster in Samos Island with actions comprising the following (Figure 8.5) among others:

- The Hydrographic Service issued a warning NavTex (NAVigational TEleX service for meteorological warnings and forecasts), for tsunami in the Aegean, based on the responsible area of the Hellenic Armed Forces, which coincides with the Search and Rescue Area of Greece.
- All units of the Hellenic Armed Forces were put on alert in the earthquake-affected Samos, Ikaria and Chios Islands, white the Unit Commanders were in constant communication and cooperation with the staff of the affected municipalities of Eastern and Western Samos in order to assist as needed.
- Operators and drivers of the Engineer Directorate were put on alert for immediate intervention. Moreover, vessels of the Hellenic Navy stayed on standby in Salamina Island. Also reserved on standby were C-130 military transport aircrafts and CH-47 Chinook helicopters of the Hellenic Air Force at Elefsina and at Megara Airports, respectively.
- A vessel remained in Vathy Bay in order to be used for temporary housing, if necessary.
- The DEFKALION rescue units of the Hellenic Army, Navy and Air Force, comprising rescue teams along with special trained dogs and appropriate equipment, were put on alert for immediate intervention.

- Teams of civil engineers were also ready to contribute to the damage assessment throughout the earthquake-affected island of Samos.
- Special flights were organized over the affected area in order to initially assess the extent of damage in Samos Island.
- Moreover, staff of the Hellenic Armed Forces contributed to the setting of the emergency shelters. They set up sturdy tents, provided meals, and repaired the road network at several sites mainly affected by rockfalls and landslides.

Immediate actions of the municipal authorities following the earthquake included:

- Suspension of operation from 2 to 4 November of municipal and private Kindergartens, Primary and Secondary Schools, including Kindergartens, Primary, Secondary and High Schools, Private Music Schools, Private Music Schools, and chamber music. The duration of suspension was related to Phase A of the rapid visual inspection of school buildings as described in Chapter 7.
- The operation of municipal and private nursery schools, creche and kindergarten, school units of the Elementary and Secondary education including elementary, middle and high schools, private music institutions, conservatories, music schools, choirs, and orchestras was temporarily suspended from November 2 to 4, 2020 until the completion of the first post-earthquake building inspection for assessing possible structural and non-structural damage.
- The operation of municipal and private nursery schools, creche and kindergarten was further suspended from November 5 to 20, 2020.
- As regards the higher education, the University of Aegean temporarily suspended its educational, research and administrative activities in its facilities located in Samos and Chios from November 2 until the completion of the first post-earthquake building inspection for the safety of all staff members and students. The entrance to all university facilities was forbidden without permission except for student residences.
- Since November 1, 2020, the affected residents had the opportunity to electronically submit damage assessment reports for their houses through a digital application specially designed for this situation.
- Water sampling checks were conducted to assess water quality and suitability.

Figure 8.5. The Hellenic Armed Forces assisted several actions comprising set up of temporary emergency shelters, distribution of food supplies and restoration of roads affected by slope failures.

8.3.3 *Guidelines through 112 emergency communications service*

The General Secretariat for Civil Protection informed residents of the islands of the northeastern part of the Aegean Sea with two messages through the single European emergency number “112” in order to take self-protection measures. The first message was sent to the inhabitants of all the islands located with the triangle Ikaria – Kos – Chios and comprised recommendations for staying away from the coasts in order to avoid the adverse effects of possible tsunami generation after the mainshock and from severely affected buildings on the verge of partial or total collapse in order to avoid falling debris in case of an aftershock (Figure 8.6). The second message was exclusively sent to the residents of Samos Island, who were recommended to stay away from buildings and remain in safe open sites away from the adverse effects of the earthquake and the induced geodynamic phenomena (Figure 8.6).

Similar information and updates were posted by the municipalities of Eastern and Western Samos on their websites with self-protection measures and information about the emergency shelters for the affected population. Recommendations included avoiding coastal areas, avoiding power lines, moving away from old and abandoned masonry buildings, away from unstable slopes, and away from streams and bridges. They also advised residents of Samos to avoid spending the night inside their homes and to stay in safe open spaces, emergency shelters or cars and away from buildings in order to avoid debris falling and buildings collapse.

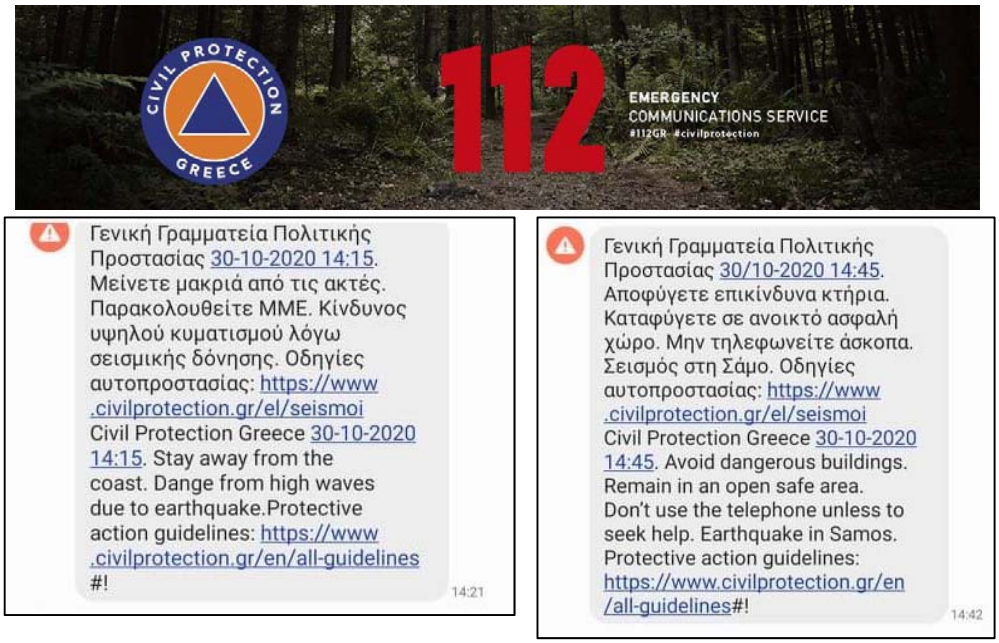

Figure 8.6. The General Secretariat for Civil Protection with 2 SMS messages through the Single European Dialing Number "112" called the residents of the North Aegean Region first and then of the Regional Unit of Samos in order to take measures of self-protection from the earthquake and its accompanying geodynamic phenomena, with emphasis on the tsunami.

8.3.4 *Search and rescue operations – First-aid treatment and medical care*

The demand for search and rescue operations in the earthquake-affected portions of Samos was minimal, because no full collapses of inhabited residential buildings occurred.

However, the Fire Service in Samos received a call shortly before 17:00 for assistance in Vathy town, located in the northeastern part of Samos, after a partial collapse of an old and abandoned masonry building. Part of its masonry collapsed, trapping two young people. Minutes after they were located, the trapped people were pulled unconscious and immediately transported to the General Hospital of Samos. The final report of the impact of the earthquake on the local population of Samos comprised 2 fatalities from the collapse site of Vathy town and 19 injured residents.

The search and rescue operations were conducted by members of the 1st Disaster Management Special Unit of the Hellenic Fire Service. The operations were supported by staff of the Hellenic Fire Service, the National Center for Emergency Assistance, the Hellenic Police and civil protection volunteers.

As regards the provision of first-aid treatment and medical care, a patient airlift was required from Samos to Athens for a 14-year-old child, who was seriously injured (multiple fractures), and for a 63-year-old woman with a fracture of the cheekbone and a partial rupture of the spleen. The patient airlift was implemented with a C-130 military aircraft. The child was transported to the General Children's Hospital of Athens "Panagiotis and Aglaia Kyriakou" and the woman to the KAT General Hospital of Attica.

At the Samos Hospital, 7 injured residents were treated and remained, all out of danger. Several residents went to the Health Center of Karlovassi, located at the northwestern part of Samos. First-aid was administered and they returned to their homes. All health centers and related medical units remained in a state of maximum readiness.

8.3.5 *Psychosocial support for the affected population*

A natural disaster, such as the October 30, 2020 earthquake in Samos, in addition to fatalities, injuries and property damage, can have adverse effects on the mental health of the affected population. Feelings of loss, grief, anger, anxiety, fear and sadness can occur in the days after the event or even weeks or months after. These feelings may be accompanied by symptoms such as: nightmares or disturbing memories of the earthquake, intense mental pain at the slightest reminder of the earthquake, disturbed sleep or lack of sleep, irritability and feelings of anger, panic attacks, anxiety, anxiety accompanied by physical symptoms such as difficulty breathing or "tightening" of the body, lack of interest in activities or social life, lack of appetite or overeating and increased alcohol and drug abuse. Thus, the psychological support of those affected by the above symptoms has been considered necessary and very important in order to deal with the earthquake disaster and its mental health effects. Such psychological support actions were undertaken by the psychological service of the Social Welfare Department of the Samos Municipalities, with which someone who was experiencing significant psychological

stress could contact. It is important to note that due to the evolving SARS-CoV-2 pandemic, sessions were also available via skype or telephone.

Psychosocial support was also provided by voluntary organizations that acted in the earthquake-affected Samos, such as the Regional Department of the Hellenic Red Cross and the Samos Department of the Hellenic Rescue Team, always in excellent cooperation with the state and the local authorities. Psychological support and counseling was provided free of charge to affected residents in specially designed spaces. Practices were applied to avoid overcrowding and to limit the spread of SARS-CoV-2 virus; such practices required appointments to be made in advance of in-person sessions along with masking and social distancing, as well as by making available remote communication via teleconference or videoconference.

8.3.6 *Awareness and education for the earthquake effects and protective measures due to the continuous aftershock sequence*

Awareness and education activities for the earthquake effects and protective measures due to the aftershock sequence were implemented by the EPPO. Five days after the earthquake, an EPPO team arrived in Samos in order to implement meetings with members of local authorities and workshops for teachers etc. (Figure 8.7).

The educational activities that took place by EPPO after the earthquake were crucial, because they helped the local community to mitigate earthquake effects, gave hope for the future and provided a sense of normality to people. In addition, these activities provided participants with the opportunity to discuss the lessons learned from the earthquake and the tsunami management, to become familiar with the idea of dealing with multiple disasters at the same time (earthquake and tsunami amid pandemic) and to continuously apply the protocols against the spread of the new SARS-CoV-2 virus.

More specifically, EPPO implemented (Figure 8.7) meetings with Eastern Samos and Western Samos Municipalities' members, workshops for Directors of primary and high schools, one in Vathy and one in Karlovassi, a workshop for child care centers' personnel of Eastern Samos Municipality and distribution of specific educational material per target group.

Figure 8.7. (Up) Workshops for Directors of primary and secondary schools, in Vathy town, located at the northeastern part of Samos. (Down) Workshops for Directors of primary and secondary schools in Karlovassi town, located at the northwestern part of Samos.

EPPO's distributed the following documents in Samos area:

- a leaflet concerning protection measures that should be taken by individuals and families during the aftershock period, and initiatives to mitigate psychosocial effects on the family members, particulalry children.
- the new EPPO's poster "Earthquake and Protection in Workplaces in case of Pandemic" that focused on prevention, preparedness, mitigation, and response to an earthquake event in case of pandemic (Figure 8.8).

The occurrence of the Samos earthquake during the SARS-CoV-2 pandemic challenged local authorities and the Samos' community to effectively manage and cope with the disaster. The trainings and exercises in 2017 allowed competent authorities and individuals to better identify, coordinate, and correct gaps of the emergency planning, problematic behavioral or physical reactions. Building earthquake preparedness takes a lot of effort, which EPPO intends to continue along with the local authorities because preparedness is important for the resilience of every community.

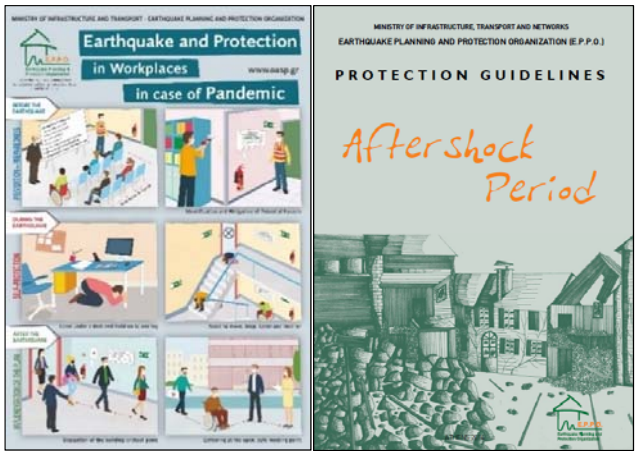

Figure 8.8. Educational material of EPPO for (left) earthquake and protection in workplaces amid pandemic and (right) protection guidelines during the aftershock period.

8.3.7 *Participation of volunteer teams*

Volunteers not only from the regional units of Samos, but also from the surrounding regional units of the North Aegean Region assisted the local authorities in the management of the earthquake disaster during the first critical hours and days of the emergency response phase. The main actions carried out by the volunteer teams included (Figures 8.9, 8.10):

- participation in search and rescue operations,
- participation in teams competent to assess damage to buildings and infrastructure including port facilities among others
- sending humanitarian aid including equipment for the homeless (blankets, aluminum blankets, sleeping bags, ranches, etc.), long-lasting food supplies and personal hygiene items (toothpaste, shower gel, soap, cotton swabs, etc.)
- distribution of humanitarian aid, gathered from various sources, including equipment for the homeless, long-term food and personal hygiene items,
- participation in the organization of temporary emergency shelters for the affected population and especially in the cleaning of the sites, in setting up of tents, in the transportation of humanitarian aid and basic necessities to the emergency shelters,
- meeting health needs of the affected people gathered in the emergency shelters,
- distribution of meals and humanitarian aid to affected people in the emergency shelters and elsewhere necessary
- assistance in organized evacuation actions from dangerous areas of towns and villages during the aftershock period,
- assistance in actions for the safe removal of religious items from temples severely affected by the earthquake
- relief actions to organizations, churches, institutions and individuals, where requested,
- providing support and guidance, especially for people with special needs and reduced mobility,
- assessment of needs of the affected population,

- daily visits to hotels and tourist facilities for homeless and affected people in order to assess health needs, provide pharmaceutical / medical supplies and train staff and guests on measures for the prevention of the spread of the new SARS-CoV-2 virus
- provision of psychological support and counseling to residents with significant psychological stress attributed to the adverse effects of the earthquake,
- information on earthquake prevention measures and
- information on protection measures against the spread of the new SARS-CoV-2 virus.

The volunteer mechanism was mobilized, proving its readiness and offering practical support to the earthquake-affected population of Samos. The participating voluntary organizations included: Association for the Protection of the Environment of Agios Kirikos Ikaria, Association of Volunteer Firefighters of Pythagorion, SOS Kokkari Volunteer Team, Hellenic Rescue Team Samos Department, and the Samos Scuba Divers Association.

8.3.8 *Donations and provision of essential emergency supplies*

There was a nationwide mobilization for emergency supplies after the 2020 Samos earthquake. Emergency relief supplies including water bottles, emergency food supplies, clothing, blankets and bedding were distributed to those in need. Several sites across Samos were converted into concentration, packaging and distribution centres of emergency supplies provided by governmental authorities and donated by individuals, volunteer teams, non-governmental organizations, charitable organizations, big supply chain companies and shipping companies. With this nationwide mobilization, Greeks sent a strong message of humanity, solidarity and hope to the earthquake-affected population of Samos Island. Despite the difficult situation due to the evolving SARS-CoV-2 pandemic, the collective effort paid off, as thousands of packages of long-lasting food and basic necessities were collected.

Figure 8.9. The Hellenic Red Cross assisted the local authorities and the Hellenic Armed Forces in short-term response activities that distributed food supplies and personal hygiene items to the earthquake-affected people of Samos and setting up temporary emergency shelters, among other activities important for effective disaster management.

Figure 8.10. The Samos Department of the Hellenic Rescue Team Volunteer participated in various short-term response actions comprising (up) the distribution of humanitarian aid, gathered from various sources, including equipment for the homeless, long-term food and personal hygiene items, (in the middle) assistance in actions for the safe removal of religious items from temples severely affected by the earthquake and (down) assistance in organized evacuation actions from dangerous areas of towns and villages during the aftershock period.

8.3.9 *Issue of Government Gazette of the Hellenic Republic for delimiting the affected areas*

The regional units of Samos, Ikaria and Chios of the North Aegean Region were formally declared affected by the earthquake generated on October 30, 2020 with the Government Gazette of the Hellenic Republic issued on December 2, 2020. This Government Gazette formalizes form a legal viewpoint the state of emergency and comprises details about processes that are going to be applied for granting housing assistance for the restoration of the damage induced to buildings after the destructive earthquake. The task of the restoration of damage to buildings from the earthquake is undertaken by the General Directorate of Natural Disaster Recovery (DAEFK).

8.3.10 *Hazard mitigation in post-disaster recovery*

Numerous hazards are present during the initial earthquake response and subsequent recovery and clean-up efforts. The most common hazards the affected population and workers will likely encounter in the aftermath of an earthquake comprise partially collapsed or dangerously unstable buildings, exposed and energized electrical wiring, natural gas leaks resulting in potentially explosive environments, water system breaks and flooded areas, exposure to hazardous materials, exposure to airborne dusts including asbestos, lead, crystalline silica and mold, confined space work that may include insufficient oxygen and toxic environments, struck-by hazards from falling objects, sharp objects from glass and debris as well as other health and safety exposure risks specific to the response site among others. Immediate actions should be taken by qualified safety professionals and be completed prior to the public approaching or even moving in any response area presenting an adverse

exposure risk. Such actions were designed and implemented by response workers in several sites throughout the earthquake-affected Samos. These actions comprise mainly (Figure 8.11):

- Identification of damage induced to electricity, water supply and regional and municipal road networks by the earthquake and repair.
- Identification of hazards and placement of markings and protective barriers
- Identification of hazards related to partially collapsed and unstable buildings by DAEFK engineers and subsequent exclusion of the areas by the Hellenic Police.
- Organized evacuation of the population from several heavily affected parts of Samos, comprising Samos town and the communities of Vathy, Kokkari, Chora and Pyrgos and hosting of residents, who evacuated, in hotels and tourist facilities. The temporary staying in hotels is free for the residents (expenses were covered by competent ministries). This decision has been considered necessary in order to ensure the safety of residents from the risks of earthquake-induced phenomena including mainly landslides and rockfalls and from extensive collapse of buildings or parts of them during the aftershock period. The well-organized evacuation of population was designed and applied by the joint teams comprising staff of the Hellenic Police, the Disaster Management Special Units of the Hellenic Fire Service, the Hellenic Fire Service, the Municipality Departments of Civil Protection in Samos, the Hellenic Red Cross and volunteers.
- Activation of a memorandum of cooperation between the General Secretariat for Civil Protection and the Hellenic Authority of Geology and Mineral Exploration, with the aim of assessing the geodynamic phenomena and their impact to buildings and infrastructures and indicating protective measures for the mitigation of the adverse effects.

Figure 8.11. Actions for the mitigation of hazards the affected population and workers will likely encounter in the aftermath of the earthquake in Samos. Supporting of buildings, removing debris from roads and pavements, placement of markings and protective barriers to severely affected buildings in order to avoid approaching, demolition of unstable buildings dangerous for cars and passersby.

- Cleaning of regional, municipal and community roads and removal of debris accumulated on the roads after landslides and rockfalls.
- Cleaning of regional, municipal and community roads and removal of debris resulting from partial and total collapse of buildings.
- Demolition of unstable and dangerous buildings after the final consent of the owners as well as abandoned buildings.

8.3.11 *Community housing and support*

Immediately after the occurrence of the earthquake, citizens evacuated their homes due to building damage or fear of aftershocks and stayed in open air sites that they considered safe. During the first hours of the emergency response, the personnel of Samos municipalities in cooperation with the officers of local police departments collected information about the number of citizens who evacuated their homes and stayed outdoors. In cooperation with the Hellenic Armed Forces and volunteer teams, they assisted in the installation, organization and operation of emergency shelters in open air sites for the immediate housing of the temporary homeless. Due to the fact that the earthquakes occurred in the middle of the autumn season, the affected people also had to face bad weather conditions including low temperatures especially during the night.

More specifically, the Municipality of Eastern Samos set up temporary emergency shelters in the Kokkari, Vathy and Chora, while the Municipality of Western Samos in Karlovassi (Figure 8.12). Temporary emergency shelters were also set up in communities of the affected municipalities. Homeless and vulnerable people stayed in hotels. It is significant to mention that the setting up of the temporary emergency shelters was significantly supported by the Hellenic Armed Forces and volunteer teams. The temporary emergency shelters included military, emergency rapid deployment tents and sanitary and personal hygiene facilities. The Ministry of Migration and Asylum has also provided tents, sleeping bags, blankets and beds to affected residents, while the United Nations High Commissioner for Refugees sent 100 tents to the island.

Furthermore, the Municipalities set up semi-permanent container-type structures in order to be used for classrooms due to the severe damage to school facilities in Samos and as temporary houses for the homeless people (Figure 8.13). The Municipality of Eastern Samos used container-type structures for temporary school facilities. These container-type structures were transported from the Municipality of Mytilene (Regional unit of Lesvos, northern part of the North Aegean Region), which proved immediately, in practice, its support to the efforts made by the affected municipality, in order to find a solution for the housing of the school units that suffered serious damage. It is significant to highlight that Lesvos suffered a destructive Mw=6.3 earthquake on June 12, 2017 with considerable impact on the natural and built environment of Lesvos Island.

Figure 8.12: Temporary emergency shelters with military tents in the earthquake-affected island of Samos. The shelters were created in safe fields and open football stadiums.

Figure 8.13: Container-type structures used as temporary housing for the homeless, for classrooms and warehouses in the earthquake-affected Samos Island. They were transported to Samos after cooperation of the Municipalities of the Western and Eastern Samos with the Municipality of Mytilene (Lesvos Island, North Aegean Sea) and the Ministry of Migration and Asylum.

8.4. Planning and Preparedness for Earthquakes in Turkey

The planning and preparedness efforts before the earthquake both in Greece and Turkey are very similar. In Turkey, a national policy is also in place to mitigate earthquake impacts and enhance preparedness at national, regional, local, workplace and family levels. This includes pre-earthquake inspection of critical infrastructure (i.e., schools and public buildings) and prioritization for strengthening based on relative risk scoring.

The Disaster and Emergency Management Authority (AFAD), an institution working to prevent disasters and minimize disaster-related damages, plan and coordinate post-disaster response, and promote cooperation among various government agencies, has a very critical role in Turkey. Turkey ranks the third in the world in terms of earthquake-related casualties and eighth with regard to the total number of people affected. Every year, the country experiences at least one M≥5 earthquake – which renders the proper management and coordination of disasters absolutely crucial. Turkey's disaster policy dates back to the aftermath of the 1939 Erzincan earthquake, which claimed nearly 33.000 lives and left at least 100.000 injured. Two decades later, the Turkish Parliament adopted the Law on Precautions to be taken due to Disaster Affecting Public Life and Assistance to be Provided (No.7269) in order to fill the long-existing legal void. The legislative effort on disaster continued with the

1988 by-law on the Principles of the Organization and Planning of Emergency Assistance Regarding Disasters.

The 1999 Marmara earthquake, however, marked the turning point in the area of disaster management and coordination. This devastating disaster clearly demonstrated the need to reform disaster management and compelled the country to establish a single government institution to single-handedly coordinate and exercise legal authority in cases of disaster and emergencies. Consistent with high levels of seismic hazard, historically three sets of Earthquake Design Codes (1947, 1953, 1961, 1968, 1975, 1998, 2007, 2018-2019) were put in effect with the aim of reducing seismically-induced damages and losses on residential structures. Additionally, seismic design codes were also in effect specific to Ports, Harbors and Railways (2007-2008, 2020).

AFAD introduced a novel disaster management model which prioritizes Turkey's transition from crisis management to risk management – which came to be known as the Integrated Disaster Management System. AFAD currently has 81 provincial branches across Turkey in addition to 11 search and rescue units. Notwithstanding its position as the authority on disasters and emergencies, AFAD cooperates with a range of government institutions and non-governmental organizations depending on the nature and severity of individual cases.

A Preparedness for Disasters Annual Program was organized by AFAD. A new movement with #BePreparedforDisasters motto during the promotion meeting held at the Disaster and Emergency Management Authority (AFAD) headquarters was introduced. 6 important disaster management projects were declared: i) Declaration of the disaster preparation year, ii) Setting up AFAD volunteering system, iii) Establishment of AFAD Accreditation System, iv) Increasing practices and make them routine activities, v) Creating the Disaster Risk Reduction Platform of Turkey, vi) Implementing Disaster Risk Reduction System.

In addition to AFAD, AKUT is another organization which serves in entirely voluntary as a non-governmental organization in searching, assisting and rescuing all who require aid after disasters. With an organizational structure that allows it to react rapidly to a wide variety of emergency situations, AKUT has the ability to make quick decisions in the face of crisis. Today, AKUT is one of the top search and rescue organization in Turkey, with its large number of members and the broadest variety of specialized skills. With local branches across 32 provinces in Turkey as well as Istanbul on call 24/7, AKUT is always standing by, ready to accept the duty of serving people in need both inside and outside Turkey, to perform operations according to its mission, provide training, organize drills, cooperate with local and international institutions, and to share its experience and knowledge at home or abroad. Figure 8.14 presents views from rescue efforts coordinated by AFAD and AKUT groups.

https://www.ehaege.com/2020/11/akut-yerleskesi-izmir-depreminde-koordinasyon-ussu-oldu-h16265.html

https://www.karamanhabercisi.com/akut-eskisehir-ekibi-deprem-bolgesinde-gorevini-tamamladi-21883h.htm

Figure 8.14. Rescue teams working in Izmir-Bayrakli after the event

Turkish Red Crescent is the largest humanitarian organization in Turkey, which is an integral part of the International Red Cross and Red Crescent Movement. After the earthquake, the Turkish Red Crescent dispatched its disaster response teams to the region and has been meeting the nutrition need of the earthquake victims.

https://www.aa.com.tr/en/turkey/turkey-foreign-students-volunteer-to-aid-quake-victims/2053073

https://www.aa.com.tr/tr/turkiye/turk-kizilaydan-izmirdeki-depremzedelere-psikososyal-destek/2027858

https://www.ehaege.com/2020/11/kizilay-izmir-icin-acil-ihtiyac-listesini-belirledi-iste-o-ihtiyac-listesi-h16123.html

https://www.aktuelintermedya.com.tr/

Figure 8.15. Turkish Red Crescent services

Turkish Red Crescent has also been meeting the needs of the rescue teams and dispatching the equipment which might be required. Turkish Red Crescent dispatched its psychosocial support teams to Izmir to handle the psychological effects of the earthquake on the victims as well as delivering hygiene kits in the COVID-19 pandemic. The Turkish Red Crescent continue to prepare the needs assessment and capacities in the crisis management center set up within the Governorship in coordination with Disaster and Emergency Management Presidency of Turkey (AFAD). Figure 8.15 presents some of the services provided by Turkish Red Crescent.

As part of the training programs, AFAD and AKUT and many more other volunteered groups have organized seminars to educate and train school directors and teachers responsible for earthquake planning. Similarly, the practice in Greece, the teachers were trained to follow specific documented preparedness and evacuation procedures in case of an earthquake and to teach basic safety concepts to students, including drills. Additionally, Training Seminars targeting a wide range of age groups covering pre-school children to elderly (Figure 8.16).

www.afad.org.tr

https://beyazgazete.com/video/webtv/guncel-1/afad-dan-cocuklara-deprem-egitimi-ankara-528182.html

https://www.yeniakit.com.tr/haber/afaddan-deprem-haftasi-etkinlikleri-637291.html

https://indigodergisi.com/2016/06/cocuklar-icin-deprem-bilinci-arttirma-programi/

Figure 8.16. Awareness and educational efforts organized by AFAD

8.5. Emergency, Search, and Rescue Efforts in Turkey

Emergency response and recovery activities after a major natural disaster, such as the recent Samos (Aegean Sea) earthquake, relates to the resilience of the affected community. It depends on pre-disaster organizational preparedness, financial, equipment and trained manpower possibilities and their mobilization capacity. Within 25 years the Izmir Metropolitan Municipality (IMM) has concluded several major projects on earthquake research and mitigation. First, between 1996 and July 1999, the IMM, in collaboration with Boğaziçi University, Kandilli Observatory and Izmir Branch of Chamber of Civil Engineers have developed "Izmir Earthquake Master Plan" in conjunction with RADIUS (Risk Assessment Tools for Diagnosis of Urban Areas against Seismic Disasters) initiative of United Nations. Then between 2011 and 2013, the IMM achieved 10,000 buildings for two sub-municipalities, Balçova and Seferihisar, which are part of the Metropolitan Municipality. In the following sections the efforts performed before, during and after the event will be discussed.

8.5.1 Initial notification of the earthquakes, earthquake alerts and announcements

The Samos (Aegean Sea) earthquake caused damage mostly in localized regions of Izmir. Izmir is Turkey's third largest city with a population of over 4.5 million. The initial notification, alerts and announcements were coordinated by AFAD. Unfortunately, many people were impacted by this earthquake. People scenes running out into the streets in panic and fear were shared in media. There were damages to the structures and infrastructures in different parts of Izmir, especially in Bayrakli, Bornova and Karsiyaka region (Figure 8.17). Videos had been posted on social media and TV showing the collapse of a multi-story building (BBC, 2020). The structural performances were discussed in Chapter 7 and will not be presented herein.

Figure 8.17. Collapsed buildings in Izmir on Friday, Oct. 30, 2020.

8.5.2 Emergency Communication Services, Mobilization, and Search and Rescue Operations response of the state authorities

AFAD informed residents of earthquake-affected regions through media as well as with short message services send to their mobile phones to take self-protection measures. Additionally, immediately after the event, search and rescue teams have arrived at Izmir (Figure 8.18) began to operate and continued their efforts uninterruptedly for six days, officially ending on 4 November 2020 (Figure 8.18). Turkey's National Medical Rescue Team (UMKE), Fire Brigades from 41 cities across Turkey, and qualified search and rescue personnel from ministries and NGO's rushed to the city to assist with search and rescue operations in the affected region. Under the coordination of AFAD, search and rescue operations were conducted with a total of 8,712 personnel, in addition to 25 search and rescue dogs. AFAD Personnel have reached out to 11,000 people in the region (AFAD, 2020) for support.

(Ali Aksoyer/AP) https://www.washingtonpost.com/

https://www.trthaber.com/

Figure 8.18. Rescue teams arriving Izmir and operating on the debris of a collapsed building

Jointly with the Izmir Municipality Fire Department along with AFAD and AKUT search and rescue teams, the citizens also participated in the search and rescue operations immediately after the event. These immediate efforts were then led by professional teams, and the citizens were not let entering the rescue operation zones (Figure 8.19).

Local people trying to help immediately after the event

Professionals in service
https://www.trthaber.com/haber/gundem/575-artci-deprem-yasandi-527300.html

Figure 8.19. Rescue operations after the event

Several buildings totally collapsed while over about 700 were heavily damaged and hundreds of people were displaced as discussed in Chapter 7. During the efforts to locate for survivors search and rescue teams worked non-stop at great risk to themselves. Rescue teams saved 107 lives from the rubble (Figure 8.20). The last recovery of a live victim from rubble has occurred 91 hours after the event. A total of 117 people lost their lives and 1,035 people were injured (AFAD, 2020). The sadness and the grief of the Turkish public were notable during the rescue operations. The news outlets continuously broadcasted the rescue missions live. The whole nation followed the news closely during this period. When a 14-year-old girl and a 3-year-old girl were rescued after 55 and 65 hours respectively, the people cheered and celebrated (Figure 8.21).

https://www.pencerehaber.com/haber/3016/afaddan-02112020-1215-itibariyla-son-dakika-deprem-duyurusu.html

https://yeniyasamgazetesi2.com/izmirde-can-kaybi-58e-yukseldi-guncelleniyor/

https://penceretv.com/guncel/izmir-depreminin-arama-kurtarma-ekipleri-anlatti-13143h

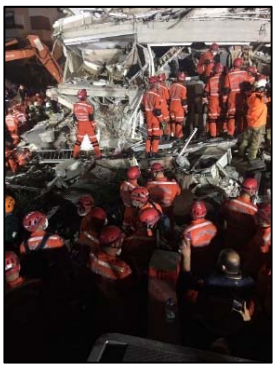

https://www.pencerehaber.com/haber/3010/afaddan-son-dakika-deprem-duyurusu.html

Figure 8.20. Continuing rescue efforts

Figure 8.21. 3-year-old girl rescued 65 hours after earthquake

https://www.aa.com.tr/en/turkey/turkey-3-year-old-girl-rescued-65-hours-after-quake/2027560

8.5.3 Psychosocial support for the affected population

As discussed earlier, feelings of loss, grief, anger, anxiety, fear and sadness can occur in the days after the event or even weeks or months after. Thus, the psychological support of those affected was necessary and very important. Such psychological support was provided by Ministry of Family, Labor and Social Services, Turkish Red Crescent, Izmir Municipality, and many more volunteered psycho-social experts. As AFAD-TAMP, its 453 personnel worked on the field in Izmir to provide people with the psychological support, to reduce their anxiety and overcome the trauma (AFAD, 2020). IMM also had 50 experts and social workers on site to give psychological support especially to children and women (Figure 8.22).

Hürriyet, 2020

BBC, 2020

https://www.dailysabah.com/

https://www.trthaber.com/haber/gundem/575-artci-deprem-yasandi-527300.html

Local residents, staying outdoors for fear of aftershocks, sit in a coffee shop in Izmir, Turkey, Oct. 31, 2020 (AP Photo) https://www.dailysabah.com/

A local resident, staying outdoors for fear of aftershocks, sits in the debris of a destroyed building as members of rescue services search for survivors in Izmir, Turkey, Saturday, Oct. 31, 2020 (AP Photo) https://www.dailysabah.com/

Figure 8.22. Psychological impacts on residents of Izmir

8.5.4 Donations and provision of essential emergency supplies

Izmir Metropolitan Municipality launched a campaign labeled “One Rent One Home,” and collected more than $5,500,000 to the victims of the quake so that they can rent flats. The good intensions of the many donors were not shared by all; apartment rents increased in the region following the earthquake.

AFAD activities during the disaster days can be summarized as follows:

- AFAD and the Turkish Red Crescent had also distributed 19,068 blankets, 11,050 beds, 11,548 sleeping bags, 2,657 kitchens and 1,023 heaters to people who are currently accommodating in these temporary shelters.
- As of 6 November 2020, food was provided to 464,395 people. Hot and cold drinks were provided to 135,034 people, 187,575 packaged food items and 161,879 bottles of water were provided to people who have been affected by the earthquake.
- A storage warehouse with a 11.500 m^2 capacity at Izmir Fair campus was used as a depot for all goods to be distributed to the people who had been affected by the disaster.
- The construction of a temporary shelter center was developed for around 7,000 people.
- In order to prevent the spread of the covid-19 virus in the disaster area, 52,360 face masks and 8,689 disinfectants were distributed to people who have been affected by the earthquake.
- In order to maintain hygiene in the disaster area, 210 hygiene sets, and 2,895 items of personal care material were delivered to people currently residing in camps. (AFAD Report)

Items distributed by the Social Services Department of Izmir Municipality included:

- Appliances such as refrigerators, washing machines etc. were distributed to 354 houses.
- 10,000 TL cash aid was given to 179 house owners with heavily damaged/destroyed structures.
- Cash aid of 5.000 TL was given to 629 tenants with medium damage.
- As of December 8, 2020, 4.643 civilian supporters transferred 20,510.000 TL in total to the families who were left homeless in the earthquake.
- 231 people opened their summerhouses for the people effected by disaster. After an examination, only 85 houses were considered to be safe for settlement. Eventually only 3 families began living in these houses.
- 60 families were settled in the Hilton Hotel.
- 160 families were settled in the apartments owned by IMM in Uzundere-İzmir. They will stay there for 1 year without paying any charge.

- IMM received a donation of 19,000,000 TL from 132 benefactors (corporate and personal) for different items such as household appliances, furniture, food, clothing and shelter.

In Aydın, a local municipality allocated nearly $6,000 from its budget to prepare aid boxes for what AFAD identified as the needs of victims. Similarly, a group of friends in Izmir gathered their savings and donated almost $600 to help survivors. Solidarity was the motto of the day.

8.5.5 Community housing and support

Immediately after the event, residents had to evacuate their homes due to building damage (Figure 8.23) or fear of aftershocks and stayed outdoors that they considered safe. Residents were advised not to return to their homes until official damage assessments of their buildings had been terminated. Under the coordination of AFAD and IMM, more than 3000 tents were set up for the families affected by the earthquake as a temporary solution. AFAD also established a "container city" of 500 temporary housing units (Figure 8.24).

Figure 8.23. Search and rescue teams on a collapsed building

Figure 8.24. Shelters set up by AFAD in Izmir

The earthquake deeply moved the Turkish people. The devastated public became more aware of the tragic realities of severe earthquakes. Days after a powerful tremor hit the country's Aegean region, people all around Turkey provided big support to the survivors of the earthquake. The Turkish government as well as some private institutions sent plentiful aid and relief packages to the region. Corporate donations funded lifelong education scholarships. Telecommunication companies, banks, associations, municipalities and various institutions launched campaigns to help victims (Figure 8.25).

Figure 8.25. Aid to citizens

Additionally, emergency relief supplies including water bottles, emergency food supplies, clothing, blankets, bedding, tents, heaters, were distributed to those in need. Portable shower, kitchen and toilet cabinets were assembled.

8.6. Earthquake Insurance Practices in Turkey

DASK (Turkish Catastrophe Insurance Pool) is an official compulsory earthquake insurance entity established in September 2000 following the devastating Kocaeli Earthquake in August 1999. It has a penetration rate of 60.9 % in Izmir, whereas the average rate is 56.6 % nationwide.

After the event there were more than 23,000 indemnity applications. To date, DASK paid about $25 million to policy holders following the investigation period.

8.7. Overall Impact on the City of Izmir

Apart from the turbulence created by the earthquake, the economic impact of the event on the local economy was limited. But observing in micro scale, one can determine the negative aspect of the disaster on local tradespeople, merchants, the owners of the shops, drugstores, groceries, etc. Fear, anxiety, anger, tension and despair were observed on the people during the catastrophic situation in Izmir. They were directly affected by the loss of their homes or loved ones. People were afraid of aftershocks and they did not always follow recommended safety protocols during the post-earthquake period. To emphasize the strength of the tremor, a retired BBC reporter who lives in Urla - Izmir was quoted as, "it was a really strong shaker almost enough to knock you off your feet. Running out of the house with my children was like a drunken wobble."

8.8. Lessons Learned in Izmir and Samos

The post-earthquake response and crisis management was satisfactory in both countries. Awareness, preparedness and the large-scale, pre-earthquake training, primarily for the case of Izmir Metropolitan area, minimized the time required to restore social and financial life in the affected region. On the other hand, damage and loss was in some cases disproportional to the intensity of earthquake ground motion for reasons discussed in Chapter 7. Therefore, extension of existing programs in both countries for pre-earthquake assessment, including rapid visual inspection of sub-standard buildings designed to previous versions of the respective national seismic code, risk-based prioritization to strengthen the residential building stock and seismic upgrade of public buildings and critical infrastructure is key for mitigating seismic losses in a future event. It is also necessary to enhance quality control and code enforcement in construction, particularly in low-income areas. The compulsory earthquake insurance system in Turkey (TCIP-Turkish Catastrophe Insurance Pool), with a penetration rate of 61% in Izmir, was very effective in speedy payment of the insured damages, which will significantly contribute to the post-earthquake recovery.

Finally, the authorities need to update emergency plans to address multiple hazards simultaneously. Post-earthquake crisis management during a global pandemic is such an example, clearly highlighting the importance of detailed scenario planning, data harvesting and retrieval protocols, multi-disciplinary and multi-authority training and possibly further cross-border collaboration for the benefit of the communities.

Acknowledgements

The authors are indebted to many volunteers and rescue workers, who have worked for the rescue operations immediate after the event. Many of the information in this chapter were attained from institutional reports, webpages and newspapers.

References

AFAD (2020), 30 October 2020 Izmir Turkey Earthquake Reports dated 6 November 2020 and December 2020, Turkey.

Anadolu Ajansı, Merve Berker (2020) "Turkey unites to help Izmir earthquake survivors; cities, companies, ordinary Turks, including children, extend helping hand to survivors", 07.11.2020.

İzmir Metropolitan Municipality (IMM) sources.

BBC news (2020), "Earthquake hits Greece and Turkey, bringing deaths and floods 30 October 2020", https://www.bbc.com/news/world-europe-54749509.

Hürriyet (2020) https://www.hurriyet.com.tr/gundem/son-dakika-korkutan-deprem-40487712

BBC Türkçe (2020), Engin Karaman, İzmir'de deprem: 'Çok deprem yaşadım, hiçbiri bu kadar uzun sürmemişti' , 30 Ekim 2020 https://www.bbc.com/turkce/haberler-turkiye-54752559

Earthquake Planning and Protection Organization (2016). Protection Guidelines - Aftershock Period. https://www.oasp.gr/sites/default/files/OASP-Aftershock%20period.pdf

Earthquake Planning and Protection Organization (2018). EPPO's Activities 2015-2017. Available at: https://www.oasp.gr/sites/default/files/DRASTIRIOTITES%2015-16-17.pdf (in Greek)

Earthquake Planning and Protection Organization (2020). Earthquake and Protection in Workplaces in case of Pandemic. Available at: https://www.oasp.gr/userfiles/Poster%20Pandemic%20ENG%20digital.pdf

Earthquake Planning and Protection Organization (2020). Instruction Manual for Planning and Organizing Earthquake Exercises. 40 p. Available at: https://www.oasp.gr/entypa (in Greek)

General Secretariat of Civil Protection (2020). Enceladus – General Plan for emergency response and immediate/short-term management of earthquakes effects. Available at: https://www.civilprotection.gr/sites/default/gscp_uploads/sxedio_egkelados.pdf

General Secretariat of Civil Protection (2020). Guidelines for Planning and Conducting Civil Protection Exercises. Available at: https://www.civilprotection.gr/sites/default/gscp_uploads/odigies_sxediasmou_askiseon_2020.pdf

Internet Links:

Earthquake Planning and Protection Organization: https://www.oasp.gr

General Secretariat of Civil Protection: http://www.civilprotection.gr

Institute of Engineering Seismology and Earthquake Engineering: http://www.itsak.gr

National Observatory of Athens – Geodynamic Institute: http://www.gein.noa.gr

Municipality of Eastern Samos: https://www.islandofsamos.gr/, https://el-gr.facebook.com/islandofsamos/

Municipality of Western Samos: http://dsamos.gr/welcome, https://www.facebook.com/dimosdytikissamou/